University of Strathclyde Glasgow

Department of Physics
Institute of Photonics
Technology and Innovation Centre
99 George Street
Glasgow G1 1RD

Development and exploitation of additive GaN micro-lenses for applications in quantum technology and micro-optics

Submitted by

Nils Kolja Freier, born Wessling

in order to fulfil the requirements for the degree of Doctor of Philosophy in Physics at the University of Strathclyde in Glasgow

Examiners:
Dr. Konstantinos Lagoudakis
Prof. Dr. Anthony Bennett

Supervisors:
Prof. Dr. Michael J. Strain
Prof. Dr. Martin D. Dawson

Sunday 15th October, 2023

Frontispiece

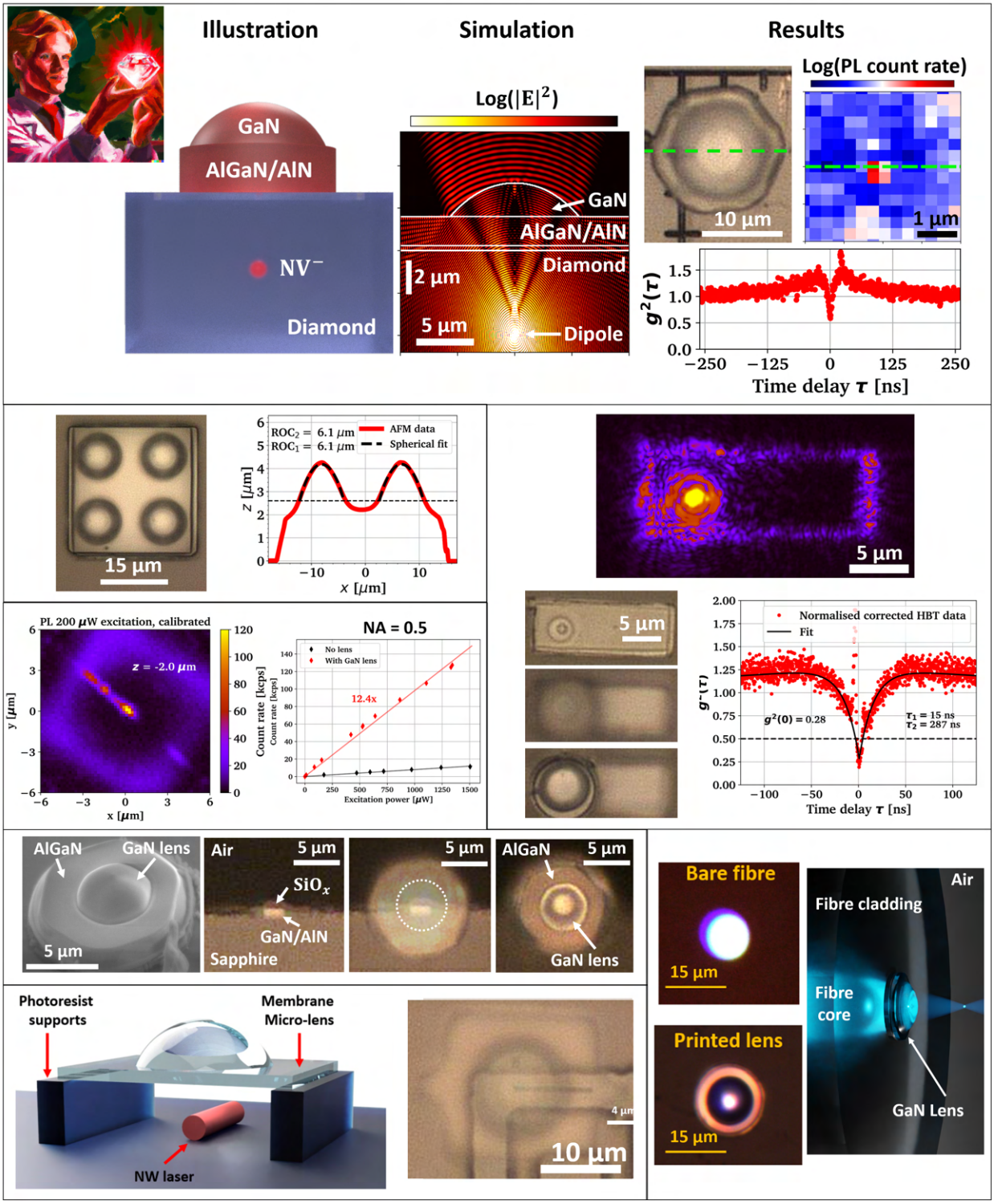

Abstract

Shaping the nanoworld has been a desire of physicists and engineers since Richard Feynman's famous talk 'Plenty of room at the bottom' in 1959. Its the gift of great visionaries to articulate and maybe even shape the Zeitgeist. Today, a vast set of tools is available to both explore and manipulate matter on the micro- and nanometer scale, offering an unprecedented and fruitful interaction between humans and base matter. This thesis is an incremental part of the overall effort to harness the unique properties of the micro- and nanocosmos for the benefit of humanity.

The field of visible optics is particularly interesting because in many atoms, molecules and materials valence electrons can couple to photons in the visible, near infra red or ultra violet parts of the electromagnetic spectrum. Light-matter interaction of this kind allows to connect remotely to the close-ranged interaction between those electrons and the atom core, other electron shells or maybe neighboring atoms in a crystal, because photons can travel vast distances in a relatively undisturbed state. A great example of harnessing electron-photon coupling in semiconductor crystals are UV-green light emitting gallium nitride diodes, which are widely used in lighting applications in our homes, cars and outdoor spaces today. Here electrons and holes are pumped into a heterogeneously doped semiconductor junction and recombine to produce light emission close to the band gap of the semiconductor material which is set by interaction of the atoms in the crystal. This blue and reasonably broad light emission is then coupled to phosphorescent material, converting some of the photons to lower wavelength and generating a white light impression after absorption by our retinas and signal processing performed by the neural tissue.

Gem stones have fascinated humans for millennia, probably due to their bright and radiant colours, their hardness and the potential to cut them into beautifully precise geometric shapes. Today we have learned that we can explain many of their properties with the quantum mechanical description of light-matter interaction. Particularly their bright colours can often be caused by well defined inclusions of foreign atoms into the crystal's lattice. These artificial atoms are well protected from the environment and as they are optically active we can use photons to investigate their inner state. At the heart of many today's efforts in the space of quantum technology like quantum sensing and quantum computing lays the idea to engineer the photon-gated interaction with the inner workings of matter to expand our ability to shape the world around us.

Micro-optical elements can facilitate efficient coupling between photons and fermionic matter. Commercialization has long reached this technology in many forms, for instance micro-lens arrays made of glass or polymer materials are used to focus light on the limited area of semiconductor light detectors, just to name one application. This thesis mainly explores the use of GaN micro-lenses for enhancing the interaction with a specific defect emitter in diamond - the nitrogen vacancy centre - in the context of transfer printing, an integration method that allows flexible combination of different preprocessed and highly specialized semiconductor devices. This method relies on careful preparation of free-standing semiconductor thin films on donor chips, and highly engineered surfaces on the receiving semiconductor chips. Transfer printing harnesses the visco-elastic properties of the polymer polydimethylsiloxane, which is used in a similar manner to carved potato stamps that children dip into ink to create colourful geometric shapes, relying on white light microscopy in combination with nanoscale precision 6-axis alignment stages.

The thesis summaries both the micro-fabrication process development of GaN micro-lenses in compar-

ison to monolithic diamond lenses as well as the integration of the GaN micro-lenses with planar and preprocessed diamond surfaces. In particular, the potential for enhanced light coupling efficiency to the nitrogen vacancy centre is investigated in three different scenarios: Laser written nitrogen vacancy centre doublets, NV clusters with $< 1\mu$m proximity to a planar diamond interface, as well as commercially available diamond probes for scanning magnetometer with a single NV centre. To properly assess the properties of the assembled micro-scale systems, a single-photon sensitive confocal microscope is built to probe the fluorescence response from nitrogen vacancy centres. In summary it is found by both simulations and experiments that transfer printed GaN micro-lenses can effectively enhance the light-matter coupling in most of the studied cases.

Other interesting and developing fields with much technological overlap are fibre optics, integrated photonic circuits and nano-scale laser sources. Printing of GaN micro-lenses on a fibre and integrated waveguide facet as well as in a 3D geometry above an optically pumped nanowire lasers is demonstrated and potential benefits are studied both experimentally and by finite difference time domain simulations. Here we mostly find marginal or limited utility for the targeted applications, but these efforts show effectively how flexible transfer printing can be as an integration method, pushing the forefront of this specialized knowledge space.

List of publications and events

Journal articles

Authors with * contributed equally to the respective article. The thesis' author's legal name today is 'Nils Kolja Freier' but is generally publishing as 'Nils Kolja Wessling'.

- **Fabrication and transfer printing based integration of free-standing GaN membrane micro-lenses onto semiconductor chips**, N. K. Wessling, S. Ghosh, B. Guilhabert, M. Kappers, A. M. Hinz, M. Toon, R. A. Oliver, M. D. Dawson, M. J. Strain, *Optical Materials Express* 12.12 (2022): 4606-4618.
- **Advanced transfer printing with in-situ optical monitoring for the integration of micron-scale devices**, B. Guilhabert*, S. P. Bommer*, N. K. Wessling*, D. Jevtics*, J. A. Smith, Z. Xia, S. Ghosh, M. Kappers, I. M. Watson, R. A. Oliver, M. D. Dawson, M. J. Strain, *EEE Journal of Selected Topics in Quantum Electronics* (2022).
- **Photonic integration of lithium niobate micro-ring resonators onto silicon nitride waveguide chips by transfer-printing**, Z. Li, J. A. Smith, M. Scullion, N. K. Wessling, L. J. McKnight, M. D. Dawson, M. J. Strain, *Optical Materials Express* 12.11 (2022): 4375-4383.
- **Additive GaN solid immersion lenses enhance light extraction efficiency from diamond colour centres**, X. Cheng*, N. K. Wessling*, S. Ghosh, R. A. Oliver, M. D. Dawson, J. Smith, P. Salter, M. J. Strain, *ACS Photonics* (2023).

Conference proceedings

- **Integration of single GaN micro-lenses with high index semiconductors by transfer printing**, N. K. Wessling, S. Ghosh, B. Guilhabert, M. Kappers, R. A. Oliver, M. D. Dawson, M. J. Strain, *CLEO: QELS_Fundamental Science*, Optica Publishing Group (2022).
- **Additive GaN micro-lenses for enhanced photon extraction efficiency from diamond color centers**, N. K. Wessling, X. Cheng, S. Ghosh, A. R. Kirkpatrick, M. J. Kappers, Y. N. D. Lekhai, G. W. Morley, R. A. Oliver, J. M. Smith, M. D. Dawson, P. S. Salter, and M. J. Strain, *DokDok 2023*, Friedrich-Schiller-Universität Jena (2023).

Scientific meetings, symposia and Fraunhofer events

- **Integration of single GaN micro-lenses with high index semiconductors by transfer printing**, N. K. Wessling, S. Ghosh, B. Guilhabert, M. Kappers, R. A. Oliver, M. D. Dawson, M. J. Strain, *UKNC Winter meeting* (2022).
- **Vertical integration of free-standing GaN micro-lenses with InP nanowire lasers by transfer printing**, N. K. Wessling, D. Jevtics, S. Ghosh, B. Guilhabert, M. Kappers, R. A. Oliver, M. D. Dawson, M. J. Strain, *Rank symposium on nanowire photonics* (2022).

- **Half-period review meeting for the QMag lighthouse project**, 15 min in person talk given, Freiburg (2022)
- **Fraunhofer conference 'Futuras in Res: The Quantum Breakthrough'**, including a workshop on quantum sensing, Berlin (2022)

Book chapters

- **'Quantum Technologies', chapter 'Fraunhofer CAP', section 4.2 'Micro-optic integration for scanning magnetometers'**, L. J. McKnight, C. H. Carson, A. Selyem, M. Warden, B. Ndagano, P. Schlosser, N. K. Wessling, M. J. Strain, H. T. Bookey, D. J. M. Stothard, M. D. Dawson, *Fraunhofer-Forschungsfokus* Fraunhofer Verlag (2022).

List of Abbreviations

AFM	Atomic force microscope
AOD	Acousto-optic deflector
AOM	Acousto-optic modulator
APD	Avalanche photo diode
BOE	Buffered oxide etch
BOX	Buffered oxide
CCD	Charged coupled device
CMOS	Complementary metal-oxide semiconductor
CMP	Chemical mechanical polishing
CVD	Chemical vapor deposition
DBR	Distributed Bragg reflector
DOI	Diamond on insulator
EC	Edge coupler
FDE	Finite difference eigenmode
FDTD	Finite difference time domain
FIB	Focused ion beam
FPGA	Field programmable gate array
FSM	Fast scanning mirror
FWHM	Full-width-half-maximum
GMR	Giant magneto resistance
HMDS	Hexamethyldisilazane
HPHT	High-pressure-high-temperature
IAF	Institute of applied solid state physics
IC	Integrated circuit
ICP-RIE, ICP	Inductively coupled plasma reactive ion etching
IPA	Isopropanol
IR	Infra red
KOH	Potassium hydroxide
LDOS	Local density of states
LED	Light emitting diode

MFM	Magnetic force microscopy
MLA	Micro-lens array
MMF	Multi mode fibre
MOCVD	Metalorganic chemical vapour deposition
MRFM	Magnetic resonance force microscopy
NV^-	Negatively charged nitrogen vacancy
PDMS	Polydimethylsiloxane
PECVD	Plasma enhanced chemical vapor deposition
PEB	Post exposure bake
PGMEA	Propylene glycol methyl ether acetate
PIC	Photonic integrated circuit
PML	Perfectly matched layers
PWB	Photonic wire bond
QPIC	Quantum photonic integrated circuit
Qubit	Quantum bit
RF	Radio frequency
RIE	Reactive ion etching
r.m.s.	Root-mean-squared
ROC	Radius of curvature
SC	Single crystalline
SCD	Single crystalline diamond
SEM	Scanning electron microscope
SiCOI	Silicon carbide on insulator
SIL	Solid immersion lens
SMF	Single mode fibre
SNR	Signal-to-noise ratio
SOI	Silicon on insulator
SPAD	Single photon avalanche diode
TaO	Tantalum pentoxide (Ta_2O_5)
UV	Ultra violet
VIS	Visible
ZPL	Zero phonon line

Contents

1 Introduction

We start this thesis with a quick overview of important physical concepts and relevant literature. More specific literature reviews are added in front of each section. Much of which is discussed in section 1.1 is based on references [1–3], while common text books on solid state physics [4] and books on optics [5, 6] have inspired the author.

1.1 Principles of light-matter interaction in semiconductors

The general formalism that to our today's knowledge describes the interaction of electrons and the atom core well is quantum mechanics, which allows the calculation of the gross energetic structure, as well as the probabilistic position and speed of single or multiple electrons in a wavefunction picture based on solving the Schrödinger equation. The Heisenberg uncertainty principle states that position and speed cannot be known at the same time with arbitrary precision and a similar relation applies to the life time and energy spread of an electronic transition. Light-matter interaction can generally be described in first or second quantization. First quantization is often called semi-classical, because it describes the atom with the theory of quantum mechanics leading to discrete energy levels of the electrons, while the light field is approximated by the classical theory summarized in the Maxwell equations. Second quantisation takes the particle-nature of light into account, which is surprisingly seldomly really necessary. Here, the light field is described by a quantum mechanical harmonic oscillator, with discrete energy levels corresponding to the number of photons, the light particle. This is the most accurate theoretical approach we have to describe light-matter interaction. In this thesis most experiments can be well described within the semi-classical approximation. Only when discussing single photon sources the quantized nature of light will become relevant.

The electronic levels of an atom inside a light field can be coupled by three main processes: Absorption, spontaneous emission and stimulated emission. The rate equations governing the relative strength of these processes is semi-classically described by the Einstein coefficients (weak-field limit) or Rabi oscillations (strong-field limit). In quantum electro dynamics spontaneous emission is often interpreted as stimulated emission in interaction with the vacuum background field (a consequence of the zero-point energy of the quantum harmonic oscillator) and retarded interactions with backscattered previously emitted photons.

Semiconductor crystals are a unique type of material whose energetic structure corresponds to that of an insulator, meaning that at temperatures close to absolute zero all electrons are localized to a few atoms and no electricity can flow if a voltage is applied at either end of the crystal. But as the temperature rises some electrons can randomly move away from their host atoms if they are receiving enough thermal energy, leaving 'holes' behind. Both electrons and holes can then conduct electricity (in a simple picture the hole can be filled by 'hopping' electrons, leading to the impression of a positive charge moving around). Depending on the necessary activation energy of the electrons, thermal activation might be very unlikely. Alternatively, an electromagnetic wave with large enough frequency can cause excitation of an electron, delivering precisely that or more than the necessary energy. Simply speaking this is why the conductivity of a semiconductor can rise if light is incident on the crystal, which is a primitive way to build a light detector.

1.1.1 Spin in quantum mechanics

A basic concept within quantum mechanics without direct classical counterpart is the spin, which similar to a charge on a circular trajectory creates a magnetic dipole moment. Matter can be divided into Bosons and Fermions based on whether their spin quantum number s is an integer or odd half-integer, respectively. This also relates to the symmetry of the wavefunction with Bosons exhibiting a symmetric and Fermions exhibiting an antisymmetric wavefunction. For example, electrons have $s = \frac{1}{2}$ and are classed as Fermions, while photons have $s = 1$ which assigns them the status of a Boson. Spins are extremely important in solid state physics as they can couple together, causing energetic splittings if for example an external magnetic field is applied. This Zeeman effect can be used to generate quantum mechanical two-level systems with variable energy spacing within the gross structure of the atom or solid, which can be useful for sensing outer magnetic fields or quantum based computation.

1.1.2 Energy bands in semiconductor crystals

A solid state crystal contains many closely spaced atoms in a periodic lattice. This lattice can have all kinds of structures with the closely packed diamond-cubic (two translated face-centre-cubic lattices) configuration being the most relevant for this thesis as it applies to both diamond and Si, compare Fig. 1.1 a). The c-plane GaN discussed in this work has a hexagonal wurtzite structure.
The interatomic separation in a crystal is so low, that the wavefunctions of neighbouring electrons overlap, which forces the electrons to form continuous energy bands due to the Pauli exclusion principle, compare Fig. 1.1 b). The activation energy previously discussed with regard to semiconductor crystals refers to the energy difference - the band gap E_g - between the valence and conduction band with electrons in the valance bands being localized to their respective atoms and electrons in the conduction band moving around in a weakly bonded electron gas, compare Fig. 1.1 c).

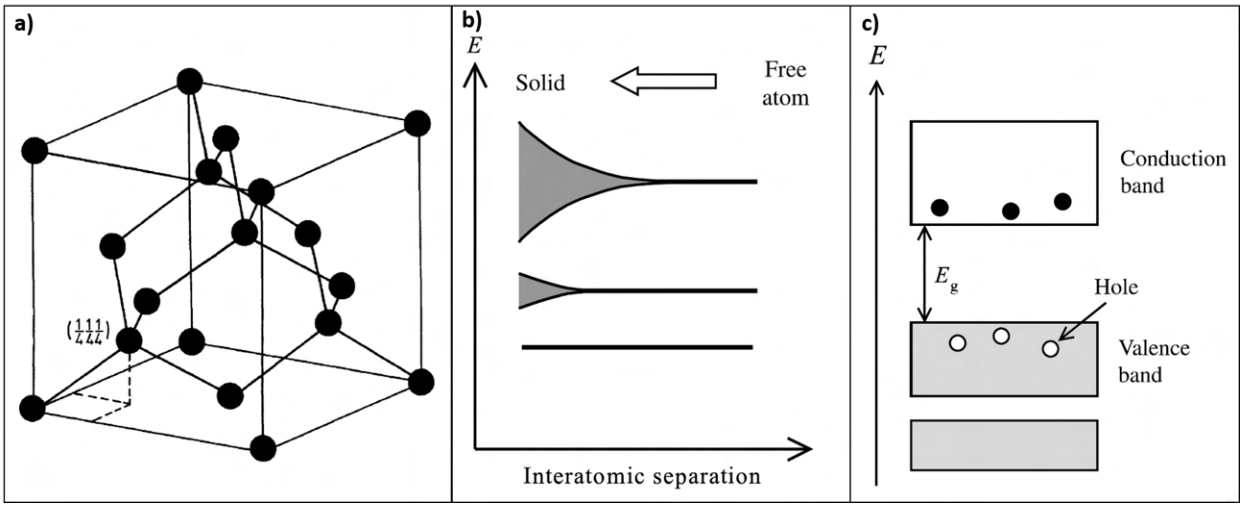

Figure 1.1: a) Illustration of the diamond cubic crystal structure adapted from [4], b) generic energy structure of atoms as function of interatomic spacing, c) simple bandstructure of a semiconductor with band gap E_g in real space, both b) and c) are adopted from [1].

1.1.3 Refraction, reflection and diffraction as described by classical electrodynamics

As this thesis discusses mostly semiconductor lenses with a diameter on the micrometer scale, reflection, refraction and diffraction are important concepts, which together describe the performance of the investigated lenses very well. In classical electrodynamics Maxwell's equations can be extended to include linear light-matter interaction by slightly modifying the vacuum equations, leading to the concept of the refractive index n caused by elastic oscillations between electrons and atom cores driven by the incoming electromagnetic wave. The refractive index describes a retardation effect, causing the speed of light c in vacuum to reduce to $\frac{c}{n}$ in a linear and transparent medium (a dielectric), such as a wide band gap semiconductor at optical frequencies (e.g. diamond and GaN).
As a consequence of the reduction of speed of light and Fermat's principle minimizing the optical path length, a plane wave in vacuum that has direction and frequency is described by a wave vector $\vec{k}$ hitting a planar dielectric interface under an angle of incidence is redirected upon transmission in a slightly different direction. This effect is called refraction and is heavily exploited in optics, for example when focusing light into a narrow spot with a lens. Due to the impedance mismatch ($n_1 \neq n_2$) between vacuum and the dielectric, part of the electromagnetic wave is reflected by flipping the wave vector component $k_\perp$ orthogonal to the interface.
We will also make use of the ray optics approximation (mostly for illustration), which describes the propagation direction of an electromagnetic wave in space with rays (with the density representing the light intensity) that are partially reflected and transmitted when hitting a dielectric interface. Snell's law and the Fresnel coefficients govern the quantitive description of these effects and can easily be derived from Maxwell's equations in matter.
Diffraction effects become relevant if for example a light beam passes an aperture which diameter is comparable to the wavelength λ of the light or if a laser beam is tightly focused into a spot with a diameter similar to the size of λ. Diffraction is caused by the wave nature of light. A plane wave can for example be described as the coherent super position of spherical waves, which if interrupted by an aperture spread out into all directions, leading to diffraction patterns caused by wavefront interference, which cannot be explained in the ray optics approximation. In the Fraunhofer approximation the far field intensity pattern of an aperture illuminated by an electromagnetic wave is described by the squared modulus of the Fourier transformation of the spatial field distribution in the aperture. As a consequence an aberration free lens, which would focus parallel incoming rays into exactly one point, still achieves only a diffraction limited spot size, which is determined both by the diameter of the illuminated part of the lens and the wavelength of the light. The Fourier transformation of a circular aperture with homogeneous illumination is called an Airy disk pattern, roughly the circular 2D equivalent to a sinc function.
In this thesis light propagation is modelled by solving Maxwell's equations on a regularly spaced grid in 3D in the time domain. The theoretical frame work is described in more detail just before it is applied for the first time. Importantly, these simulations take refraction, reflection and diffraction effects into account to properly describe the micro-lens performance.

1.1.4 Atomic defects: Energy levels within the bandgap

Atomic impurities have been crucial for harvesting the properties of semiconductor crystals for advanced technology such as integrated circuits. If we use the group IV semiconductor silicon as an example, and if either boron (group III, *p*-type doping) or phosphor (group V, *n*-type doping) are added in small concentrations to the otherwise perfectly crystalline material, these foreign atoms appear as electron acceptor or donor respectively, meaning that much less energy than E_g is needed to add/remove an electron to/from the impurity atom, respectively. Therefore they create additional discrete energy levels within the band gap of the semiconductor (but often close to the edge of the valence/conduction band). This allows for example to switch the material's conductivity by applying electric fields, which is used in MOSFET transistor architectures.
Fundamentally speaking a defect breaks the periodicity of the crystal and lifts the Pauli exclusion principle that led to the formation of the energy bands of the pure crystal in the first place. Because the outer electrons contributing to the defect experience a different environment than the typical valance electrons in the lattice, these discrete energy levels similar to molecular orbitals can reside within the band gap (but they dont have to). Viewing solid state defects as molecules is a semi-empirical model rather than a first principle's approach which starts from the Schrödinger equation or the calculation of the Eigenvalues of the Hamiltonian (ab initio) [7].
In this thesis we are going discuss an atomic defect - the nitrogen vacancy centre - within single crystalline diamond with discrete electronic levels inside the large band gap of this semiconductor. This means that the ground and excited state of the NV^- centre are coupled by an optical frequency much smaller than the minimum frequency necessary to cause absorption in diamond, which allows us to view this defect as an artificial atom that is sitting well protected inside the diamond lattice. The semiconductor GaN is mostly approximated as an insulator with high refractive index, because we are making use of its dielectric properties only. Still, impurities in GaN cause fluorescence emission in the same spectral region as the nitrogen vacancy centre [8], which is relevant for the applications we are going to discuss.

1.1.5 Photon statistics of single photon sources

Single optically active emitters such as the nitrogen vacancy centre can only emit a photon at a time, which allows us to look into the quantum mechanical properties of light. To investigate the temporal distribution of the photons in such a beam (photon statistic) makes it necessary to consider a second quantization approach, meaning the particle nature of light is considered in the picture of a quantized harmonic oscillator as shown in Fig. 1.2 a).
A classical monochromatic electromagnetic plane wave is described in quantum electrodynamics by a coherent state, representing light with a Poissonian photon number statistic, meaning that the average photon number $\overline{n}$ within the measurement interval[1] is proportional to the classical light intensity. The intensity noise is then defined by the standard deviation of the photon number given by $\Delta n = \sqrt{\overline{n}}$. Therefore the relative fluctuations of the intensity of coherent light fall with rising average photon number according to

$$\frac{\Delta n}{\overline{n}} = \frac{\sqrt{\overline{n}}}{\overline{n}} = \frac{1}{\sqrt{\overline{n}}} \tag{1.1}$$

[1] unfortunately n is also used for the real part of the refractive index

Typically, laser light produces an approximately coherent photon stream with random time spacing between photons.

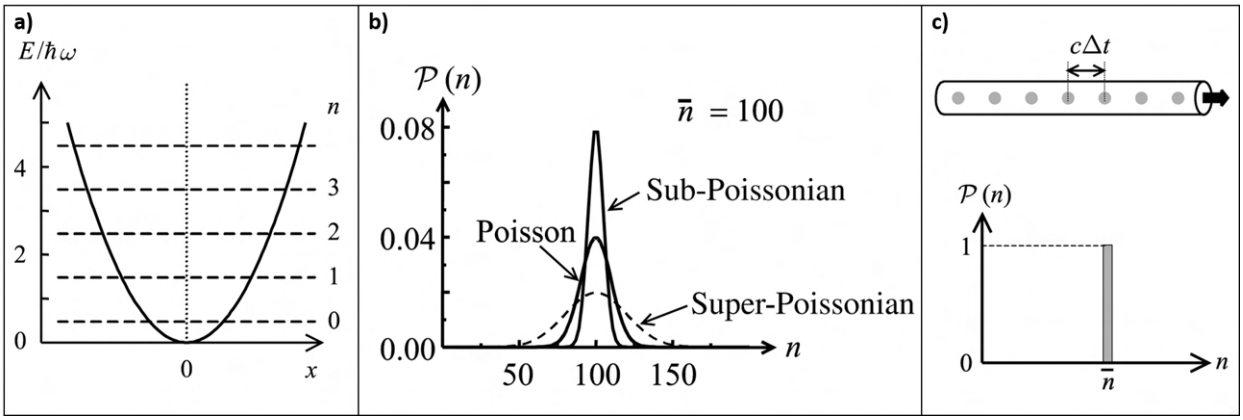

Figure 1.2: a) Energy levels of the quantized harmonic oscillator, b) exemplary photon statistics for an average photon number $\bar{n} = 100$ in the measured time interval, c) the photon statistic of a photon number state with equal time spacing Δt between photons. All graphics are adopted from [1].

A light source emitting photons with a narrower photon number distribution is called sub-Poissonian, while a broader photon number distribution indicates super-Poissonian light, compare Fig. 1.2 b). Classical descriptions of electromagnetic waves always lead to light with either Poissonian or super-Poissonian intensity noise and cannot explain the occurrence of sub-Poissonian noise levels. Therefore, Poissonian levels of intensity noise are often referred to as the shot-noise limit. Photon number states, which statistic is depicted in Fig. 1.2 c), correspond to a stream of perfectly spaced single photons, which lead to a constant average photon number within the integration time without any fluctuations.
A common measurement technique to identify the photon statistic of light sources is based on the work of Hanbury Brown and Twiss (HBT), who split the light emitted from a star on two separate detectors and then correlated the measured intensities as function of detector distance to estimate the diameter of the star based on the spatial coherence of the light hitting the two detectors. This intensity interferometry can also be applied to photons with an experimental arrangement similar to what is shown in Fig. 1.3 a). The degree of second order temporal coherence of the photon stream can here be accessed by calculating the second order autocorrelation function

$$g^{(2)}(\tau) = \frac{\langle n_1(t) n_2(t+\tau) \rangle}{\langle n_1(t) \rangle \langle n_2(t+\tau) \rangle} \tag{1.2}$$

with the measured photon counts $n_i(t)$ on the respective detector at time t with the brackets indicating a time average. The second order autocorrelation function is the intensity equivalent to the first order autocorrelation function which corresponds to electrical field strength and indicates interference fringe visibility. The photon stream can then be classified as

- **bunched** if $g^{(2)}(0) > 1$,
- **coherent** if $g^{(2)}(0) = 1$,
- **anti-bunched** if $g^{(2)}(0) < 1$.

and in most cases anti-bunched light also exhibits sub-Poissonian photon statistics. Anti-bunching is similarly a clear indication of the quantum nature of light and cannot be explained classically. The

illustration in Fig. 1.3 b) shows exemplary photon streams that fall into the three different classes. Light from a single spectral line of an arc discharge lamp is an example for chaotic light that creates photon bunching.

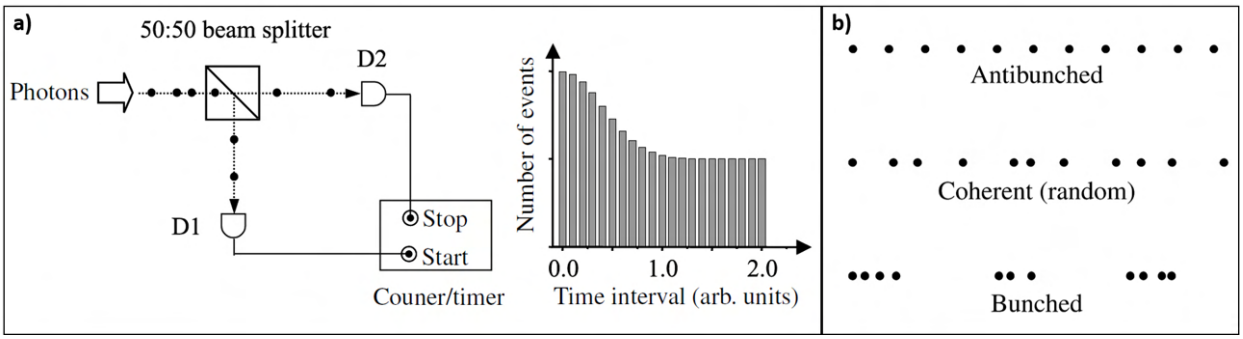

Figure 1.3: a) Generic HBT experiment for photons with single photon detectors D1 and D2 with the time difference between start and stop pulses being recorded, the graph on the right shows a one sided histogram of a potential measurement result corresponding to bunched light, b) illustration of the time intervals between photons in a photon stream and the resulting classification of the light. All graphs are adopted from [1].

For a photon number state with constant $\overline{n}$, we expect

$$g^{(2)}(0) = \frac{\overline{n}(\overline{n}-1)}{\overline{n}^2} \tag{1.3}$$

Therefore ideal single photon sources with $\overline{n} = 1$ are expected to deliver $g^{(2)}(0) = 0$, while for example two closely spaced single photon sources that are probed simultaneously leading to $\overline{n} = 2$ are expected to show $g^{(2)}(0) = 0.5$.

The discussion of isolated atomic defects in semiconductor host crystals naturally leads to the concept of single photon sources. Quantum mechanics allows us to describe the defect in a superposition of ground and excited state, but if it decays it can only emit one photon at a time before it can be excited again to cause the next emission. Therefore, a single nitrogen vacancy centre in diamond is an optically excitable single photon emitter, which has sub-Poissonian photon statistics.

1.2 Synthetic single crystalline diamond

Single crystalline diamond (SCD) is an extremely promising material for the semiconductor industry. SCD is exceptionally hard [9] and its inertness enables its application in harsh chemical environments, but both properties make diamond fabrication challenging [10]. Diamond's large band gap (5.5 eV), huge break down field strength ($\approx$ 13 MV/cm) as well as high electron and hole mobility ($\approx$ 4000 cm^2/V·s) might allow its use in highly efficient high-power switching electronics, an industrial space currently occupied by GaN and SiC [11]. SCD shows the largest heat conduction of all known bulk materials at room temperature (2000-3500 W/m·K) [11, 12], which enables its use as heat spreader in various applications such as optically pumped solid state disk lasers [13]. Additionally, it has an extremely wide transparency window from $\lambda = 250 - 2500$ nm in the UV to Mid-IR and above $\lambda = 7\,\mu$m [14–16].

But diamond is also highly interesting for quantum technological applications. A variety of optically active artificial atoms are energetically shielded within the large band gap and can act as quantum bits

or allow quantum sensing of temperature or magnetic fields via optical control of collective electron spins [17–22]. Even though diamond's χ^3 non-linear coefficient is relatively low and χ^2 is absent because of the inversion symmetry of the lattice, diamond is suitable for non-linear applications: The large band gap damps two-photon absorption even at visible (VIS) wavelengths and the high heat conduction and low thermo-optic coefficients allow high power throughput to enable for example four-wave mixing [23].

Natural and synthetic diamond can be classified based on the type and density of impurities as well as the quality of the diamond lattice. Though for defect centre applications specific impurities are even desired, those usually compromise the optical properties of diamond [24]. The purest quality grade of single crystalline diamond (SCD) is type IIa with an nitrogen impurity level below 5 ppb [16]. Nitrogen impurities can create undesirable noise due to unpaired electron spins [7]. Many different methods exist to generate desired defect centres within such a high quality host crystal [25–32], which we will review in more detail in the beginning of Chapter 4.

Today, several methods are known to produce SCD synthetically. To create nanometer-seized diamonds (nanodiamonds) graphite discharge methods can be used, while high-pressure-high-temperature (HPHT) and chemical vapor deposition (CVD) methods produce macroscopic diamond samples [17, 33–39]. CVD relies on high quality seed diamonds as growth substrate, often delivered by the HPHT method. The production of SCD on other single crystalline materials than diamond (heteroepitaxial growth) is challenging and has so far inhibited the production of large diamond wafers with high quality (typical commercially available CVD grown SCD substrates are 2x2 or 4x4 mm in size [16]), even though some promising results for SCD wafer growth on iridium have been demonstrated [38]. Synthetic diamond production is generally difficult because graphite is the thermodynamically favourable solid phase of carbon, which is a barrier that needs to be overcome by the growth technique [34]. After growth SCDs substrates usually need to be carefully separated from their growth substrate and polished, which contributes significantly to their cost [40].

Thin polycrystalline diamond films can easily be grown on various substrates via CVD methods, but the polycrystalline nature makes the implantation of high quality colour centres for advanced quantum technology schemes impossible [17].

1.2.1 The nitrogen vacancy centre

Over 400 defect centres have been discovered in diamond, but the negatively charged nitrogen vacancy has been investigated most intensively, partly due to its bright room temperature emission and long electron spin decoherence time T_2 (see references [7, 41, 42] for review articles). There is much written and ongoing research on the rich physics of this defect and we are going to cover some of the basic properties only [7]. More recently, the silicon and tin vacancy centres are attracting growing attention due desirable properties such as their weaker coupling to the diamond lattice leading to a larger proportion of emission into the zero-phonon line and their lower sensitivity to electronic charges in the environment [7, 10, 17, 43–48].

The negatively charged nitrogen vacancy (NV^-) centre in diamond consists of a substitutional nitrogen atom next to a vacancy in the diamond lattice, as shown schematically in Fig. 1.4 a). In a simple molecular model, two unpaired electrons from the nitrogen, three unpaired electrons from the carbon atoms around the vacancy and one additional electron captured from the environment (typically a

nitrogen donor) contribute to its energetic structure, filling the sp^3 hybridized molecular orbitals of the dangling bonds of the nitrogen and carbon atoms around the vacancy [7, 41, 49]. As shown in Fig. 1.4 b), four of these six electrons are assumed to occupy discrete energy states within the diamond band gap, of which two electrons remain unpaired, forming a spin triplet. The excited state of the NV^- centre refers to the additional promotion of an electron from the a_1 to an e state, allowing us to view the negatively charged nitrogen vacancy centre as an artificial ion inside the diamond matrix. The resulting photoluminescence spectrum of a single NV^- centre under non-resonant green laser excitation at room temperature is shown in Fig. 1.4 c). The photoluminescence emission is bright due to nearly pure radiative relaxation ($> 85\%$ [48]) of the lower $m_s = 0$ transition (see Fig. 1.5 a) and stable without blinking or bleaching [7]. The fluorescence life time of the excited electronic states of the NV^- in bulk SCD is reported in the range between 8-15 ns [7, 49], but depends on the host crystal quality, temperature, the dielectric environment (nanodiamonds, cavities, waveguides) as well as the exact spin sub-levels involved [7]. Typical optical experiments with single NV's average over many excitation and spontaneous emission cycles to for example built up the life time statistic of the emitter. The captured charge of the NV^- centre can be lost by photo excitation, leading to cycling charge state conversions into the neutral nitrogen vacancy centre NV^0 (with associated loss of optical read out of its spin state) under resonant and non-resonant laser excitation [7, 49, 50].

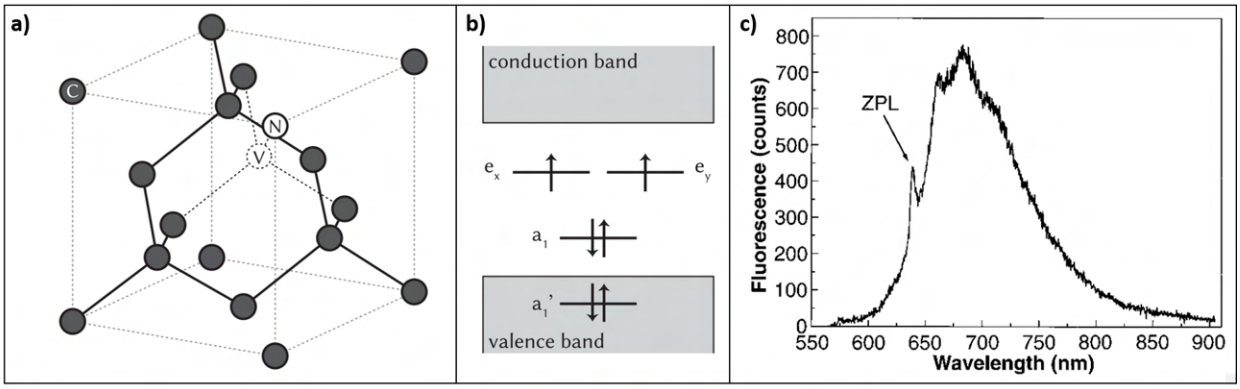

Figure 1.4: a) Schematic of the NV^- centre inside the diamond crystal lattice, adapted from [49], b) ground state electronic structure of the NV^- centre with respect to the diamond band gap, adapted from [7, 49], c) photoluminescence emission spectrum of a single NV^- centre excited at $\lambda = 514$ nm, adapted from [51].

The NV^- centre can be approximately described as a dipole emitter. It can be excited with laser light that is linearly polarized perpendicular to its $< 111 >$ symmetry axis due to its two similarly strong orthogonal dipole moments in the (111) plane, so that its optical photoluminescence emission is approximately unpolarized if viewed along the [111] direction [52]. But if the degeneracy of the spin triplet sub-levels is lifted by the application of an external magnetic field, one might selectively prepare the NV^- in a state where it emits orthogonal circularly polarized photons depending on the spin state after relaxation, entangling the electronic spin state with the emitted photon polarization [53]. The photoluminescence peak at $\lambda = 637$ nm marks the emission without coupling to the diamond lattice and is called the zero phonon line (ZPL). An undesirable property of the NV^- centre is its small emission efficiency of ca. 3-4% into the ZPL (Debye-Waller factor) [48], which makes embedding NV centres into cavities an attractive research field. A well designed optical cavity can enhance the emission efficiency at 637 nm via the Purcell effect [10].

1.2.2 Optically detected magnetic resonance

The previously discussed ground state $^3A_2$ (as shown in Fig. 1.4 b) of the NV$^-$ is believed to be split in $m_s = 0$ and $m_s = \pm 1$ states (m_s being the secondary spin quantum number) by spin-spin interactions on the order of $D_{gs} = 12\,\mu$eV [7]. The detailed energy structure is shown in Fig. 1.5 a). The thermal energy at room temperature is on the order of $K_B T = 25$ meV with the Boltzmann constant K_B, indicating that both levels are equally occupied under ambient conditions.
Under low-power, non-resonant laser excitation (green arrow), the relaxation to the excited state ^3E (black arrow) maintains m_s. In addition the $m_s = \pm 1$ states seem to contribute less to the fluorescence signal (red arrows) because a non-radiative decay channel via the metastable singlet state ending in the $m_s = 0$ ground state is available (black dotted arrows). Therefore the quantum state of the NV$^-$ can be polarized in the $m_s = 0$ ground state after a few cycles of excitation with state preparation fidelity approximately ranging from 46-96 %, for example depending on temperature and crystal strain [7, 49]. If a population transfer between the $m_s = 0$ and $m_s = \pm 1$ triplet states is then driven by a coherent resonant microwave field, Rabi oscillations can be observed in the time-dependent fluorescence emission spectrum [54]. If the microwave frequency is swept, the steady-state fluorescence can be collected and the count rate shows a dip at the resonant microwave frequency due to a partial population transfer to the less emissive $m_s = \pm 1$ states. The result of such a measurement is called an optically detected magnetic resonance (ODMR) spectrum and is shown in Fig. 1.5 b). It corresponds to an optical readout of the spin state of the defect centre. The full bandwidth of the NV$^-$ emission can be exploited in ODMR experiments and remarkably an ODMR dip can be measured even at room temperature [55].

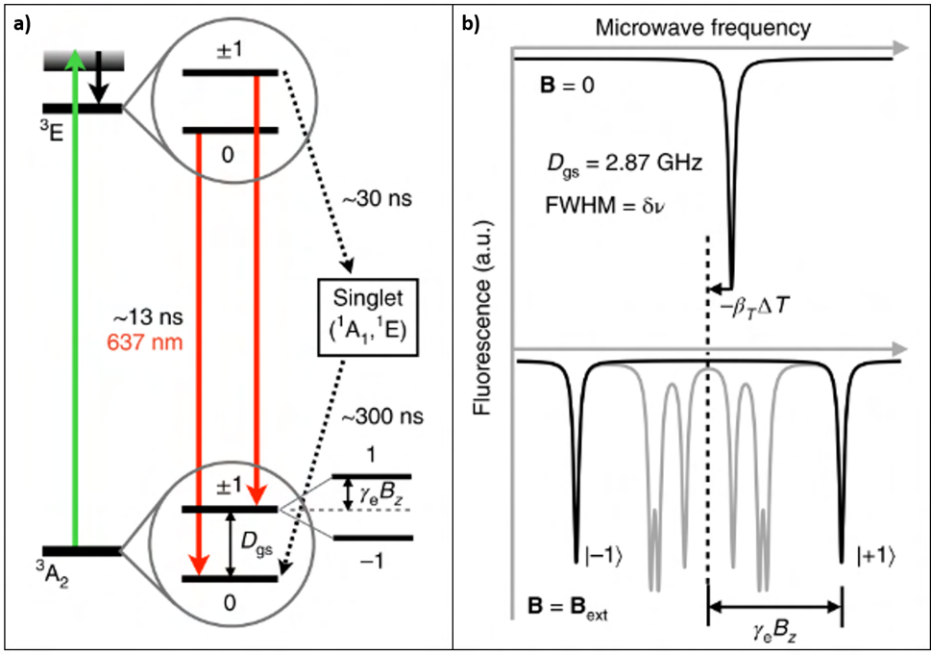

Figure 1.5: Energy scheme of the NV$^-$ centre's unpaired electrons and ODMR spectrum as function of the applied microwave field frequency, taken from [18]. The gray dips in the bottom graph of b) relate to additional lines that appear if an ensemble of NV centres with all four possible crystal orientations is exposed to the same external field in the z direction.

These properties can be utilized to measure an outer magnetic field B and/or the local temperature T. The position of dip in the ODMR spectrum depends on T, while the $m_s = +1$ and $m_s = -1$ spin

states can be Zeeman-split by the magnetic field component B_z along the NV$^-$ axis. This leads to a splitting of the dip in the ODMR spectrum, which is via the gyromagnetic ratio $\gamma_e \approx 2.8$MHz/G directly proportional to B_z, compare the bottom graph of Fig. 1.5 b).
Alternatively, the splitting of the $m_s = \pm 1$ states in an external magnetic field can be exploited to define a 2-level quantum system with the ground state $|0\rangle$ assigned to $m_s = 0$ and the excited state $|1\rangle$ assigned to either $m_s = +1$ or $m_s = -1$, forming a quantum bit, a qubit [49]. In such cases the NV$^-$ is usually cryogenically cooled to reduce thermal excitation of the ground state spin, enhance the emission into the ZPL and access the hyperfine splitting to address nearby nuclear spins [7]. Strain and electric fields can effect the electronic structure of the NV$^-$ excited state at cryogenic temperatures, which can be exploited for sensing or tuning of the NV$^-$ emission spectrum [7, 21, 49].
The time period in which a polarized spin quantum state maintains a coherent phase is measured by a Spin-Hahn echo and is called the spin-coherence time T_2 [54]. In the picture of the Bloch sphere, which is often used to describe quantum mechanical 2-level systems, T_2 corresponds to a transverse relaxiation of the Bloch vector from the surface of the sphere to its z-axis, indicating a loss of phase coherence reducing a linear superposition state to a statistical mixture that does not exhibit wave function interference [1]. Depending on the quality of the diamond lattice, impurity concentration, nuclear isotope composition and distance of the NV$^-$ to the diamond surface, T_2 for single NV$^-$ centres can be on the order of up to 2 ms even at room temperature [7, 55]. These long times are partially a consequence of the isolation the NVs electronic states from the bulk states due to the large band gap of diamond (5.5 eV). With pulsed decoupling schemes T_2 can be enhanced to hundreds of ms [56, 57]. Coupling to external nuclear or electron spins are suspected to be the main contributions for decoherence of single NV$^-$ centres (for example the nuclear spin bath from ^{13}C isotopes), but this spin-spin interaction allows to utilize the NV$^-$ centre as a 'photon gate' interacting with surrounding nuclear spins for quantum computation and networking applications [48, 49].
T_2 is a figure of merit for the detection limit in AC and DC magnetic field measurements, which is defined by the noise floor. A higher T_2 allows longer signal accumulation for AC magnetic field sensing [58]. But a long T_2 similarly indicates high crystal quality and therefore a low ODMR linewidth, which increases the ability to detect small absolute DC fields.

1.3 Limited photon extraction efficiency from diamond colour centres

Both DC and AC magnetic field sensitivity as well as the correct and fast readout of the NV$^-$ spin or coupled nuclear spin states rely on the signal-to-noise ratio of the fluorescence signal collected from the NV$^-$ centre [7, 48]. But extracting fluorescent light from diamond is challenging due to its high refractive index ($n_{\lambda=637\,\mathrm{nm}} = 2.38$) [59]. Photons emitted from inside a diamond substrate can easily be trapped due to total internal reflection with the critical angle as low as $\Theta_{\mathrm{TIR}} = 25°$. Additionally, a significant amount of photons that can leave the diamond substrate are refracted to such high angles that even a microscope objective with high numerical aperture placed above the diamond sample cannot collect them. For example an air objective with NA = 0.95 has a collection half angle of only 72°.

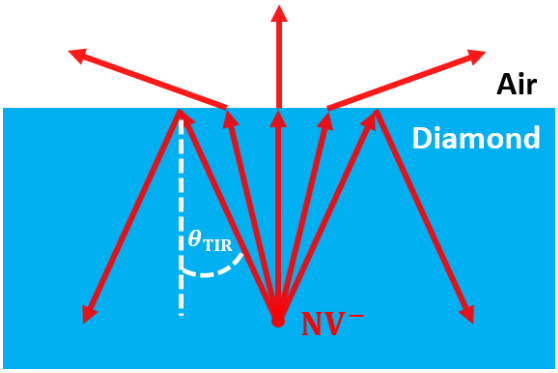

Figure 1.6: Schematic illustrating the refraction at a planar diamond-air interface for photons emitted from a single NV^- centre. The critical angle of total internal reflection $\Theta_{TIR} = 25°$ is given at the zero-phonon line of the NV^- emission spectrum.

The main motivation behind the work in this thesis is to fabricate micron-scale solid immersion lenses with similar refractive index to diamond and its deterministic alignment to NV^- centres in order to enhance the photon extraction efficiency for quantum applications. We will discuss quantum computing [60–62] and quantum networking [48, 63, 64] approaches with the NV^- in more detail in the beginning of Chapter 4 and explore the state of the art of NV^- scanning magnetometry in Sec. 4.3.
In the following we will quickly review general miniaturization trends in optics to set the context for the micro-lens development in this work.

1.4 The drive towards miniaturization in optics

Miniaturization of electronics has led to the enormous computational and networking capability that we use today to manipulate and share information. The reduction of transistor size and parallel fabrication techniques described by the CMOS industry standards have enabled the exponential growth of transistor density on integrated circuits (IC) since the 1970s [65]. Their impact on technology and society was and is tremendous, as it has changed how we cooperate with modern computers for our own benefit in nearly all aspects of our life.
Photons offer both less interaction with the environment (no charge) and easier multiplexing schemes (wavelength) than electrons, which is why they are employed in remote communication schemes, such as radio, other wireless and infra red fibre optics networks, just to name a few. Fibre optic cables are a good example of using miniaturized optics for data transfer which is powering the world wide web today. We will discuss both photonic integrated circuits (PICs), which work on the same principle as fibre optic cables but are smaller in size and micro optical components, which might be classified as typical free space optics components with reduced dimensions. Both fields follow the drive to offer the same capability as bulky free-space optics systems on smaller space with less material cost and energy consumption.

1.4.1 Photonic integrated circuits

Even though optical chips are not the main focus of this thesis we will briefly introduce them due to their immense significance in the field of optics and micro-optics today. Interest in integrated optics has become vast in recent years with specialized chip foundries growing all over the globe [66] to

produce the specific semiconductor layer-stacks needed for this type of technology [67]. In principle, photonic integrated circuits (PICs) follow the trends of the integrated circuit (IC) industry, leveraging micro-fabrication techniques such as photolithography and plasma dry etching to create complex optical arrangements by targeted material removal and deposition in a layer-by-layer fashion with minimal device foot print [68]. In most cases light of optical wavelength (UV to Mid-IR) is guided in the 2D plane of the chip surface by dielectric waveguides, which exhibit a higher refractive index than their environment, allowing the trapping of light by total internal reflection [67, 69]. This waveguiding concept was suggested as early as 1969 [70, 71] and is similar to how optical fibres operate. Some of the drawings from the original proposal are shown in Fig. 1.7, with b) illustrating two closely spaced parallel waveguides that allow light transfer by coupling of the evanescent tail of the propagating electromagnetic wave.

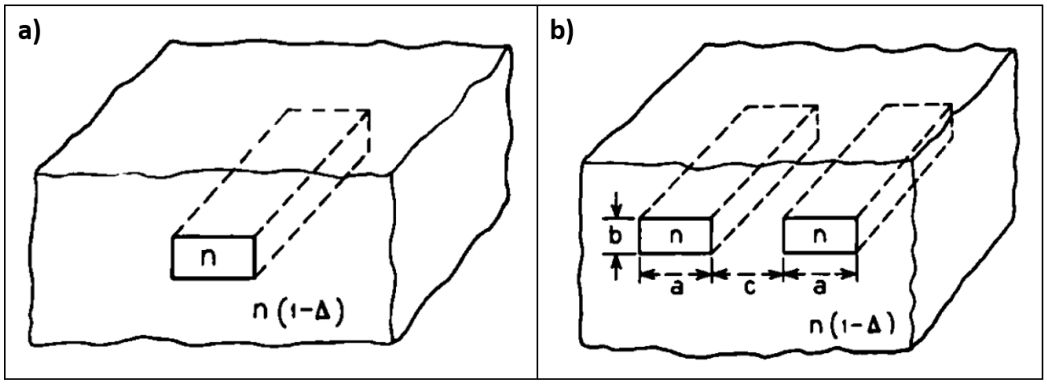

Figure 1.7: Original proposal for the geometry of a buried (a) dielectric waveguide and (b) directional coupler with the refractive index n of the waveguide core indicated and $\Delta > 0$, adapted from [71]. Today PIC waveguides are often etched into a high-index dielectric thin film on top of a low-index buffer with successive overgrowth of a low-index cladding layer.

The use of photons instead of electrons gives rise to many interesting properties such as immense band width for information transfer [68] and miniaturization of the rich fields of quantum [66] and non-linear optics [72, 73], the latter benefiting from the high field concentration within the waveguides [72]. Some applications at different stages of development include

- Optical communication e.g. based on Si and InP transceivers (main application today) [69, 74–76],
- Bio-chemical sensing based on refractive index change or on-chip spectroscopy [68, 72, 77–80],
- Optical implementation of neural networks [68, 80],
- Quantum computation, cryptography and sensing [10, 18, 68, 73, 81–87].

A generic PIC might contain integrated elements such as light sources, waveguides, couplers, resonators, phase and amplitude modulators, mixers and filters, amplifiers and attenuators, other non-linear elements and detectors [74]. It can be fixed and application specific or programmable like a field programmable gate array (FPGA)) in electronics [68]. It can work with light in the classical or the quantum regime, the latter chips are sometimes described as quantum PICs (qPICs) [66]. Regardless of application the PIC can be expected to be co-packed or fully integrated with control and read-out electronics with varying degree of achieved integration.
The following figures Fig. 1.8 and 1.9 give an example from the field of programmable qPICs. In Fig. 1.8

a generic schematic of a universal unitary 2x2 optical coupler is shown that controls the coupling ratio κ and the phase $\Delta\phi$ of the fields b_i in the output waveguides with respect to the fields in the input waveguides a_i. As shown in Fig. 1.9 a mesh of such couplers could be used as programmable linear weights in a quantum optical neural network, ideally with fully integrated single photon sources and detectors as well as a non-linear interaction region. On a hardware basis such a programmable coupler (red box in Fig. 1.8) could be realized by two static 2x2 multimode interference couplers forming a Mach-Zehnder interferometer with a variable phase shifter in one arm to control the coupling ratio of the outputs. The use of such specialized hardware might allow to harness the full power of artificial intelligence by minimizing the power consumption at higher data throughput rates [68].

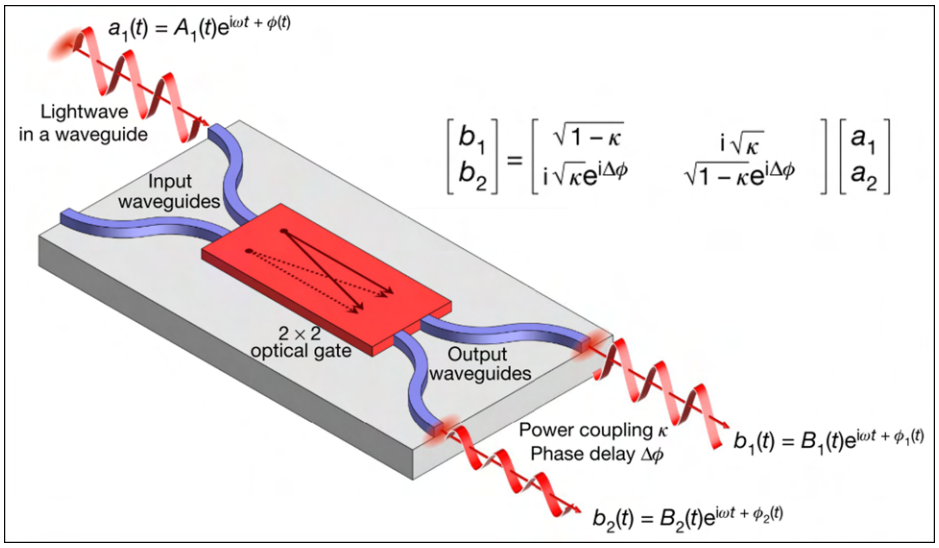

Figure 1.8: a) Schematic of a universal 2x2 optical gate for programmable photonic integrated circuits, adapted from [68].

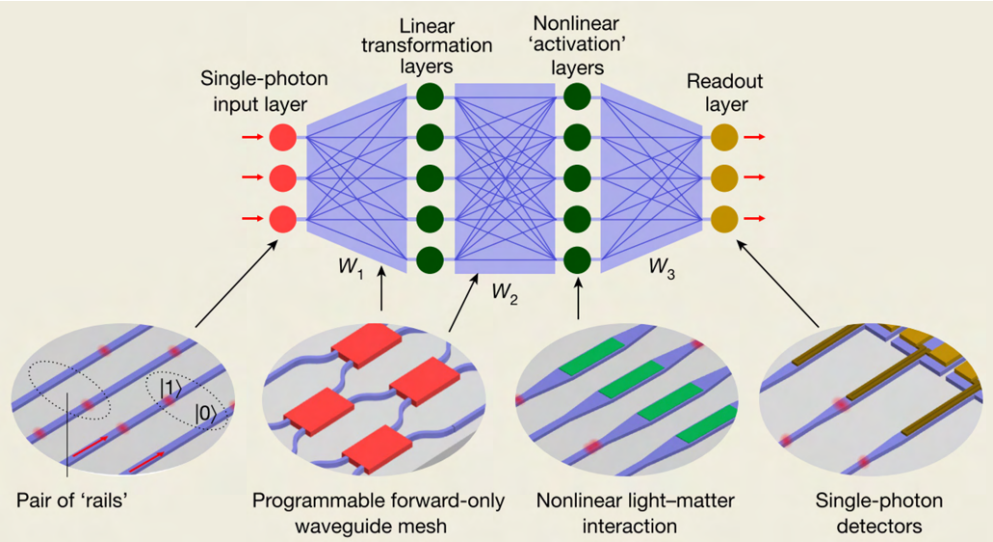

Figure 1.9: Application example: Potential layout of a quantum optical neural network and the integrated photonic components necessary for its implementation, adapted from [68].

The material platforms for integrated photonics are in constant development and the interested reader is referred to the following review articles that give a broad overview over the different properties and

applications [66, 67, 73, 74, 78, 80, 88–92]. The main layer of 2D PIC usually consists of a high-index semiconductor thin film bonded or grown on a several μm-thick insulating buffer layer such as SiO_2 often called BOX (Buffered oxide) on top of a mm-thick carrier wafer for mechanical handling. For this thesis the most relevant platforms are silicon on insulator with a standard of 220 nm Si thin film bonded on SiO_2 (NIR), as well as GaN on sapphire, tantalum pentoxide on insulator and polymer waveguides on insulator (VIS and NIR).

To date no isolated material platform seems to allow the efficient implementation of all passive and active PIC components due to demanding properties such as low propagation loss for passive elements such as waveguides and ring resonators, a direct semiconductor band gap for efficient light emission and detection or simply the existence of high-quality defect centres as sources of quantum light [66, 67, 69, 74]. Therefore the field of hybrid and heterogeneous integration is of crucial relevance to create highly functional PICs, meaning the assembly and packaging of multiple semiconductor materials and devices on the surface of the same base-chip. Wafer or die bonding, selective area epitaxy and μm-precise pick-and-place methods such as transfer printing can be used to achieve this [74, 91]. A simple example shortly discussed in this thesis is the incorporation of diamond nitrogen vacancy centres as bright single photon sources into a low-loss waveguide platform such as SiN or AlN on insulator [93, 94].

1.4.2 Micro optics

We are quickly going to review some typical and state of the art micro-optical elements to give a short introduction into the topic. Further details will be given in front of the relevant chapters. This subsection is partly based on [95].

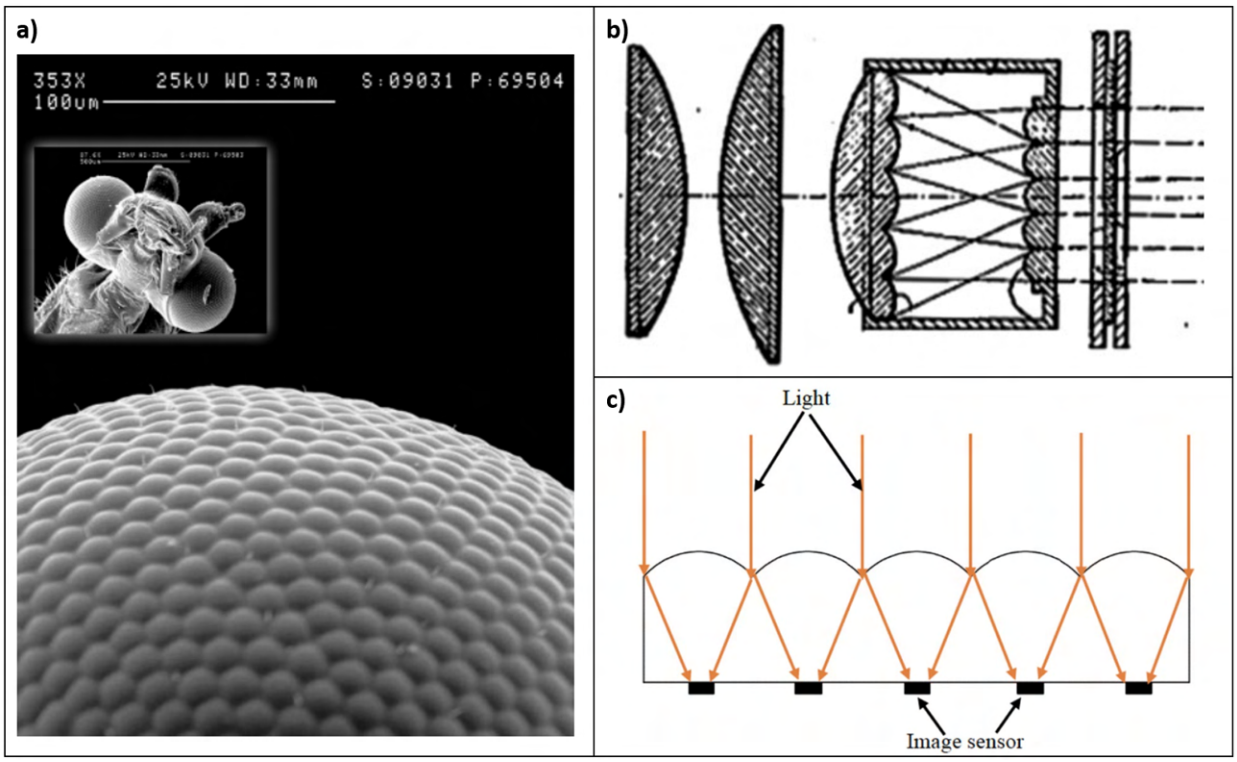

Figure 1.10: a) SEM image of the superposition compound eye of the moth 'Ephestia Kuehniella', adapted from [96], b) Köhler integrator for illuminating a film with uniform light adapted from [97], c) a regular micro-lens array increasing the fill factor of a solid state light sensor, adapted from [98].

Micron-sized optical elements are important components for the coupling of light between free-space and matter based systems. In nature, we find that evolution has designed insects to use micro-lens arrays (MLA) in their compound eyes to increase their field of view while keeping the eye volume small (compare Fig. 1.10 a), while dielectric micro-lens arrays are commercially available and commonly used as illumination homogenizers [99] (compare Fig. 1.10 b) or to focus light onto the photon-sensitive regions of charged coupled device (CCD) [100] and complementary metal-oxide semiconductor (CMOS) [101] photo-detector arrays, in order to increase quantum efficiency (Fig. 1.10 c). Micro-optics are also used to improve the efficiency of light extraction from light emitting diodes (LEDs) [102] and μ-LEDs [103], for coupling to integrated photonic circuits (PICs) [104] as well as for improving pump and collection efficiency between microscope systems and semiconductor based solid state quantum emitters [105]. This latter application is particularly challenging due to the often random positioning of the quantum emitters and the large refractive index of the host material that leads to total internal reflection at the interface between the material and free-space and which is the focus of this thesis.

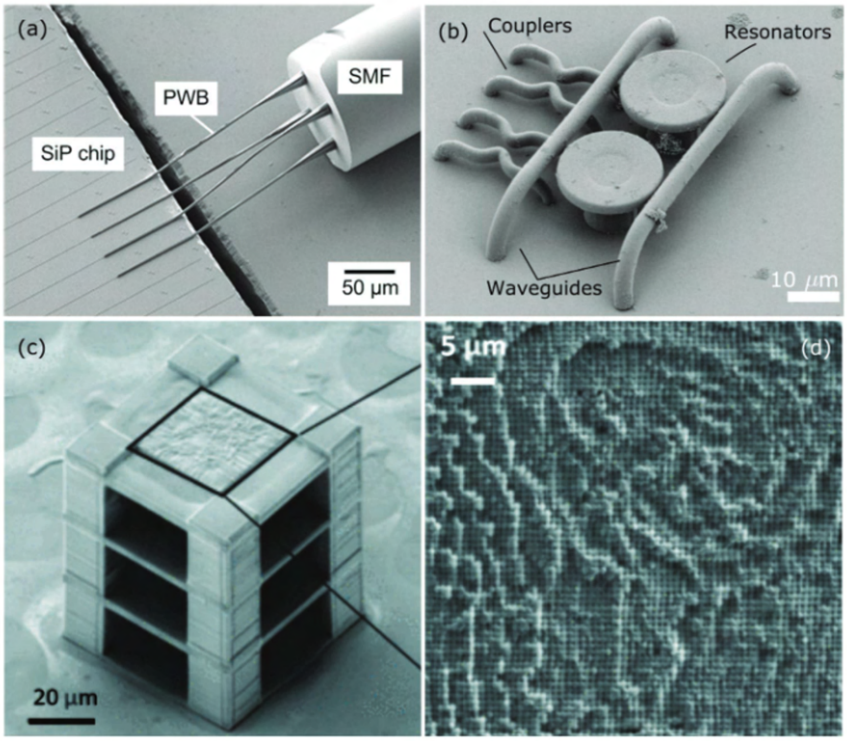

Figure 1.11: SEM images of multiple micro-optical elements fabricated by two photon polymerization, a) photonic wire bonds (PWB) adiabatically connecting waveguide edge couplers and multiple single mode cores of a fibre, b) dielectric waveguides, couplers and resonators in a 3D architecture, c)/d) full view and close up of stacks of fixed arrays of pixels with varying material thickness used as passive diffractive layers in a multilayer artificial network, adapted from [122].

There are two main routes to fabrication of micro-optics on semiconductor substrates, either additive materials patterning on the substrate, or direct fabrication of optical surfaces into the material itself. There are a number of techniques available for the fabrication of additive components, including imprint lithography [106–108], two-photon polymerization [109–111], thermal reflow [108, 112–114], and inkjet printing [108, 115, 116]. Structures formed by these methods are commonly used as the final optical element themselves, but may also be used as a mask for a dry-etch shape transfer into the

semiconductor.

Two photon polymerization (TPP) is a particularly flexible method and can be used to fabricate complex micro-optical systems such as multi-lens beam expanders on fibre tips [109] as well as vertical and end-fire couplers to PICs [110, 111]. Some examples of micro-optical elements fabricated with this powerful technique are shown in Fig. 1.13 b), 1.11 and 1.12. But the relatively low refractive index n of TPP resins ($n = 1.5 - 1.6$ [117] compared with common semiconductor materials $n > 2.0$ [59, 118–121]) limits the achievable numerical aperture (NA) of the polymer lenses. Furthermore, polymeric materials are susceptible to catastrophic optical damage at watt-level optical power [110].

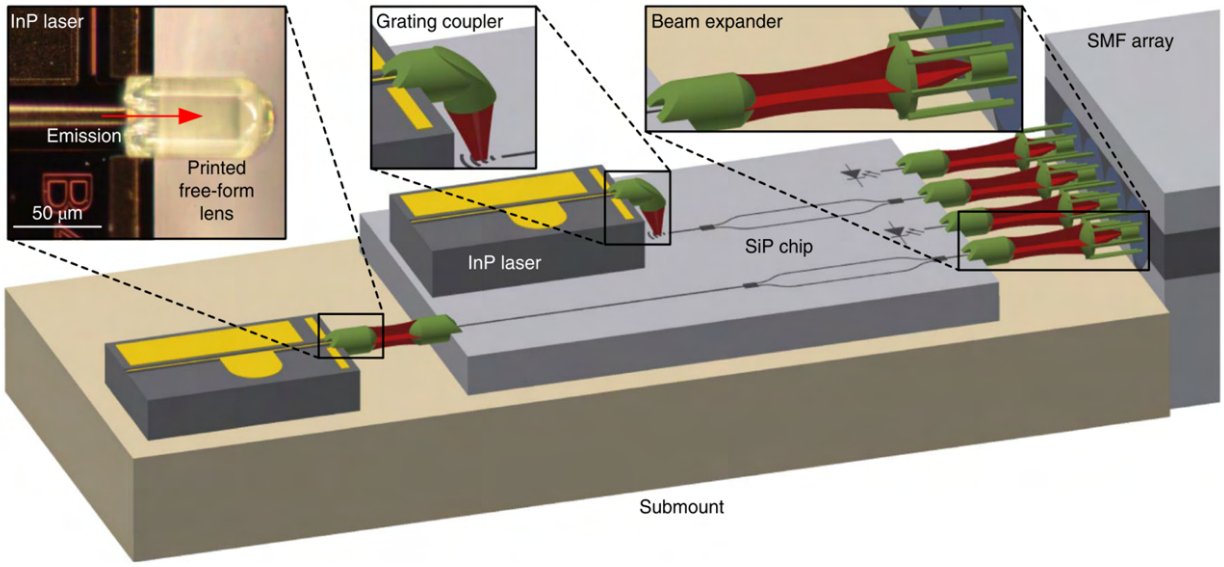

Figure 1.12: Schematic showing how 3D polymer micro-lenses can be used to assist in the co-packing of photonic integrated circuits for PIC-to-PIC coupling in end-fire (left) and vertical geometry (middle) as well as fibre-to-PIC coupling (right), adapted from [133]. The inset in the top left shows a fabricated lens.

Alternatively, solid immersion lenses (SIL) can be formed directly into semiconductor materials by focused ion-beam milling [123–125] (compare Fig. 1.13 a), laser-micromachining [126, 127], photoresist reflow in combination with reactive ion etching [128, 129], dual masking [130] and diamond turning [131, 132]. These methods make use of the high refractive index of the material itself to avoid refractive index contrast at interface layers, produce high NA performance and are robust to optical damage. Individual lenses can be fabricated with high positional accuracy but require either serial, time consuming processing [124, 125], or in the case of diamond substrates are limited in the form factors that can be achieved due to the mask-to-semiconductor etch selectivity [128, 129].

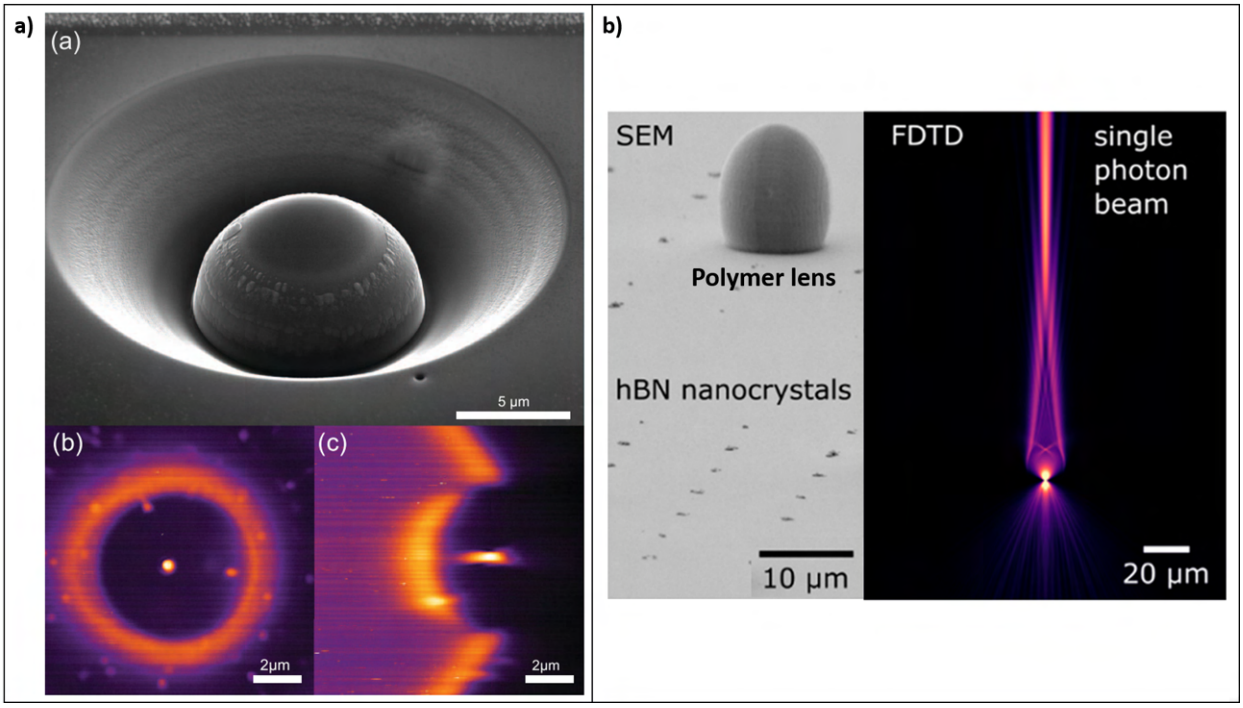

Figure 1.13: a) Monolithic diamond solid immersion lens fabricated around a single NV^- emitter by focused ion beam milling with confocal photoluminescence scans in the horizontal and vertical planes through the emitter, adapted from [125], b) elliptical 3D polymer micro-lens fabricated by two-photon polymerization on top of hexagonal boron nitride (hBN) nanorystals containing single photon emitters emitting at visible wavelength and the corresponding cross section through a simulation showing the formation of a narrow emission cone in the far field above the lens, adapted from [134].

1.5 Growth of single crystalline GaN thin films on Si

We are interested in GaN thin films because of two reasons: First, the refractive index of GaN and diamond are nearly matched around the emission wavelength of the diamond NV^- centre ($n_{\mathrm{GaN},\lambda=637\,\mathrm{nm}} = 2.38$) [120] and GaN also has a wide transparency window spanning from 365 nm to 7 μm [135], which makes both materials nearly equivalent in terms of dielectric properties. This similarly holds for the AlN/AlGaN buffer layer necessary for successful thin film growth, which will be discussed in more detail later on.

Secondly, we want to fabricate micro-lenses that can be transferred to a foreign substrate, which means that we need to suspend the lenses after fabrication. The following Fig. 1.14 illustrates the process flow that was developed in this thesis to process GaN thin films into semiconductor lens platelets. The assembly above nitrogen vacancy centres aims to break the influence of total internal reflection similar to the monolithic diamond hemisphere shown in Fig. 1.13 a). We precisely move to GaN because it offers much higher etch selectivity compared to diamond lenses if parallel plasma etching of resist micro-lenses is used for the fabrication. We therefore aim to offer a scalable alternative to focused ion beam milling of monolithic diamond lenses.

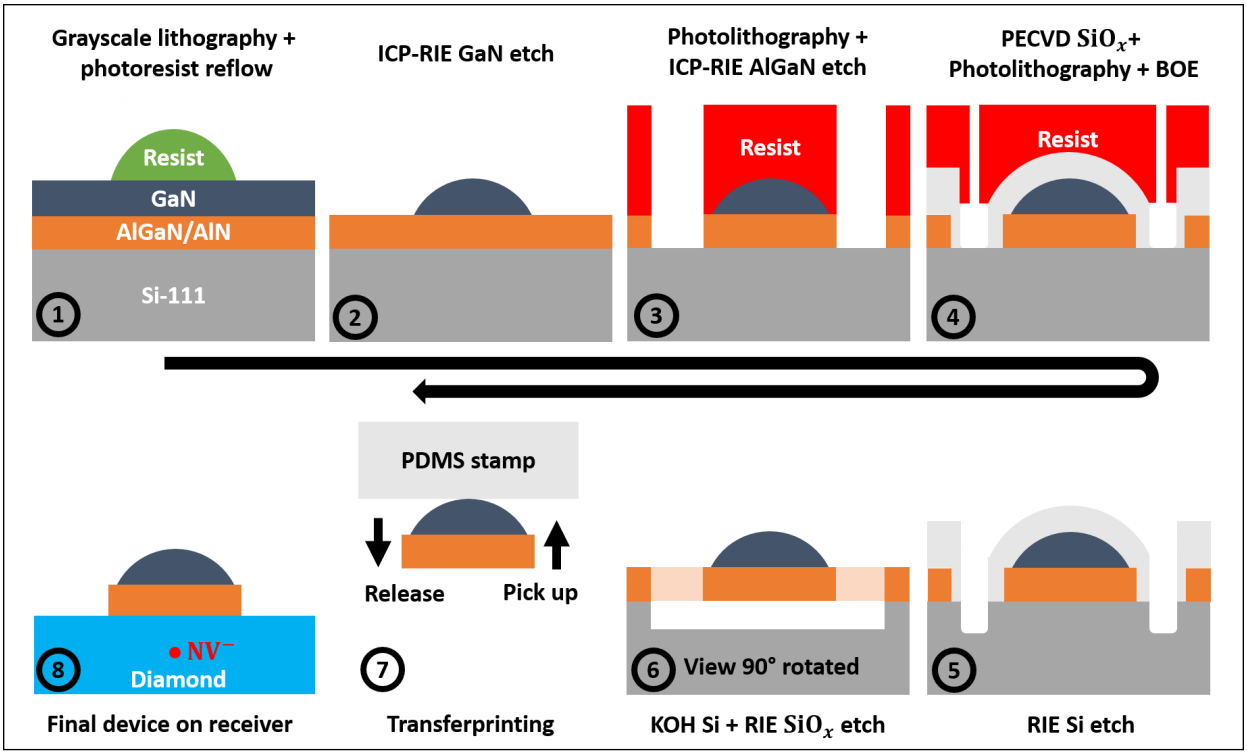

Figure 1.14: Full process flow developed in this work that allows to integrate GaN thin-film micro-lenses with the diamond NV^- centre. Details will be given in the following chapters.

There exist other techniques for device suspension from bulk crystals instead from thin films, such as angled Faraday cage [136–139] or quasi-isotropic inductively coupled plasma (ICP) dry etching [140–146]. But the first unfortunately generates a triangular bottom profile, while the second requires specialized ICP machines with very high plasma densities for efficient chemical etching without bias. Semiconductor thin films on the other hand offer the use of chemical wet and gas etching for suspension of large device areas with a flat bottom profile, as indicated in Fig. 1.14 [91, 147–150]. Crystalline GaN thin films can be grown by metal-organic chemical vapour deposition (MOCVD, also known as MOVPE or OMVPE) on various foreign substrates, such as sapphire, SiC and Si [151, 152]. In MOCVD the growth substrate is placed into a pressurized vacuum chamber at a controlled process temperature, typically around 1000 °C for GaN [153], and precursor gases are injected at a controlled flow rate, with the vent valve regulating the pressure built up. The metal-organic gas precursors (metals or semiconductors in an organic compound) react at the sample surface, depositing a semiconductor thin film, while the organic components evaporate and are removed by the vacuum pump [154]. Unfortunately carbon atoms can be incorporated into the lattice during growth which might be linked to red emission under green laser excitation, competing with the NV^- centre emission [8].

Due to differing lattice constants and thermal expansion coefficients (see Fig. 1.15), thin film cracking and wafer bow caused by significant stress is a typical problem if GaN is grown on Si substrates (less severe so when grown on sapphire or SiC [151]), which can be addressed by adding a AlN/AlGaN buffer layer to add compressive strain during growth [153, 155, 156]. We will look at the thin film stress and growth conditions in more detail when the heterogeneous integration of GaN thin film lenses with diamond is discussed in Chapter 3, because it is crucial for the generation of a flat bottom surface of the lens membranes as shown in Fig. 1.14.

The commercial interest in high-electron mobility transistor technology on the GaN-on-Si platform [157]

is a significant advantage over the diamond platform, because Si wafers are available in large sizes. The growth wafers used in this work had a diameter of 150 mm.

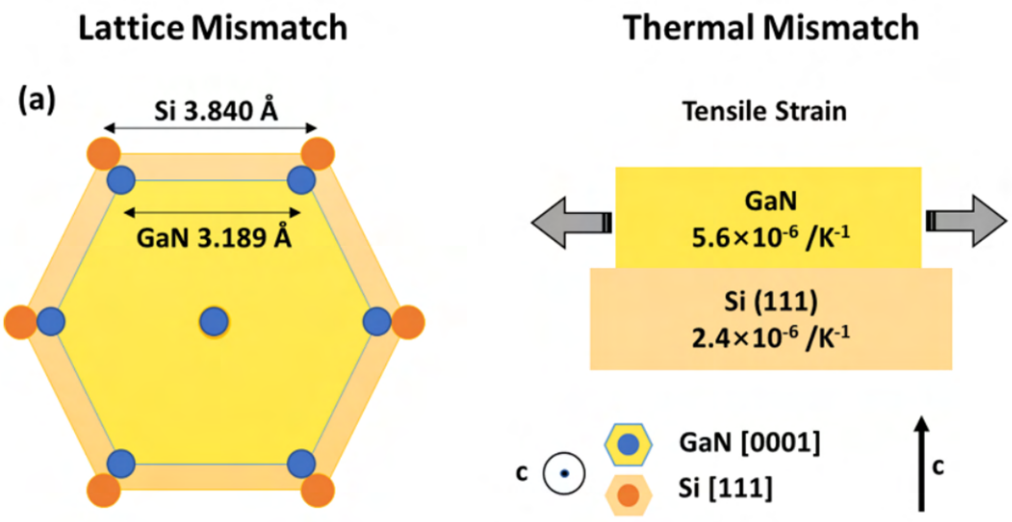

Figure 1.15: Lattice and thermal expansion mismatch of GaN and Si, taken from [158]. Because MOCVD growth takes place at elevated temperatures, the cooling of the epitaxial layer to room temperature after growth causes the GaN to shrink faster than the Si substrate, leading to tensile strain (the GaN is stretched).

1.6 Thesis outline

This thesis is dedicated to the development of high-aspect ratio GaN solid immersion lenses with diameters around 10 μm with the explicit potential for scalable and flexible integration.
In **Chapter 2** we will review some micro-lens fabrication methods in more detail and discuss in depth how the micro-lenses in this work are created in GaN and diamond materials. We will find that the use of the III-N material enables the fabrication of much higher aspect ratio lenses than in diamond while retaining a close refractive index match.
In **Chapter 3** some literature on polymer based μ-transfer printing and heterogeneous integration of GaN membrane devices is highlighted. This sets the context for the demonstrated fabrication of suspended micro-lens membranes consisting of a GaN/AlGaN/AlN epilayer grown on Si substrates and their successive transfer print integration with single crystalline diamond. The printed GaN micro-lenses are optically characterized and compared to monolithically etched diamond lenses finding much short focal length for the GaN micro-lenses.
In **Chapter 4** we will discuss the integration of GaN lenses with NV centres in various configurations which was the main target of this work. We will show that by including a GaN micro-lens on the diamond substrate, the effective collection angle from a point emitter is significantly reduced, improving potential coupling efficiency to external optics and mitigating total internal reflection losses. We experiment with the printing of GaN lenses on scanning NV^- magnetometry probes, finding that the integration is challenging, but possible.
In **Chapter 5** we will look into the results of more adventures printing processes targeting 3D resist structures, photonic integrated circuit waveguide and optical fibre facets. We find that GaN micro-lenses can be released with μm-precise accuracy in these unconventional configurations and investigate potential photonic benefits by simulation and experiment.
In **Chapter 6** we will summarize the results, critically illuminating some gaps in the gained knowledge about hybrid lens integration and discuss potential future directions of further work.
The **Appendix** add a significant amount of detailed information that might be necessary to reproduce the results of the micro-fabrication, including the micro-fabrication methods used. It also includes the detailed development of a single photon sensitive confocal microscope setup that is developed for this work.

2 Fabrication of high-index micro-lenses

Many fabrication methods are known to create micro-lenses from semiconductor materials. We will initially review diamond micro-lenses specifically as these are the most relevant. Afterwards we will discuss two different methods used in this work to create micro-lenses from photoresist before we go into the details of the shape transfer into single crystalline diamond and GaN using inductively coupled plasma (ICP) etching. The detailed description of the experimental methods used for the micro-fabrication are given in the Appendix.

2.1 Review: Diamond micro-lenses

As discussed in the introduction diamond is difficult to machine due to its high bond strength. We will review methods for the creation of diamond micro-lenses that are targeted at the integration with colour centres (focused ion beam milling), but also look into methods that have not yet been used for this purpose (reflow method, hard mask approaches).
Noticeably other geometries than lenses can be used to enhance the extraction efficiency from diamond colour centres, including for example coupling to diamond bullseye gratings [159] or plasmonic antennas [160, 161] and implementation into inverted nanocones [139], parabolic reflectors [162] or nanowires [163]. Approaches utilizing integrated photonic circuits and/or cavities are particularly attractive due to miniaturization, waveguide confinement and exploitation of Purcell enhancement [43, 94, 164–169].

2.1.1 Focused ion beam milling

A particularly common approach to fabricate diamond micro-lenses - sometimes also referred to as solid immersion lenses (SILs) - is focused ion beam (FIB) milling in which the diamond surface is bombarded with a stream ions that break the diamond bonds by physical sputtering [49, 123, 125, 170–172].
For diamond milling the beam typically consists of Ga ions and is focused on the surface while carefully controlling energy and flux, which allows the successive layer by layer removal as a function of position, carving the diamond into a lens shape. If a single diamond NV^- centre is identified by confocal photoluminescence microscopy in reference to alignment markers that can also be identified in the FIB system, the centre of the fabricated lens can be matched to the emitter position. In this way the pumping and light collection efficiency is reported to increase drastically after integration with the lens. Fig. 2.1 gives an overview of the first report combining a single NV^- centre with a FIB SIL.
A standard milling process is stated to take around 0.5-4 h per lens [49, 125] and is therefore challenging to scale, but significant collection improvements of up to 10× have been reported. Even though no detrimental effects of the milling process on the coherence properties of NV^- centers are documented [172], there are some concerns that the ion bombardment might cause additional strain around the defect of interest [173, 174]. An outer conducting layer (ca. 30 nm deep) of the SIL that contains implanted ions from the fabrication process and remaining debris on the surface can be removed using wet chemical and RIE etching [49, 172, 175].
Work at the forefront of NV-based quantum computing and quantum networking reports the use of such

monolithic SILs for faster measurement time and reduced error rate due to enhanced signal-to-noise ratio, illustrating the practical significance of this method [49, 176, 177].

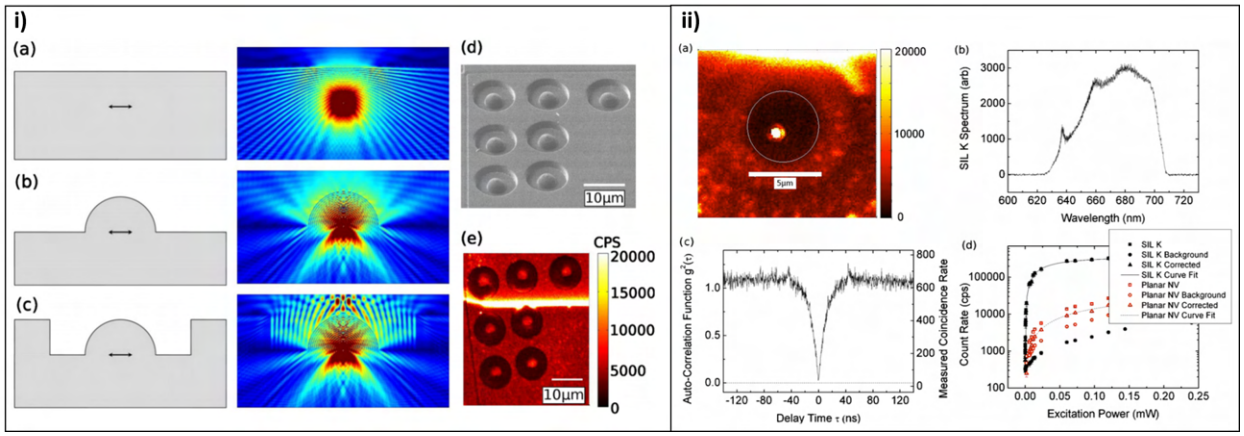

Figure 2.1: Example of focused ion beam milling (FIB) creating a diamond hemisphere referenced to a single NV^- centre in diamond, adapted from [123]. i) a,b,c) Schematics and cross section through finite difference time domain simulations (FDTD) showing the electrical field intensity emitted by a dipol source in the midpoint of a monolithic diamond hemisphere with 5 μm diameter, d) FIB image of fabricated lenses, e) confocal photoluminescence (PL) image of the same area, ii) zoom into the PL map of one hemisphere containing a single NV^- centre which is identified by b) a spectral measurement and c) a g^2 autocorrelation measurement, while d) contains the results of an excitation power series taken on the single NV^- below the lens and another single NV^- below the planar diamond interface, showing roughly 10x improvement of the saturated fluorescent count rate.

2.1.2 Photoresist reflow method

The photoresist reflow method has been commonly used to fabricate lithographically defined polymer micro-lenses that are then transferred into the semiconductor by inductively coupled plasma etching [108, 113, 114, 128, 129, 178–185]. The basic principle is illustrated in Fig. 2.2 and some SEM images of photoresist lenses fabricated with this method in this work are added. Initially circular resist pedestals are lithographically defined and then the resist is heated above its glass transition temperature, leading to a mobilization of its polymer chains. In a simplified picture the surface energy is then minimized by approaching a spherical shape typical for the droplets of a liquid on a flat surface surrounded by a gas. For an ideal liquid the contact angle between resist and substrate surface depends on the substrates surface energy and the resist's surface tension, essentially pulling an energetically unfavourable structure apart till an equilibrium is reached.

Photoresists do not behave like ideal liquids as they are complex compound materials. For example the unexpected evolution of an edge bulge under thermal reflow [185] and an unusual constant contact line between substrate and resist are typically observed [181]. Partially this might be due to competing processes in the resist, such as the evaporation of remaining solvent after development, thermally induced cross-linking of the polymer chains, embrittlement at elevated temperatures due to reactions with oxygen and increasing surface adhesion [181].

Still reflowed photoresists tend to form spherical profiles with exceedingly low surface roughness [186], which makes them extremely attractive for the fabrication of semiconductor lenses. Other geometric shapes such as spherical reflectors [186], cylindrical or ring lenses [187] are similarly possible to achieve with this method. A modern approach is the combination of photoresist reflow with grayscale lithography

for surface smoothening and shape optimization [181, 186], which we will also exploit in this work. If we are assuming that the resist lens forms a spherical surface after reflow and that the radius of the resist pedestal and micro-lens remain the same, we can roughly calculate the lens height h_2 that we expect for a certain resist pedestal height h_1 by assuming a constant overall volume:

$$\pi r^2 h_1 = \frac{1}{6}\pi h_2 (3r^2 + h_2^2) \tag{2.1}$$

If we then assume a fully anisotropic and linear etch transfer into the semiconductor substrate during ICP etching we expect a semiconductor micro-lens with height h_3 depending on the etch selectivity s between both materials:

$$h_3 = s \cdot h_2 \tag{2.2}$$

If s is not too far from one and the initial resist profile was spherical we can then assume that the semiconductor micro-lens is also reasonably spherical and can calculate the radius of curvature (ROC) of the final lens with the following equation:

$$\mathrm{ROC} = \frac{r^2 + h_3^2}{2h_3} \tag{2.3}$$

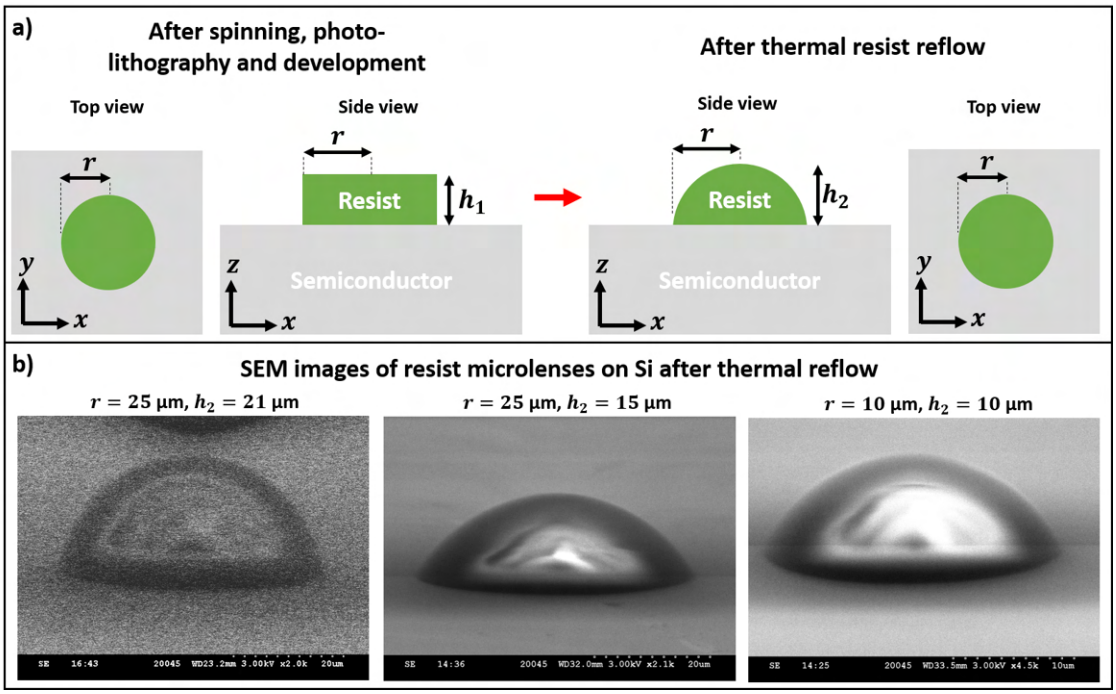

Figure 2.2: a) Schematic showing the principle of the photoresist reflow method to create spherical droplets on semiconductor substrates, b) 80-85° tilted SEM images of SPR220-7.0 photoresist droplets on Si substrate fabricated with a mask aligner and 190°C (left lens) / 210°C (two right lenses) thermal reflow applied on a hotplate. The nominal radius is given and the height estimated from the SEM image and Dektak data. h_1 is different for the left and the two right lenses. The real reflow temperature is likely to be much lower due to the missing calibration of the hot plates used (probably 130-150°C).

In literature the reflow method has been very successfully applied to fabricated shallow diamond micro-lenses with both Ar/O_2 and Ar/Cl_2 plasma based ICP etching recipes [113, 128, 129, 184, 185, 188], compare Fig. 2.3 a) and b) for two examples. The reported etch selectivity ranges between

$s \approx 0.1-0.16$ which limits the aspect ratio that can be achieved. For example a highly aspherical resist lens would be needed to generate a diamond hemisphere, which is not energetically favourable and thus not achievable with the reflow method alone. To our knowledge the highest aspect ratio diamond micro-lens fabricated by the reflow method and ICP etching is reported in [128] using an Ar/O_2 plasma: A diameter $d = 18\,\mu$m and a height $h = 1.5\,\mu$m was achieved, leading to ROC$= 28\,\mu$m.
GaN micro-lenses can also be fabricated using the reflow method. Cl_2 plasma based resist micro-lens transfer into GaN-on-sapphire has been reported as early as 1997 [182], with the schematic process flow shown in Fig. 2.3 c) and an etch selectivity $s \approx 1$. Gu et. al. later reported the fabrication and optical fabrication of negative and bifocal GaN micro-lenses using the reflow method, achieving focal length on the order of $f \approx 70-130\,\mu$m using Ar/Cl_2 etching [183]. We will built on this approach in this work due to its massive parallelism that allows to create 1000s of micro-lenses in one process run, offering a significant speed advantage over serial methods such as focused ion beam milling.

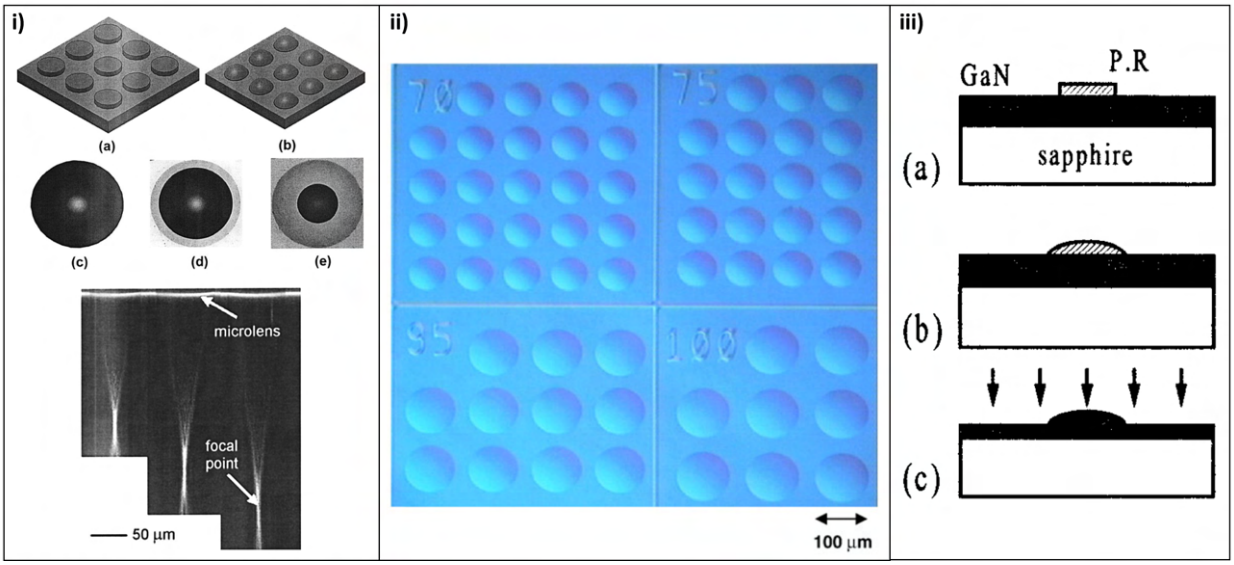

Figure 2.3: Examples of using the photoresist reflow method for the generation of circular micro-lenses in a) SC diamond based on Ar/O_2 ICP etching, adapted from [113], b) SC diamond based on Ar/Cl_2 ICP etching, adapted from [129], c) GaN based on Cl_2 ICP etching, adapted from [182].

2.1.3 Hard mask approaches

Intuitively one might assume that another semiconductor material or dielectric would provide higher etch selectivity towards diamond than a soft organic polymer, which is indeed correct. Both Si and SiO_x hard masks have been successfully used to create high aspect ratio diamond micro-lenses [130, 189]. Two results are shown in Fig. 2.4 (SiO_x) and Fig. 2.5 (Si).
The first approach employs the drop-casting of homogeneous silica micro-spheres as an etch mask and the authors show that they can tune the selectivity in the range $s = 0.26-0.52$ by adding O_2 to a Ar/Cl_2 ICP plasma. This allows them to create nominally hemispherical diamond micro-lenses with 2.5 μm diameter by exploiting the fact that the full diameter of the silica sphere is used as mask - the silica hemispheres are etched twice. The SEM images show that for $s \approx 0.5$ the etched lenses are clearly aspherical with a sharp pointed tip which leaves doubts about how well the lenses would perform optically which is not demonstrated by the authors. This technique is not necessarily well suited for alignment to quantum emitter locations as the drop-casting of the spheres is random. But one might

initially etch a shallow etch pattern in diamond to guide the positioning of the spheres.

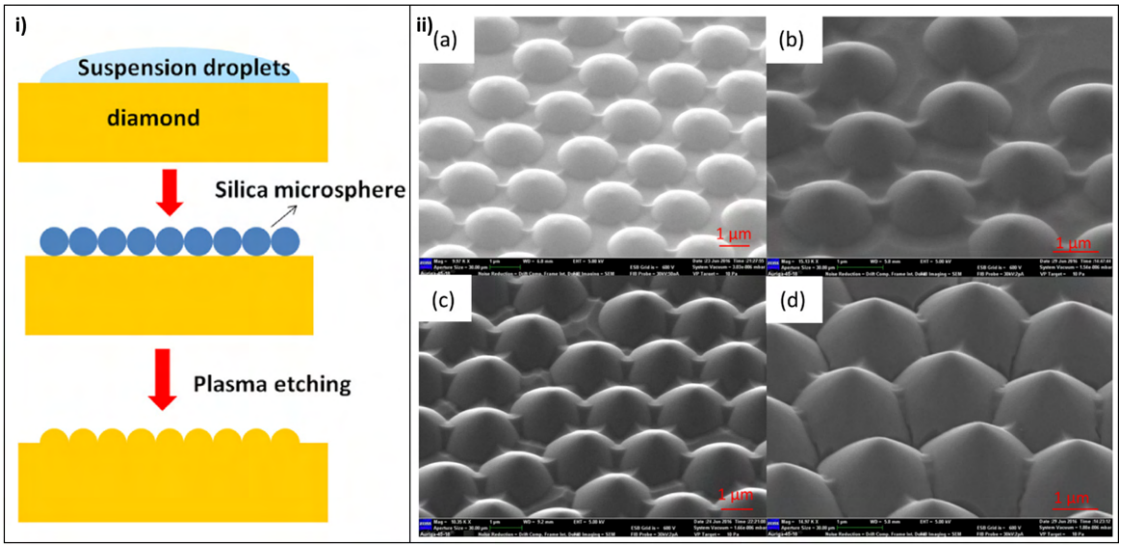

Figure 2.4: i) Drop-casting of SiO_x microspheres (diameter $d = 2.5\,\mu$m) from solution on a diamond substrate with successive $Ar/Cl_2/O_2$ ICP etching, ii) resulting etched diamond micro-lens arrays in a hexagonal lattice with varying height and shape due to increased added amount of O_2 to the Ar/Cl_2 base plasma, adapted from [189].

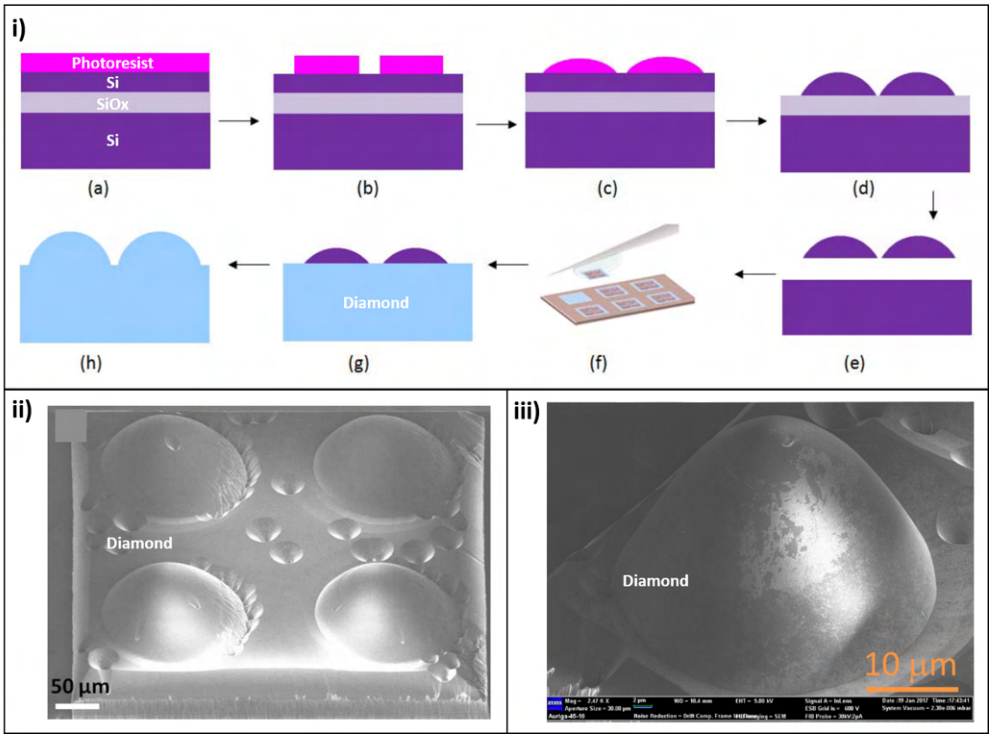

Figure 2.5: i) Schematic showing a dual mask processing approach with initial fabrication of Si micro-lenses on a silicon-on-insulator wafer with successive polymer based transfer to a single crystalline diamond substrate and etch based shape transfer of the Si lens into the diamond substrate via ICP etching, ii)/iii) yielded results showing very high aspect ratio micro-lenses with limited surface quality, adapted from [130].

The second method exploits pick and place of a transferred Si hard mask which exhibits very high etch selectivity towards diamond in O_2-based ICP etching, a technique initially exploited to etch diamond

photonic crystal cavities [190–192]. In the demonstration shown here [130] lenses are etched into a SOI wafer using the reflow method and an O_2/SF_6 RIE plasma. The Si lenses are then suspended from their growth substrate using a buffered oxide etch and transferred to diamond with a polymer micro-probe. By adding SF_6 to an Ar/O_2 ICP-plasma the etch selectivity between Si and diamond can be tuned in the range $s = 7 - 13$ achieving high aspect-ratio diamond lenses from shallow Si lenses. Some drawbacks of the technique seem to be bad surface quality due to micro-masking and surface residues, as well as conical lens shapes. Shape control is overall difficult, because both etch processes probably behave isotropic to some degree, leading to lateral shrinkage of the initially spherical resist lens profile, something we will also observe in this thesis. If both PR/Si and Si/diamond etch processes could be optimized towards $s \approx 1$ and high anisotropy while yielding a higher surface quality, this process might be very viable for diamond micro-lens fabrication with deterministic shape and position.
The approach to micro-lens fabrication in this thesis is very similar to this dual-mask process with the difference that we will use GaN instead of Si and the GaN works as the micro-optical element itself, rather than transferring the shape into diamond. This simplifies the lens shape control significantly.

2.2 Defining polymer micro-lenses

We will briefly discuss how polymer micro-lenses with high aspect ratio are created in this work. We employ a commerical direct write laser lithography system (DWL66+, Heidelberg Instruments) with a 8-bit grayscale capability. The working principle is illustrated in Fig. 2.6. A 375 nm UV laser is raster-scanned over the sample surface, while the local dosage can be controlled with an acusto-optical modulator that is synchronized with the scanning motion. The grayscale pixel size is 50 nm with a laser spot size of around 200 nm (full-width-half-maximum, FWHM).

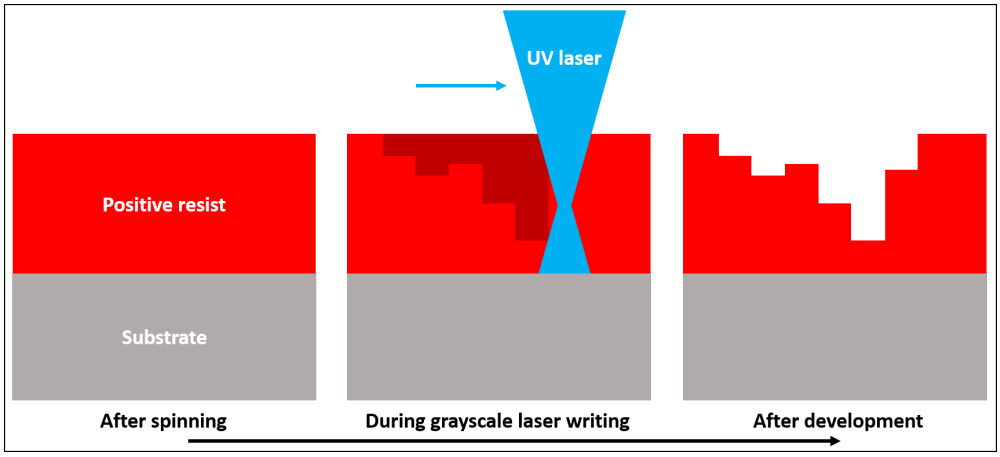

Figure 2.6: Working principle of grayscale lithography using positive photoresist and direct laser writing. The laser focus is kept constant from pixel to pixel, while the acusto-optical modulator of the DWL66+ rapidly adjusts the intensity from pixel to pixel, varying the dosage. For simplicity, the proximity effect is ignored in this schematic, in reality the laser beam diameter is larger than the pixel size by about a factor of 4.

We employ positive photoresist so that local dosage variations vary the development speed as function of position, leading to 3D shapes of the photoresist after a fixed development period.

2.2.1 Resist reflow combined with grayscale preshaping

We exploit the grayscale capability to preshape photoresist pillars before applying a thermal reflow procedure on a hotplate. The size dependent results are displayed in Fig. 2.7. The procedure allows us to avoid resist wrinkling that can occur if high aspect ratio resist pedestals with vertical sidewalls are reflowed. An example of fully processed and etched diamond micro-lenses from such high aspect resist pedestals as shown here is displayed later on in Fig. 2.16, showing a misshaped surface profile. We believe that a strong kink in the resist is difficult to flatten by thermal reflow if the lenses are close to a hemispherical shape. The energetically favourable resist droplet conditions probably implies a widening of the lens radius which would reduce the contact angle.

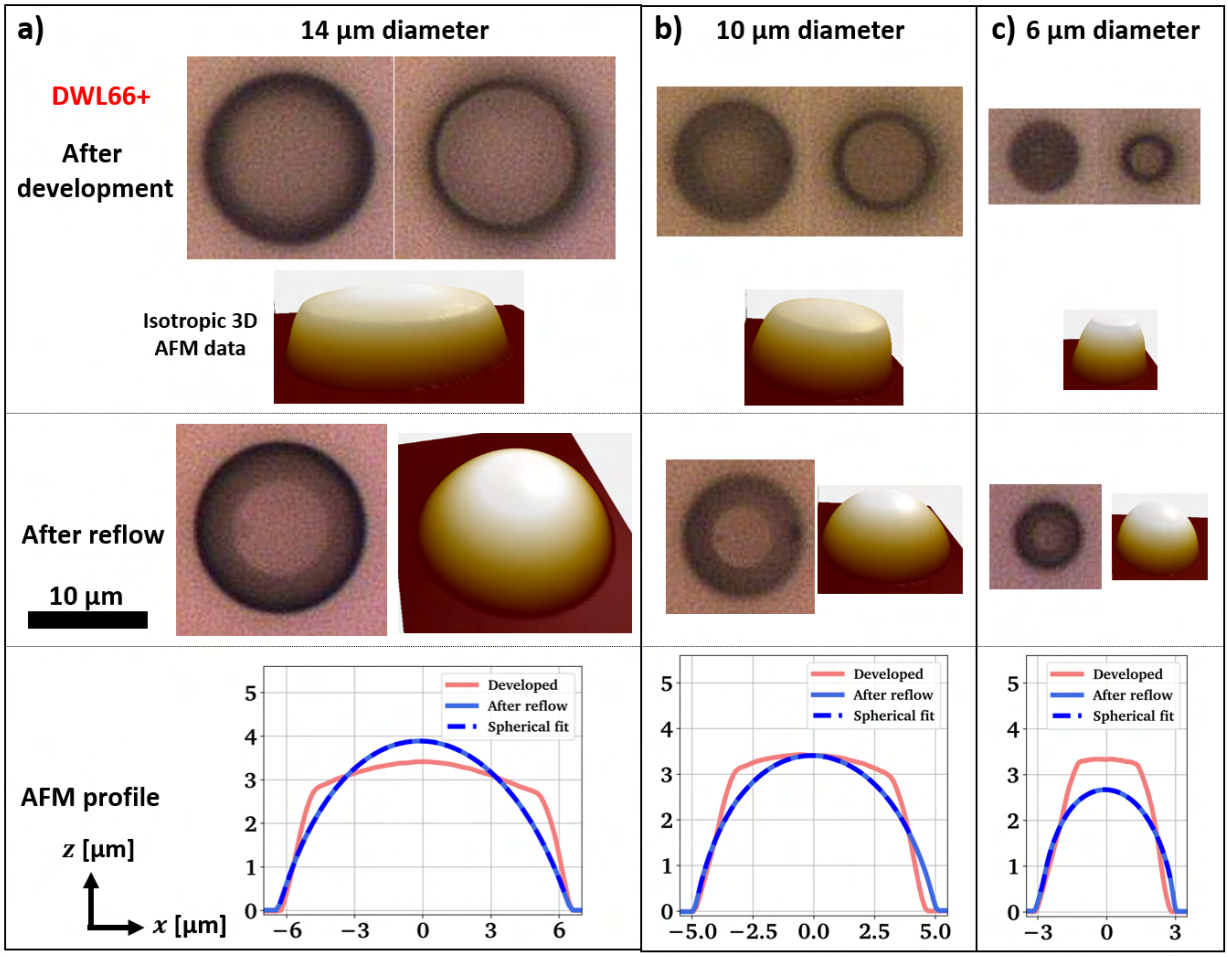

Figure 2.7: Microscope images and AFM data (NSC15) of SPR220-4.5 photoresist lenses fabricated with the DWL66+ laser lithography system with grayscale preshaping and thermal reflow. The nominal diameters of a) 14 μm (135 °C), b) 10 μm (150 °C), c) 6 μm (145 °C) are given. The scale bar applies to all microscope images in the figure. The closely neighboured images in the top part correspond to the bottom (left) and top (right) focus respectively.

In our interpretation the preshaping of the resist pedestal into a slightly rounded form eases the transformation of the droplet into a smooth meta-stable shape with high aspect ratio. We show that this procedure allows to generate nearly hemispherical resist lenses with a diameter as small as 6 μm (Fig. 2.7 c). The preshaping is performed by gradually increasing the exposure dose with increasing radius. This procedure also allows to carefully tune the height of the resist pedestal by variations of the

minimum exposure dose, which together with a staged increase of the reflow temperature allows height control on the order of 100-200 nm in successive runs, compare with the Appendix for more detailed information.

2.2.2 Pure grayscale lithography

The grayscale capability of the DWL66+ can also be used to directly create a desired resist shape. In the example shown in Fig. 2.8 we aimed to fabricate spherical resist lenses with a diameter $d = 15\,\mu$m and height $h = 3.5\,\mu$m. Using a self written Python script the lens shape is transferred into a .bmp grayscale map. Initial optimization included to find the correct dose level at fixed development time that would slightly develop the top part of the lens and leave a 200-400 nm bottom resist layer undeveloped. This trick is employed to avoid interface effects that can lead to additional significant non-linearity in the resist response. The first iteration shown in Fig. 2.8 a) refers to the application of a linear dependence of the exposure dose on the grayscale value in each pixel. The atomic force microscope (AFM) measurements show that the photoresist does not respond perfectly linear, meaning that within the resist bulk the development depth does not linearly depend on the applied UV dosage. Using self-written python code we are able to calibrate the exposure dose that corresponds to each grayvalue to compensate the non-linear resist response, improving the result significantly in only one iteration.

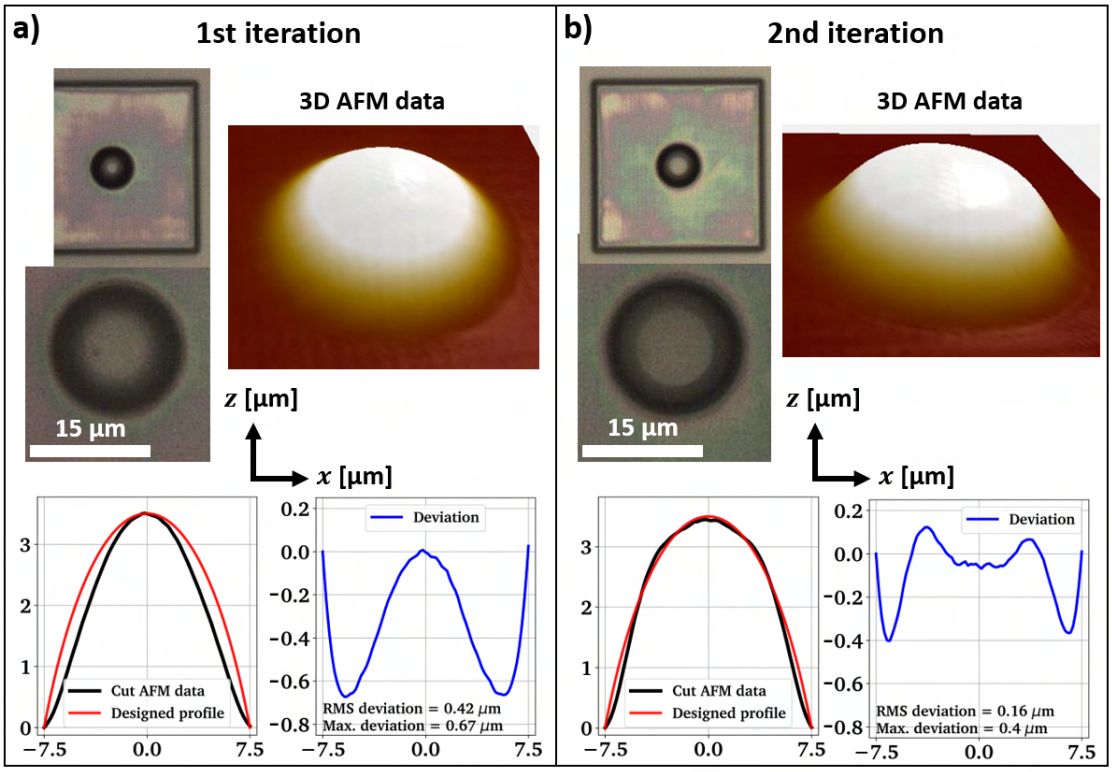

Figure 2.8: Grayscale optimisation for a spherical resist lens (SPR220-4.5) with 15 μm nominal diameter and 3.5 μm targeted height after a) 1st and b) 2nd iteration based on proportional correction.

A significant challenge in the optimization of grayscale lens profiles with a diameter $< 10\,\mu$m are proximity effects. In the most simple picture this refers to the overlap of the laser spot when targeting neighbouring pixels, but it also contains light scattering and reflections withing the resist thin film and depends on the resists dark erosion (resist removal in the development solution without UV exposure).

An illustration of the spot size overlap is shown in Fig. 2.9 a). The single pixel in the centre is affected by the exposure dose delivered on the neighbouring pixels, which makes the calibration of the grayvalue to exposure dose curve a function of the geometry. The effect is reasonably low if the height varies sufficiently slow with position, but the measured AFM profiles in Fig. 2.9 b) indicate that proximity effects become quite strong for lens diameters below 10 μm. In principle these could be compensated by methods of deconvolution, taking the shape of the laser spot into account, which is unfortunately not known. There are commercial software suits such as 'Beamer' (GenISys) that borrow from the experience on proximity effects in SEM imaging and allow to precompensate the design file to reach a targeted shape. For simple micro-lenses as investigated in this work a non-linear precompensation of the calibration curve in combination with iterative adjustment is found to be sufficient to generate highly spherical GaN micro-lenses, something that we will discuss in more detail in subsection 2.3.2.

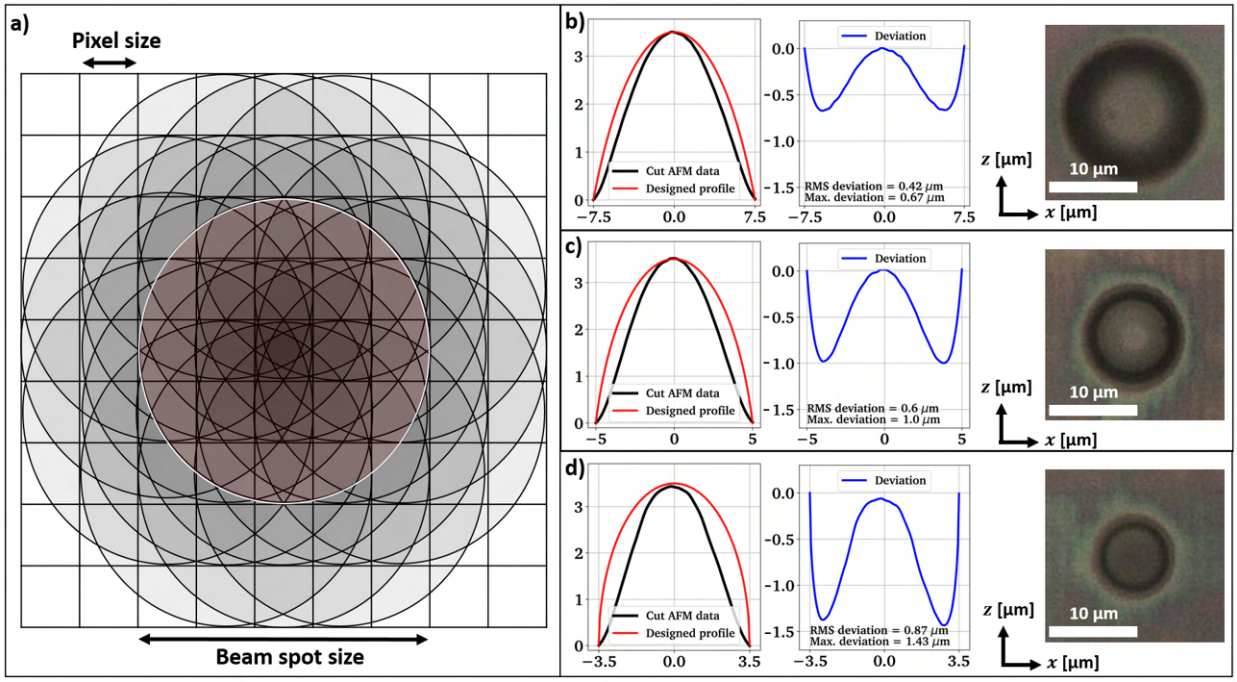

Figure 2.9: a) Illustration of the simplest version of the proximity effect. The pixel grid of the grayscale lithography map is overlaid by circles mimicking the beam size of the UV laser of the DWL66+. The exposure dose of the central pixel depends on the exposure dose applied to roughly the 2nd nearest neighbour, b)-d) AFM profile data (NSC15) and microscope images of successively shrinking spherical resist lenses (SPR220-4.5) from 15 to 7 μm nominal diameter. All data corresponds to 1st iteration optimisation, applying a linearly rising exposure dose with gray value.

The following example of a fabrication attempt aiming to create a Fresnel lens shows that investment into a commercial software suit or a self-written compensation software might allow to generate more advanced micro-optical elements: In Fig. 2.10 a simple Fresnel lens shape with 5 segments was exposed using an optimized grayscale calibration curve previously used for simple resist lenses. It is clearly visible that the local dosage at the transition points between the lens segments is much higher than intended due to proximity effects, making it impossible to create such high-contrast shapes without design precompensation.

Other complex shapes proved to be simpler to achieve. The following Fig. 2.11 shows a dense array of resist micro-lenses that overlap laterally. One would expect that proximity effects would also affect this anisotropic shape differently in x or y direction compared to the diagonal (using the same global

grayscale-to-exposure dose calibration). Luckily the effect is not very pronounced, which allows us to fabricate such complex micro-lens array devices after a few rounds of optimization.

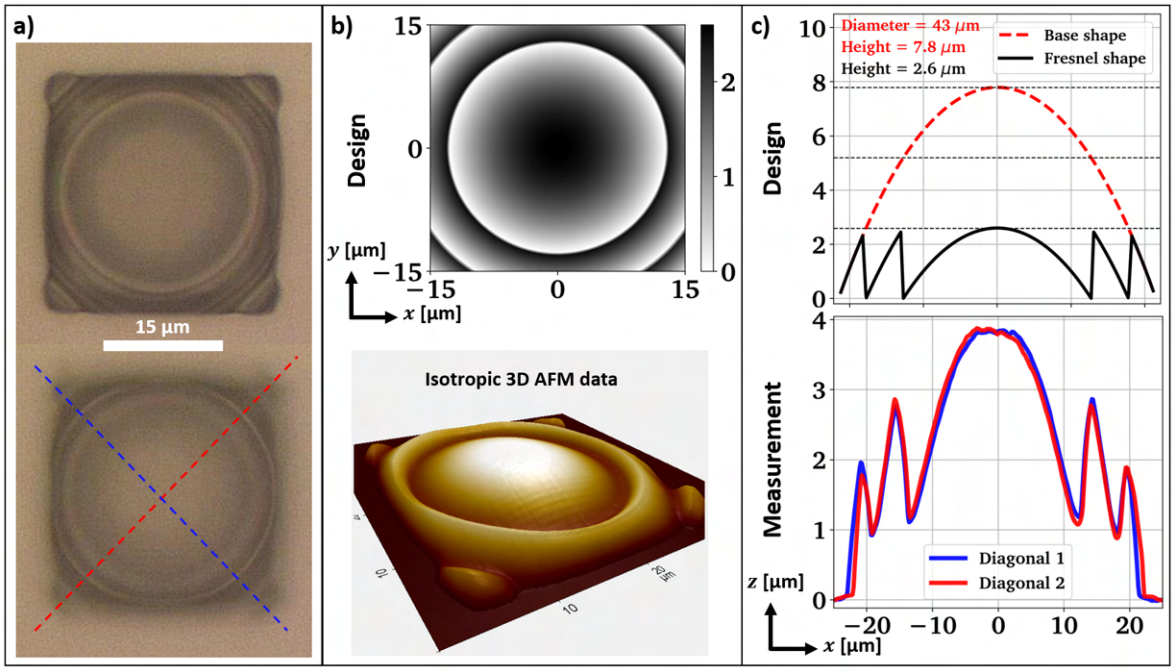

Figure 2.10: Grayscale exposure of a simple spherical resist Fresnel lens with 5 segments (SPR220-4.5), a) shows the microscope image after exposure, b) the design file and 3D AFM data (NSC15), c) designed and measured profile with AFM (NSC15).

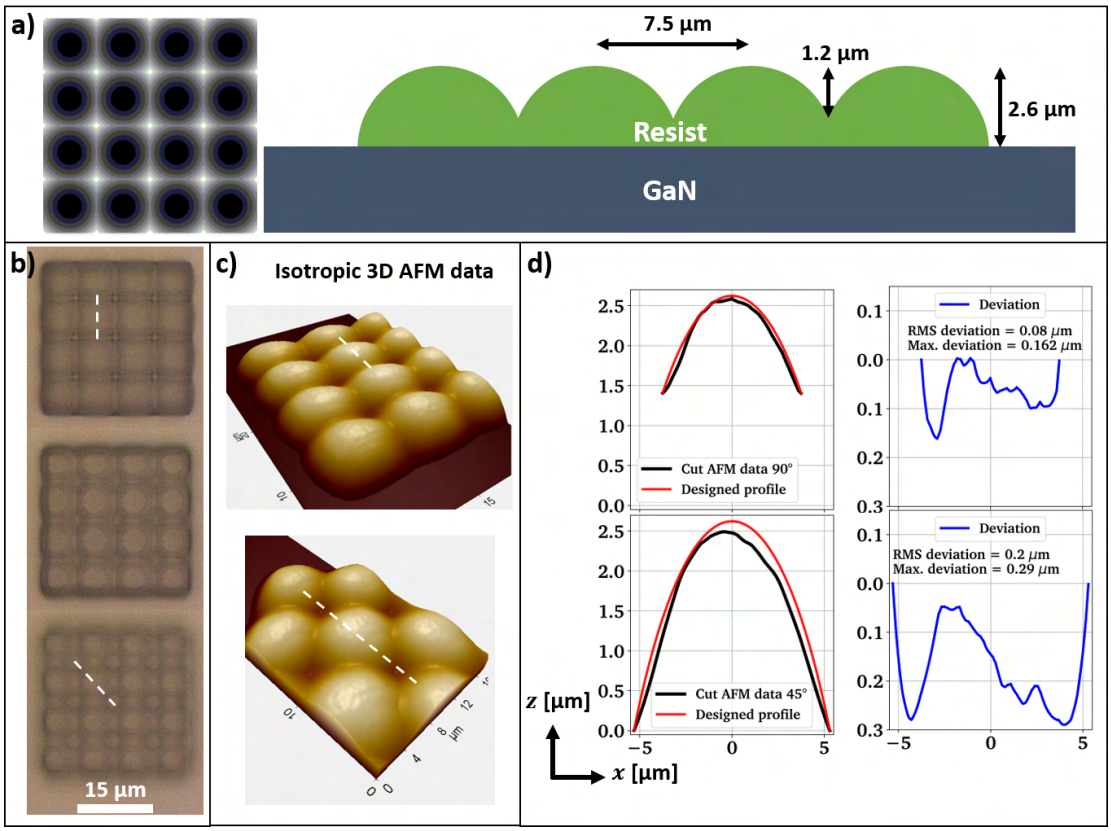

Figure 2.11: Dense array of spherical resist micro-lenses (SPR220-4.5) with 11 μm nominal diameter on a square grid with 7.5 μm pitch, fabricated using optimised grayscale lithography with the intensity rising to the power of 1.4 with grayvalue, a) contains a schematic explaining the dimensions and the .bmp file layout, b) shows microscope images at different focus positions, c) contains 3D AFM data, while d) compares the measured profile data with the design (all NSC15).

2.3 Micro-lens transfer into the semiconductor

In the following we will discuss the transfer of resist micro-lenses into diamond and GaN substrates by inductively coupled reactive ion etching (ICP-RIE). The detailed etch recipes used in this section are given in the Appendix. The plasma dry etching based transfer adds to the complexity of the lens-shape control, because ICP etching can contain both vertical and lateral etch components. Purely vertical etching is called anisotropic, which is the ideal case for our purposes. But the etch recipes used contain strongly chemically reactive species that can create volatile etch components even without the assistance of ion bombardment, leading to a lateral etch progression which distorts the lens shape. The following Fig. 2.12 illustrates the principle of reactive ion plasma dry etching. A detailed description is given in the Appendix.

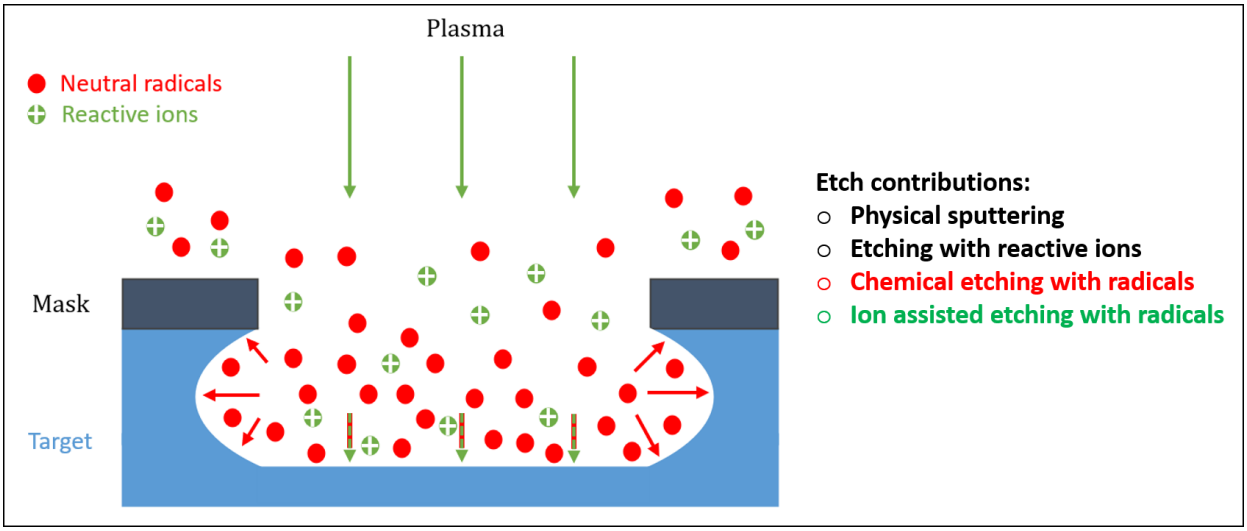

Figure 2.12: Illustration of the different contributions to 'reactive ion etching': Sputtering with ions and fast neutrals (mainly anisotropic), chemical etching with reactive ions (anisotropic), thermally-induced chemical etching with neutral radicals (isotropic), ion-assisted chemical etching with neutral radicals (anisotropic). Radicals are indicated in red and ions in green with + signs, based on [193].

2.3.1 Monolithic diamond micro-lenses

The basic process flow of micro-lens fabrication with the reflow method and successive ICP etch transfer into a diamond substrate is shown in Fig. 2.13. Anisotropic ICP etching is favourable for a controlled shape transfer, because it would linearly transfer the resist shape into the diamond substrate in a top-down manner. A complication of the lens shape transfer into diamond is the low etch selectivity $s \approx 0.1$ in Ar/Cl_2 based ICP plasma, which we use here. Therefore a nearly spherical high-aspect resist lens is transformed into an aspherical diamond lens even if perfect anisotropy is given. We do not attempt to correct for this effect by gray scale lithography, but simply show fabrication results for diamond micro-lenses fabricated from standard resist pillars patterned with a mask aligner and the DWL66+.

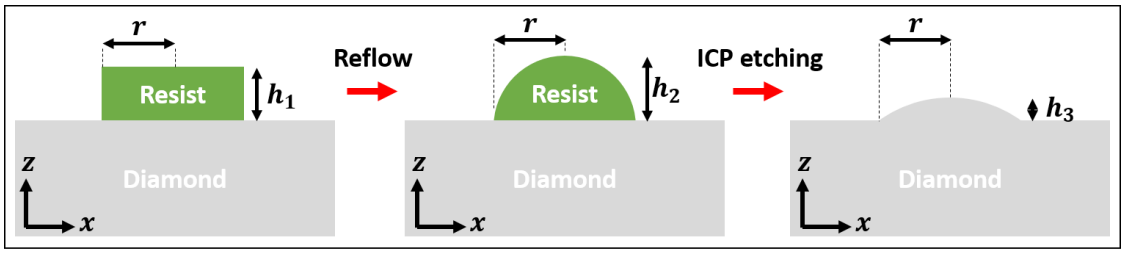

Figure 2.13: Plasma etching based process flow to generate micro-lenses in diamond with the reflow method employed in the following figures.

A significant disadvantage of single crystalline diamond substrates is their small size. With photoresist thickness of $> 5\,\mu$m bulging of the resist at the substrate edge becomes a significant problem, reducing the size of the substrate that can be used for processing and prohibiting close contact of a photomask in a mask aligner. We employ an embedding procedure of the CVD overgrown and polished HTHP diamond substrates into an optical adhesive, which is given in more detail in the Appendix. Essentially the diamond substrate size is artificially enlarged by inlaying it into a layer of the adhesive with similar

thickness. This reduces the photoresist edge bulge effect significantly.

The fabrication results are displayed in Fig. 2.14 with AFM profiles of diamond lenses etched from a standard and extra thick layer of photoresist displayed in Fig. 2.15 and Fig. 2.16, respectively. The etching generated a smooth surface finish, but slightly aspherical lens shapes. The extra thick photoresist layer processing with the DWL66+ led to small lenses with around 12 μm diameter and reasonable height, breaking the previous record for the smallest ROC of a ICP etched diamond lens (24 μm vs. 28 μm [128]). This result might be further improved by grayscale lithography, which was not applied here but which would be extremely cumbersome to optimize on small diamond substrates. We are aiming for a ROC $<$ 10 μm to effectively couple to diamond colour centres. Therefore monolithic diamond ICP etching proves to be impractical for this application. We also attempted to reproduce the slightly enhanced reported etch selectivity of $s \approx 0.16$ [113, 128, 184] in a Ar/O_2 plasma without success leading to similarly shallow lenses as in Ar/Cl_2 plasma chemistry. Some additional data on the shown lenses is provided in the Appendix.

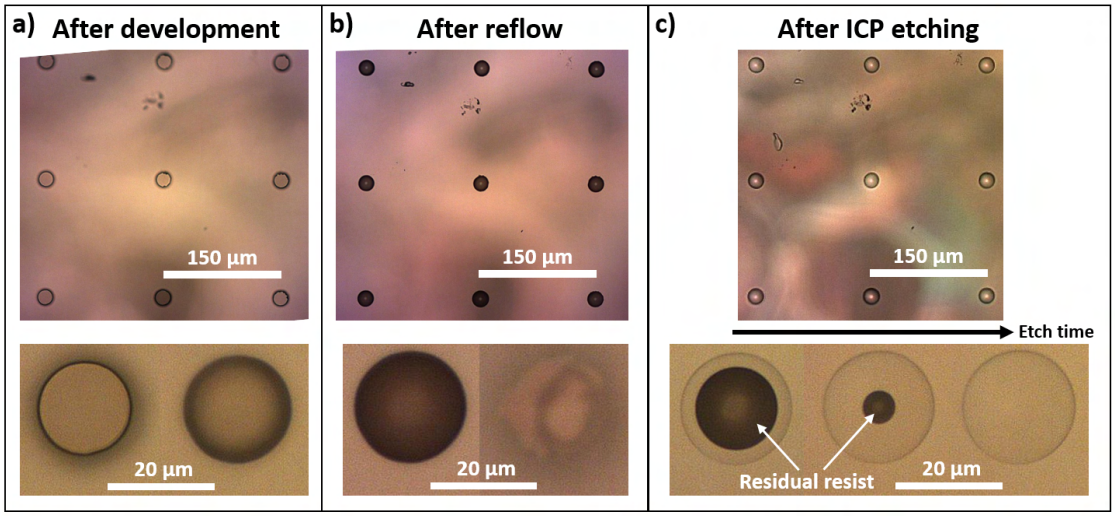

Figure 2.14: Fabrication results of diamond micro-lens fabrication using a layer of SPR220-7.0 (ca. 7 μm) and Ar/Cl_2 based ICP etching. The nominal lens diameter is 20 μm. a) Photoresist pedestals after development using the mask aligner, b) lenses after applying 135 °C on a hotplate for 3 min, c) final etch result and intermediate etch progression after 5, 10 and 13.5 min.

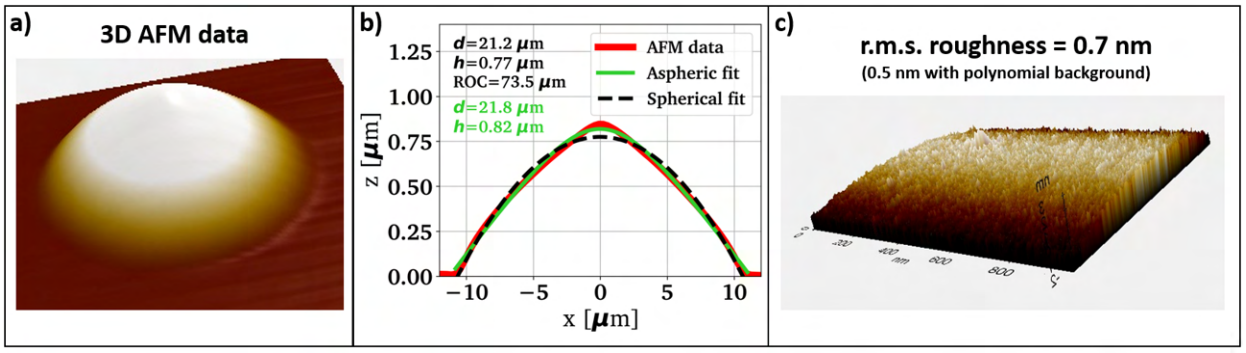

Figure 2.15: AFM analysis of the etched diamond micro-lenses (NSC15), a) 3D representation, b) line profile and c) surface roughness measured on top of the lens.

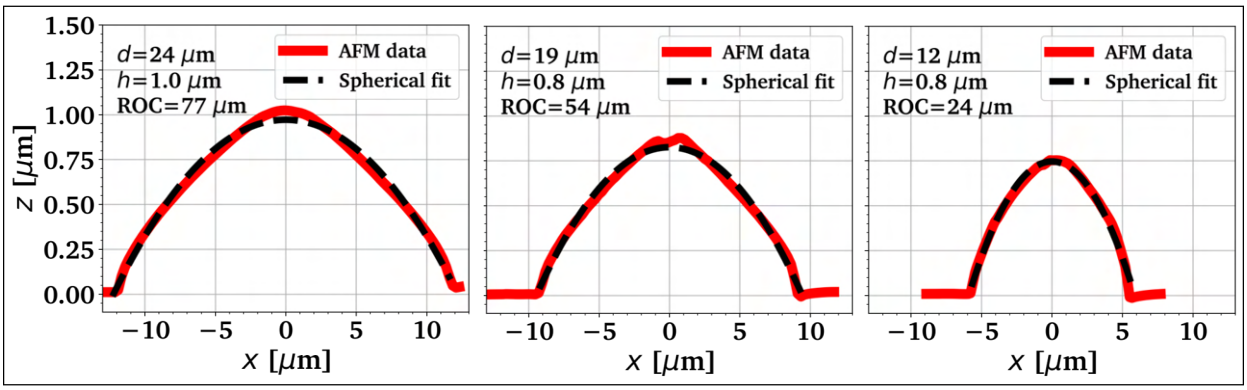

Figure 2.16: AFM profiles (NSC15) of etched diamond lenses with nominal diameters of 20, 15 and 10 μm created by extra thick layer processing of SPR220-7.0 (ca. 14 μm) using the DWL66+ laser lithography system and Ar/Cl_2 based ICP etching.

2.3.2 Single GaN micro-lenses

We will now look into the GaN micro-lens fabrication on GaN-on-Si substrates (MOCVD growth), using both a grayscale preshaping combined with resist reflow and a pure grayscale lithography approach. The process flow for grayscale preshaping, resist reflow and ICP etch transfer into the GaN-on-Si epilayer is shown in Fig. 2.17 with the corresponding fabrication results shown in Fig. 2.18.

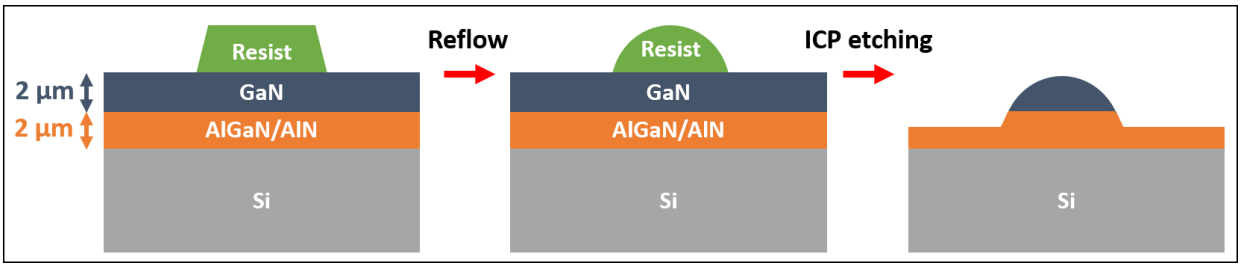

Figure 2.17: Process flow for etching GaN micro-lenses on Si substrates. The AlGaN/AlN buffer layer mitigates the lattice mismatch between GaN and Si. Grayscale lithography is used to slightly preshape the resist pedestals to ease the reflow process, especially at small diameters.

There are a few interesting observations to make:

- The selectivity between GaN and resist is around $s \approx 0.77$ (compare red and blue curves, Fig. 2.18 c)
- The etched GaN lens profile exhibits significant lateral shrinkage compared to a fully anisotropic etch process (compare blue and green curve, Fig. 2.18 c))
- The lateral etch component seems to exhibit a selectivity towards the crystal planes of the Wurtzite GaN, leading to hexagonal faceting at this particularly large etch depth

The hexagonal faceting can be clearly observed in the SEM images shown in Fig. 2.19, especially at small lens diameters. Luckily this effect largely disappears if the etching is restricted to the GaN epilayer (upper 2 μm in the optimized GaN-on-Si substrates used). Fitting of the AFM profile data for three different lens sizes in Fig. 2.20 shows reasonable agreement with a spherical lens shape, but a simple parabolic fit can describe the data slightly better. This effect can also be attributed to lateral etching of the lenses during the resist shape transfer. This is probably a combination of lateral resist and lateral

GaN/AlGaN/AlN etching, as the centre parts of the lens are etched last and are mostly protected by a resist cap during the etching process, which is also exposed to and etched by the plasma.

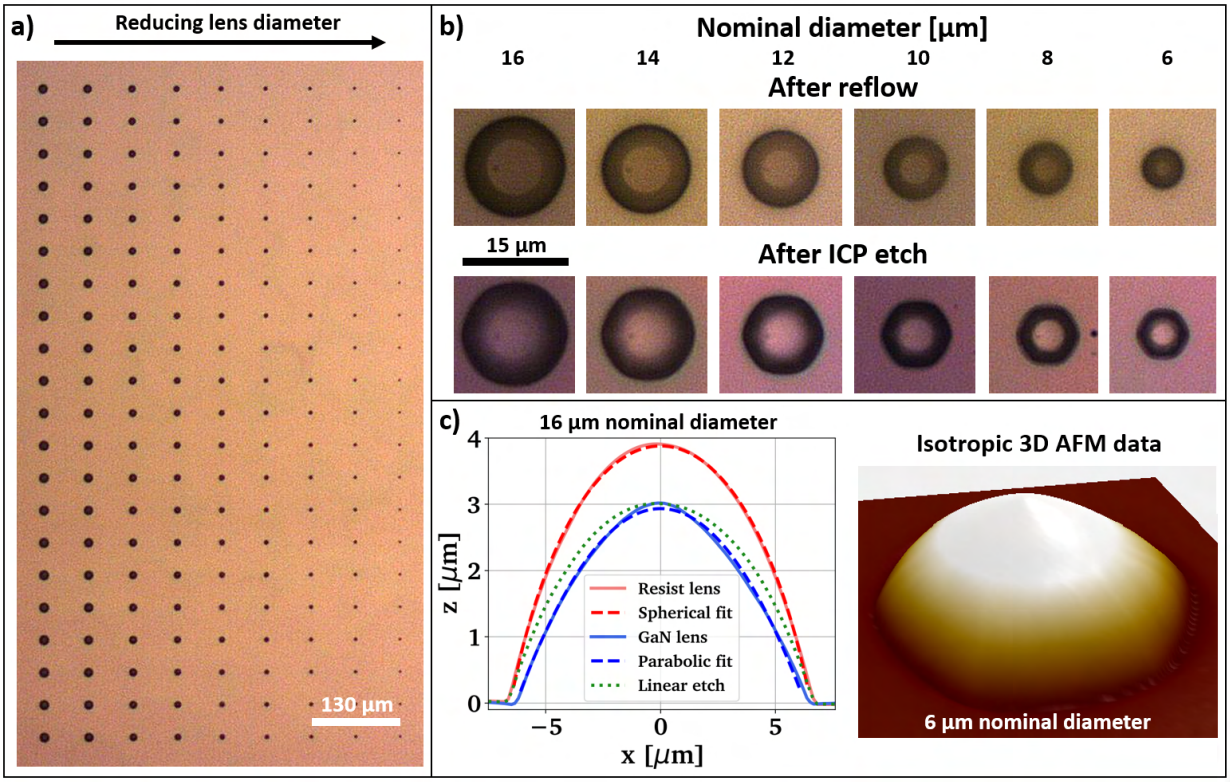

Figure 2.18: Etching GaN micro-lenses on Si substrate using SPR220-4.5 and the DWL66+. a) Sample overview after reflow, b) microscope images after reflow and Ar/Cl_2 based optimised low bias ICP etching to avoid resist burning, the scale bar applies to all images, c) AFM linescan showing the resist to semiconductor shape transformation and real scale 3D AFM data of a high-aspect ratio GaN lens (NSC15).

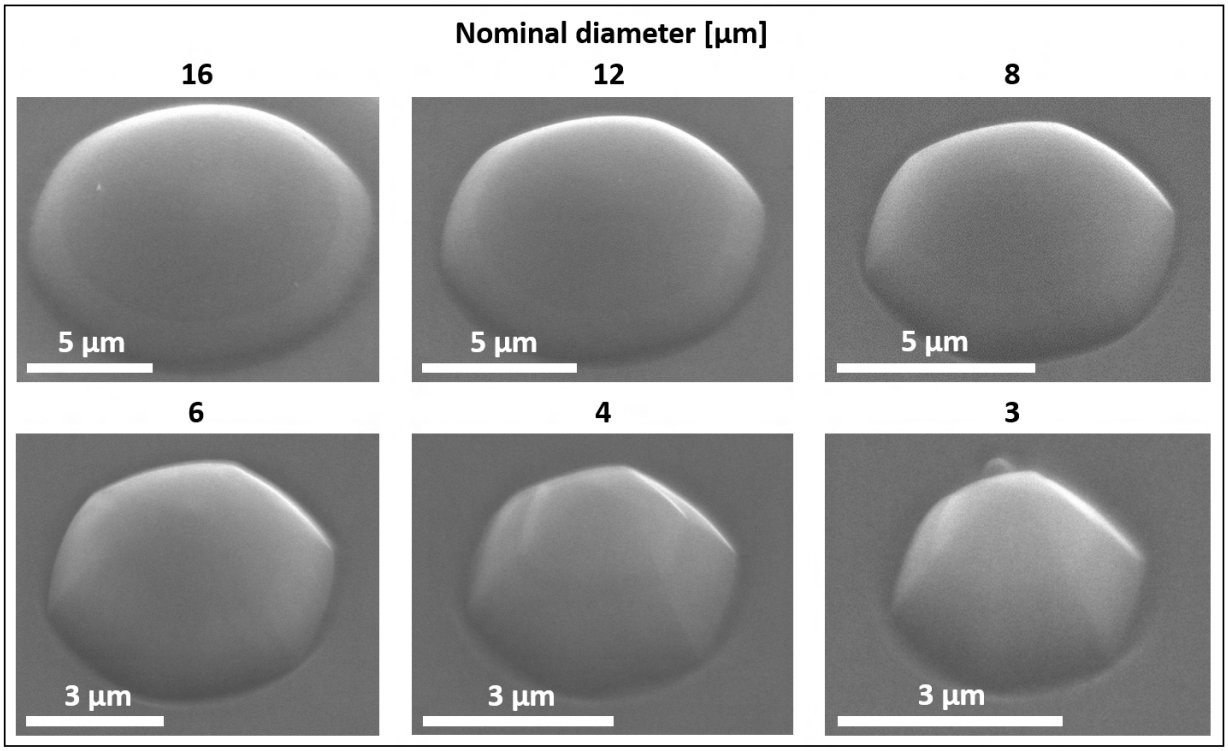

Figure 2.19: SEM images (40° tilt) of GaN micro-lenses with various diameters after lens etching.

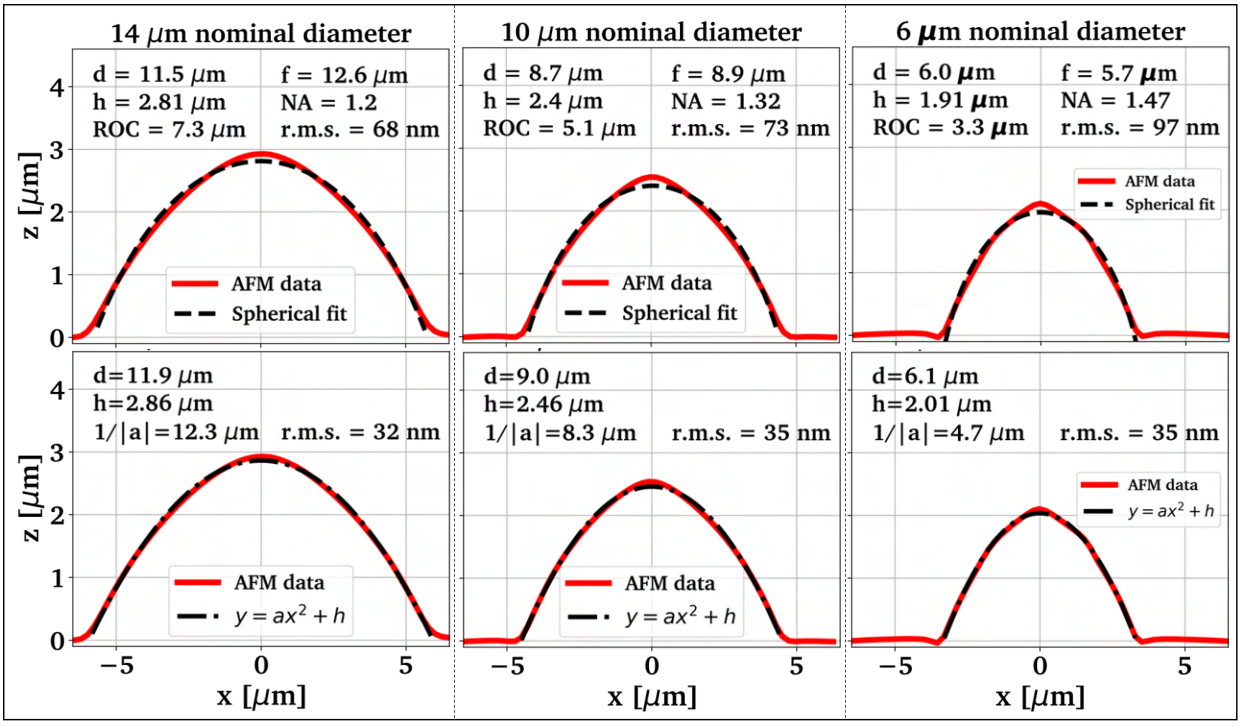

Figure 2.20: Detailed AFM profile analysis (NSC15) of three GaN micro-lenses in different size categories. The upper plots contains a spherical fit while the lower plots compare the same AFM data to a simple parabolic fit. The focal length and NA correspond to a possible integration with diamond and are calculated using the ray optics approximation and assuming a monolithic layer stack. The r.m.s. value shows the root-mean-square deviation of the data from the fit in each case.

We can counter act the undesirable shape transformation during ICP etching by

- limiting the etch depth to around 2 μm which reduces the exposure of the lens to the lateral etch and faceting contributions
- taking lateral etching into account by adapting the grayscale shape of the resist lens by adding a simple parabolic function on top of the linearly stretched ($s \approx 0.77$) spherical resist shape and performing iterative grayscale optimization on the resist lens without applying any reflow

The latter point simply means that we add material laterally to the resist lens to widen it in comparison to the GaN micro-lens targeted with the parabolic overlay function as a best guess. By varying the resulting difference between resist lens and GaN lens diameter (which we call 'gap'), we are able to fine control the lens diameter while achieving spherical GaN micro-lenses with one and two dimensional r.m.s. deviation below 33 nm, which is equivalent to fulfilling the Maréchal criterion for diffraction limited optics at $\lambda = 650$ nm. 33 nm r.m.s surface deviation corresponds to wavefront error over the full aperture of $\lambda/14$ if weighted with the index contrast $n-1$ [95, 194]. The results are displayed in Fig. 2.21 and 2.22 for lenses in two different size categories with a diameter between 6-11 μm and a ROC between 4-10 μm. At the same time a low r.m.s. surface roughness of 3.0 nm is maintained on the lens surface even in pure grayscale mode. With grayscale preshaping and resist reflow the roughness can be as low as 1.4 nm probably due to the reflow surface smoothening effect (see Appendix for data). These surface roughness values can be estimated to correspond to 0.1 % and 0.03 % scattering losses respectively [195] which can be considered insignificant.
In short we are able to create nearly hemispherical GaN micro-lenses with excellent surface properties both in terms of three dimensional shape and roughness which creates a nearly ideal micro-optics platform. Further information on the details of the grayscale shape optimization are included in the Appendix.

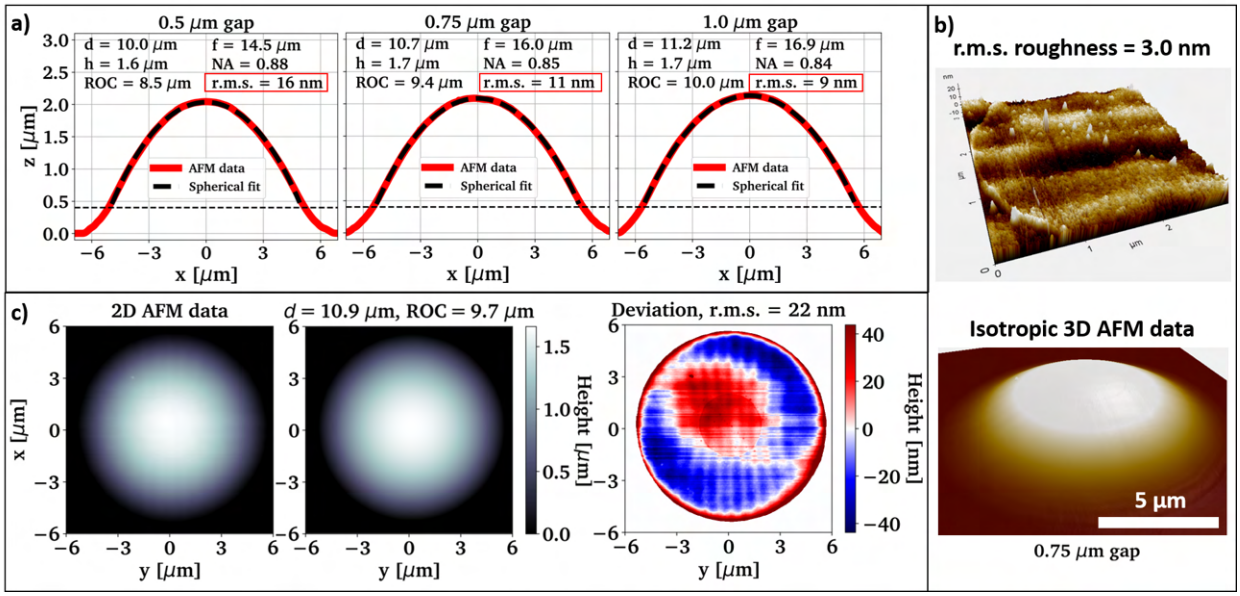

Figure 2.21: Detailed AFM analysis of the etched 11 μm diameter GaN-on-Si micro-lenses (SSS-NCH), a) linescan data with spherical fits in dependence of the design gap, b) surface roughness measured on top of a GaN micro-lens with real scale 3D representation, c) 2D spherical fitting of a micro-lens with 0.75 μm gap.

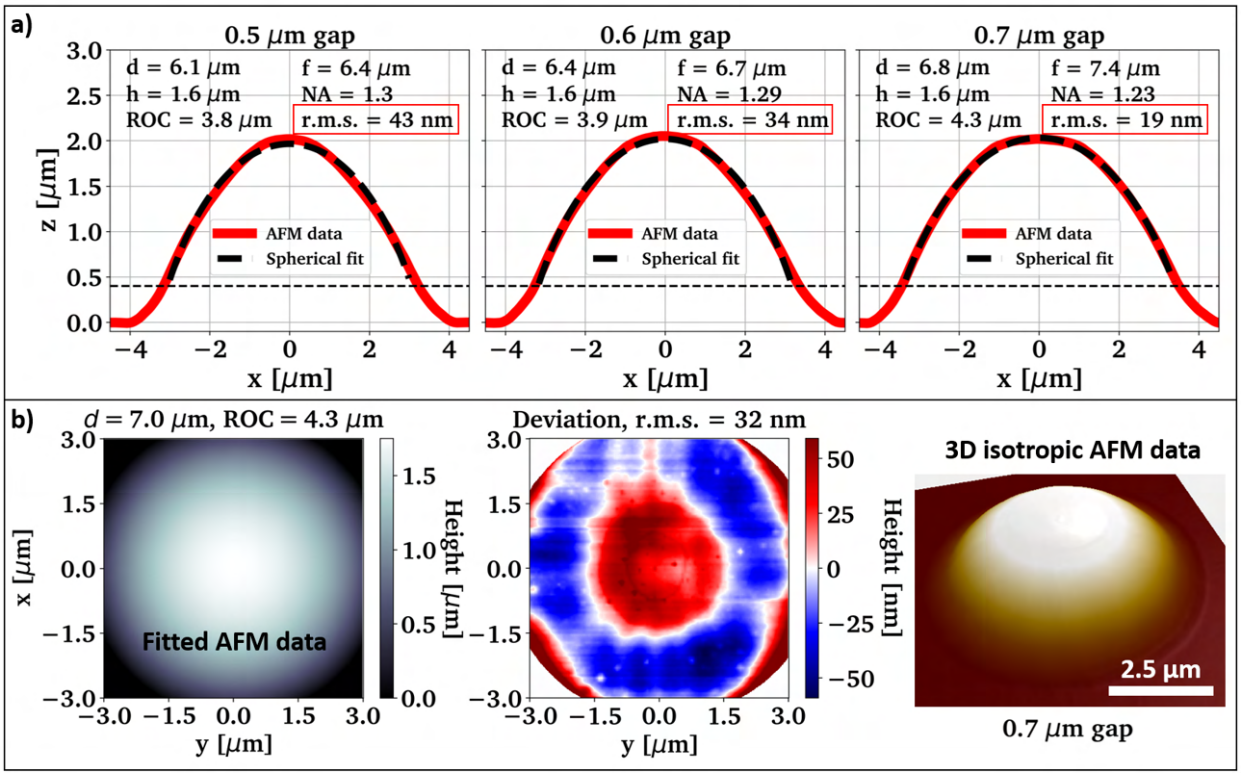

Figure 2.22: Detailed AFM analysis of the etched 7 μm diameter GaN-on-Si micro-lenses (SSS-NCH), a) linescan data with spherical fits in dependence of the design gap, b) 2D spherical fitting of a micro-lens with 0.7 μm gap and 3D real scale representation.

2.3.3 GaN micro-lens arrays

The grayscale lithography capability also allows for efficient scaling of the micro-lens fabrication. So far we mostly discussed single micro-lenses and we will see how these are individually suspended in Chapter 3. If we suspend multiple closely spaced micro-lenses on one membrane platelet we can reduce the number of transfer processes which can significantly improve throughput of the integration process. Fig. 2.23 and 2.24 show the processing of 2x2 and 4x4 lens arrays fabricated with pure grayscale lithography and ICP etch transfer into the GaN-on-Si substrate. We deliberately choose to leave a buffer resist layer at the bottom of the lenses, which was aimed to benefit the transfer process and will be discussed in Chapter 3. Unfortunately this measure increases the lateral etching of the resist micro-lenses, because they are significantly longer exposed to the plasma before their shape is transferred into the semiconductor. For these devices no 'gap' overlay is used, which deteriorates the shape achieved. Still from the AFM profile scans we can expect that both lens array types will perform reasonably well optically. The 2D fit in Fig. 2.24 indicates that there exists anisotropy in these lenses most probably due to the discussed proximity effects during grayscale lithography.

A challenge in micro-lens array fabrication is the different environment lenses experience at different positions in the array, because the lithography and etching process can be sensitive to the structures themselves. For example we find that the lenses in the outer parts of the dense 4x4 micro-lens arrays shown in Fig. 2.24 are significantly shallower than the lenses in the center part, probably due to a mixture of UV straylight during exposure, physical access of the development solution or ion-channelling effects during etching.

Some additional processing results of etched GaN micro-lens arrays are shown in the Appendix.

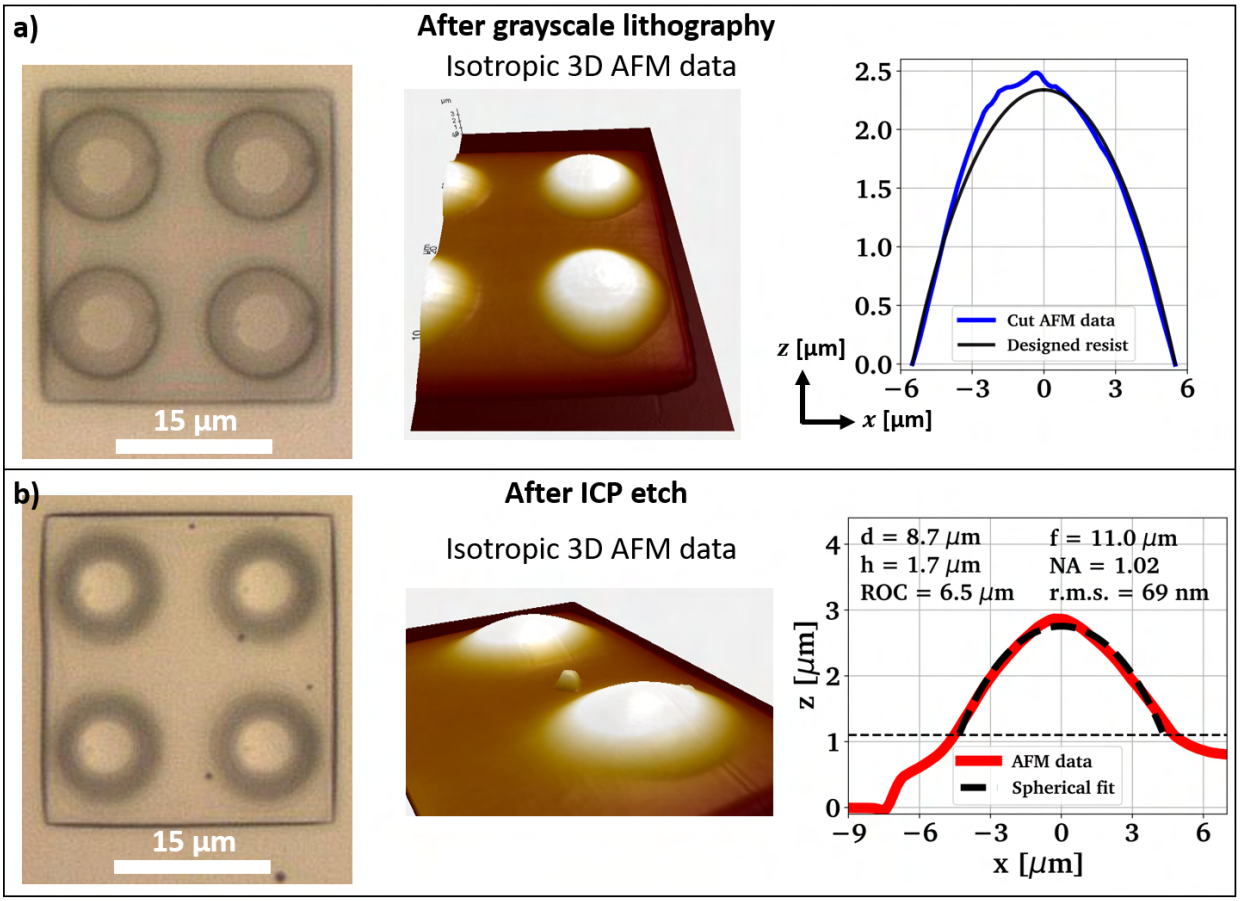

Figure 2.23: 2x2 micro-lens array on a 30x30 μm^2 mesa and nominally 11 μm lens diameter with 15 μm pitch. Microscope images of a) photoresist lenses after optimised grayscale lithography and b) after low-bias Ar/Cl_2 etch transfer into the GaN-on-Si layer with corresponding AFM data (NSC15).

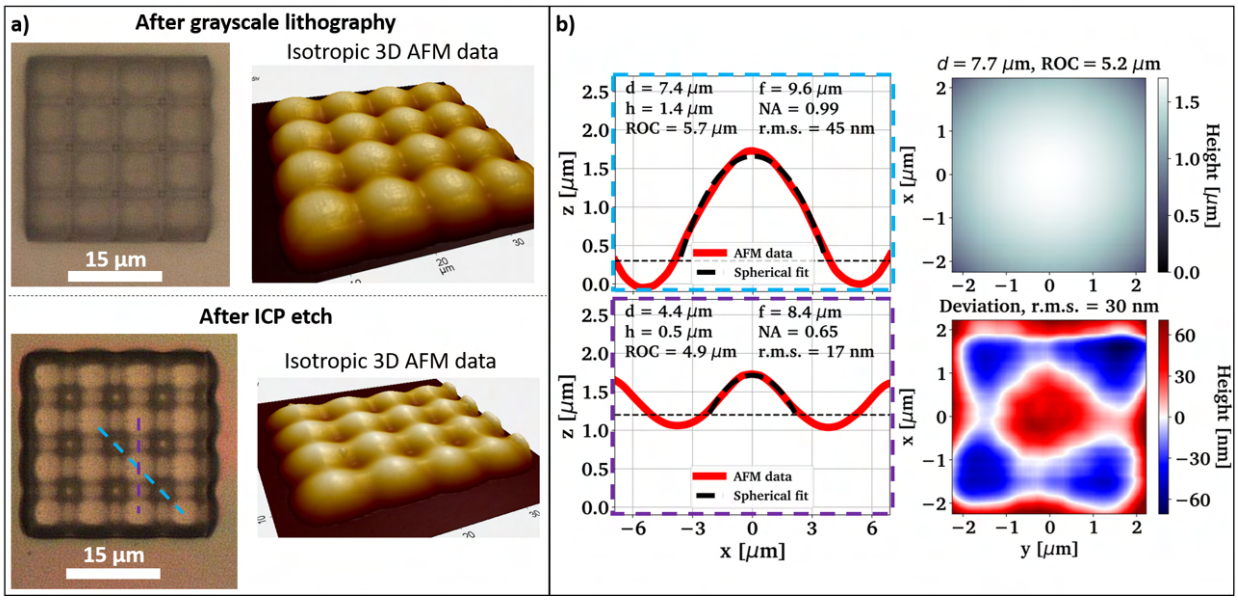

Figure 2.24: 4x4 dense micro-lens array on a 30x30 μm^2 mesa and nominally 11 μm lens diameter with 7.5 μm pitch. The photoresist lens array was already discussed in Fig. 2.11. a) Microscope images of the photoresist lenses after optimised grayscale lithography and after low-bias Ar/Cl_2 etch transfer into the GaN-on-Si layer with corresponding 3D AFM data representation (NSC15), b) detailed AFM profile analysis of the etched GaN lens profile with spherical fits in 1D and 2D (SSS-NCH).

2.4 Summary

In short we have seen that GaN thin films offer fabrication of highly spherical micro-lenses with high aspect ratio and excellent surface quality using inductively coupled plasma etching. This fabrication method allows for rapid scaling as parallel wafer-scale compatible micro-fabrication methods are used to create the lenses which stands in contrast to serial methods such as focused ion beam milling.
Moving to the GaN platform eliminates the difficulty to create large arrays of high-aspect ratio micro-lenses in diamond without losing control of the lens shape and surface quality. The obvious cost of this approach is that we need to suspend the GaN micro-lens devices from their growth substrate to transfer them to diamond, which is usually performed in a serial manner. To mitigate the bottleneck of serial micro-lens placement we show the fabrication of GaN micro-lens arrays which improves the potential integration speed.
We will now focus in depth on the GaN micro-lens suspension and integration with planar diamond substrates.

3 Hybrid integration of GaN micro-lens membrane platelets with diamond

After an initial review of the field of transfer printing and its implementation in this work, we will discuss the basic principles of membrane and wafer bow in GaN-on-Si thin films as these are highly relevant to achieve a gap-less interface between GaN thin-film devices and diamond. Afterwards we will describe in detail how GaN micro-lens platelets are successfully suspended from their growth substrate while maintaining the shape and high surface quality of the previously fabricated micro-lenses using an optimized process flow to suspend 2x2 GaN micro-lens array membranes as an example. To illustrate the key insights leading to a flat and smooth bottom surface and recovered lens profiles after suspension, we will show some failed approaches which finally lead to the successful integration of single GaN micro-lenses with diamond.
We will then assess the optical performance of single printed GaN lenses on single crystalline diamond and compare it to expectations from theory and experimental data from the monolithically etched diamond lenses discussed in Chapter 2. Finally we discuss the transfer printing of additional suspended GaN micro-lens arrays in detail to highlight a road map towards scalable integration.
The novelty of the discussed approach stems from the direct use of a heterogeneously integrated solid state micro-lenses as optical elements that solve the difficulty of scalable high aspect ratio micro-lens production in diamond, which led to the publication of some of the presented work in [95].

3.1 Transfer printing methodology

Pick-and-place techniques are commonly applied in research facilities to achieve novel geometries on the micron- and nanoscale and refer to the device or material removal from one substrate (donor) and its targeted release on another (receiver) [91, 196–198]. In the context of microfabrication this usually infers the use of an imaging system and automated translation and rotation stages with micro- to nanometer scale resolution. Typical examples are the micro-manipulation with sharp metallic probes in a SEM environment [93, 199, 200] or polymer stamp based transfer printing under an optical microscope [91, 196, 201–207]. Pick-and-place technology has partially reached industrial usage for devices such as micro-LED displays [91, 208, 209].
In the following we will quickly review polydimethylsiloxane (PDMS) based optical transfer printing as an integration technique. We will cover the visco-elastic properties of PDMS, a typical process flow for device suspension and printing, as well as examples for transfer printing based integration of photonic devices such as lasers, single photon sources and GaN micro-LEDs.

3.1.1 Review: Visco-elastic properties of PDMS

Polydimethylsiloxane (PDMS) is an elastomeric polymer meaning that it can be flexibly deformed but returns into its original shape if applied stress is released. Additionally it has visco-elastic properties which means that its surface adhesion can be kinetically controlled [210, 211]. Fig. 3.1 a) illustrates this process: A thin film of PDMS is brought into contact with generic devices that adhere to a donor

surface (blue). If the PDMS is peeled away very quickly, its surface adhesion is high and the devices may stick to it. Those devices can then be brought into contact with a receiver surface (red), and if the PDMS is now peeled away very slowly the devices might then stick instead to the receiver surface, because the adhesion of PDMS is significantly lowered if the peeling speed is low. In short for a successful PDMS lift off the device adhesion to the donor surface needs to be lower than the adhesion to PDMS at high retraction speed, while the device adhesion to the receiver surface needs to be stronger than the adhesion to PDMS at low peeling speed.

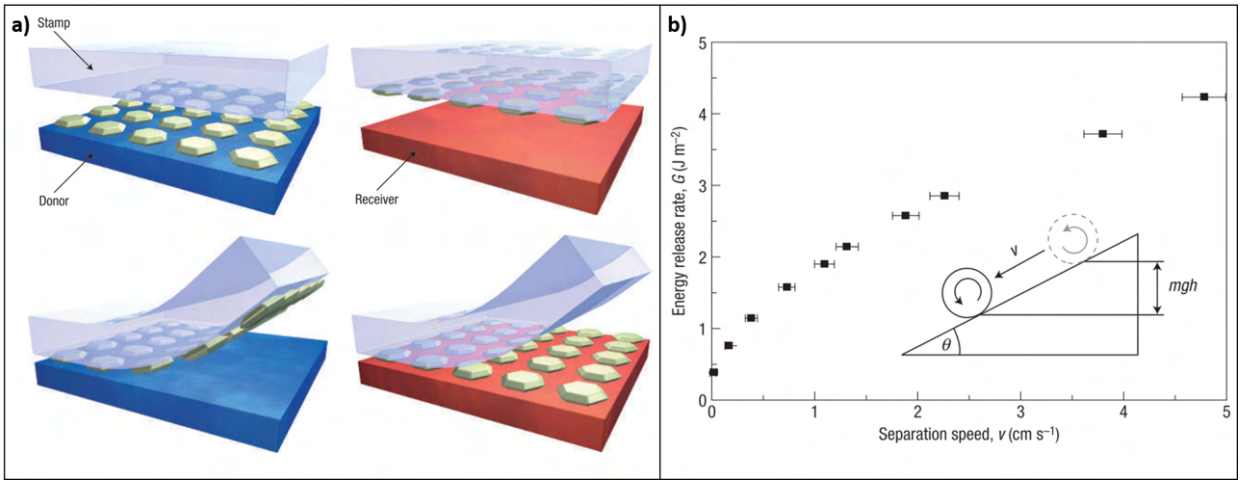

Figure 3.1: a) PDMS based transfer of generic solid devices from a donor chip (blue, fast peel) to a receiver chip (red, slow peel) by kinetically controlled peeling of the PDMS thin film, b) experiment demonstrating the speed-dependent adhesion of a steel cylinder rolling down an inclined plane covered with a PDMS thin film: The 'Separation speed' refers to the constant peeling speed of the cylinder's circumference that is reached in equilibrium at varying incline angles Θ of the plane. The energy release rate of the contact line is calculated from the length of the cylinder and the loss of gravitational potential. The cylinder adopts a constant speed exactly because of the speed dependent adhesion forces of PDMS: If the velocity increases from the equilibrium speed, the adhesion increases, slowing it down, and if the velocity decreases below the equilibrium speed the adhesion decreases allowing the cylinder to accelerate back till the adhesion balances the gravitational force. Therefore the measured energy release rate corresponds roughly to the adhesion strength of PDMS at a set peeling speed. Both a) and b) are adapted from [210].

A clever experiment with a steel roller is shown in Fig. 3.1 b), illustrating that the adhesion to PDMS can be kinetically varied by about one order of magnitude. In addition to the kinetic control, one might cool the donor and heat the receiver to enhance the asymmetric adhesion even further [210, 211]. The adhesion strength might also be permanently tuned by changing the ratio between curing agent and polymer base substance when mixing the PDMS precursors.

The adhesion to the polymer and its competing surfaces is generally thought to be dominated by short ranged dipole-dipole interactions caused by quantum fluctuations called van der Waals forces. These forces can become sufficiently strong to bond macroscopic devices together if their respective surface roughness is on the low end of the nm-scale and the contact area is sufficiently large, an effect extensively exploited in the field of 2D materials [210–214]. For surface separations on the 10s of nm to μm scale Casimir forces can become important and might play a role in the peeling process [214]. Casimir forces have been historically attributed to originate from the zero-point energy of the quantized electro-magnetic field, which nowadays seems to be doubted [214, 215]. Generally both van der Waals and Casimir forces are today assumed to originate from dipolar quantum fluctuations [214, 215].

Adhesion might additionally contain contributions from capillary forces caused by ambient humidity and electro-static forces induced by contact charge transfer [216].

3.1.2 Review: Transfer printing for photonic integrated circuits

Back-end targeted integration of photonic devices to non-native chip-platforms can be effectively facilitated using the visco-elastic properties of PDMS in conjunction with a white light microscope that operates in transmission, observing the donor and receiver substrates mounted below through a PDMS μ-stamp [91]. A μ-stamp generally refers to a microfabricated extrusion in PDMS that allows to target single devices. Multiple extrusions can be employed to print several devices with a given pitch in parallel [217]. Fig. 3.2 shows an overview of a generic transfer print process for a thin-film grown on a sacrificial layer [91]. For suspended devices like this the device adhesion to the donor surface is dominated by the chemical bond strength to the remaining epilayer, which competes with the van der Waals adhesion forces attracting the device to the PDMS stamp after contacting and during stamp retraction.

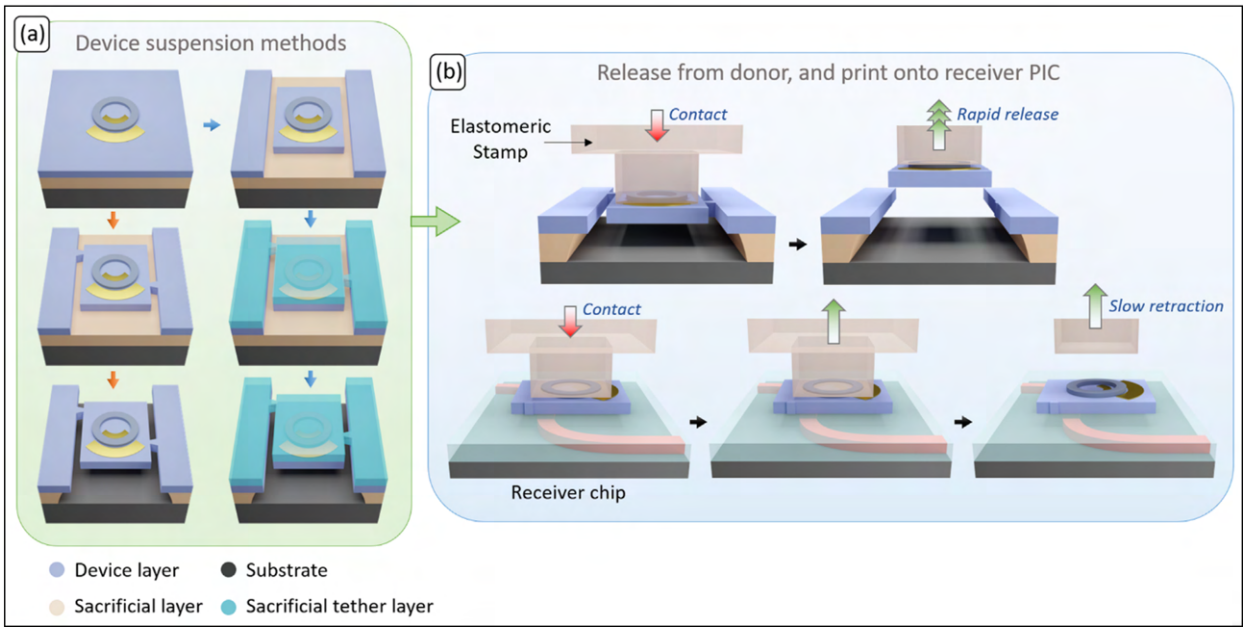

Figure 3.2: a) Generic suspension of a functional device from a semiconductor thin-film grown on a sacrificial layer that is released by wet or dry etching techniques, either with tether structures in the device material or a sacrificial tether layer that can be removed after the printing process is conducted, b) generic transfer print process using a PDMS extrusion stamp with fast retreat to capture the device after contact and slow release at the targeted surface, adapted from [91].

Many different device architectures have been successfully integrated with photonic circuits using pick-and-place techniques and two examples are shown in Fig. 3.3. In a) the integration of a III/V semiconductor laser with a silicon-on-insulator PIC is shown using vertical directional coupler (PDMS based μ-transfer printing) [206], while b) shows the impressive placement of a multitude of single photon emitters inside a diamond waveguide chiplet on a AlN-on-sapphire PIC (metallic probe manipulation in SEM) [93]. Recent review articles with more examples and alternative integration techniques in the context of integrated circuits can be found in [91, 197, 198].

Generally PDMS based μ-transfer printing decouples the fabrication processes on donor and receiver

substrates, reduces material waste and allows dense device integration [218] with potentially sub-μm placement precision in an automated way using techniques such as cross correlation based alignment marker detection [219]. Thus transfer printing can relax the difficulties arising from the larger device variety required to create high-end PICs compared to purely electrical ICs [69, 74, 91]. We will make use of the same advantages for the dense integration of high-aspect ratio GaN micro-lenses on polished SC diamond surfaces, avoiding damage to the diamond crystal caused by microfabrication techniques and increasing the potential integration speed compared to milled FIB lenses.

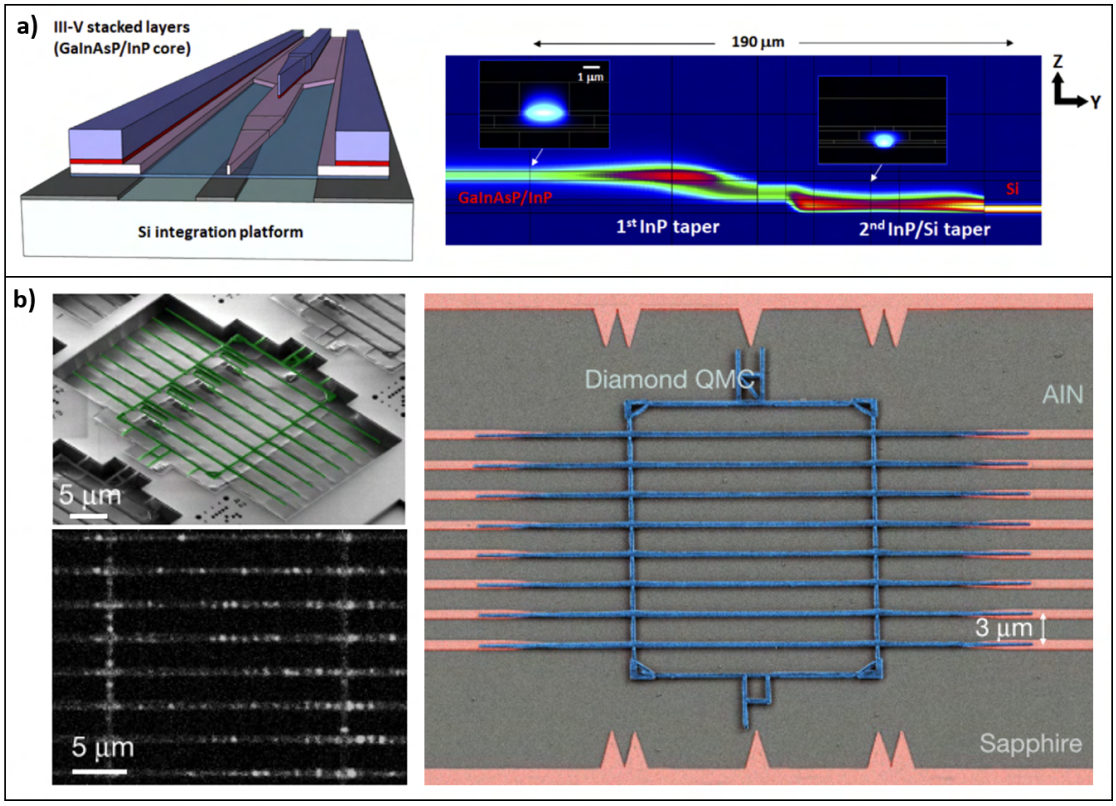

Figure 3.3: a) Integration of a GaInAsP/InP laser with an underlying SOI waveguide using vertical adiabatic coupling in a double taper geometry, the left images shows a schematic of the device and the right a cross section through the simulation of the light intensity showing the mode conversion between the waveguides, adapted from [206], b) (top left) SEM image of suspended diamond waveguides with tapered ends containing germanium (GeV) and silicon vacancy (SiV) centres with (bottom left) a PL map of SiV centres inside the diamond waveguides, and (right) the printed waveguide chiplet vertically coupled to tapered AlN-on-sapphire waveguides to optically address and read-out the colour centres, adapted from [93]

3.1.3 Review: Transfer printed GaN micro-LEDs

The GaN-on-Si micro-lens platelet fabrication and its placement on foreign substrates is based on the previously developed transfer printing of GaN-on-Si micro-LEDs [147, 220–222]. Fig. 3.4 illustrates a typical process flow and shows some electrically contacted devices on a flexible PDMS/PET (polyethyleneterephthalate) substrate after transfer printing [147]. Implementing micro-LEDs onto flexible substrates like this might be useful to create displays or visible light communication transceivers for wearable-electronics applications due to the micron-scale device foot print and high modulation band width facilitated by the low device capacitance [196, 202, 207, 221–223].
In this chapter we will discuss how the planar GaN micro-LED process flow is adapted with a modi-

fied layer stack containing unintentionally doped GaN instead of a quantum well structure to achieve high-aspect ratio micro-lens platelets.

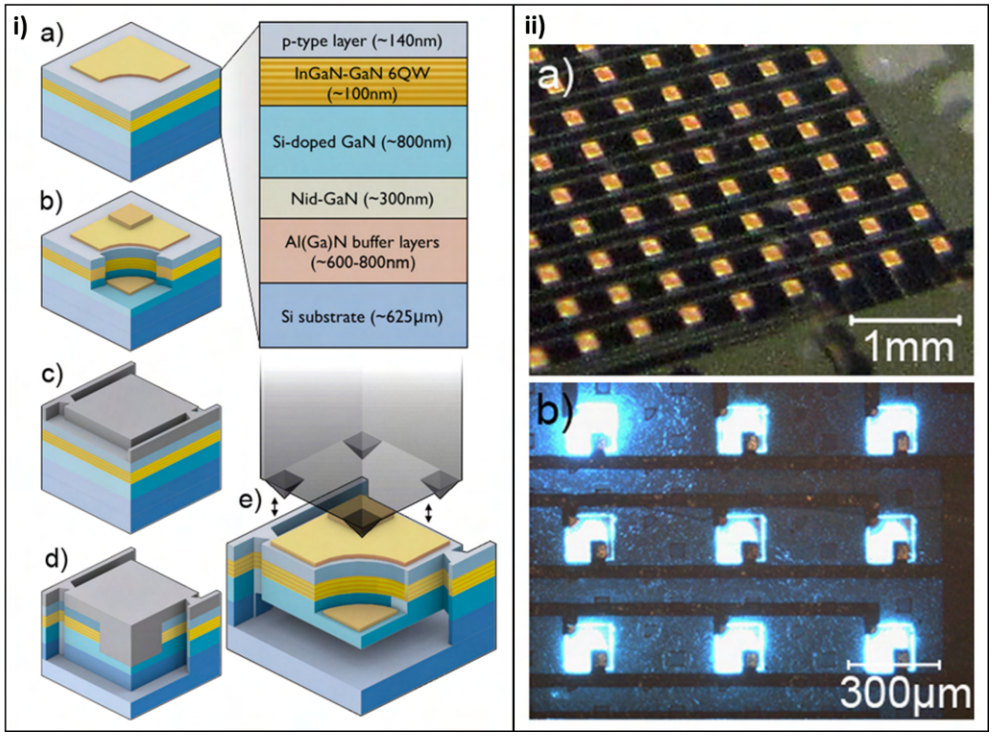

Figure 3.4: Fabrication and chip-scale integration of GaN micro-LEDs using PDMS based transfer printing, i) schematic showing the process flow with a)/b) electrical contacting, c)/d) device membrane vertical ICP etching to expose the Si substrate using a SiO_x hard mask and e) KOH based lateral Si removal for device suspension and successive hard mask removal, ii) a) photograph and b) microscope image of a transfer printed GaN LED array on a flexible PDMS/PET substrate with electrical contact lines. The operating devices is shown in b). The sub figures are adapted from [147].

3.1.4 Implementation in this work

Fig. 3.5 a) shows a schematic of the general transfer print process of suspended GaN micro-lens platelets. A modified commercial dip-pen lithography system with a 6-axis automated stage is employed, some photographs are shown in Fig. 3.6. In this tool the microscope column can be adjusted to the statically mounted μ-stamp using micrometer screws. As illustrated in Fig. 3.5 b) the sample stage is moved upwards to contact both donor and receiver substrate with nanometre scale closed-loop precision ($\Delta x/y = \pm 25\,\text{nm}$, $\Delta z = \pm 75\,\text{nm}$, $\Delta\phi/\theta/\alpha = \pm 4.4\mu\text{rad}$ [219]). The microscope objective used is 20x PLAN APO with long working distance imaging on a 1.4 megapixel CCD. The optical column has a zoom capability. We employ commercially available Sylgard 184 PDMS (6:1), which we shape into flat 30x30 μm^2 stamps with around 35 μm extrusion height compared to the bulk PDMS. The μ-stamp fabrication is described in detail in the Appendix.

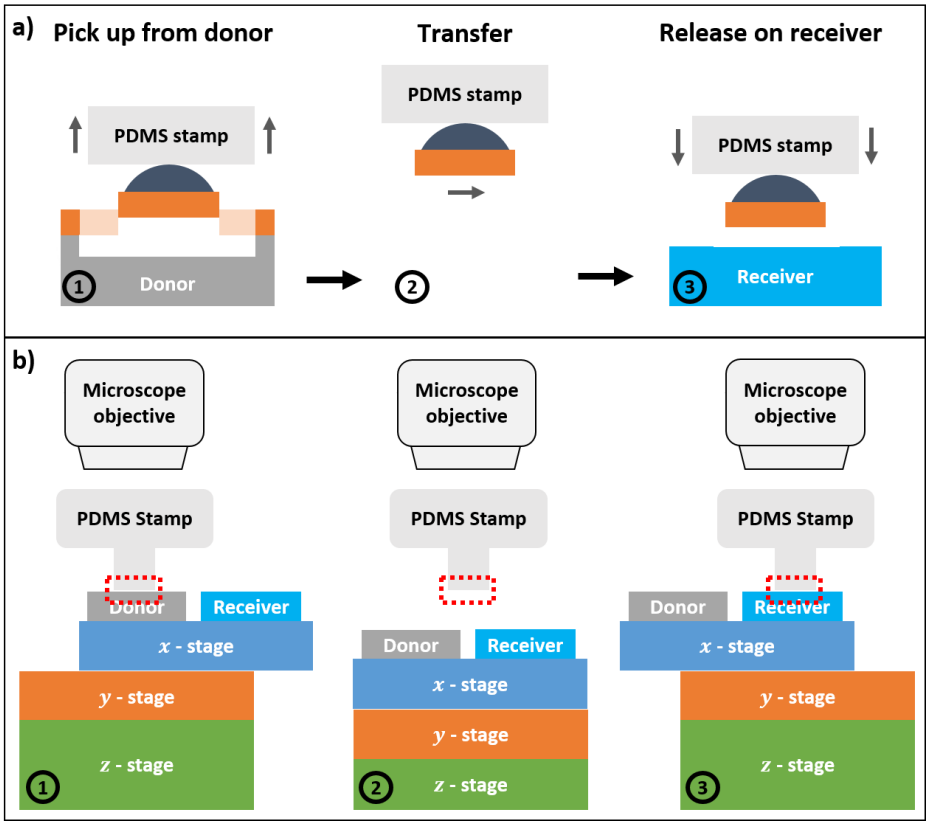

Figure 3.5: Schematics explaining the transfer-print method using PDMS-based polymer stamps. a) A suspended membrane device (in this case a suspended GaN micro-lens) is contacted with a PDMS μ-stamp, adheres to it durig a fast upwards movement and is placed on the receiver chip. Release can be achieved by slowly retracting the PDMS stamp relying on van-der-Waals bonds between the receiver top surface and the device membrane bottom surface, b) illustration of the stage movements in the particular system used in this work corresponding to steps (1), (2) and (3) in a).

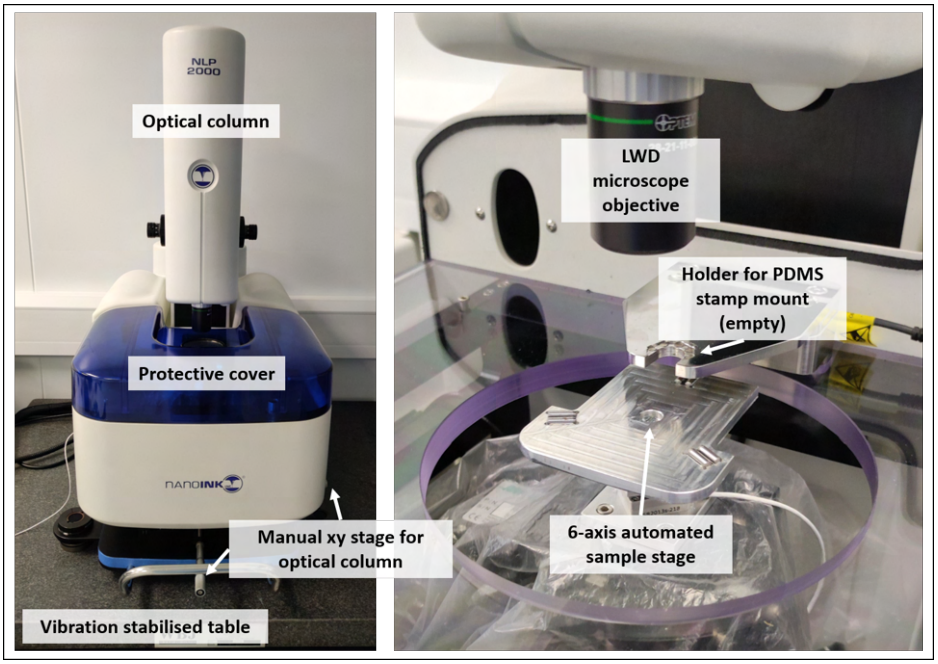

Figure 3.6: Transfer print tool used during this work. The commercial nanoink dip-pen system 'NLP 2000' is adapted with an additional 360° rotational stage (SmarAct).

3.2 Membrane device fabrication

In the following we will look into the micro-lens membrane processing which is a key achievement in this work. With micro-LED devices the flatness of the LED-membranes is not as crucial as for the application of GaN lenses to extract light from diamond colour centres and was not optimized previously. We therefore start with looking into the details of the GaN thin film growth process to gain some understanding of the forces that lead to wafer and membrane deflection due to stresses in the epitaxial thin film.

3.2.1 GaN-on-Si wafer and membrane bow

We are considering in-plane forces and the resulting bending moments in a stress analysis of the Si growth wafer and the GaN/AlGaN/AlN thin film grown on top. These forces and moments can lead to deformation of the initially flat growth wafer by the addition of the strained epilayer thin film as well as to the deformation of the released epilayer membrane devices in which we are ultimately interested [224].
As discussed in Chapter 1 and illustrated in Fig. 3.7 a) the difference in thermal expansion coefficients between GaN and Si induces tensile in-plane stress in the GaN thin film after cooling to room temperature. This stress usually leads to wafer deformation called wafer bow, which can cause thin-film cracking [151, 152, 224]. In this simplified picture of a stress-free as grown wafer at 1050°C we assume that the lattice mismatch between GaN and Si is fully relaxed by the introduction of dislocations into the thin film during growth, which is generally not the case [224].
The tensile stress between GaN and Si due to the mismatch in thermal expansion coefficient is commonly precompensated by the addition of an AlN/AlGaN buffer layer that induces compressive stress during the growth. The relaxed lattice constant rises from AlN over AlGaN to GaN, therefore the successive layers effectively pull those above inwards during the growth [95]. After cooling the overall bending moment exerted by the epilayer on the wafer system can then be close to zero, leading to crack-free wafers and reasonable wafer bowing, compare Fig. 3.7 b). This simplified explanation omits many of the intricate details of this thin film growth process, such as the formation of AlN nanocrystals at the Si interface in the AlN nucleation phase and dislocation progression during growth. The interested reader is referred to more specialized works [224].
But we are interested in the release of flat GaN/AlGaN/AlN thin film devices, and not necessarily flat growth wafers as long as the wafers do not crack during growth or the dislocation density is heavily increased. The Si substrate removal may release substantial stress exerted on the epilayer into strain, potentially leading to a completely new stress and momentum balance. Fig. 3.7 c) shows three different cases in a simplified illustration of how restoring forces in different parts of the thin film can cause bowing of the membrane after transfer printing on a diamond substrate. The position of the dotted 'bending' line can be understood as a geometric average of the individual layer thickness weighted by their respective Young's modulus [225]. The transfer print process might induce additional plastic deformation of the membrane, while the van der Waals adhesion forces might also be able to counteract small levels of bowing [226].

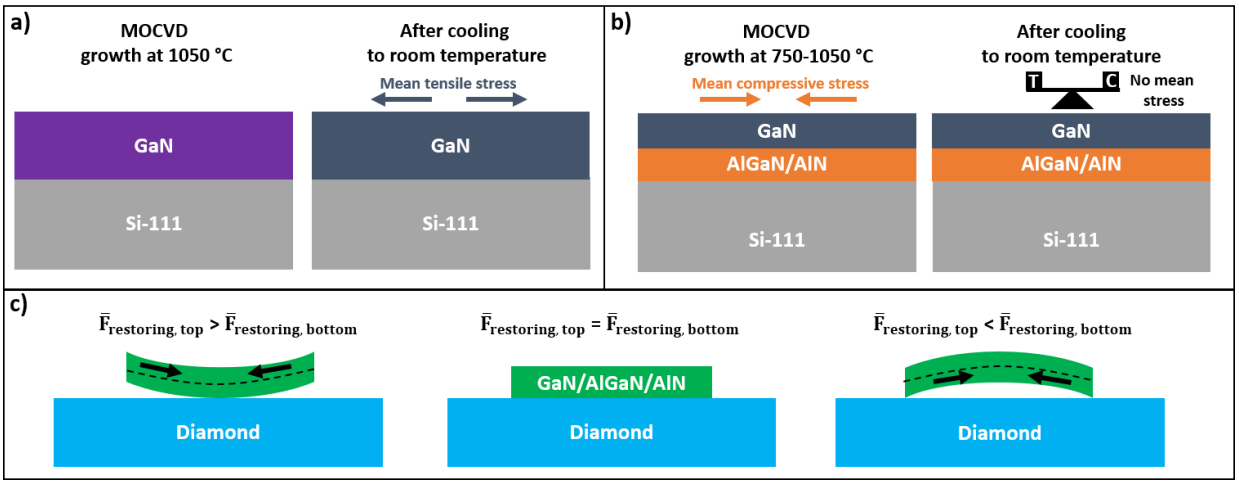

Figure 3.7: a) Schematics showing direct heteroepitaxial growth of GaN on Si substrates by high temperature MOCVD. The larger thermal expansion coefficent of GaN causes tensile stress in the epilayer after cool down. The arrows indicate the direction of the stress caused by the Si substrate, while the restoring force in the GaN layer would be directed in the opposite direction, b) schematics showing the effect of AlN and AlGaN buffer layer with stepwise or linearly increasing Ga content towards the GaN layer. Due to the rising lattice constant with decreasing Al content, compressive stress develops during the growth, with each successive layer trying to expand outwards while the seed crystal keeps the lattice in place. This counteracts the tensile stress caused by the cool down, potentially leading to a film with no mean stress that does not exert a bending moment on the full wafer system thus reducing wafer bow, c) schematics showing different cases for membrane deformation after Si substrate removal. $\bar{F}$ refers to the net in-plane restoring force above and below the 'bending' line of the membrane, leading to either concave, flat or convex membrane devices. We arbitrarily assign '-' to tensile forces and '+' to compressive forces and the 'bending' line position depends on the Young's modulus of the individual layers of the thin film [225].

A recent study found that the overall stress levels in GaN/AlGaN/AlN thin films specifically can be related to the wafer bow, with low bow indicating low overall stress levels [226]. But this is not a conclusion that can be generalized to other material platforms or growth methods: For example flat wafers after growth can yield heavily bowed thin films after release in principle, because opposite signs of equally strong net forces above and below the 'bending' line in the released epilayer can cause significant membrane bow, even if the resulting net force on the Si wafer before removal is negligible. This is because the 'bending' line shifts from inside the Si substrate to inside the epilayer after release. The same applies the other way around: A flat membrane after release might cause significant wafer bow, for example if the thin film is homogeneously stressed after growth, leading to the exertion of a bending moment on the wafer system and therefore wafer bow. But this stress might be relaxed into homogenous strain along the membrane thickness after substrate removal, yielding a flat thin film device.

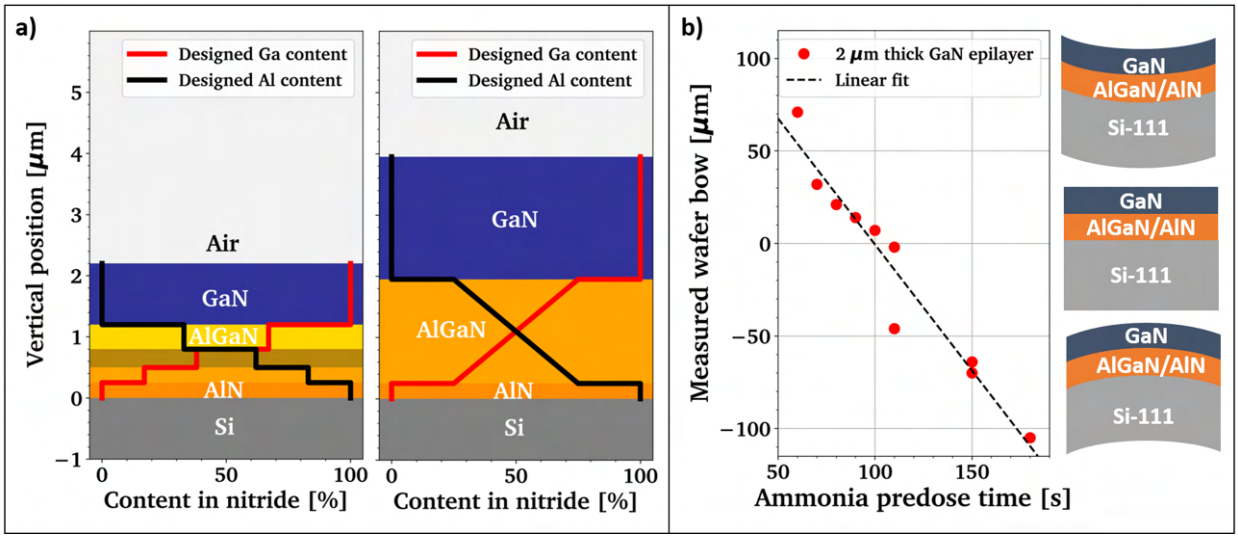

Figure 3.8: a) Schematics showing the different MOCVD epilayer of GaN-on-Si employed in this work, b) wafer bow optimisation by tuning the ammonia predose of the Si substrate immediately before the epilayer growth for the 2 μm thick GaN epilayer shown on the right hand side of a). This tuning of the wafer bow is used to balance the strain in the AlN/AlGaN/GaN epilayer to suspend flat micro-lens devices and indicates that the AlN nucleation on the Si substrate has a tremendous impact on the film properties.

Fig. 3.8 a) includes schematics of the two epilayer structures that are used in this work and are provided by the 'Cambridge Centre for Gallium Nitride'. The left structure is mainly employed for testing purposes with functional lenses being created from the right multilayer which consists of a 0.25 μm AlN nucleation layer, a 1.7 μm graded $Al_xGa_{1-x}N$ buffer with the AlN mole fraction x decreasing from 75% to 25%, and a 2 μm GaN layer, leading to a total thickness of ca. 4 μm nitride material. No intentional doping is used during the growth to create the highest possible optical quality material with low absorption coefficient. The film thickness is monitored during the growth by reflectometer measurements at both the wafer centre and close to the edge to ensure uniformity, which is found to be on the order of ±75 nm. The growers can also monitor the bowing of the wafer during growth [224] which allows them to gain insight whether the growth currently induces compressive or tensile stress. The more detail on the growth conditions can be found in [224]. Trimethylgallium (TMGa), trimethylaluminum (TMAl), and ammonia (NH_3) are used as the precursor gases and hydrogen (H_2) as the carrier gas with 1 mm thick p-type Si(111) substrates at 150 mm wafer diameter.

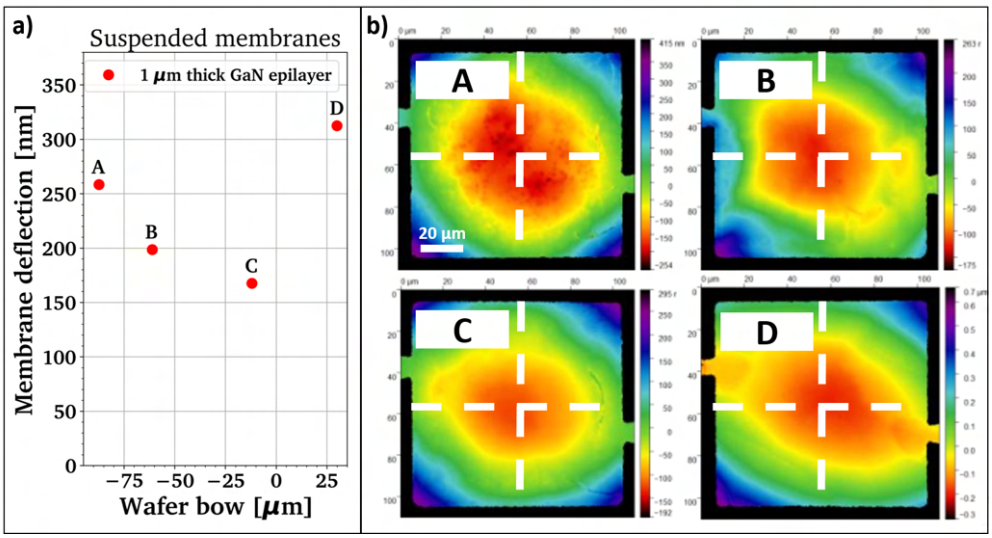

Figure 3.9: Data from a previous study on suspended GaN/AlGaN/AlN membrane deflection in dependence of the wafer bow after GaN-on-Si deposition. Minimal membrane deflection of the 100x100 μm^2 membranes is found close to minimal wafer bow. Therefore, we chose to work with optimised 2 μm GaN epilayer substrates exhibiting minimal wafer bow in the following (+7 and -2 μm on 6 inch wafers), hoping that this indicates low levels of stress in the membrane. Courtesy to Benoit Guilhabert and Miles Toon for providing this data.

Before the growth is started, the Si substrate is exposed to ammonia to prevent the Si etch-back effect, which is the release of Si into the epilayer creating unwanted n-type doping [152]. Fortunately for us, this process causes two things: First, it creates a disordered SiN_x interlayer at the bottom of the epilayer film [152, 227] which very effectively protects it from the chemical wet etch (KOH) that we apply to suspend the thin film devices from the Si growth substrate. This SiN_x interlayer is also extremely smooth with an r.m.s. roughness on the order of 0.4 nm which facilitates the van der Waals bonding between the GaN thin film devices and diamond. Both of these points are of crucial importance for this work. Data on the measured surface roughness on the backside of a suspended GaN/AlGaN/AlN membrane is provided in the Appendix.

Secondly, the time duration of the ammonia predose of the Si substrate is found to heavily influence the wafer bow as shown in Fig. 3.8 b). This effect has been linked by the growers to a reduction of edge type dislocation density in GaN observed by high-resolution X-ray diffraction spectroscopy, leading to overall increasing mean compressive stress in the epilayer tuning the wafer bow from concave to convex.

Earlier work on the membrane fabrication process with the pre-dose duration varying (without any lens fabrication) used a series of wafers in which a 1 μm GaN epilayer was grown on top of similar underlying buffer layers as shown here. These trials indicated that minimizing the wafer bow also yielded the least bowed membrane, compare Fig. 3.9. Based on this information we use material from two nearly-flat wafers with 2 μm GaN epilayer having respective bow values of +7 μm and −2 μm for the optimized micro-lens fabrication. We will find that the processing of the GaN/AlGaN/AlN thin film into micro-lens membrane devices crucially affects the device flatness as one would expect from the understanding developed in this section.

3.2.2 Optimized multilayer process flow: Example of 2x2 GaN micro-lens arrays

In the following we will discuss the optimized GaN micro-lens membrane device fabrication in detail. The full process flow including micro-lens fabrication (1-3), device suspension (4-11) and transfer printing (12-15) is shown in Fig. 3.10.

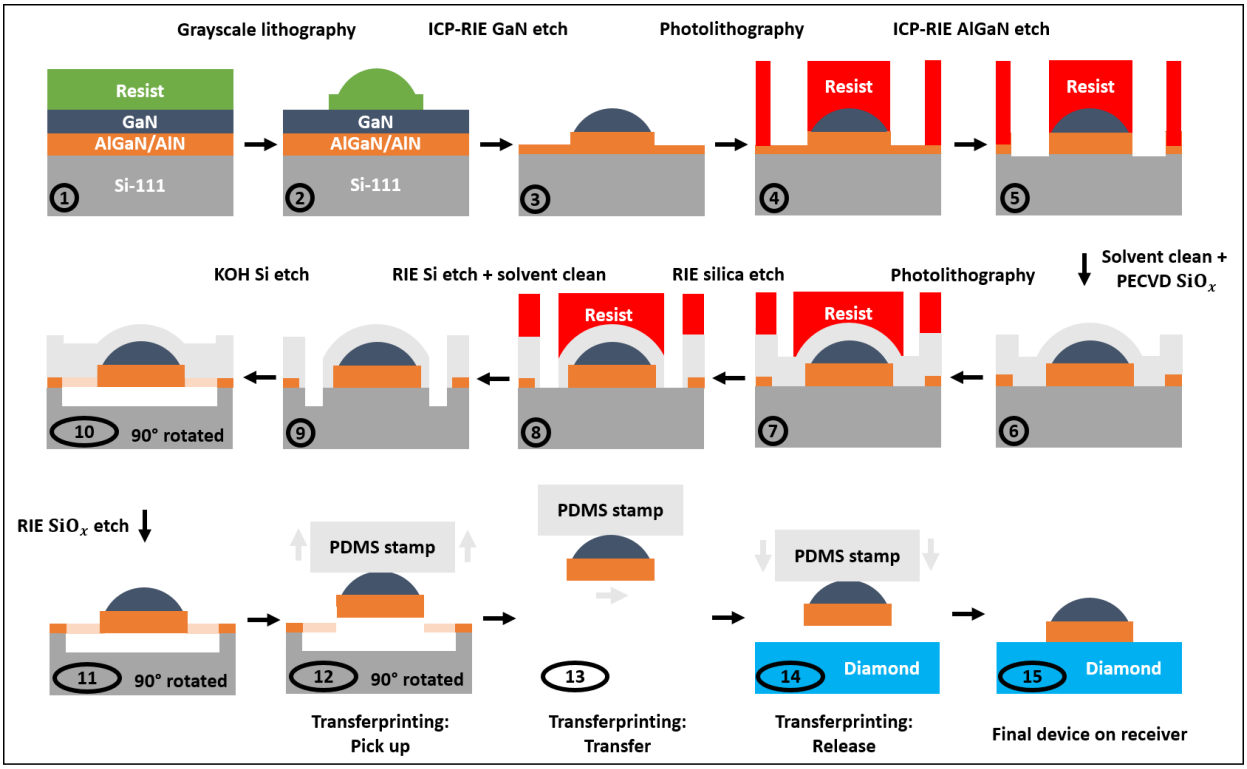

Figure 3.10: Detailed process flow to fabricate suspended GaN micro-lenses on AlGaN/AlN membranes followed by their transfer-print integration with a diamond substrate. This process is the result of careful optimization to protect the micro-lens during the KOH lateral Si etch that suspends the devices (9-10). The mesa around the lens (2,3) causes thinning of the surrounding epilayer which weakens the mechanical stability of the tethers that hold the device in step (11). Photoresists SPR220-4.5 (green) and SPR220-7.0 (red) are used in this process.

Before processing it is crucial to align the cut die towards the correct crystal orientation. We are interested in harvesting the fast anisotropic etch progression of potassium hydroxide wet etching along the (110) crystal plane in Si which is a vertical plane in our (111) Si substrates exhibiting a hexagonal symmetry if viewed from above. We are going to fabricate a trench based etch pattern that is aligned to one of the three equivalent (110) planes and therefore need to make sure that the wafer notch direction is transferred to each square die after dicing. We align two parallel edges of the substrate to one (110) plane and fabricate the pattern orientated towards these particular substrate edges.

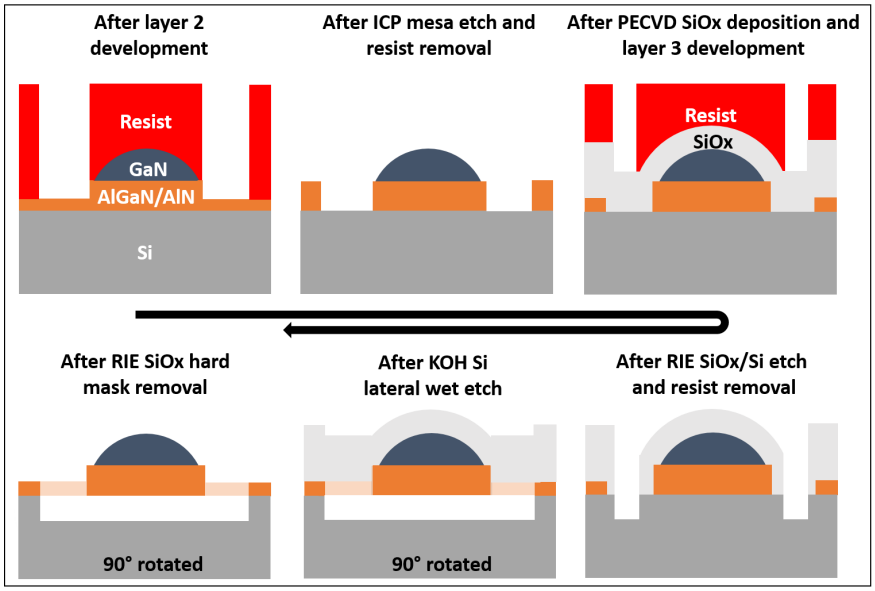

Figure 3.11: Example process: 2x2 micro-lens arrays. Schematics referring to the microscope images shown in Fig. 3.12.

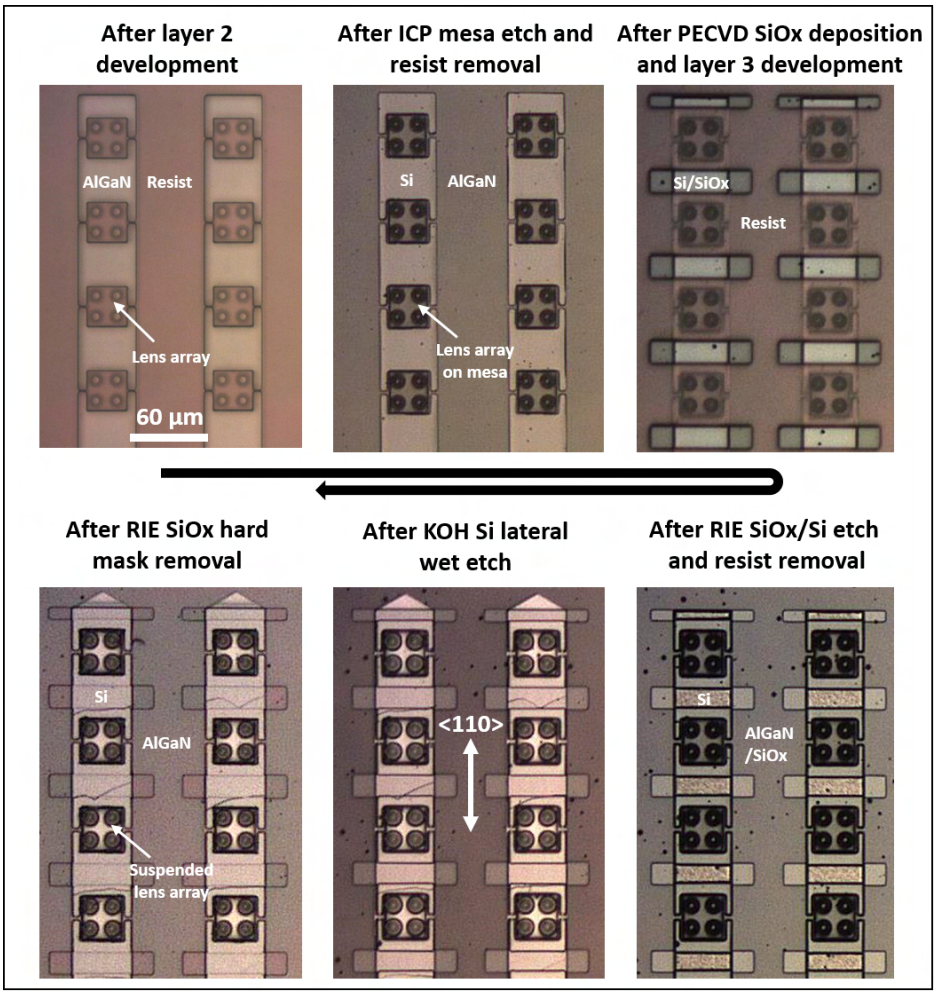

Figure 3.12: Example process: 2x2 micro-lens arrays. Microscope images corresponding to various stages between process step (4) and (11) in Fig. 3.10 with direct mapping of the images to the schematic shown in Fig. 3.11. The 2x2 micro-lens array fabrication on 30x30 μm^2 membranes is previously shown in Fig. 2.23. The scale bar applies to all images.

For completeness we add the experimental detail of the micro-lens fabrication whose general principles were discussed in the previous chapter. A wafer die is spin coated with 'Microposit SPR220-4.5' photoresist and micro-lenses are defined in the resist using grayscale lithography, leaving a bottom layer of resist unexposed (1,2). We use this effect to thin the membrane anchors to ease their break off during transfer printing. An Ar/Cl_2-based ICP-RIE (200 W coil power, 70 W platen power, 30 sccm Cl_2, 10 sccm Ar, 20 mTorr) is used to transfer the lens shape into the GaN (3). The ICP recipe yields etch rates of 200 nm/min for SPR220-4.5 and 155 nm/min for GaN/AlGaN, leading to a selectivity $s \approx 0.77$. The etch rate drops to around 120 nm/min for AlGaN with Al content $x > 60\,\%$ and in the AlN layer.

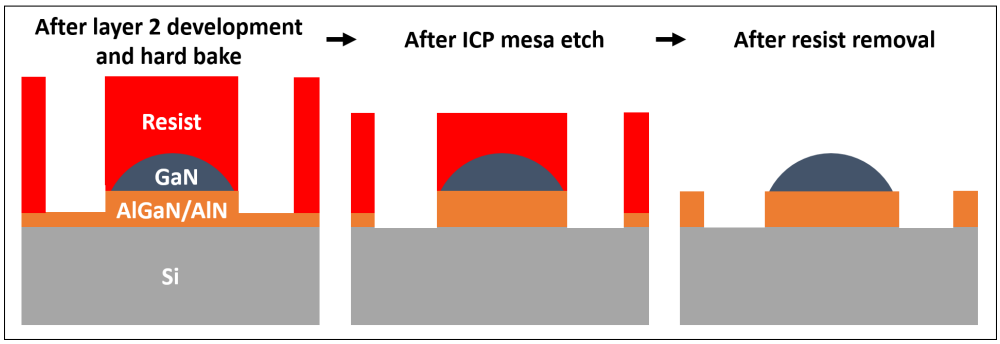

Figure 3.13: Example process: 2x2 micro-lens arrays. Schematics referring to the microscope images shown in Fig. 3.14.

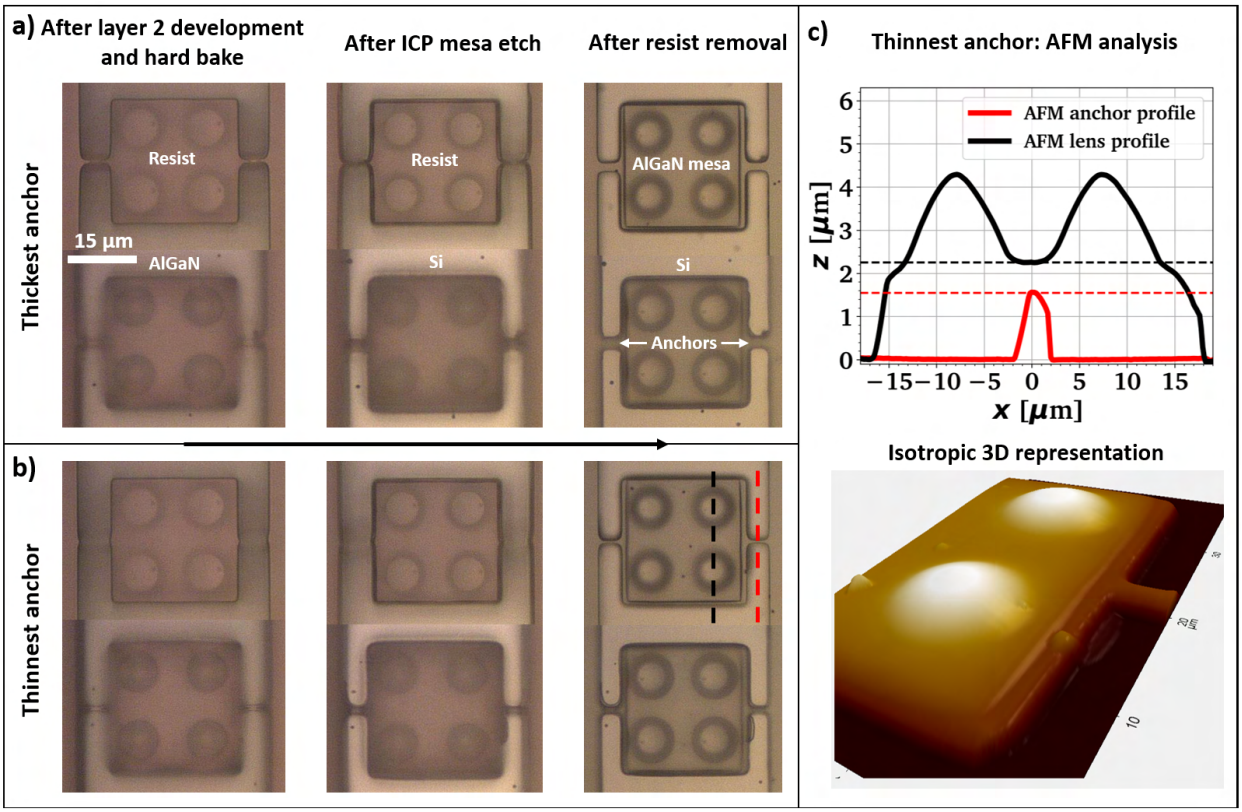

Figure 3.14: Example process: 2x2 micro-lens arrays. a,b) Detailed microscope images corresponding to process steps (4) and (5) with direct correspondence to the schematics shown in Fig. 3.13. The nominal anchor widths shown are 2.5 and 1.25 μm for the thickest and thinnest anchor respectively. After the ICP etch, the Si substrate is exposed between the membranes, c) AFM profile analysis of the thinnest anchor, showing ca. 4 μm total etch depth corresponding to the total epilayer thickness and revealing a several 100 nm thinner anchor.

We will now focus on the micro-lens membrane fabrication (4-11) using the example of 2x2 micro-lens arrays with 30x30 μm^2 membrane foot print. Fig. 3.12 contains microscope images during these steps to give an overview of the designed patterns with the corresponding schematics shown in Fig. 3.11. The defined GaN lenses are overlaid with a mesa pattern including suspension anchors using 'Microposit SPR220-7.0' photoresist. The previously detailed ICP-RIE recipe is employed to remove the remaining AlGaN and AlN layers, leading to a slight overetch into Si (4-5). Fig. 3.13 shows the corresponding schematics in more detail with matching a microscope images shown in Fig. 3.14 a), illustrating the etched anchor and mesa pattern defined in this processing step. The 7 μm thick photoresist is needed to successfully protect the GaN lens surface from the plasma, as about 2-3 μm resist is sacrificed during the etching and the spin coated resist is slightly thinner than the full 7 μm thickness over the protruding lens features. The AFM profiles in Fig. 3.14 b) show that the anchor is effectively thinned with respect to the rest of the AlGaN/AlN membrane that carries the GaN lenses. As shown the GaN micro-lenses are etched into the top 2 μm of the epilayer.

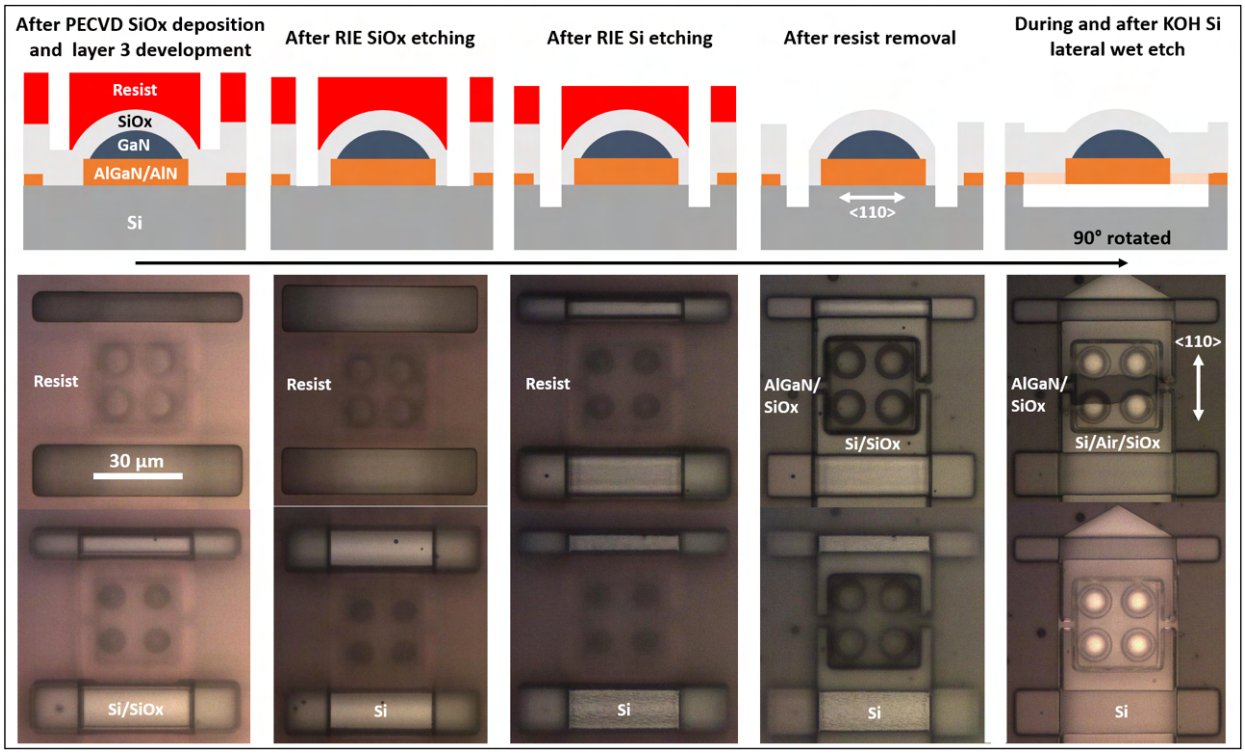

Figure 3.15: Example process: 2x2 micro-lens arrays. Microscope images referring to processing steps (6-10). SPR220-7.0 is used to open windows between PECVD overgrown membranes to etch a trench into the Si substrate which directs the KOH wet etch effectively, while protecting the membrane and lens. In the most right hand side image, the SiO_x hard mask is still present, additionally stabilizing the device mechanically. The scale bar on the left hand side corresponds to all images.

After resist removal, a conformal layer of ca. 2.0 μm thick SiO_x is deposited in step (6) by plasma enhanced chemical vapor deposition (PECVD, 70 W RF power, 170 sccm SiH_4, 710 sccm N_2O, 1 Torr, $T = 300\,°C$). This hard mask protects the GaN lens from the potassium hydroxide (KOH) wet etch in step (9-10), with thinner layers demonstrating susceptibility to local failure and subsequent chemical etching of the micro-lens features. Detailed microscope images with corresponding schematics of this and the following processing steps are shown in Fig. 3.15. SPR220-7.0 is used as a lithography mask to open windows at the bottom of the etched trenches and carefully dried to avoid resist carbonisation

during plasma exposure (7). The SiO_x hard mask is then patterned using reactive ion etching (RIE, 120 W RF, 5 sccm CHF_3, 15 sccm Ar, 30 mTorr) in process step (8), followed by etching 3 μm deep into the Si substrate (50 W RF, 100 sccm SF_6, 8 sccm O_2, 25 mTorr) exposing the (110) plane surface plane on the sidewalls towards the membrane devices. Successively the resist is removed by solvent cleaning (9). The resultant trench allows the KOH wet etch solution (40 % in weight, 85 °C) to access the (110) crystal plane, selectively removing the Si below the lens-mesa along the fast <110> etch direction (10) with the detailed etch progression shown in Fig. 3.15 on the most right hand side. The schematic is here rotated indicating the anchors as semitransparent areas and showing the anisotropic nature of the KOH etch in Si-(111). As confirmed in previous studies by scanning transmission electron microscopy [227, 228], a nm-thin disordered $AlSi_yN_x$ interlayer is formed between Si substrate and AlN nucleation layer, which provides an effective bottom protection against the KOH solution. The smoothness of the mesa bottom surface after KOH etching is confirmed by atomic force microscopy (AFM) measurements after flipping a flat suspended membrane device with a PDMS stamp, yielding 0.4 nm r.m.s. roughness.

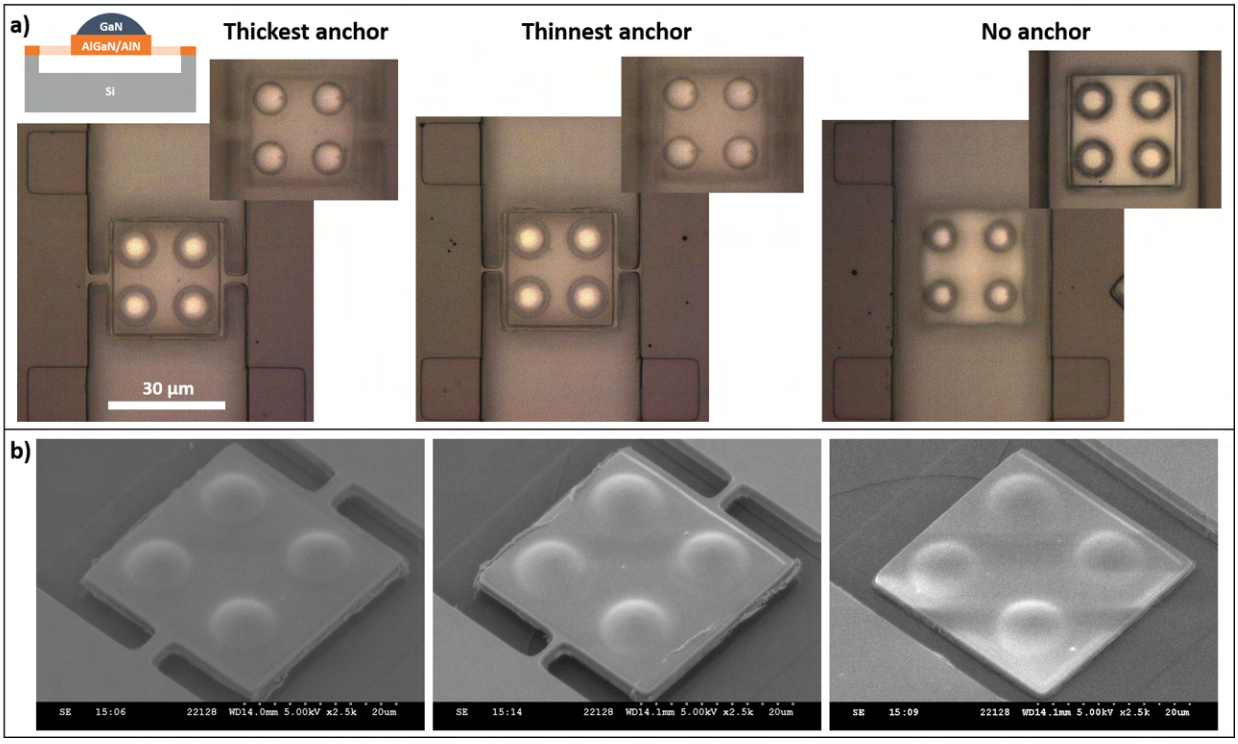

Figure 3.16: Example process: 2x2 micro-lens arrays. Finished donor fabrication (11) with a) microscope images and b) tilted SEM images (40°) for the thickest and thinnest anchor, as well as a device without anchor that collapsed on the Si substrate. The scale bar in a) applies to all images.

Finally, the SiO_x protection layer is removed by RIE dry etching (5 sccm CHF_3, 15 sccm Ar, 30 mTorr, 120-200 W RF-power) to restore the GaN lens surface (11). Microscope and SEM images of the finalized devices shown in Fig. 3.16. AFM surface roughness analysis on a single GaN micro-lens after SiO_x removal show a r.m.s. roughness on the order of 1.4 nm (device generated by grayscale prehaping and resist reflow, data shown in the appendix). As a beneficial side effect the SiO_x protection layer holds the devices firmly in place during the suspension etch. We exploit this in order to fabricate devices without any anchors as shown on the right hand side of Fig. 3.16. Unfortunately such devices can flip during the hard mask removal, reducing the yield for anchor-free devices significantly (near 100% yield with anchors vs. $\approx$ 62% without anchors for membrane array devices with 30-60 μm edge length).

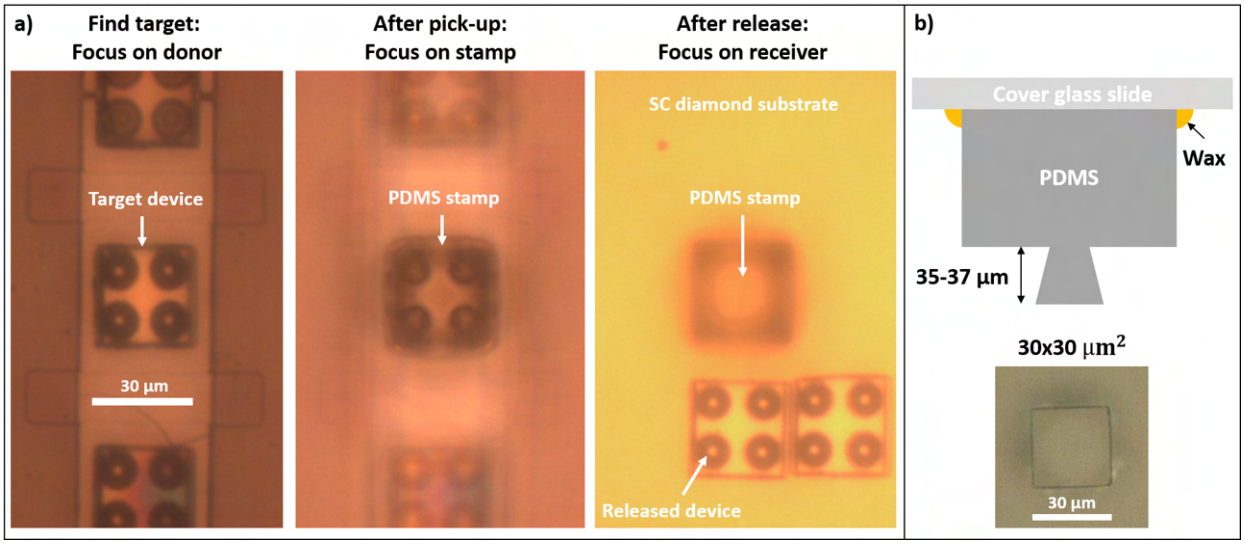

Figure 3.17: Example process: 2x2 micro-lens arrays. a) In-situ microscope images during transfer print integration with a single crystalline diamond sample as in process step (12)-(15), the scale bar applies to all images, b) schematic and image of the μ-stamp design generally used for transfer printing of GaN micro-lens devices.

We now turn to the transfer printing based integration of the micro-lens platelets to polished single crystalline diamond substrates with r.m.s. surface roughness on the order of 0.5 nm (12-15), the roughness data is included in the appendix. The lenses are removed from their growth substrate using a soft polymer stamp fabricated using a 6:1 ratio Sylgard PDMS with a contact area of 30x30 μm^2 and fast retraction speed after firm contact with the device (12). Unfortunately we find that most anchors are still too stiff to allow a device release, something that might be solved in future runs by adding only a single anchor. We therefore focus on the devices without any attached anchors.

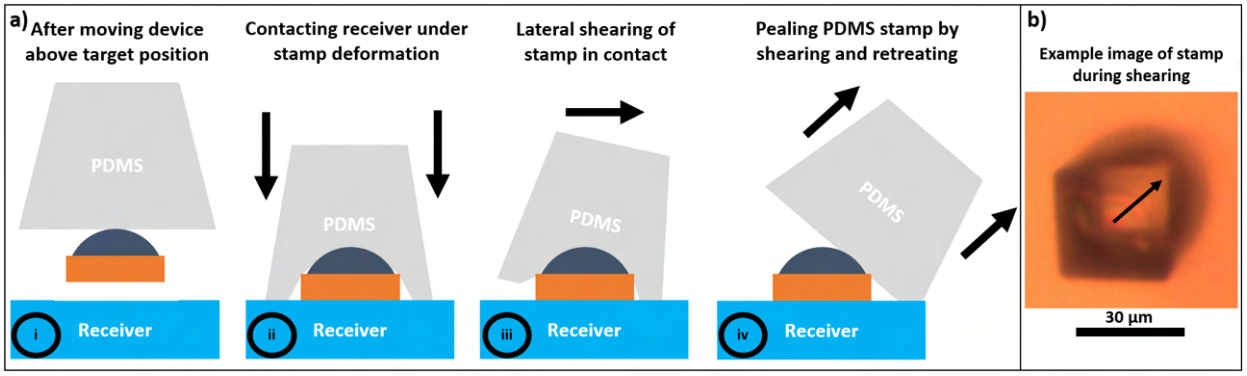

Figure 3.18: a) Schematics explaining the shear printing which proved to work very effectively with suspended GaN micro-lens devices, b) in-situ microscope image the stamp being sheared laterally (iii) after pushing receiver (Diamond) and device (AlGaN) into contact (ii). As can be seen, the μ-stamp surface adheres at least partially to the surface, while the μ-stamp connection point to the PDMS bulk piece moves laterally, generating a shear force slowly peeling the PDMS off the receiver and device.

The micro-lens membrane chiplet is then transported to the receiver substrate (13) and aligned to a target position (14), relying on the adhesion strength of the smooth membrane bottom and diamond top surface created by van-der-Waals interaction (15). Fig. 3.17 documents the transfer printing process step-by-step, while the schematic in Fig. 3.18 illustrates the shear-release technique that was successfully

employed with GaN micro-lens devices throughout this work. It relies on the weakened adhesion forces of PDMS during slow retraction in addition to a successive peeling of the stamp surface from the device surface, which allows to release the devices without noticeable lateral movement.

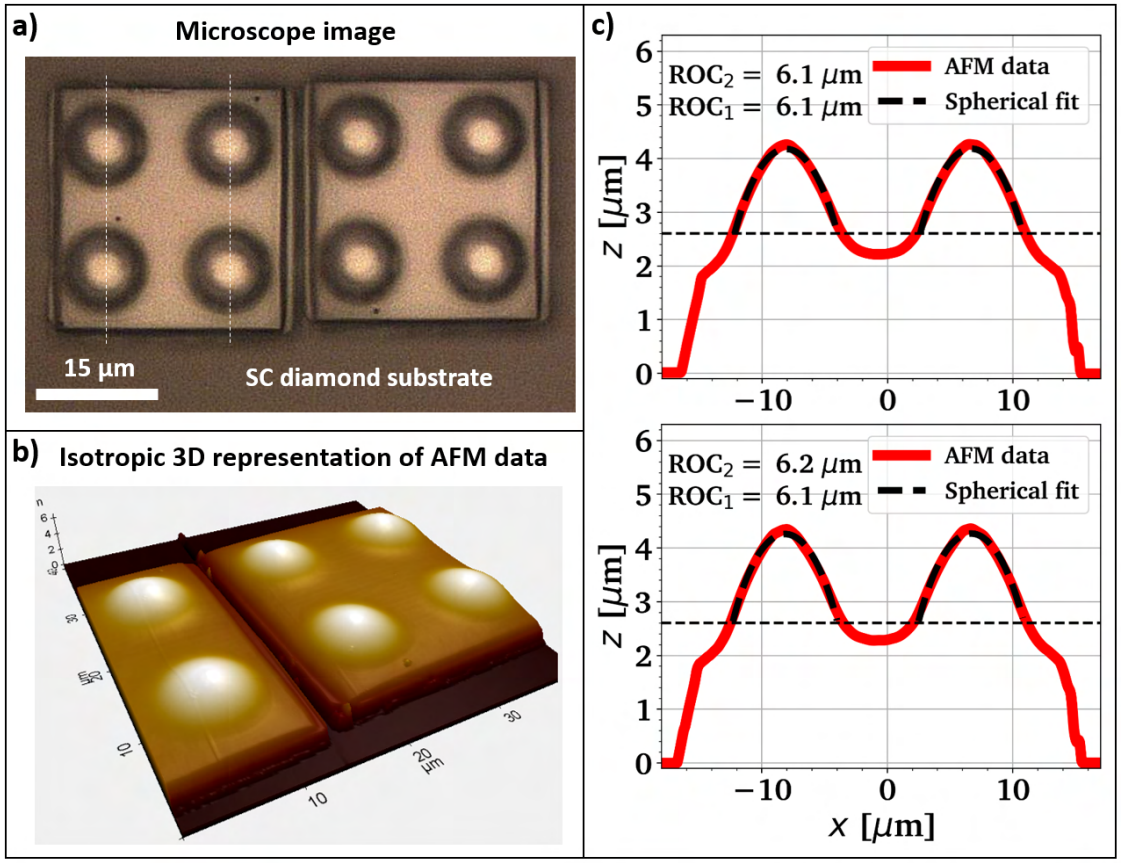

Figure 3.19: Example process: 2x2 micro-lens arrays. Detailed analysis of printed arrays on a single crystalline diamond substrate. a) Microscope images indicating the AFM profile lines, b) real scale 3D AFM representation and c) fitted line scan data of the printed lens arrays (SSS-NCH).

Microscope images and AFM scan data of transfer printed GaN-micro-lens arrays on diamond are shown in Fig. 3.19. The absence of any colour fringes in the microscope images in a) indicate an air-gap free contact between GaN micro-lens devices and diamond, while the AFM profile scans show that the surface quality and shape is maintained after the printing process is completed. The power of integrating multiple micro-lenses on one membrane lays in the reduction of printing processes needed, potentially yielding arrays of closely spaced GaN micro-lenses on diamond.

A larger scale study with printed GaN lens arrays on diamond is shown in Fig. 3.20. Here we compare devices without (left, red) and devices with anchors (right, blue). To facilitate the device release of the devices with anchors we break these with a contact mode AFM cantilever mounted in the transfer print tool and then pick the devices afterwards with a PDMS stamp (microscope images contained in appendix). For the devices in Fig. 3.20 we can see that 2 out of 6 lens arrays without anchors exhibit color fringes, while all 6 devices with anchors show coloration, indicating the presence of a significant air-gap on the order of $> 100\,\text{nm}$ between the membrane device and the diamond surface. Even though frustrated total internal reflection might still be possible, such an air gap is expected to degrade the lens performance if photons from an NV centre are to be extracted from the diamond substrate. This experiment shows that the usage of anchors, especially thinned ones, seem to prevent good contact to

the diamond substrate because they might be strained and buckle downwards. So far the yield of the full suspension process and hard mask removal has been near 100% only for anchored devices, leaving room for further optimization.

A potential solution for this yield problem is the pick-up of anchor-free GaN micro-lens devices while the SiO_x mask is still present, mechanically stabilizing the devices. The final removal of the hard mask could then be conducted after printing release on diamond by exposure to a reactive ion etcher. Alternatively a quarter wavelength thick ($\approx 70\,nm$) high quality SiN_x/AlN_x layer could be applied to the GaN lens device before depositing the SiO_x hard mask. Then the SiO_x layer could be removed on the donor substrate after suspension while the SiN_x/AlN_x mask could mechanically stabilize the device till pick-up and then serve as an anti-reflection coating further enhancing the micro-lens performance [229].

We now turn to some key insights that facilitated the development of the optimized process flow described in this Chapter.

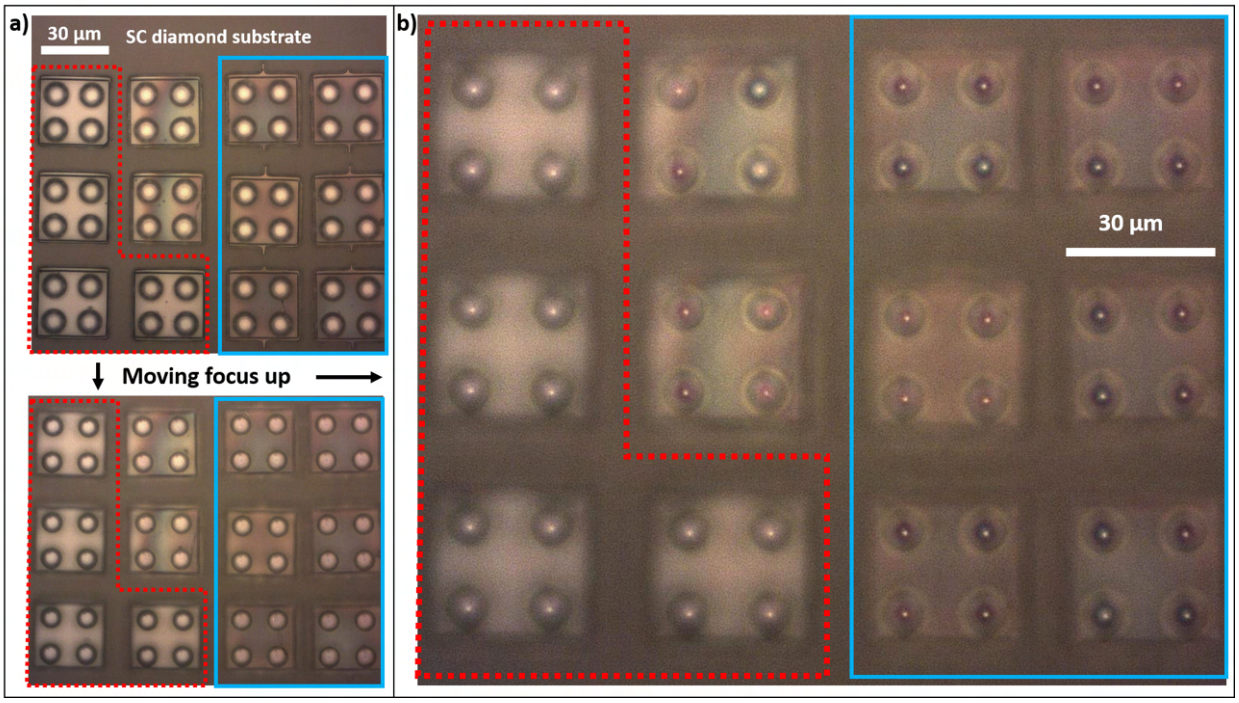

Figure 3.20: Transfer printed GaN lens arrays with similar AlGaN/AlN membrane thickness (same total laser power) without (left) and with anchors (right). 4 out of 6 devices without anchor seem to exhibit good contact with the single crystalline diamond substrate below (red), while 2 exhibit colour fringes potentially due to debris (unmarked). All six devices with anchors were broken off with the AFM cantilever prior printing (see appendix) and exhibit significant colouring after print integration, suggesting that the anchor points prevent a full device contact (blue).

3.2.3 Milestone: Suspension yield and micro-lens protection

A crucial part of fabricating suspended GaN-on-Si membrane devices is

- the preparation of a (110) Si plane to guide the KOH suspension etch without termination
- the protection of the GaN/AlGaN/AlN membrane which is attacked by the KOH solution

The standard μ-LED suspension process developed in previous work [147, 220–222] is illustrated on the left hand side of Fig. 3.21. A usually 2-4 μm thick epilayer is protected by a PECVD SiO_x hard mask

after trench etching that exposes the Si substrate. Due to the flat device architecture thin photoresist (Microposit S1805, ≈ 500 nm thickness) can be used to pattern the trench and the high aspect ratio of the sidewalls generates pinch-points at the bottom of the nearly vertical sidewalls which allows the KOH solution to access the (110) plane effectively after a few seconds of SiO_x removal.
In the optimized GaN micro-lens process flow discussed above this is achieved by a second lithography step, because we find that the standard μ-LED process stops to work effectively if the epilayer thickness is roughly $< 2\,\mu$m and μm-thick photoresist is used for the trench etching. Thick photoresist generally suffers from significant positive sidewall slope, which is suspected to additionally mitigate the pinch point formation. Three different potential strategies to suspend thin epilayers are shown on the right hand side of Fig. 3.21, of which we tested the two most right approaches in different geometries. Detailed information about the systematic studies conducted can be found in the appendix.
The thickness of PECVD hard mask needed to protect the lens during the KOH suspension etch depends on the size of the membrane device and the selectivity between Si and the hard mask. For PECVD SiO_x usually around $1-2\,\mu$m thickness are needed to survive the under etch process of membranes with $10-30\,\mu$m edge length. Therefore a thin epilayer with a shallow trench etched into Si is expected to yield conformal mask built up preventing the KOH to effectively penetrate the hard mask at the bottom of the trench. This is illustrated in the second schematic in Fig. 3.21.

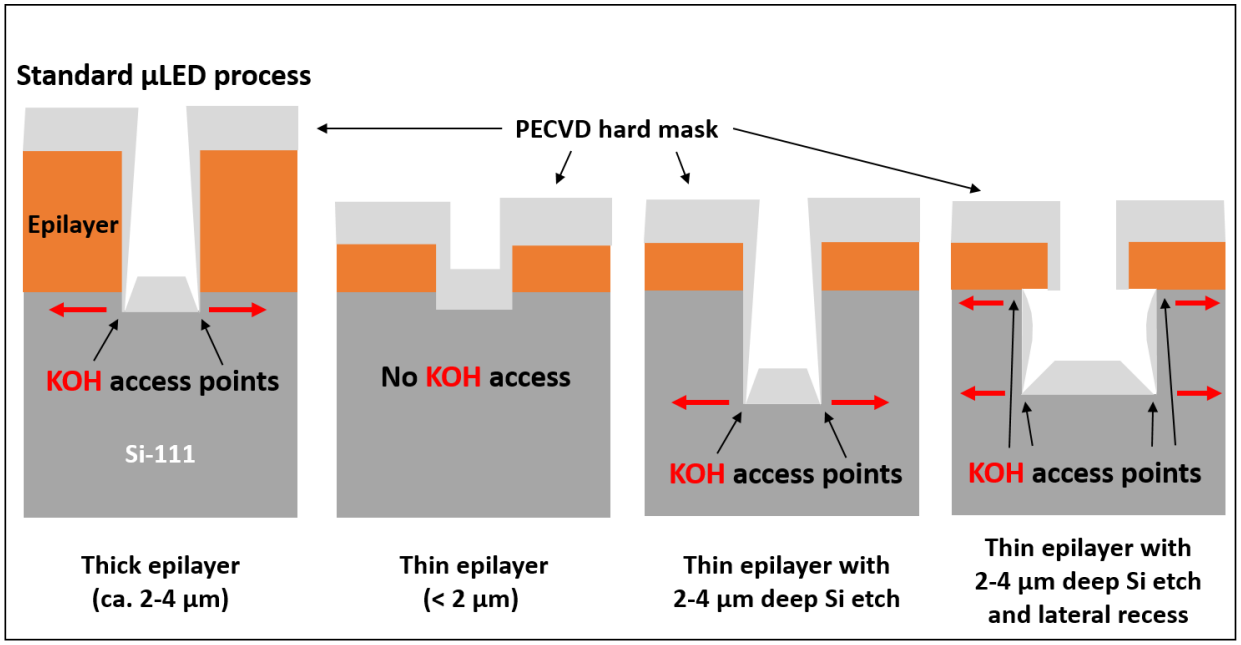

Figure 3.21: Discussion of membrane protection and KOH access if the same trenches are used for. Schematics explaining variations of epilayer thickness and Si etch depth with constant hard mask thickness, the later depending on the size of the membrane that is to be suspended. The most right schematic indicates the use of an isotropic Si RIE step.

Fig. 3.22 contains the results if a thin AlGaN membrane is overlayed by $1\,\mu$m PECVD SiO_x after $2\,\mu$m deep Si trench etching in a single lithography step with thick photoresist and ICP etching used to define the lens mesa. The suspension works, but the lens and membrane gets attacked by the KOH solution and the suspension yield is low, probably due to terrace forming and self termination (ca. 30%). The positive sidewall slope caused by the thick photoresist used is suspected to contribute to this effect, but thin resist cannot be employed as it would leave the GaN micro-lenses unprotected during the

AlGaN/AlN mesa etching.

We also test lateral recess etching into the Si substrate below the membrane using isotropic RIE etching corresponding to the most right schematic in Fig. 3.21. The detailed process flow is shown in Fig. 3.23. The aim of the recess is to avoid the accumulation of the hard mask at the Si sidewalls immediately below the membrane to allow KOH access, which proved to work well in terms of suspension yield for various thicknesses of SiO_x and SiN_x hard masks (see appendix). But unfortunately the approach undermines the device protection. In Fig. 3.24 we show results using a PECVD SiN_x hard mask instead of SiO_x hoping that it would persist longer in the KOH solution.

The SEM images indicate that indeed the SiN hard mask can indeed sustain the exposure to the KOH solution well, but it seems that the mask is too porous to protect the underlying lens devices, leading to their destruction. Alternatively or additionally the systematic study shown in the appendix indicates that the isotropic Si recess etch could actually remove the protective SiN_x bottom layer of the GaN/AlGaN/AlN membrane device, allowing the KOH solution to access the devices from the bottom, which leads to heavy membrane and lens etching in the KOH solution. But we note that this effect is stronger the deeper the micro-lens is etched into the epilayer. So the reduction of the micro-lens etch depth to 2 μm also contributes to the overall device protection. We provide additional data on the systematic testing of the micro-lens protection and these fabrication results in the Appendix.

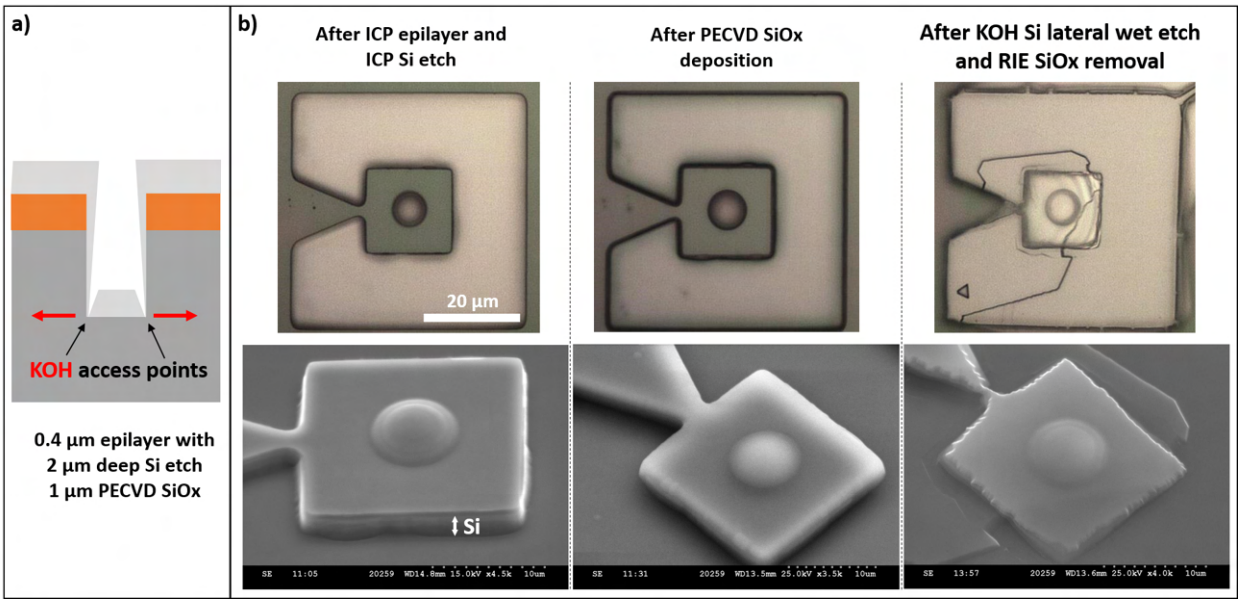

Figure 3.22: Case 3: Thin epilayer and deep anisotropic Si etch using the GaN-on-Si material shown on the left hand side of Fig. 3.8 a). a) Schematic of the epilayer corresponding to the shown microscope and SEM images (40° tilt) of processed membranes in b). SPR220-4.5 was applied to both define the membranes and lenses. The scale bar applies to all three microscope images.

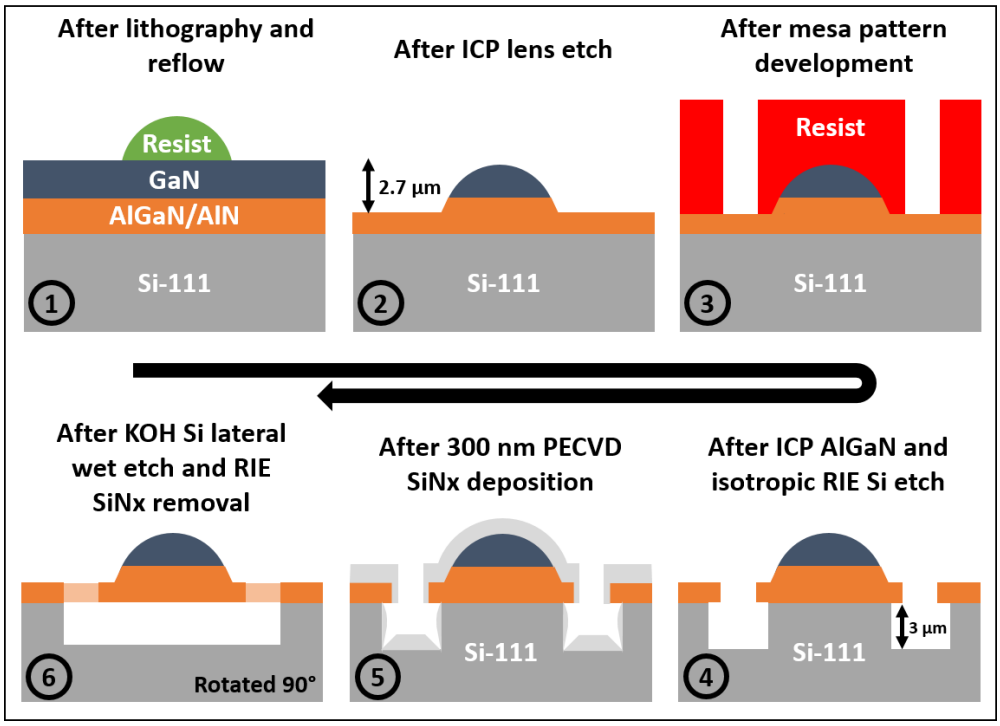

Figure 3.23: Process flow for test of Si recess etch with SiN hard mask and optimized epilayer stack (-2 μm wafer bow, 2 μm thick GaN epilayer). Lenses are fabricated from SPR220-4.5 (green) and platelets are formed with SPR220-7.0 (red).

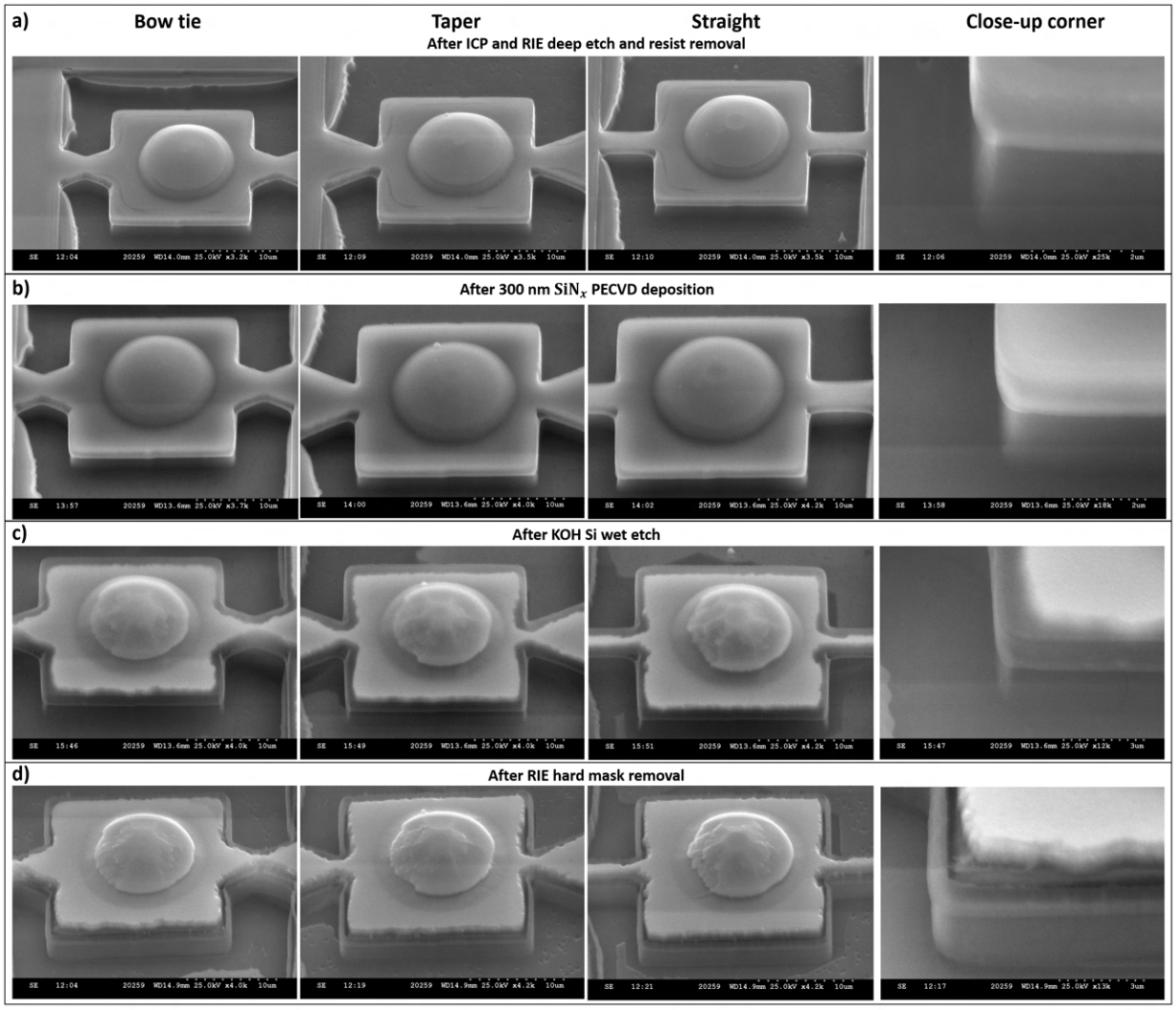

Figure 3.24: Test of Si recess etch with SiN hard mask and optimised epilayer stack (-2 μm wafer bow). Tilted SEM images (40°) of the three different anchor geometries for the smallest anchor width (3 μm) and lenses with 16 μm nominal diameter, after a) Si deep etch (4), b) SiN_x deposition (5), c) KOH lateral Si etch for device suspension and d) removal of the remaining SiN_x hard mask with RIE (6). The same device is imaged in each column after the respective process step.

As already indicated in the optimized process flow shown in Fig. 3.10 the suspension yield and device protection issues are solved by the addition of a third lithography step. This step is used to etch trenches into the Si substrate after the membrane mesa etch that removes the remaining buffer layer. This then leaves a several μm thick SiO_x buffer layer between the KOH access point and the membrane device. The process flow that worked for the first time is shown in Fig. 3.25 a) with b) containing a top view of the devices after suspension and hard mask removal, indicating the fast <110> KOH etch direction. For these particular devices the SiO_x was removed in step (4) using a buffered oxide wet etch, which proved to be unreliable in later trials and was replaced by RIE etching.

Fig. 3.26 contains some SEM images after various processing steps. This simple added separation between the KOH access point and the membrane device proved to allow micro-lens membranes suspension with high yield while protecting the GaN micro-lenses from the KOH solution, even though membranes and anchors are still attacked by the KOH. The high yield of this process flow is indicated in Fig. 3.27 with more detailed data shown in the Appendix.

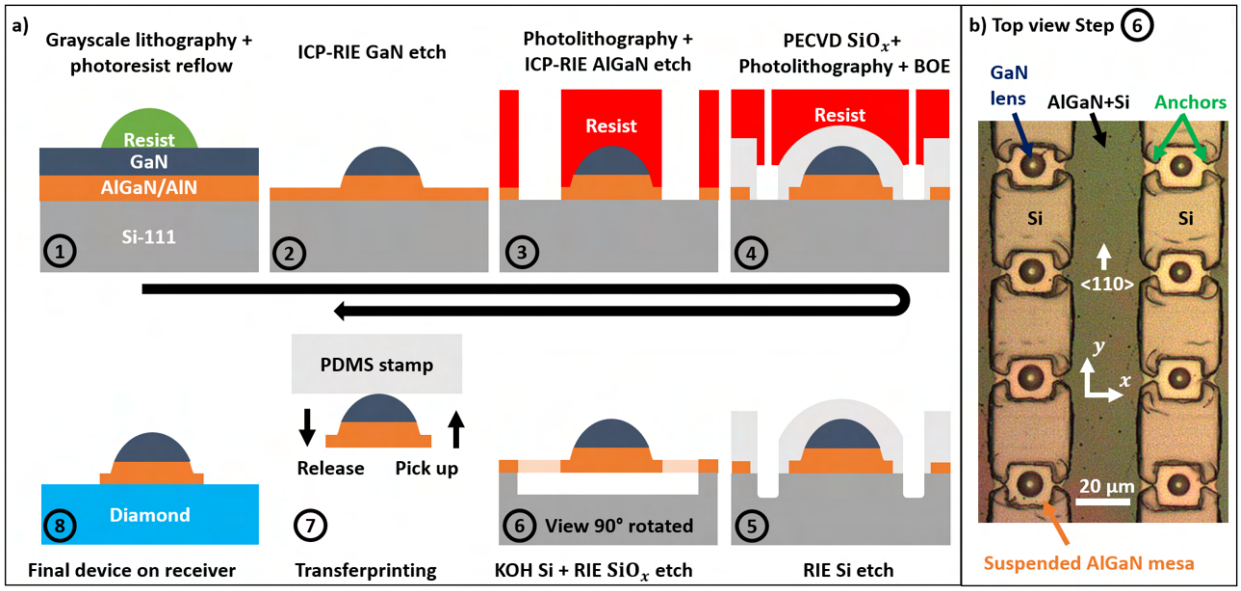

Figure 3.25: 1st fabrication with conserved GaN lenses after suspension and hard mask removal. a) Schematics of the process flow. The key change appears in step (4) with adding an extra layer of SiO_x protection to the sidewalls of the membrane devices. For lens fabrication SPR220-4.5 is used (ca. 3 μm etch depth in the μm thick epilayer), while both layer two and layer three (3,4) are formed with SPR220-7.0, b) microscope image showing the successfully suspended GaN micro-lenses on square platelets, using tapered anchors.

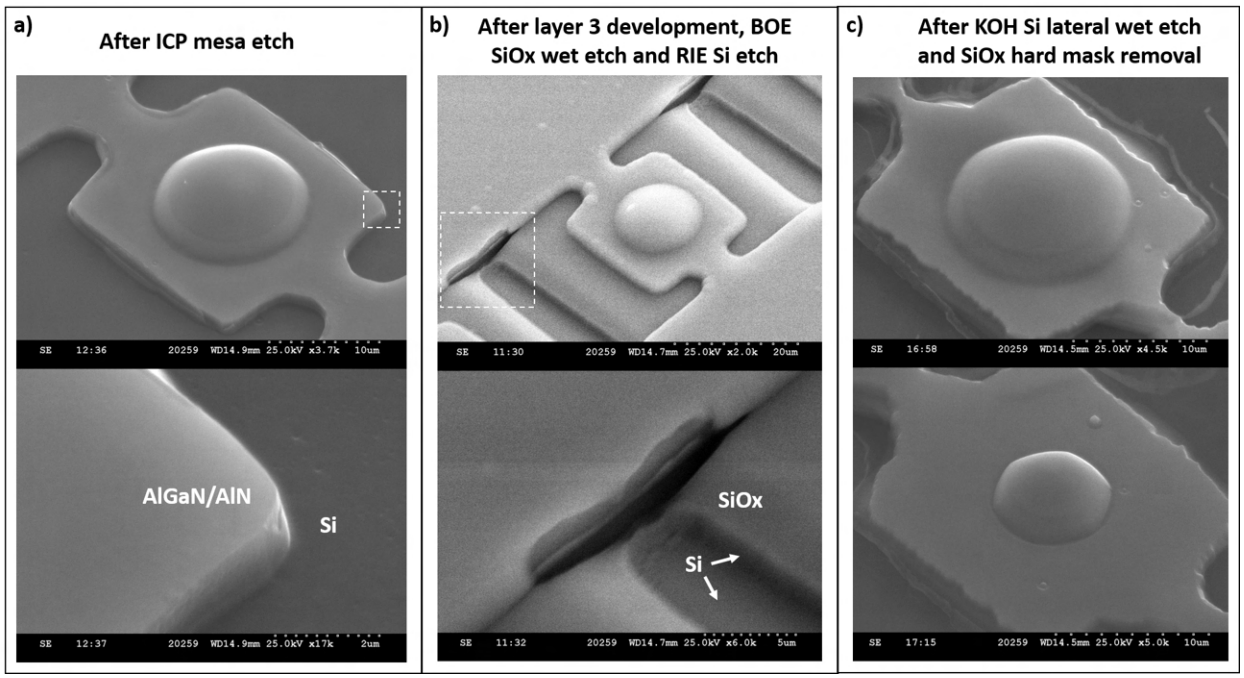

Figure 3.26: 1st fabrication with conserved GaN lenses after suspension and hard mask removal. Tilted SEM images (40°) of different devices after successive processing steps, with magnified views in a) and b) showing the sidewall of the AlGaN mesa and the wet and dry etching profile in SiO_x and Si respectively. c) shows two suspended membrane devices after hard mask removal with conserved GaN microlenses of 16 and 8 μm nominal diameter.

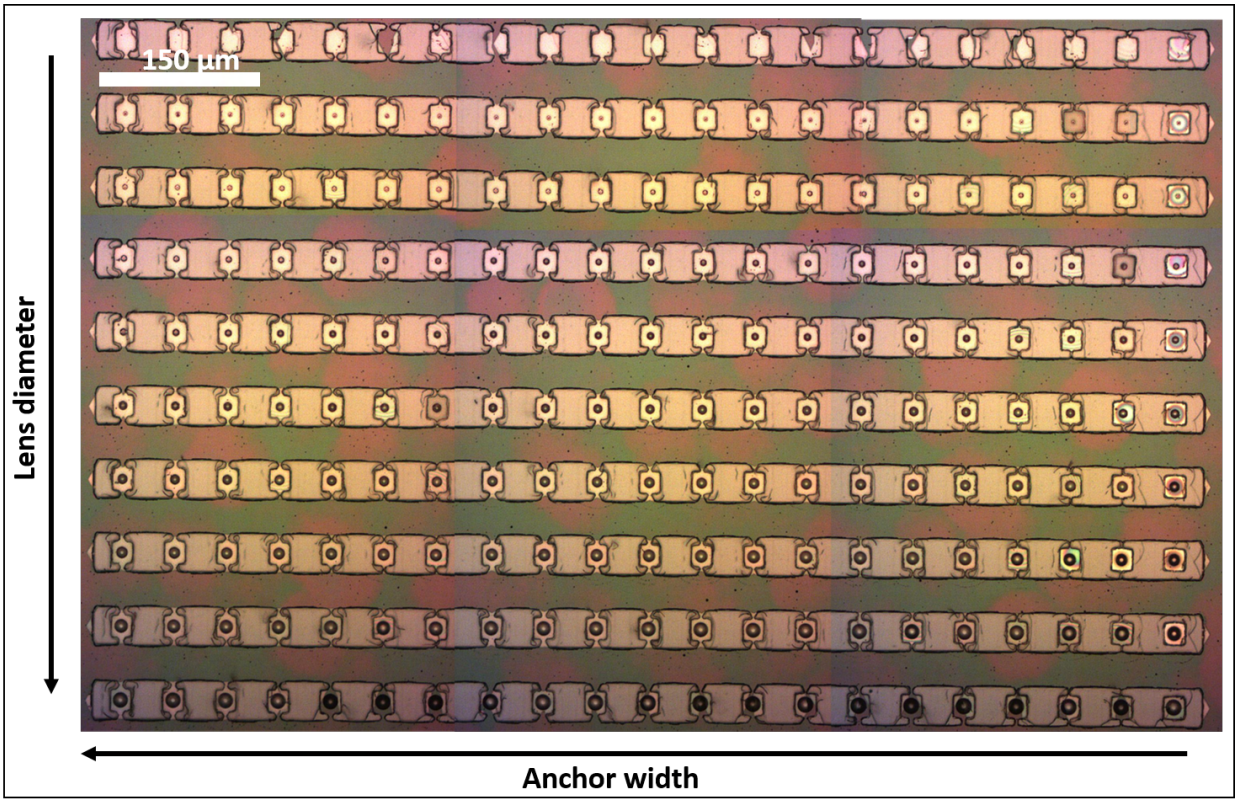

Figure 3.27: 1st fabrication with conserved GaN lenses after suspension and hard mask removal. Device yield on the full die. Some devices in the top and bottom row are not successfully suspended, otherwise the suspension yield is 99 %.

3.2.4 Milestone: Flat membrane bottom surface

The second significant optimization applied to fabricate functional GaN micro-lens devices is to restrict the etch depth of the micro-lens to the 2 μm thick GaN epilayer above the buffer layer (which also benefits the lens and membrane protection). Without this adjustment the membrane devices exhibit significant convex bowing. For example, Fig. 3.28 a) shows a test membrane with a planar surface (i.e. no lens topology) where material was removed by ICP-RIE until 1.2 μm of the combined graded AlGaN buffer and AlN nucleation layer remained. Though the source wafer had near-zero bow, when the resulting AlGaN/AlN membrane is transferred to a diamond substrate, a clear interference fringe pattern appears. This indicates an air gap below the device. An AFM scan confirms convex bowing of the membrane, showing that the maximum width of the air gap is on the order of 250 nm.
Membranes with micro-lens topology are also bowed when etched to this same remaining thickness of 1.2 μm, as shown in Fig. 3.28 b). These devices refer to the processing just shown in Fig. 3.25 to 3.27. However, the effect is observed to be most pronounced for the smallest micro-lens whose colour fringes closely resemble the planar membrane device in Fig. 3.28 a). As the lens diameter increases, the coloured fringes decrease in spatial frequency, indicating a reduced membrane bow. This can be explained by the fact that in membranes where the original layer thicknesses are maintained, the summation of bending moments arising from each layer are balanced. Once the thicknesses and/or volumes are altered (e.g. by partial etching of the layers to create a lens geometry), this balance is disrupted, so that the membrane starts to bow, creating an additional bending stress restoring equilibrium. This effect is here further

enhanced, since lens height and the diameter are for these particular devices positively correlated, with the height rising from 2 μm to 3 μm, compare Fig. 2.20 for the AFM data shown in Chapter 2. As more material is removed, like in the case of small radius of curvature lens structures, the bow of the devices becomes larger. Hence, the optimized micro-lenses are designed to leave more of the epitaxial stack intact by limiting the lens etch depth to 2 μm, matching the thickness of the GaN epilayer. Additionally we adjust the size of the membrane to the lens size and experiment with round, square and hexagonal membrane shapes without anchors. As shown in Fig. 3.28 c), this balanced height of GaN micro-lens and AlGaN/AlN mesa and the adjusted shapes did not result in air cavity induced colour fringes after the transfer step. The flatness of these membranes can be further confirmed by the tilted SEM image in Fig. 3.28 d) which shows a micro-lens membrane from a side-view.

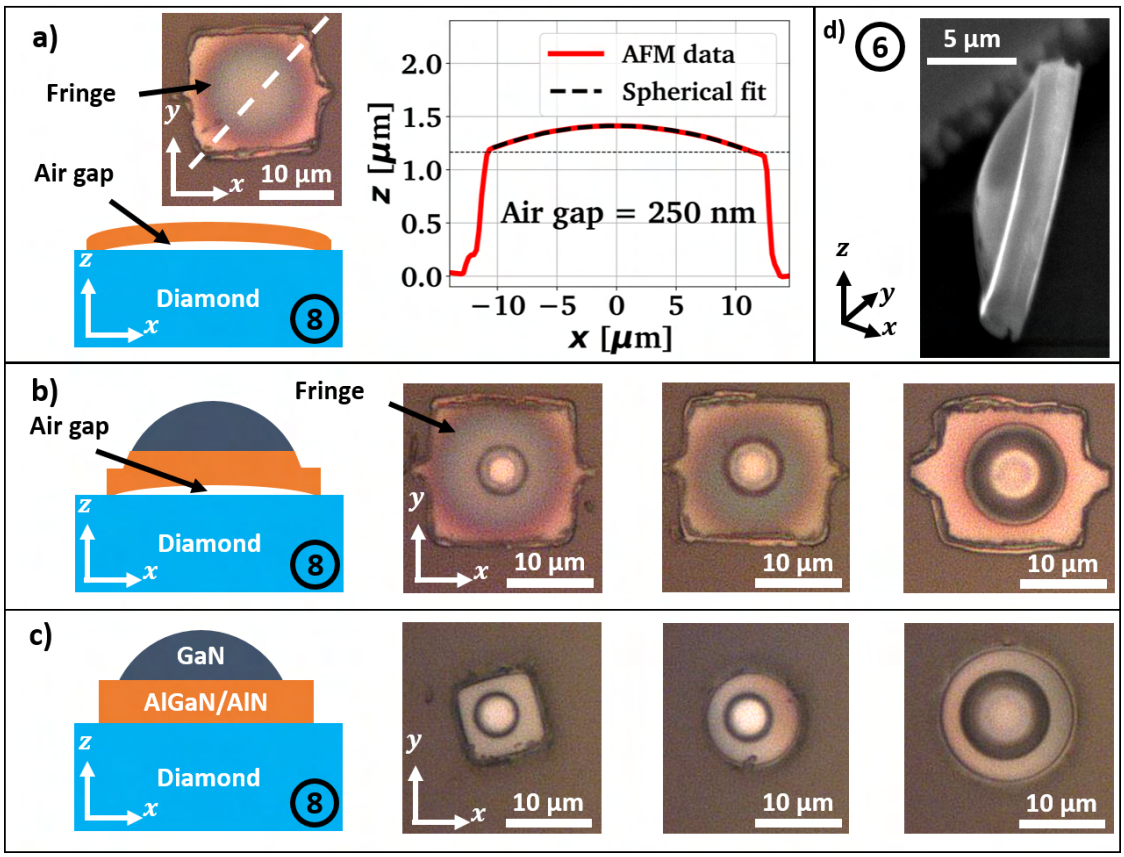

Figure 3.28: Optimized etch depth and device membrane size. a) Microscope image and AFM line scan (NSC15) on a transfer printed 1.2 μm thick AlGaN membrane on diamond without micro-lens from the fabrication run in the previous subsection, showing convex bowing. b) Transfer printed GaN micro-lens membrane devices on diamond with increasing micro-lens diameter and $2-3\,\mu$m height from the fabrication run in the previous subsection indicating a reduction of convex bowing with micro-lens diameter, c) similar fabrication run with reduced lens etch depth (2 μm) confining the lens to the GaN epilayer, reduced membrane sizes and optimized membrane shapes (all shown devices without anchors), leading to flat membrane devices without circular interference fringes, d) SEM image (40° tilt) of a 2 μm high GaN micro-lens with a circular matched 2 μm thick AlGaN/AlN membrane with flat bottom surface as shown in the most right image of c), standing upright on the Si growth substrate after SiO_x hard mask removal.

Fig. 3.29 a) shows SEM images of devices without anchoring tethers collapsed to the Si surface after KOH etch and SiO_x mask removal. For optical testing we selected three simlar micro-lenses with varying diameter (1,2,3) printed on a electronic grade single crystalline CVD diamond membrane from Element6

[2x2 mm^2, N < 5 ppb], see Fig. 3.29 b) for microscope images. AFM profile scans of these devices are plotted in c) and fitted both with a spherical and parabolic function. The lenses are fabricated by grayscale preshaping and resist reflow.

Both fits match the data well, but the parabolic fit performs slightly better, showing r.m.s. deviation from the data of 30, 35 and 55 nm compared to 40, 60 and 105 nm for the spherical fit, ordered left to right according to device (1), (2) and (3). The Maréchal criterion defines an optical focussing system as diffraction limited when the r.m.s. wavefront error is smaller than $\lambda/14$ across the full aperture [194]. For a wavelength of $\lambda = 650$ nm, this corresponds to roughly 33 nm r.m.s. surface deviation (weighted by the index contrast $n-1$). Devices (1) and (2) show surface variations from the spherical and parabolic fit close to this threshold, so we do not expect significant loss of optical performance. The smallest micro-lens, device (3), shows reasonable agreement with the parabolic shape, which should make it effective at collimating light from its focal position close to the diamond surface.

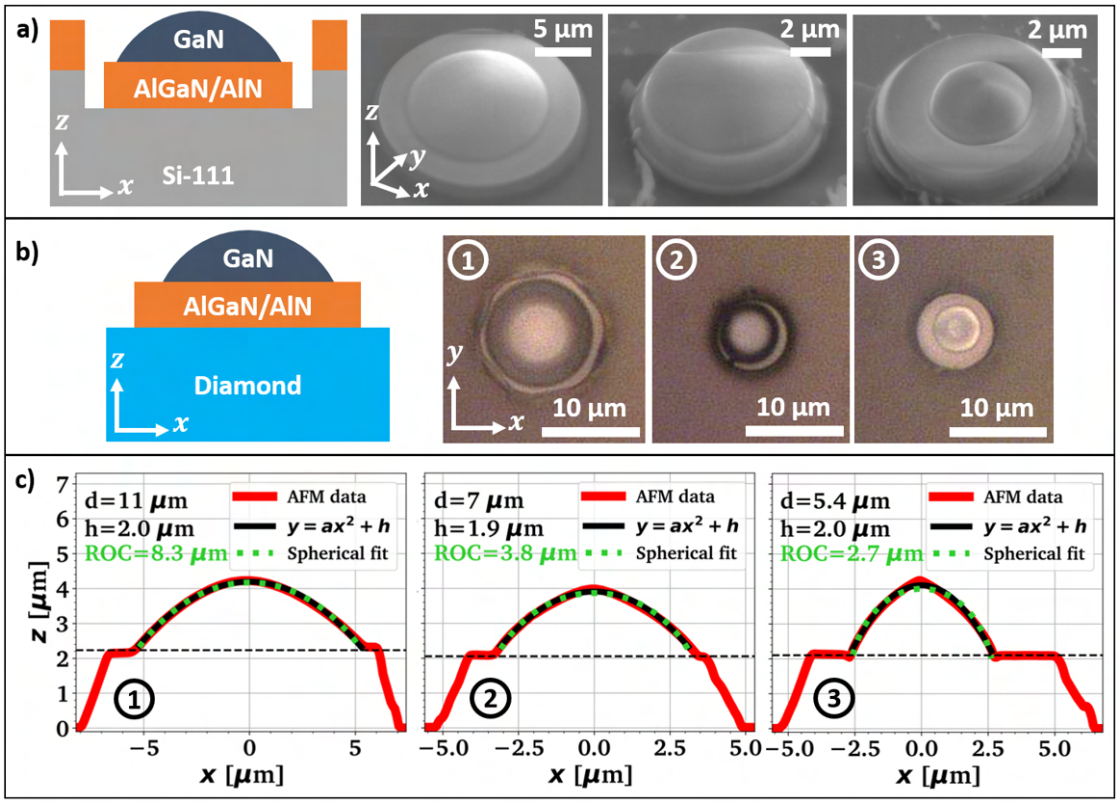

Figure 3.29: Optimized etch depth and device membrane size. a) SEM images (40° tilt) of collapsed membrane devices after suspension etch and hard mask removal with varying lens and membrane sizes, b) transfer printed GaN micro-lens platelets of similar size as shown in a) on a polished single crystalline diamond receiver substrate, c) corresponding AFM line scans across the transfer printed devices on diamond shown in b) (NSC15) with spherical and parabolic fits.

3.3 Optical performance: Measurement of focal length in air

To assess the optical performance of the transfer printed micro-lenses we measure their focal length in air and compare the results to finite difference time domain (FDTD) simulations (Ansys Lumerical) and the measured focal length of monolithic diamond lenses. In a FDTD simulation the classical matter-based Maxwell equations are solved on two interspaced grids in the time domain, probing the simulation

geometry with light from a pulsed source. Fourier transformation then allows to backcalculate the continuous wave solution at a specific time point for all frequencies involved in the excitation pulse. Further details on this simulation method are given in the Appendix.

3.3.1 Setup

The focal lengths of the three lenses printed onto a SC diamond substrate, shown in Fig. 3.29 b)/c), are measured using a custom built infinity-corrected microscope illustrated in Fig. 3.30, which is based on [230]. The light from a tungsten lamp (Ocean optics HL-2000-FHSA) is collimated with a convex lens (CL) and passed through a colour filter (CF) primarily transmitting green light. For additional spectral selection, only the green pixel channel of the CCD colour camera with a Bayer filter (Allied Vision Prosilica GC650-C) is used for the analysis, leading to a total of 10 dB rejection in the $\lambda = 525 \pm 50$ nm wavelength range. The transmission spectrum of the setup is shown in Fig. 3.31. The refractive index of GaN varies only by ca. 2 % in this wavelength range [120].

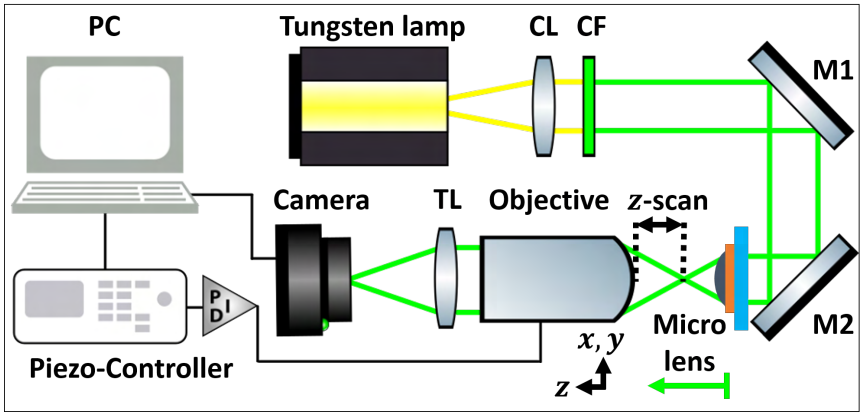

Figure 3.30: Optical setup used to evaluate the focal length of GaN micro-lenses printed onto diamond, based on [230]. The convex lens CL, green colour filter CF, mirrors M1 and M2 and tube lens TL are annotated. Illustrations are taken from [231]

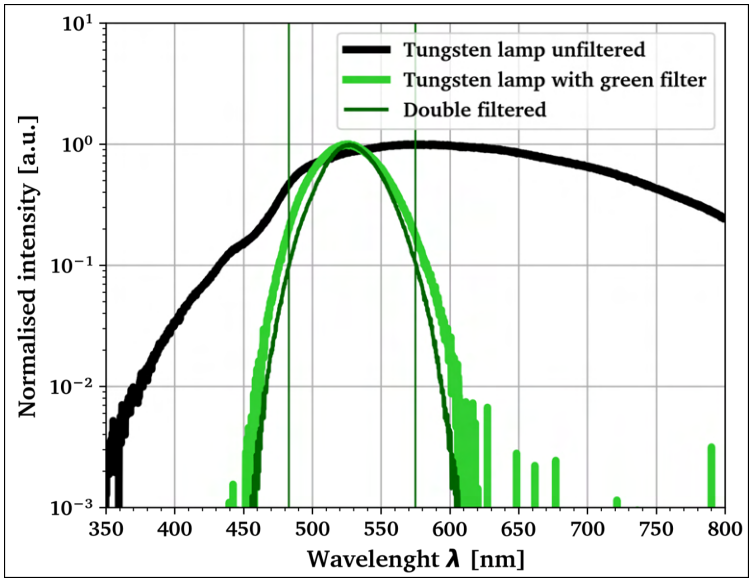

Figure 3.31: Light source spectra used for optical analysis taken with a ocean optics USB4000 fibrecoupled spectrometer (black and lime green curve) and multiplied with quantum efficiency of the green pixel of our colour camera extracted from data sheet (dark green).

The collimated beam is coupled through the back-side of the diamond substrate and then through the printed GaN micro-lenses on the opposite face. The wide field illumination allows imaging of the micro-lenses with an infinity-corrected 60x objective (Nikon Plan Fluor, NA = 0.85), using a 200 mm tube lens (TL, Thorlabs LA1708-A) to image onto a CCD array. A calibrated piezo controller (PI P-725.4CD with E-665CR) is used to manipulate the objective's z-position with sub-micron accuracy. Automated z-scans are constructed by taking images in synchronisation with the piezo position.
One aspect that obscures the measurement of the point spread function of high-index high aspect ratio micro-lenses in this bottom illumination configuration is total internal reflection. Fig. 3.32 illustrates the effect with a ray tracing simulation and a parallel beam of light rays illuminating a high-index hemisphere from the bottom.

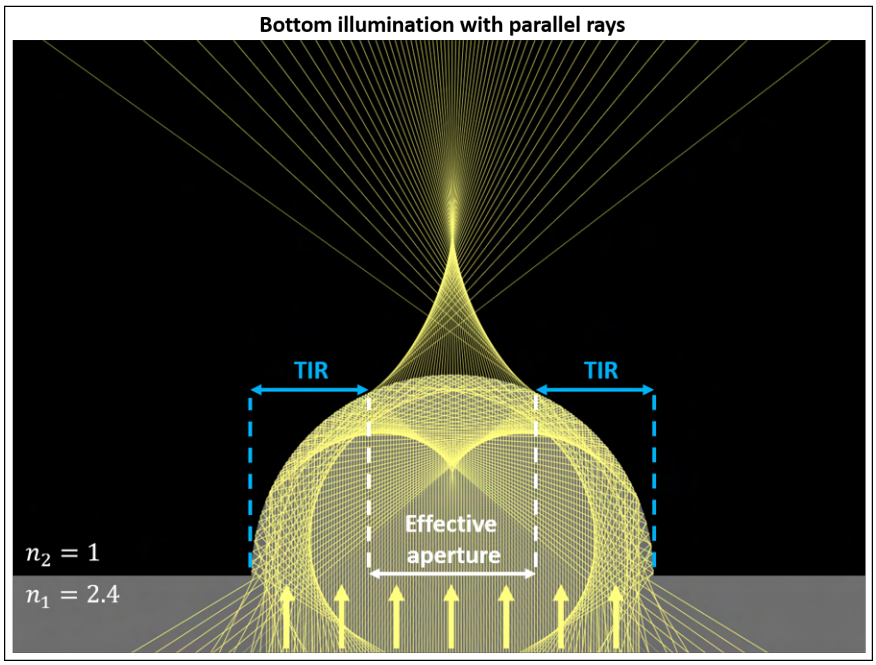

Figure 3.32: Ray tracing calculation of the focusing behaviour of a monolithic high index (n_1) hemispherical lens that is illuminated through the high index material (n_1) from the bottom. Total internal reflection (TIR) occurs at the outer parts of the lens diameter, effectively reducing the lens aperture in this arrangement, similar to the experimental results shown in Fig. 3.33.

3.3.2 Measurement results in comparison to simulations

The focal length f_{air} of the micro-lens in air is extracted from the z-scan as a bright spot on the CCD camera, which is generated if the focal spot of the objective and micro-lens overlap. We then compare the z-travel distance between a sharp image of the micro-lens mesa and the image of the focal spot to extract f_{air}. The reasonably broadband source is used in these measurements to avoid the obscuring interference fringes generated by monochromatic sources.

The expected focal length of the three example micro-lenses is calculated using 3D FDTD simulations (Lumerical) in which the lenses are created to match the form factor of the measured devices, based on the AFM profiles shown in Fig. 3.29 c). The refractive index model for the micro-lens structure consisting of GaN, AlGaN and AlN is based on [59, 120, 121, 232], using $Al_xGa_{1-x}N$ with $x = 38\,\%$ to model the AlGaN part of the buffer layer.

Fig. 3.33 a) shows the simulated electric field strength squared for a plane wave injected from the diamond substrate upwards through the micro-lens geometry at $\lambda = 525\,\text{nm}$ wavelength. We chose the apparent symmetry point of the focal spot to evaluate the focal length f_{air} measured from the GaN micro-lens tip. The results are displayed in Tab. 3.1 and compared to what would be expected from the geometric optics (GO) approximation for a spherical surface with index $n_{\text{GaN},\lambda=525\,\text{nm}} = 2.43$ [120] (compared to $n_{\text{dia},\lambda=525\,\text{nm}} = 2.43$ [59]). We evaluate the following equations [233] with the lens diameter d and height h found in the spherical fit in Fig. 3.29 c):

$$\text{ROC} = \frac{\left(\frac{d}{2}\right)^2 + h^2}{2h} \qquad f_{air} = \text{ROC} \cdot \frac{1}{n_{\text{GaN},\lambda=525\,\text{nm}} - 1}$$

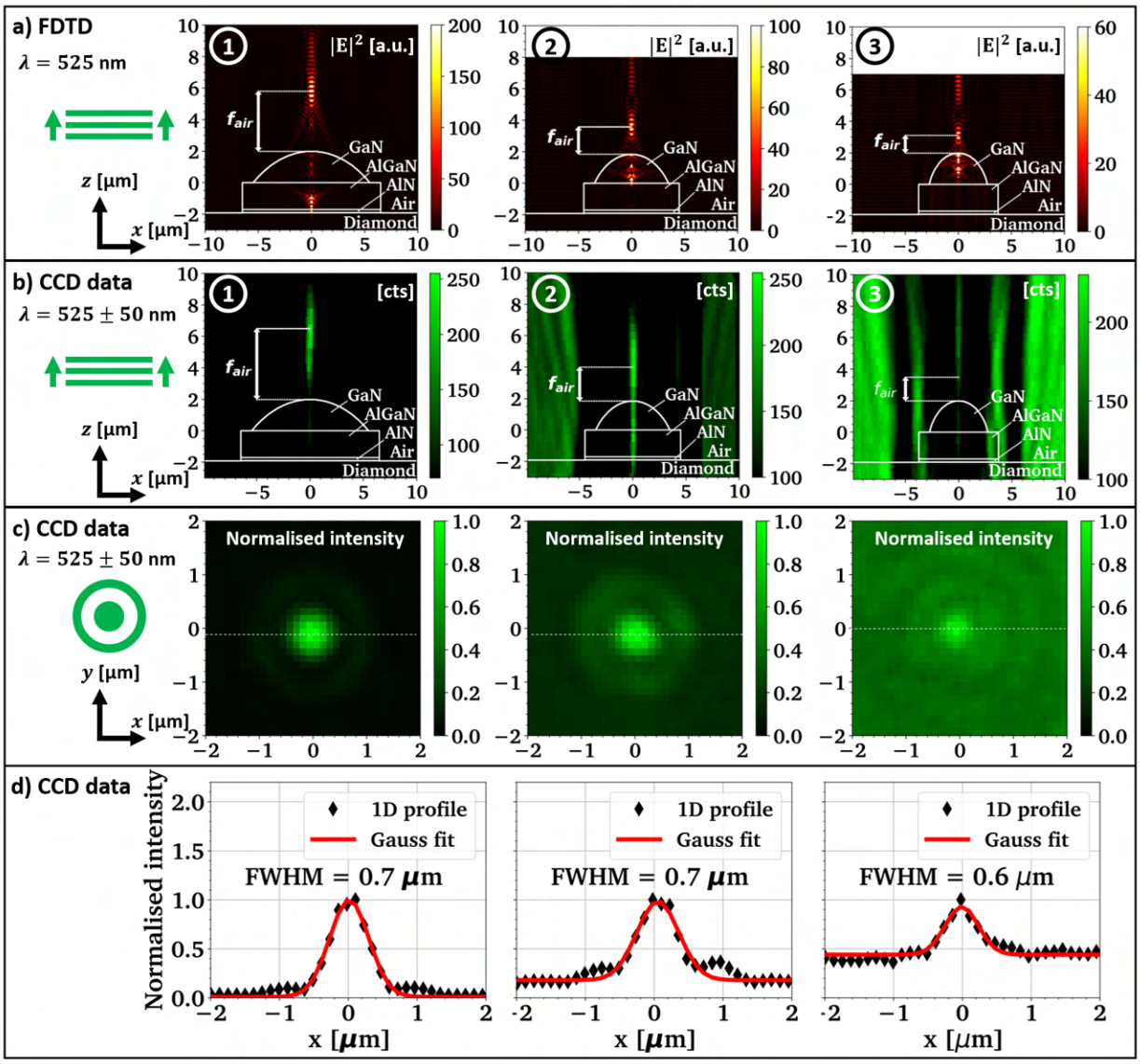

Figure 3.33: Optical analysis of the GaN micro-lenses on diamond shown in Fig 3.29 b),c): a) FDTD simulations of the electric field squared with a linearly polarised plane wave injected at $\lambda = 525$ nm wavelength from diamond through spherical lens profiles, b) Measured z-scan of the x-profile through the xy-CCD data evaluated on the lenses with the setup shown in Fig. 3.30, overlayed with contours from the FDTD simulations in a), c) normalized xy-CCD data at the objective's focal position matching f_{air} in b), d) normalized line scans through the micro-lens focus shown in c) with fitted Gauss curves.

The shortened focal lengths found in the FDTD simulations in comparison to the GO approximation shows the necessity to use a full Maxwell solver to accurately predict the micro-lens performance. The diffraction effect evident in the simulations is known as focal shift and is well documented for small scale micro-optics [234–236]. Diffraction is also reported to account for the visible 'funneling' of light into a tube, rather than a distinct focal spot [234], and can be seen in Fig. 3.33 a).

Table 3.1: Results of the AFM and optical analysis of the lenses shown in Fig. 3.29 b)/c). Diameter d, height h, radius of curvature (ROC) and focal length f are given for the geometric optics (GO) approximation and FDTD simulations and compared to the experimental data (EXP). f_{air} is simulated at $\lambda = 525\,\text{nm}$, while f_{dia} is simulated at $\lambda = 700\,\text{nm}$ wavelength.

	d	h	ROC	f_{air} GO	f_{air} FDTD	f_{air} EXP	f_{dia} FDTD	NA_{dia}
#	[μm]	[μm]	[μm]	[μm]	[μm]	[μm]	[μm]	
(1)	11	2.0	8	6	4	4.5 ± 1.0	14	1.0
(2)	7	1.9	4	3	2	2.0 ± 1.0	7	1.4
(3)	5.5	2.0	3	2	1	1.5 ± 1.0	5	1.7

Fig. 3.33 b) shows the measured z-scan sections with 0.5 μm step size for each micro-lens. The lens geometries from the FDTD simulations are overlaid as a guide to the eye, with their locations defined by imaging the mesa structures. The measured position of the focal point is extracted as the highest intensity spot above the lens surface in air and is presented alongside the simulation values in Tab. 3.1. The measurement errors are dominated by the uncertainty regarding the lens surface position (found from the z-position of the mesa image) and the μm-large measured depth of focus in the measurement setup.

The xy-view of the selected focal spot is shown in Fig. 3.33 c). The full-width-half-maximum (FWHM) of the measured focal spot size is extracted from line scans shown in d) and is on the order of 0.6-0.7 μm exhibiting reasonable circular symmetry. This is relatively close to the diffraction limited spot size of FWHM $\approx 500-750\,\text{nm}$ for $\lambda = 525\,\text{nm}$ and simulated NA in air of $\approx 0.5, 0.4$ and 0.35 for devices (1), (2) and (3), respectively [230] even though we use a broadband beam with low coherence. The decreasing numerical aperture is due to the reduction of the effective NA due to the rising influence of total internal reflection, which we combine with the FDTD simulation result to calculate the effective NA in air.

Expected and measured focal lengths agree well for lenses (1) and (2), but the results for the highest-aspect ratio micro-lens (3) are more challenging to extract due to the lack of a clear signature of the focal spot. This may be partially due to the reduction of contrast due to the decreasing lens aperture, which is additionally masked by increasing total internal reflections when transitioning to a higher aspect ratio lens. Within the geometric optics approximation we can estimate that only 40%, 23% and 18% of the area of the aperture actually transmits light for devices (1), (2) and (3) respectively. The resulting loss of contrast is visible in Fig. 3.33 c) and d). Aberration from the slightly pointed tip of this smallest lens and astigmatism might also lead to a wider spread of the focus along the z-axis for device (3).

Due to the substrate thickness and high index contrast, it is experimentally challenging to measure the focal length f_{dia} of the micro-lenses in diamond. But as there is overall reasonable agreement between measured results and FDTD simulations, f_{dia} can be estimated by inverting the FDTD simulations, see Fig. 3.34 b). In this case, a linearly polarised plane wave is injected from the top of the sample through the lens and into the substrate. Here we use $\lambda = 700\,\text{nm}$ wavelength corresponding to the central wavelength of NV^- emission at room temperature [51], with $n_{\text{GaN},\lambda=700\,\text{nm}} = 2.37$ [120] and $n_{\text{dia},\lambda=700\,\text{nm}} = 2.41$ [59].

In Fig. 3.34 a) we show two different cases of potential emitter placement with respect to lens. The lens can either act to extract the wavefront without significant refraction if the emitter is placed in the midpoint of the spherical lens surface, or it can collimate the light beam into lower numerical collection

optics at the cost of reduced collection efficiency.

The focal length f_{dia} in diamond in reference to the GaN lens tip is assessed by identifying the symmetry point of the apparent focal spot, which leads to the results presented in Tab. 3.1. These values imply that the fabricated micro-lenses could be used to couple to NV^- centres both in nm-proximity to the diamond surface and in up to 10 μm depth using the different arrangement shown in Fig. 3.34 a). To illustrate the light collection potential of our demonstrated micro-lenses, we calculate the numerical aperture for collection from diamond using the following expression:

$$\mathrm{NA}_{dia} = n_{dia} \cdot \sin\left(\arctan\left(\frac{d}{2(f_{dia}-h)}\right)\right)$$

which indicates potentially comparable performance to high-end oil immersion objectives, compare the last column in Tab. 3.1.

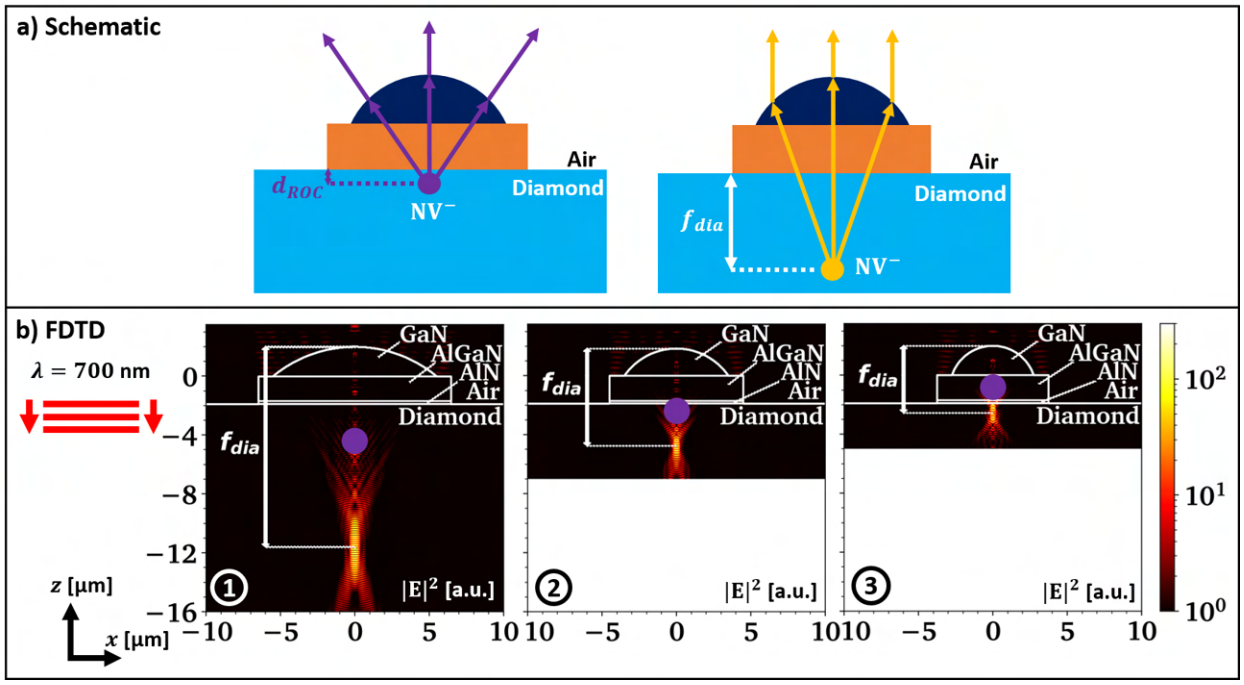

Figure 3.34: a) Schematics showing potential coupling geometries of GaN micro-lenses to nitrogen vacancy centres in diamond, b) FDTD simulations of the electric field squared with a linearly polarised plane wave injected at $\lambda = 700$ nm from air into the indicated spherical micro-lenses on diamond, matching the devices discussed in Fig. 3.33 and 3.29 b),c). Both the focal length f_{dia} in diamond and the midpoint of the spherical lens profile (purple disk) are indicated for reference.

3.3.3 Comparison with monolithic diamond micro-lenses

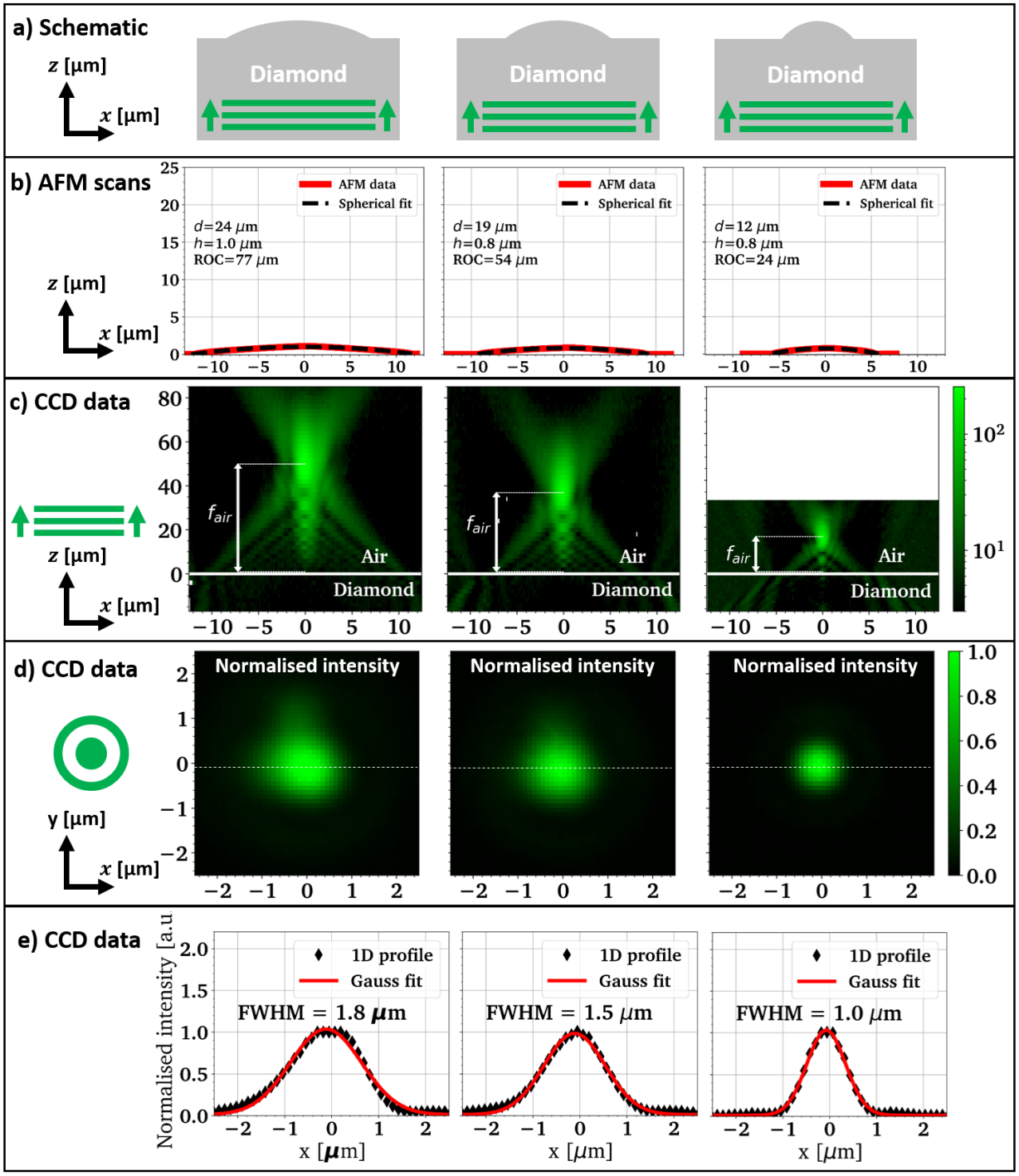

Figure 3.35: Optical analysis of monolithic diamond micro-lenses shown in Fig. 2.16: a) Schematics of the experimental arrangement and shrinking lens diameter, b) AFM line scans close to equal x and z scaling depicting the low aspect ratio of these lenses, c) Measured z-scan of the x-profile through the xy-CCD data evaluated on the lenses with the setup shown in Fig. 3.30, d) normalized xy-CCD data at the objective's focal position matching f_{air} in c), e) normalized line scans through lens focus shown in d) with fitted Gauss curves.

To further demonstrate the refractive power of the created GaN micro-lenses we compare their optical performance to the highest aspect ratio monolithically etched diamond micro-lenses that we are able to

create and which are discussed in Chapter 2. The experimental results are shown in Fig. 3.35, with a schematic of the experimental arrangement in a) and the AFM profile scans of the investigated devices in b). We highlight the low aspect ratio of these lenses by plotting x and z axis on a similar scale. In c)-d) the position of the measured point spread function and its lateral shape and extend are analysed in analogy to the results shown for the GaN micro-lenses.
The measured focal length in air are $f_{air} = 49$, 36 and 15 μm respectively, roughly matching the expectation using a geometric optics approximation leading to $f_{air,GO} = 54$, 38 and 17 μm respectively. The focal length in diamond at $\lambda = 700$ nm can then be estimated to $f_{dia,GO} = 132$, 92 and 41 μm respectively, which shows that the focal length of the diamond micro-lenses is around 1 order of magnitude larger than those of the GaN lenses.

3.4 Micro-lens array printing yield

Before we move to the exciting prospect of coupling GaN micro-lenses to nitrogen vacancy centres we will briefly discuss some additional printing results of GaN micro-lens arrays on diamond. We previously saw that anchors might prevent intimate contact with the diamond substrate and we therefore look at devices without anchor geometries only. Detailed fabrication results and yields of the GaN array processing are added for completeness to the Appendix.

3.4.1 4x4 micro-lens arrays on 30x30 μm^2 membranes

Fig. 3.36 shows printing results from dense micro-lens arrays created by grayscale lithography and the optimized membrane processing flow discussed earlier in this Chapter using the example of 2x2 micro-lens arrays. Printing of these devices is extremely straightforward, but as discussed the micro-lenses in the array are expected to show inhomogenities in their optical performance due to varying lens height depending on their position and the local environment during exposure, development and etching. Similar lens types are marked in three different colours. We can also see that all devices exhibit slight coloration if the microscope objective focus is moved upwards, indicating a residual gap below the devices.
As in these arrays much less GaN material is removed during the lens etching a change in the strain balance after device suspension is expected even if similar overall etch depth is achieved. To make such devices work effectively, additional optimization of the etch depth or a variation of the initial wafer bow might yield good results.

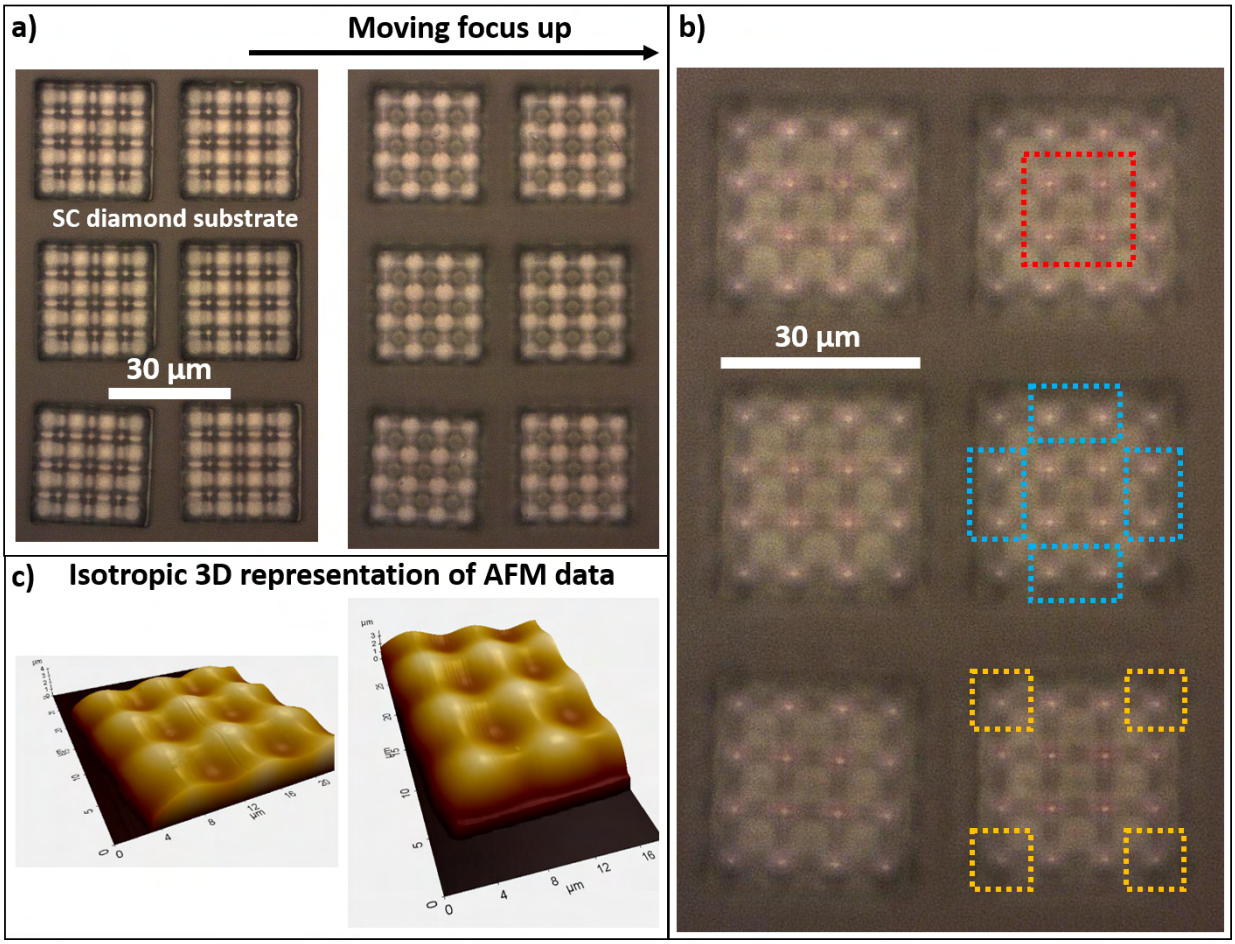

Figure 3.36: Transfer printing of dense 4x4 micro-lens arrays on 30x30 μm^2 footprint without anchors onto single crystalline diamond substrates. When moving the focus upwards from a) to b), slight coloration of the GaN lens foci appears. These devices were preselected on their Si growth substrate (collapsed) for minimal coloration indicating device flatness and are probably the flattest devices available. The marked lenses refer to a similar environment, as edge effects are observed to have influenced the lens height in dependence on position within the array, c) real scale 3D AFM representation of similar transfer printed devices on a different diamond substrate (SSS-NCH).

3.4.2 4x4 micro-lens arrays on 60x60 μm^2 membranes

To further scale the micro-lens array fabrication we also tested the integration of large scale GaN lens membranes which are very similar to the 2x2 GaN lens array devices discussed in much detail in this Chapter. Unfortunately at similar overall etch depth we see significant colour fringes in the devices after transfer printing to a single crystalline diamond surface, as illustrated by Fig. 3.37. This indicates that the membrane stiffness might be heavily influenced by the edge of the device, making a optimization of etch depth and wafer bow necessary for further scaling. But this approach would allow very fast integration of large scale GaN micro-lens arrays on diamond.

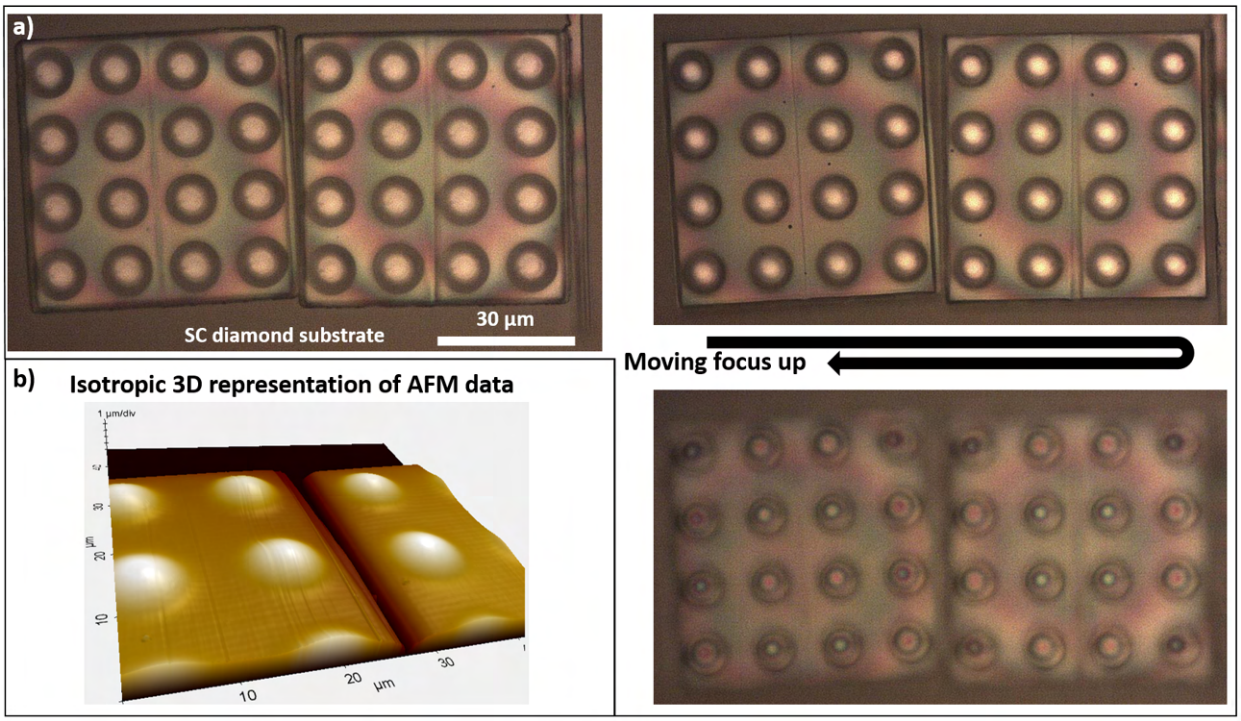

Figure 3.37: Transfer printing of 4x4 micro-lens arrays on 30x30 μm^2 footprint without anchors onto single crystalline diamond substrates. Clear color fringing appear throughout the membranes, b) real scale 3D AFM representation of these transfer printed devices (SSS-NCH).

3.4.3 6x6 micro-pillar arrays on 30x30 μm^2 membranes

Lastly we also attempt the fabrication of GaN micro-pillars, using grayscale lithography to create high aspect ratio resist pillars. Unfortunately these seem to reflow during the etching process yielding nearly hemispherical micro-lenses with around 2 μm diameter with high density instead. This test run was performed on a wafer with signifant bow, yielding quite substantially bowed membranes as can be observed in the SEM image taken on an upright standing membrane after suspension and hard mask removal shown in the bottom left of Fig. 3.38.

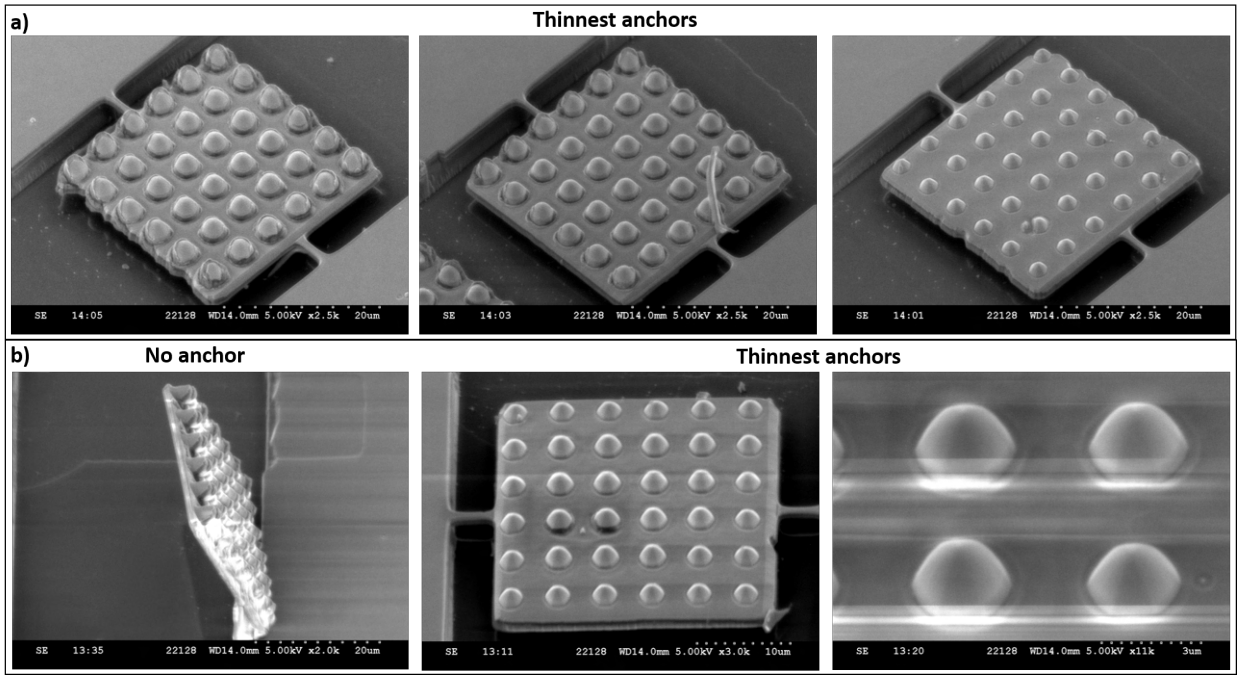

Figure 3.38: SEM images (40° tilt) of 6x6 micro-pillar arrays on 30x30 μm^2 footprint after finalized micro-fabrication. a) shows devices with increasing exposure dose yielding smaller devices at similar membrane thickness, b) shows some additional examples, including an image of an upright standing membrane exhibiting a clear bow (this wafer had -46 μm wafer bow).

3.5 Summary

We have seen that GaN micro-lenses can be suspended from their Si growth substrate with high yield, preserving the excellent surface quality and shape of the lenses after the donor fabrication is completed. We find that, after optimization of the etch depth and wafer bow, flat membrane devices with an atomically smooth bottom surface can be created and transferred to single crystalline diamond surfaces with PDMS-based transfer printing.

The optical properties of the lenses is found to agree well with the theoretical expectation and confirm that the heterogeneous integration method offers significant advantages over monolithic diamond micro-lens etching. To our knowledge this is the first demonstration of the integration of semiconductor micro-lenses with around 10 μm diameter and radius of curvature that are successfully shown to operate as micro-optical devices on a foreign receiver crystal.

Future work might include the addition of an anti-reflection coating that could also serve as a tether layer and the optimization of the scaling of GaN micro-lenses into membrane arrays, which has been started but not fully completed in this work. Remaining issues are the etch depth and wafer bow optimization in dependence of the created micro-optical element as well as the overall size of the membrane.

4 Integration of GaN micro-lenses with the nitrogen vacancy centre in diamond

We are going to discuss how GaN micro-lenses can enhance the light-matter coupling between the nitrogen vacancy centre in diamond and collection optics with various numerical aperture. The novel combination of additive GaN micro-lenses with diamond colour centres is the main motivation behind the development work in this thesis and we will see that the GaN lenses have the potential to significantly increase the photon extraction efficiency without damaging the diamond host crystal, potentially offering a new scalable route to micro-system assembly.
We will also learn that PDMS based transfer printing is a viable integration method that allows sufficiently accurate placement of the lenses with respect to targeted emitters. We discover that GaN micro-lenses can even be beneficial for applications such as scanning NV magnetometry, and show that the transfer print integration with commercially available scanning probes is challenging due to the poor top surface quality of the probes.
For the work presented in this Chapter we receive delta-doped diamond samples from Fraunhofer Institute for Applied Solid State Physics (IAF) in Freiburg, who also provide commercially available diamond magnetometry probes. The collaboration is coordinated by the Fraunhofer lighthouse project 'QMag' led by IAF. The University of Oxford contributes their laser writing and confocal analysis tools for the data shown in the second section.

4.1 Near-surface NV clusters in CVD grown delta doped diamond

We will start this Chapter with the deterministic alignment of GaN micro-lenses to NV^- emitter clusters in single crystalline HTHP diamond that is overgrown by chemical vapour deposition to create a delta-doped emitter layer at targeted depth. In order to properly assess the enhancement of light-matter coupling to the NV centres a confocal microscope system with single photon sensitivity is developed and discussed in the outline of this work.

4.1.1 Outline

We receive single crystalline diamond substrates overgrown with CVD that contain a nitrogen rich diamond layer at targeted depth from Fraunhofer IAF. The fabrication process flow including the lens integration is shown in Fig. 4.1. The ca. 500 nm thin delta-doped nitrogen rich layer is overgrown by additional 6 μm of unintentionally doped diamond and then Scaife polished (using a spinning wheel with a retaining agent and diamond dust) to achieve a layer of naturally forming NV^- defects in μm-proximity to the flat diamond surface with low surface roughness. This process is intended to allow placement of lenses at arbitrary positions to quickly test the photon extraction and pump focusing enhancement provided by suitable GaN micro-lenses.

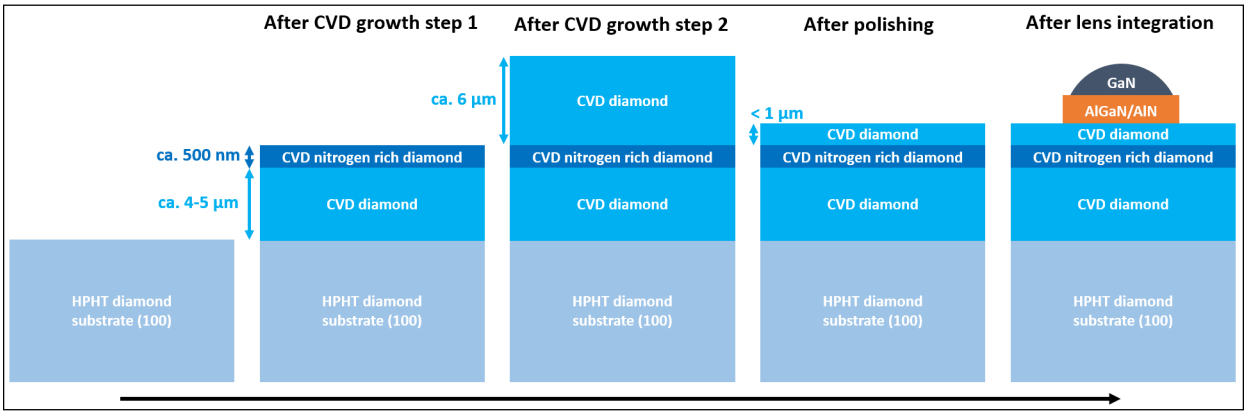

Figure 4.1: Chemical vapour deposition based growth process (Fraunhofer IAF) including a 500 nm thin delta doped layer with NV^- centers (ca. 30 ppb) forming from nitrogen impurities (ca. 10 ppm). Overgrowth of the nitrogen rich layer with successive Scaife polishing was used to achieve vertical position control and a smooth surface finish.

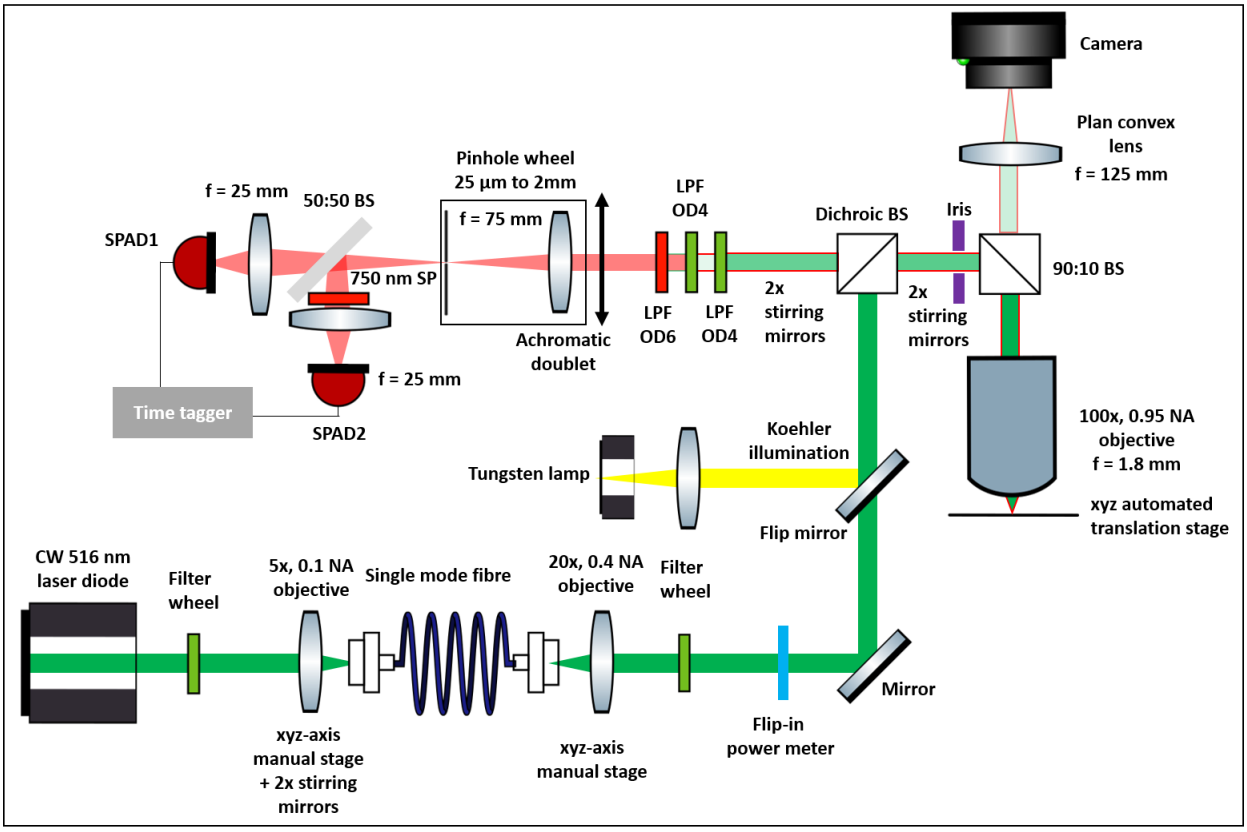

Figure 4.2: Schematic showing the components of the home-built confocal microscope system with single photon sensitivity with closed-loop automated stage movements for scanning the laser spot over the sample. The setup is optimised for the 100x objective lens, but 50x and 10x objectives can also be easily mounted. Abbreviations are long pass filter (LPF), short pass (SP) filter, beam splitter (BS), numerical aperature (NA), continuous wave (CW), single photon avalanche photodiode (SPAD).

In order to assess the enhancement of the photon extraction efficiency from the colour centres we design and build a confocal microscope system with single photon sensitivity. Confocal microscopy offers the rejection of background light by coaligning the focal spot of the excitation laser to a pinhole in front of the detection optics. Thus it gives rise to a z-sectioning ability, mostly collecting photons from the same focal volume that is excited by the laser. In contrast to wide field microcopy the sample or laser needs

to be scanned across the sample surface to generate an image.
The system is designed to fulfil the following requirements:

- Collect photoluminescence from a diffraction limited three dimensional volume for tomography of complex samples with the option to switch to a larger detection area
- Single photon sensitivity in the $\lambda = 600 - 900$ nm wavelength window
- Gathering $g^{(2)}(\tau)$ second order autocorrelation statistics of the detected photon stream from targeted positions
- Relative position detection of emitter distributions with respect to alignment markers

A schematic of the home-built confocal microscope setup is shown in Fig. 4.2. The detailed description of the setup, its optical performance and the developed graphical user interface are given in the Appendix. We will here quickly introduce the main components and capabilities only.
A single mode green laser diode (Sharp GH0521DE2G, 130 mW) with measured $\lambda = 517 \pm 2$ nm wavelength is mounted in an actively cooled housing (Thorlabs LDM56) and operated with a constant current power supply (Thorlabs LDC200C) while the temperature is monitored and corrected by a thermoelectric temperature controller (Thorlabs TED200C). The laser beam is collimated using an anti-reflection coated asphere and reflected twice via silver mirrors while passing through a filter wheel with optical density filters before the beam is focused on the facet of an angled single mode fibre (Thorlabs P3-460B-FC-2) with a 5x objective lens system (infinity corrected, NA= 0.1) for spatial cleaning of the asymmetric laser diode mode profile, delivering 5-6 mW stable output power.
The cleaned laser mode exits the single mode fibre and is collimated using an infinity corrected 20x objective (Olympus ULDW MSPlan, NA= 0.4) leading to a Gaussian beam profile with a diameter of approximately 2-3 mm. A manual and an automated filter wheel (Thorlabs FW102C) loaded with a wide range of neutral density filters give control of the laser power which is measured by a photo diode power sensor (Thorlabs S120VC,$<$ 50 mW 200-1100 nm) on a flip mount. The laser is then aligned to the cage system containing the optical microscope column via two silver mirrors. The first optical element in the cage system is the dichroic mirror (Thorlabs DMPL567).
Another part of this section of the setup is the white light illumination source employed to navigate the sample. The filament of a tungsten lamp (Ocean optics HL-2000-FHSA) is imaged onto a nearly closed iris ($\approx \varnothing 1$ mm) using a collector lens ($f \approx$10s of mm, plano-convex). A field lens ($f = 200$ mm, plano-convex) reimages the filament onto the back focal plane of the 100x objective to achieve reasonably homogenous illumination conditions in a Köhler like arrangement. The white light path in is coupled into the microscope cage system via a flip mirror.
The cage-mounted optical column contains the dichroic mirror employed to prefilter the laser reflected light and transmit excited photoluminescence above $\lambda = 567$ nm to the detector section. Two periscope mirrors increase the height of the beam path which is then split vertically by a 90R/10T beam splitter cube (Thorlabs BS028, A coated) focusing most of the laser light through the 100x objective on the sample surface. The beam splitter cube allows to image the sample surface on a CCD camera (Thorlabs DCC1645C) with a tube lens (Thorlabs LA1986-A, $f = 125$ mm). The sample is mounted on an automated closed-loop xyz slip-stick piezo stage with 31x31x12 mm large travel (Smaract SOM-505020, uni-directional repeatability of 50-100 nm with MSC2 controller).
The emitted fluorescent light from the excited sample volume is recollimated through the 100x objective

in reflection mode, passes the periscope and dichroic in the opposite direction and is aligned to the detection path with two silver mirrors. A cage based filter section (Thorlabs CFS1/M) allows to add three filters into the beam path: 2x soft coated 550 nm long pass (Measured around OD4, Thorlabs FEL0550), 1x hard coated 650 nm long pass (Thorlabs FELH0650). By default all three are used in photoluminescence experiments, which effectively means that the phonon sideband of the NV^- centre is detected without the ZPL. The detection of the ZPL is not of importance for the experiments conducted because the ZPL does not heavily contribute to the photon emission of the NV^- centre at room temperature [51].

The filter section is aligned to the second cage system containing an HBT arrangement of two silicon single photon avalanche photodiodes (SPAD, IDQuantique ID120-500-800) with an automated pinhole wheel (Thorlabs MPH16-B, 25 μm-2 mm pinhole diameter) inserted in between. This contains a B-coated achromatic doublet with $f = 75$ mm to focus the collimated beam onto the pinhole. Without recollimation the beam now passes a 50:50 plate beam splitter (Thorlabs BSW29R, B-coated) and is focused on the ca. 500 μm large detector area of the respective SPAD using B-coated plano-convex lenses (Thorlabs LA1951-B) mounted with xy manual translation stages.

Si SPADs emit light between $\lambda = 700 - 1000$ nm wavelength due to the "break down flash" [237] which causes false counts on the complementary detector in this arrangement. A 750 nm short pass filter (Thorlabs FESH0750) is permanently added in front of SPAD2 to reduce the effect without cutting into the NV^- centre emission spectrum.

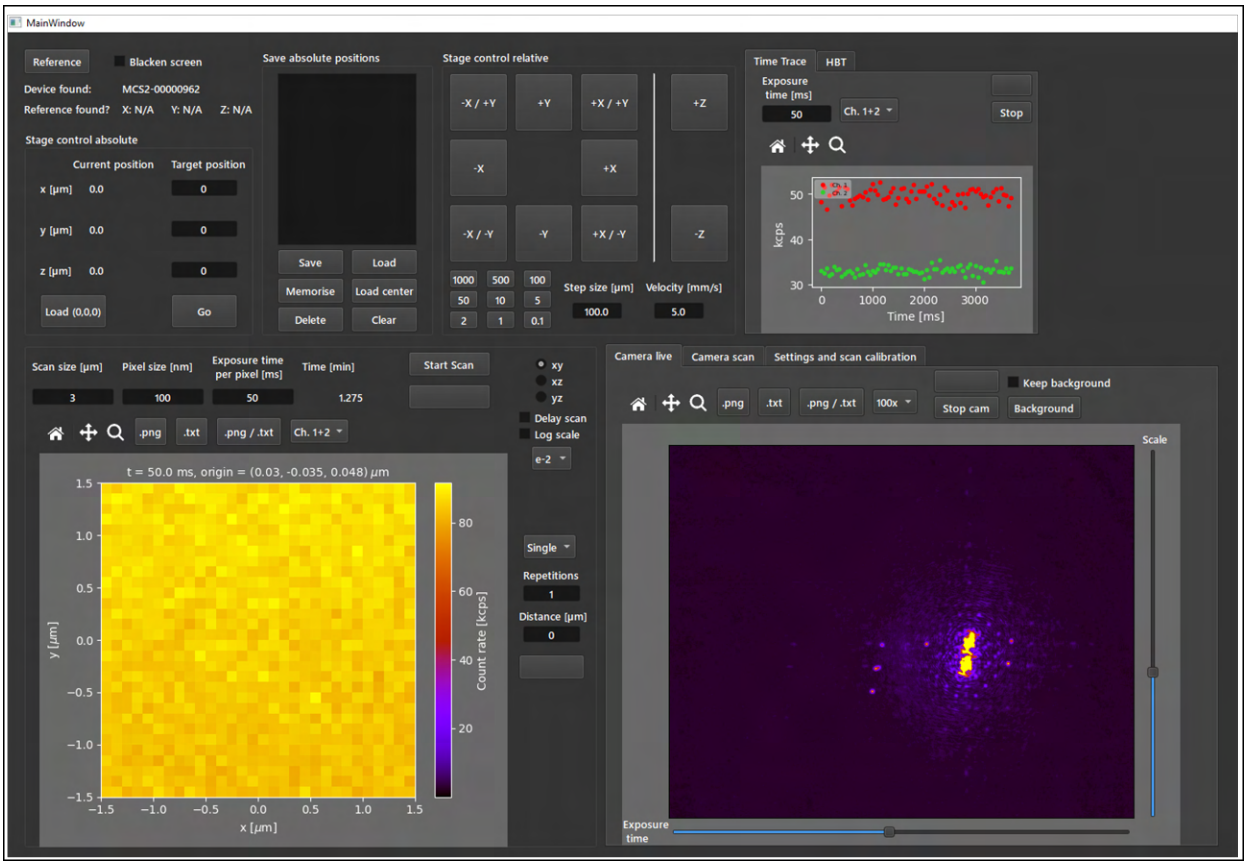

Figure 4.3: Python based graphical user interface of the home-built confocal setup. The user can access the stage, record time traces and photon statistics, perform confocal imaging scans in 3D and interact with the camera live view. Both scan and camera panels have a 'click to extract position' feature, that allows the user to quickly navigate on the sample.

The detection events triggered on both SPADs are collected via a time tagger (Swabian Instruments Time Tagger 20) which is interfaced with the PC via USB. Detection events and sample position are synchronized using a self-developed Python-based GUI with the main panel of the software shown in Fig. 4.3. The software allows to control the stage movement in a relative and absolute manner, can be used to save positions and calculate the geometric average between marker points. A live time trace and camera image are shown to the user who can quickly collect 2D and 3D confocal scan maps along the xy, xz and yz axis (no rotation capability). Normalized HBT measurements can be directly taken with the second tab behind the time trace window.

4.1.2 Experimental results

Unfortunately the control of material removal in the Scaife polishing proved very challenging, which left us with one sample with an intact nitrogen doped layer showing bright photoluminescence from the top surface but high r.m.s. surface roughness of around 7.5 nm and another sample where the polishing left a smooth surface finish, but most parts of the nitrogen rich CVD layer are removed. We will focus our discussion on this latter sample with sparsely distributed clusters of NV^- scattered around the surface, see Fig. 4.4. AFM and photoluminescence (PL) measurements for the other substrate and a rough as grown CVD surface are shown in the Appendix for completeness.

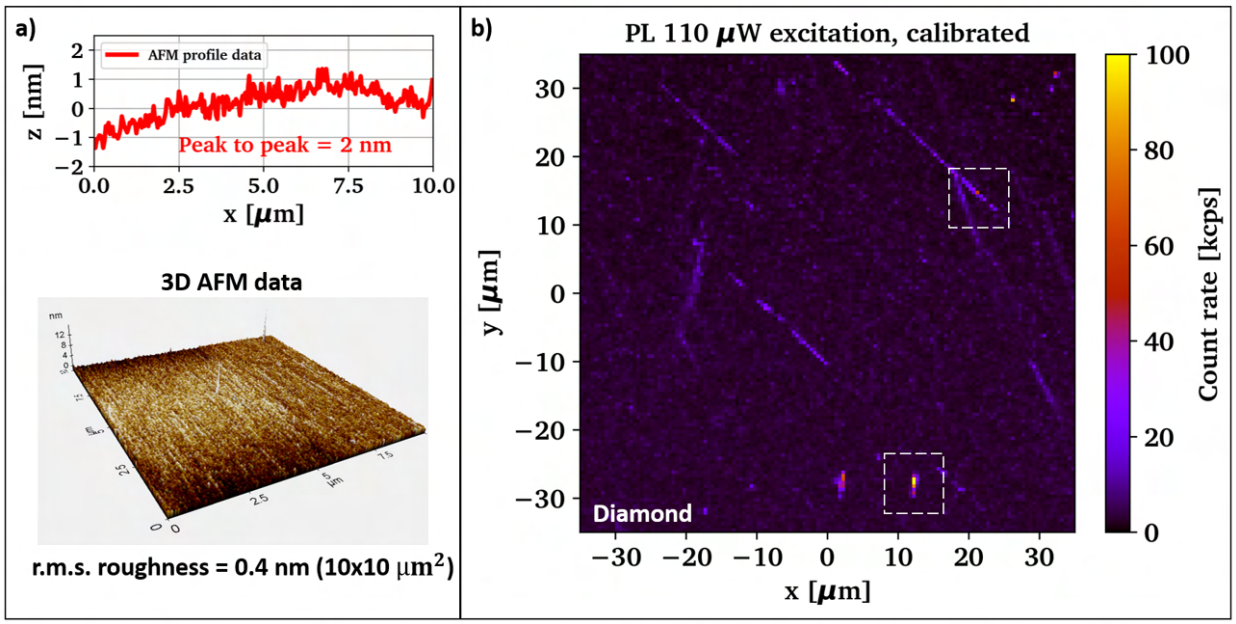

Figure 4.4: Diamond sample with a successfully polished surface, but the nitrogen rich layer seems to have been removed to a large extent (after Piranha acid clean, see Appendix). a) AFM line scan and 3D presentation of the surface roughness (SSS-NCH) taken close to the sample centre, b) xy PL map in the surface layer with two interesting emitter formations marked (100x objective, 40 μm pinhole, 2x 550 nm LP, 1x 650 nm LP). The scan origin matches the origin of the whole sample, using the corners of the diamond as alignment markers. The following transfer print process was based on the here retrieved emitter positions (1st round of printing).

We can only estimate the exact depth of the NV^- clusters on the smooth sample, but the partial removal of the layer indicates that we are in a regime of < 500 nm depth. Because our setup lacks a spectrometer we have actually not confirmed the identification of the PL light to stem from nitrogen vacancy centres, but they should be the main emitters present on this highly engineered sample.

We select two types of lenses for our testing, a single GaN micro-lens with a radius of curvature around 5 μm and a 2x2 GaN micro-lens array with around ROC $\approx$ 6 μm. Corresponding microscope images and AFM profile scans taken after transfer printing to a single crystalline diamond surface are shown in Fig. 4.5. Both devices are selected for their apparent excellent contact to the diamond receiver surface indicating very low membrane bow.

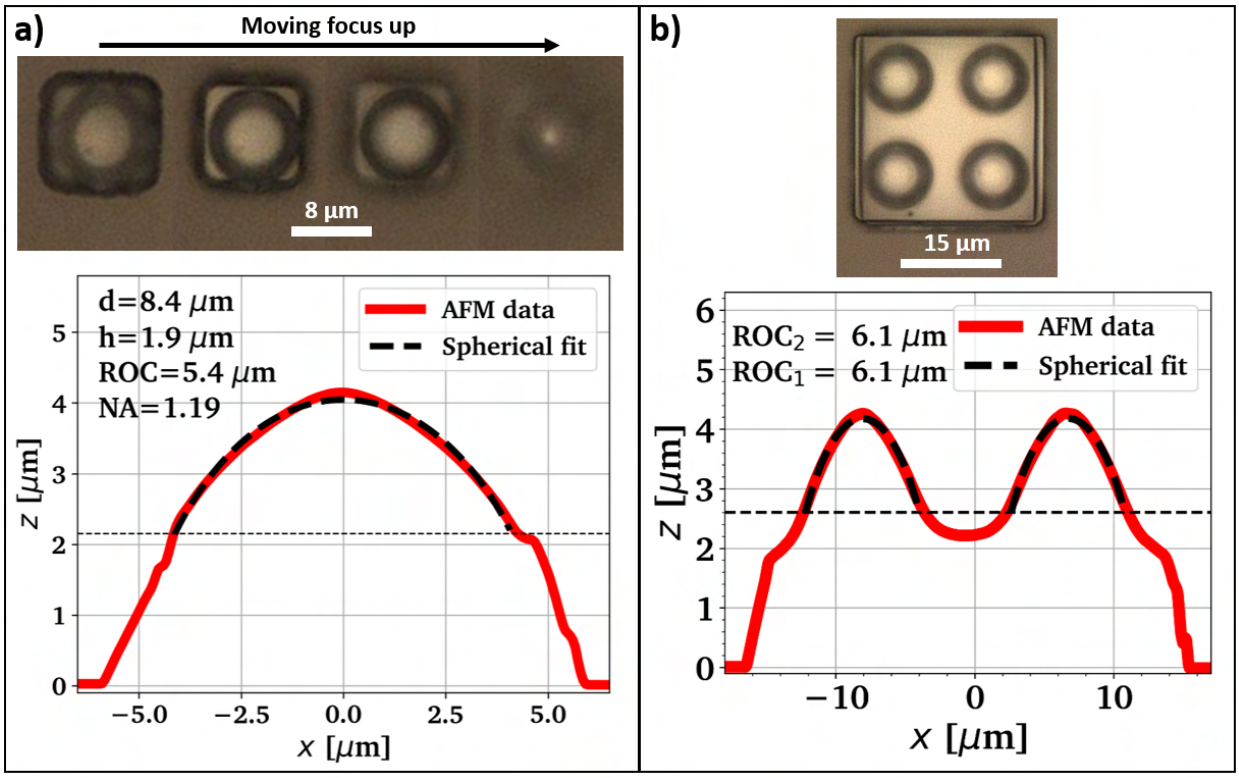

Figure 4.5: Microscope images and AFM line scans (SSS-NCH) of the single micro-lens and a representative micro-lens array used for the coupling experiments to shallow NV centres in this subsection.

We quantify the expected collection improvement in dependence of the numerical aperture by running FDTD simulations with the results presented in Fig. 4.6. We focus on the potential improvement using the single GaN lens with ROC $\approx$ 5 μm. In a) we see a cross section through the simulation region observing the electrical field strength squared emitted by two classical dipole sources 200 nm below the diamond surface on a logarithmic scale, comparing the case of a planar diamond interface and with a transfer printed GaN micro-lens membrane device mimicking the device shown in Fig. 4.5 a). We monitor the emission pattern at the green lines in the near field above the device and calculate the far field emission pattern, which is shown in Fig. 4.6 b).

Because the Purcell enhancement is close to unity in both cases and the far field pattern does not vary significantly with wavelength we can average both far field pattern and the light transmission through the green detector surfaces between $\lambda = 650 - 750$ nm to extract the integrated photon extraction efficiency as a function of the maximum far field cone angle collected (or the numerical aperture NA of the collection optics) used in an optical experiment. The result is shown in Fig. 4.6 c), comparing both cases and indicating the expected enhancement as function of collection NA in the lower plot. We see that a significant photon extraction enhancement of 4-5x is expected for microscope objectives with an NA varying between 0.5 and 0.95.

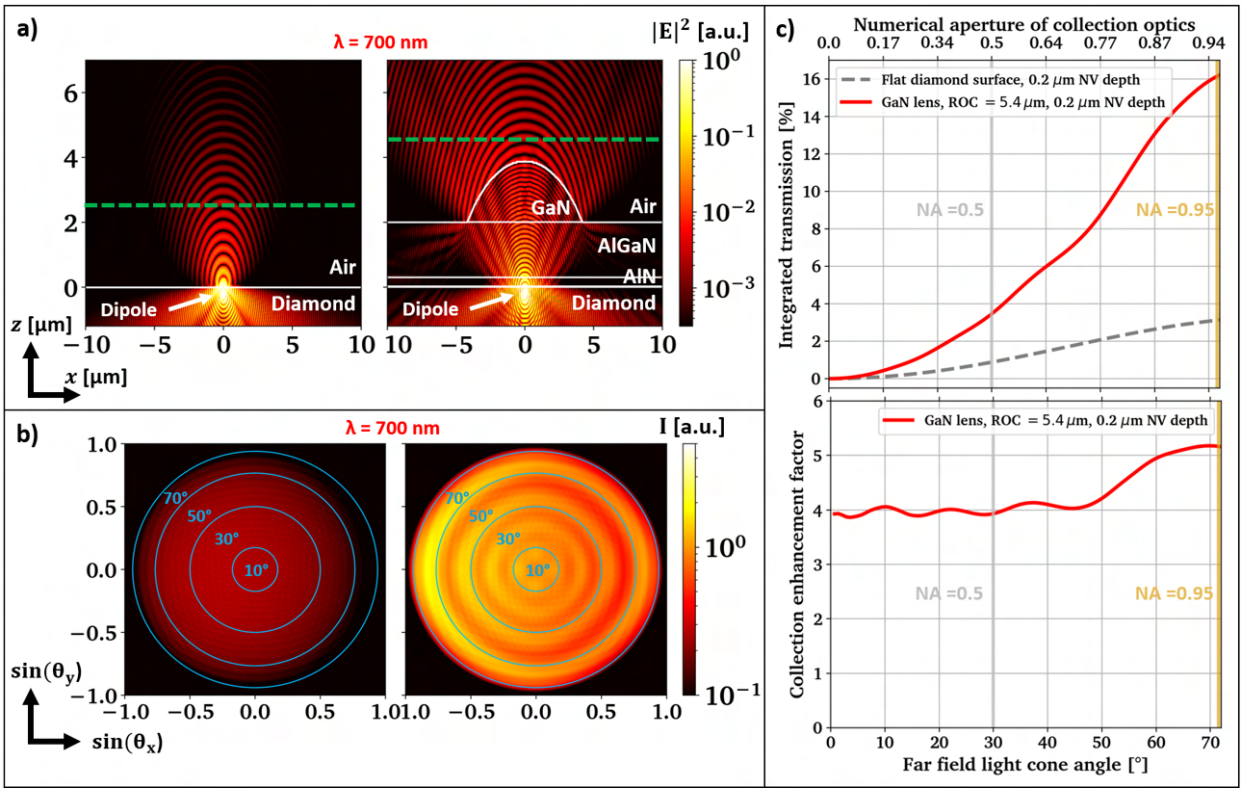

Figure 4.6: FDTD simulations showing the emission characteristic of a two orthogonal dipole emitter mimicking an NV^- centre in 200 nm depth below a planar (100) diamond substrate without and with a spherical GaN micro-lens ($d = 8.4\,\mu$m, $h = 1.9\,\mu$m) matching the lens device used in the experiments shown in Fig. 4.5 a). Simulation cross sections (a) and far field projections (b) along 2D monitors positioned at the indicated green lines in a) are taken at $\lambda = 700$ nm, c) averaged transmission ($\lambda = 650-750$ nm) through the monitors above the device in a) and collection enhancement based on the comparison of both curves (gray and red).

Because we are going to probe clusters of NV^- centres we will not see a saturation of the photoluminescence typically observed if only a few emitters are present. Usually the saturation effect can be exploited to differentiate between more efficient pump laser delivery and enhanced photon collection efficiency. In order to gain insight into the improvement of light delivery to the NV centres in close surface proximity, we are running FDTD simulations with Gaussian beam sources that correspond to different numerical aperture of the microscope objectives used in the experiment. The findings are shown in Fig. 4.7, comparing focusing efficiency in roughly 200 nm depth below the diamond surface without and with a single added GaN micro-lens mapped on the device shown in Fig. 4.5 a).
At a comparable wavelength to the excitation laser used in the experiment and optimizing the electrical field strength at the targeted position by varying the position of the Gaussian beam waist, we find around 3.5x and 2.1x expected enhancement of the maximum field intensity around 200 nm depth. This is probably partially due to mitigation of spherical aberration observed when focusing into a planar high-index material. We also observe that the GaN micro-lens can significantly reduce the FWHM of the focal spot due to enhancement of the overall system NA.

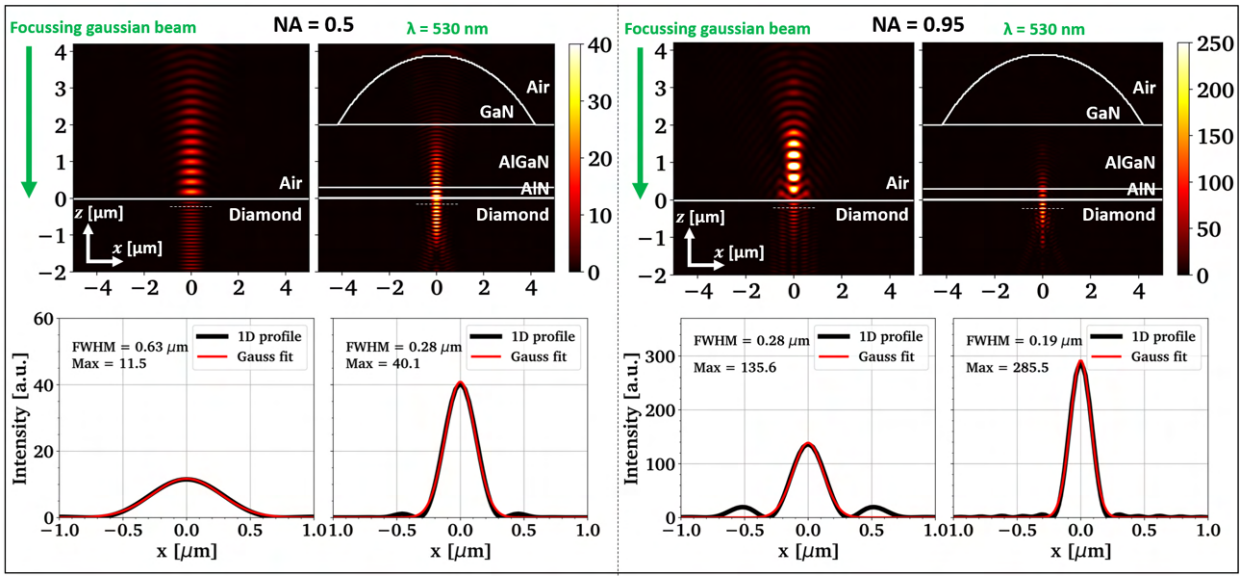

Figure 4.7: FDTD simulations of a Gaussian beam focusing from above at 200 nm depth in a diamond substrate with and without a spherical micro-lens ($d = 8.4\,\mu$m, $h = 1.9\,\mu$m, same geometry as in Fig. 4.6). The numerical aperture (NA= 0.5 on the left vs. NA= 0.95 on the right) is chosen in the beam setting, referring to a full vectorial representation of the Gaussian beam source at $\lambda = 530$ nm, roughly matching the emission wavelength of the pump laser used in the experiments. The beam waist position is varied to maximize the intensity at 200 nm depth. The line scans below are taken with ±50 nm deviation around this depth to cut through the most adjacent field maximum. The cross section plots show the electric field amplitude squared in arbitrary units.

We now turn to the experimental results. Fig. 4.8 contains a confocal PL depth scan taken through the single GaN micro-lens device shown in Fig. 4.5 a) that is placed centrally above an emitter cluster. We observe significant PL response from the sidewalls of the GaN/AlGaN/AlN membrane device and significant PL background from the GaN micro-lens itself at high z-positions.

The targeted printing of the lens is facilitated by marking the positions of the substrate corners in the confocal microscope setup. The PL map shown in Fig. 4.4 has its origin at the geometric average of the corner positions and we transfer this coordinate system to the transfer print tool. The main error is expected to stem from rotational misalignment and the manual marker identification. The position that was acutally targeted for the lens printing is the bright cluster visible at ca. (-1,1) μm in the PL map shown in Fig. 4.9 b) on the right hand side. We therefore performed a targeted printing process without any dedicated marker structures with around 1 μm placement accuracy in x and y.

Because the emitter is suspected to be placed in nm-proximity to the surface, we would not expect a dramatic shift of the emitter position in z due to the introduction of the micro-lens when considering a geometric optics picture. Generally emitters below planar diamond surfaces appear to lay closer to the surface than they are due to the strong refraction at the interface. The micro-lens mitigates most of the refraction, moving the optimal focus position closer to the 'real' position of the emitter. As shown by the xz scan displayed in Fig. 4.9 a), we find the apparent position of the emitter cluster ca. 3 μm below the diamond surface which is identified by the PL response from the GaN micro-lens membrane. This shift could be explained if the real emitter position is actually in a few μm depth below the surface. This increased z-separation between emitter cluster and micro-lens device benefits the rejection of background light emitted by the GaN micro-lens by the confocal arrangement.

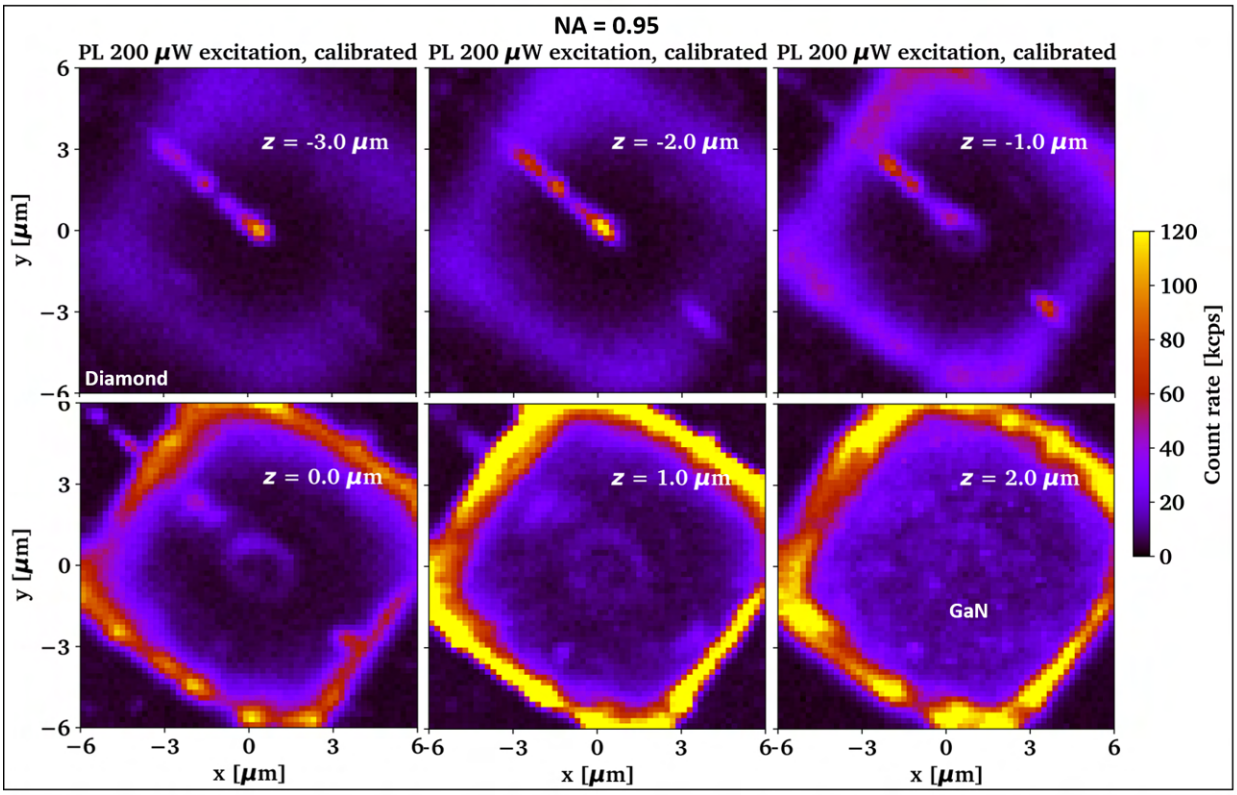

Figure 4.8: Single GaN lens above an emitter cluster (centre of image, diagonal features are further emitter clusters) measured with an objective NA= 0.95: xy photoluminescence maps at different sample depth after transfer printing the single GaN micro-lens shown Fig. 4.5 a). Alignment was performed using the PL map in Fig. 4.4 b), the lens was found to be misplaced by ca. 1 μm in both x and y direction. Still a localised emitter cluster was found centrally below the micro-lens. PL maps are linearised (compare appendix H for procedure) and taken with 100x objective, 40 μm pinhole, 2x 550 nm LP, 1x 650 nm LP.

In order to assess the collection improvement caused by the lens we take a power series with the micro-lens in place and immediately after removing the micro-lens via transfer printing with the setup left in the same alignment conditions. In order to extract the maximum count rate at each excitation power level we take a series of 2D scans with slightly varying z position around the ideal emitter position and extract the difference between the average of the three highest and lowest intensity pixels after correcting for the non-linear SPAD response (see Appendix). The result is shown in Fig. 4.9 b) for NA = 0.95 yielding ca. 2.7x improvement. The subplots in c) show the investigated emitter cluster after lens removal in an xz and xy confocal PL scan. We repeat the same procedure for NA = 0.5 yielding 12.4x improvement after discounting for 10% background light that could be stemming from the GaN micro-lens and is not rejected by the lowered z-sectioning ability at higher microscope NA. For this lower NA we perform an iterative printing and PL mapping process to place the device above the bright emitter cluster missed by 1 μm along x and y in the initial printing attempt. We did not perform the measurements of varying NA at the same lens position, because we wanted to avoid any setup changes between the measurement with and without lens. Therefore we remove and replace the lens between these measurements.

The simulations have predicted ca. $\approx 5{\cdot}2 \approx 10$x (NA = 0.95) and $\approx 4{\cdot}3.5 \approx 14$x (NA = 0.5) improvement of the combined photon extraction and pumping efficiency. Interestingly the measured enhancement agrees quite well for NA = 0.5, while the discrepancy is large for NA = 0.95. If the real emitter position

would against our expectation lay in a few μm depth, we could expect a significantly reduced collection enhancement due to lowered coverage of the angular space above the emitter by the micro-lens aperture.

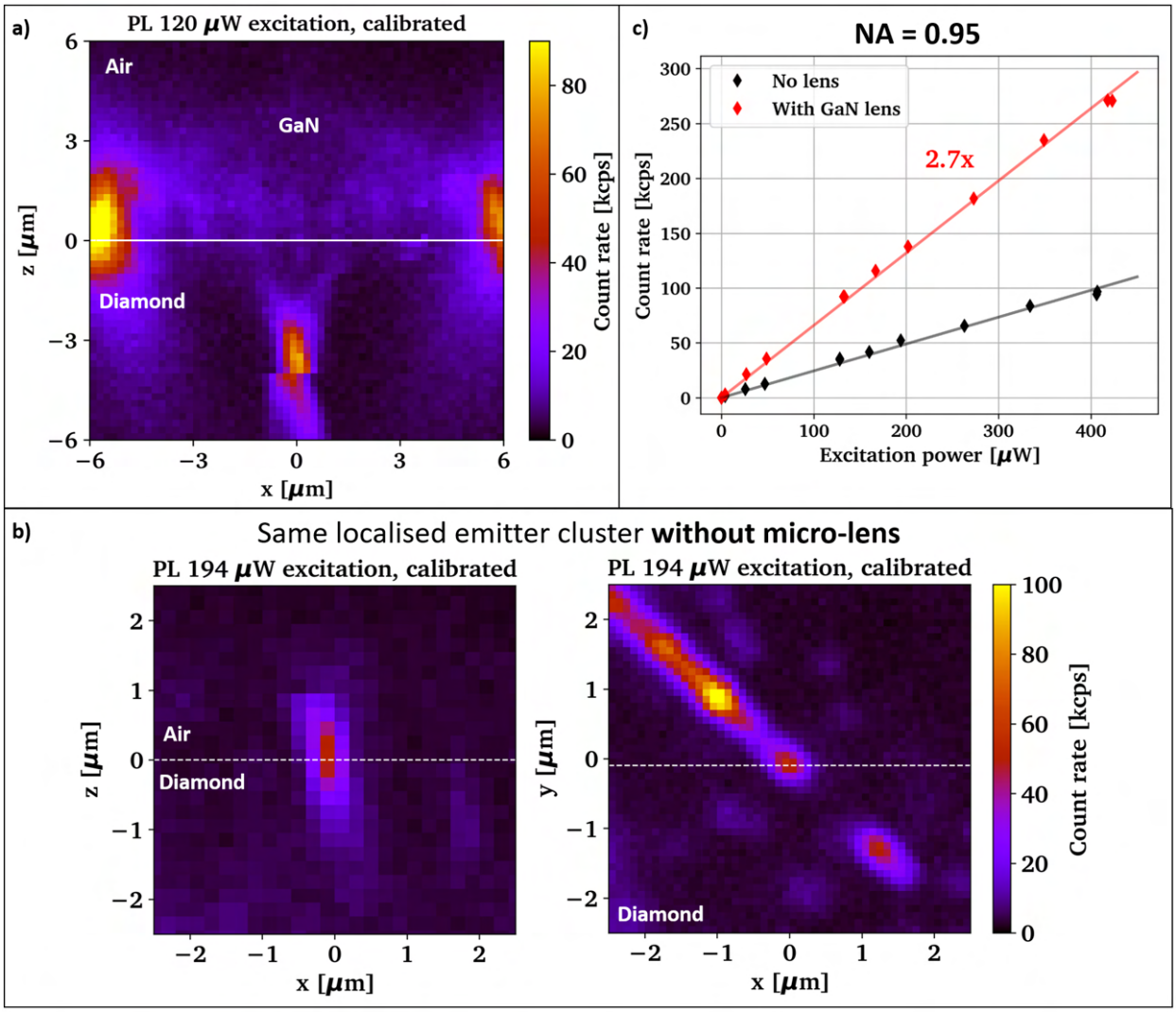

Figure 4.9: Single GaN lens above an emitter cluster measured with an objective NA= 0.95: a) xz PL scan through the emitter cluster below the single GaN micro-lens shown in Fig. 4.8, b) PL maps of the same localised emitter cluster after the micro-lens was removed, with the white dotted lines indicating the shared plane between the two scans. The transfer print process was aimed at the brighter emitter cluster at ca. (-1,1) μm in the right map, the diagonal feature is a series of emitter clusters inside the sample, c) linearised power series taken on the same local emitter cluster without and with micro-lens. Background light is subtracted and the maximum intensity of a 3D emitter scan is shown. Both power series were taken without any changes to the optical beam path. PL data is linearised (compare appendix H for procedure) and taken with 100x objective, 40 μm pinhole, 2x 550 nm LP, 1x 650 nm LP.

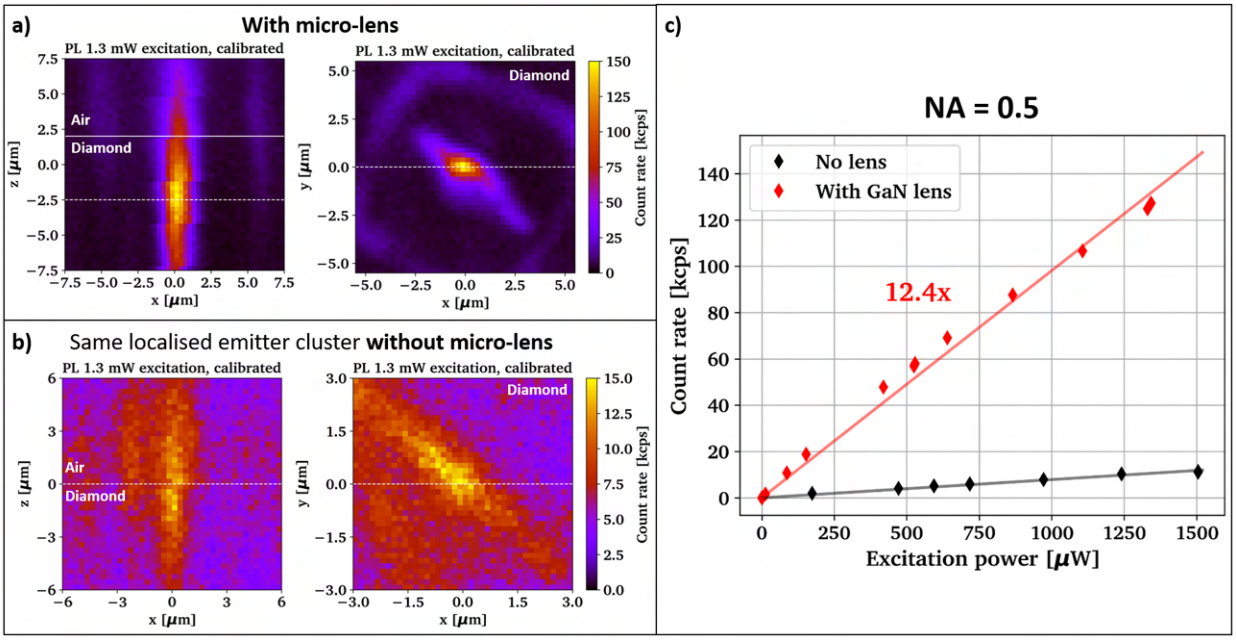

Figure 4.10: Single GaN lens above an emitter cluster measured with an objective NA= 0.5: a) xz and xy PL scans through a different emitter cluster below the single GaN micro-lens shown in Fig. 4.8 with the white dotted lines indicating the shared plane between the two scans, b) PL maps of the same localised emitter cluster after the micro-lens was removed, with the white dotted lines indicating the shared plane between the two scans, c) Linearised power series taken on the same local emitter cluster without and with micro-lens. Background light is subtracted and the maximum intensity of a 3D emitter scan is shown. Both power series were taken without any changes to the optical beam path. To take PL background from the GaN micro-lens into account, the PL signal with micro-lens is reduced by 10 % (compare Fig. 4.11 a). PL data is linearised (compare appendix H for procedure) and taken with 50x objective, 25 μm pinhole, 2x 550 nm LP, 1x 650 nm LP.

We want to highlight two further interesting experimental results displayed in Fig. 4.11. In a) we see a yz and xy confocal PL scan through the single GaN micro-lens device printed on a location without significant emission from the diamond substrate taken at NA = 0.5. We can see that at high excitation power significant background fluorescence is observed in the centre of the lens, potentially overlapping with emitters in μm proximity to the diamond surface. This GaN/AlGaN/AlN PL emission is an undesirable side effect of the heterogeneous integration scheme, which we will be discussing in more detail in the next section. It would reduce the photon purity in any quantum based experiment adding noise to the measurements. But a high NA objective lens system seems to be able to filter the light sufficiently even for emitters in nm-proximity to the diamond surface, even though it is not fully clear whether this is what we are observing in these tests.

Fig. 4.11 b) contains the comparison of a shallow emitter cluster that is combined with the GaN micro-lens array device shown in Fig. 4.5 b). Even though we tried several alignment positions between lens and emitter, we are not able to create significant count rate enhancement. Due to the relatively small aperture of these lenses this could be explained if the emitter cluster is several micron deeper below the diamond surface than expected. Another explanation could be the existence of an air-gap on the order of 50-100 nm, which would not generate any significant colourization of the devices but which might increase reflection losses. We will find in the next section that such an effect is expected to be reasonably weak. Generally the quality of the GaN micro-lenses in the array is not optimal with r.m.s. deviation of around 50-60 nm from the ideal spherical shape, which could additionally contribute to

reduced photon extraction and pump focus enhancement.

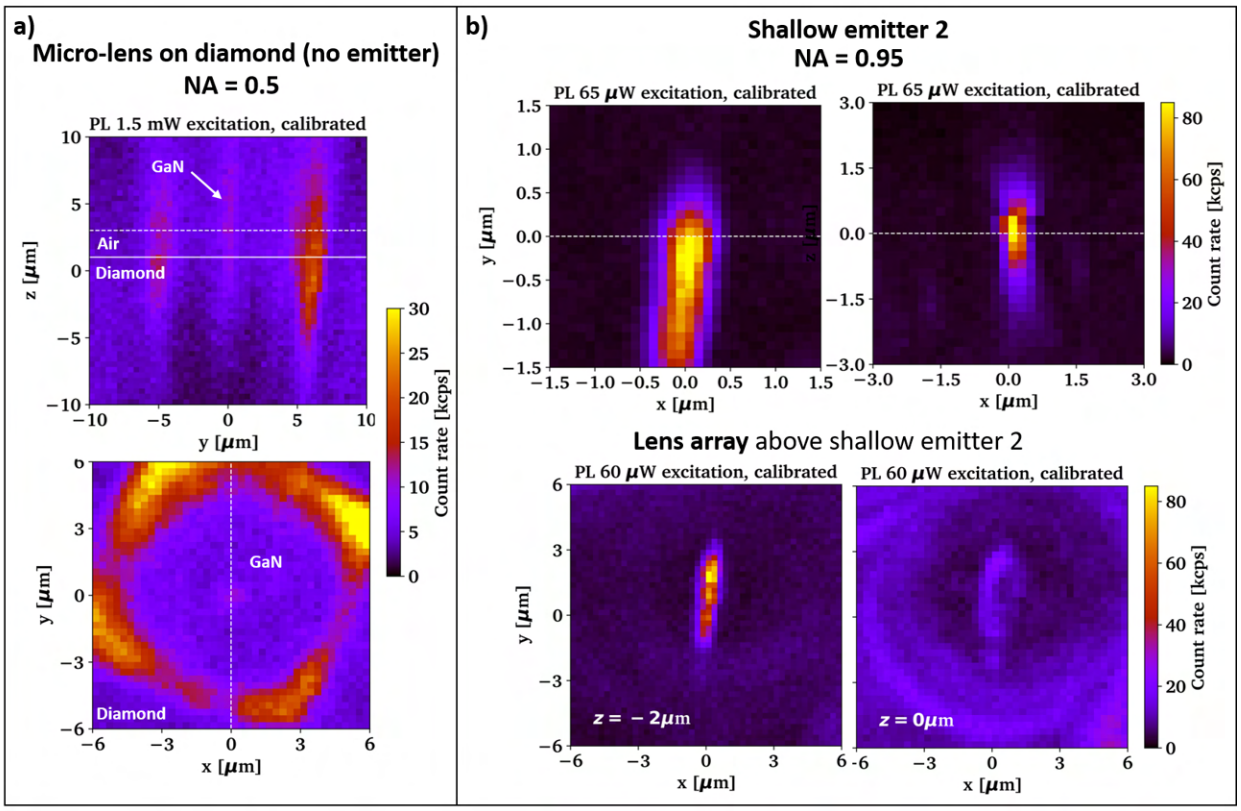

Figure 4.11: a) Emission signature of the GaN micro-lens if the objective with NA= 0.5 is used (50x objective, 25 μm pinhole, 2x 550 nm LP, 1x 650 nm LP), the shared plane between the scans is indicated with the white dotted lines. In 2.5 μm depth a background of around 10 kcps is observed in the very centre of the lens, b) Test integration of a GaN micro-lens array similar to the device shown in Fig. 4.5 b) with the emitter cluster shown in the bottom part of Fig. 4.4 b). PL maps at similar excitation power before (top) and after lens integration (bottom) are shown on the same scale for comparison, indicating no effective enhancement of the PL emission from this emitter cluster (PL data is linearised (compare appendix H for procedure) and taken with 100x objective, 40 μm pinhole, 2x 550 nm LP, 1x 650 nm LP.)

4.1.3 Summary

We find significant improvement of light matter coupling between suspected clusters of NV^- centres and a single GaN micro-lens. The experiments leave doubt about the exact depth of the emitter investigated, because a deeper position of the clusters could explain several main observations, including the absence of enhancement from a GaN micro-lens array. We additionally demonstrate that GaN micro-lenses can be placed accurately above targeted emitter clusters in diamond.

4.2 Laser written diamond NV centres for quantum computing and quantum networking applications

With these promising initial results in hand we move to the discussion of coupling GaN micro-lenses to NV^- centre doublets created at targeted positions by direct laser writing. With that we are entering the quantum regime and a highly engineered system space with potential applications in quantum networking and computing. Due to the novelty of the presented micro-system assembly approach and practical significance for diamond colour centre research most results in this section are published in [238]. The NV centres discussed in this section are created and measured using the dedicated setups of our collaborators at the University of Oxford.
We will start this section with a quick review of the relevant NV centre applications to highlight the importance of photon extraction efficiency in quantum applications.

4.2.1 Review: Quantum computing and networking with NV centres

Today there is immense research interest in 'quantum technologies' which usually refer to quantum communication, computing and sensing schemes that directly exploit purely quantum mechanical effects like superposition and entanglement to enhance the performance in the respective application space compared to traditional technologies that build on effects that can be explained by classical physical theories [239, 240].
In the sub-field of quantum computing the basic idea is to isolate and control the wave function of 2-level quantum systems in terms of population and phase to gain access to the immense information density that can be stored in quantum systems. A simple example is given by Nielson and Chuang in their famous book on the basics of quantum information theory: The Hilbert space of only 500 2-level quantum systems (qubits) has more degrees of freedom than the number of atoms that exist in the observable universe and still the information one might associate with the population and phase of these systems seems to be constantly and correctly be tracked by nature. The language used here adapts the perspective of information theory and assumes that quantum mechanics appropriately represents how nature operates [81]. The main motivation behind investigating quantum computation is to harness some of this immense computational power for the benefit of humanity.
The NV^- centre in diamond stands at the forefront of early demonstrations of so-called quantum networks that are used to remotely entangle distant 2-level quantum systems, so far on a few qubit scale [48, 61–64, 176, 177, 241, 242]. The idea of a 'quantum internet' has been proposed [48, 64, 243] to secure information exchange beyond the factoring based RSA encryption used today and enhance quantum computation and sensing capabilities [48]. To enhance quantum computation, network nodes could contain a 'quantum processor' with several data qubits that can be controlled by quantum logic gates [81] and are to be combined by exchanging photons as flying qubits that transfer entanglement between distant nodes, potentially easing the scaling of these complicated and hardware intensive systems while avoiding cross-talk. The idea is very similar to the combination of many sub-processing units in a classical data-centre or supercomputer.
The NV^- centre in diamond is specifically interesting because its electron spin can couple via dipole-dipole interaction to the native ^{14}N and surrounding ^{13}C nuclear spins. ^{13}C occurs naturally at a percentage of

roughly 1.1% around otherwise spin-free ^{12}C atoms. The nuclear spins are highly decoupled from their environment due to their weak dipole moment, leading to long spin decoherence times which allows to store 2-level quantum information efficiently [48, 49]. The interaction with the electronic spin of the NV$^-$ centre is facilitated by driving population transfer between the hyper-fine levels of the overall system, entangling nuclear and electronic spin states, compare Fig. 4.12 a).

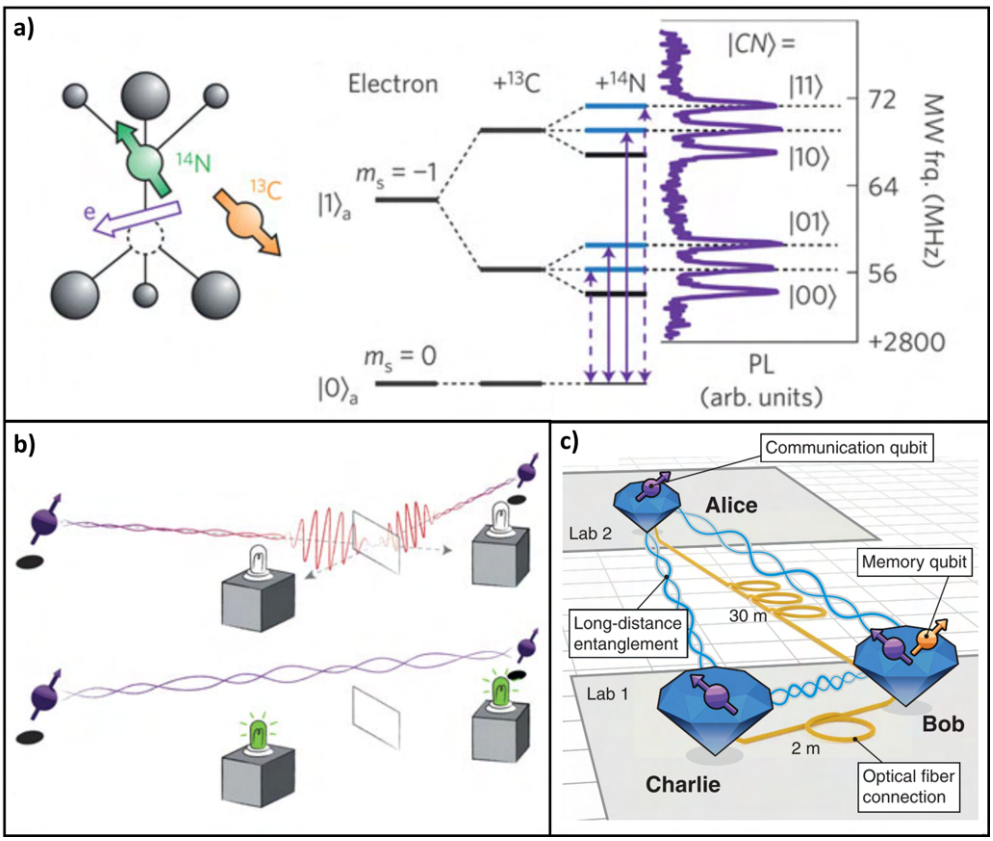

Figure 4.12: a) Schematic showing relevant electron and nuclear spins in the surrounding of the diamond NV centre and the resulting hyper-fine splitting of the $m_s = -1$ spin state that can be used to address nearby nuclear spins using MHz drive frequencies and optical read-out, b) measurement based remote entanglement scheme using a 50:50 beam splitter and single photon detectors. The quantum-interference effect removes the 'which-path' information leading to the collapse of the wave function of the spin-photon state into a remote spin-spin bell state [49, 241], a)/b) adapted from [63], c) demonstration of a multi-node quantum network with entanglement shared between two electron and one nuclear spin state, adapted from [177].

Remote entangling of electronic and nuclear spins has been demonstrated by spin-photon entanglement and successive 2-photon quantum interference using a 50:50 beam splitter and single photon detectors [49, 63, 241], compare Fig. 4.12 b). This leads to the recent demonstration of a multi-node quantum network, entangling two electron spins and a nuclear spin in separate cryostats [177], compare Fig. 4.12 c). Another recent demonstration shows how five ^{13}C spins in nm-proximity to a single NV$^-$ centre can be separately addressed and a quantum error correction code is implemented to achieve a logical qubit, compare Fig. 4.13.

To date all remote entanglement experiments reported with diamond NVs use hemispherical FIB solid immersion lenses (SILs) to enhance spin-photon coupling [48]. One of the reasons for using SILs in favour of other microstructures is that the indistinguishability of photons emitted by separate NV centres is reported to deteriorate if the emitters are in nm-proximity to the surface [48]. Fig. 4.14

summarizes the typically chosen architecture with microstructured strip lines delivering a static electric field for resonance tuning and microwave and radio frequency pulse series. In addition optical on- and off resonant pulsed excitation, charge state recovery and optical readout is delivered through fibre coupled SILs while an outer magnetic field is applied along the NV centre axis. Effective light collection is demonstrated using multimode fibres and an anti-reflection coating that is applied on top of the monolithic diamond lens [49].

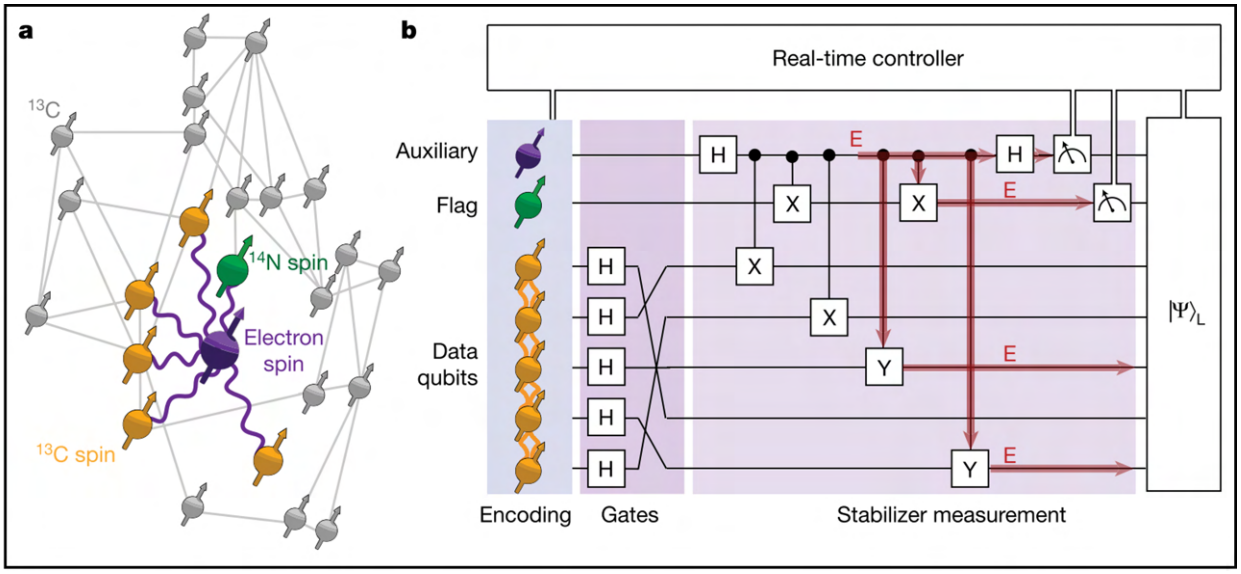

Figure 4.13: a) Schematic showing how five physical data qubits based on ^{13}C nuclear spin in the vicinity of a single NV$^-$ centre and the nuclear spin of the nitrogen atom are coupled to the colour centre's electron spin, which allows the optical read-out of the nuclear spin states, b) illustration of a five qubit error correction code with quantum gates (Hadamard, controlled Pauli-X, controlled Pauli-Y, SWAP) performing 1 and 2 qubit logic operations building a single logical qubit from the 7 involved spin states, adapted from [176].

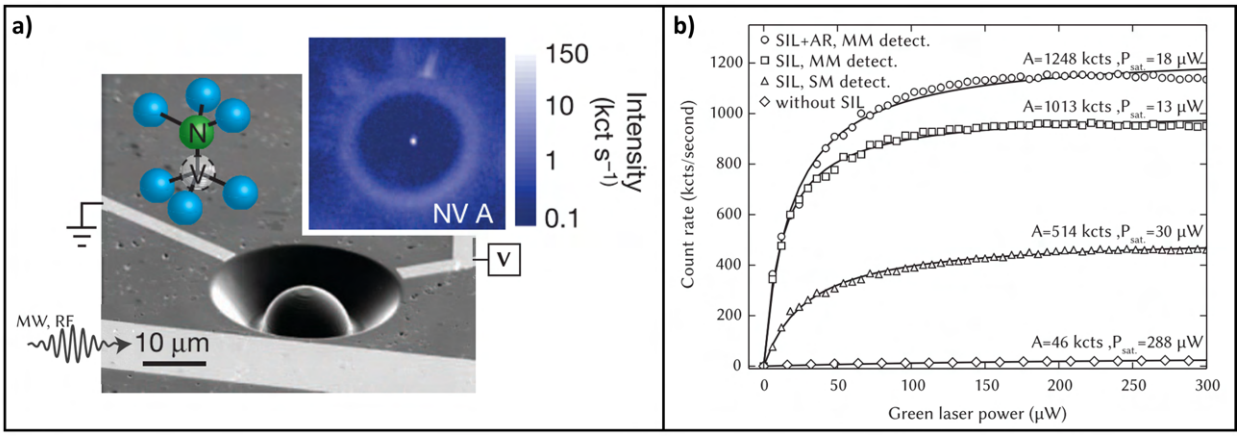

Figure 4.14: a) Typical experimental arrangement in quantum networking and computing demonstrations using the NV$^-$ centre: A focused ion beam milled solid immersion lens is carved around a single emitter and electrical strip lines are used to apply a static electric field for tuning the ZPL of the NV$^-$ centre as well as for the application of resonant microwave and radio frequency pulses for coherent control of the electronic and nuclear spin states associated with the emitter. The sample is then cooled to cryogenic temperatures and a static outer magnetic field is applied along the symmetry axis of the NV centre, adapted from [242], b) single (SM) and multimode (MM) fibre coupled photoluminescence count rates of a single NV$^-$ centre without and with SIL. A single thin layer of AlO_x serves as an anti-reflection coating, adapted from [49].

Even though these early quantum demonstrations with NV centres coupled to monolithic SILs are promising, the entanglement generation rate is limited to $< 100\,\mathrm{Hz}$ [48]. Embedding NV centres into in nanophotonic cavities is challenging due to their charge sensitivity which leads to decoherence, but open cavity approaches with NVs in thin SC membranes are promising to speed up entanglement rates by up to 2 orders of magnitude [48]. The interaction between NV and cavity mode might be additionally enhanced by an appropriately designed micro-optical element, depending on the cavity design.

4.2.2 Outline of the work

In this section we investigate whether additive GaN micro-lenses can replace monolithic diamond SILs fabricated by focused ion beam milling in the context of quantum applications, while offering enhanced scalability. Doing this we want to keep in mind that cavity based coupling approaches are likely to offer much stronger benefits for this application than simple lenses alone.

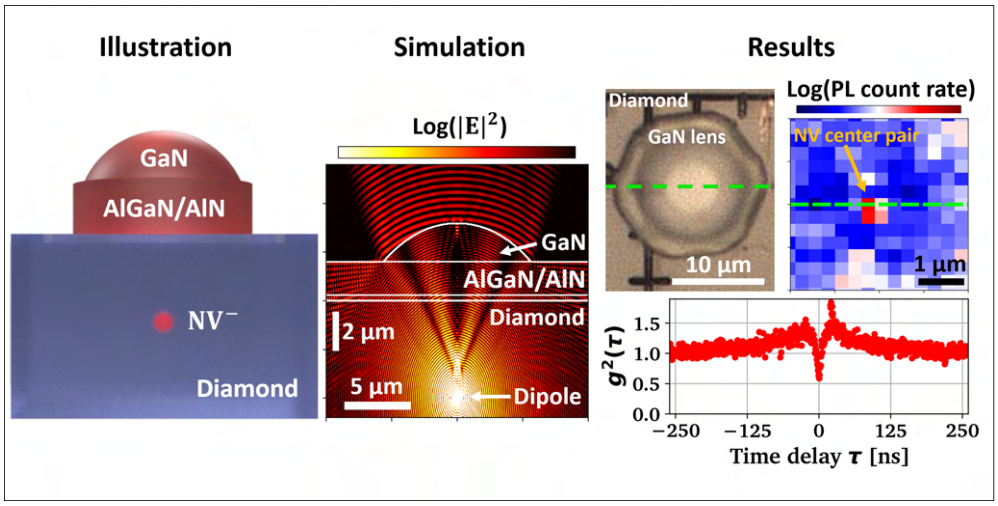

Figure 4.15: Illustration of the device geometry in this subsection, FDTD simuation results for a GaN lens combined with a dipole emitter in 5 μm depth, and transfer printing result, PL map and 2nd order autocorrelation measurement of an emitter pair through a GaN lens. All these results are discussed in more detail in the following figures.

We report increased fluorescent light collection efficiency from laser-written nitrogen vacancy centres (NV) in bulk diamond facilitated by micro-transfer printed GaN solid immersion lenses. In recent years there has been significant progress in developing techniques for fabricating NV centres in diamond, including ion implantation [25, 26], and low energy electron beam irradiation [27, 28] with post-treatment annealing. Laser writing has emerged as a particularly attractive fabrication technique due to the unique non-linear light-matter interaction mechanism so that single NV^- centres can be fabricated deterministically with minimal residual lattice damage and precision positioning inside host materials [29–32]. Both laser-writing of NV centres and transfer printing of micro-lens structures are compatible with high spatial resolution, enabling deterministic fabrication routes towards future scalable systems development. The micro-lenses are integrated in a non-invasive manner, as they are added on top of the unstructured diamond surface and bond by van-der-Waals forces. This heterogeneous integration approach allows the decoupling of the lens fabrication processing from the vacancy centre definition and selection, while significantly speeding up the lens fabrication due to the use of wafer scale compatible parallel wet and dry etching techniques. As discussed the GaN lenses are realized using the balanced etch selectivity of

photoresist and GaN in inductively coupled plasma (ICP) etching creating high aspect ratio lenses, which cannot commonly be achieved when processing diamond with ICP etching [95]. For emitters at 5 μm depth, we find approximately 2× improvement of fluorescent light collection using an air objective with a numerical aperture of NA = 0.95 in good agreement with simulations. Similarly, the solid immersion lenses strongly enhance light collection when using an objective with NA = 0.5, significantly improving the signal-to-noise ratio of the NV centre emission while maintaining the NV's quantum properties after integration.

4.2.3 Fabrication flow and measurement methods

A schematic of the process flow is indicated in Fig. 4.16 while corresponding experimental results are shown in Fig. 4.17.

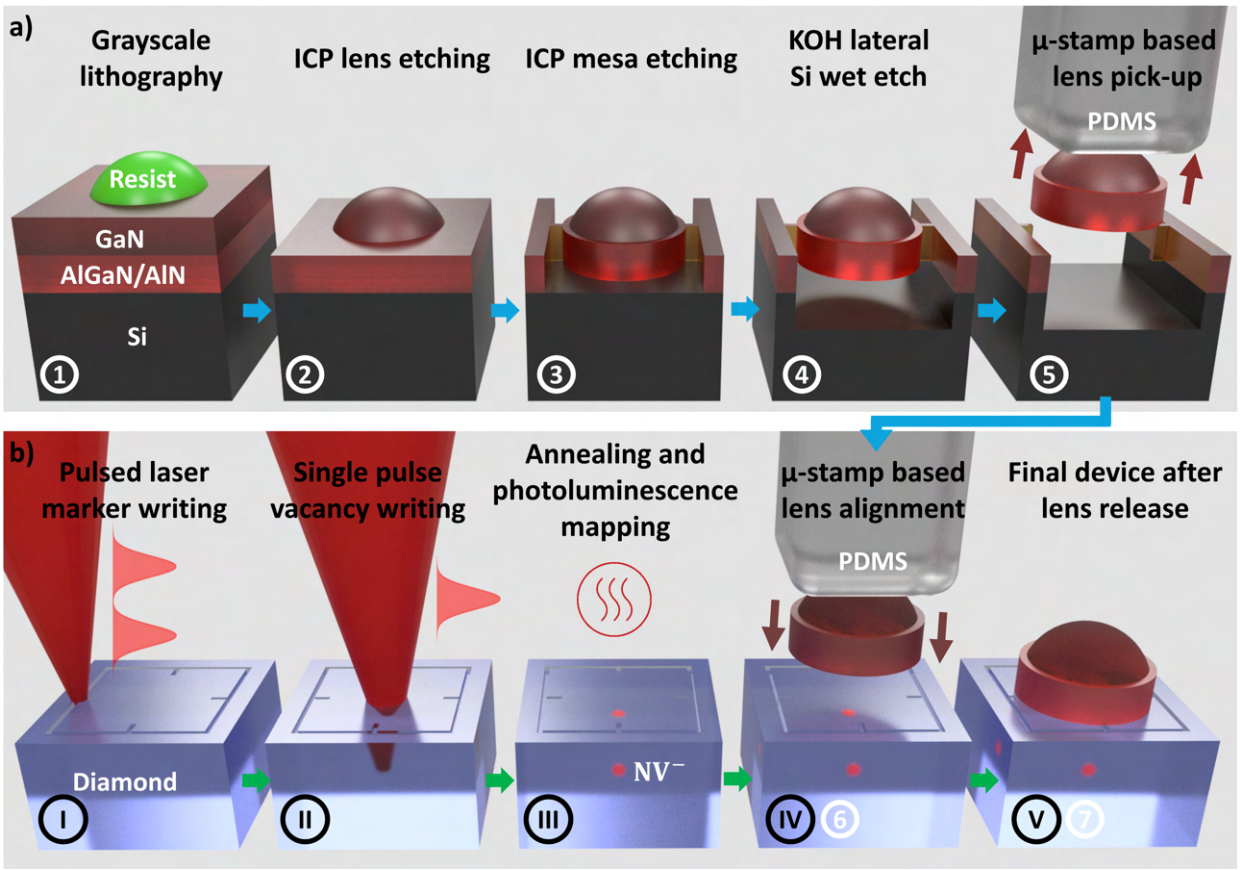

Figure 4.16: Schematics describing the process flow, (a) suspended GaN solid immersion lenses are fabricated by parallel plasma dry and wet etching techniques, (b) after initial marker writing, a NV^- defect centre is generated in single crystalline diamond by pulsed laser writing and subsequent thermal annealing, and the suspended GaN lenses are assembled above the defect centre with micro-transfer printing.

Fig. 4.16 a) illustrates how the GaN solid immersion lenses are defined and suspended on a strain-optimised heteroepitaxially grown GaN-on-Si chip [224, 226, 244] based on the wafer-scale compatible microfabrication process and transfer printing integration discussed in Chapter 2 and 3.
The fabrication of diamond nitrogen vacancy centres at targeted positions and successive GaN SIL integration is illustrated in Fig. 4.16 b). A commercially available electronic-grade single crystalline [100] diamond grown by chemical vapour deposition with nitrogen density < 5 ppb is used as substrate.

Laser writing is implemented using a regeneratively amplified Ti:Sapphire source producing laser pulses with 150 fs duration, 790 nm wavelength and a repetition rate of 1 kHz which is focused using a high-NA oil immersion objective lens (Olympus 60×, 1.4 NA). Initially a high laser pulse energy is used to break down the diamond lattice and create square graphite markers in regions with low intrinsic color centre concentration (I). These surface markers are easily visible in an optical microscope, aiding the localization of the writing sites and later the transfer printing process, as shown in Fig. 4.17 b).
A single pulse from the femtosecond laser is focused inside the electronic grade diamond substrate to introduce an ensemble of Frenkel defects at the target position determined by the markers in 5 μm depth (II). Optical aberrations related to refraction at the diamond interface are corrected using a liquid crystal spatial light modulator [245, 246]. The sample is then subjected to a 1000 °C anneal for 3 hours under nitrogen flow to mobilise the vacancies, some of which combine with intrinsic substitutional nitrogen atoms in the diamond lattice to form stable NV centres (III) [29, 247].
The laser-processed areas of the diamond sample are initially characterized by collecting the photoluminescence (PL) emission with a home-built confocal microscope using an oil immersion objective (NA = 1.25) (III). A 532 nm continuous-wave (CW) laser (GEM 532) is used as excitation source and the collected epi-fluorescence signal is focused on a single photon avalanche diode detector (SPAD), filtering in the spectral range from 600 nm to 740 nm. The setup is described in more detail at the end of this subsection.

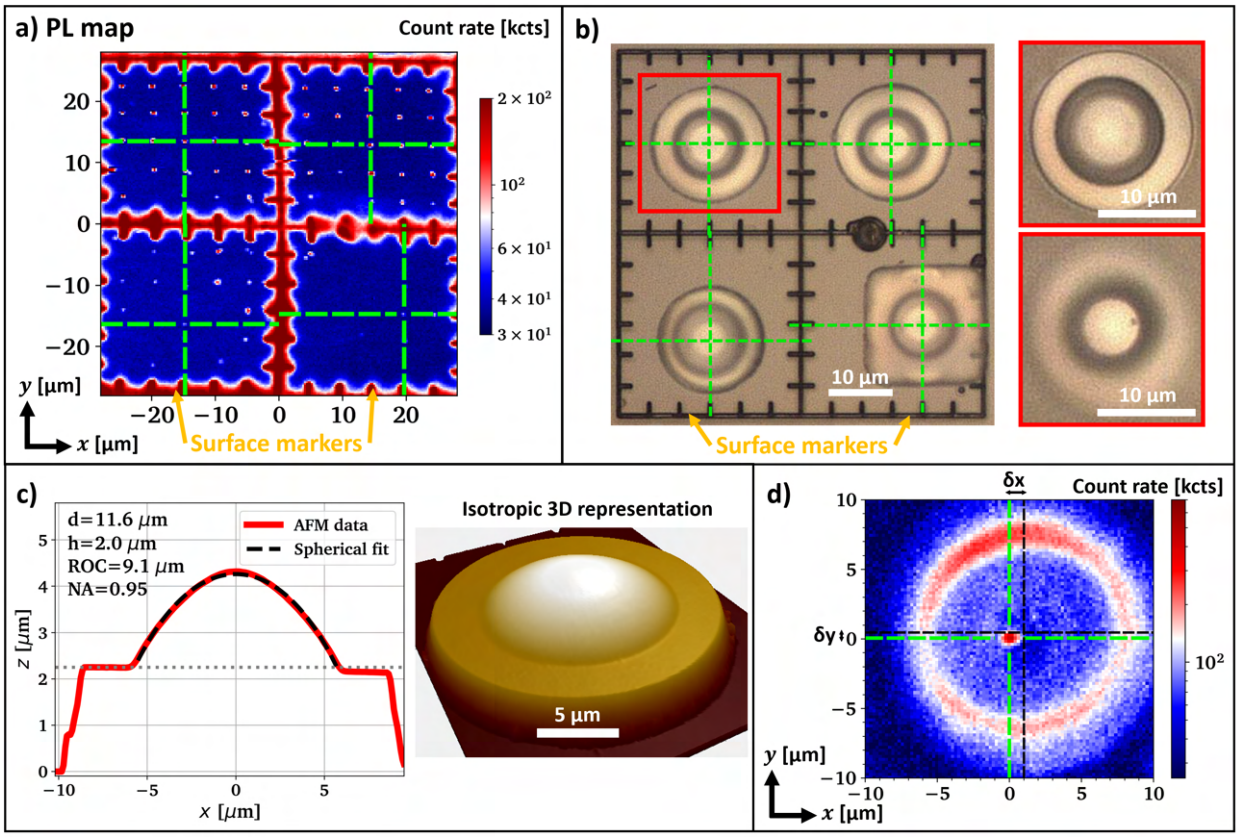

Figure 4.17: a) Photoluminescence image of an example region after laser writing and annealing. The image was recorded using an oil immersion objective with NA = 1.25. Targeted emitter locations are marked with green crosses, b) Microscope images of the assembled GaN SILs above the marked emitters in a), c) AFM data of the GaN SIL with the red frame (top left quadrant) in b), d) Photoluminescence image of a graphitised spot below the SIL from c), recorded using an air objective with NA = 0.5.

Photoluminescence maps of the created emitters were obtained at room temperature (setup description below), with an example shown in Fig. 4.17 a). As can be seen here, each marker quadrant contains an array of 5×5 writing sites with 5 μm spacing. Each site is irradiated by a single laser pulse, with pulse energy kept constant within a particular row but modified between rows. The laser pulse energy range straddles the narrow transition between the regime of lattice breakdown and graphitization to the regime of creating vacancy ensembles without any sp^2-bonded carbon content. The in-plane placement accuracy of the NV centres is expected to be within 250 nm with respect to the grid [29]. The upper two quadrants of the array typically contain graphitised points while the lower two quadrants show vacancy ensembles. Anti-bunched photon emission is identified by collecting $g^{(2)}(\tau)$ autocorrelation statistics using two SPAD detectors and the positions of promising emitters are noted to guide the transfer printing of the GaN micro-lenses.

Using the detailed spatially resolved precharacterization of the photo-emitters, GaN SILs with a radius of curvature (ROC) matching the emitter depth are preselected, removed from their growth substrate and deterministically placed above targeted NV^- centres using the laser written marker structures as alignment guide, as illustrated in Fig. 4.16 a) (IV)/(6). The related experimental results after lens release (V)/(7) are shown in Fig. 4.17 b).

Here multiple micro-lenses are integrated on a small footprint, with a single GaN lens placed in each quadrant of a pre-characterized marker region. The corresponding PL map shown in Fig. 4.17 a) is used to adjust the print position according to the most promising emitter locations. Alignment is mainly limited by image distortions in the PL map and the markers are solely used for visual guidance without applying any numerical methods.

Before transfer printing, an ultrasonic solvent clean and a boiling acid treatment in 95 % sulfuric acid mixed with 30 % H_2O_2 with 3:1 volume ratio is applied to the diamond surface to remove any surface debris remaining after laser writing the surface markers. The laser written marker structures themselves appear as trenches in the diamond surface and do not inhibit bonding after the acid clean is applied. The adhesion of the GaN micro-lens to the diamond surface relies solely on van-der-Waals forces without the use of any adhesion layers. This type of bonding depends on both μm-scale flatness and nm-scale local roughness of the participating surfaces. The micro-lens height is restricted to the 2 μm thick GaN epilayer to achieve a flat bottom surface as discussed in Chapter 3.

The combination of grayscale lithography and resist reflow is used to fabricate spherical and smooth lens profiles with highly engineered lens dimensions. Fig. 4.17 c) shows an atomic force microscopy (AFM) line scan and a true-scale 3D representation of the AFM data of the marked device in Fig. 4.17 b), indicating a smooth symmetrical lens with a fitted ROC = 9 μm, taking 4 μm overall device thickness into account.

After lens integration, we reevaluate the photoluminescence emission from the targeted emitter ensembles though the GaN SILs using air objective lenses. Fig. 4.17 d) shows the emission from a graphitized spot in the top left quadrant using an objective lens with NA = 0.5. The SIL is expected to contribute a magnification similar to its refractive index $n = 2.4$ if the emitter is placed in the geometric centre of the lens sphere [248]. The visible lateral displacement between emitter and lens centre accounts to roughly $(\delta x, \delta y) = (1.0, 0.4)\,\mu$m, indicating a real displacement of $(\Delta x, \Delta y) = (0.4, 0.2)\,\mu$m. Our simulations show, that the gross expected collection enhancement is maintained for both collection optics with NA = 0.5 and NA = 0.95 if the real lateral displacement does not exceed $\pm 1\,\mu$m, see Fig. 4.22.

Noticeably the apparent emitter depth increases due to the printed SIL in agreement with expectation:

Without lens, refraction at the planar diamond interface causes the apparent emitter depth to lie much closer to the diamond air interface than its actual position inside the crystal [125].
The PL map in Fig. 4.17 d) reveals significant background fluorescence from the edges of the lens but the much weaker light emission from the centre of the GaN lens is largely rejected by the confocal microscope arrangement. The photoluminescence emission spectrum of the GaN/AlGaN/AlN layer stack under green CW laser excitation is broad, covering 550-800 nm wavelength at room temperature, compare Fig. 4.18. Therefore spectral filtering can only be partially applied to isolate the NV^- emission. The low-temperature photoluminescence characterization of the printed GaN lens devices under green laser excitation is still an outstanding experimental task. Depending on the mechanism that creates the broad red emission (for example if the broadening is phonon related) cooling might reduce the emission or change the spectral shape which could benefit the removal of the PL by filtering. In literature usually excitation above the band-gap is applied, and a broad emission called the yellow band similarly covering the yellow-to-red visible spectral region is observed in MOCVD grown samples at cryogenic temperatures [249]. This emission is linked to carbon inclusions into the lattice [8], which are hard to avoid if metal-organic precursor gases are used as in the employed MOCVD growth method.

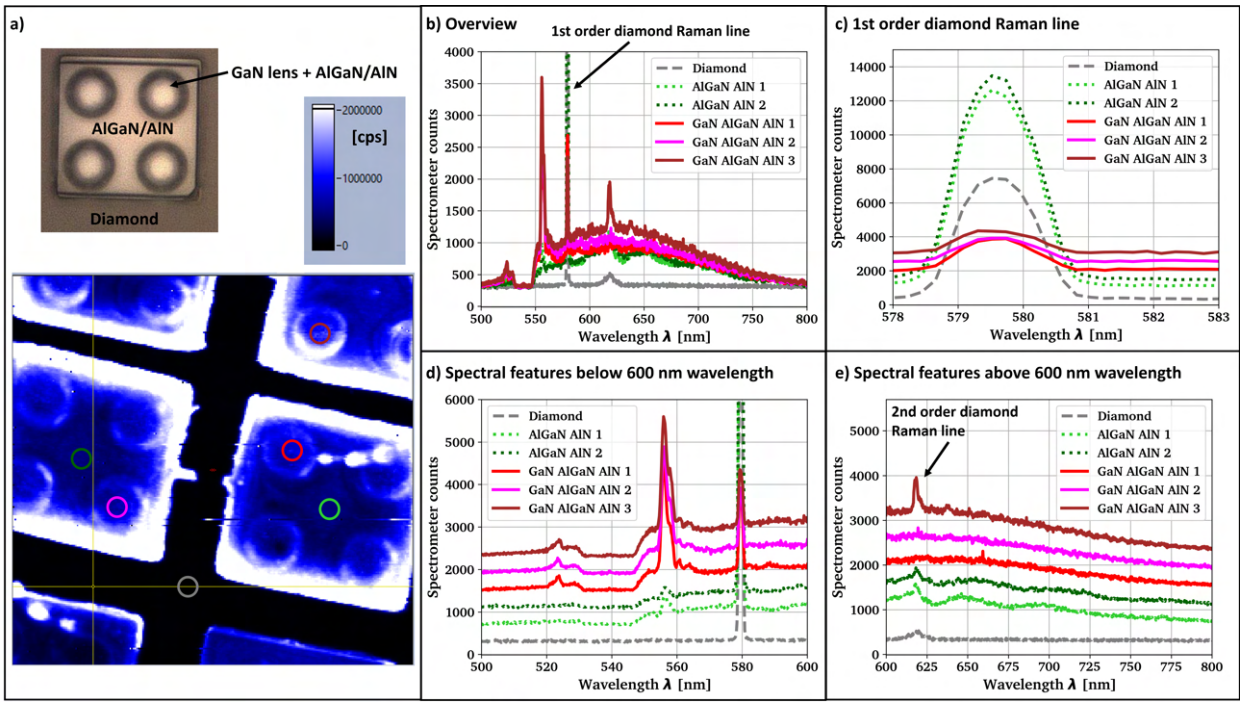

Figure 4.18: Room temperature photoluminescence spectra of transfer printed GaN lens arrays on AlGaN/AlN mesa structures on a single crystalline CVD grown polished diamond sample taken using a 550 nm long pass filter and 532 nm notch filter in a confocal arrangement. a) Microscope image showing a lens array on diamond for reference and confocal PL maps taken at Oxford with the measurement positions indicated with coloured circles matching the spectra in b)-e). b)-e) show the same spectral data, which is separated linearly in c)-e) for better visibility.

Overall, we demonstrate three dimensional deterministic matching of emitters and SILs using targeted colour centre laser writing, grayscale lens-shape control and micro-transfer printing, moving towards novel micro systems development with scaling potential. We will end this section by quickly describing the two confocal setups that were used to analyse the results and guide the printing, both stationed at the University of Oxford. Our home-built confocal setup was finished after the work presented in this section was finalized.

The confocal photoluminescence setup that is used to gather power series, autocorrelation and spectral measurements with a NA = 0.95 air lens is depicted in Fig. 4.19. A NA = 1.25 oil lens is used in the same setup to get spatial distribution information of the emitter arrays before lens printing with best signal-to-noise ratio as presented above. A continuous wave 532 nm laser (GEM532) excitation source with 1 mW output power is used, the fluorescence signal is collected back through the same objective lens and spectral filtering of the excitation laser is applied before detection.
Fig. 4.20 shows the setup used for measurements with a NA = 0.5 air objective. A continuous-wave 532 nm laser (GEM532) with 6 mW output power is used as excitation source. Photoluminescence maps of the sample before and after lens integration are taken with both setups.

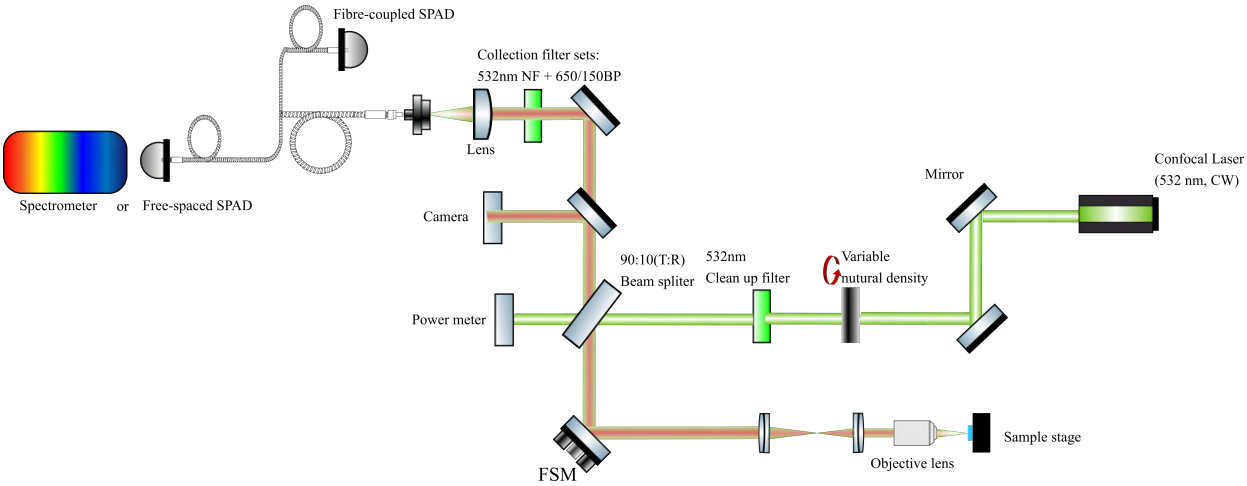

Figure 4.19: University of Oxford: Home-built confocal microscope used with air (NA = 0.95) and oil (NA = 1.25) objective lenses. The results in this subsection were obtained before our own confocal microscope was built. The lens system between the fast scanning mirror (FSM) and the objective is a tele-centric lens system used to image the back focal plane of the objective onto the scanning mirror surface.

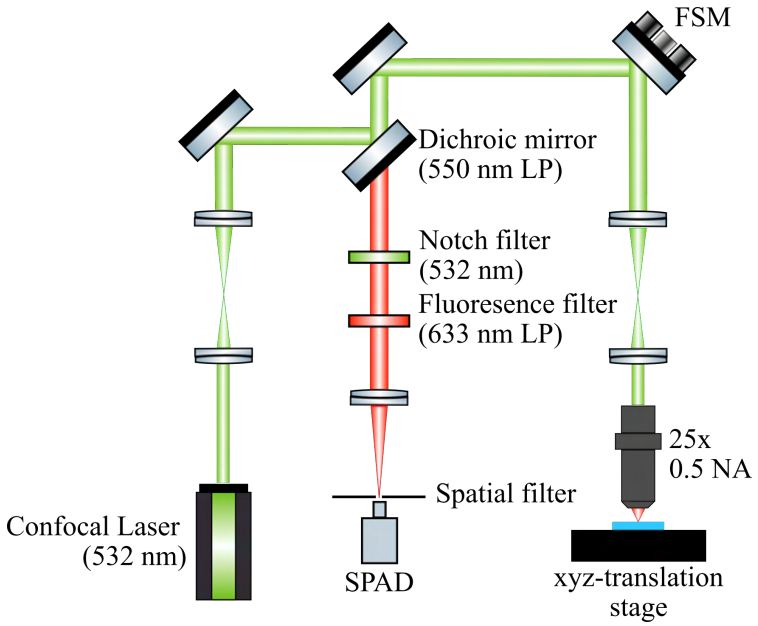

Figure 4.20: University of Oxford: Home-built confocal microscope used with the NA = 0.5 objective lens. The results in this subsection were obtained before our own confocal microscope was built.

4.2.4 Simulated light extraction efficiency

In order to quantify the potential collection efficiency improvement from NV^- centres caused by the transfer printed GaN SILs, three different scenarios are investigated with finite difference time domain simulations (FDTD): (i) a flat diamond substrate, (ii) a flat diamond substrate with added GaN micro-lens and (iii) a monolithic hemispherical solid immersion lens fabricated around the emitter, as can typically be achieved by FIB milling. Fig. 4.21 a) illustrates all three cases. The GaN lens in simulation (ii) closely resembles the fabricated micro-lens shown in Fig. 4.17 c). The emitter position overlaps with the midpoint of the lens sphere for both the GaN and the diamond lens. The commercial simulation software 'Ansys Lumerical FDTD' is used with absorbing boundary conditions.

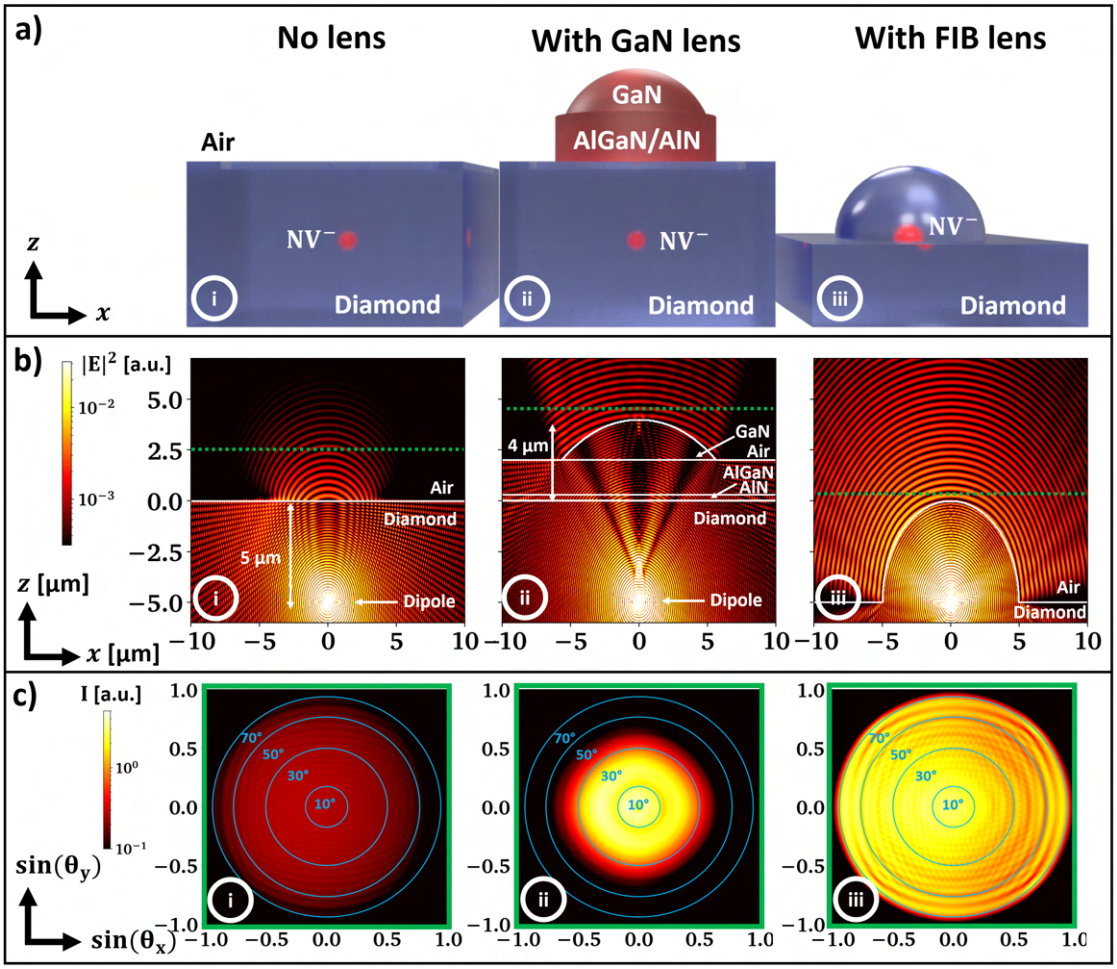

Figure 4.21: a) Schematics introducing three different cases of NV-to-free-space coupling with b) corresponding device cross sections from finite difference time domain simulations at $\lambda = 700$ nm wavelength with two dipole emitters mimicking the NV defect centre in 5 μm depth and c) the far field projection in free-space above the emitter derived from the simulations in b), similarly taken at $\lambda = 700$ nm wavelength.

In all three scenarios, the nitrogen vacancy centre is modelled by two dipole emitters at 5 μm depth below the (100) diamond surface. Two separate simulations are run and the intensity averaged to account for the two different dipole moments of the NV^- centre, one of which is tilted by (90-54.7) ° with respect to the surface normal, while the other dipole moment is parallel to the diamond surface. The NV symmetry axis is tilted by 54.7 ° towards the surface normal and both dipole moments are

orientated perpendicular to the NV axis and with respect to each other. We can see the slight asymmetry generated by the tilt of one of the two dipole moments in Fig. 4.21 b) and c). All four possible NV orientations in (100) diamond are rotationally invariant when viewed from the top, so all four are modelled at once.

Fig. 4.21 b) shows the intensity cross section taken at $\lambda = 700\,\text{nm}$ wavelength through each simulation region. In the case of the flat diamond surface the emitted wavefront exhibits strong curvature after passing the diamond-air interface, indicating large angles of the k-vector towards the surface normal caused by refraction. Additionally, total internal reflection (TIR) traps significant amounts of the upwards traveling light in the diamond slab. In contrast, both GaN and monolithic SILs allow the wavefront to maintain its shape after passing through the semiconductor materials because their radius of curvature (ROC) is matched to the position of the dipole emitter. Additionally, the GaN micro-lens visibly reduces the negative impact of total internal reflection while the FIB lens can eliminate TIR fully. The upwards directed far-field emission pattern is recorded using monitors positioned at the green lines in Fig. 4.21 b), assessing the theoretical collection efficiency and its dependence on the numerical aperture (NA) of the collection optics. The result of the far field projections is displayed in Fig. 4.21 c). As expected the intensity distribution is comparably weak and spread over wide angles if no SIL is in place, while both SILs increase the maximum light intensity by about one order of magnitude for this specific NV centre depth and diamond orientation. Due to the buffer layer thickness and additive nature of the assembly process, the far field above the GaN micro-lens indicates strong improvement primarily when collection optics with low numerical aperture (NA < 0.6) are considered. For collection optics with NA > 0.6, not much additional gain in absolute collection efficiency is expected as a function of increasing NA, compare with the red line in Fig. 4.22 b). Lower numerical aperture collection optics could be used to address arrays of multiple quantum emitters in a significantly enlarged field of view, which might offer a route to scaling of such quantum systems using spatial light modulators and free-space emitting photonic integrated circuits for beam delivery [250].

The expected collection efficiency is calculated by averaging the transmission through the detector surface above the lens (indicated in green) multiplied with the projected far field distribution from the same detector, choosing $\lambda = 650 - 750\,\text{nm}$ wavelength to match the spectral emission region of the NV^- centre. Both transmission and far field projection are found to be insensitive towards wavelength changes in this spectral regime, allowing us to ignore the spectral density distribution of the emission spectrum. The integrated transmission refers to the percentage of total light emitted by the dipole that is caught within the respective angular acceptance cone. The simulations take Purcell enhancement into account, which is found to be $< 5\,\%$ within the given spectral region.

The effect of lateral and vertical displacement of the emitter with respect to the same micro-lens with ROC $= 9\,\mu$m is discussed in Fig. 4.22 and 4.23. We illustrate the effects of a slightly larger radius of curvature accompanied by a larger diameter of the micro-lens on the collection improvement as function of an air gap between diamond and the AlN bottom surface of the lens platelet in Fig. 4.24. We will come back to these simulation results when discussing the experimental data in the next subsection.

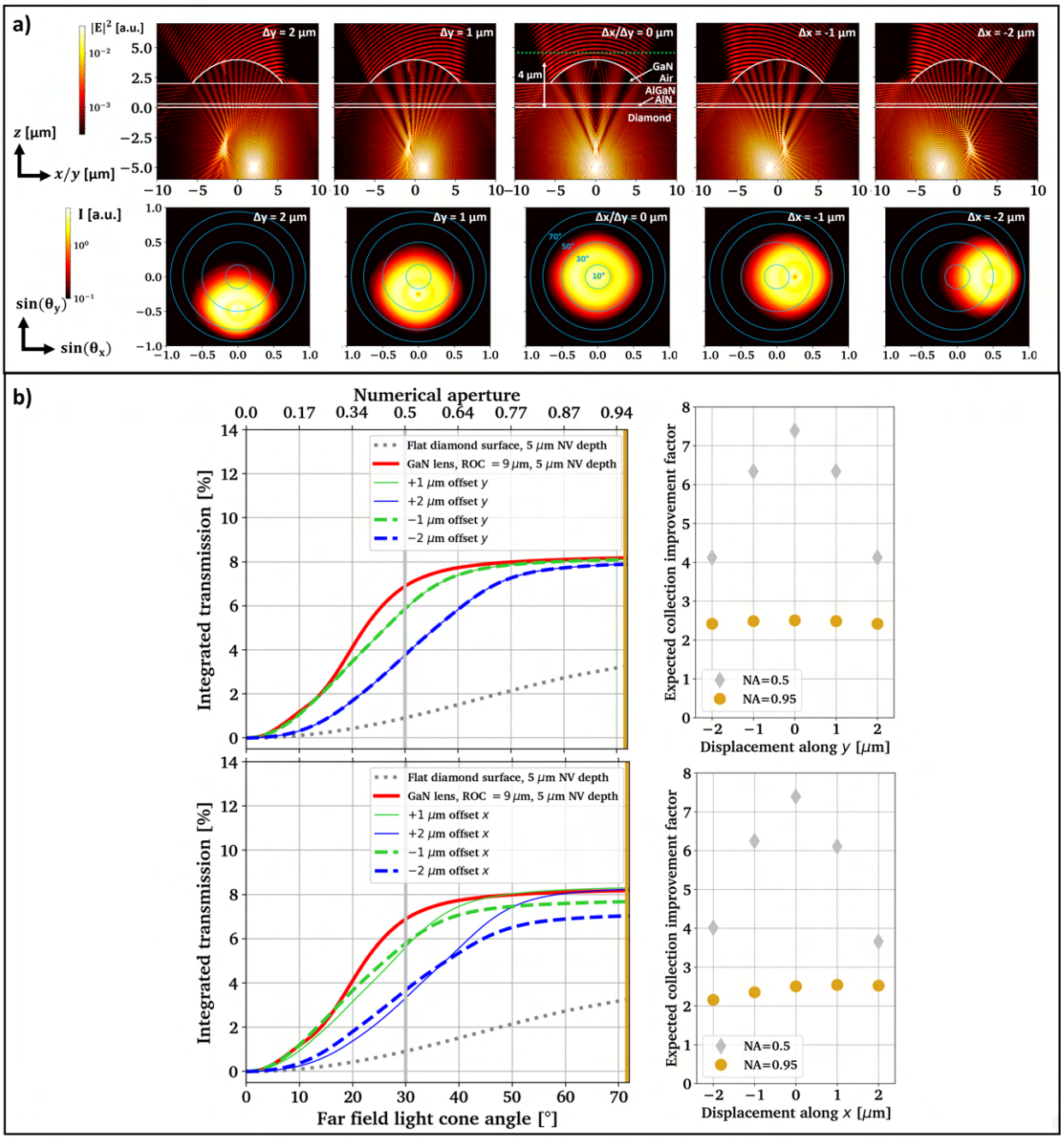

Figure 4.22: Influence of x and y displacement on the expected collection efficiency from the two dipole emitter. The radius of curvature of the GaN micro-lens is matched to the emitter depth of 5 μm. Cross sections (a) are taken at $\lambda = 700$ nm wavelength and the transmission (b) is averaged between $\lambda = 650 - 750$ nm wavelength.

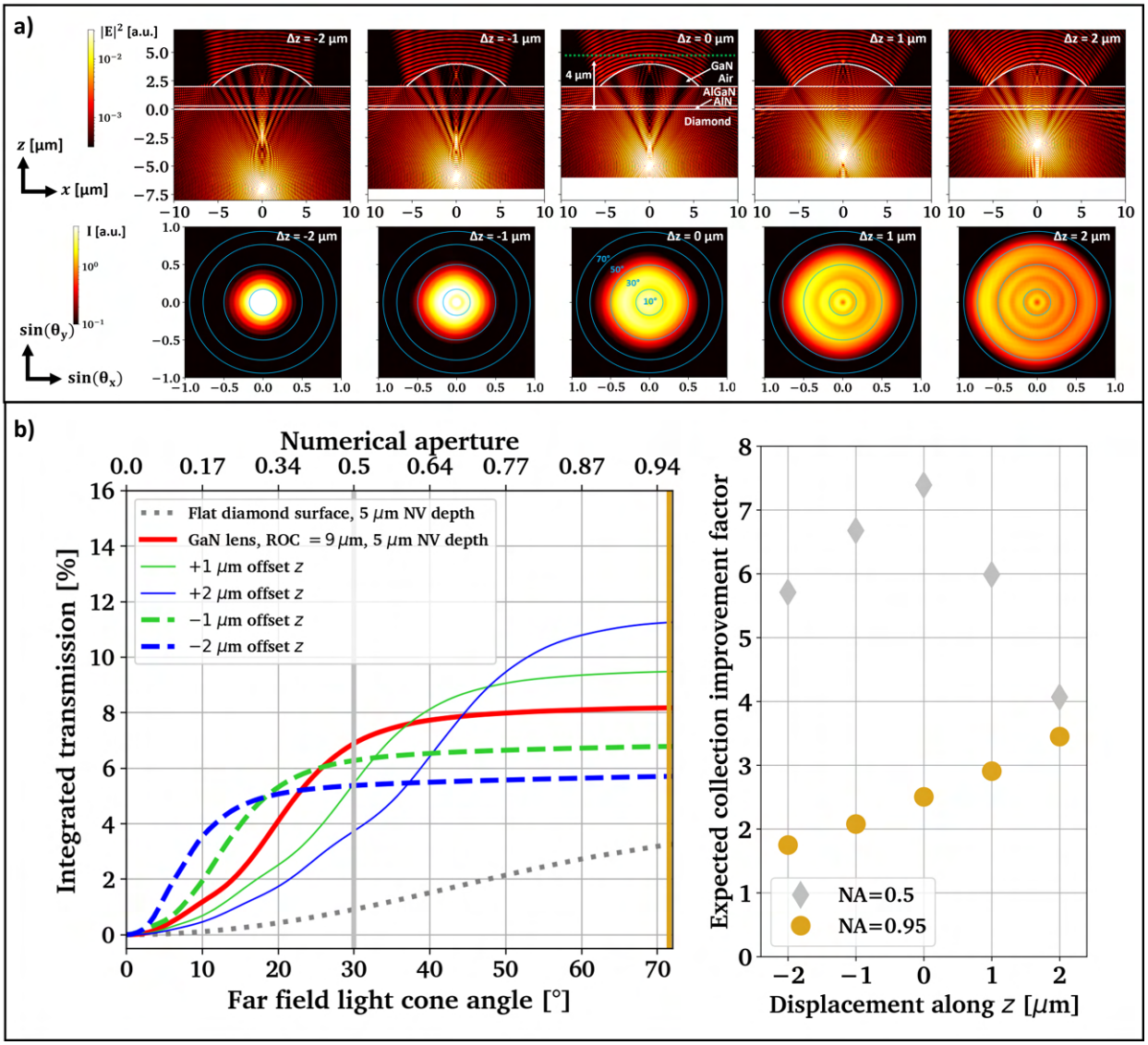

Figure 4.23: Influence of z displacement on the expected collection efficiency from the two dipole emitter. The radius of curvature of the GaN micro-lens is matched to the emitter depth of 5 μm. Cross sections (a) are taken at $\lambda = 700$ nm wavelength and the transmission (b) is averaged between $\lambda = 650-750$ nm wavelength.

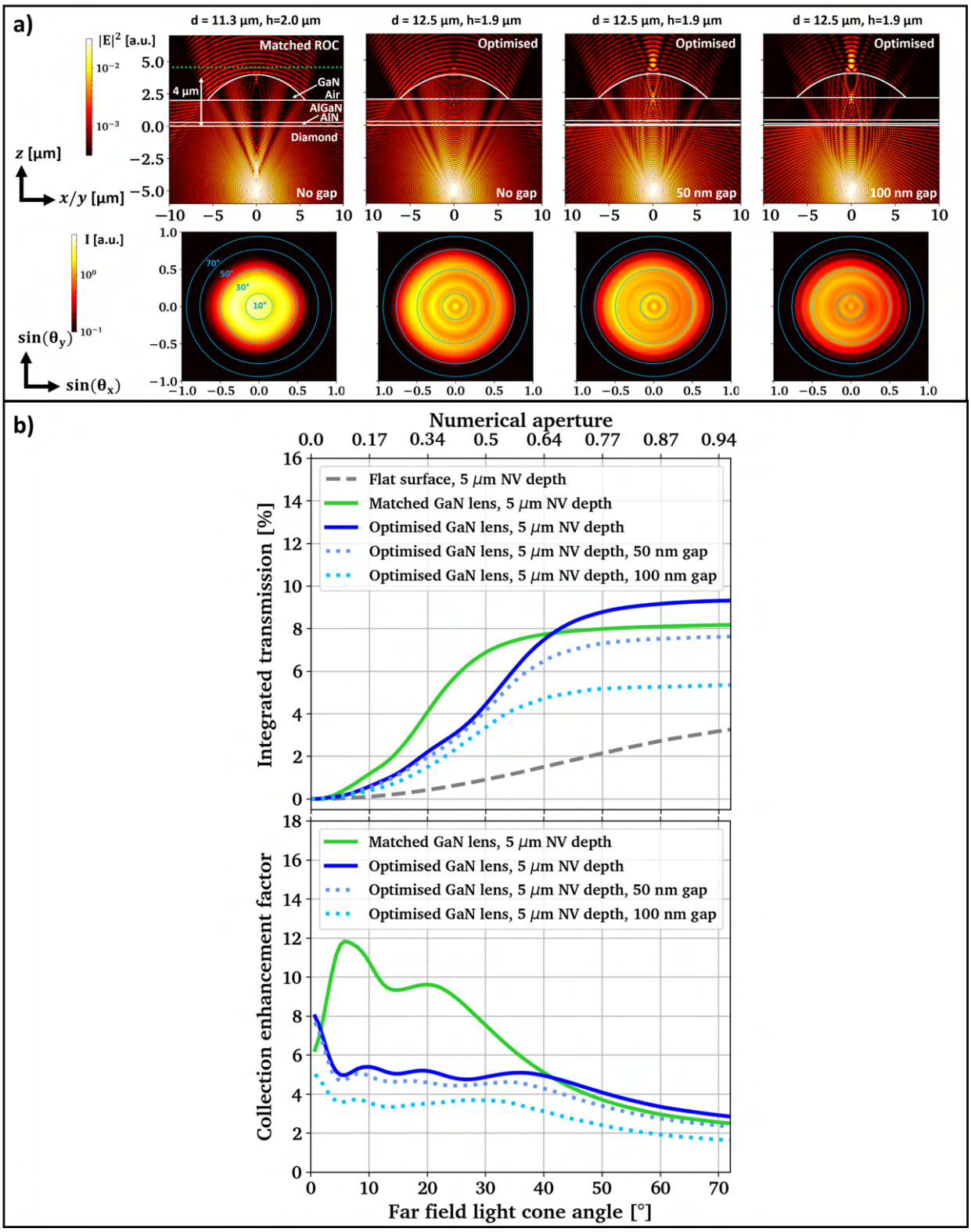

Figure 4.24: FDTD simulations taking the measured AFM profile from the lens above emitter pair 1 (Fig. 4.25, a, 4.26, a and 4.27 a) into account. The most left cross section and far field plot show the previously discussed GaN lens with matched radius of curvature for reference. Additionally, the effect of an air gap between diamond and AlN bottom layer of the GaN lens layer stack is investigated on the right hand side of a). Cross sections (a) are taken at $\lambda = 700\,\text{nm}$ wavelength and the transmission (b) is averaged between $\lambda = 650 - 750\,\text{nm}$ wavelength.

4.2.5 Measured signal enhancement and single photon purity

The improvement of PL collection efficiency is experimentally assessed by comparing two sites where we combine NV^- centre pairs with GaN lenses. We additionally show that anti-bunching in the photon statistic is maintained after lens integration. The previously introduced two home-built confocal microscopes are used to measure the effects of varying NA of the collection optics (NA = 0.5, 0.95 and 1.25). The setups are qualitatively similar, but we cannot directly compare count rates quantitatively between them.

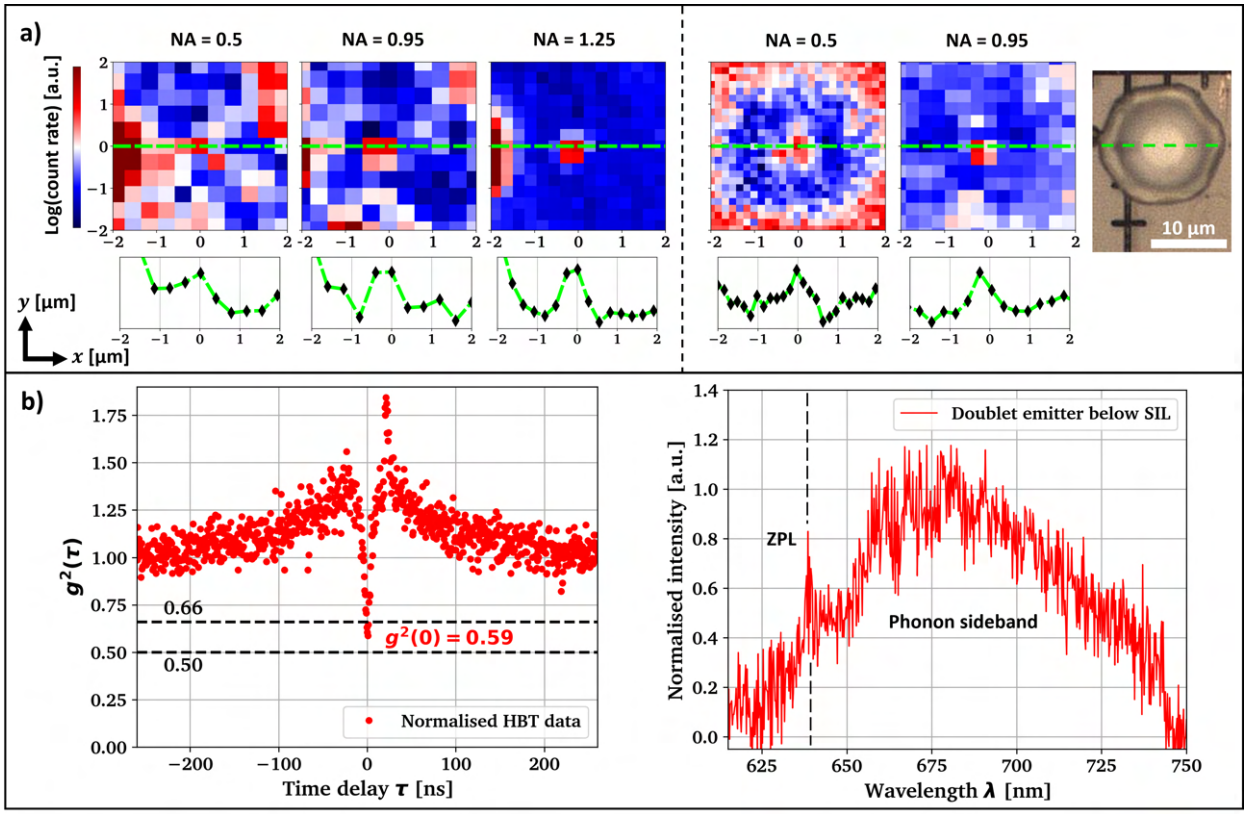

Figure 4.25: a) PL images of the same emitter after the initial laser writing and annealing (left) and after GaN SIL integration (right) showing dependence on the numerical aperture of the collection optics. Line profiles are taken along the green lines in the maps, b) normalised autocorrelation without background correction and background corrected spectral data from the emitter discussed in a) after SIL integration using the objective with NA = 0.95.

Fig. 4.25 a) includes PL maps of one writing site which is identified as a NV^- centre pair. The PL signal is compared for different objective lens NAs with and without a GaN SIL in place. Prior to SIL integration, the written site is barely visible when imaged with NA = 0.5, but with increasing the objective lens NA, the signal to noise ratio (SNR) increases significantly due to more efficient collection from the heavily refracted emitted light. After adding a GaN micro-lens on top of the same emitter, we are now able to clearly resolve the emission using NA = 0.5, noting a roughly 5× enhanced count rate when the emitter is pumped to saturation (no data shown). But the low SNR before lens integration makes it difficult to quantify the improvement with much accuracy. The magnification effect of the SIL additionally separates the emitter more clearly from the emitting surface marker structure in the left part of the PL map. The logarithmic line scans through the emitter PL signal reveal significantly improved SNR when comparing both NA = 0.5 and NA = 0.95 before and after lens integration.

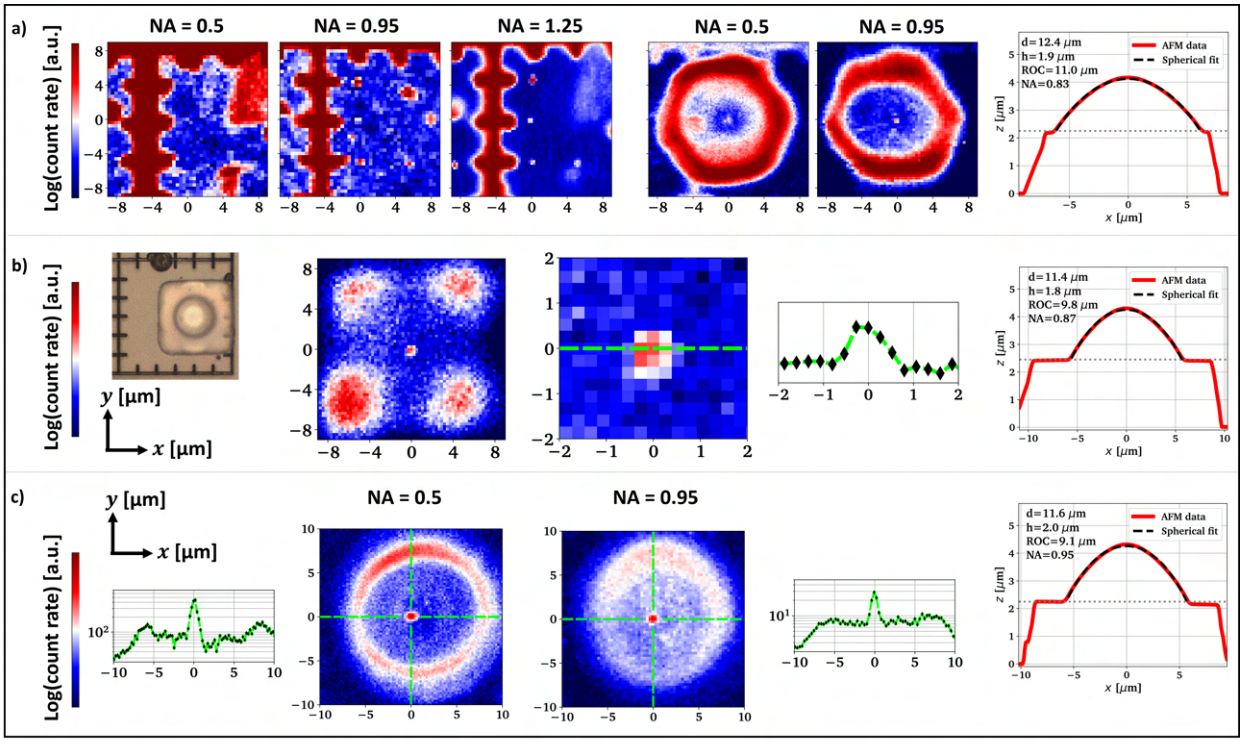

Figure 4.26: Photoluminescence and AFM measurements regarding a) doublet emitter 1 shown in Fig. 4.25 a), b) doublet emitter 2 included in the power saturation measurement shown in Fig. 4.27 a), c) the micro-lens in the top left quadrant discussed in Fig. 4.17.

To provide some additional data from the investigated emitters, Fig. 4.26 a) includes a larger field of view of the photoluminescence plots shown in Fig. 4.25 a) as well as an AFM line scan of this particular SIL with slightly larger diameter matched to the simulations shown in Fig. 4.24. Fig. 4.26 b) also includes photoluminescence maps and an AFM line scan of the lens above of the second emitter pair which we use to take a power saturation series assessing the collection improvement. Fig. 4.26 c) illustrates the NA dependency of the PL map taken on the graphitized emitter spot discussed in Fig. 4.17.

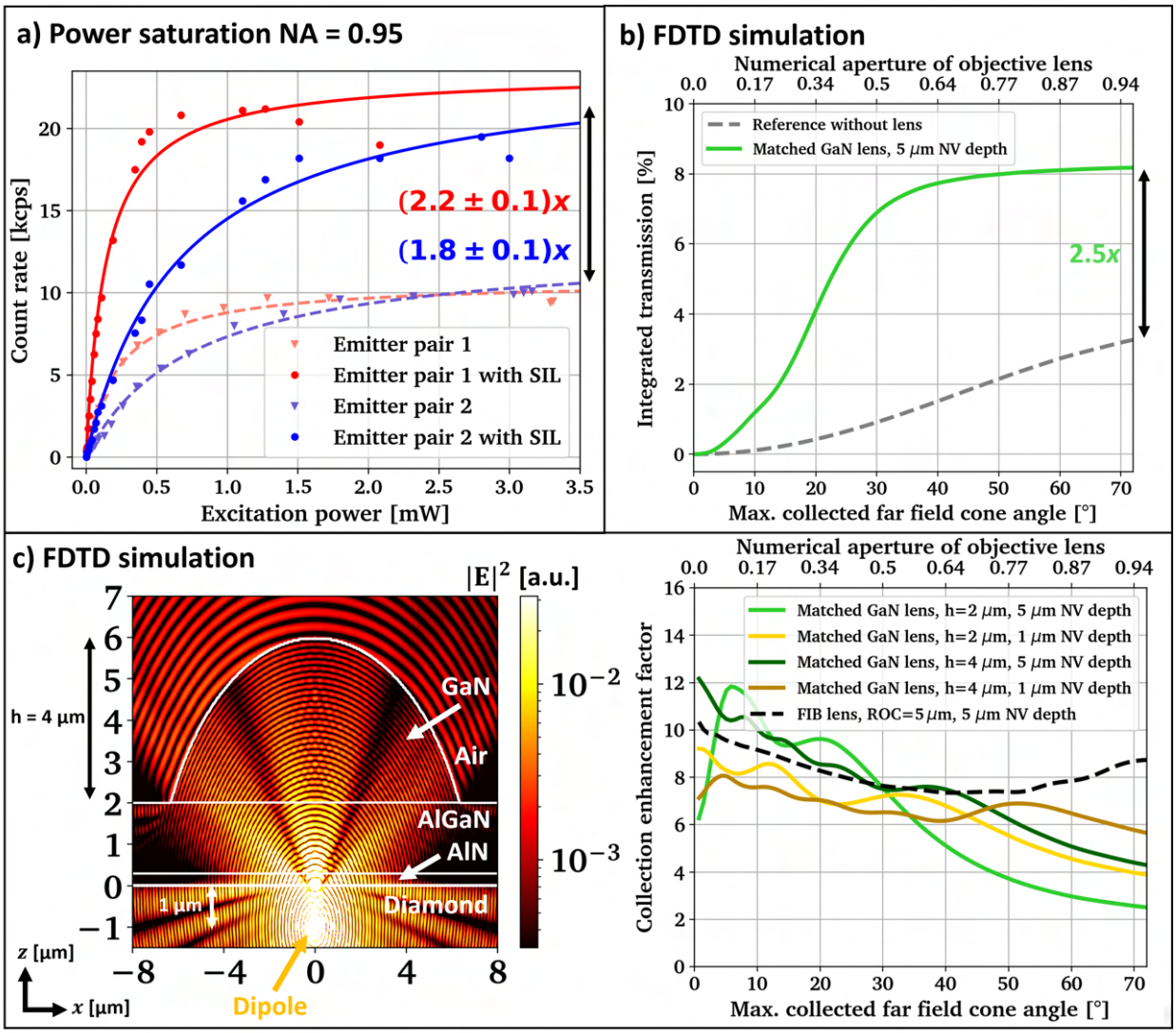

Figure 4.27: a) Fitted power saturation measurements of two NV^- centre pairs with and without GaN SIL using an objective with NA = 0.95, b) expected free space collection improvement in dependence of the objective's NA derived from the FDTD simulations shown in Fig. 4.21, c) cross section though a simulation region with a GaN SIL matched to a dipole emitter at $\lambda = 700$ nm wavelength and the expected corresponding free space collection enhancement in reference to a planar diamond-air interface in dependence of the emitter depth and GaN lens height. The ROC of the GaN lenses is matched to the respective emitter depth and the result for a monolithic diamond hemisphere ('FIB lens') is shown for comparison.

To confirm the compatibility of the GaN micro-lenses with measurements in the quantum regime, $g^{(2)}(\tau)$ autocorrelation measurements are taken after lens integration. As mentioned in the thesis introduction intensity autocorrelation is a well-established technique often used to verify the existence of single photon sources in solid state physics and goes back to the work of Hanbury Brown and Twiss (HBT) [251–253]. To collect the $g^{(2)}(\tau)$ statistic, the PL signal is split between a free-space SPAD and a fiber-coupled SPAD with timing jitter $\Delta\tau \approx 500$ ps using a 50:50 beamsplitter. For these measurements the objective lens with NA = 0.95 is used. A spectral filter in the optical path of one SPAD prevents potential optical cross-talk due to the breakdown flash commonly observed in Si APDs and SPADs [237].

Fig. 4.25 b) contains the HBT measurement result from the emitter depicted in Fig. 4.25 a) and we find $0.5 < g^{(2)}(0) = 0.59 < 0.66$ after lens integration, indicating that the ensemble consists of two

closely spaced NV^- centres, which cannot be resolved separately. The data is taken as is, no background correction is applied and the finite detector response time is not taken into account. Due to the large depth of $> 5\,\mu$m of the emitter below the SIL we don't expect significant PL background contributions from the micro-lens after integration if high NA objective lenses are used. We can confirm this by comparing the PL data collected with the oil immersion objective (NA = 1.25) without SIL and the data collected after lens integration with an air objective (NA = 0.95) where we find very similar signal-to-noise ratio.

In the histogram in Fig. 4.25 b) we find an asymmetric spike-like feature on the right-hand side at $\tau \approx 20$ ns delay time, which is most probably due to optical cross-talk between the SPADs. The break down flash in one SPAD is emitting IR photons which can be detected by the second SPAD. The asymmetry between the left and right hand side of the histogram arises from unbalanced reflections and coupling between the two different SPADs used: one is free space coupled and the other fibre coupled. Similar spiking features can be observed in the histogram before lens printing at $\tau \approx \pm 20$ ns, indicating that this effect is not due to the GaN SIL. Before integration of the GaN SIL we measure $g^{(2)}(0) = 0.72$ due to the NV centre pair being heavily saturated (data not shown). The high pump power leads here to significant charge state conversion and to the introduction of additional background light, both contributing to reduced visibility of the $g^{(2)}(0)$ value.

Fig. 4.25 b) also includes a background corrected spectral measurement of the discussed emitter taken through the lens, exhibiting a sharp zero-phonon line (ZPL) centred at 637 nm and a phonon sideband of approximately 100 nm width, as is characteristic of the NV^- centre in diamond [42, 254]. The long wavelength transmission edge of the 665/150 nm band-pass filter can be seen around 740 nm wavelength. For the $g^{(2)}(\tau)$ measurement, a 600 nm long-pass filter is added to remove the first order diamond Raman line from the background signal. Both measurements demonstrate that the photophysics of the emitters remain undisturbed after passing through the GaN SIL. Furthermore, the GaN SIL enhances the photon count rate to enable faster measurements with similar SNR.

To quantify this enhancement caused by the SILs, power saturation measurements are taken on two NV^- centre pairs before and after SIL printing using the air objective lens with NA = 0.95. The results are shown in Fig. 4.27 a) and as expected, the count rates of the NV centres increase with increasing laser power up to a certain saturation level, after which the count rates plateau. Pair 1 corresponds to the emitter discussed in Fig. 4.25, while pair 2 is shown in the bottom right quadrant of the region discussed in Fig. 4.17 with additional information on both lenses and emitters discussed in Fig. 4.26. The data is fitted with the sum of two saturation curves derived for two-level quantum systems, allowing both emitters in the focal volume their own saturation power P_{sat} and intensity I_{sat}:

$$I(P) = \frac{I_{\text{sat1}} \cdot P}{P + P_{\text{sat1}}} + \frac{I_{\text{sat2}} \cdot P}{P + P_{\text{sat2}}} \tag{4.1}$$

A single saturation curve fit describes the data equally well. With this, $(2.2 \pm 0.1)\times$ and $(1.8 \pm 0.1)\times$ enhancement of I_{sat} is found for pair 1 and pair 2, respectively. Similarly a slight reduction in saturation pump power by a factor of $(1.7 \pm 0.3)\times$ for pair 1 and $(1.2 \pm 0.2)\times$ for pair 2 is observed. This is likely due to reduction in the spherical aberration that occurs at a planar interface with high index contrast [125]. Here we do not expect additional substantial narrowing of the point spread function of the pump laser caused by the SIL because objective lens and SIL exhibit similar numerical aperture, compare Fig. 4.26. The pump efficiency enhancement would likely be more noticeable when using

a lower NA objective, because the SIL is then expected to reduce the diffraction limited spot size, as illustrated by the simulation results shown in section 4.1.

The measurement results are compared to the expected collection enhancement as function of far field angle derived from the simulations shown in Fig. 4.21 with the result displayed in Fig. 4.27 b). Here we compare the planar diamond surface to one with a printed GaN micro-lens with its radius of curvature matched to the emitter depth and ideal lateral alignment.

The simulations predict an improvement factor of around 2.5× for an objective lens with NA = 0.95, which is a bit higher than what is found in the experiment. For both NV^- centre pairs the real lateral displacement is less than the predicted critical value of $\pm 1\,\mu$m, but vertical misalignment might lead to lower collection enhancement, if the emitter is actually placed deeper inside the crystal than intended. We estimate that an emitter that lays $1\,\mu$m too low, could cause the enhancement to drop to around a factor of 2×, compare Fig. 4.23. Note that the SIL placed above NV^- centre pair 1 was chosen to have a slightly larger diameter, leading to a larger ROC, for which the simulations predict increased collection at large collection NA, compare Fig. 4.24 and Fig. 4.26. Another reason for the slight discrepancy between measured and simulated enhancement might be interference effects from the sidewalls of the AlGaN/AlN buffer layer, which are not taken into account in the simulations. But due to the sloped sidewall angle of our AlGaN/AlN membranes these are more likely to allow photons to leave the semiconductor layer stack rather than reflecting them into the lens aperture causing interference.

Further collection enhancement could be achieved by placing the colour centre closer to the diamond surface and increasing the GaN epilayer thickness. In our current work, the $5\,\mu$m depth of the NV emitters, the $2\,\mu$m thick AlGaN/AlN buffer layer and the epilayer constrained GaN lens height ($2\,\mu$m) limit the enhancement expected from the SILs, because these parameters affect how much the lens aperture covers the angular space above the emitter. The simulated enhancement factors for ROC-matched GaN lenses combined with emitters at various depths and varying GaN lens height compared to a hemispherical monolithic SIL are depicted in Fig. 4.27 c).

These results show that a $2\,\mu$m high GaN micro-lens is expected to increase the light collection efficiency up to 7× (NA = 0.5), 6× (NA = 0.7) and 4× (NA = 0.95), if the emitter is placed in $1\,\mu$m proximity to the surface, compare with the yellow curve in Fig. 4.27 c). In particular the overall absolute collection is not expected to deviate much between an NA of 0.7 and 0.95, potentially offering larger field of view without any losses if a suitable GaN SIL is used. But we note that with moving both to lower NA and lower emitter depth the confocal rejection of the PL from the GaN/AlGaN/AlN layer stack is likely to decrease.

In addition, the GaN epilayer thickness could be increased to e.g. $4\,\mu$m, which allows to increase the lens diameter while maintaining the midpoint position of the spherical lens profile. Thus, the effective angular coverage of the lens aperture above the emitter would rise, improving the photon extraction regardless of emitter depth, compare the dark green and dark golden curves in Fig. 4.27 c) with the light colored curves. This approach is expected to require tuning of the strain profile in the epilayer including the redesign of the buffer layer [95, 224].

Overall, the derived collection efficiency for the planar diamond surface and the monolithic diamond SIL are in good agreement with previous experimental and theoretical work [123, 125, 170–172, 248, 255, 256], indicating the validity of the simulations. We added the expected enhancement and absolute collection efficiency for various emitter depths and different GaN epilayer thickness both for (100) and (111) crystal orientation in Fig. 4.28, with the overall trends being very similar to what is shown in

Fig. 4.27 c).

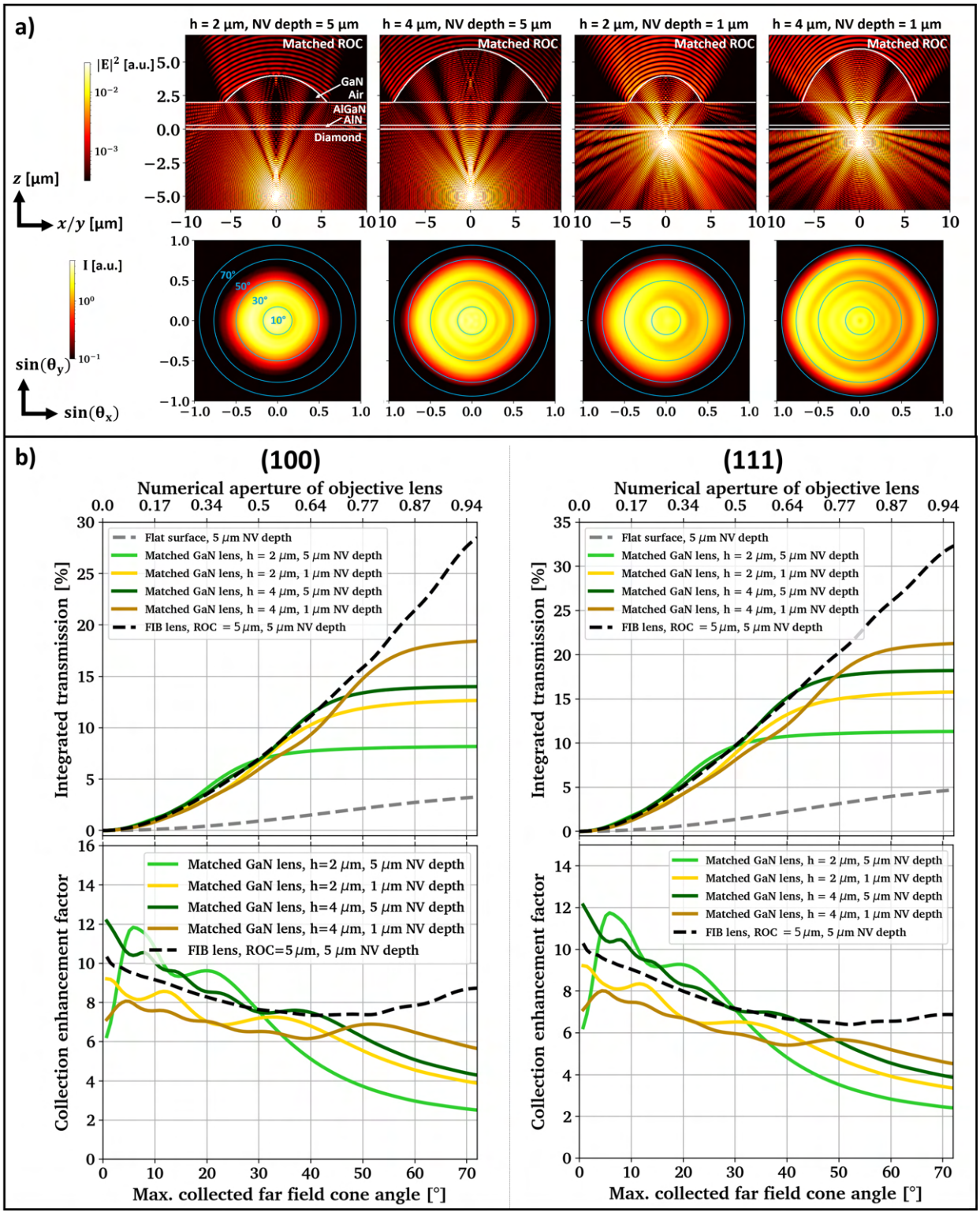

Figure 4.28: Light collection and its enhancement in dependence of emitter depth and GaN lens height expected from FDTD simulations. The emitter position is matched to the geometric centre of each lens. The cross sections (a) are taken for (100) diamond surface orientation, while the plots in b) distinguish between (100) and (111), assuming an ideally aligned emitter in the (111) case. Cross sections (a) are taken at $\lambda = 700$ nm wavelength and the transmission (b) is averaged between $\lambda = 650-750$ nm wavelength.

4.2.6 Cooling printed lens arrays to cryogenic temperatures

During this work we needed to send samples with printed lenses across the UK by post, which tested the reliability of the van-der-Waals bonding. Unfortunately some lenses actually moved before arriving in Oxford, see Fig. 4.29. Furthermore our collaborators found that the other lenses detached from the diamond surface after adding them into a vacuum chamber which prevented further cryogenic studies. At Strathclyde printed lenses and other devices are commonly exposed to vacuum chamber conditions, either in the SEM or the RIE machines and we do not usually observe such device movement or even loss. It is not clear how the sample was handled upon transport to cause this severe effect.

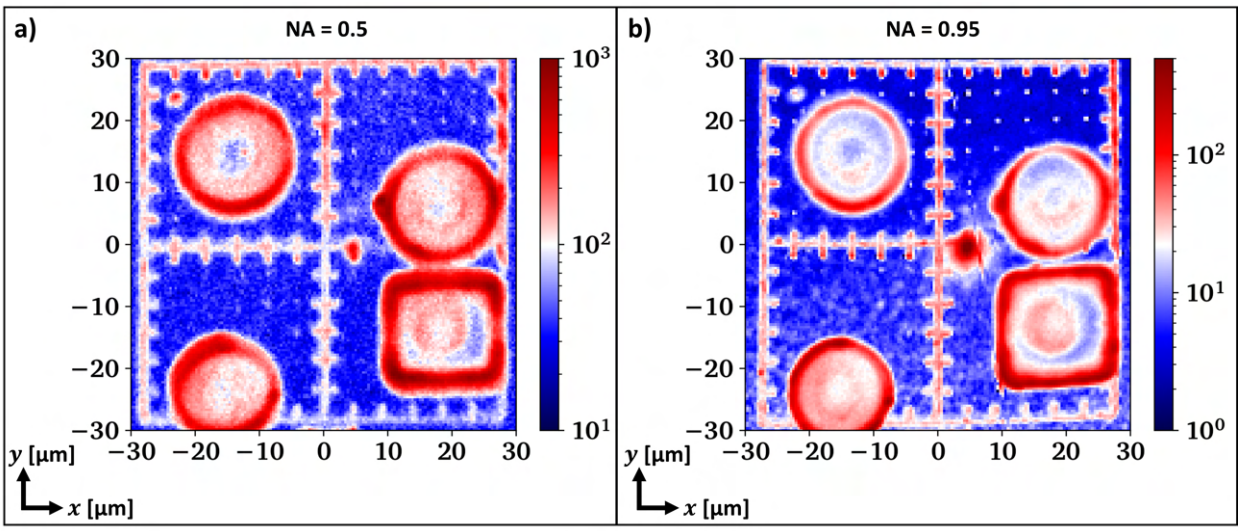

Figure 4.29: Movement of lenses during transport from Glasgow (fabrication site) to Oxford (optical characterization site) illustrated by two overview PL maps taken with a) NA= 0.5 and b) NA= 0.95. If compared to the freshly assembled lenses in Fig. 4.17 b), the bottom left and top right lens have moved significantly. The sample was shipped via DHL in a sticky sample box.

In order to clarify that the mechanical bond strength of the GaN SILs to the diamond surface is sufficient to survive typical conditions used in NV^- quantum experiments we test cryogenic cooling of seemingly flat 2x2 GaN micro-lens arrays printed on Si and diamond substrates. We additionally investigate whether the application of a thin layer of PECVD SiN_x or a thick layer of photoresist which is lithographically opened above the lens devices can mechanically stabilize the devices. In the used cryostat (CTI Cryogenics 22) the samples are exposed to a high vacuum environment and severe vibrations caused by the closed-cycle helium pumping. We expect that differences in thermal expansion coefficients between diamond, GaN, AlGaN and AlN might cause either bowing of the membrane itself or loosening of the bond van-der-Waals bond under the generated lateral stress.
The results are shown in Fig. 4.30 and 4.31. We find that the lens arrays do not detach under several cooling cycles in any of the two scenarios. We are able to observe the devices with a microscope column in-situ at low temperatures and cannot detect any changes in colour that might indicate a change in membrane bow. Therefore these results are a promising indicator that additive GaN micro-lenses are cryostat compatible.

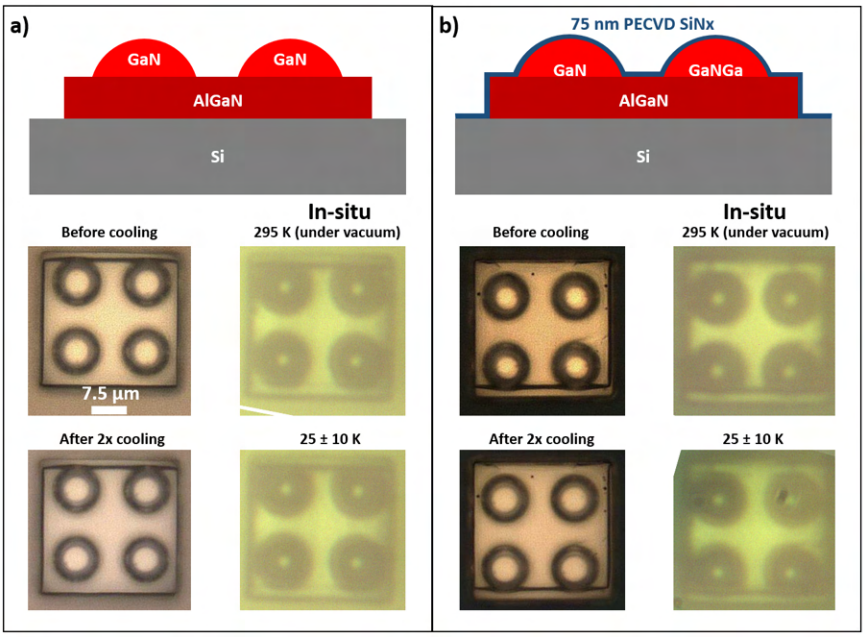

Figure 4.30: Results of closed-cycle cryostat cooling of flat 2x2 micro-lens arrays without anchors transfer printed on Si to test potential dilamination due to differences in thermal expansion coefficients. a) Printed membranes before and after 2x cooling cycles and in-situ images in the cryostat at room temperature and at 15 K measured at the bottom of the cold finger, b) shows the same experiment with a thin layer of SiN_x that was applied to potentially stabilize the devices if necessary. The scale bar applies to all images, the schematics on top show a side view. Both devices were loaded in the cryostat in parallel.

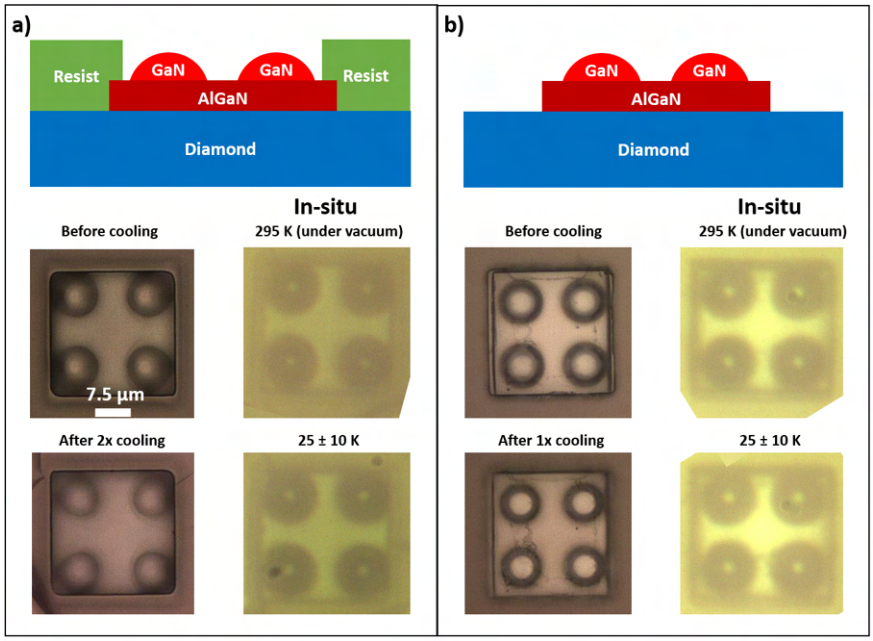

Figure 4.31: Results of closed-cycle cryostat cooling of flat 2x2 micro-lens arrays without anchors transfer printed on single crystalline diamond to test potential dilamination due to differences in thermal expansion coefficients. a) Printed membranes with SPR220-4.5 resist protection before and after 2x cooling cycles and in-situ in the cryostat at room temperature and 15 K measured at the bottom of the cold finger, b) shows the same experiment repeated after the resist was removed from the same device as shown in a). The scale bar applies to all images, the schematics on top show a side view.

4.2.7 Summary and outlook

In summary, we have investigated how additive GaN micro-lenses can be used to enhance the photon collection from diamond color centres, using laser written negatively charged nitrogen vacancy centres as an example. To our knowledge, this is the first work that deterministically combines ca. 10 μm large semiconductor micro-lenses with colour centres in a foreign host crystal, showing the potential of additive high-NA micro-optical components for quantum technology based systems in general. We find evidence of collection improvement on the order of 2× in good agreement with finite difference time domain simulations. The main advantages that transfer printed GaN solid immersion lenses offer over monolithic diamond hemispheres fabricated with focused ion beam milling are the potentially much faster fabrication speed and their additive nature that eliminates damage to the diamond lattice which could affect the colour centre properties.

Further improvement of photon collection efficiency is expected by placing the colour centre closer to the diamond-air interface. We find that a dipole emitter in 1 μm proximity to the surface might experience 4-7× collection improvement. Still, the highest possible collection efficiency offered by these additive lenses remains limited in comparison to monolithic hemispheres due to the 2 μm thick buffer layer. This might be mitigated by increasing the GaN epilayer thickness to 4 μm, potentially achieving lenses with larger diameter but same midpoint of the lens sphere, covering a larger angular space above the emitter. When using an objective lens with NA $= 0.7$ in this arrangement, the simulations predict that collection is relatively on par with what can be achieved with a hemispherical diamond lens, using the same collection optics.

Deterministic laser writing of colour centres has been reported with near unity yield [31], making regular high quality colour centre arrays possible which could be combined with regularly spaced micro-optical elements for effective collection improvement. The GaN lens fabrication uses highly parallel ICP etching, enabling thousands of device to be fabricated in one wafer run, potentially utilizing 6 inch GaN-on-Si wafer technology. The stamp-based transfer printing process is conducted manually here, but can easily be automated while maintaining μm-precise placement accuracy using optically visible marker structures [257, 258].

Combined with a multi-stamp head approach [217], a device throughput of $> 100-200$ devices per hour is conceivable after initial alignment of donor and receiver chip and highly optimized processing. Alternatively continuous roller transfer printing might offer a way to scale the transfer process, but still needs further development in terms of overlay alignment accuracy [259]. Further scaling could be achieved by using printable arrays, thus reducing the number of transfer print processes. Lens arrays could either be integrated with arrays of deterministically generated color centres or deterministic writing could be performed through the GaN lenses themselves after printing [31]. The latter approach could allow the reduction of depth at which vacancies can be created by laser writing and would additionally auto-align the respective color centre close to the midpoint of the lens sphere [260]. We also find promising evidence for the cryostat compatibility of fabricated GaN lens arrays opening the doors towards the use of GaN SILs in quantum applications.

There still remain significant challenges in terms of system scalability. Even with large arrays of micro-lenses in place high numerical aperture objective lenses with a confocal measurement arrangement are needed to collect the light emitted by the colour centres. The parallelization of the spin-photon channels via fibre or free-space optics approaches need development. Fibre coupling of each separate emitter is

likely to increase device foot print, while for parallel free-space coupling fast spatial light modulators could be used to create excitation spots over the whole field of view [250], while selectively guiding the collected light from each emitter to separate detectors. Crucially a quasi-confocal arrangement would need to be maintained to spatially filter the photoluminescence response.

4.3 Diamond scanning probe magnetometry

We have seen in the introduction that the energetic structure of the electron-spin sub-levels of the NV^- centre are sensitive to the projection of an external magnetic field along the NV's symmetry axis. The projected field strength can be mapped on the photoluminescence intensity because an applied microwave field can excite spin-state population transfer on resonance leading to a dip in the optically detected magnetic resonance (ODMR) spectrum. This effect can be exploited to build highly sensitive magnetometers with potentially nanoscale resolution if single NV^- emitters are used [21, 22, 84, 85, 252, 261–269]. NV ensemble magnetometers with partial CMOS integration (photodiode and microwave source) and vector field reconstruction have also been demonstrated [18, 270–272].
In this section we will investigate how GaN micro-lenses can support the optical readout of the NV^- fluorescence signal that carries the information about the magnetic field strength. We will use commercially available monolithic diamond probes containing single emitters designed specifically for scanning NV magnetometry. We will find that the integration of GaN SILs with these probes is challenging due to varying quality of the diamond top surface. We demonstrate the successful integration with a functional probe containing a single NV but will measure negligible count rate improvement. Still we confirm single photon emission via a $g^{(2)}$ autocorrelation measurement through a GaN SIL coupled to a low NA microscope objective (NA = 0.5).

4.3.1 Review: Scanning NV^- magnetometry

The field of magnetometry is vast and many different technologies such as flux-gate, hall-effect or optically pumped vapour cell magentometers are available targeting different sensitivity and field frequency domains [273, 274]. Techniques such as giant magnetic resistance (GMR) read heads [274], magnetic force microscopy (MFM, MFRM) [275, 276] or scanning superconducting quantum interference devices (SQUID) [22] combine magnetic field imaging or even quantitive read-out with high spatial resolution. Similar to these scanning based techniques the NV^- centre can be used as a quantitative scanning magnetic field sensor with the earliest demonstration using a diamond nanocrystal containing a single NV attached to a conventional AFM probe [261]. Advantages of NV based magnetometry include sensitivity to weak fields (AC and DC, pT to $\mu T/\sqrt{Hz}$), nanometer-scale spatial resolution (≈ 10 nm possible) as well as large operation temperature (from cryogenic to above room temperature) and pressure (ultra-high vacuum to > 60 GPa) range [22].
Monolithic diamond probes containing single NV centres for scanning magnetometry are today commercially available with the first demonstrated device geometry shown in Fig. 4.32. In this initial demonstration the authors show that they can image magnetic domains with around 40 nm width, with the results displayed in Fig. 4.33. Minimizing the distance between NV and sample is a crucial factor to achieve high spatial resolution resulting in a trade-off because the NV coherence properties are known to deteriorate close to the surface, affecting the sensitivtiy negatively[22]. In this first monolithic probe demonstration [262] the NVs are placed only 10 nm away from the diamond surface, a distance still typical for commercial probes today [277, 278].
With such a device, single electron spin detection at ambient conditions has been achieved, demonstrating spatial resolution on the nm-scale and nT-scale field sensitivity [85]. This fantastic result involved periodic flipping of the targeted spin (a second NV) which allowed the use of dynamic decoupling pulse

sequences [56–58] extending the NV^- decoherence time. Pulsed decoupling can only be applied in AC field sensing. The measurement took 42 min which shows that the technique has some practical limits. The sensitivity of a magnetometer is generally measured in $T/\sqrt{Hz}$ with the minimum detectable field normalized by the square root of the measurement band width. For a NV based magnetometer the sensitivity η depends on the number N of NVs involved, the free spin precession time τ, the spin state's dephasing time T, the contrast C of the optical spin readout technique applied, the overhead time (how quickly a measurement can be initialized (t_i) and read-out (t_R)) and the average photon number n_{avg} collected [22]:

$$\eta = \alpha \frac{1}{2\pi\gamma} \frac{1}{\sqrt{N\tau}} \frac{1}{e^{-(\tau/T)^p}} \sqrt{1 + \frac{1}{C^2 n_{avg}}} \sqrt{\frac{t_I + \tau + t_R}{\tau}} \tag{4.2}$$

with the electron gyromagnetic ratio γ, a constant α and the exponential spin bath parameter p.
We are targeting an increase in collection efficiency to improve the sensitivity of scanning magnetometry probes, which could either be used to shorten the image acquisition time at similar SNR or decrease the minimal field that can be reliably detected with the technique. It is reported that the sensitivity is proportional to the square root of the average photon number collected in the limit of low contrast (it might be confusing that low sensitivity stands for a smaller minimum detectable field strength) [22, 279]. This means that at constant measurement time 4x more photons are needed to half the minimum detectable field at the same bandwidth, making large improvements necessary to yield practical significance.

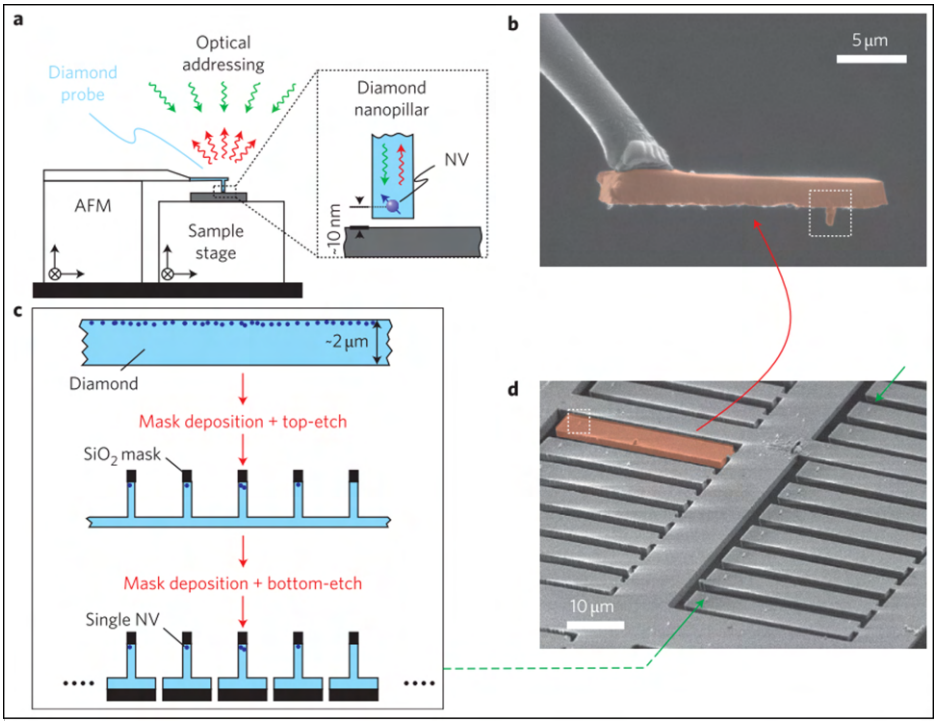

Figure 4.32: (a) Measurement setup for AFM like scanning NV^- magnetometry, (b) membrane and pillar attached to the AFM cantilever, (c) pillar nanofabrication from a (100) diamond membrane using e-beam lithography and dry etching, (d) array of freestanding diamond cantilever devices before detachment, taken from [262].

Current applications of scanning NV magnetrometry generally focus on investigating the magnetic properties of 'traditional' and emerging materials such as superconductors and van-der-Waals thin-films in greater detail than possible before [22]. This usually includes imaging and characterization of spins

and currents on the surface of these materials on the nanometre scale. Two examples are given in Fig. 4.34, highlighting the significance of this method for modern material science.

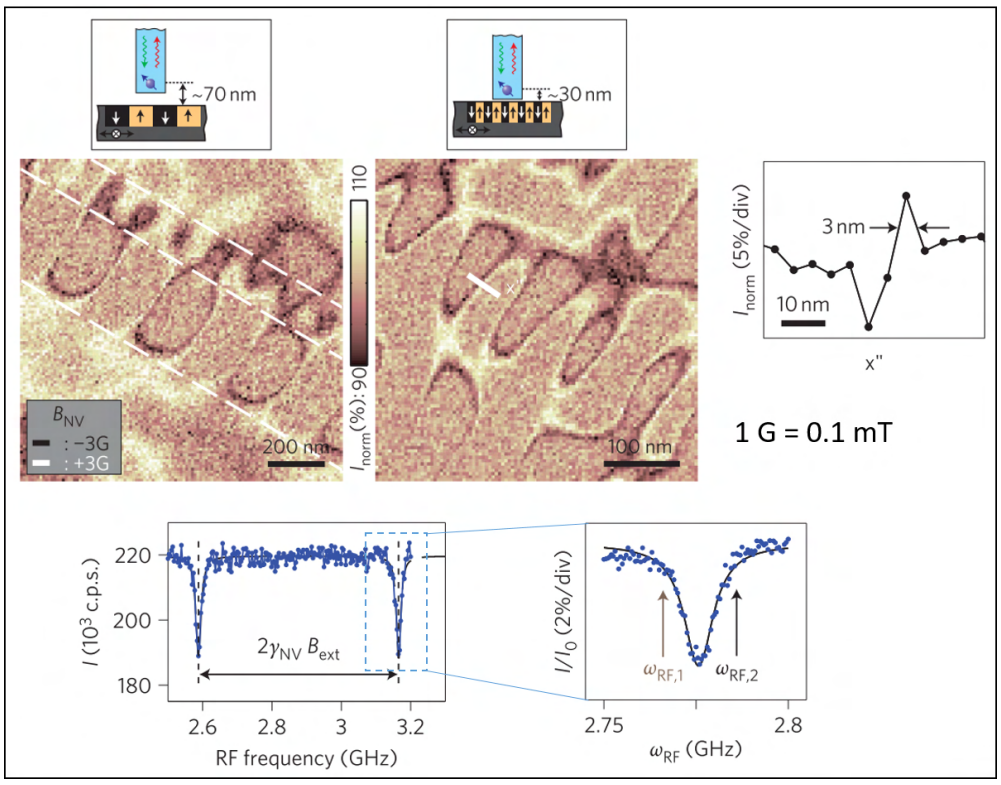

Figure 4.33: Visualization of magnetic domains on a HDD memory disk in DC imaging mode generated by scanning a monolithic diamond tip including a single NV^- centre across the surface. An external magnetic field is applied creating two split peaks in the ODMR spectrum and a microwave drive is set on resonance with the externally applied field reducing the fluorescence count rate. The image then yielded the contours generated by the magnetic stray field of the sample. The run is repeated while mixing the RF side bands $\omega_{RF,1}$ and $\omega_{RF,2}$ ($\pm$10 MHz) into the microwave drive and the sign of the field deviation is extracted from comparing both data sets. As shown the spatial resolution is a function of NV to sample distance with the lateral resolution here limited to around 40 nm at ca. 30 nm distance of the NV to the sample surface, taken from [262].

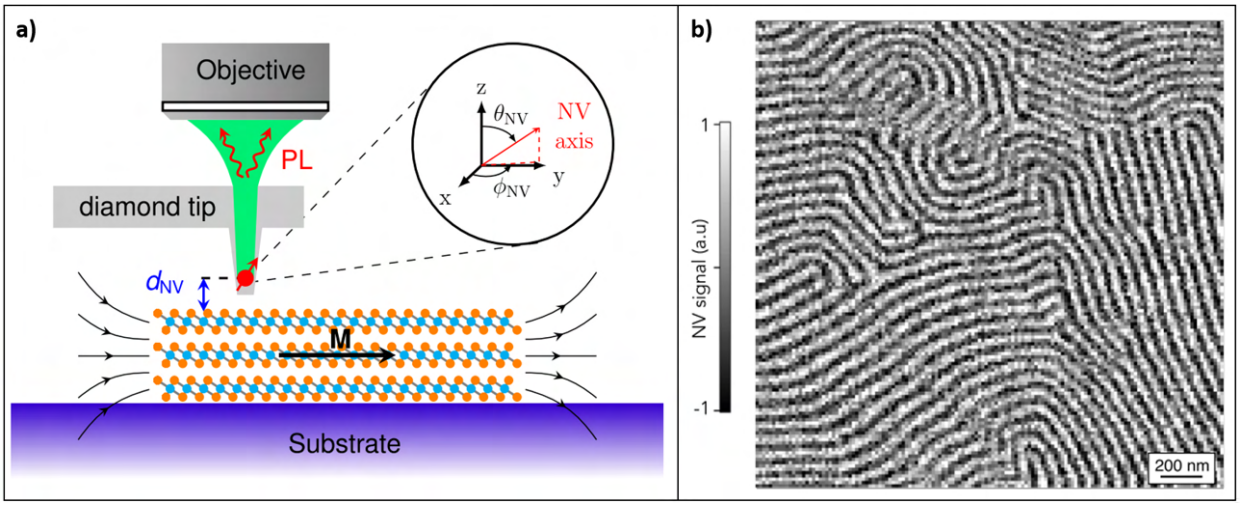

Figure 4.34: Recent publications applying scanning magnetometry using a commercially available monolithic diamond probe with a single NV^- centre close to its tip. The scanning probe is used to investigate a) the in-plane magnetization of the van-der-Waals thin-film ferromagnetic material $CrTe_2$ at room temperature, taken from [280], b) the surface of a bulk $BiFeO_3$ crystal showing the formation of topological defects of antiferromagnetic domains, taken from [281].

4.3.2 Outline of the work

We aim to increase the collection and pump efficiency from a single negatively charged nitrogen vacancy (NV^-) centre in the tip of monolithic diamond micropillar, which is a geometry suitable for sensitive, high spatial resolution AFM-like scanning magnetometry. Increased collection efficiency increases the magnetic field sensitivity as discussed in the previous section.

A schematic of the typical experimental arrangement in a scanning diamond probe system is shown in Fig. 4.35. Such systems are essentially a combination of a single photon sensitive confocal microscope setup, an AFM setup, microwave source and antenna (mostly a simple wire that is brought close to or integrated with the probe tip) and a magnet with adjustable position [282]. The optical addressing and read-out of the NV^- makes the detection of the cantilever deflection via laser reflection difficult and the probes are therefore usually attached to a piezoelectric tuning fork deflecting up and down under an applied electric field or mapping such a deflection onto a voltage that can be read-out [283, 284].

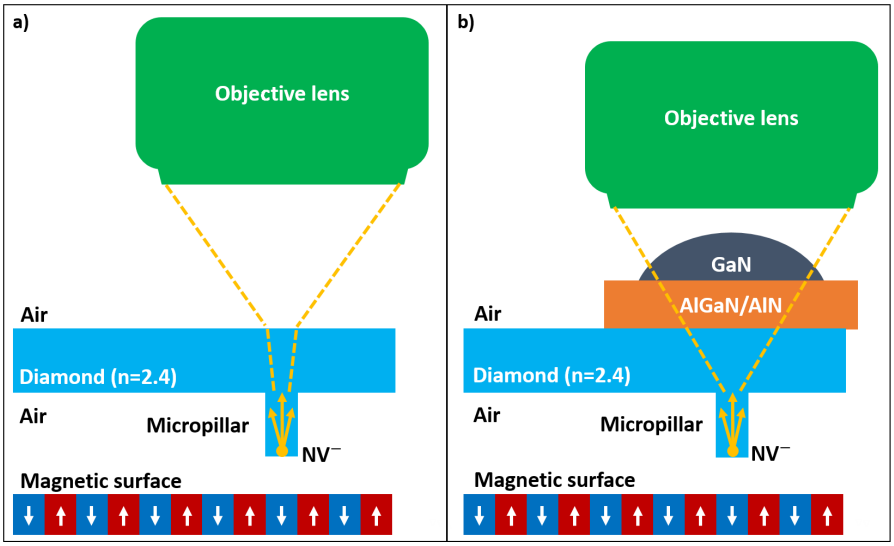

Figure 4.35: a) Schematic showing a typical measurement arrangement for scanning magnetometry with diamond NVs. Due to strong refraction at the top diamond air interface only light from a narrow emission cone can be collected with the free space optics above, b) proposal to integrate an additive GaN micro-lens with a diamond cantilever probe to enhance the collection efficiency by mitigating refraction at the interface.

Currently the two companies 'Qnami' and 'QZabre' offer single crystalline diamond magnetometry probes and compatible scanning systems. Fraunhofer IAF purchased systems and probes from both companies for the QMag project. The diamond scanning probes from Qnami offer easier integration with our relatively bulky GaN SILs, and we therefore focus on their diamond probes in the following, which are provided to us by IAF.

The two most recent generations of magnetometry probes from 'Qnami' are shown in Fig. 4.36 a) and b), with c) containing illustrations of the different NV orientations that are available on demand. The shape design of the newest generation of tips ('MX+') is based on [268] and the performance is illustrated in Fig. 4.37. Compared to the tapered 'MX' tips, saturation count rates are reported to have increased up to 3x by achieving a parabolic tip shape. Interestingly Fig. 4.37 b) shows that even such a moderate improvement can lead to a $>$ 10x reduction in acquisition time per pixel for a similar SNR of 4.

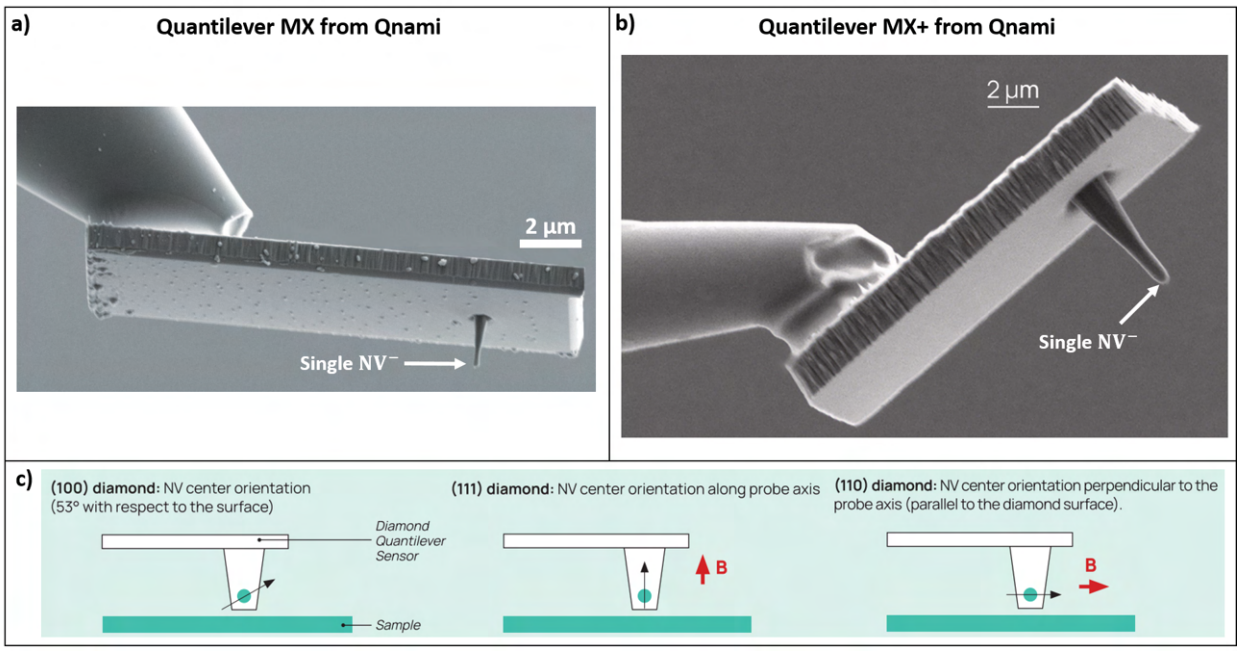

Figure 4.36: Commercially available diamond probes from 'Qnami'. a) Previous generation of diamond probes which are available for this work, b) newest optimized diamond probes with parabolic tip shape for enhanced collection, c) the different crystal orientations 'Qnami' offers for their probes resulting in different sensitivity for certain field directions. SEM images and schematics are adapted from [277, 278].

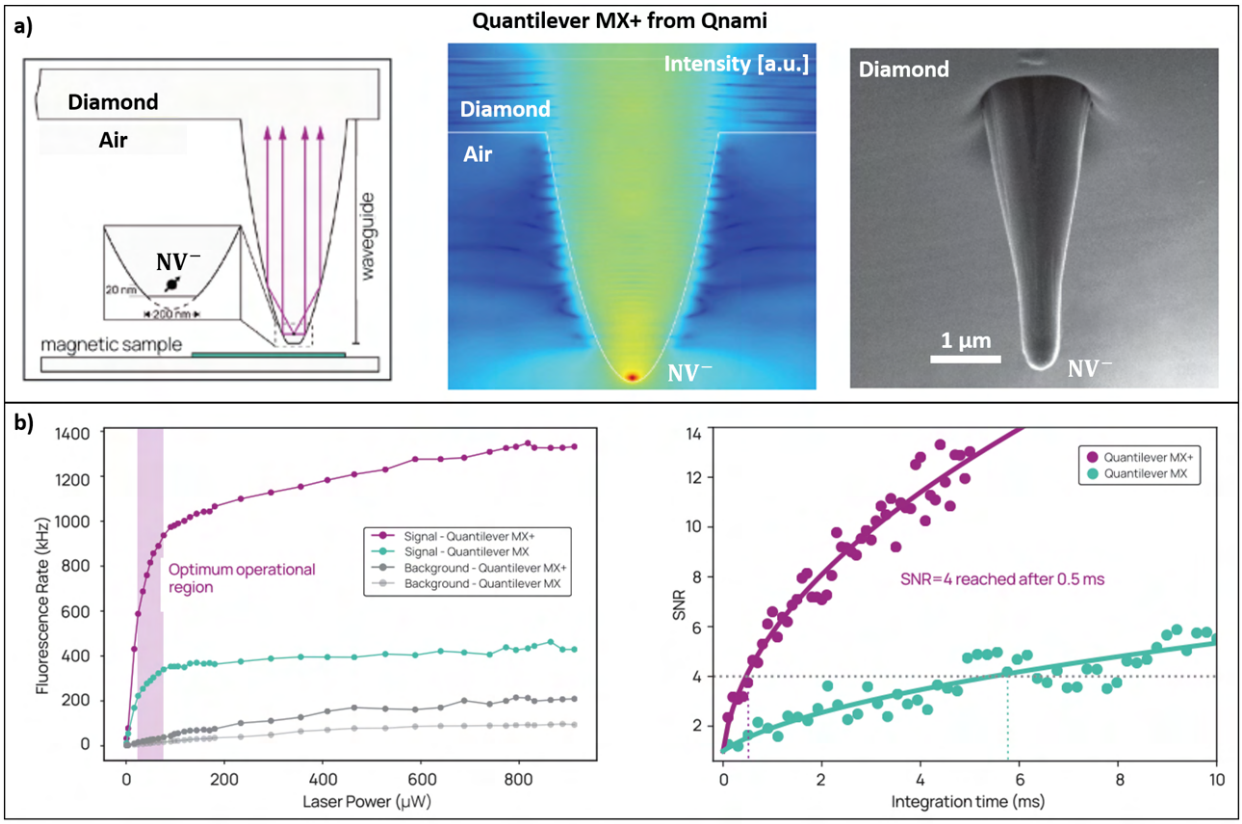

Figure 4.37: Newest generation of commercially available diamond probes from 'Qnami' ('MX+'). a) Schematic, FDTD simulation and SEM image of probes with single NV⁻ centres close to the tip, b) (left) measured fluorescence rate under increasing laser power using the same collection optics and (right) integration time needed to reach a certain signal-to-noise ratio. Adapted from [278].

4.3.3 Simulation results

We use FDTD simulations to assess the interplay of GaN micro-lenses with different pillar geometries with the results shown in Fig. 4.38 with b) depicting the four different pillar geometries used. The pillars with pink and golden frame are modelled on the available SEM images of the 'MX' and 'MX+' probes from 'Qnami'.

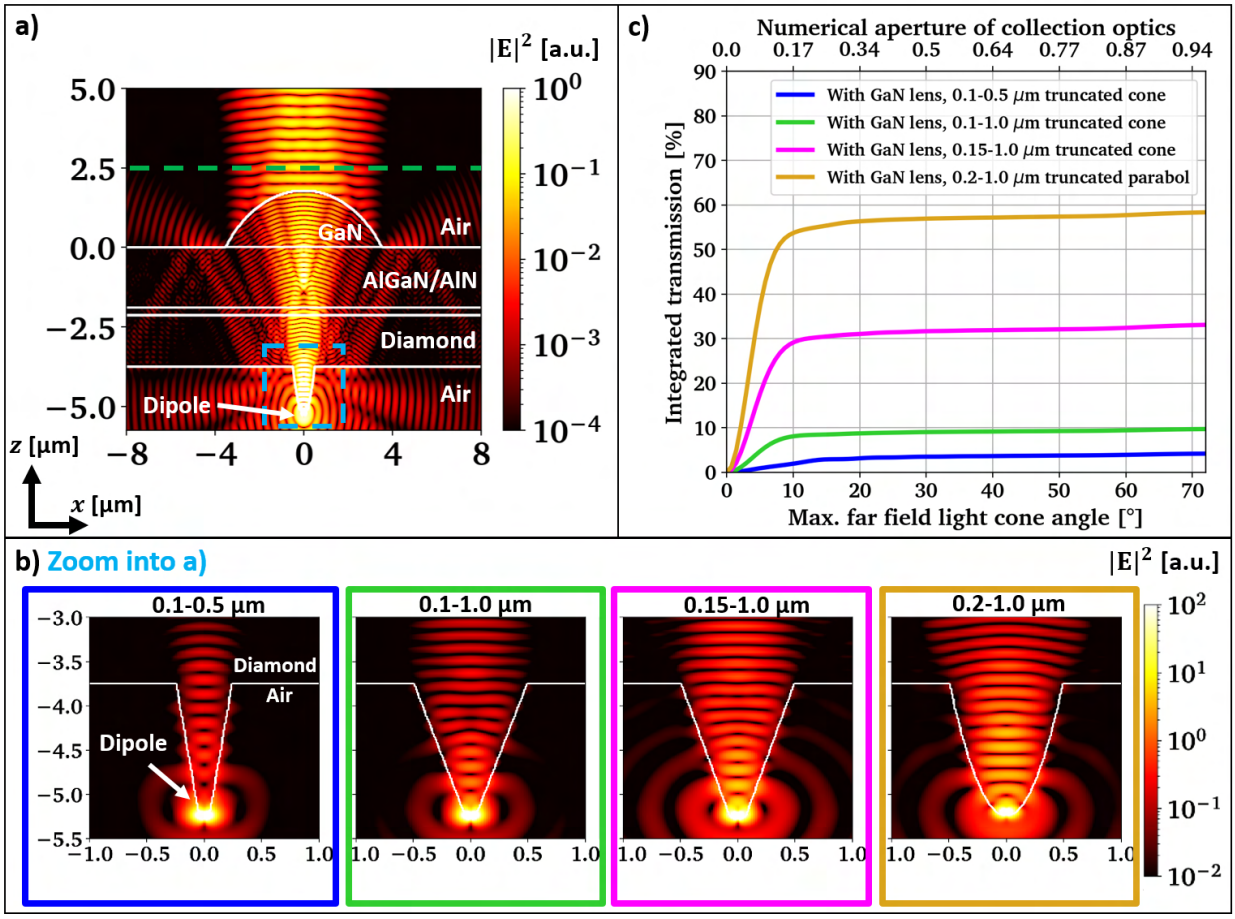

Figure 4.38: FDTD simulations investigating the interplay of different micro-pillar geometries with a spherical GaN micro-lens ($d = 7.1\,\mu$m, $h = 1.8\,\mu$m) for an ideally aligned dipole in (111) crystal orientation mimicking the NV^- centre in 10 nm proximity to the pillar tip. All pillars are 1.5 μm long and the diamond membrane has 1.6 μm thickness, which is based on AFM and SEM measurements of the commercial diamond probes. a) Cross section through the simulation region at $\lambda = 700$ nm wavelength, here for the parabolic tip (golden curve), b) Zoom into the circular micro-pillars with four different variations of the top and bottom diameter and a shape variation between truncated cones (blue, green and purple) and a truncated rotated parabola (gold), c) integrated transmission in dependence of the maximum far field angle taken from the monitor above the micro-lens (green dotted line in a).

We see in b) that the shape of the diamond micro-pillar plays a crucial role in terms of guiding the light towards the top surface of the membrane. Due to variations in the available local density of states, upwards transmission is strongly suppressed if the tapered diamond pillar is too narrow or too steep in agreement with literature [285]. The slightly enlarged size of the truncated parabola (golden curve) seems to offer the best compromise in terms of low Purcell suppression (Purcell factor close to 1 in the emission window of the NV^-) and reduced diffraction at the pillar-membrane interface, yielding a reasonably precollimated beam propagating upwards into the diamond membrane. Purcell

enhancement and how it can be calculated with classical Maxwell solvers is discussed in appendix G. The same GaN micro-lens is used in all four simulations leading to efficient extraction of photons into a narrow emission cone of around 10° in all cases, compare Fig. 4.38 c). Similar to previously discussed FDTD simulation results the transmission through a 2D monitor indicated in green is averaged between $\lambda = 650 - 750$ nm wavelength and multiplied with the averaged far field projection at 650, 700 and 750 nm to extract the integrated transmission within a given emission cone. The Purcell factor falls in all cases linearly with wavelength, which allows us to ignore the exact spectral shape of the NV^- emission, which is roughly symmetrical around 700 nm wavelength. A higher Purcell factor at 650 nm is balanced by a lower Purcell factor at 750 nm wavelength, see Appendix for a discussion of the Purcell effect and how it is modelled in FDTD simulations.

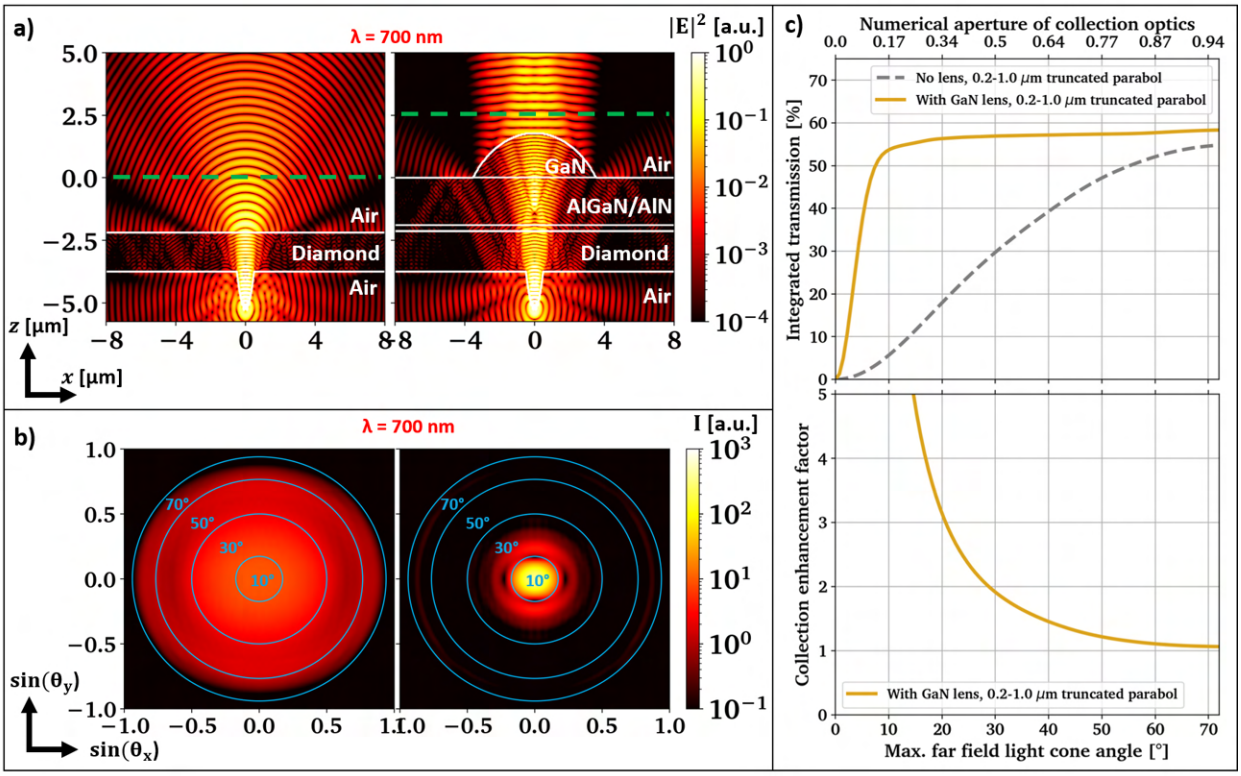

Figure 4.39: FDTD simulations of the optimised parabolic micro-pillar shape based on the newest generation of the 'Qnami' probes (MX+) comparing the cantilever without and with a spherical GaN micro-lens ($d = 7.1\,\mu$m, $h = 1.8\,\mu$m) for an ideally aligned dipole in (111) crystal orientation mimicking the NV^- centre in 10 nm proximity to the pillar tip. All pillars are 1.5 μm long and the diamond membrane has 1.6 μm thickness, which is based on AFM and SEM measurements of the commercial diamond probes. a) Cross sections through the simulation region at $\lambda = 700$ nm wavelength, b) corresponding far field emission without and with micro-lens at $\lambda = 700$ nm wavelength, c) integrated transmission and enhancement (comparing gray and golden line) in dependence of the maximum far field angle taken from the monitor above the pillar or micro-lens (green dotted lines in a).

To illustrate that the addition of a GaN lens is not only expected to flatten the angular response from the diamond micro-pillars but also enhances the light collection, we compare the modelled 'MX+' probe without and with added micro-lens, with the FDTD simulation results shown in Fig. 4.39. From these simulations we can expect that the addition of optimized GaN micro-lenses might allow 2x improved collection efficiency even from the already highly optimized 'MX+' probes while further reducing the required microscope objective NA to 0.5. Further reduction of the NA is likely not possible due to the

added fluorescence signal from the GaN micro-lenses themselves. We also see that at high collection NA the benefit from adding the GaN micro-lens is expected to nearly disappear.
At the time of this work we only had access to 'MX' diamond probes from 'Qnami' and our experimental demonstrations will focus on these probes. Therefore, we also modelled the expected improvement from this tip by adding a GaN micro-lens, with the results shown in Fig. 4.40. The lens dimensions are modelled on the GaN lens device we will later print onto the cantilever probe and we include a thin layer of an optical adhesive into the simulations, which proved to be necessary to facilitate bonding in the experiment.
As visible in Fig. 4.40 we expect moderate enhancement of around 1.5x at a collection NA of 0.5, which could deliver significant acquisition speed-up and a low sensitivity boost. The improvements essentially vanish when moving to an NA of 0.77, therefore the market will decide whether the lens integration into the probe-fabrication process flow can be cost-effective. We additionally see that the adhesive layer is only expected to minimally effect the overall upwards transmission.

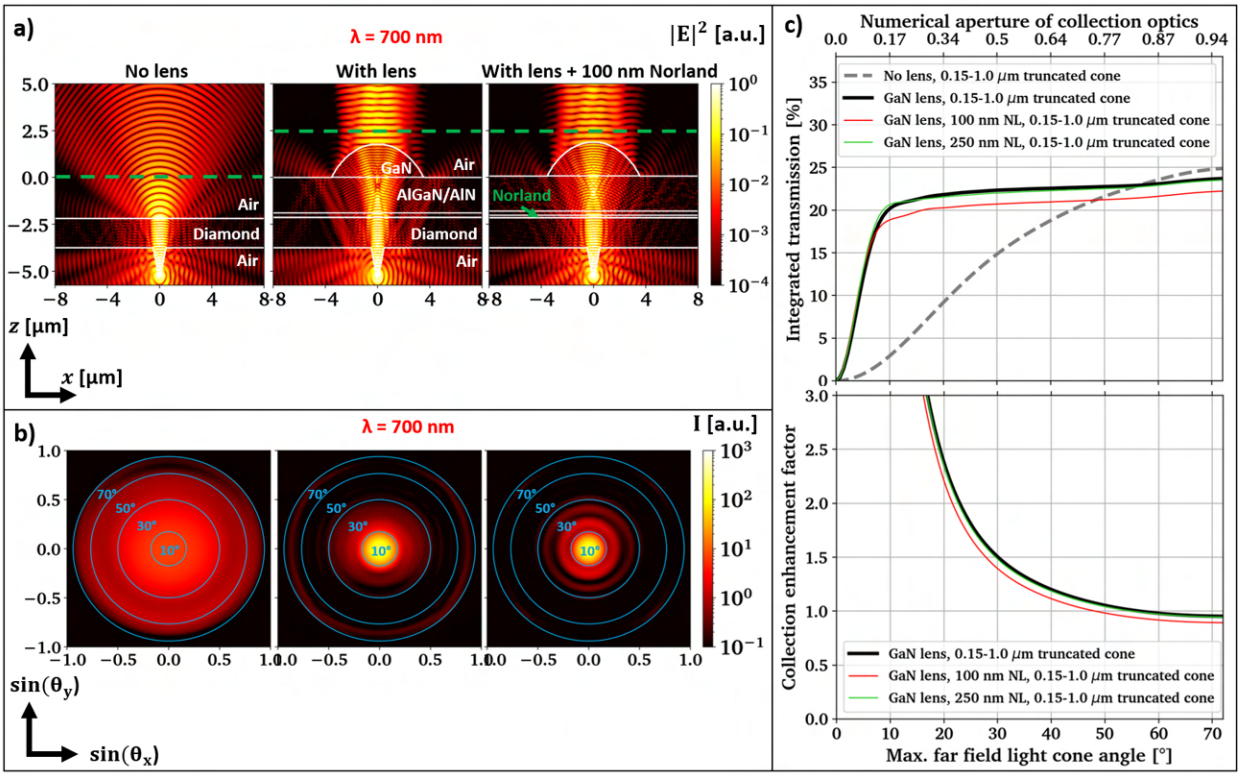

Figure 4.40: Based on the performed experiment: FDTD simulations of a micro-pillar shaped like a truncated cone with $d_{bottom} = 150$ nm and $d_{top} = 1000$ nm based on the available 'Qnami' probes (MX) comparing the cantilever without and with a spherical GaN micro-lens ($d = 7.1\,\mu$m, $h = 1.8\,\mu$m) for two dipole emitters mimicking the NV^- centre in 10 nm proximity to the pillar tip in (100) crystal orientation. This pillar shape is shown in more detail in Fig. 4.38 b) (purple graph). In the third simulation, a 100 nm (250 nm, not shown) thick adhesive layer of Norland 61 is added to investigate the effect of a bonding layer. All pillars are 1.5 μm long and the diamond membrane has 1.6 μm thickness, which is based on AFM and SEM measurements of the commercial diamond probes. a) Cross sections through the simulation region at $\lambda = 700$ nm wavelength, b) corresponding far field emission without, with micro-lens and with micro-lens and 100 nm Norland 61 at $\lambda = 700$ nm wavelength, c) integrated transmission and enhancement (comparing the gray with the other curves) in dependence of the maximum far field angle taken from the monitor above the pillar or micro-lens (green dotted lines in a).

4.3.4 Experimental results

We test two different schemes to integrate the GaN micro-lenses on top of the diamond cantilever probes, Fig. 4.41 includes schematics of both. In a) the full back-end integration is described and refers to printing lenses on the fully assembled diamond micro-probe ready for NV scanning magnetometry. The height difference between diamond NV and tuning fork as well as the reasonably steep angle of the mounting needle necessitate the careful cutting of the micro-stamp to avoid contact between PDMS and other parts of the probe.

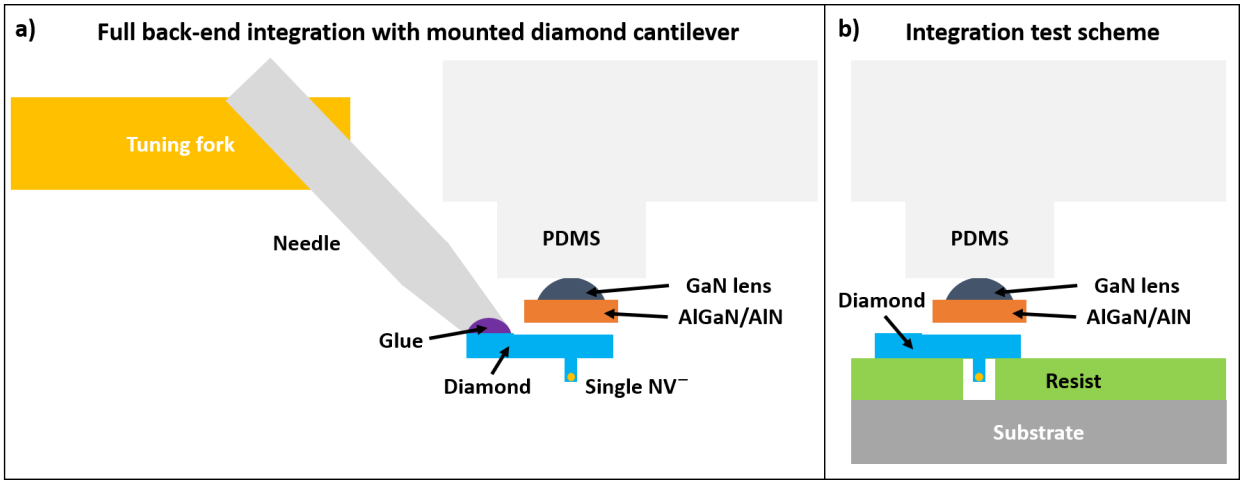

Figure 4.41: Schematics of the two tested schemes for micro-lens integration with the commercial diamond cantilevers, which are fully mounted on piezo electric tuning forks used to electrically stimulate tip oscillations for tapping mode operation. a) Back-end integration of the GaN micro-lens on the mounted diamond cantilever tips with an appropriately cut PDMS stamp, b) proof-of-principle test scheme mimicking GaN lens integration on the diamond host substrate before mounting. Here, the diamond cantilevers are removed from the fully assembled scanning probes and released on a resist pattern with holes for the micro-pillars by transfer printing.

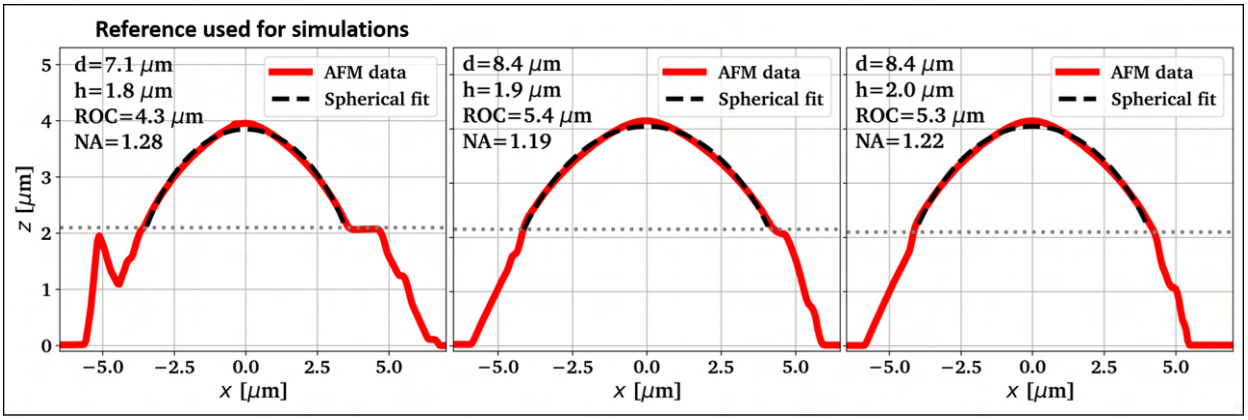

Figure 4.42: AFM line scans of three different single GaN micro-lenses printed on a flat diamond substrate employed in the following test schemes (all SSS-NCH, type of tip, see appendix D). The most left device is used as reference for the simulations in the figures above and is successfully integrated with a 'MX' cantilever from 'Qnami' printed on a SU8 resist hole pattern (compare Fig. 4.48). The shown line scans correspond to the three microscope images of lens devices shown in the following Fig. 4.43 b) at the top.

In b) we mimic the assembly of the lens on the diamond cantilever donor substrate after microfabrication,

see Fig. 4.32 d) for an image of such a donor. Diamond is a very stiff material that can be expected to bend minimally under pressure from a PDMS micro-stamp. The tether connection between cantilever and remaining diamond substrate is reported to be cut by focused ion beam milling [262]. Because we do not have access to the growth substrate, we mimic this geometry by removing already mounted diamond probes by transfer printing and release them on a prepatterned resist substrate with sufficiently large holes to allow for free-standing micro-pillar diamond probes in air. Afterwards we shortly reflow the resist to 'glue' the diamond probe into place and successively print the GaN micro-lens. In this section we use 40x40 μm^2 and 50x50 μm^2 micro-stamps following the two different designs shown in the Appendix.

The AFM profiles of three GaN micro-lenses that are used for the following print experiments are depicted in Fig. 4.42. The FDTD simulations are based on the most left device, which is successfully integrated with one of the probes following the scheme depicted in Fig. 4.41 b).

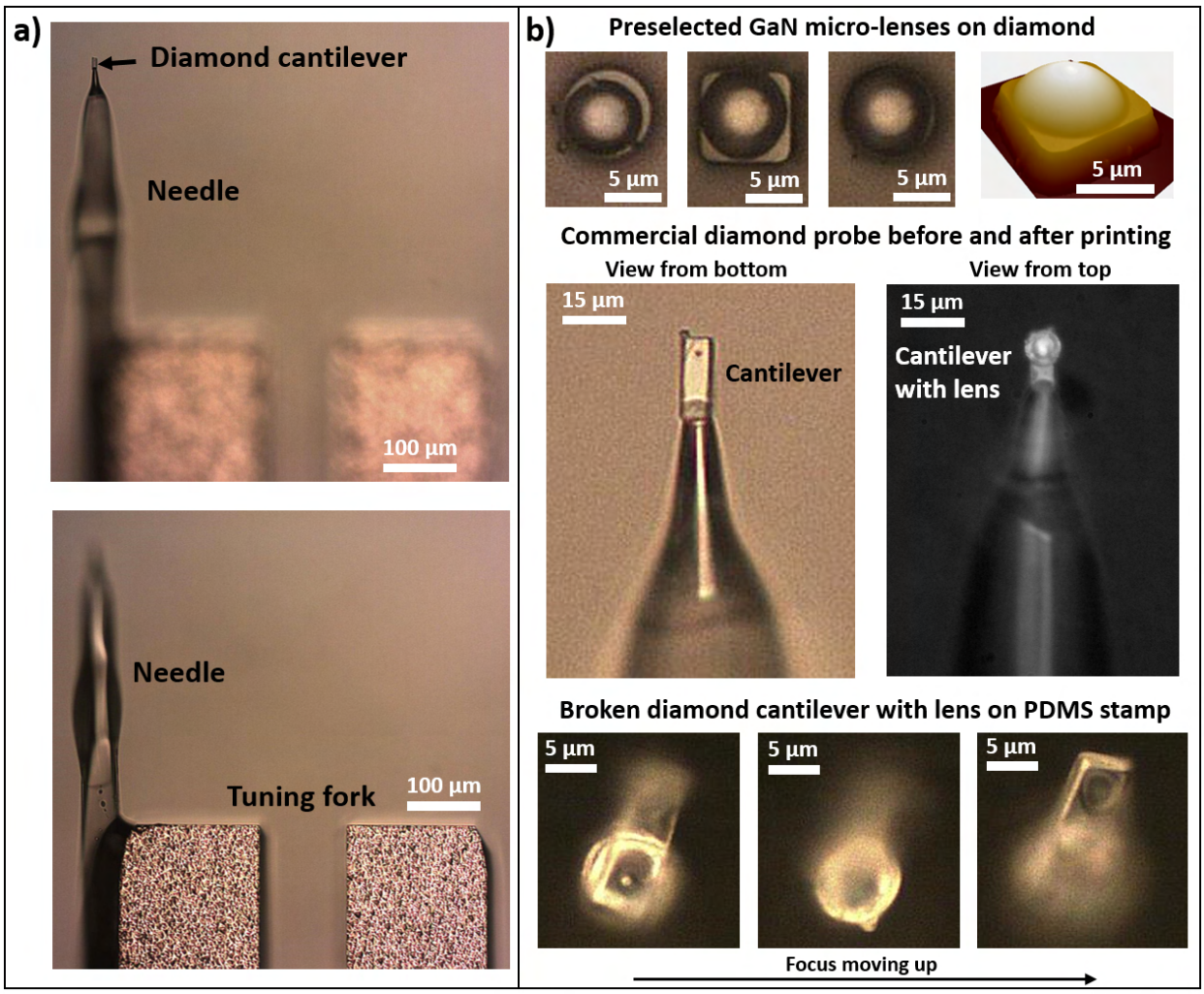

Figure 4.43: Back-end GaN micro-lens integration attempts on the mounted diamond cantilever devices from 'Qnami', following the scheme shown in Fig. 4.41 a). a) Large scale microscope images of the diamond cantilever mounted at the end of a needle attached to a tuning fork (two different focal positions), b) (top) Microscope images of three promising single GaN micro-lenses on a flat diamond substrate preselected for integration with the 'Qnami' probes (AFM line scans of these devices are shown in the previous figure), including a 3D isotropic representation of AFM data taken on the middle lens (SSS-NCH), (middle) successful release of the most left micro-lens on a mounted cantilever probe with sub-optimal alignment accuracy (the two images are taken from the bottom and the top of the cantilever respectively), (bottom) a broken diamond cantilever after failed integration with the most right micro-lens attached to it, both adhering to the PDMS stamp used for the transfer attempt (3 different focus positions).

Microscope images showing pure back-end printing attempts can be viewed in Fig. 4.43. In a) we can see the substantial height difference between the tuning fork and diamond cantilever mounted at the tip of a transparent needle. As visible in the middle of b) we are able to successfully transfer a GaN micro-lens on top of a diamond cantilever, but unfortunately the shearing print release technique proves not straight forward on a flexible substrate which additionally has smaller surface area than the full lens membrane. This leads to significant misalignment between lens and micro-pillar.

We find that some cantilevers are very weakly bonded to the attached needle, leading to mechanical deformation of the probe during printing attempts. This resulted in the complete loss of one probe and unplanned breaking of another during the transfer print process. The latter diamond probe got attached to the PDMS stamp and is then released on the resist hole pattern together with the adhered

lens, compare Fig. 4.43 b) at the bottom and 4.44 b). This particular device is marked with the red frame with the three bottom images showing the cantilever-lens system immediately after printing. We observe several μm misalignment between lens and micro-pillar. We therefore remove the lens and investigate the top surface of three printed diamond cantilever devices with AFM, compare the three top images in Fig. 4.44 b).

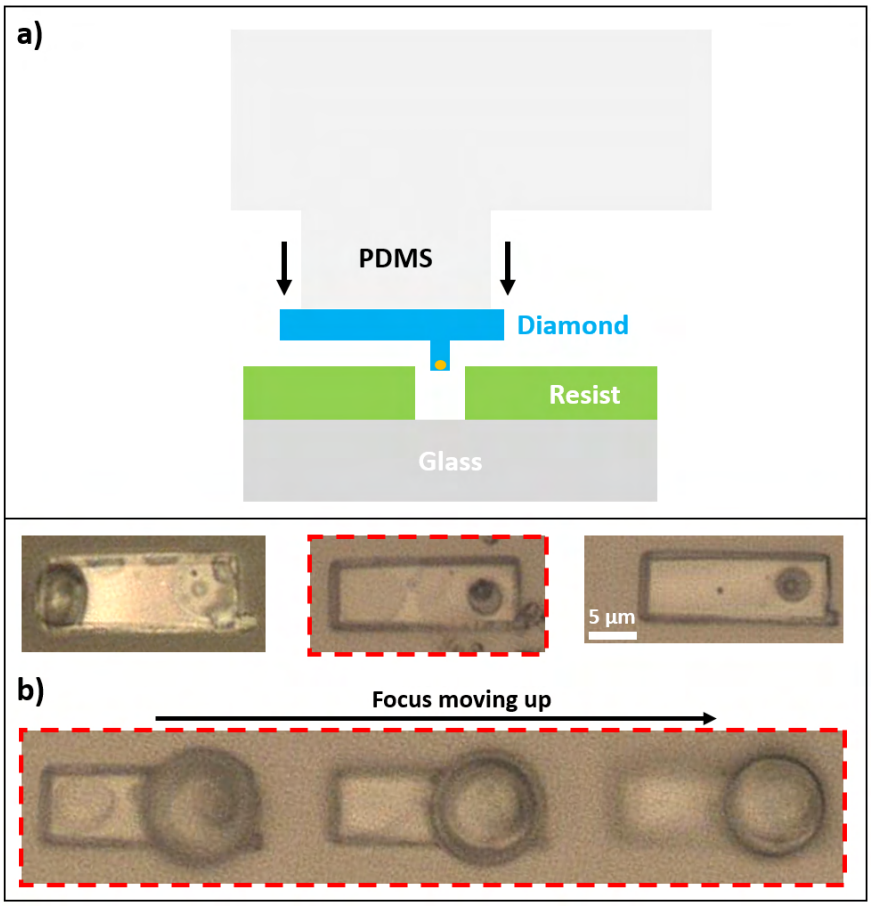

Figure 4.44: a) Schematic showing the transfer printing based integration of a diamond cantilever with a resist hole pattern, b) three different transferred diamond cantilevers on SU8-5 with the micro-pillar aligned to a lithographically defined resist hole (DWL66+) on low-autofluorescence cover glass slides (Thorlabs, precision cut). The middle device with the red dotted frame corresponds to the same device which broke during the lens integration attempt in the bottom of Fig. 4.43 b). The three bottom images show this device immediately after printing on SU8-5, with the micro-lens showing a significant offset compared to the micro-pillar position. Reprinting attempts with better positioning failed, therefore the GaN micro-lens was removed. The scale bar applies to all images.

The results of this AFM analysis is shown in Fig. 4.45 for the two cantilever devices that appear 'cleaner' in the microscope images after printing, compare Fig. 4.44 b). We can observe substantial differences in surface quality, with the cantilever in b) showing a reasonably flat top-surface and smooth surface finish. Still spiking features are observed in both small and large area scans. Unfortunately our AFM tool can show spiking artefacts at the edges of high-aspect ratio structures which leaves some uncertainty whether the observed spikes at the cantilever edges in Fig. 4.45 b) are real.

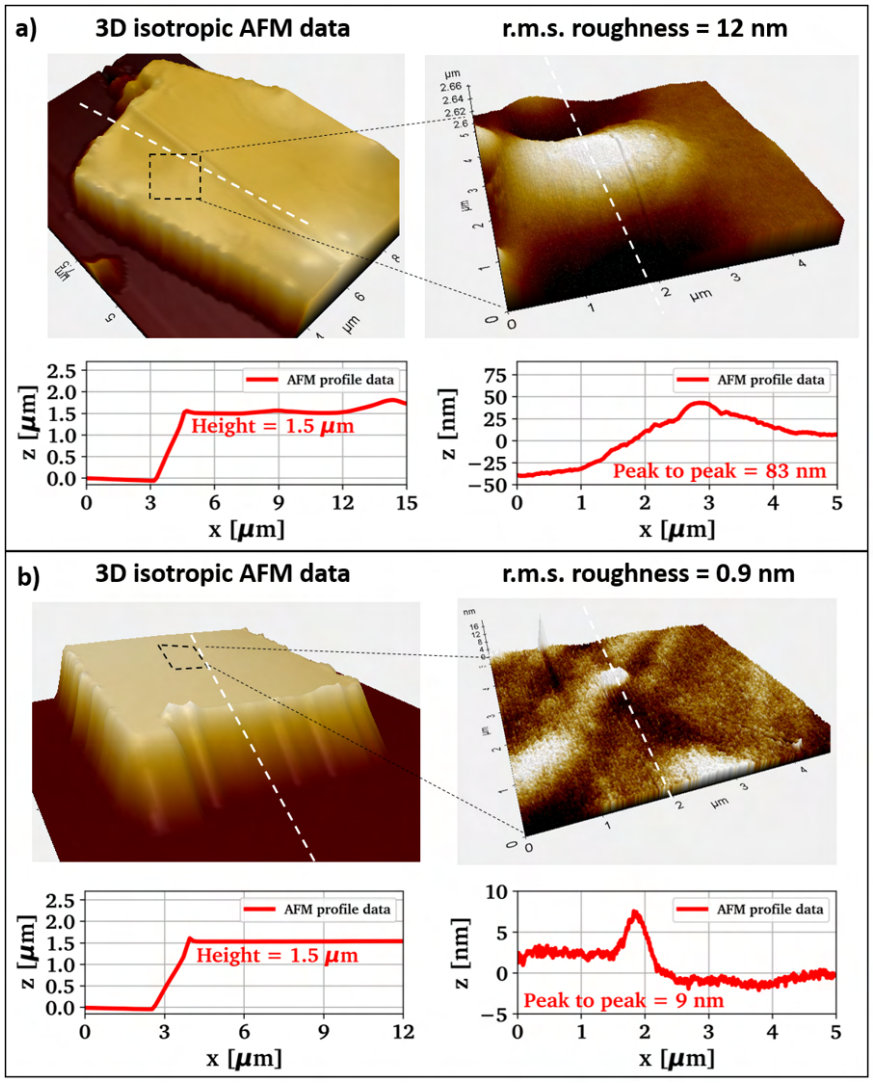

Figure 4.45: AFM analysis of two diamond cantilevers printed on SU8-5 (SSS-NCH). 3D representations of the AFM data with a roughness scan taken on top of the cantilever (position indicated by the black dotted lines). Line scans correspond roughly to the white dotted lines in the respective 3D representations. a) corresponds to the middle device and b) to the most right diamond cantilever device (3S9) shown in Fig. 4.44 b) (three top images). Before the AFM scan, a short hard bake at 85 °C is applied to 'glue' the cantilever to the resist.

Encouraged by the relatively positive AFM result on the cantilever top surface shown in Fig. 4.45 b), we analyse this transfer printed cantilever device optically in our home-built confocal microscope setup introduced at the beginning of this Chapter. The resulting power series, xy and xz PL maps for objective lenses with NA = 0.5 and NA = 0.95 taken on the single NV^- centre inside the commercial diamond probe are shown in Fig. 4.46.

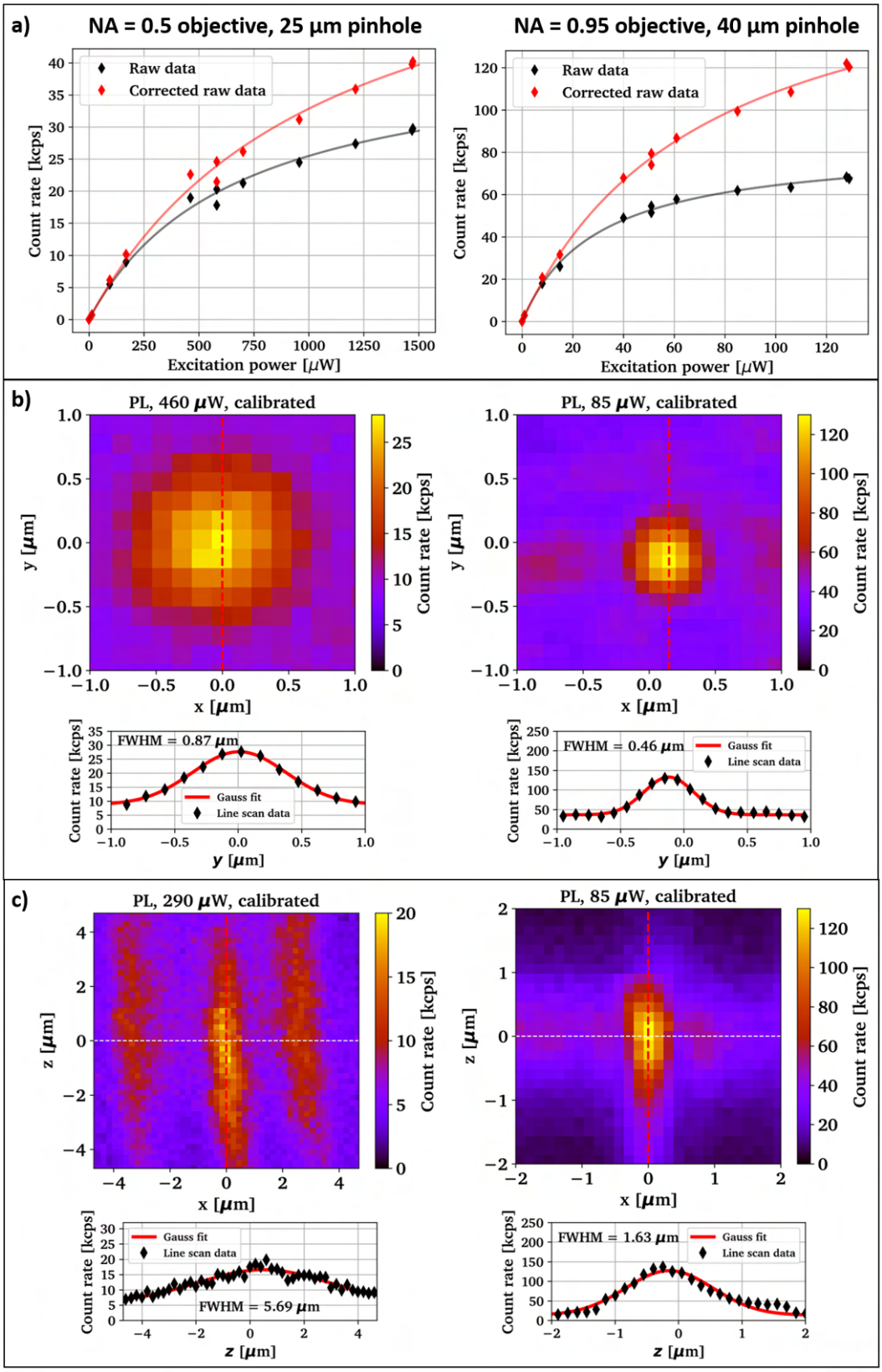

Figure 4.46: Precharacterisation of the most promising diamond cantilever printed on SU8-5 corresponding to the device 3S9 analysed in Fig. 4.45 b), using two different microscope objective lenses in the home-built confocal microscope PL setup (2x 550 nm LP, 1x 650 nm LP, maps and power series are linearised). a) Power saturation series on the single emitter fitted with a simple power law function, b) xy PL maps and fitted linescans through the red dotted lines in the scan, c) xz PL maps and fitted linescans through the red dotted lines in the scan, the white dotted lines indicate the plane of the xy scan in b).

In a) we show the effect of the data calibration necessary to account for the detector saturation behaviour. The plots in b) contain the lateral xy scan maps with a FWHM close to what one would expect from the diffraction limited spot size of 0.71 μm and 0.38 μm for a NA of 0.5 and 0.95 at $\lambda = 700$ nm, respectively (see Appendix for the employed equations). The found axial resolution measured in c) matches the prediction for light collection with diffraction limited spot size reasonably similarly well, we expect a FWHM of 4.7 μm and 1.2 μm from theory for a NA of 0.5 and 0.95, respectively (we take the pinhole size into account, see Appendix). This is not too surprising as the micro-pillar dimensions at the tip are smaller than the diffraction limited spot size.

A $g^{(2)}$ autocorrelation measurement performed on the same device is shown in Fig. 4.47 indicating single photon emission from the diamond micro-pillar. Even though low-autofluorescence cover glass slides are used as substrate, significant background counts are observed, which reduce the single photon purity significantly and we attempt to correct for these using the procedure indicated in [94, 286, 287]. The remaining $g^{(2)}(0) > 0$ value might be due to the finite detector response function which can be taken into account by applying a deconvolution procedure [288].

The normalized $g^{(2)}(\tau)$ autocorrelation data is fitted according to a three level model of the NV emission, based on continually increasing photoionization of the NV^- centre with increasing optical power, leading to NV^--NV^0-NV^- charge state conversion and shelving of the emission [50]. The shelving generates a bunching effect that overlays the single photon emission for delays τ longer than the emitter life time [7, 286, 289–292]. This bunching occurs because if the NV^- centre is excited it might be cycled through the charge conversion process, leading to a delayed emission characteristic following the time scale of the conversion process. At low excitation powers this bunching effect is reported to vanish and it is not expected to change the value of $g^{(2)}(0)$ at any power [290]. But usually high pump rates increase the amount of background light collected from the environment.

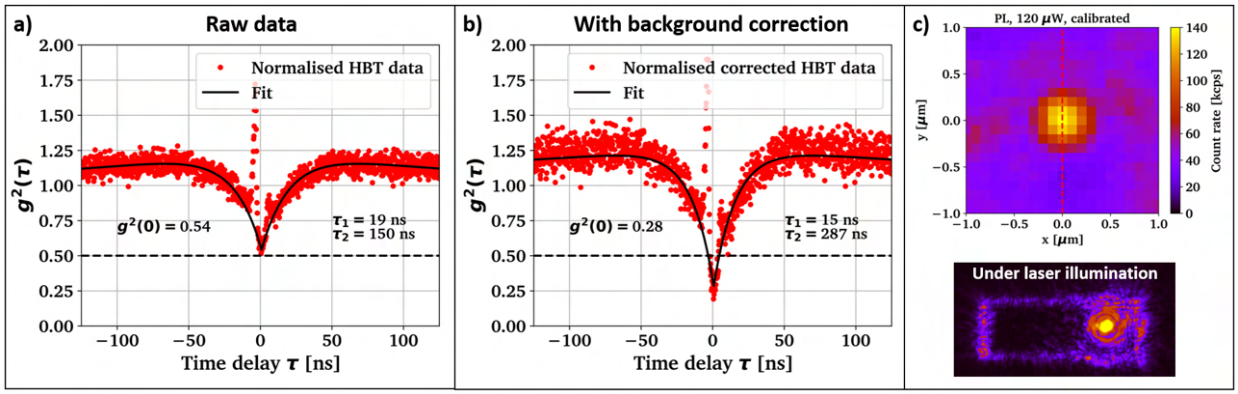

Figure 4.47: $g^{(2)}$ autocorrelation measurement of the single NV^- centre in the most promising diamond cantilever (3S9) after printing on SU8-5. The lens arrangement in front of the two SPAD detectors is optimized for minimal optical cross talk, using two SPADs with low dark count rates (< 100 Hz). a) Normalised $g^{(2)}(\tau)$ generated by the time tagger, b) the same data taking the surrounding level of background fluorescence into account using the formula given in [94, 286, 287], c) xy PL map of the emitter and camera image of the diamond cantilever with the laser focused on the micro-pillar. All measurements are performed with the 100x objective and 40 μm pinhole, using 2x 550 nm LP, 1x 650 nm LP. The uprising data points close to $\tau = 0$ are due to asymmetric optical cross talk, with detector 1 picking up a significant amount of photons that are emitted by detector 2.

With these results at hand we attempt the transfer print based integration of the preselected GaN micro-lens on which the FDTD simulation geometry is based. Initial dry printing attempts failed, and

we therefore apply the optical adhesive Norland 61 in a PDMS based dip-ink fashion to the cantilever top-surface to facilitate bonding even though spiking features on the order of 10-100 nm might be present in the topology as indicated by the AFM scans. The results of this two staged 'wet' transfer printing are shown in Fig. 4.48. After several failed attempts the release of the device on top of the cantilever succeeded and we use a contact mode AFM cantilever mounted in the transfer print tool to push the lens in a visually well aligned state above the diamond micro-pillar and apply a short (5-10 min) UV cure with a multilamp photoreactor. Due to the relatively 'messy' transfer printing a thin layer of the optical adhesive is found on top of the lens, but disregarded for the time being.

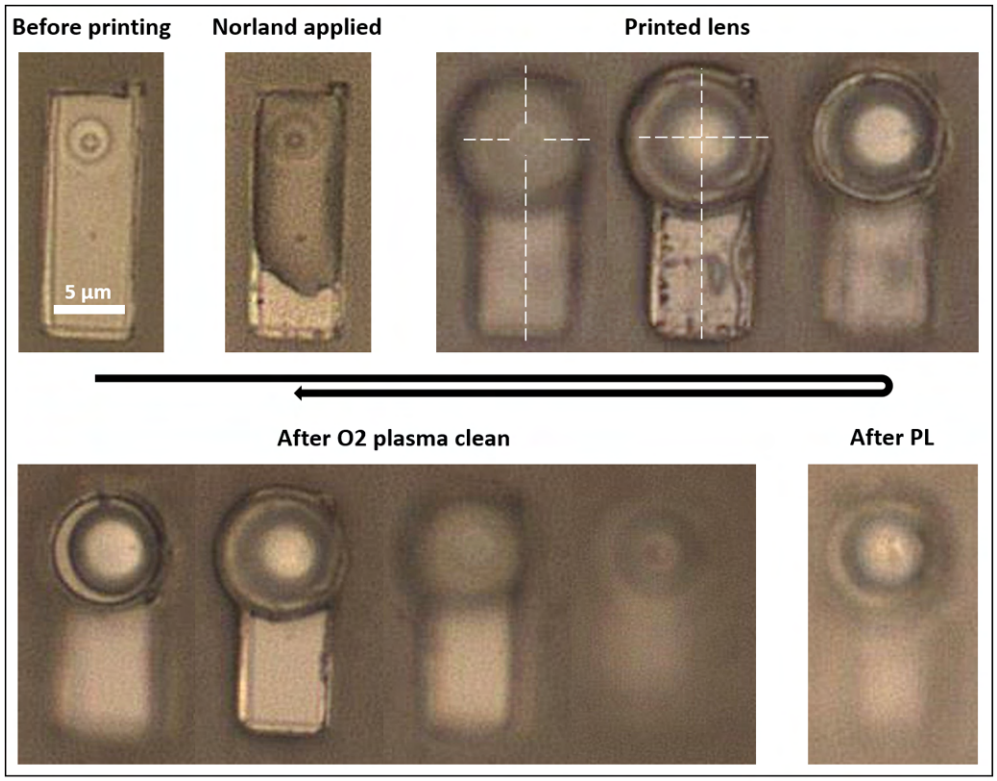

Figure 4.48: Transfer print based integration of a single GaN micro-lens with the most promising diamond cantilever 3S9 containing a single NV^- centre. Printing failed without the use of an adhesive layer, so a thin layer of the optical adhesive Norland 61 is applied to the cantilever by dipping a PDMS stamp into a bigger Norland bubble on a Si substrate and transferring the picked Norland to the target location. The lens is released on top in a well aligned position to the diamond micro-pillar below (the white dotted lines indicate the pillar position). A PL measurement is performed and after strong laser excitation (1.5 mW) a defect is found in the lens surface, suggesting that Norland 61 has migrated to the top of the micro-lens (bottom right image). These Norland residues are removed by applying ca. 20 min of oxygen plasma at room temperature to the sample (Barrel asher), revealing a burned spot when focusing through the lens on the micro-pillar (most right image after plasma clean). Potentially the Norland between micro-lens and diamond cantilever broke down under laser excitation.

We repeat the analysis of the resulting lens-cantilever structure with the confocal microscope using the objective with NA = 0.5 and the results are shown in Fig. 4.49 with a comparison of spot size and count rate before and after lens integration displayed in Fig. 4.50 a). We observe in Fig. 4.49 a) a seemingly elongated response from the lens-micropillar device. We are only able to observe anti-bunching in the bottom parts of the elongated vertical stripe with the best result displayed in Fig. 4.49 b), the measurement position is marked with white dotted lines in the left plot in a). This indicates that the

optical adhesive below the micro-lens contributes significant photoluminescence counts, because the effect persisted after the micro-lens top surface is cleaned by exposure to an O_2 plasma, see bottom part of Fig. 4.48.
The slight lateral magnification of the spot size on the right hand side of Fig. 4.49 a) might simply stem from the added SIL, theory predicts a magnification of around 2.4 if the emitter is placed at the centre of a spherical lens sphere but the magnification probably varies at other positions.
The autocorrelation measurement shown in Fig. 4.49 b) indicates compatibility of the GaN lens platform with single NV emitters even in 1-2 μm proximity to a fluorescent adhesive layer while a low collection NA is used. This is a promising result for combing GaN SILs with NV centres close to planar diamond surfaces as discussed in section 4.2.

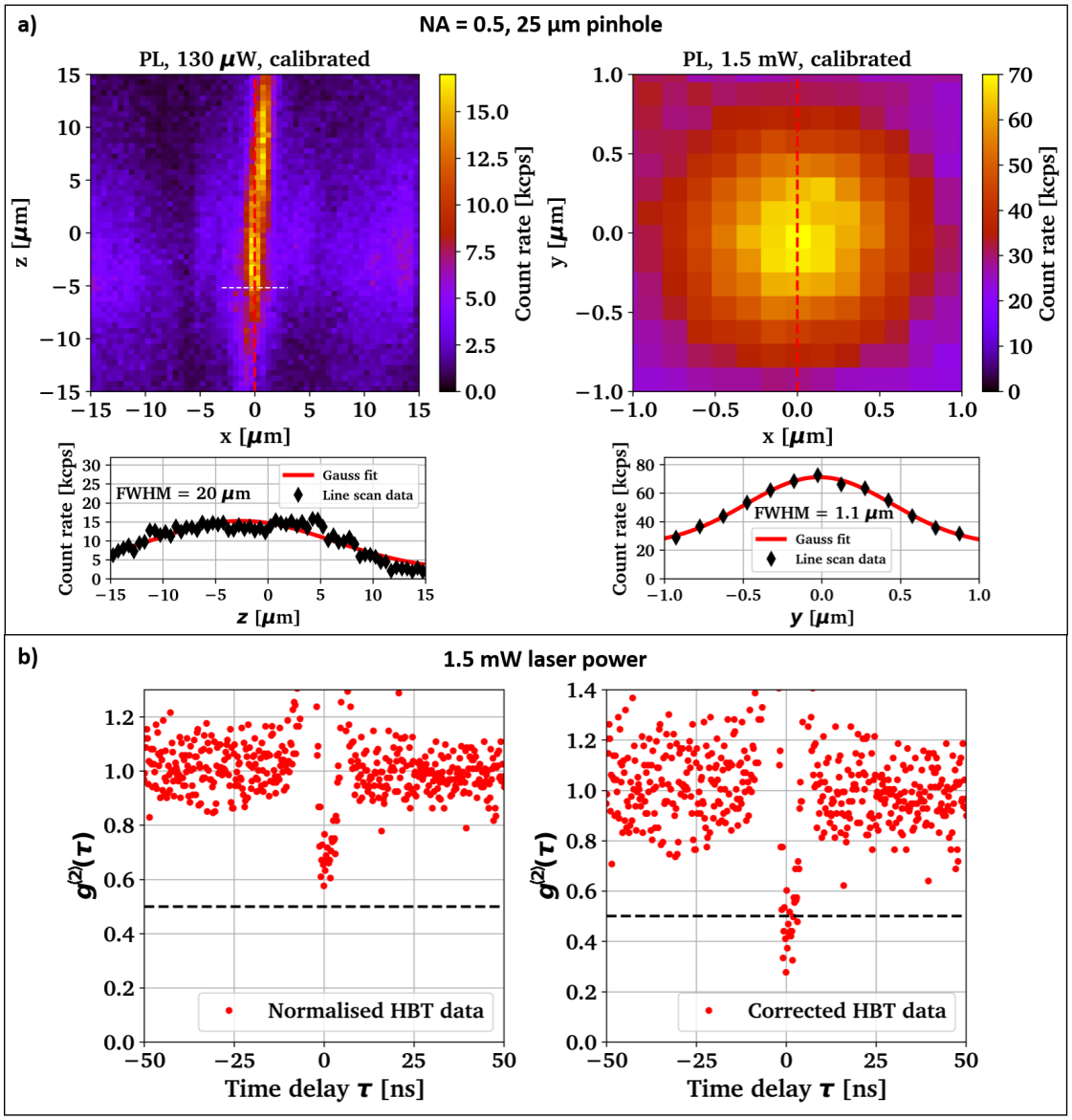

Figure 4.49: PL characterisation of the single photon emitter below the GaN micro-lens before the optical adhesive started to become unstable and before applying the O_2 cleaning procedure, using the 50x objective with 25 μm pinhole, 2x 550 nm LP and 1x 650 nm LP filter. a) xz and xy PL scans with line scans corresponding to the red dotted lines in each graph, the xy scan is taken in the plane indicated by the white dotted line in the top left graph, b) $g^{(2)}(\tau)$ autocorrelation measurement without and with background correction corresponding to the origin of the xy scan shown in a). As above, a simple background correction is done according to [94, 286, 287], assuming same background conditions at the emitter position as well as the used reference point in the same PL map.

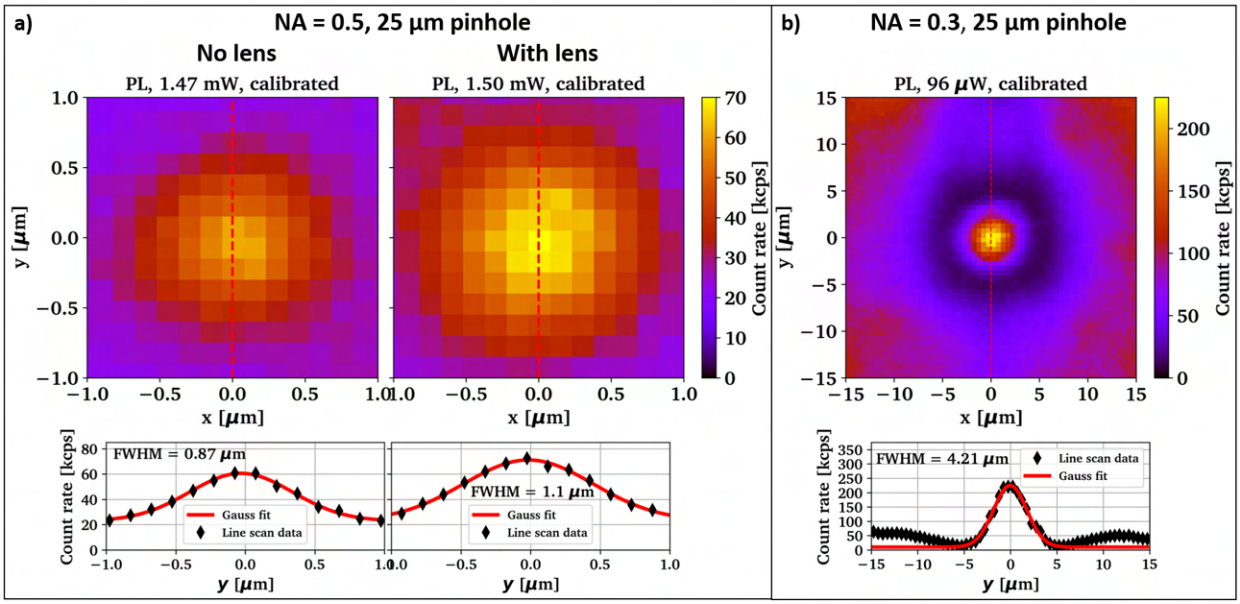

Figure 4.50: a) Direct comparison of the collected photoluminescence emission from the single NV^- centre in cantilever 3S9 printed on the SU8-5 hole pattern without and with micro-lens on the same scale under similar laser excitation power, using 50x objective with 25 μm pinhole and 2x 550 nm LP and 1x 650 nm LP filter. The right image corresponds to the position at which the $g^{(2)}(\tau)$ measurement shown in Fig. 4.49 b) is taken, b) xy PL map and line scan (corresponding to the red dotted line) of the GaN micro-lens on top of cantilever 3S9 using a 10x objective with 25 μm pinhole and 2x 550 nm LP and 1x 650 nm LP filter. This PL scan is performed after removing the optical Norland from the top surface of the lens.

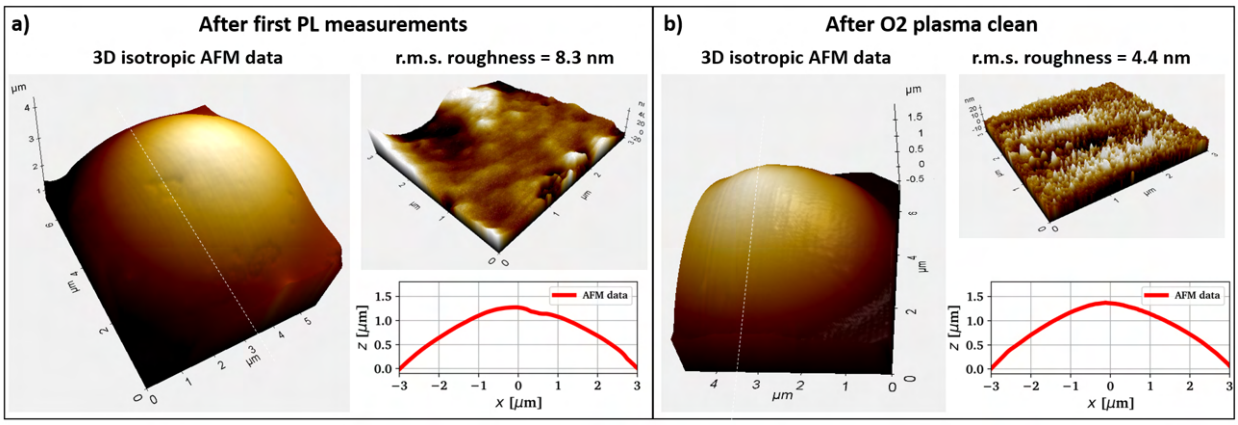

Figure 4.51: AFM analysis (SSS-NCH) of Norland residues on top of the transfer printed GaN micro-lens discussed in the previous figures (3S9 cantilever) with 3D AFM representations of the lens and surface roughness scans taken on top of the lens and with the positions of the line scans roughly indicated by the white dotted lines. Plots in a) corresponds to the micro-lens after print release and the first PL measurements, while b) shows the recovered lens profile after applying 14 min O_2 plasma in the barrel asher.

The AFM scans in Fig. 4.51 show significant residues of the optical adhesive on top of the micro-lens, which might have affected the optical performance of the lens and degraded the relatively low count rate improvement of 1.1-1.2x which we find from Fig. 4.50 a). Unfortunately the optical adhesive becomes optically unstable under highly focused green laser light (ca. 1.5 mW), leading to increasingly bright emission that rises over time under continuous laser excitation. This behaviour prevented any further systematic optical analysis even after the Norland on top of the lens is removed and additional UV curing

is applied, indicating that the Norland between lens and diamond causes the issues. We can distinguish a discoloured spot next to the micro-pillar after the O_2 plasma clean, compare the the images at the bottom of Fig. 4.48. This might indicate material degradation.
A final measurement using an objective with NA = 0.3 after lens cleaning and additional UV cure is shown in Fig. 4.50 b). A $g^{(2)}(\tau)$ measurement showed no anti-bunching even though bright emission is found from the micro-lens, suggesting efficient light collection from the Norland below the micro-lens at relatively low excitation power (ca. 100 μW). Much weaker fluorescence is collected from the other diamond cantilevers with this objective lens with no clear signature from the micro-pillar.

4.3.5 Summary

We attempted the integration of GaN SILs with scanning NV magnetometry probes to enhance collection efficiency and with that the magnetic field sensitivity.
Experimentally we have seen that the low quality of diamond cantilever top surface challenges the transfer print integration method. Integration succeeded using an adhesive layer, but the layer proved unstable under the strong field intensities necessary for confocal microscopy. Another material or longer UV curing might enhance the performance. We find very moderate improvement between 1.1-1.2x count rate enhancement at NA = 0.5 which potentially includes combined gain in collection and pumping efficiency. 1.5x collection enhancement is predicted in the investigated configuration, which could indicate that the found Norland residues on top of the micro-lens might have caused the lowered performance.
On the simulation side we have seen how important the pillar shape is for the upwards transmitted photon rate and that GaN micro-lenses are expected to offer moderate improvement on the order of 2x if integrated with the newest generation of commercial probes if an objective with NA = 0.5 is used. Because the minimum detectable field would only rise by $\sqrt{2} \approx 1.4$ and substantial effort might be needed for reliable lens integration with the scanning probes, the overall benefits for this technology space are doubtful and the improvement nearly vanishes for higher NA collection optics. Still the probe manufacturer shows that even moderate count rate improvements can cause significant reduction in measurement time at same SNR, which might justify further investigations.

4.4 Summary

In short we have investigated in this Chapter how GaN micro-lenses can be coupled to NV centres in diamond. We looked at NV clusters close to a planar diamond surface, emitter pairs in 5 μm depth and single emitters placed at the tip of diamond micropillars attached to scanning magnetometry probes. The main findings are:

- Optical microscopy based transfer printing in combination with confocal photoluminescence characterization allows for sub-micron accurate lateral printing of GaN micro-lenses on top of high-surface quality planar diamond substrates
- Grayscale preshaping in combination with resist reflow allows to fabricate GaN lenses with their radius of curvature matched to the emitter depth, here demonstrated in all three investigated NV configurations, meaning that we can match emitter and SILs in three spatial dimensions. Full grayscale lithography is not employed in combination with NV centres but the results shown in Chapter 2 indicate that it would increase the vertical dimension control further
- Depending on the numerical aperture we observe $\approx$ 2x-3x improvement of collection efficiency from NV centres in different configurations experimentally, with our simulations predicting that for objective lenses with NA$>$ 0.77 we can expect 4-6x improvement from the current GaN SIL architecture depending on the emitter depth and diamond crystal orientation
- In simulations we find that an increase of the GaN epilayer thickness to 4 μm would allow GaN micro-lenses to operate nearly on-par with monolithic diamond hemispheres if an objective lens with NA$\approx$ 0.77 is used, leading to 6-7x improvement in photon extraction efficiency
- Depending on the emitter configuration we find 1.2x-3x pump efficiency enhancement provided by the GaN SIL which is probably caused by a combination of increased system NA and mitigated spherical aberration at a planar diamond interface
- A significant amount of photoluminescence is emitted by the GaN SILs with spectral overlap with the NV^- emission characteristic. Further investigations of the strength of the emission at cryogenic temperatures and in dependence of the excitation wavelength are remaining experimental tasks. The emission puts a lower limit to the numerical aperture of the collection optics that can be employed depending on emitter depth. We estimate that an objective with NA$\approx$ 0.77 ($\approx 2\,\mu$m FWHM axial resolution) is sufficient to reject most PL counts from the GaN lenses by the confocal arrangement even for shallow emitters in $< 1\,\mu$m depth below a planar diamond
- GaN SILs can be combined with 1-2 NV emitters without significant deterioration of the photon purity in $g^{(2)}$ autocorrelation measurements and cooling of GaN micro-lens arrays to cryogenic temperatures without detachment or significant change of membrane bow indicates compatibility with typical experimental conditions in quantum computing and networking applications
- Integration of GaN SILs with scanning magnetometry probes proves cumbersome and reasonable alignment is only achieved by adjusting the lens position with an AFM cantilever. Experimentally we find minimal count rate improvement around 1.1x-1.2x, potentially due to a thin layer of optical adhesive on top of the lens distorting the shape. Our simulations predict that the GaN lenses

can increase photon collection up to 2x at NA $\approx$ 0.5 for the current state of the art commercial scanning probes, but the benefits are predicted to diminish if higher NA collection optics are used

All in all we can see the potential for GaN micro-lenses to replace monolithic diamond hemispheres fabricated with focused ion beam milling in the realm of quantum computation and networking with diamond colour centres. For an effective and scalable platform the GaN epilayer thickness might be increased to 4 μm and large scale (4x4-16x16) ROC-matched highly spherical GaN micro-lens membrane arrays could be fabricated and printed onto highly pure single crystalline diamond membranes. The lens array could facilitate writing of diamond colour centres in shallow depth below the diamond surface while being automatically addressed to the lens centre position. Significant remaining challenges are the development of high-quality shallow emitter writing in high purity single crystalline diamond substrates through the GaN SILs, the strain optimization after increase of the epilayer thickness and membrane size increase as well as the development of a 'parallel' confocal microscopy technique, potentially employing an array of pinholes. One might combine transfer printed GaN micro-lenses with the deposition of distributed Bragg mirrors on the lens surface and the diamond membrane backside to create local micro-cavities around each emitter to enhance the emission into the ZPL via the Purcell effect. Such rarge scale cavity-coupled diamond colour centre arrays could open the door towards future quantum computing and networking applications.
The use of GaN micro-lenses in combination with diamond NV scanning magnetometry probes is probably not worth the potential cost due to the significant integration challenge and relatively minor gain in terms of photon collection efficiency in this specific application space.

5 Applications of transfer printed GaN micro-lenses on non-standard substrates

In this last thesis Chapter we are discussing the integration of GaN micro-lenses with nanowire laser devices, photonic waveguides and optical fibres. We will see that GaN micro-lenses will not deliver significant optical benefit for the investigated systems, but the results show how versatile the transfer printing method can be applied to assemble micro-optical systems in non-standard geometries. As usual, we compare experimental results to FDTD simulations to gain insight into potential benefits delivered by the GaN lenses.
This Chapter is a result of collaborative work, with printing and optical characterization of nanowire lasers performed by Dimitars Jevtics, photonic integrated circuits provided by Jack Smith (IOP), Michael Strain (IOP) and 'Octave Photonics' and an optical fibre facet cleaved by Craig Hunter (Fraunhofer CAP).

5.1 3D integration with nanowire laser

Initially we will discuss printing of GaN micro-lenses on top of nanowire lasers to collect emitted photons more effectively from above. The lenses are assembled on photoresist frames leaving an air-gap between lasers and lenses while maintaining micrometer-precise placement accuracy which has not been demonstrated before. Some of the shown results are published in [293] and presented at the 'Rank Prize Symposium for Nanowire Photonics 2022'.

5.1.1 Review: Nanowire lasers

Nanowires generally refer to structures with cross sectional dimensions $< 500\,\text{nm}$ but are potentially several μm-mm long leading to a high aspect ratio [294, 295]. Similar to quantum dots which are confined in all three spatial dimensions to the nm-scale, the dimensions of the wire can strongly influence its physical properties such as the band gap in the case of semiconductors [294, 295]. Fig. 5.1 shows several examples of semiconductor nanowires which today can be grown in many material platforms in a bottom-up manner [294, 295]. The plots in e) and f) show how tuning the composition of the wires affects the crystal structure and photoluminescence emission wavelength of such devices.

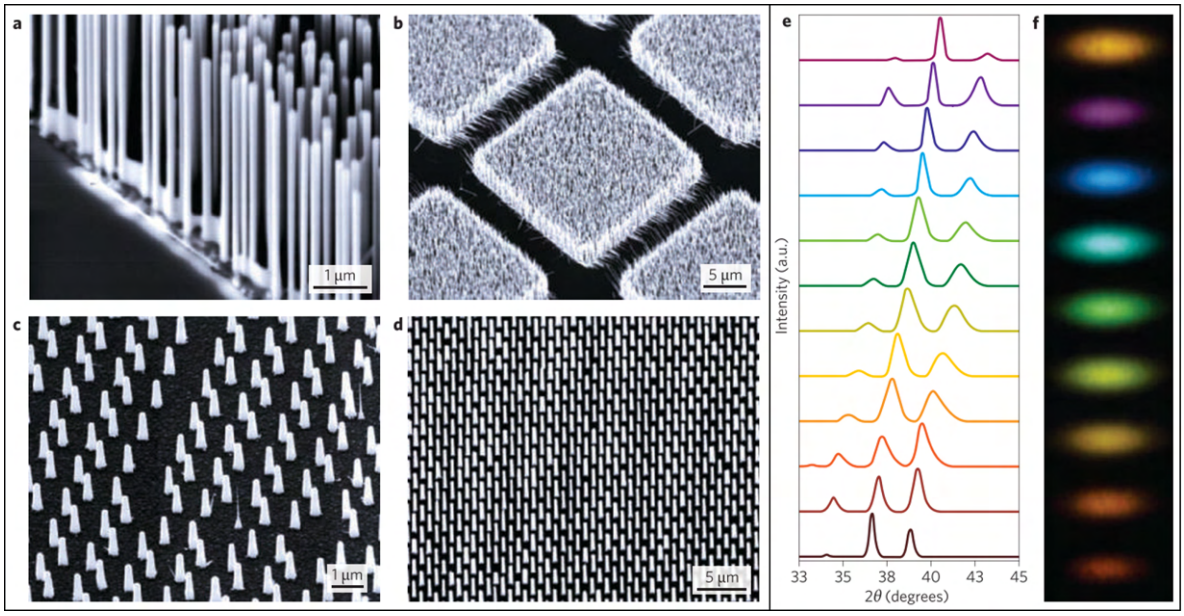

Figure 5.1: SEM images of semiconductor nanowires on their growth substrate, a) ZnO, b) GaN, c) InP, d) InP/INAs/InP, e)/f) X-ray diffraction and visual photoluminescence emission from InGaN nanowires with tuned In concentration, adapted from [294].

We are specifically interested in nanowire lasers [295–300], which are to date mostly optically pumped semiconductor nanowires which achieve lasing due to the high reflectivity of their end facets in combination with effective waveguiding along the wire which is facilitated by their high refractive index and sub-wavelength cross section [295]. We will use optically pumped InP nanowire lasers for our demonstration which can be grown by selective area MOCVD with very high crystalline quality in the Wurtzite phase [301], compare Fig. 5.2 for TEM images of such a wire.

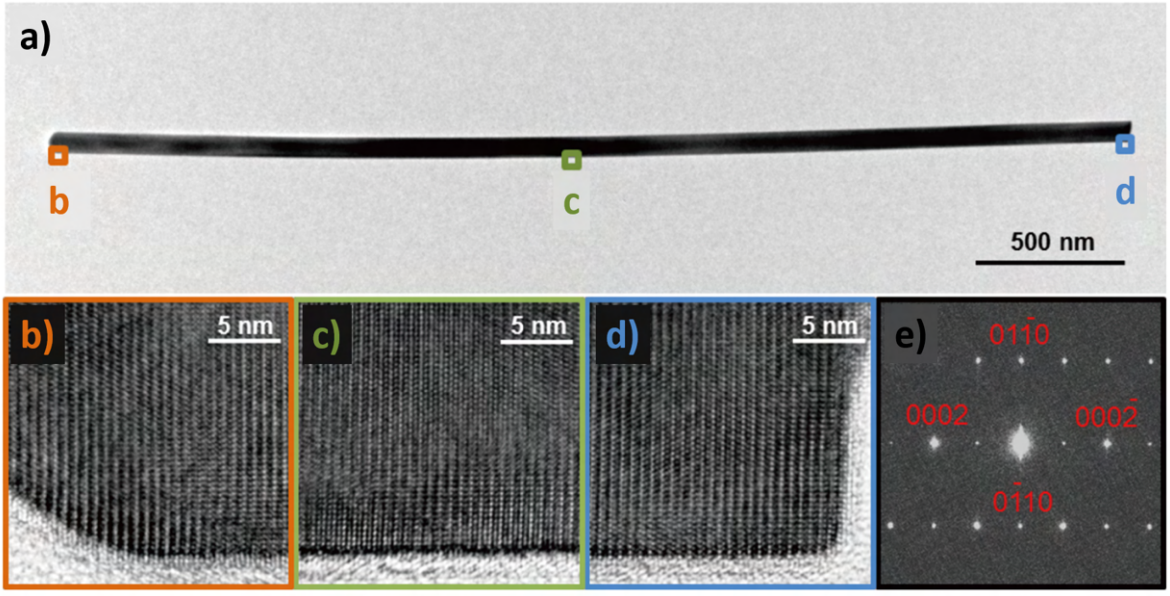

Figure 5.2: a) TEM image of single crystalline InP nanowire grown by selective area MOCVD growth, b)-d) high resolution TEM images of the nanowire shown above revealing high quality Wurtzite crystal structure and an atomically smooth surface, e) electron diffraction pattern confirming the high crystalline quality, adapted from [301].

In previous work [302–305] the selective integration of lasing nanowires with photonic structures such as

polymer waveguides [303] and cat's eye antennas [304] has been demonstrated using optimized PDMS based transfer printing. The general procedure is indicated in Fig. 5.3: High quality InP nanowires are removed from their growth substrate and scattered on an intermediate surface for photoluminescence characterization. Lasing devices are selected and can then be printed to targeted locations.
A typical challenge for effective pumping and light extraction from nanowire lasers is that they are mostly placed in a horizontal geometry with emitted photons diffracting upwards from both end facets under laser excitation, leading to reduced directionality of the emitted photons compared to conventional laser systems [294]. For integrated photonic applications the typical horizontal arrangement of wires on a substrate is desirable [303], but vertical light coupling into microscope objective is needed in most experimental test settings. Effective vertical coupling has already been demonstrated using a cat's eye antenna and we are not aiming to improve this excellent result, shown in Fig. 5.3 b). Instead we will use transfer printed InP nanowire lasers as a test field for accurate assembly of micro-optical elements in three dimensions with micrometer-precise accuracy.

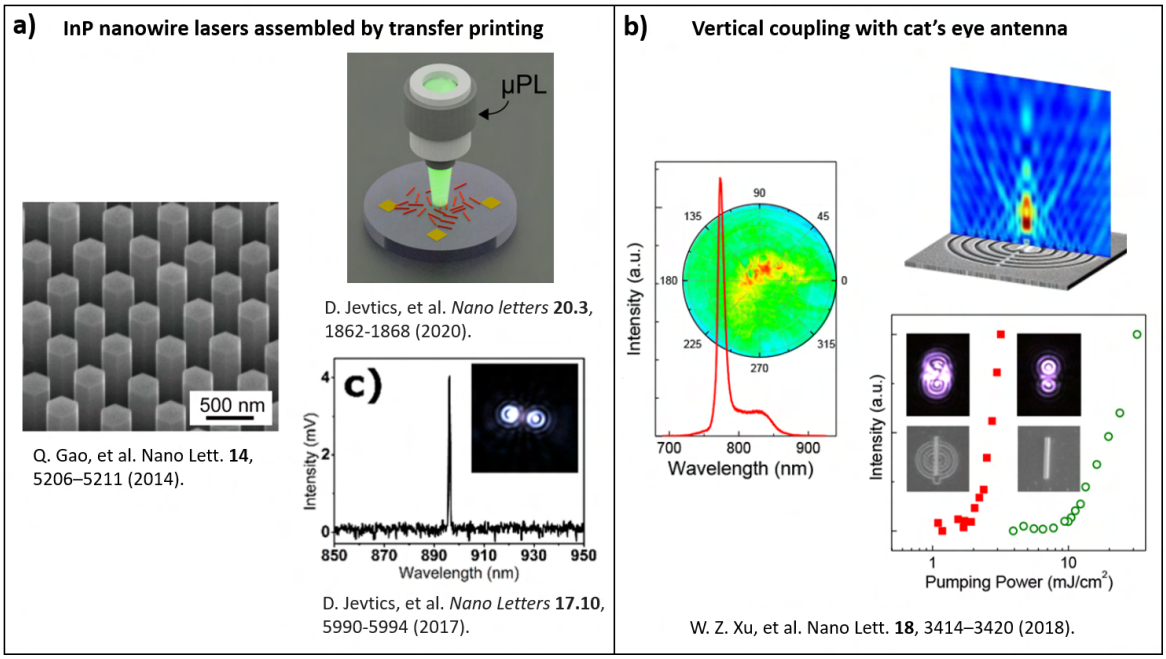

Figure 5.3: a) SEM image of hexagonal InP nanowires on their growth substrate [301] and a schematic showing the PL characterization of nanowires that are 'broken off' their growth substrate [305]. Lasing devices can then be selected and placed at targeted positions on a receiver substrate using PDMS based transfer printing, the bottom image shows a typical lasing spectrum of a laying nanowire on a silica substrate [303], b) lasing spectrum and measured far field intensity distribution (left) for a InP nanowire coupled to a cat's eye antenna with a simulation of the near field above the antenna (top right). Reduced lasing threshold is demonstrated after integration with the antenna (bottom right), adapted from [304].

5.1.2 Outline of the work

A render of the targeted geometry is shown in Fig. 5.4 with the centre of a GaN micro-lens laterally aligned to the end facet of an InP nanowire laser below. This challenging printing geometry with minimal surface contact between micro-lens and photoresist frames is used to test the boundaries of high accuracy transfer printing.

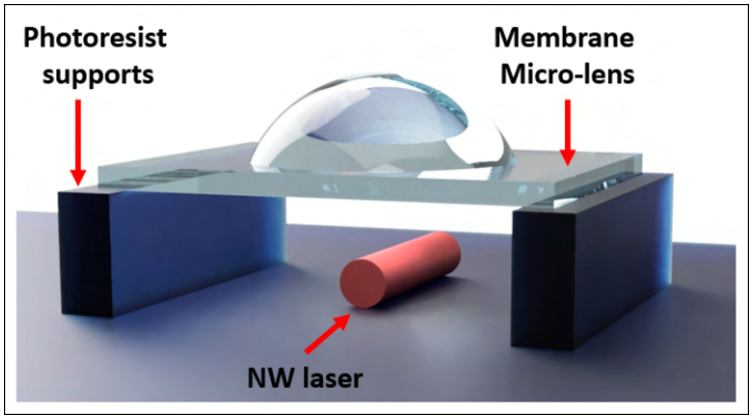

Figure 5.4: 3D illustration of the device geometry in this subsection. A nanowire laser is transfer printed between photoresist ridges, followed by the integration of a GaN micro-lens to enhance upwards collection from the nanowire end-facet under top illumination and collection, adapted from [293].

Following the process flow in Fig. 5.5 nanowire lasers are removed from their growth substrate to an intermediate carrier and then printed between photoresist frames fabricated on a glass substrate. Afterwards the micro-lens is assembled above with its centre aligned to one end facet of the wire. We use GaN micro-lens devices with significant membrane bow generated by 3 μm etch depth as indicated in the schematic. We use these devices because the lenses have both a large aperture to potentially collect a wide angular spread of emitted photons from the wire facet while maintaining low ROC and therefore micron-scale focal length to achieve a dense vertical integration.

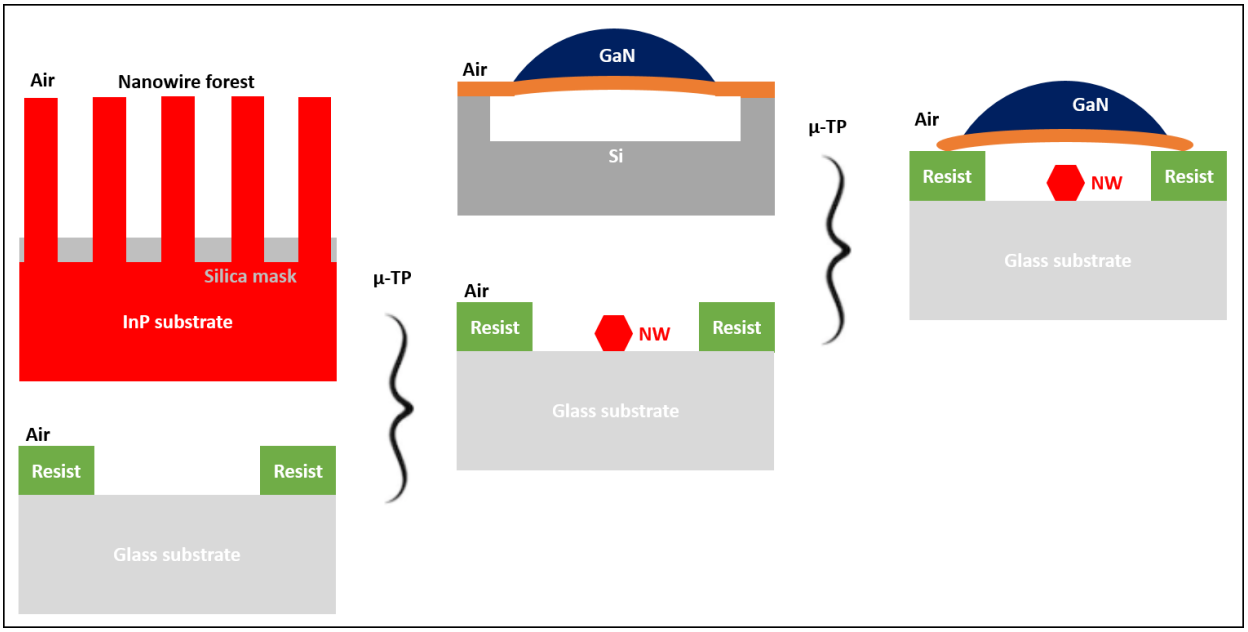

Figure 5.5: Schematics of the process flow. InP nanowires (ca. 10 μm length and 260 nm diameter) are removed from their host substrate and transferred to an intermediate PDMS substrate. Promising devices are selected, repicked and printed between photoresist ridges (Shipley S1818) prefabricated on a borosilicate cover glass substrate. The printing is performed by Dimitars Jevtics and the photoresist frames are fabricated by Zhongyi Xia. Finally bowed GaN micro-lenses with up to 3 μm height are picked from their growth substrate and aligned to the end facets of the laterally placed nanowire lasers. The GaN lens devices used in this section have been shown previously in Fig. 3.25 to 3.27.

5.1.3 Simulation results

We simulate the focal length in air below free-standing GaN micro-lenses with 3 μm etch depth, with the results depicted in Fig. 5.6. The simulations are based on the measured AFM line profiles of typical devices in two size categories with around 12 μm and 9 μm diameter. With a plane wave injected at the nanowire emission wavelength from above we find very short focal length below the lens device ranging between 1-3 μm. We use a fixed photoresist height of 1.7 μm and by comparison with the FDTD simulations we can anticipate that the two lens sizes will cause slightly different optical effects, which are schematically drawn in Fig. 5.6 c).

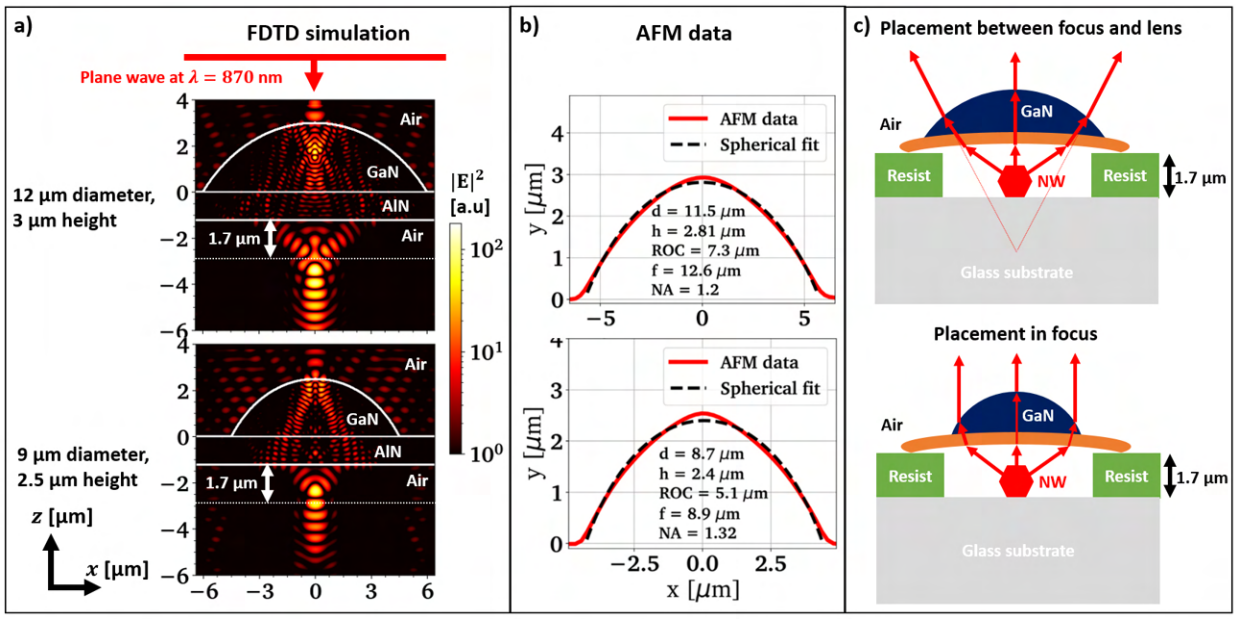

Figure 5.6: a) Cross sections through FDTD simulations run at $\lambda = 870$ nm wavelength with a plane wave source propagating downwards through suspended GaN micro-lenses (two selected sizes) from the top. The constant photoresist height of 1.7 μm is included to reference the focus position, b) AFM line scans of representative micro-lens devices of the two selected size categories (NSC15), focal length f and NA given in these graphs assume monolithic integration with diamond for comparison, c) schematics illustrating potential ray paths of emitted nanowire laser light based on the FDTD simulations and the chosen resist height.

5.1.4 Experimental results

In a first test we print GaN lenses from these two size categories on top of InP nanowires that are fully embedded into SU8 photoresist, see Fig. 5.7. We find that we can align well to the nanowire end-facet using the optical microscope column of the transfer print tool. Additionally we observe that we can close the air-gap between the bowed GaN membrane devices and photoresist by reflow, which might be useful in future micro-systems development in the packaging stage.

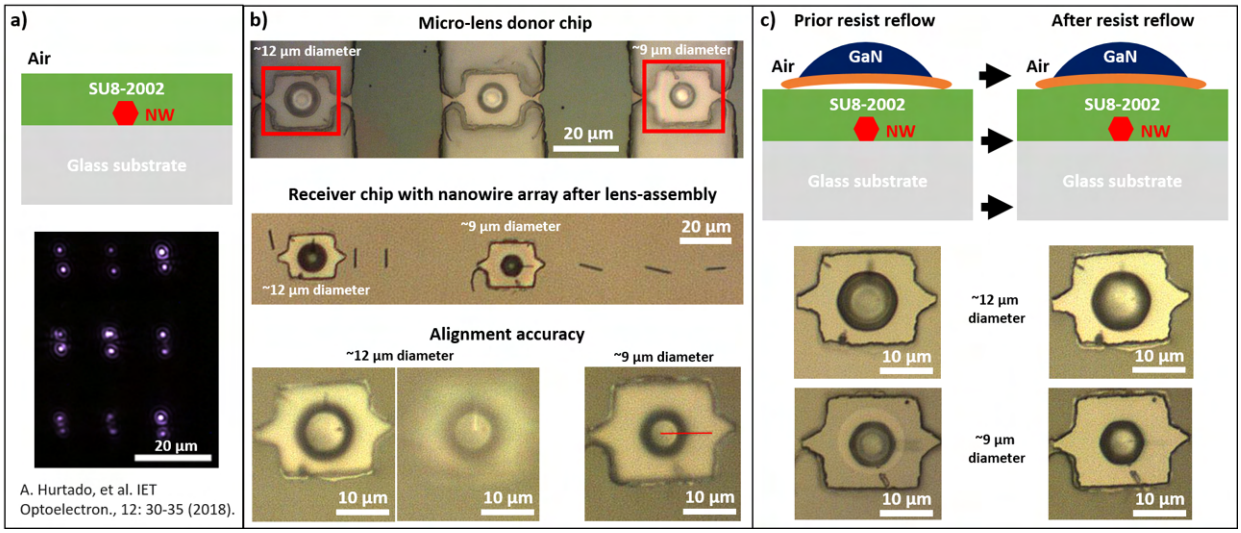

Figure 5.7: First test run with unpatterned photoresist (SU8-2002) that is spun on the substrate after InP nanowires are printed on a borosilicate cover glass substrate. The nanowire printing and resist spinning is performed by George Ivens. a) Schematic showing the nanowires embedded into the photoresist and a widefield PL image showing the characteristic emission from the end facets of these optically pumped nanowire devices emitting around 870 nm wavelength, b) microscope images showing the assembly process with the bottom images taken after thermal resist reflow, which (c) allows to close the air gap between micro-lens and photoresist. Nominal diameters of the respective micro-lenses are given.

We now move to the process flow indicated in Fig. 5.5. After printing the nanowire laser between resist frames we confirm optical emission and lasing from the nanowire using a defocused pulsed excitation laser in a wide field PL setup relatively similar to our home-built confocal setup but directly mapping the PL emission onto the CCD camera without the use of a pinhole. A typical result is presented in Fig. 5.8 with diffraction limited upwards emission from the nanowire facets visible as Airy rings in b). The fact that we mainly see emission from the end facets rather than photoluminescence emission from the full wire indicates effective waveguiding within the wire. We further confirm lasing operation by threshold and spectral measurements, see Fig. 5.14.

With an closed-loop nm-precise sample stage we are able to record the z-position at which the objective focal spot overlaps with the nanowire facet by applying a simple Gauss fitting procedure to approximate the main lobe of the Airy disk pattern, see Fig. 5.8 c). We evaluate the position of maximum photon count rate by integrating the 1D Gaussian' fit function at different z-positions.

After the PL characterization of the printed nanowire laser we assemble micro-lenses from both size categories above, the printing results are displayed in Fig. 5.9. An overlay of the images before and after printing allows us to roughly assess the placement accuracy which we estimate to around $\pm 1\,\mu$m even without the use of any dedicated marker structures and despite the reduced surface contact to the receiver chip. Release is achieved by the shear-contact technique described in Chapter 3.

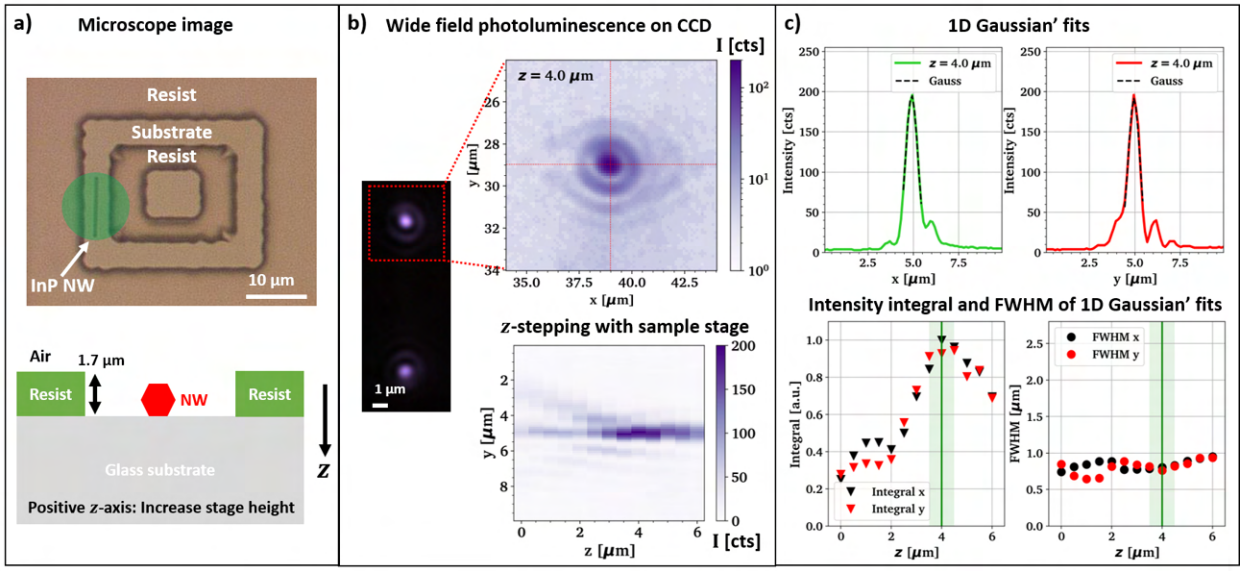

Figure 5.8: Photoluminescence characterisation after nanowire printing. The measurements are performed by Dimitars Jevtics with a widefield micro-PL setup (objective NA= 0.75) using a frequency doubled pulsed solid state laser source (532 nm, 0.5 ns pulse length, 7 kHz repetition rate). a) Microscope image of the printed nanowire laser within the resist pattern and schematic showing the geometry and choice of z-axis. The pump laser is defocused to around 10 μm spot size, as indicated by the green disk, b) wide field IR photoluminescence response from the nanowire laser shown on the left. A series of images at different z-positions is taken with the closed loop stage, c) the main lobe of the diffraction limited emission from the nanowire facet is fitted with a Gaussian line shape, which allows us to extract the focus position by comparing both the integrated intensity in the main lobe (area of the Gauss) and its FWHM.

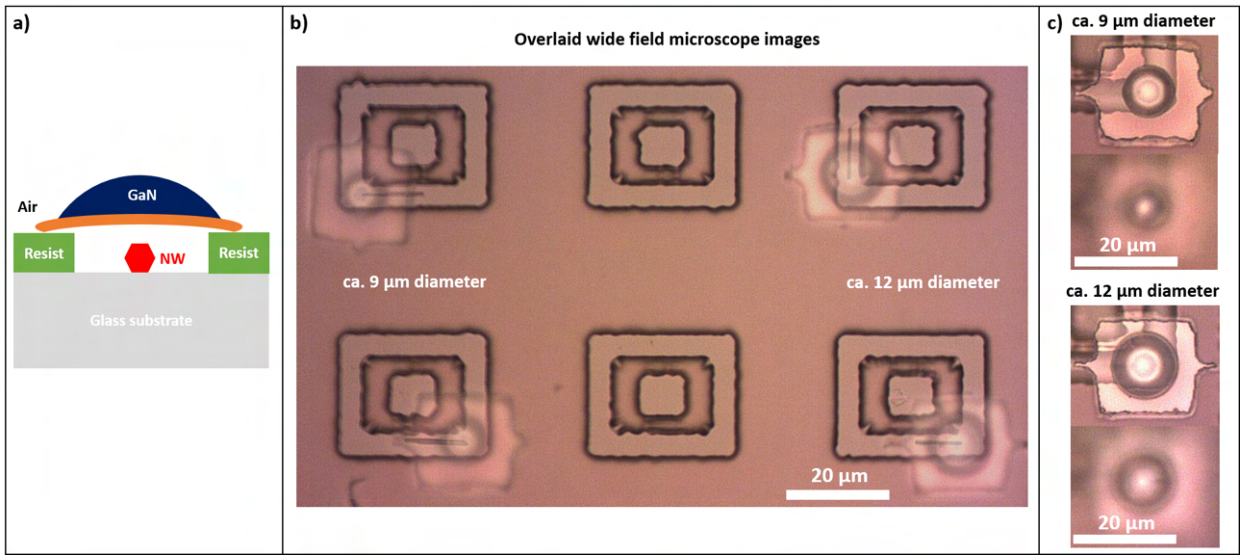

Figure 5.9: After micro-lens assembly process. a) Schematic of the geometry, b) four micro-lenses in two size categories integrated with four different nanowire lasers on a small foot print, the microscope images before and after printing are overlayed to visualize the alignment accuracy, c) images of two micro-lenses after printing at different focus positions.

We repeat the photoluminescence characterization after lens integration. A before-to-after comparison is not straight forward because we can expect that the lens changes the pumping characteristic. Fortunately the nanowires have sufficient length so that one facet is not covered by the lens. Still the facet is covered by the AlGaN/AlN membrane which can be expected to induce additional reflection losses. We again use

a defocused pump hoping that thus the excitation conditions of the nanowire vary slowly with changes in sample height.

The results of the repeated PL analysis for a lens with ca. 12 μm diameter are shown in Fig. 5.10. Following our expectation the nanowire facet below the lens appears 5 μm lower (larger z) than the facet without micro-optical element. Our analysis in Fig. 5.11 shows that the FWHM of the Airy disk main lobe is enlarged from around 0.8 μm to 1.6 μm at the position of maximum photon counts due to a magnification effect provided by the lens.

We can see in Fig. 5.11 b) and c) that the amount of collected photons is significantly increased (around 2x) for the nanowire facet with micro-lens. This is most probably due to reduced angular spread caused by the refractive power of the lens. On a system level the comparison is somewhat unfair, because we introduce unnecessary Fresnel reflection losses of up to 30% to the facet which is not covered by the lens but the membrane alone. If we discount for these losses the improvement reduces to around 25%.

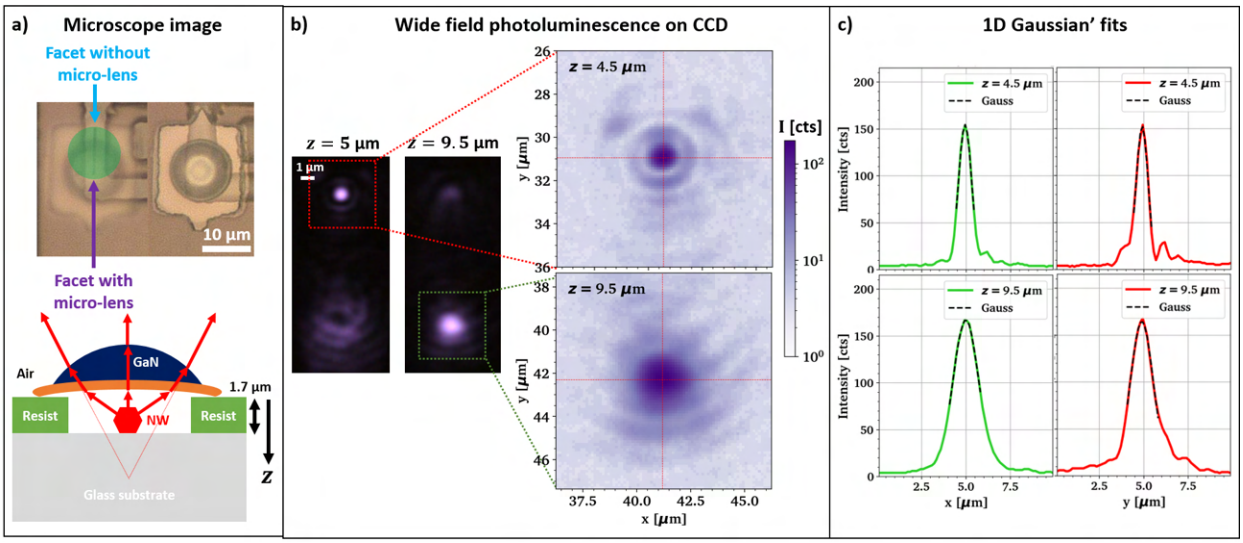

Figure 5.10: Photoluminescence recharacterisation after micro-lens printing ($d = 12\,\mu$m nominal diameter). The measurements are performed by Dimitars Jevtics with a widefield micro-PL setup (objective NA= 0.75) using a frequency doubled pulsed solid state laser source (532 nm, 0.5 ns pulse length, 7 kHz repetition rate). a) Microscope image of the printed nanowire laser and lens, with the schematic showing the geometry and choice of z-axis. The pump laser is defocused to around 10 μm spot size, as indicated by the green disk. As can be seen, one facet of the nanowire is covered by the micro-lens while the other is covered by the AlGaN/AlN membrane, b) wide field IR photoluminescence response from the nanowire laser shown on the left. A series of images at different z-positions is taken with the closed-loop piezo stage, c) line scans from the PL images shown on the left, the main lobe of the diffraction limited emission from the nanowire facet is fitted with a Gaussian line shape which allows us to extract the focus position by comparing both the integrated intensity in the main lobe (area of the Gauss) and its FWHM.

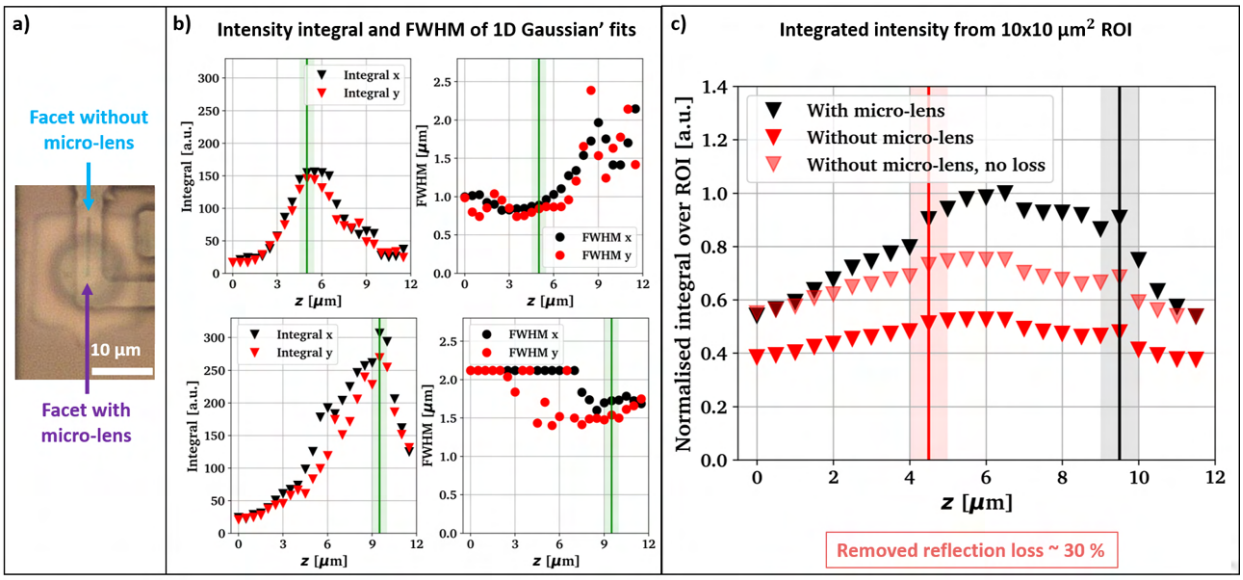

Figure 5.11: Summary of the analysis of the PL measurements shown in Fig. 5.10. a) Microscope image marking the two facets with b) the corresponding integrated intensity of the Gaussian fit and the extracted FWHM of the main lobe from 1D line scans through the 2D PL images, the potential focus positions are marked, c) comparison of the normalized intensity integral over a 10x10 μm^2 region around the respective nanowire facet. The result for the nanowire facet without micro-lens is corrected by the expected Fresnel reflection losses caused by the air-AlN and AlGaN-air interfaces (thickness not considered).

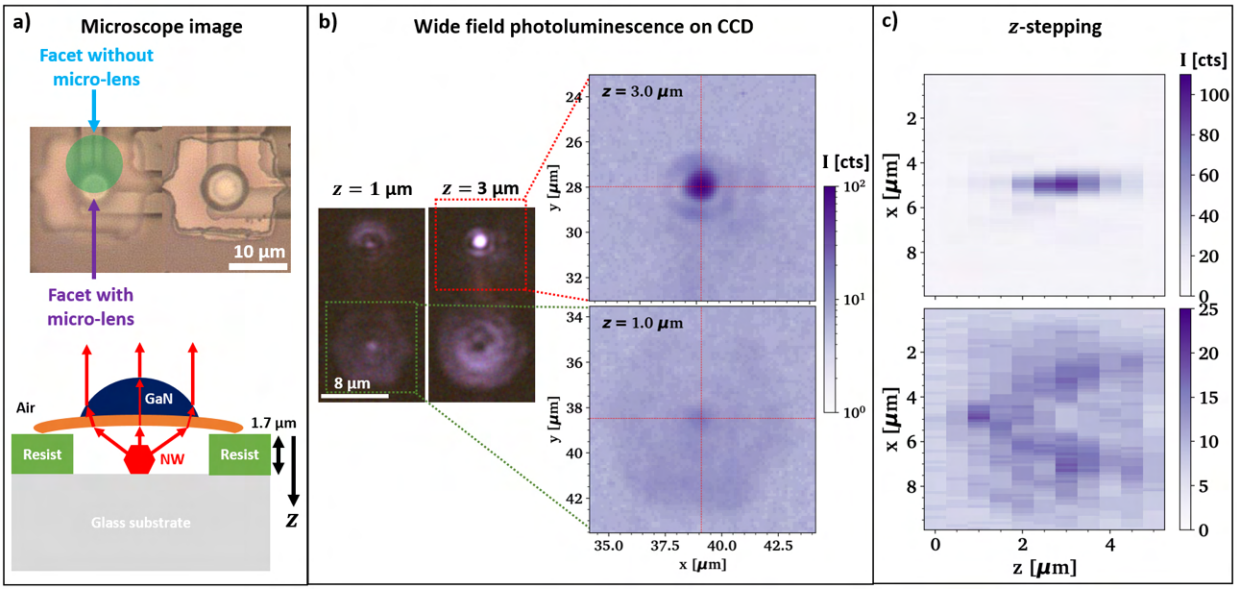

Figure 5.12: Photoluminescence recharacterisation after micro-lens printing ($d = 9\,\mu$m nominal diameter). The measurements are performed by Dimitars Jevtics with a widefield micro-PL setup (objective NA= 0.75) using a frequency doubled pulsed solid state laser source (532 nm, 0.5 ns pulse length, 7 kHz repetition rate). a) Microscope image of the printed nanowire laser and lens, with the schematic showing the geometry and choice of z-axis. The pump laser is defocused to around 10 μm spot size, as indicated by the green disk. As can be seen, one facet of the nanowire is covered by the micro-lens while the other is covered by the AlGaN/AlN membrane, b) wide field IR photoluminescence response from the nanowire laser shown on the left. A series of images at different z-positions is taken with the closed-loop piezo stage, c) stitched xz scans showing the axial characteristic of the PL response.

From the smaller micro-lenses with reduced radius of curvature and focal length we expect that the lens roughly collimates the upwards emitted photons into a narrow cone. The experimental results are displayed in Fig. 5.12 and seem to confirm this effect even though strong interference caused by the narrow emission wavelength (see Fig. 5.14 b)) reduces the visibility. Still we are able to observe nanowire lasing emission across the full aperture of the micro-lens over a z-range of ca. 4 μm and find that hexagonal lens faceting affects the emission shape.

The detailed data analysis is summarized in Fig. 5.13. We observe no clear photon collection maximum for the facet below the micro-lens and find that after discounting for Fresnel reflection losses the lens seems to reduce the amount of collected photons, compare with the plot in c). This might be explained by the reduced lens aperture in this configuration that covers less angular space above the facet. The acceptance angle of the objective used in the experiment (NA = 0.75) is around 49° and we can estimate that the lens covers an emission cone with 56° half angle above the device which should result in a significant improvement, but reflection losses and potentially lens aberrations seem to outweigh the effect.

Finally we confirm that the micro-lens addition does not affect the lasing performance of the wire with a before and after comparison of lasing threshold and spectrum. We find neglibile differences that might be caused by slight differences in the optical excitation of the wires due to the addition of the lens, see Fig. 5.14.

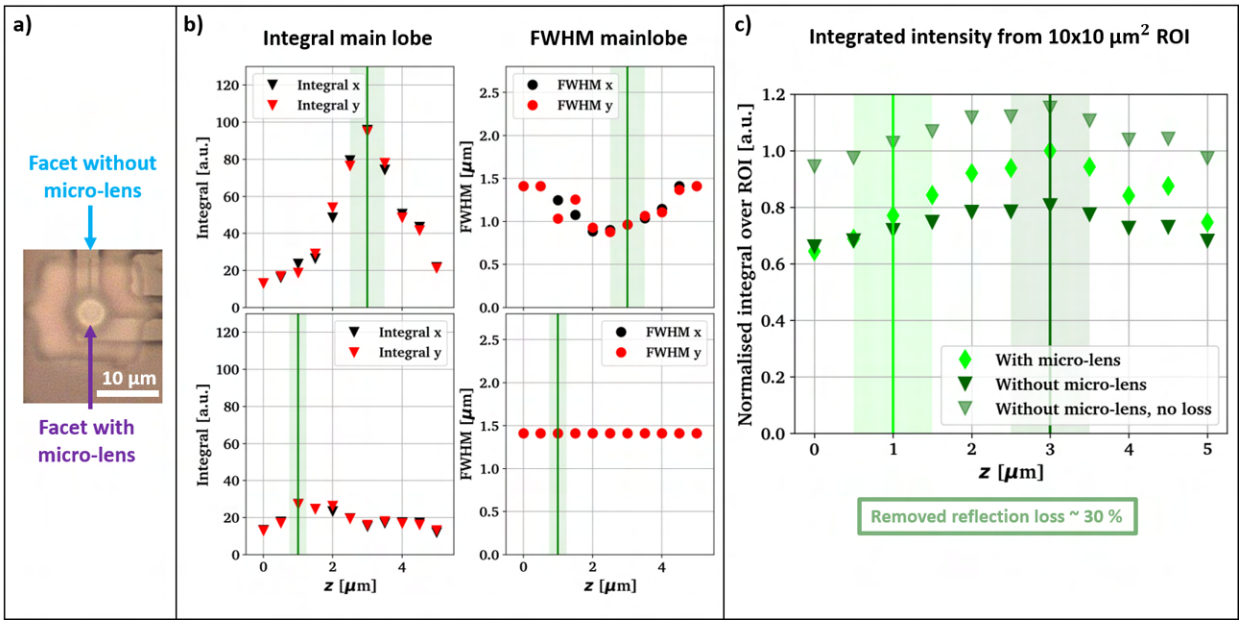

Figure 5.13: Summary of the analysis of the PL measurements displayed in Fig. 5.12. a) Microscope image marking the two facets with b) the corresponding integrated intensity of the Gaussian fit and the extracted FWHM of the main lobe from 1D line scans through the 2D PL images, the potential focus positions are marked. The FWHM is fixed for the facet with micro-lens to allow fitting of the main lobe only, c) comparison of the normalized intensity integral over a 10x10 μm^2 region around the respective nanowire facet. The result for the nanowire facet without micro-lens is corrected by the expected Fresnel reflection losses caused by the air-AlN and AlGaN-air interfaces (thickness not considered).

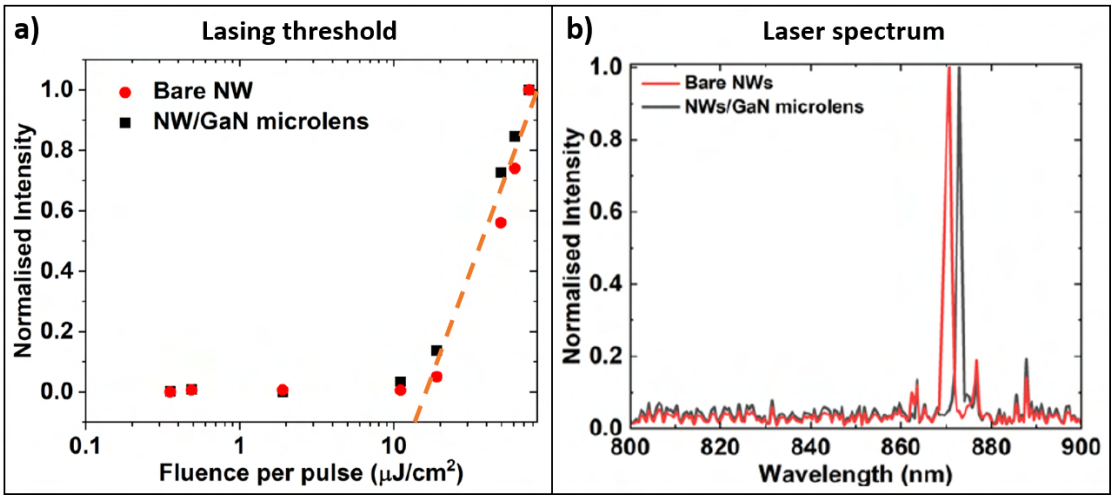

Figure 5.14: Performance analysis of the nanowire lasers carried out by Dimitars Jevtics (plots are similarly adapted from him) with the described wide field PL setup. a) Lasing threshold before and after lens integration using a micro-lens with $d = 12\,\mu$m nominal diameter, b) nanowire laser spectrum before and after lens integration collected with a fibre coupled spectrometer (Avantes, up to 0.14 nm spectral resolution).

5.1.5 Summary

In short we have seen that GaN micro-lenses can be assembled into an unconventional 3D architecture while maintaining micro-meter precise placement even without the use of dedicated marker structures. We find that lenses with ca. $12\,\mu$m diameter can increase the photon collection rate into a moderate NA air objective (NA$= 0.75$) by roughly 25%, while a smaller lens with ca. $9\,\mu$m diameter seems to collimate the light from the nanowire facet in reasonable agreement with FDTD simulations.
All in all this demonstration might inspire future heterogeneous micro-optic assembly schemes.

5.2 Fibre to integrated waveguide coupling

We have seen in the introduction that photonic integrated circuits (PICs) are an immensely interesting research field concerning itself with the development of cheap, low-power and reliable miniaturized photonic device for a wide range of applications. Light coupling with PICs is still a significant packaging problem affecting chip performance. In this section we will quickly review stat-of-the-art PIC coupling schemes and then investigate whether the developed additive GaN micro-lenses can be beneficial for this particular application by assessing both simulations, performing test prints and transmission experiments through simple PICs.
The photonic integrated circuits used in this section are provided by Jack Smith, Michael Strain and 'Octave Photonics'.

5.2.1 Review: Fibre-to-PIC light coupler

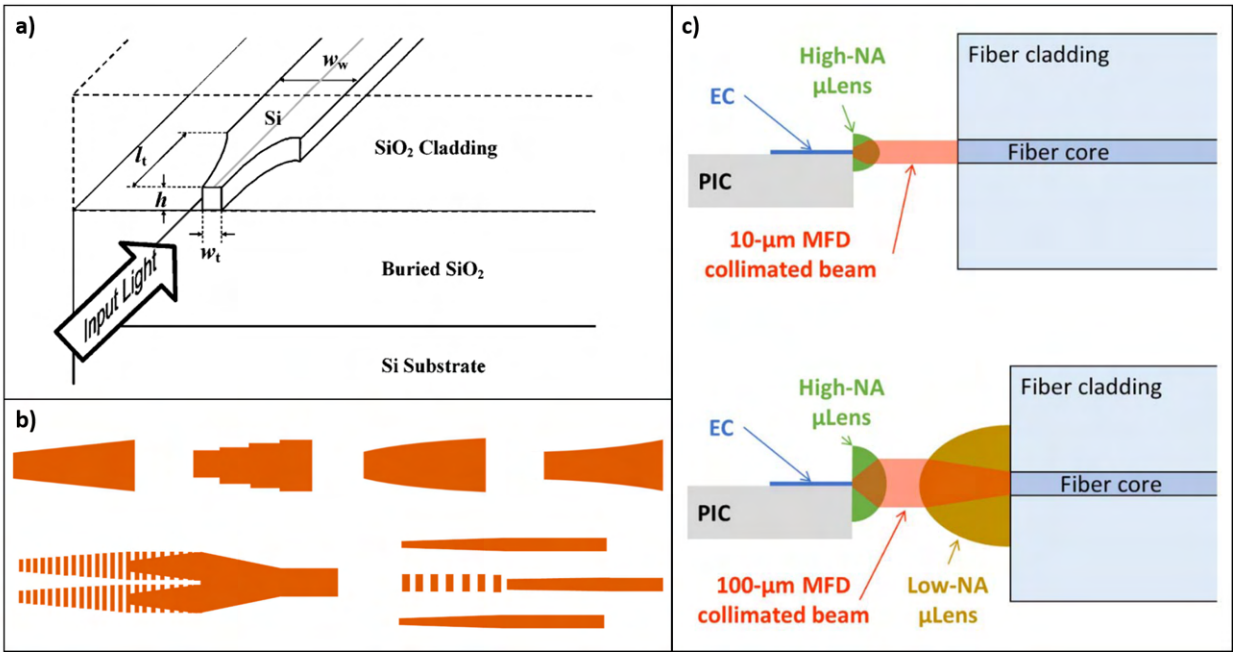

Figure 5.15: a) Initially proposed design of a nanotaper at the edge of a photonic integrated waveguide that allows extension of the mode field diameter by adiabatically squeezing the waveguided mode into the SiO_2 cladding, adapted from [306], b) typical taper designs employed in literature with multi-sub-wavelength tapers leading to reduced coupler foot-print, adapted from [307], c) schematics proposing how micro-optical elements could support light coupling between PIC and fibre, adapted from [104].

The fundamental problem of fibre-to-chip coupling in the field of integrated photonics is the difference in mode field diameter between single mode fibres (ca. 3-10 μm) and single mode semiconductor waveguides (ca. 0.2-0.5 μm) [104, 306, 307]. In-plane or out-of-plane coupling schemes can be employed affecting the wider chip integration strategy [104, 307]. In-plane couplers, also referred to as edge couplers (EC), end-fire couplers or butt-couplers, can effectively solve the mode field mismatch by employing inverse taper geometries in one or multiple layers close to the waveguide edge [307], compare Fig. 5.15 a) and b). The tapered waveguide allows the waveguide mode to slowly expand into the lower-index cladding leading to coupling losses on the order of 0.2-2 dB, depending on the coupler

geometry [307].

Generally coupling loss, footprint, bandwidth as well as fabrication and alignment tolerance are important factors when deciding which specific coupler to use when targeting a specific application [307]. For example difference in thermal expansion coefficients or mechanical vibrations might affect a highly efficient coupler if it has sub-to-few micron level alignment tolerance. As proposed in Fig. 5.15 c), micro-lenses could assist optimized edge couplers to increase alignment tolerances which might allow to use standard manufacturing techniques when packaging PICs [104, 308].

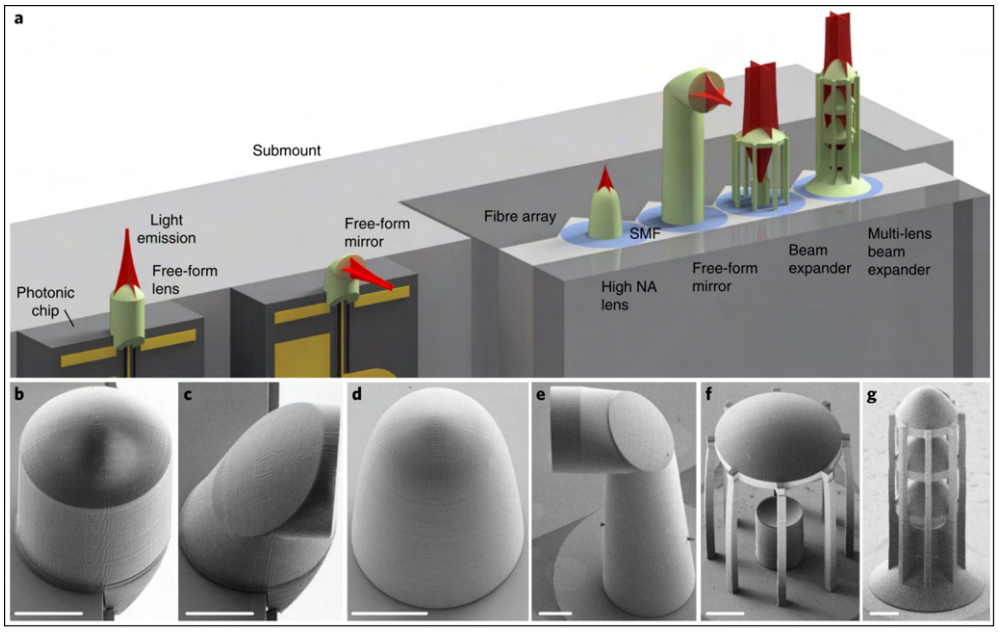

Figure 5.16: a) Schematics showing edge-coupled 3D printed optical elements using two photon polymerization on fibre and chip facets, b)-g) SEM images of fabricated devices with 20 μm scale bars, adapted from [133].

Impressive examples of 3D printed optical elements on waveguide and fibre facets [133] and direct polymer interconnects called photonic wire bonds [310, 311] have been demonstrated using two-photon polymerization (TPP), see also Fig. 5.16. In [110] free space polymer-to-polymer lenses facilitated fibre-to-chip coupling with 0.8 dB loss and a 1 dB lateral alignment tolerance of ca. 10 μm which is a very promising result. TPP based 3D printing also allow the fabrication of broadband vertical couplers for both IR and VIS wavelength [309, 312, 313], compare Fig. 5.17.

As already discussed TPP resins suffer from much lower refractive index than typical semiconductor materials. In this section we therefore investigate whether high-index high-NA GaN micro-optics could facilitate efficient fibre-to-chip coupling. Additionally semiconductor lens couplers might provide higher damage threshold than polymer lenses which are reported to break down at sufficient field strength [110]. This might be specifically interesting for non-linear applications which we will be discussing in the context of TaO PICs.

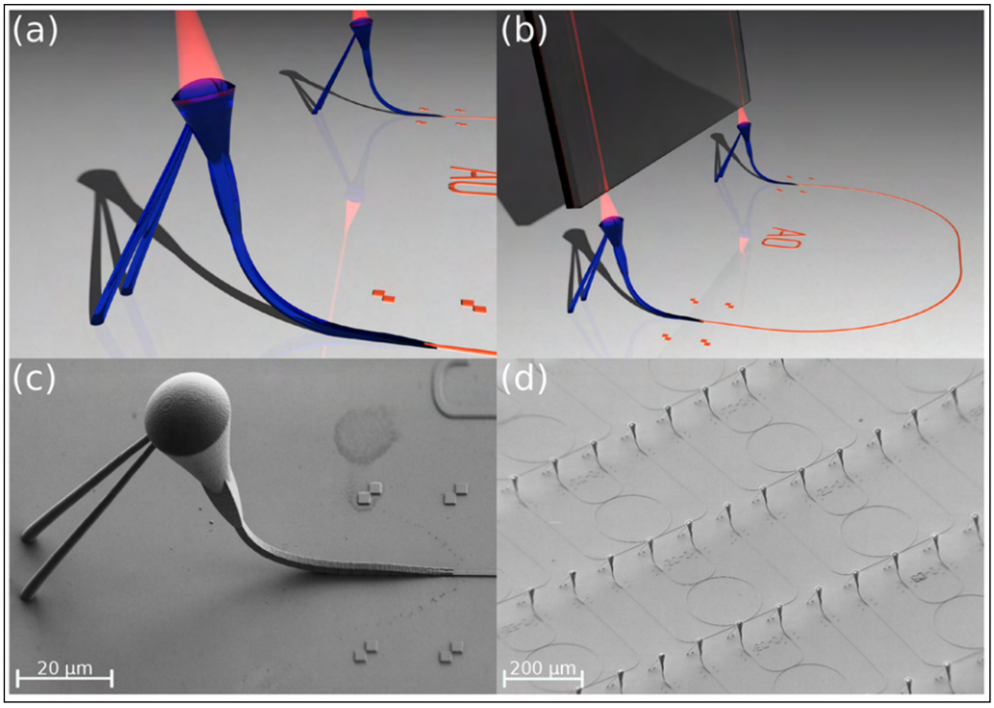

Figure 5.17: Low-loss vertical coupler featuring a combination of 3D printed micro-lens and polymer waveguide tapering, leading to ca. -1.7 dB insertion loss over the full C-band, adapted from [309].

5.2.2 Outline of the work

In the following we will demonstrate transfer printing of nearly hemispherical GaN micro-lenses onto the edges of cleaved GaN-on-sapphire, Si-on-insulator and RIE etched TaO-on-insulator photonic chips, while aligning the micro-lens centre to waveguides and an inverse taper. The printing geometry is shown in Fig. 5.18 a) and the setup used to evaluate the transmission performance is drawn schematically in c). We will use FDTD simulations to assess potential coupling improvement and increased alignment tolerance to external optical fibres. We start with considering two test geometries with simple GaN and Si waveguides without any edge coupler geometries and then combine a GaN micro-lens with a TaO inverse taper.

We will find that printing with sufficient accuracy is possible on all three unoptimized device edges, while the optical experiments will not show enhanced coupling to a polarization maintaining fibre at IR wavelength. In simulations we find that the combination of an inverse taper with the GaN micro-lenses is not expected to yield immediate benefit without redesigning the photonic chip.

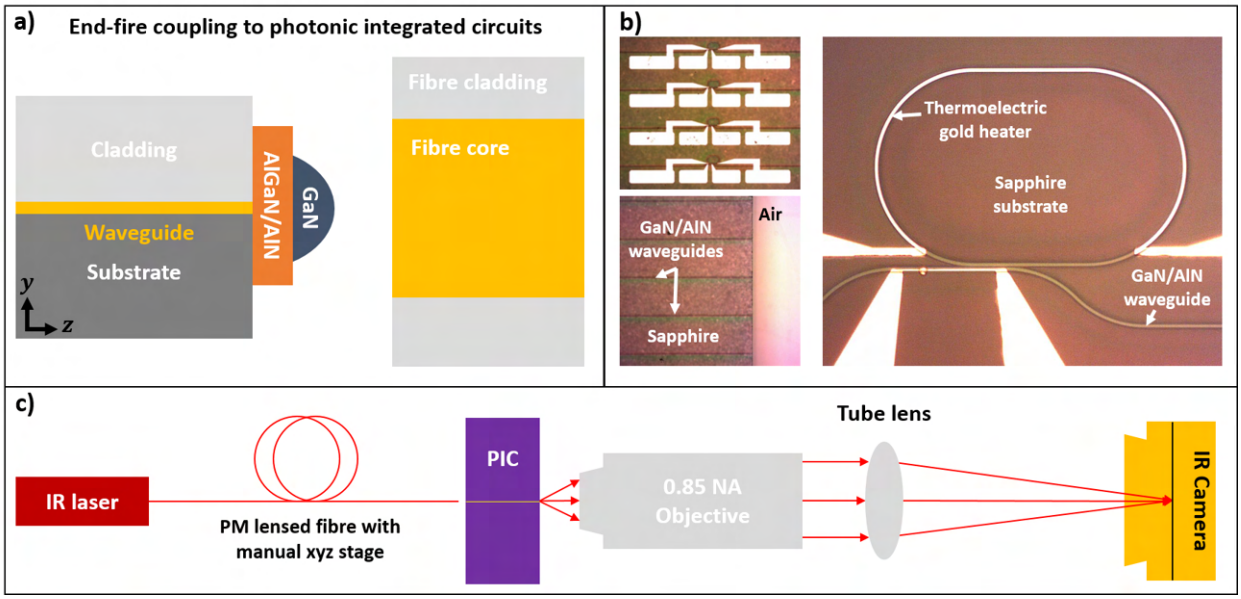

Figure 5.18: a) Schematic of the proposed geometry: A GaN micro-lens is printed on the end-fire facet of an integrated waveguide to mitigate coupling to an external optical fibre, b) microscope images of a GaN on sapphire test chip used in the first set of experiments, here shown to illustrate the concept of photonic integrated circuits with racetrack resonators and thermal heaters for varying the transmission wavelength of the resonators (designed by Jack Smith and fabricated in the James Watt nanofabrication centre), c) schematic of a simple fibre transmission setup used to investigate the fibre to PIC coupling using a tuneable IR laser (Agilent B164B, B1640A) in the C-band that is coupled to the device of interest (PIC) via a polarisation maintaining lensed fibre. The transmitted light is then collected with an objective lens (NA= 0.85) and focused on an IR camera (Xentics XS-1.7-320).

5.2.3 GaN-on-Sapphire test PIC

To show the compatibility of the free-standing micro-lens transfer with photonic waveguide edges, we integrated a high-aspect ratio micro-lens onto the polished facet of a straight waveguide on a GaN-on-sapphire PIC with a 600 nm thin SiO_2 upper-cladding layer, see Fig. 5.18 b) for a top view of this chip. The GaN/AlN waveguides have a total thickness of 1.2 μm, with 850 nm GaN on top of a 350 nm AlN nucleation layer. The waveguide width is 2 μm at the facet, but is tapered down to 1 μm on the chip. See Fig. 5.19 for the corresponding FDTD simulations which predict that the micro-lens might support coupling to optical fibres with NA < 0.5, but we only see moderate enlargement of the mode field diameter in the near field.

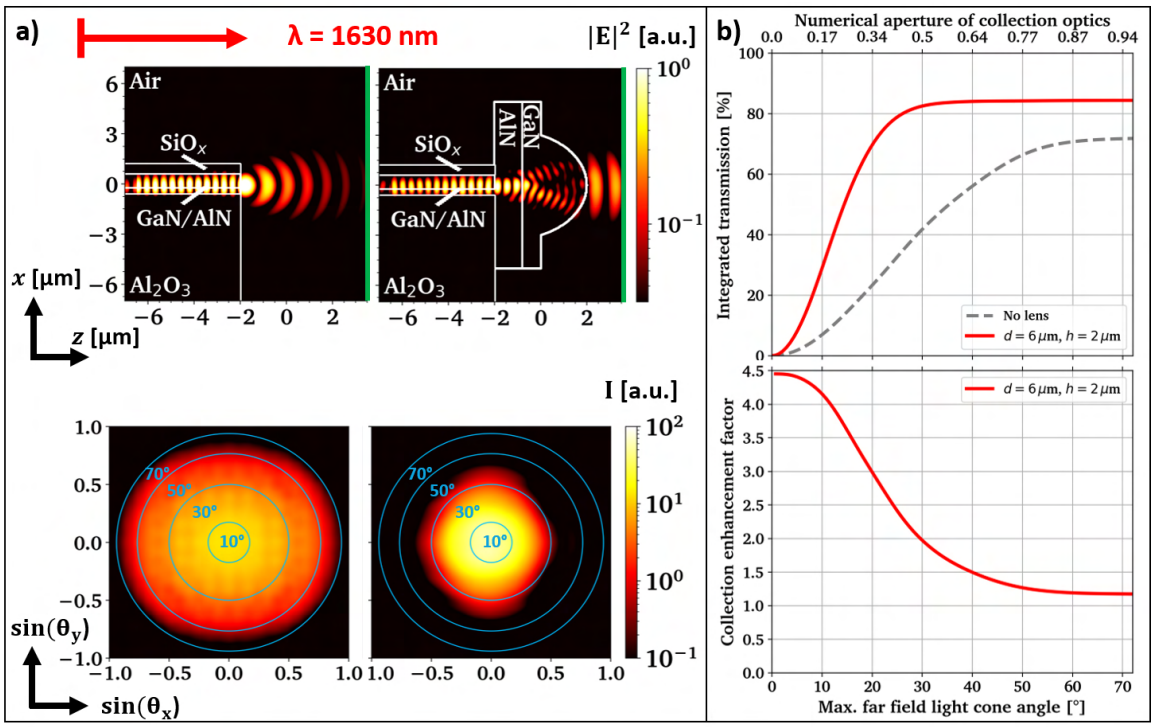

Figure 5.19: Initial test combining GaN/AlN waveguides on a sapphire substrate (2 μm width, 350 nm AlN thickness, 850 nm GaN thickness) with a GaN micro-lens ($d = 6\,\mu$m, $h = 2\,\mu$m, with a 2 μm buffer consisting of GaN and AlN). The fundamental TE mode is injected into the waveguide, propagating towards free space. a) Cross sections of the simulation region ($\lambda = 1630$ nm) without and with micro-lens on the end facet and the corresponding far field emission patterns generated from the monitors indicated by the green lines in the cross sections, b) integrated transmission and predicted collection enhancement (comparing gray and red curve) of light intensity passing through the free space monitors (indicated by the green lines in the cross section in a) in dependence of the maximally collected far field cone angle averaged between 1500-1700 nm wavelength.

A tilted SEM image of the micro-lens before printing is shown in Fig. 5.20 a), while microscope images of the waveguide facet before and after printing are shown in c), including an overlay of images before and after printing in the centre. This chip does not contain any local alignment markers to guide a print on the facet, which restricts the alignment accuracy to around $\pm 1\,\mu$m. The cladding layer is very thin, which causes roughly a third of the micro-lens to remain suspended in air, demonstrating the versatility of the transfer printing integration approach and the flatness of the printed device. As previous work has shown nm-scale accuracy with transfer printing [219], alignment to a chip with dedicated markers and a thicker cladding layer should allow placement accuracy with sub-micron precision.

We image the light output from the waveguide facet through the micro-lens using a 60x objective with a 500 mm tube lens to reach 150x magnification using the setup shown in Fig. 5.18 c). The output mode at $\lambda = 1630$ nm wavelength is shown in Fig. 5.20 d), indicating the transparency of the lens in this wavelength region. The top view image in Fig. 5.20 b) shows the lens after optical characterization, validating the mechanical stability of the bond between lens and the polished facet even with the limited bond area. We did not test enhancement of fibre-to-chip coupling through the micro-lens in this geometry. The test print presented here is published in [95].

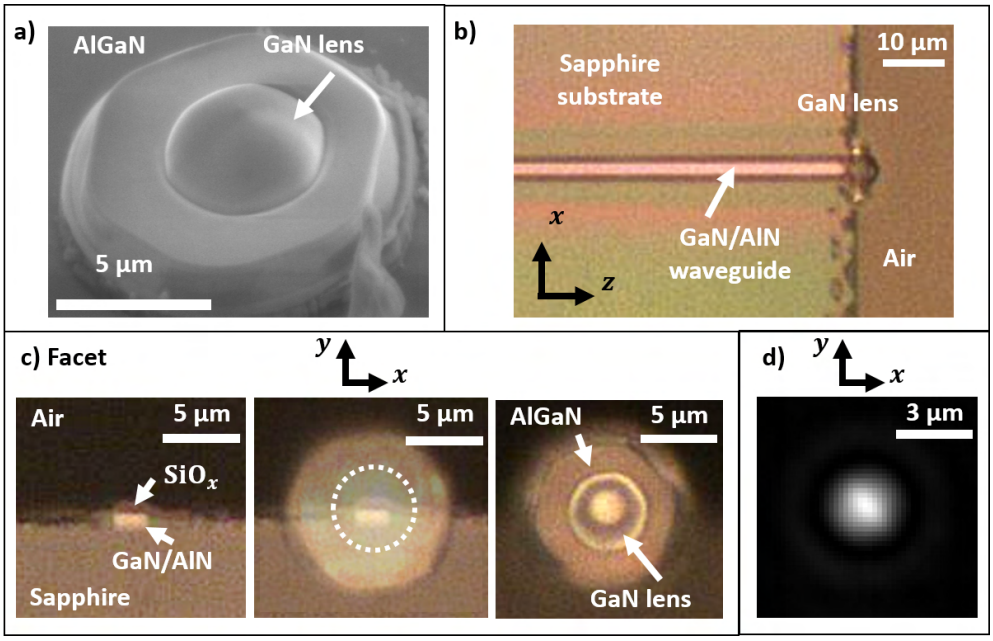

Figure 5.20: High-aspect ratio GaN micro-lens printed on GaN-on-sapphire waveguide facet. a) 40 ° tilted SEM image of the micro-lens on the donor sample, b) top view of the printed micro-lens on the output facet, c) microscope images of the waveguide facet (1.2x2 μm^2) before (left) and after (right) transfer printing, the centre image shows an overlay, d) imaged output waveguide facet with printed micro-lens at $\lambda = 1630$ nm wavelength at 150x magnification, taken with the setup shown in Fig. 5.18 c).

5.2.4 Silicon-on-Insulator test PIC

We repeat a similar printing experiment on the facet of a simple SOI waveguide, which due its small size (450x220 nm^2) and high refractive index ($n \approx 3.5$) suffers from both high diffraction and reflective losses. FDTD simulations with a GaN micro-lens acting as output coupler are displayed in Fig. 5.21, showing that in this geometry we can expect substantially improved coupling to low-NA optics with effective mode field expansion realized by the reasonably broad emission cone.

We estimate how effective the lens might support input coupling into the SOI waveguide by monitoring the power coupled into the waveguide if a Gaussian beam source of different size (flat and lensed fibre) is injected into the waveguide from air, mimicking the output light of an optical fibre. The FDTD simulation results are displayed in Fig. 5.22, indicating that even though the micro-lens is expected to enhance coupling by up to 8-10 dB in the C-band, the overall coupling loss is with 6-9 dB much higher than what can be achieved with optimized coupler geometries as discussed in the review section.

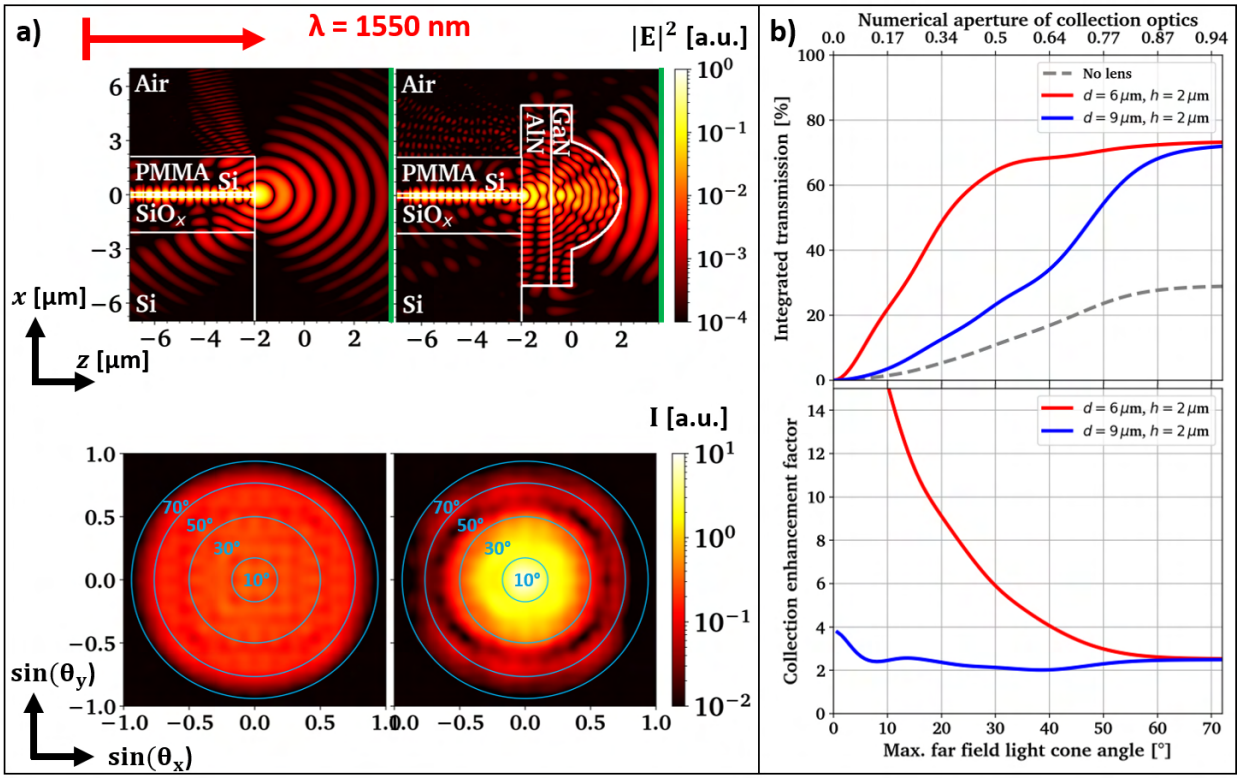

Figure 5.21: Combination of SOI waveguides (450 nm width and 220 nm high Si waveguides on a 2 μm thick SiO_x buffer with 2 μm thick PMMA cladding fabricated by Michael Strain at the James Watt centre for nanofabrication) with a GaN micro-lens ($d = 6\,\mu$m, $h = 2\,\mu$m, with a 2 μm buffer consisting of GaN and AlN). The fundamental TE mode is injected into the waveguide, propagating towards free space. a) Cross sections of the simulation region ($\lambda = 1550$ nm) without and with micro-lens on the end facet and the corresponding far field emission patterns generated from the monitors indicated by the green lines in the cross sections, b) integrated transmission and predicted collection enhancement (comparing gray and coloured curves) of light intensity passing through the free space monitors (indicated by the green lines in the cross section in a) in dependence of the maximally collected far field cone angle averaged between 1530-1565 nm wavelength.

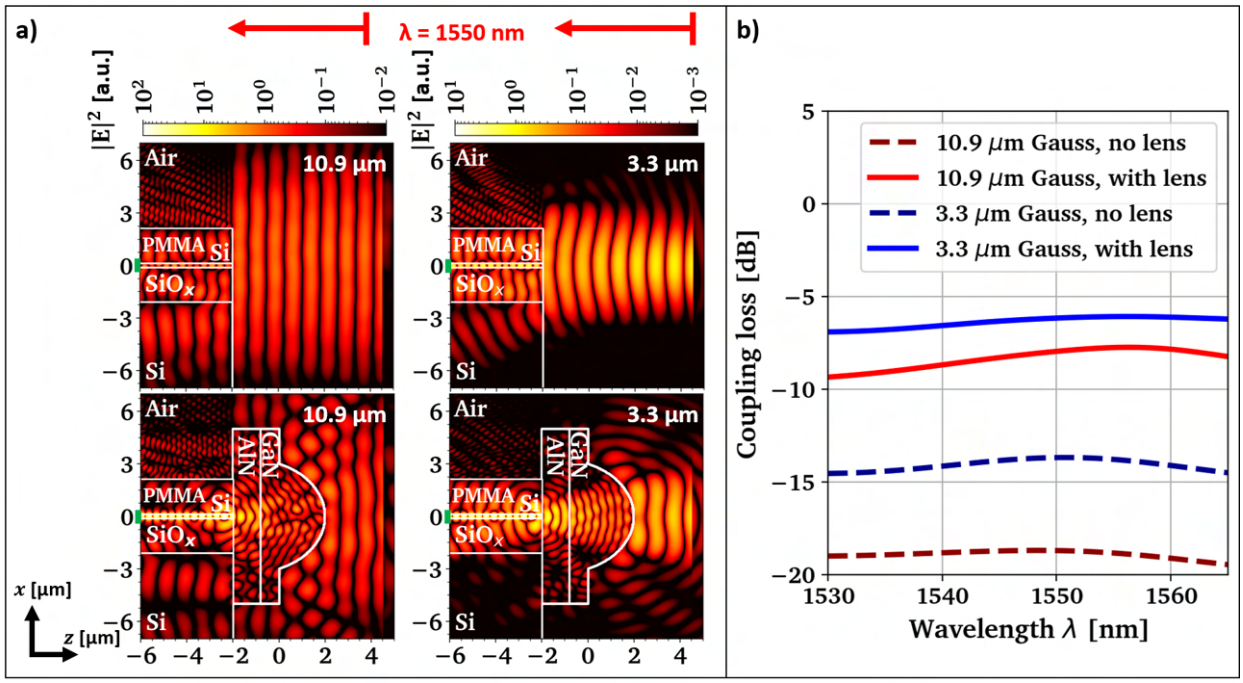

Figure 5.22: Coupling of light output from a standard (10.9 μm beam waist) and lensed fibre (3.3 μm beam waist) at $\lambda = 1550$ nm wavelength modelled by a Gaussian beam source propagating towards the SOI waveguide (450 nm width and 220 nm high Si waveguides on a 2 μm thick SiO_x buffer with 2 μm thick PMMA cladding) without and with a GaN micro-lens ($d = 6\,\mu$m, $h = 2\,\mu$m, with a 2 μm buffer consisting of GaN and AlN). a) Cross sections of the simulation region without and with micro-lens on the end facet, b) coupling loss estimation into the fundamental waveguide mode based on small monitors (950x520 nm^2) covering the waveguide core indicated by the green lines in the cross section in a).

The experimental printing results are shown in Fig. 5.23. The cleaved Si substrate shows significant roughness, but we are still able to release a GaN micro-lens close to the waveguide, even though we note significant misalignment on the order of 2-3 μm in the lateral dimension. As during the first print demonstration we use the surrounding waveguides as visual guides to aid the correct height and lateral position, because the waveguides cannot be observed through the lens during the printing release.
We are able to use the lens both as input and output coupler in the measurement configuration shown in Fig. 5.18 c), but we do not find reliable improvement of transmission with the micro-lens used as fibre-to-PIC input coupler (compare Fig. 5.18 a). This might simply be due to the large misalignment between lens and waveguide. We noted signifcant improvement of horizontal coupling tolerance facilitated by the lens experimentally without quantifying the effect.

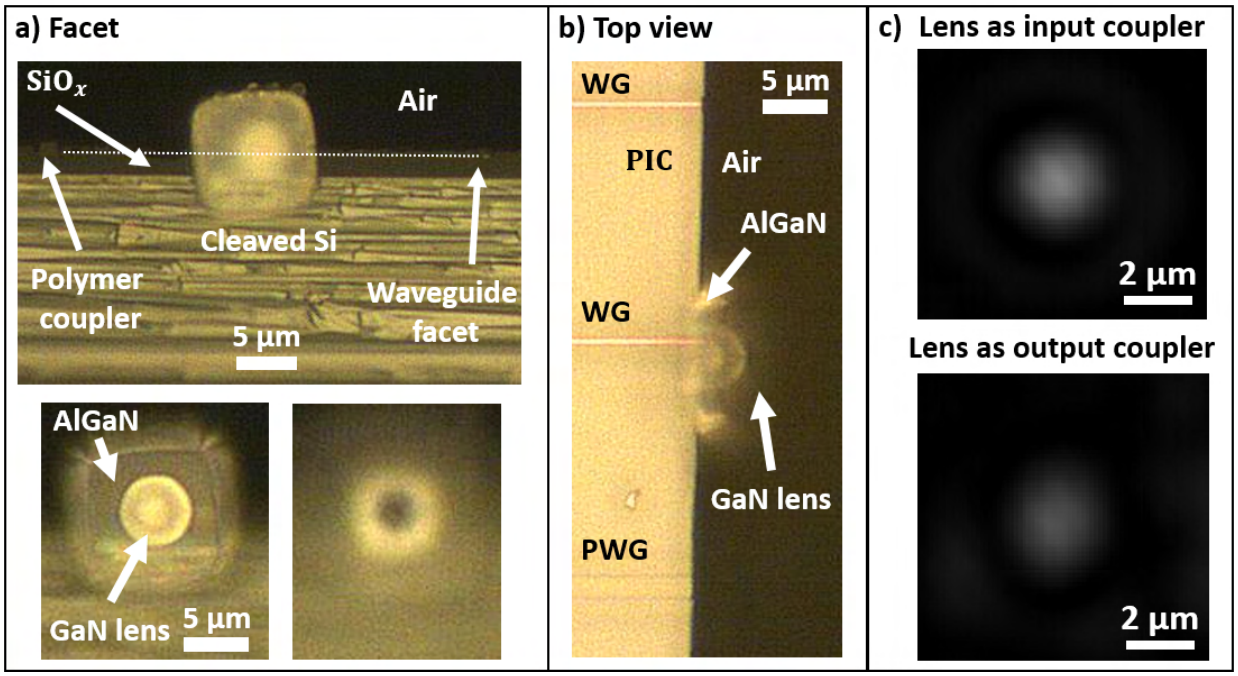

Figure 5.23: Successful printing attempt of a high aspect ratio GaN micro-lens onto a SOI waveguide end facet matching the simulations shown in the previous two figures. a) Microscope images at different focus positions of the printed lens on the waveguide facet, the white dotted line in the top image indicates the vertical position of the waveguide, b) microscope top view of the same printed lens, showing lateral misalignment, PWG stands for polymer waveguide, c) results of IR transmission experiments (CCD image) taken with the setup shown in Fig. 5.18 c), with the lens on the input or output facet of the waveguide (300x magnification). No significant enhancement of the transmission was found either way, potentially caused by the lateral misalignment of the micro-lens.

5.2.5 TaO-on-Insulator PIC for supercontinuum generation

With these promising mechanical print demonstrations at hand we perform simulations and a test run with tantalum pentoxide (TaO) waveguides provided by 'Octave Photonics' in a collaborative project. The goal of the work is to increase the lateral alignment tolerances of edge fibre coupling to the TaO waveguides which are used for super continuum generation with watt level input and output average power covering the VIS to NIR wavelength regime. A typically packaged single PIC device can be seen in Fig. 5.24 a) and the broad output spectrum from the waveguides that are excited by a < 200 fs laser pulse is shown in b). We aim here to exploit the broad transparency window of the GaN/AlGaN/AlN layer stack while hoping that a semiconductor lens coupler can withstand the high optical power in this application.

'Octave photonics' reports to achieve low coupling loss for ideal alignment ($> 85\%$ reported in [314]), but for some applications they desire 1 dB coupling stability in a temperature range between -40°C to 80°C, which might translate to several micron misalignment tolerance due to thermal expansion mismatch. We receive 2 chips with an optimized linear inverse taper geometry with 200 μm length for print and optical testing.

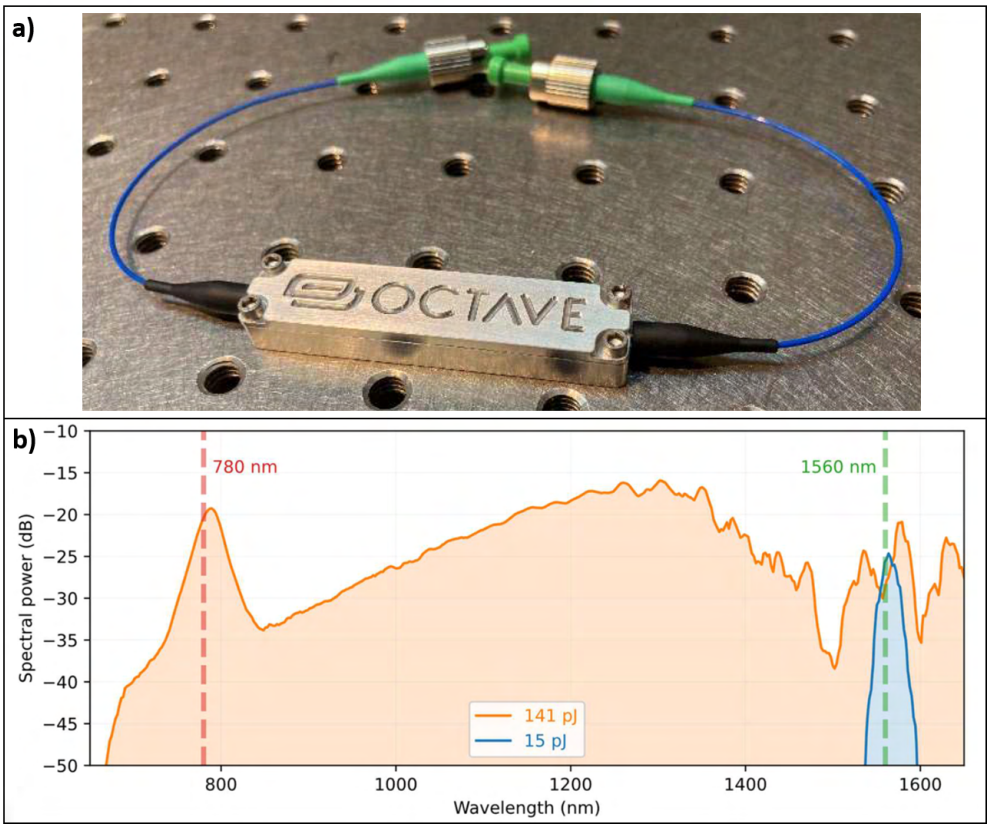

Figure 5.24: a) Packaged fibre-coupled PIC for supercontinuum generation from 'Octave Photonics', b) adapted from [315].

Using the dimensions given in the .gds file of the received chips, we simulated the propagation of the fundamental TE mode injected into a 200 μm long taper with 1.6 μm to 0.18 μm linearly varying width and 800 nm height. BOX and TOX thicknesses were set to 3 μm and 2 μm, respectively. To keep the simulation effort in a practical range, we chose a simulation region of about 9x9x60 μm^3 with absorbing boundary conditions and a grid pitch varying between 20 nm and 50 nm. We chose the C-band as wavelength window, with all simulation cross sections taken at $\lambda = 1550$ nm. The wave propagation direction is in all simulations from bottom to top.

Fig. 5.25 a) shows cross sections of the electric field amplitude squared inside the simulation region without and with a GaN micro-lens on the waveguide facet. The lower two graphs show a close-up view of the waveguide facet. The GaN micro-lens has 2 μm height, 11 μm diameter, and is carried on a 2 μm thick membrane, consisting of 1.2 μm AlN and 800 nm GaN, similar to currently available devices.

Both simulations are plotted on the same logarithmic scale, visualizing that the lens can planarise the wave front, but cannot effectively enlarge the mode-field diameter in the near field of the waveguide facet. This is simply due to the fact, that our GaN lenses are quite thin and the angular spread from the inverse taper into air / the GaN lens membrane is low, as visible in the most left image of Fig. 5.26 a). Therefore the aperture of the lens is by far not filled.

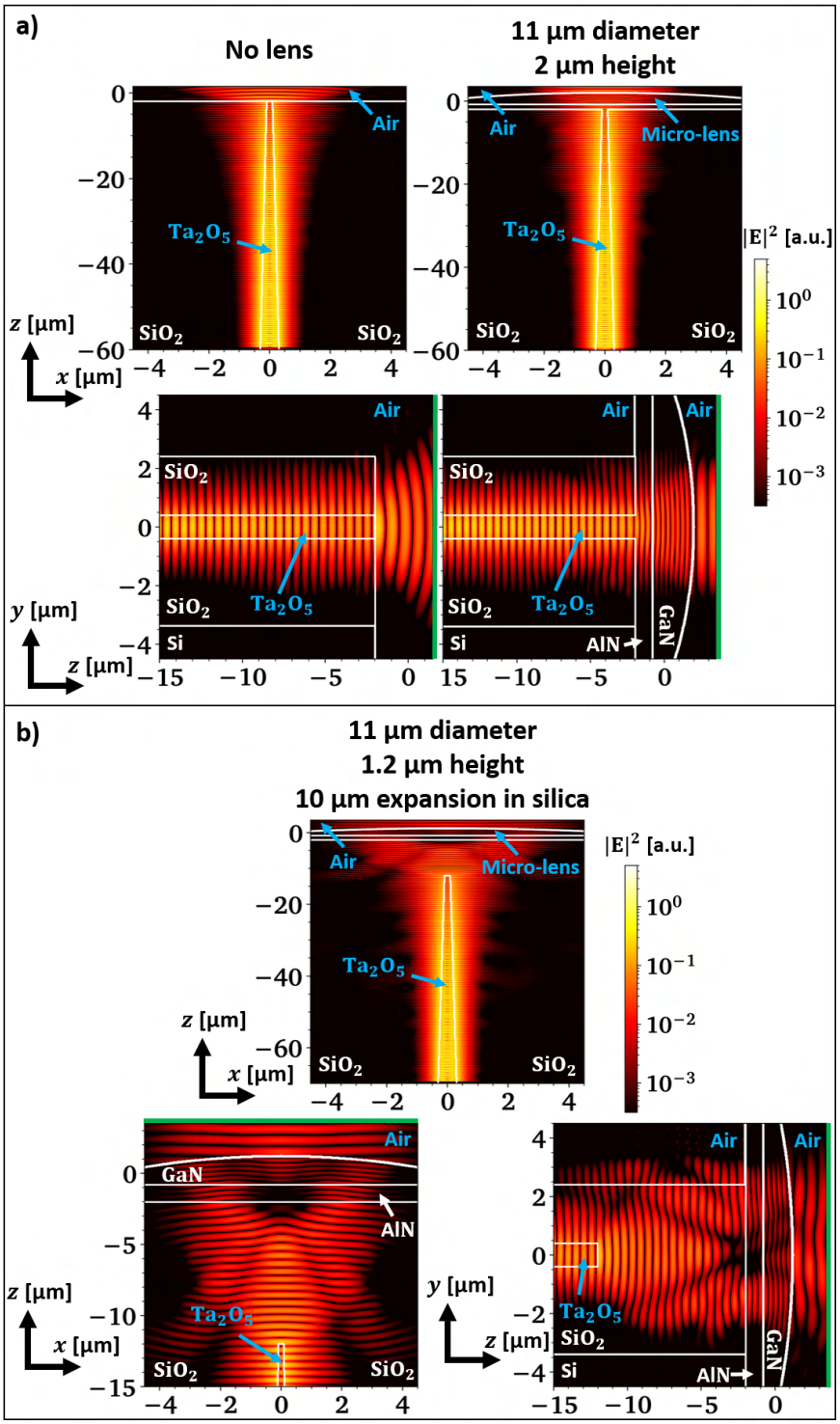

Figure 5.25: Collaboration with 'Octave Photonics': FDTD simulations of waveguides with inversed taper end-fire couplers fabricated from tantalum pentoxide on insulator platform (TaO: 800 nm height, 1600 nm to 180 nm taper over 200 μm length on 3 μm SiO_x buffer with 2 μm SiO_x cladding). a) Cross sections of the full simulation region without and with a printed GaN micro-lens on the end facet ($d = 11\,\mu$m, $h = 2\,\mu$m with a 2 μm buffer consisting of GaN and AlN) viewed from the top (upper two graphs) taken at $\lambda = 1550$ nm wavelength, the bottom images show a close up in side view with the recording transmission monitors marked with the green lines, b) adding a 10 μm long beam expansion area to the PIC edge: Cross sections of the full simulation region with a printed GaN micro-lens on the end facet ($d = 11\,\mu$m, $h = 1.2\,\mu$m with a 2 μm buffer consisting of GaN and AlN) viewed from the top (upper graph) taken at $\lambda = 1550$ nm wavelength, the bottom images show a close up in top and side view with the recording transmission monitors marked with the green lines.

To achieve aperture filling, a different device geometry could be used. If the taper is ended for example 10 μm away from the etched chip facet, the mode can expand inside the BOX and TOX layer. Fig. 5.25 b) shows the resulting simulated $|E|^2$ distribution with a modified micro-lens height to match the increased distance to the waveguide (increasing the radius of curvature). The two bottom images show a close up of the waveguide facet and the terminated waveguide taper. It is visible that the mode-field diameter can be significantly increased in both horizontal and vertical direction, but the thickness of the BOX and TOX layer limit the expansion vertically, leading to wave front distortion in the near field. Interference effects between the upwards propagating main beam and reflections from the AlN/SiO2 and GaN/Air interface are additionally visible, which might affect the overall coupling efficiency.

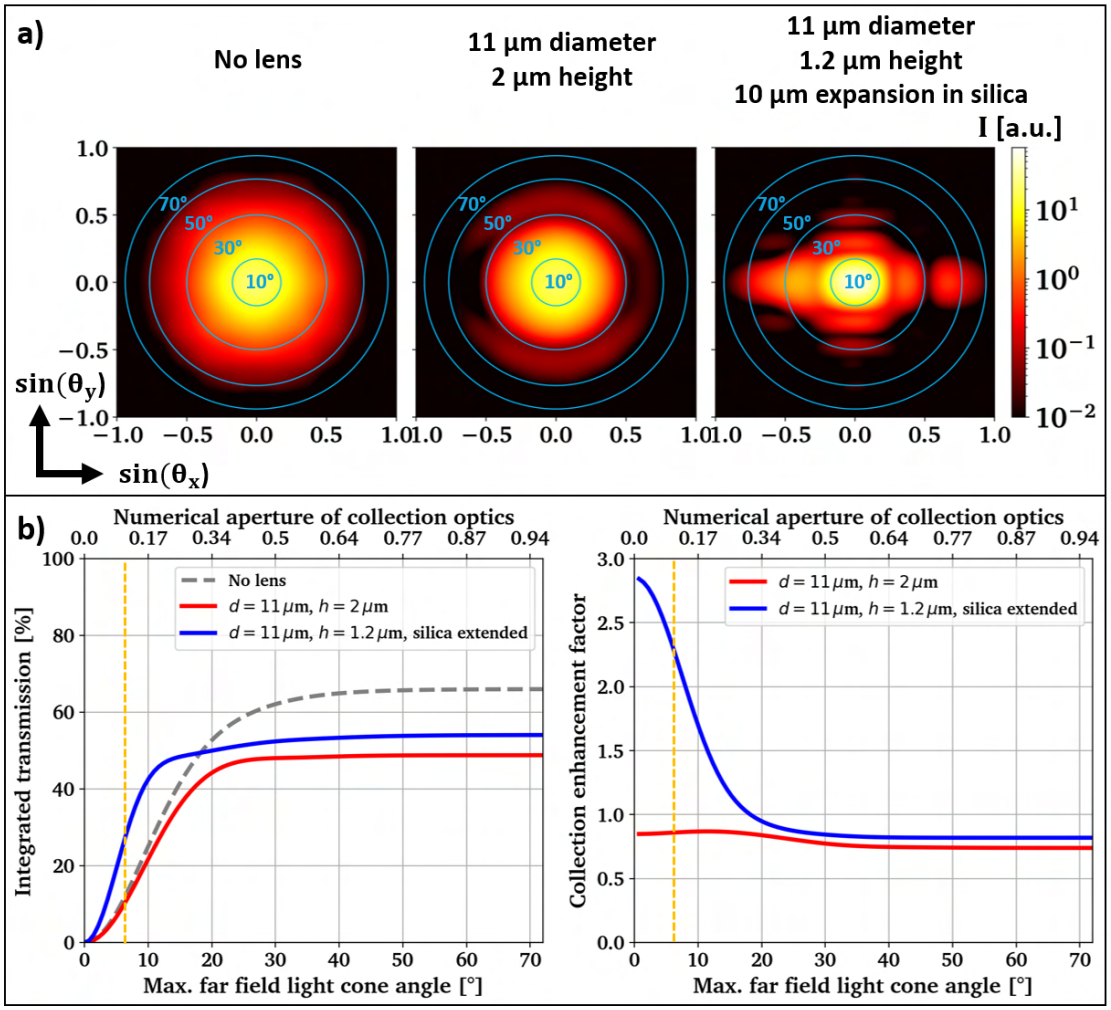

Figure 5.26: Collaboration with 'Octave Photonics': a) Projected far field intensity using the green monitors in the previous figure for all three investigated scenarios, b) integrated transmission and expected enhancement compared to the case without micro-lens (gray curve) in dependence of the maximally collected far field cone angle averaged between 1530-1565 nm wavelength recorded at the green monitors in the previous figure.

Fig. 5.26 a) shows the far field intensity distribution on the upper detector surface (marked green in Fig. 5.25) as a function of the incident angle for all 3 simulated geometries. The strongest reduction of angular spread is expected with the mode expansion inside the BOX and TOX layer shown in Fig. 5.25 b), compare the most right far field plot in Fig. 5.26 a). The asymmetry and slight intensity cloud outside of the 10° centre ring here are probably due to the stronger light confinement and wave front distortions

which can be seen if geometry is viewed from the side (bottom right graph in Fig. 5.25 b). Both might reduce the coupling efficiency to a circular fibre mode.
The results are quantified in Fig. 5.26 b) by considering the amount of light hitting the upper detector surface marked in green in Fig. 5.25. The left hand side plot in Fig. 5.26 b) shows the total transmission averaged over the C-band as function of the angular distribution in the far field based on Fig. 5.26 a). Visibly, the additional index contrast introduced by the AlN/SiO2 and GaN/Air interface increase Fresnel reflections, limiting the transmitted light through the GaN micro-lens on the facet. The right hand side plot in Fig. 5.26 b) illustrates the potential enhancement factor provided by the added GaN micro-lenses in both discussed geometries in comparison to the inverse taper alone. We find that with mode expansion inside the silica, the GaN micro-lens could give a performance boost for light cones $< 15°$. The yellow line indicates 7.5° collection from a typical single mode fibre at 1550 nm with 10 μm mode field diameter (NA$= 0.13$), demonstrating that the light loss due to Fresnel reflections could be compensated by the focusing effect of the micro-lens if low NA fibres are used for coupling. As the coupling between waveguide and fibre relies on matching both mode field diameter and NA, the graph probably underestimated the increase of coupling efficiency in this regime because the lens can be expected to increase the mode field diameter.
Overall, GaN micro-lenses could help to mitigate some losses that would be expected when using fibres with large mode field diameters for increased alignment tolerance. But as the simulations indicate the power throughput is expected to be worse compared to coupling the inverse taper input/output directly to a high NA lensed fibre with low mode field diameter at the waveguide facet, which is Octave's current choice.

To demonstrate the feasibility of printing our micro-lens devices on the etched waveguide facets of Octave's PICs, we printed a low-quality micro-lens with high accuracy on the waveguide facet corresponding to 0.5 μm width without additional marker structures. The following microscope images in Fig. 5.27 and 5.28 show the device before and after printing in top and side view. The alignment is estimated to be better than 1 μm in both dimensions. This result is achieved after trying two different lens devices, with the second device printed with few attempt. The waveguide facet is visible in high magnification before the print (c5.28, bottom left), which eases the alignment. The print worked even though the interface shows some visible etch artefacts (black).

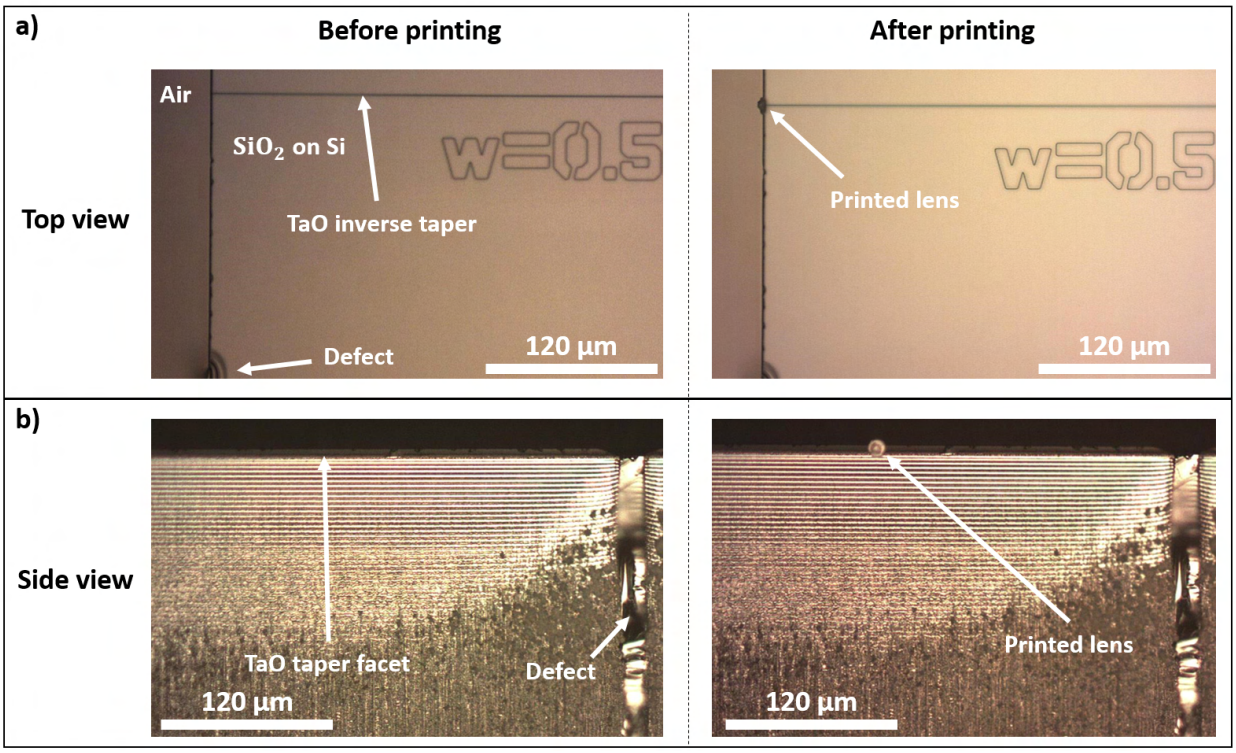

Figure 5.27: Collaboration with 'Octave Photonics': Test print result of a defective GaN micro-lens onto the waveguide facet of a TaO taper with 500 nm initial and 180 nm final design width. The PIC layer dimensions are similar to what is specified for the simulations in Fig. 5.25. Microscope images in a) top and b) side view under low magnification before and after lens printing.

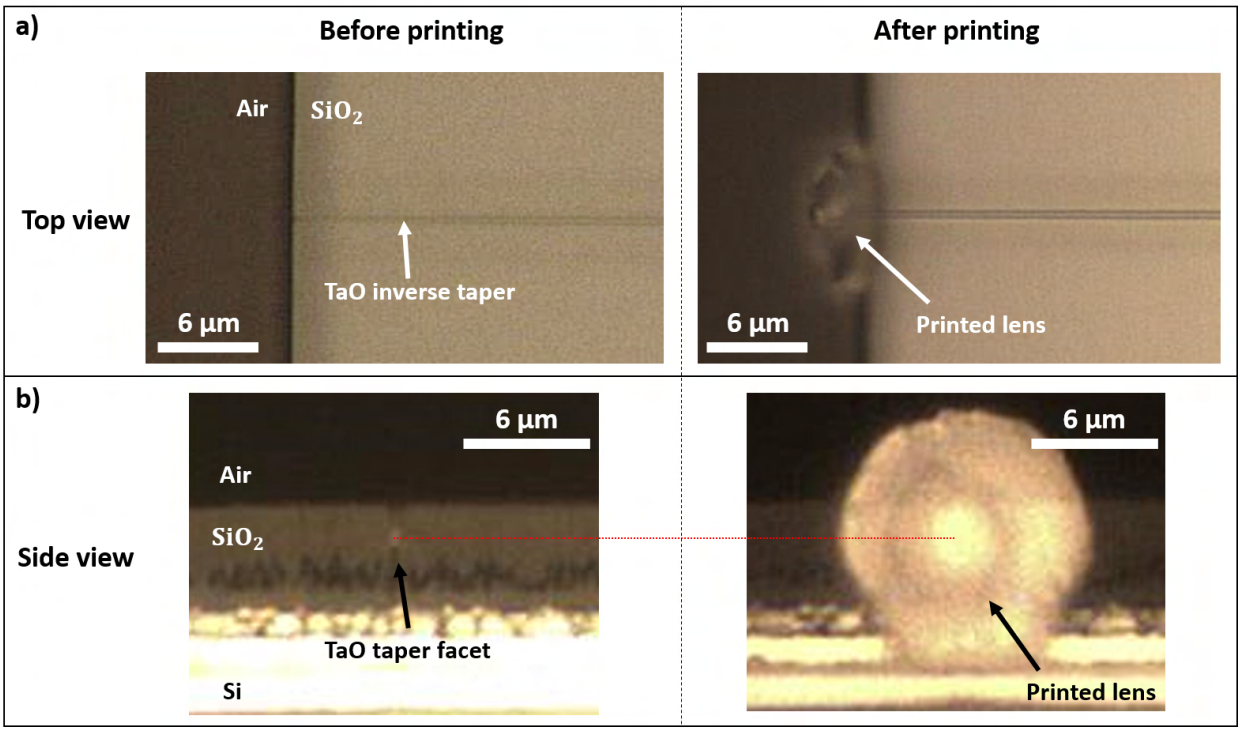

Figure 5.28: Collaboration with 'Octave Photonics': Test print result of a defective GaN micro-lens onto the waveguide facet of a TaO taper with 500 nm initial and 180 nm final design width. The PIC layer dimensions are similar to what is specified for the simulations in Fig. 5.25. Microscope images in a) top and b) side view under high magnification before and after lens printing.

5.2.6 Summary

In short we show that GaN micro-lenses can be released on PIC waveguide facets using the transfer printing method even if very little material is present to support the lenses. These half suspended lens devices prove to be mechanically robust enough to be analysed optically. The printing accuracy varies from device to device and probably depends on the surface quality of the waveguide facet and its surroundings with sub-micron accuracy achieved in the best case. With an optimized low-surface roughness etched waveguide facet that includes a cladding layer to support the micro-lens and suitable edge-marker structures incorporated into the PIC design, reliable printing could be achieved.
In optical tests we find that the lenses are sufficiently transparent in the IR spectral region but we do not find expected improvement of input coupling to SOI waveguides, probably due to strong misalignment between waveguide and lens.
We discussed the interesting application of semiconductor couplers for high-power non-linear PICs, such as the supercontinuum source TaO chips from 'Octave Photonics'. Even though we are able to release a test lens device on a TaO chip, our simulations predict that the GaN micro-lenses cannot effectively support the inverse taper edge coupler as it is and redevelopment would be needed to achieve improvement of alignment tolerances. As a first thought experiment we extend the distance between nanotaper and chip facet by 10 μm to expand the mode into the micro-lens and find a trade-off between potential increase of alignment tolerance under the cost of reduced overall coupling efficiency which is not desirable for this application.
Still this work might inspire future PIC-micro-optical integration schemes and pave the way to novel device geometries easing packing of photonic integrated circuits.

5.3 Transfer printing on a flat single mode fibre facet

In this final thesis section we are going to discuss the integration of micro-optical elements with fibre facets and demonstrate potential active alignment methods in the context of transfer printing. GaN micro-lenses will serve as an example donor devices.

5.3.1 Review: Micro-optics on fibre facets

The facet of an optical fibre offers unique opportunities for photon-mediated remote sensing in fields such as surface-enhanced Raman scattering [316, 317], scanning near-field optical microscopy [2, 316] or endoscopy for biological in-vitro imaging applications [109, 318], which all rely on modifications of the standard fibre tip geometry. Alignment accuracy, high-throughput by parallelization and packaging are important factors when considering and comparing methods to functionalize the optical fibre tip for advanced applications [316].

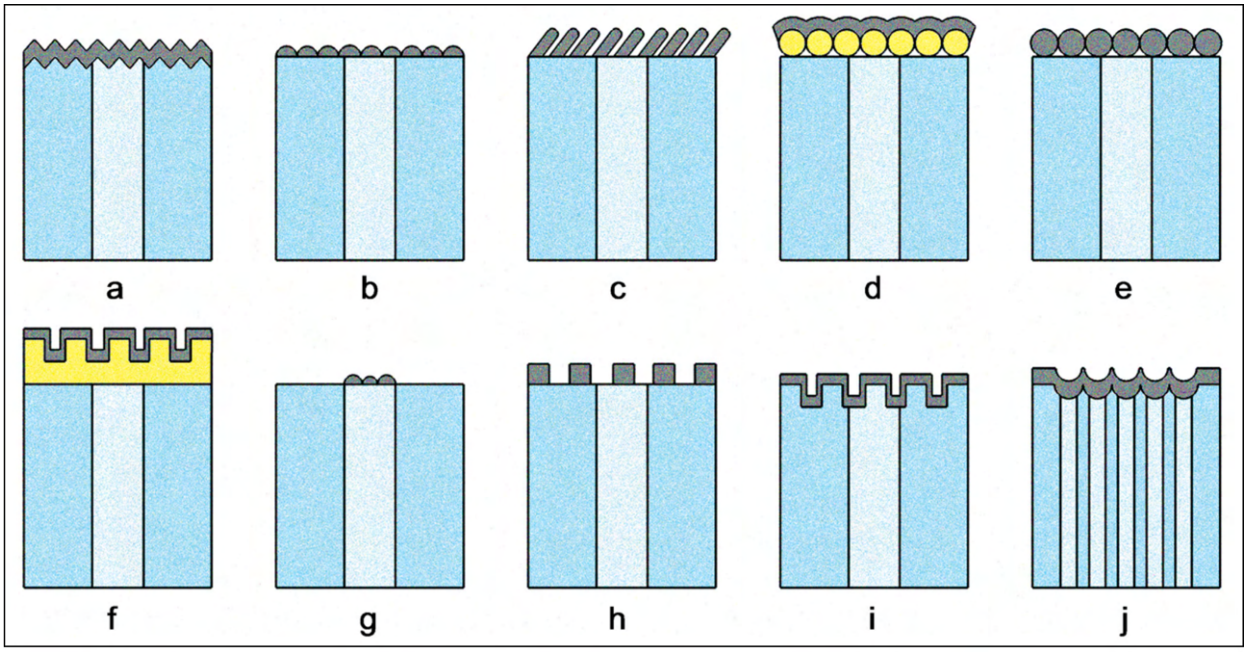

Figure 5.29: Schematics showing processing results to functionalize a fibre tip for surface-enhanced Raman scattering, the fibre core is shown in light blue, the cladding in blue, metals in gray and dielectrics/polymers in yellow: a) Mechanical abrasion, b) thin film deposition, c) glancing angle deposition, d) self assembly, e) coating with nanoparticles, f) nanoimprint lithography, g) through fibre photoreduction, h) nano-transfer, i) interference lithography and etching, j) selective etching of a multicore fibre, adapted from [316].

A clean optical fibre facet can be prepared by mechanical polishing, CO_2 laser cutting or mechanical cleavage yielding a mirror finish for the optical mode that is confined in the higher index core [316]. And even though traditional micro-fabrication methods are optimized for large, flat surfaces, much work has been focused on alterations of the optical fibre tip geometry with some techniques depicted in Fig. 5.29. Other approaches include focused ion beam milling, femtosecond laser ablation, photo- and electron-beam lithography as well as thermal reflow of the fibre tip material [316, 317].
Two-photon polymerization has shown to yield impressive fabrication results achieving various complex micro-optical elements on the fibre tip relevant for both integrated photonics and endoscopic imaging

applications [109, 133, 316–318], compare Fig. 5.30 for some examples.

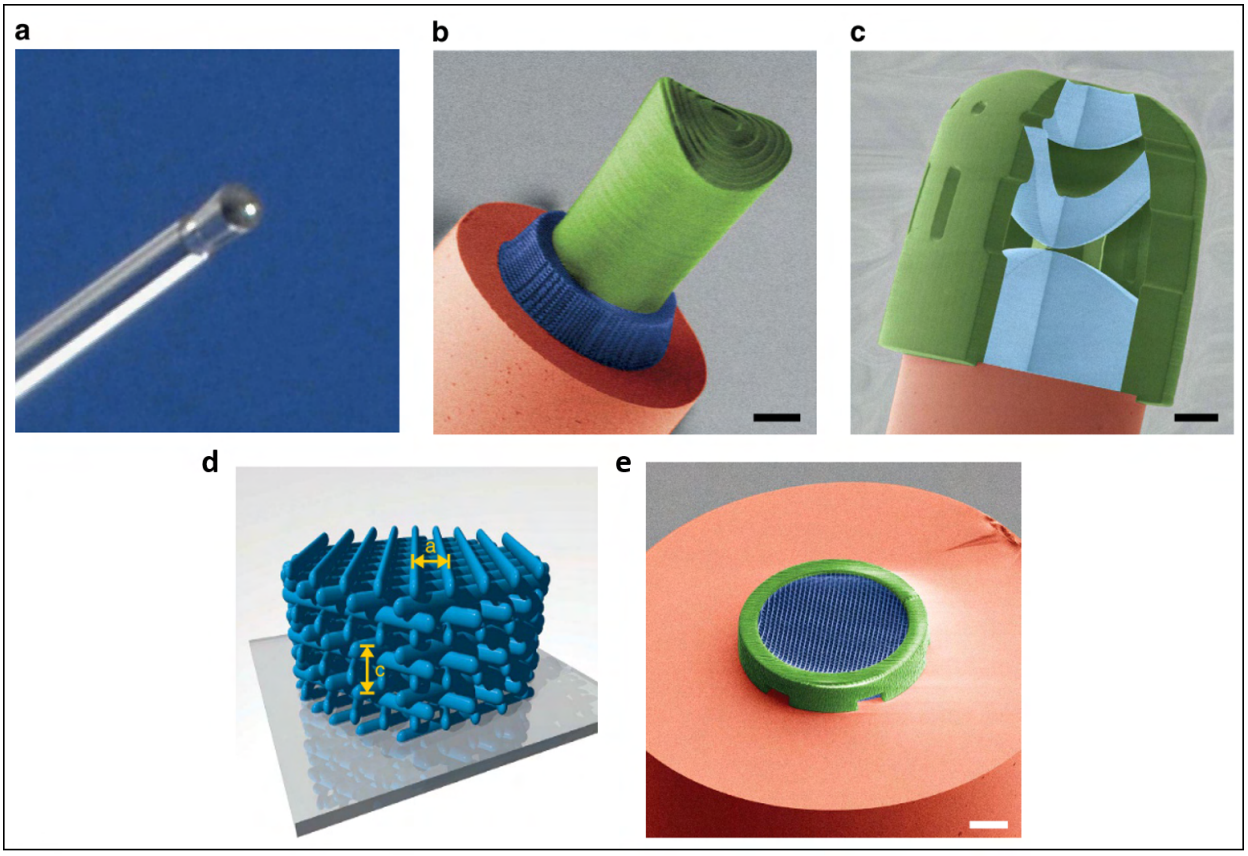

Figure 5.30: Microscope (a) and false colour SEM images (b,c,e) of micro-optical elements fabricated with two-photon polymerization on the facet of an optical fibre. d) Schematic of a chiral 3D photonic crystal polarization filter, with the corresponding fabrication result shown in e), adapted from [318].

Also μ-transfer of resist sleeve templates or nano-transfer of predefined device structures and even full photonic integrated circuits via metallic probes or direct fibre imprint onto the donor substrate - sometimes using PDMS to transfer thin films - have been demonstrated [316, 317, 319–321]. Here the quality of the optical fibre tip surface as well as the flatness and bottom roughness of the transferred device play a crucial role for reliable transfer which relies on van-der-Waals forces, even though adhesion layers might be employed [316, 317, 319].
To our knowledge PDMS-based actively aligned transfer printing of a single micro-optical element on an optical fibre tip has so far not been demonstrated, and the printing results in this section thus extend the fabrication techniques available for deterministic assembly of functional micro-systems on the tip of an optical fibre.

5.3.2 Outline of the work

We demonstrate transfer printing of a GaN micro-lens onto an a mechanically cleaved optical fibre facet leading to μm-scale focal length and investigate how active optical alignment during transfer printing can either be achieved by back- or top-illumination. We show that the printed and aligned GaN micro-lens enhances fibre-to-chip coupling compared to the bare fibre facet, using the same SOI waveguides discussed in the previous section as an example.

The following Fig. 5.31 illustrates the basic printing arrangement and contains the results from FDTD simulations of the device architecture predicting μm-scale focal length of the fibre-lens system. We note that GaN micro-lenses are due to their refractive index mismatch to standard silica fibres not an ideal optical system ($n_{\text{fibre}} \approx 1.4-1.5$), but use the platform to demonstrate the versatility of the transfer printing method. Parts of this chapter are published in [293] demonstrating advancement in the capabilities of PDMS-based optical transfer printing. This section is based on a collaborative effort with Sean P. Bommer and Benoit Guilhabert.

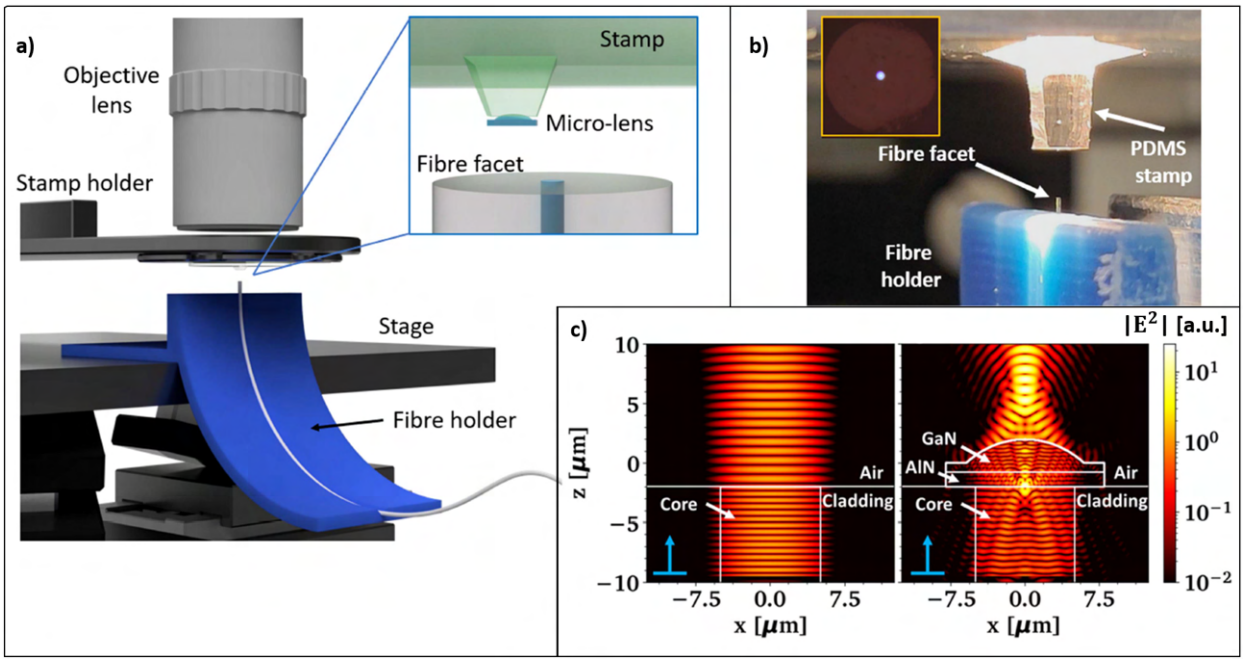

Figure 5.31: Integration of a GaN micro-lens with a cleaved fibre facet. a) Schematic showing how the fibre is mounted on a custom 3D printed holder in the home-built transfer print tool, with the inset showing a zoom into the arrangement of μ-stamp, lens and fibre facet before release (Courtesy to Sean P. Bommer), b) a photograph of the real world implementation with the inset showing the fibre facet through the optical microscope column with illumination from the back, c) cross sections through FDTD simulations ($\lambda = 1550$ nm wavelength) of the fibre facet (assuming 10 μm core diameter) with and without micro-lens ($d = 12\,\mu$m, $h = 2\,\mu$m with a 2 μm buffer consisting of GaN and AlN) with the fundamental mode injected from the bottom.

5.3.3 Results

An advantage of using an optical fibre as a substrate is that the core can be used to transmit light during the device transfer process to guide optimal device release without additional marker structures, as such are challenging to fabricate on a high-aspect ratio template. Fig. 5.32 shows microscope images taken inside our standard transfer print tool that illustrate how μm-precise optical alignment can be achieved by backside illumination of the optical fibre while monitoring the micro-lens position in close proximity to the fibre facet within the optical column of the printing system.

Challenging aspects of the printing process include the flexibility of the fibre in our improvised holder which allows the fibre to slightly deform during the transfer process. After several unsuccessful print release attempts with a different lens device we wet the surface of the fibre with a drop of IPA to facilitate the printing, which remained unsuccessful. To remove residues we clean the fibre facet with low adhesive tape. We note that printing with a second lens device is achieved after this surface treatment and it

might be possible that glue from the tape dissolved in the IPA and has modified the surface adhesion.

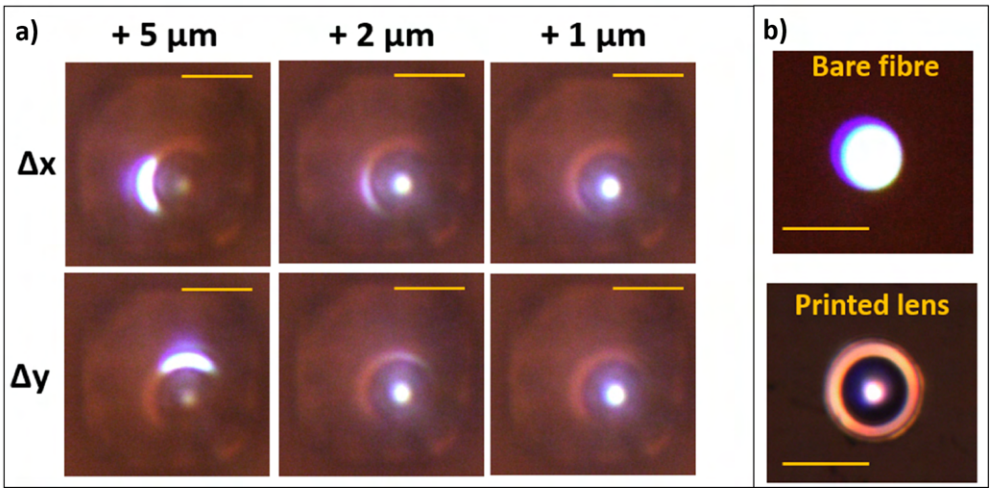

Figure 5.32: Relative alignment of the cleaved optical fibre facet with a GaN micro-lens with white light (VIS) injected at the remote end of the fibre performed in our standard transfer print tool. (a) Microscope images during transfer printing: The micro-lens on the stamp (stationary in the field of view of the optical imaging system) is brought into few μm proximity of the illuminated fibre core, which is laterally shifted at various x and y positions. (b) Micrograph showing in-situ measurement of the fibre facet emission before (top) and after (bottom) integration of the micro-lens. Scale bars are 15 μm.

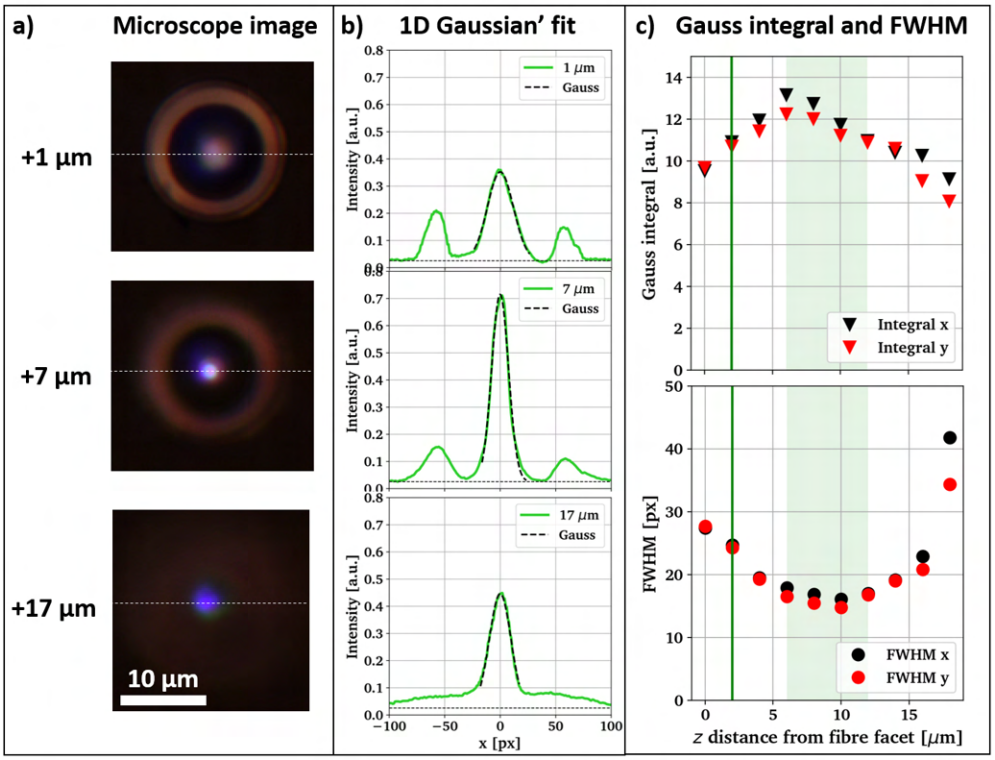

Figure 5.33: Measured focal length of the fibre-lens system after transfer printing. a) Microscope images of the micro-lens at the fibre facet under white light (VIS) back-illumination recorded inside our standard transfer print tool at different z-positions of the stage, b) 1D line scans extracted from the images in a) corresponding to the white dotted lines with the main lobe fitted by a Gaussian lineshape, c) comparison of the fitted integral and FWHM of the main lobe in b) in dependence of the distance of the microscope focus from the fibre facet (marked with the green vertical line).

After printing we observe strong focusing behaviour at $6 \pm 2\,\mu$m distance from the fibre facet under broadband VIS back-illumination, as illustrated in Fig. 5.33. This matches well with the expectation of the simulations shown in Fig. 5.31 c), even though these are run in the IR spectral region and the IR fibre (mechanically cleaved[2] tapered single mode NANONICS, $\lambda = 1300 - 1550$ nm) is expected to operate in a multimode regime under VIS illumination.
We confirm the positive impact of the focusing behaviour on fibre-to-chip coupling with the results depicted in Fig. 5.34 b) showing ca. 6.5x (TE) and 2.5x (TM) enhancement of coupling efficiency provided by the GaN micro-lens.

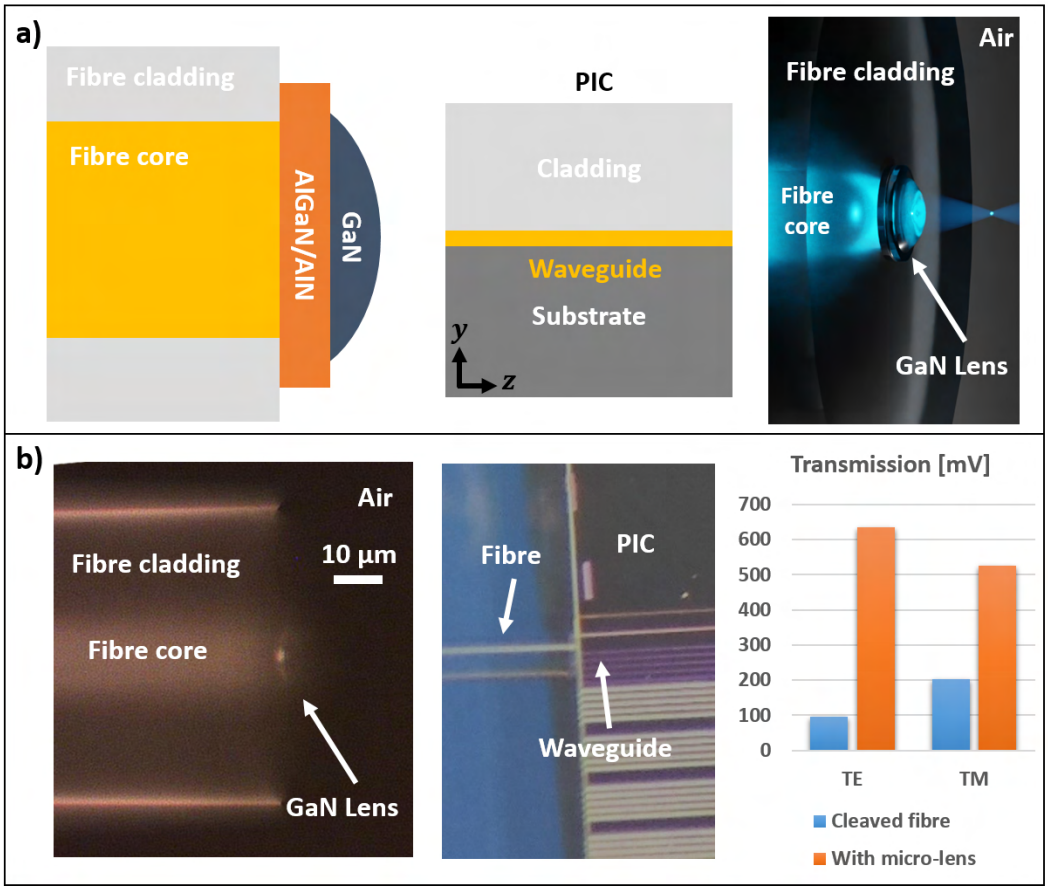

Figure 5.34: Enhanced fibre-to-PIC coupling. a) Schematic showing the experimental arrangement, including a 3D graphical render of the back-illuminated fibre with integrated lens, b) (left) microscope image of the cleaved fibre facet with the attached micro-lens in side view, (middle) microscope image of this fibre approaching a SOI PIC edge (the same as discussed in subsection 5.2.4), (right) results of an IR transmission experiment recorded with the setup shown schematically in Fig. 5.18 c) performed on the same waveguides without and with added micro-lens. The initial transmission measurement are performed before printing and light coupling is optimized in each case.

Sometimes it may not be possible to illuminate the remote end of the fibre/on-chip structure - but instead light might be coupled to the fibre/chip via top-injection using for example a photodetector or reflected light from the substrate to guide the alignment. In a second home-built transfer print tool a laser injection path with scanning mirrors and a tele-centric lens system is added to the optical column to facilitate device illumination from the top (courtesy to Benoit Guilhabert and Sean P. Bommer for this work). This additional optical injection column can be used to illuminate the structure of interest and

[2]Courtesy to Craig Hunter for performing the cleave

the coupled light can be monitored to assess the alignment of the printing in-situ, compare Fig. 5.35 for schematics of the home-built transfer print tool.
Without back-illumination aligning a micro-lens to the fibre core is more difficult since the structure is essentially invisible to the microscope imaging system, compare Fig. 5.36 a). We use the optical top injection setup to illuminate the fibre core through the printing system and monitor the coupled light with a photodetector at the remote fibre end, as illustrated on the left hand side of Fig. 5.36 b).
We fix the optical injection spot in position and the translation stage is scanned while the power received at the remote fibre end is monitored as a function of the stage (fibre core) position. The plot on the right hand side of Fig. 5.36 b) shows the measured photodetector output as a function of lateral translations of the motion control stage in x and y directions from the initial coarsely aligned (0,0) position. The peak intensity corresponds to the maximum optical power coupled through the fibre to the detector, which should be the case when the fibre core and optical injection spot are aligned in the transfer print instrument and we can place the micro-lens at this position.
Fig. 5.36 c) illustrates this process with the last image showing the released micro-lens on the back-illuminated fibre core after printing. We see a clear offset compared to the optimal lens position above the core, revealing a systematic offset between the best position for laser input coupling into the fibre facet and the ideal centre position of the fibre core. This might be due to insufficient beam-verticality in the optical path or focus asymmetry leading to a lateral offset and could either be corrected within the tool or could be calibrated for in successive prints.

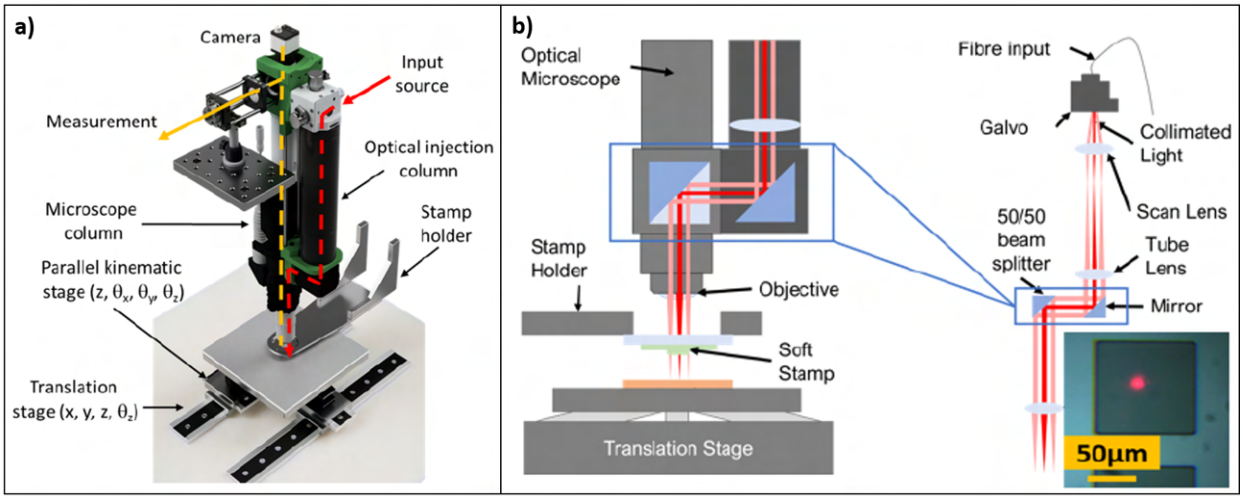

Figure 5.35: Schematics showing the home-built transfer print tool (courtesy to Sean P. Bommer) with laser scanning injection column. a) Overview of the stage, optical column and stamp holder, b) schematic of the incorporated laser scanning system that is used to inject laser or LED light through the micro-stamp to the sample from the top with a microscope image of a focused spot on the surface of a sample with square mesa structures.

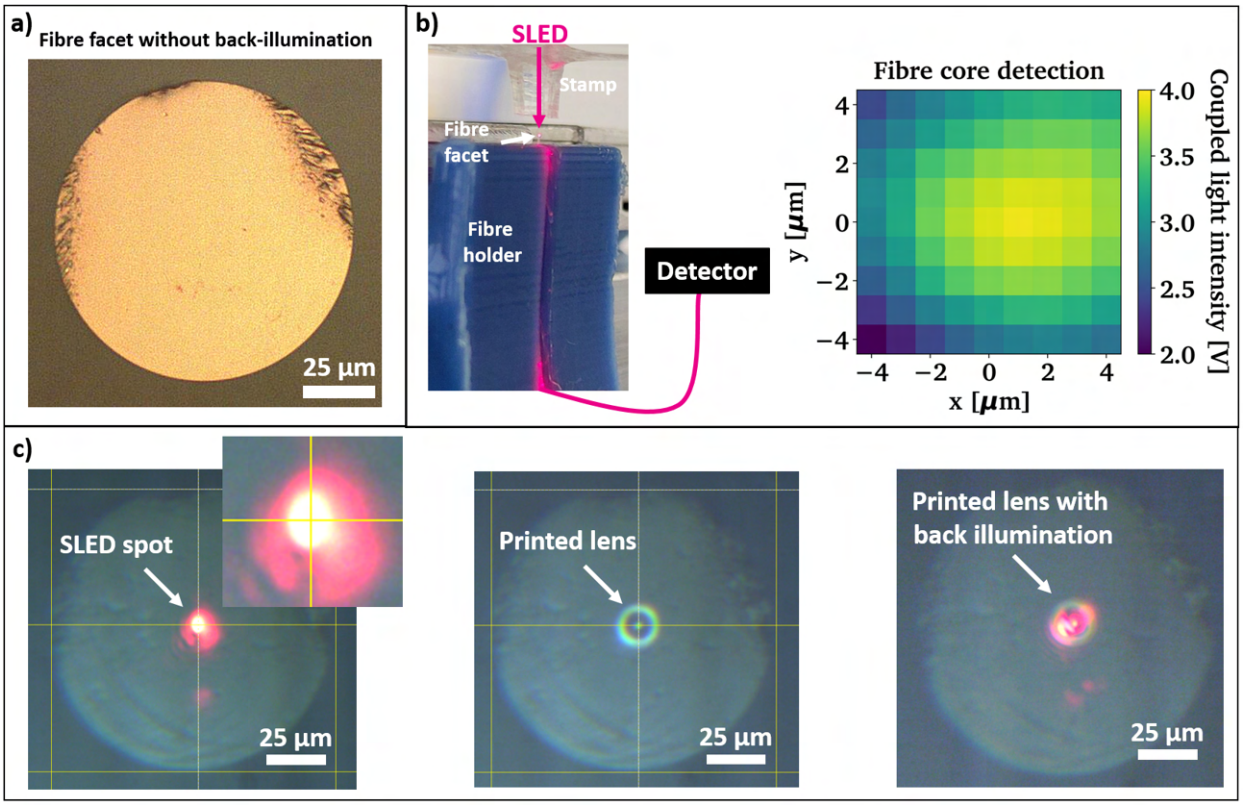

Figure 5.36: Active alignment of micro-lens and fibre core facilitated by top injection of light from a red SLED with the home-built transfer print tool. a) Microscope image of the cleaved fibre facet without micro-lens, showing that the fibre core does not deliver any optical contrast without back-illumination, b) schematic of the experimental arrangement and the experimental data collected before printing, identifying the fibre core position in the coordinate system of the stage, c) in-situ microscope images illustrating the printing procedure guided by top injected light: (left) The centre of the reflection of the SLED spot is chosen as origin - tracking the position with screen markers - then the fibre core detection shown in b) is run, (middle) the micro-lens on the stamp is moved into the field of view by the manual stage that controls the stamp head position and the micro-lens centre is overlapped with the marked SLED middle spot position, then the device is released at the position found by the scan, (right) back-illumination with the SLED is switched on after the actively guided device release.

5.3.4 Summary

In short, we demonstrate successful release of a single GaN micro-lens on the cleaved facet of a standard single mode IR fibre. We investigate both back- and top side illumination strategies to guide the lens-to-core alignment actively, finding that backside illumination immediately allows for well aligned lens integration while top-side illumination might need to take a systematic calibration offset into account. This result advances and professionalizes micro-system assembly on optical fibre tips. PDMS-based transfer printing fibre-device integration could be parallelized by bundling multiple optical fibres closely together, employing multiple print heads and by optimizing the device arrangement on the donor chip to match the correct pitches.

Mechanical cleavage is reported to create a lower quality surface compared to polishing and laser cutting techniques [316] but is much simpler to achieve. Therefore the successful print release on such a surface is a promising result for van-der-Waals based photonics device bonding. For functional systems, packaging methods might need to be considered to protect assembled devices from mechanical or thermal shocks.

5.4 Summary

In this Chapter we have investigated three challenging transfer print geometries using GaN micro-lenses as exemplary devices:

- 3D printing on photoresist support frames limiting the device contact area above an air gap and therefore reducing the strength of the van-der-Waals bond
- Device transfer on cleaved and etched photonic integrated circuit facets with varying surface quality, half suspended in air
- Micro-lens release on the semi-flexible tip of an optical fibre using active alignment procedures

In all cases we find that the transfer printing based integration (i) can be successful and (ii) can retain μm-precise alignment precision even without dedicated marker structures.
We can summarize the main optical results:

- GaN micro-lenses can enhance the collection of of laser light that is emitted upwards from the facet of a nanowire laser, demonstrating a mediocre 25% improvement using a NA$=0.75$ objective lens
- Our simulations show that standard inverse taper PIC edge couplers might need significant redesign before GaN micro-lenses could improve alignment tolerances without inducing additional losses to a fibre-to-chip coupling interface. The index mismatch between the mainly cladding guided mode at the waveguide edge and the high-index GaN/AlGaN/AlN layer stack is a significant challenge in this respect
- We show that GaN micro-lenses can effectively focus the light output from a cleaved optical fibre facet at around 6 μm distance and enhance edge coupling to a SOI PIC if compared to the bare fibre. Commercially available tapered fibre facets can similarly achieve μm-sized working distance and spot size with a numerical aperture up to 0.4, and therefore the benefit of adding a even higher NA GaN micro-lens competes with the added Fresnel reflection losses due to the high index mismatch between GaN and silica

We conclude that GaN micro-lenses are able to interact with nanowire lasers, integrated and fibre-based waveguides over a wide wavelength range spanning the VIS to NIR spectral region. For the specific arrangements discussed in this Chapter we are not able to claim any significant optical benefits from the integration with GaN micro-lenses, but the mechanical print demonstrations inspire future systems design with semiconductor membrane devices in general.
Especially the deterministic micro assembly of heterogeneous material systems in complex geometries including air gapes and exceedingly low surface contact area on surfaces prepared by standard methods significantly advance transfer printing as a packaging method.

6 Summary and Outlook

In **Chapter 1** we have given a short introduction into the relevant concepts, including basic solid state physics and single photon sources, focusing on the high-band-gap semiconductors diamond and gallium nitride. The nitrogen vacancy centre in diamond is discussed as a promising colour centre for quantum applications and we shortly introduced the main problem that is targeted with this work: The extraction of light from solid state spin systems hosted in high index semiconductors, here approached by the fabrication high-index solid immersion lenses with high aspect ratio. We noted that this thesis generally fits into the technology space of miniaturized photonics.

In **Chapter 2** we have demonstrated that GaN thin films offer fabrication of highly spherical micro-lenses with high aspect ratio and excellent surface quality using inductively coupled plasma etching. This fabrication method allows for rapid scaling as parallel wafer-scale compatible micro-fabrication methods are used to create the lenses which stands in contrast to serial methods such as focused ion beam milling. We have shown that optimized grayscale lithography can be used to shape the resist template lens before ICP etching, leading to deviations from an ideal spherical lens profile on the order of 22 nm r.m.s. over the full GaN lens aperture while maintaining a r.m.s. surface roughness as low as 3 nm.
Moving to the GaN platform therefore eliminates the difficulty to create large arrays of high-aspect ratio micro-lenses in diamond without losing control of the lens shape and surface quality. The obvious cost of this approach is that we need to suspend the GaN micro-lens devices from their growth substrate to transfer them to diamond, which is usually performed in a serial manner. To mitigate the bottleneck of serial micro-lens placement we show the fabrication of GaN micro-lens arrays which improves the potential integration speed.

In **Chapter 3** we have seen that GaN micro-lenses can be suspended from their Si growth substrate with high yield, preserving the excellent surface quality and shape of the lenses after the donor fabrication is completed. We find that, after optimization of the etch depth and wafer bow, flat membrane devices with an atomically smooth bottom surface can be created and transferred to single crystalline diamond surfaces with PDMS-based transfer printing.
The optical properties of the lenses is found to agree well with the theoretical expectation and confirm that the heterogeneous integration method offers significant advantages over monolithic diamond micro-lens etching. To our knowledge this is the first demonstration of the integration of semiconductor micro-lenses with around 10 μm diameter and radius of curvature that are successfully shown to operate as micro-optical devices on a foreign receiver crystal.
Additionally we find that anchor or tether structures - especially if thinned - might prohibit good contact between the micro-optical membrane device and the receiver surface. A potential solution for this yield problem is the pick-up of anchor-free GaN micro-lens devices while the SiO_x mask is still present, mechanically stabilizing the devices. The final removal of the hard mask could then be conducted after printing release on diamond by exposure to a reactive ion etcher. Alternatively a quarter wavelength thick ($\approx$ 70 nm) high quality SiN_x/AlN_x layer could be applied to the GaN lens device before depositing the SiO_x hard mask. Then the SiO_x layer could be removed on the donor substrate after suspension while the SiN_x/AlN_x mask could mechanically stabilize the device till pick-up and then serve as an

anti-reflection coating further enhancing the micro-lens performance [229].
Future work might include the optimization of the scaling of GaN micro-lenses into membrane arrays, which has been started but not fully completed in this work. Remaining issues are the etch depth and wafer bow optimization in dependence of the created micro-optical element as well as the overall size of the membrane.

In **Chapter 4** we have investigated how GaN micro-lenses can be coupled to NV centres in diamond. We looked at NV clusters close to a planar diamond surface, emitter pairs in 5 μm depth and single emitters placed at the tip of diamond micropillars attached to scanning magnetometry probes. The main findings are:

- Optical microscopy based transfer printing in combination with confocal photoluminescence characterization allows for sub-micron accurate lateral printing of GaN micro-lenses on top of high-surface quality planar diamond substrates
- Grayscale preshaping in combination with resist reflow allows to fabricate GaN lenses with their radius of curvature matched to the emitter depth, here demonstrated in all three investigated NV configurations, meaning that we can match emitter and SILs in three spatial dimensions. Full grayscale lithography is not employed in combination with NV centres but the results shown in Chapter 2 indicate that it would increase the vertical dimension control further
- Depending on the numerical aperture we observe $\approx$ 2x-3x improvement of collection efficiency from NV centres in different configurations experimentally, with our simulations predicting that for objective lenses with NA $>$ 0.77 we can expect 4-6x improvement from the current GaN SIL architecture depending on the emitter depth and diamond crystal orientation
- In simulations we find that an increase of the GaN epilayer thickness to 4 μm would allow GaN micro-lenses to operate nearly on-par with monolithic diamond hemispheres if an objective lens with NA $\approx$ 0.77 is used, leading to 6-7x improvement in photon extraction efficiency
- Depending on the emitter configuration we find 1.2x-3x pump efficiency enhancement provided by the GaN SIL which is probably caused by a combination of increased system NA and mitigated spherical aberration at a planar diamond interface
- A significant amount of photoluminescence is emitted by the GaN SILs with spectral overlap with the NV^- emission characteristic. The emission puts a lower limit to the numerical aperture of the collection optics that can be employed depending on emitter depth. We estimate that an objective with NA $\approx$ 0.77 ($\approx$ 2 μm FWHM axial resolution) is sufficient to reject most PL counts from the GaN lenses by the confocal arrangement even for shallow emitters in $<$ 1 μm depth below a planar diamond
- GaN SILs can be combined with 1-2 NV emitters without significant deterioration of the photon purity in $g^{(2)}$ autocorrelation measurements and cooling of GaN micro-lens arrays to cryogenic temperatures without detachment or significant change of membrane bow indicates compatibility with typical experimental conditions in quantum computing and networking applications

- Integration of GaN SILs with scanning magnetormetry probes proves cumbersome and reasonable alignment is only achieved by adjusting the lens position with an AFM cantilever. Experimentally we find minimal count rate improvement around 1.1x-1.2x, potentially due to a thin layer of optical adhesive on top of the lens distorting the shape. Our simulations predict that the GaN lenses can increase photon collection up to 2x at NA$\approx$0.5 for the current state of the art commercial scanning probes, but the benefits are predicted to diminish if higher NA collection optics are used

From the work on scanning NV magnetometry we conclude that the use of GaN micro-lenses in this technology space is probably not worth the potential cost due to the significant integration challenge and relatively minor gain in terms of photon collection efficiency in this specific application space.
From the work presented in this Chapter we can see the potential for GaN micro-lenses to replace monolithic diamond hemispheres fabricated with focused ion beam milling in the realm of quantum computation and networking with diamond colour centres. For an effective and scalable platform the GaN epilayer thickness might be increased to 4 μm and large scale (4x4-16x16) ROC-matched highly spherical GaN micro-lens membrane arrays could be fabricated and printed onto highly pure single crystalline diamond membranes. The lens array could facilitate writing of diamond colour centres in shallow depth below the diamond surface while being automatically addressed to the lens centre position.
Significant remaining challenges are the development of high-quality shallow emitter writing in high purity single crystalline diamond substrates through the GaN SILs, the strain optimization after increase of the epilayer thickness and membrane size increase as well as the development of a 'parallel' confocal microscopy technique, potentially employing an array of pinholes. One might combine transfer printed GaN micro-lenses with the deposition of distributed Bragg mirrors on the lens surface and the diamond membrane backside to create local micro-cavities around each emitter to enhance the emission into the ZPL via the Purcell effect. Such rarge scale cavity-coupled diamond colour centre arrays could open the door towards future quantum computing and networking applications.
Further investigations of the strength of the GaN emission at cryogenic temperatures and in dependence of the excitation wavelength are remaining experimental tasks which could further enhance the ability of GaN micro-lenses to interact with NV^- centres. With other more red shifted colour centres such as the Si vacancy ($\lambda \approx 740$ nm [322]) the GaN emission might simply be removed by spectral filtering.

In **Chapter 5** we have looked at three challenging transfer print geometries using GaN micro-lenses as exemplary devices: 3D printing on photoresist support frames limiting the device contact area and therefore strength of the van-der-Waals bond, device transfer on cleaved and etched photonic integrated circuit facets with varying surface quality and finally micro-lens release on the tip of an optical fibre. In all cases we find that the transfer printing based integration (i) can be successful and (ii) can retain μm-precise alignment precision even without dedicated markers.
We can summarize the main optical results:

- GaN micro-lenses can enhance the collection of of laser light that is emitted upwards from the facet of a nanowire laser, demonstrating a mediocre 25% improvement using a NA = 0.75 objective lens

- Our simulations show that standard inverse taper PIC edge couplers might need significant redesign before GaN micro-lenses could improve alignment tolerances without inducing additional losses to a fibre-to-chip coupling interface. The index mismatch between the mainly cladding guided mode

at the waveguide edge and the high-index GaN/AlGaN/AlN layer stack is a significant challenge in this respect

- We show that GaN micro-lenses can effectively focus the light output from a cleaved optical fibre facet at around 6 μm distance and enhance edge coupling to a SOI PIC if compared to the bare fibre. Commercially available tapered fibre facets can similarly achieve μm-sized working distance and spot size with a numerical aperture up to 0.4, and therefore the benefit of adding a even higher NA GaN micro-lens competes with the added Fresnel reflection losses due to the high index mismatch between GaN and silica

From this Chapter we conclude that GaN micro-lenses are able to interact with nanowire lasers, integrated and fibre-based waveguides over a wide wavelength range spanning the VIS to NIR spectral region. For the specific arrangements discussed in this Chapter we are not able to claim any significant optical benefits from the integration with GaN micro-lenses, but the mechanical print demonstrations inspire future systems design with semiconductor membrane devices in general.
Especially the deterministic micro assembly of heterogeneous material systems in complex geometries including air gapes and exceedingly low surface contact area on surfaces prepared by standard methods significantly advance transfer printing as a packaging method.

We note that GaN is reported to host bright single colour centres emitting at room temperature when grown on sapphire substrates [323–326]. If high quality single defects would be found and could be engineered in GaN grown on Si, this might directly allow flexible transfer printing based integration of single photon sources with foreign receiver chips.
More generally the proposed direct transfer printing of solid state micro-optical elements could be extended to other material platforms such as SiC, which hosts high-quality colour centres on its own [327–333] and some demonstrations include optical spin read-out and coupling to nuclear spins in the environment [327, 328, 333, 334]. Additionally SiC is being supported by mature semiconductor manufacturing technology partially due to its use in high power electronics and for IC applications under harsh environmental conditions [335, 336].
Different polytypes of single crystalline SiC thin films have successfully been combined with Si wafers to create an integrated photonics platform, either with a SiO_2 BOX layer (SiC-on-insulator, for example achieved by wafer bonding and thinning of bulk SiC) or by suspending SiC devices fabricated from epitaxial thin films grown on Si by partial removal of the Si substrate [332, 337–342].
Such approaches could be extended to a form a μm thick SiC layer bonded on top of a sacrificial Si or SiO_2 layer for device transfer printing. Mature ICP based micro-lens fabrication is similarly available for SiC with reported demonstrations of nearly hemispherical lenses and 1:1 etch selectivity towards photoresist [343, 344].
Combining for example a SiC-on-insulator chip with micro-lens fabrication would easily allow the suspension of high quality lens devices using BOE wet etching for device suspension which does not attack SiC [345]. Thus hemispherical and transferable micro-lens platelets containing single emitters might be placed at target locations forming integrated single photon sources or qubits. This could additionally be combined with mirror coatings on both sides of the micro-lens platelet: The lens might be printed on a DBR mirror substrate while a lower reflectivity DBR is deposited on top of the SiC lens creating a plan-convex cavity design to access the qubit inside the SIL. Compared to an integrated

photonics approach the μm-scale distance from spin defects to device surfaces might deliver a significant advantage in terms of spin decoherence time.

Recently photoresist reflow on ultra-smooth substrates combined with ICP etching was demonstrated to act as highly miniaturized external cavities for laser linewidth stabilization [186, 346]. Building on these results, grayscale lithography might be combined with targeted reflow for resist smoothing to create transferable mirror devices with low surface roughness and controllable ROC. The GaN-on-Si architecture might be directly applicable for this technology space if a highly reflective DBR mirror coating can be deposited on the finalized device.

Instead of using GaN micro-lenses in combination with diamond, more effort could be taken to optimize a Si hard mask process reviewed in Chapter 2 [130, 190–192] to generate high quality hemispherical single crystalline diamond lenses with parallel ICP etch processing: To achieve this first anisotropic ICP etching with near 1:1 selectivity would need to be developed to create hemispherical Si lenses from hemispherical resist lenses shaped by grayscale lithography. Then these hemispherical Si lenses could be transferred into diamond while aiming for 1:1 etch selectivity and anisotropy to avoid micro-masking and shape distortions. Such a project might require access to Ar/Cl_2 ICP etching to create the Si lenses with sufficient quality (from test etches performed in this work), while $Ar/O_2/SF_6$ ICP etching seems most suitable for the Si-to-diamond transfer as reported in literature.

All in all this thesis contributed to the overall efforts towards miniaturization of photonics and system scaling by addressing the challenge of heterogeneous GaN micro-lens fabrication and integration with diamond colour centres. This work shows how versatile PDMS based transfer printing can be used to assemble micro-optical components at desired locations with high reliability if the surfaces are properly engineered and thus extends today's perspective on micro-system design.

A References

1. Fox, A. M. *Quantum optics: an introduction* (Oxford University Press, USA, 2006).
2. Novotny, L. & Hecht, B. *Principles of nano-optics* (Cambridge university press, 2012).
3. Sinzinger, S. & Jahns, J. *Microoptics* (John Wiley & Sons, 2006).
4. Ibach, H. & Lüth, H. *Solid-state physics: an introduction to principles of materials science* (Springer Science & Business Media, 2009).
5. Meschede, D. *Optics, light and lasers: the practical approach to modern aspects of photonics and laser physics* (John Wiley & Sons, 2017).
6. Demtröder, W. *Experimentalphysik 2* (Springer, 2004).
7. Doherty, M. W. *et al.* The nitrogen-vacancy colour centre in diamond. *Physics Reports* **528,** 1–45. arXiv: 1302.3288 (2013).
8. Reshchikov, M. A. Measurement and analysis of photoluminescence in GaN. *Journal of Applied Physics* **129** (2021).
9. Field, J. The mechanical and strength properties of diamond. *Reports on Progress in Physics* **75,** 126505 (2012).
10. Johnson, S., Dolan, P. R. & Smith, J. M. Diamond photonics for distributed quantum networks. *Progress in Quantum Electronics* **55,** 129–165 (2017).
11. Geis, M. W. *et al.* Progress toward diamond power field-effect transistors. *physica status solidi (a)* **215,** 1800681 (2018).
12. Inyushkin, A. V. *et al.* Thermal conductivity of high purity synthetic single crystal diamonds. *Physical Review B* **97,** 1–10 (2018).
13. Maclean, A. J. *et al.* Continuous tuning and efficient intracavity second-harmonic generation in a semiconductor disk laser with an intracavity diamond heatspreader. *IEEE Journal of Quantum Electronics* **44,** 216–225 (2008).
14. Coe, S. E. & Sussmann, R. S. Optical, thermal and mechanical properties of CVD diamond. *Diamond and Related Materials* **9,** 1726–1729 (2000).
15. Mollart, T. P., Lewis, K. L., Pickles, C. S. & Wort, C. J. Factors affecting the optical performance of CVD diamond infrared optics. *Semiconductor Science and Technology* **18** (2003).
16. *The element six CVD diamond handbook* tech. rep. (2020).
17. Aharonovich, I., Greentree, A. D. & Prawer, S. Diamond photonics. *Nature Photonics* **5,** 397–405 (2011).
18. Kim, D. *et al.* A CMOS-integrated quantum sensor based on nitrogen–vacancy centres. *Nature Electronics* **2,** 284–289 (2019).
19. Boretti, A., Rosa, L., Blackledge, J. & Castelletto, S. Nitrogen-vacancy centers in diamond for nanoscale magnetic resonance imaging applications. *Beilstein journal of nanotechnology* **10,** 2128–2151 (2019).

20. Hernández-Gómez, S. & Fabbri, N. Quantum control for nanoscale spectroscopy with diamond nitrogen-vacancy centers: a short review. *Frontiers in Physics* **8,** 610868 (2021).

21. Ho, K. O. *et al.* Diamond quantum sensors: From physics to applications on condensed matter research. *Functional Diamond* **1,** 160–173 (2022).

22. Xu, Y., Zhang, W. & Tian, C. Recent advances on applications of NV- magnetometry in condensed matter physics. *Photonics Research* **11,** 393–412 (2023).

23. Hausmann, B. J., Bulu, I., Venkataraman, V., Deotare, P. & Loncar, M. Diamond nonlinear photonics. *Nature Photonics* **8,** 369–374 (2014).

24. Zaitsev, A. M. *Optical properties of diamond: a data handbook* (Springer Science and Business Media, 2013).

25. Cui, J. M. *et al.* Generation of nitrogen-vacancy centers in diamond with ion implantation. *Chinese Physics Letters* **29** (2012).

26. Sangtawesin, S., Brundage, T. O., Atkins, Z. J. & Petta, J. R. Highly tunable formation of nitrogen-vacancy centers via ion implantation. *Applied Physics Letters* **105.** arXiv: 1407.1434 (2014).

27. Chu, Y. *et al.* Coherent optical transitions in implanted nitrogen vacancy centers. *Nano Letters* **14,** 1982–1986 (2014).

28. McLellan, C. A. *et al.* Patterned Formation of Highly Coherent Nitrogen-Vacancy Centers Using a Focused Electron Irradiation Technique. *Nano Letters* **16,** 2450–2454 (2016).

29. Chen, Y. C. *et al.* Laser writing of coherent colour centres in diamond. *Nature Photonics* **11,** 77–80 (2017).

30. Hadden, J. *et al.* Integrated waveguides and deterministically positioned nitrogen vacancy centers in diamond created by femtosecond laser writing. *Optics letters* **43,** 3586–3589 (2018).

31. Chen, Y. C. *et al.* Laser writing of scalable single color centers in silicon carbide. *Nano Letters* **19,** 2377–2383. eprint: 1812.04284 (2019).

32. Wang, X. J., Fang, H. H., Sun, F. W. & Sun, H. B. Laser Writing of Color Centers. *Laser and Photonics Reviews* **16,** 1–15 (2022).

33. Bachmann, P. K. *et al.* Diamond chemical vapor deposition: gas compositions and film properties. *MRS Online Proceedings Library* **339,** 267–277 (1994).

34. May, P. W. Diamond thin films: a 21st-century material. *Philosophical Transactions of the Royal Society of London. Series A: Mathematical, Physical and Engineering Sciences* **358,** 473–495 (2000).

35. Ferro, S. Synthesis of diamond. *Journal of Materials Chemistry* **12,** 2843–2855 (2002).

36. Yamada, H., Chayahara, A., Mokuno, Y., Tsubouchi, N. & Shikata, S.-i. Uniform growth and repeatable fabrication of inch-sized wafers of a single-crystal diamond. *Diamond and Related Materials* **33,** 27–31 (2013).

37. Kasu, M. Diamond epitaxy: Basics and applications. *Progress in Crystal Growth and Characterization of Materials* **62,** 317–328 (2016).

38. Schreck, M., Gsell, S., Brescia, R. & Fischer, M. Ion bombardment induced buried lateral growth: the key mechanism for the synthesis of single crystal diamond wafers. *Scientific reports* **7,** 44462 (2017).

39. Arnault, J.-C., Saada, S. & Ralchenko, V. Chemical vapor deposition single-crystal diamond: a review. *physica status solidi (RRL)–Rapid Research Letters* **16,** 2100354 (2022).

40. Schuelke, T. & Grotjohn, T. A. Diamond polishing. *Diamond and Related Materials* **32,** 17–26 (2013).

41. Doherty, M. W., Manson, N. B., Delaney, P. & Hollenberg, L. C. The negatively charged nitrogen-vacancy centre in diamond: the electronic solution. *New Journal of Physics* **13,** 025019 (2011).

42. Jelezko, F. & Wrachtrup, J. Single defect centres in diamond: A review. *Physica Status Solidi (A) Applications and Materials Science* **203,** 3207–3225 (2006).

43. Bradac, C., Gao, W., Forneris, J., Trusheim, M. E. & Aharonovich, I. Quantum nanophotonics with group IV defects in diamond. *Nature communications* **10,** 5625 (2019).

44. Debroux, R. *et al.* Quantum control of the tin-vacancy spin qubit in diamond. *Physical Review X* **11,** 041041 (2021).

45. Chen, D. *et al.* Quantum interference of resonance fluorescence from Germanium-vacancy color centers in diamond. *Nano Letters* **22,** 6306–6312 (2022).

46. Malykhin, S., Mindarava, Y., Ismagilov, R., Jelezko, F. & Obraztsov, A. Control of NV, SiV and GeV centers formation in single crystal diamond needles. *Diamond and Related Materials* **125,** 109007 (2022).

47. Ju, Z., Lin, J., Shen, S., Wu, B. & Wu, E. Preparations and applications of single color centers in diamond. *Advances in Physics: X* **6,** 1858721 (2021).

48. Ruf, M., Wan, N. H., Choi, H., Englund, D. & Hanson, R. Quantum networks based on color centers in diamond. *Journal of Applied Physics* **130** (2021).

49. Bernien, H. *Control, measurement and entanglement of remote quantum spin registers in diamond.* PhD thesis (Citeseer, 2014).

50. Beha, K., Batalov, A., Manson, N. B., Bratschitsch, R. & Leitenstorfer, A. Optimum photoluminescence excitation and recharging cycle of single nitrogen-vacancy centers in ultrapure diamond. *Physical review letters* **109,** 097404 (2012).

51. Gruber, A. *et al.* Scanning confocal optical microscopy and magnetic resonance on single defect centers. *Science* **276,** 2012–2014 (1997).

52. Alegre, T. P., Santori, C., Medeiros-Ribeiro, G. & Beausoleil, R. G. Polarization-selective excitation of nitrogen vacancy centers in diamond. *Physical Review B - Condensed Matter and Materials Physics* **76,** 1–5 (2007).

53. Togan, E. *et al.* Quantum entanglement between an optical photon and a solid-state spin qubit. *Nature* **466,** 730–734 (2010).

54. Jelezko, F., Gaebel, T., Popa, I., Gruber, A. & Wrachtrup, J. Observation of coherent oscillations in a single electron spin. *Physical Review Letters* **92,** 1–4 (2004).

55. Maletinsky, P. *et al.* A robust scanning diamond sensor for nanoscale imaging with single nitrogen-vacancy centres. *Nature Nanotechnology* **7,** 320–324 (2012).

56. De Lange, G., Wang, Z. H., Riste, D., Dobrovitski, V. V. & Hanson, R. Universal dynamical decoupling of a single solid-state spin from a spin bath. *Science* **330,** 60–64 (2010).

57. Bar-Gill, N., Pham, L. M., Jarmola, A., Budker, D. & Walsworth, R. L. Solid-state electronic spin coherence time approaching one second. *Nature Communications* **4.** arXiv: 1211.7094 (2013).

58. De Lange, G., Ristè, D., Dobrovitski, V. V. & Hanson, R. Single-spin magnetometry with multipulse sensing sequences. *Physical Review Letters* **106,** 1–4. arXiv: 1008.4395 (2011).

59. Phillip, H. R. & Taft, E. A. Kramers-Kronig analysis of reflectance data for diamond. *Physical Review* **136** (1964).

60. O'brien, J. L. Optical quantum computing. *Science* **318,** 1567–1570 (2007).

61. Prawer, S. & Aharonovich, I. *Quantum information processing with diamond: principles and applications* (Elsevier, 2014).

62. Pezzagna, S. & Meijer, J. Quantum computer based on color centers in diamond. *Applied Physics Reviews* **8** (2021).

63. Childress, L. & Hanson, R. Diamond NV centers for quantum computing and quantum networks. *MRS bulletin* **38,** 134–138 (2013).

64. Wehner, S., Elkouss, D. & Hanson, R. Quantum internet: A vision for the road ahead. *Science* **362,** eaam9288 (2018).

65. Nigam, T., Yiang, K.-Y. & Marathe, A. Moores law: Technology scaling and reliability challenges. *Microelectronics to Nanoelectronics: Materials, Devices & Manufacturability,* 1 (2012).

66. Pelucchi, E. *et al.* The potential and global outlook of integrated photonics for quantum technologies. *Nature Reviews Physics* **4,** 194–208 (2022).

67. Bogdanov, S., Shalaginov, M. Y. Boltasseva, A. & Shalaev, V. M. Material platforms for integrated quantum photonics. *Optical Materials Express* **7,** 111–132. arXiv: 1609.02851 (2017).

68. Bogaerts, W. *et al.* Programmable photonic circuits. *Nature* **586,** 207–216 (2020).

69. Liang, D & Bowers, J. Photonic integration: Si or InP substrates? *Electronics Letters* **45,** 578–581 (2009).

70. Miller, S. E. Integrated optics: An introduction. *The Bell System Technical Journal* **48,** 2059–2069 (1969).

71. Marcatili, E. A. Dielectric rectangular waveguide and directional coupler for integrated optics. *The Bell System Technical Journal* **48,** 2071–2102 (1969).

72. Gaeta, A. L., Lipson, M. & Kippenberg, T. J. Photonic-chip-based frequency combs. *nature photonics* **13,** 158–169 (2019).

73. Moody, G., Chang, L., Steiner, T. J. & Bowers, J. E. Chip-scale nonlinear photonics for quantum light generation. *AVS Quantum Science* **2** (2020).

74. Kish, F. *et al.* System-on-chip photonic integrated circuits. *IEEE Journal of Selected Topics in Quantum Electronics* **24,** 1–20 (2017).

75. Hu, H. & Oxenløwe, L. K. Chip-based optical frequency combs for high-capacity optical communications. *Nanophotonics* **10,** 1367–1385 (2021).

76. Liu, Y. *et al.* Silicon photonic transceivers in the field of optical communication. *Nano Communication Networks* **31,** 100379 (2022).

77. Xu, Y. *et al.* Optical refractive index sensors with plasmonic and photonic structures: promising and inconvenient truth. *Advanced Optical Materials* **7,** 1801433 (2019).

78. Karabchevsky, A., Katiyi, A., Ang, A. S. & Hazan, A. On-chip nanophotonics and future challenges. *Nanophotonics* **9,** 3733–3753 (2020).

79. Steglich, P., Lecci, G. & Mai, A. Surface plasmon resonance (SPR) spectroscopy and photonic integrated circuit (PIC) biosensors: A comparative review. *Sensors* **22,** 2901 (2022).

80. Zhou, Z. *et al.* Prospects and applications of on-chip lasers. *Elight* **3,** 1–25 (2023).

81. Nielsen, M. A. & Chuang, I. L. Quantum information and quantum computation. *Cambridge: Cambridge University Press* **2,** 23 (2000).

82. Knill, E., Laflamme, R. & Milburn, G. J. A scheme for efficient quantum computation with linear optics. *Nature* **409,** 46–52 (2001).

83. Koshiba, T. Quantum cryptography. *Handbook of Natural Computing* **3-4,** 1521–1543 (2012).

84. Neumann, P. *et al.* High-precision nanoscale temperature sensing using single defects in diamond. *Nano Letters* **13,** 2738–2742. arXiv: 1304.0688 (2013).

85. Grinolds, M. S. *et al.* Nanoscale magnetic imaging of a single electron spin under ambient conditions. *Nature Physics* **9,** 215–219. arXiv: 1209.0203 (2013).

86. Carolan, J. *et al.* Universal linear optics. *Science* **349,** 711–716 (2015).

87. Hassija, V. *et al.* Present landscape of quantum computing. *IET Quantum Communication* **1,** 42–48 (2020).

88. Signorini, S & Pavesi, L. On-chip heralded single photon sources. *AVS Quantum Science* **2** (2020).

89. Blumenthal, D. J. Photonic integration for UV to IR applications. *APL Photonics* **5** (2020).

90. Zhu, D. *et al.* Integrated photonics on thin-film lithium niobate. *Advances in Optics and Photonics* **13,** 242–352 (2021).

91. Smith, J., Jevtics, D, Guilhabert, B, Dawson, M. & Strain, M. Hybrid integration of chipscale photonic devices using accurate transfer printing methods. *Applied Physics Reviews* **9** (2022).

92. Chang, L. *et al.* Second order nonlinear photonic integrated platforms for optical signal processing. *IEEE Journal of Selected Topics in Quantum Electronics* **27,** 1–11 (2020).

93. Wan, N. H. *et al.* Large-scale integration of artificial atoms in hybrid photonic circuits. *Nature* **583,** 226–231 (2020).

94. Schrinner, P. P., Olthaus, J., Reiter, D. E. & Schuck, C. Integration of diamond-based quantum emitters with nanophotonic circuits. *Nano Letters* **20,** 8170–8177 (2020).

95. Wessling, N. K. *et al.* Fabrication and transfer printing based integration of free-standing GaN membrane micro-lenses onto semiconductor chips. *Optical Materials Express* **12,** 4606. arXiv: 2208.05275 (2022).

96. Duparré, J. & Wippermann, F. Micro-optical artificial compound eyes. *Bioinspiration & biomimetics* **1,** R1 (2006).

97. Voelkel, R. Wafer-scale micro-optics fabrication. *Advanced Optical Technologies* **1,** 135–150 (2012).

98. Yuan, W., Li, L.-H., Lee, W.-B. & Chan, C.-Y. Fabrication of microlens array and its application: a review. *Chinese Journal of Mechanical Engineering* **31,** 1–9 (2018).

99. Voelkel, R. & Weible, K. J. *Laser beam homogenizing: limitations and constraints* in *Optical Fabrication, Testing, and Metrology III* **7102** (2008), 222–233.

100. Stevens, R. & Miyashita, T. Review of standards for microlenses and microlens arrays. *The Imaging Science Journal* **58,** 202–212 (2010).

101. Douglas A. Baillie, J. E. G. Zero-space microlenses for CMOS image sensors: optical modeling and lithographic process development. *Optical Microlithography* **XVII** (2004).

102. Braeuer, A., Dannberg, P., Zeitner, U., Mann, G. & Karthe, W. Application oriented complex polymer microoptics. *Microsystem Technologies* **9,** 304–307 (2003).

103. Choi, H. W., Gu, E., Girkin, J. M. & Dawson, M. D. Nitride micro-display with integrated microlenses. *Physica Status Solidi C: Conferences* **2,** 2903–2906 (2005).

104. Marchetti, R., Lacava, C., Carroll, L., Gradkowski, K. & Minzioni, P. Coupling strategies for silicon photonics integrated chips [Invited]. *Photonics Research* **7,** 201 (2019).

105. Bogucki, A. *et al.* Ultra-long-working-distance spectroscopy of single nanostructures with aspherical solid immersion microlenses. *Light: Science and Applications* **9,** 1–11 (2020).

106. Voelkel, R. Wafer-scale micro-optics fabrication. *Advanced Optical Technologies* **1,** 135–150 (2012).

107. Moharana, A. R., Außerhuber, H. M., Mitteramskogler, T., Haslinger, M. J. & Mühlberger, M. M. Multilayer nanoimprinting to create hierarchical stamp masters for nanoimprinting of optical micro-and nanostructures. *Coatings* **10** (2020).

108. Cai, S. *et al.* Microlenses arrays: Fabrication, materials, and applications. *Microscopy Research and Technique* **84,** 2784–2806 (2021).

109. Gissibl, T., Thiele, S., Herkommer, A. & Giessen, H. Two-photon direct laser writing of ultracompact multi-lens objectives. *Nature Photonics* **10,** 554–560 (2016).

110. Dietrich, P. I. *et al.* In situ 3D nanoprinting of free-form coupling elements for hybrid photonic integration. *Nature Photonics* **12,** 241–247. arXiv: 1802.00051 (2018).

111. Gehring, H., Eich, A., Schuck, C. & Pernice, W. H. P. Broadband out-of-plane coupling at visible wavelengths. *Optics Letters* **44,** 5089 (2019).

112. Oder, T. N., Shakya, J., Lin, J. Y. & Jiang, H. X. Nitride microlens arrays for blue and ultraviolet wavelength applications. *Applied Physics Letters* **82,** 3692–3694 (2003).

113. Choi, H. W. *et al.* Fabrication of natural diamond microlenses by plasma etching. *Journal of Vacuum Science and Technology B: Microelectronics and Nanometer Structures* **23,** 130–132 (2005).

114. Sardi, F *et al.* Scalable production of solid-immersion lenses for quantum emitters in silicon carbide. *Applied Physics Letters* **117** (2020).

115. Zolfaghari, A., Chen, T. & Yi, A. Y. Additive manufacturing of precision optics at micro and nanoscale. *International Journal of Extreme Manufacturing* **1** (2019).

116. Fischer, A. C., Mäntysalo, M. & Niklaus, F. in *Handbook of Silicon Based MEMS Materials and Technologies* 531–545 (2020).

117. NanoScribe GmbH & Co. KG. *https://www.nanoscribe.com/en/products/ip-resins* 2022.

118. Self-consistent optical parameters of intrinsic silicon at 300 K including temperature coefficients. *Solar Energy Materials and Solar Cells* **92,** 1305–1310 (2008).

119. Xu, C. *et al.* Temperature dependence of refractive indices for 4H- and 6H-SiC. *Journal of Applied Physics* **115,** 2–5 (2014).

120. Barker, A. S. & Ilegems, M. Infrared lattice vibrations and free-electron dispersion in GaN. *Physical Review B* **7,** 743–750 (1973).

121. Pastrnak, J & Roskovcova, L. Refraction index measurements on AlN single crystals. *Physica Status Solidi (B)* **14** (1966).

122. Gonzalez-Hernandez, D., Varapnickas, S., Bertoncini, A., Liberale, C. & Malinauskas, M. Micro-Optics 3D Printed via Multi-Photon Laser Lithography. *Advanced Optical Materials* **11,** 2201701 (2023).

123. Hadden, J. *et al.* Strongly enhanced photon collection from diamond defect centers under microfabricated integrated solid immersion lenses. *Applied Physics Letters* **97,** 241901 (2010).

124. Marseglia, L. *et al.* Nanofabricated solid immersion lenses registered to single emitters in diamond. *Applied Physics Letters* **98,** 3–5. arXiv: 1012.1135 (2011).

125. Jamali, M. *et al.* Microscopic diamond solid-immersion-lenses fabricated around single defect centers by focused ion beam milling. *Review of Scientific Instruments* **85,** 123703 (2014).

126. Presby, H. M., Benner, A. F. & Edwards, C. A. Laser micromachining of efficient fiber microlenses. *Applied Optics* **29,** 2692 (1990).

127. Hao, B. *et al.* Versatile route to gapless microlens arrays using laser-tunable wet-etched curved surfaces. *Optics Express* **20,** 12939 (2012).

128. Gu, E. *et al.* Reflection/transmission confocal microscopy characterization of single-crystal diamond microlens arrays. *Applied Physics Letters* **84,** 2754–2756 (2004).

129. Lee, C. L., Gu, E., Dawson, M. D., Friel, I. & Scarsbrook, G. A. Etching and micro-optics fabrication in diamond using chlorine-based inductively-coupled plasma. *Diamond and Related Materials* **17,** 1292–1296 (2008).

130. Zhang, Y. *et al.* Demonstration of diamond microlens structures by a three-dimensional (3D) dual-mask method. *Optics Express* **25,** 15572 (2017).

131. To, S., Zhu, Z. & Wang, H. Virtual spindle based tool servo diamond turning of discontinuously structured microoptics arrays. *CIRP Annals - Manufacturing Technology* **65,** 475–478 (2016).

132. Mukaida, M. & Yan, J. Fabrication of hexagonal microlens arrays on single-crystal silicon using the tool-servo driven segment turning method. *Micromachines* **8** (2017).

133. Dietrich, P.-I. *et al.* In situ 3D nanoprinting of free-form coupling elements for hybrid photonic integration. *Nature Photonics* **12,** 241–247 (2018).

134. Preuß, J. A. *et al.* Low-divergence hbn single-photon source with a 3D-printed low-fluorescence elliptical polymer microlens. *Nano Letters* **23,** 407–413 (2022).

135. Hite, J. *et al.* Development of periodically oriented gallium nitride for non-linear optics. *Optical Materials Express* **2,** 1203–1208 (2012).

136. Boyd, G., Coldren, L. & Storz, F. Directional reactive ion etching at oblique angles. *Applied Physics Letters* **36,** 583–585 (1980).

137. Latawiec, P., Burek, M. J., Sohn, Y.-I. & Lončar, M. Faraday cage angled-etching of nanostructures in bulk dielectrics. *Journal of Vacuum Science & Technology B* **34** (2016).

138. Burek, M. J. *et al.* Free-standing mechanical and photonic nanostructures in single-crystal diamond. *Nano letters* **12,** 6084–6089 (2012).

139. Jeon, S.-W. *et al.* Bright nitrogen-vacancy centers in diamond inverted nanocones. *Acs Photonics* **7,** 2739–2747 (2020).

140. Khanaliloo, B., Mitchell, M., Hryciw, A. C. & Barclay, P. E. High-Q/V monolithic diamond microdisks fabricated with quasi-isotropic etching. *Nano letters* **15,** 5131–5136 (2015).

141. Mouradian, S., Wan, N. H., Schröder, T. & Englund, D. Rectangular photonic crystal nanobeam cavities in bulk diamond. *Applied Physics Letters* **111** (2017).

142. Barclay, P. *Diamond nano-optomechanical devices* in *Diamond Photonics-Physics, Technologies and Applications* (2019), 127.

143. Mitchell, M., Lake, D. P. & Barclay, P. E. Realizing Q> 300 000 in diamond microdisks for optomechanics via etch optimization. *Apl Photonics* **4** (2019).

144. Rugar, A. E. *et al.* Narrow-linewidth tin-vacancy centers in a diamond waveguide. *ACS Photonics* **7,** 2356–2361 (2020).

145. Kuruma, K. *et al.* Coupling of a single tin-vacancy center to a photonic crystal cavity in diamond. *Applied Physics Letters* **118** (2021).

146. Zohari, E. *et al. Optomechanical Crystal Nanobeam Cavities in Single Crystal Diamond* in *2022 IEEE Photonics Conference (IPC)* (2022), 1–2.

147. Trindade, A. *et al.* Nanoscale-accuracy transfer printing of ultra-thin AlInGaN light-emitting diodes onto mechanically flexible substrates. *Applied Physics Letters* **103** (2013).

148. Sekiya, T., Sasaki, T. & Hane, K. Design, fabrication, and optical characteristics of freestanding GaN waveguides on silicon substrate. *Journal of Vacuum Science & Technology B* **33** (2015).

149. Bruch, A. W. *et al.* Electrochemically sliced low loss AlGaN optical microresonators. *Applied Physics Letters* **110** (2017).

150. Li, Z. *et al.* Photonic integration of lithium niobate micro-ring resonators onto silicon nitride waveguide chips by transfer-printing. *Optical Materials Express* **12,** 4375–4383 (2022).

151. Liu, L & Edgar, J. H. Substrates for gallium nitride epitaxy. *Materials Science and Engineering: R: Reports* **37,** 61–127 (2002).

152. Pal, S. & Jacob, C. Silicon - A new substrate for GaN growth. *Bulletin of Materials Science* **27,** 501–504 (2004).

153. Ghosh, S. *et al.* Design of step-graded AlGaN buffers for GaN-on-Si heterostructures grown by MOCVD. *Semiconductor Science and Technology* **38** (2023).

154. Jones, A. Metalorganic precursors for vapour phase epitaxy. *Journal of crystal growth* **129,** 728–773 (1993).

155. Amano, H., Sawaki, N, Akasaki, I & Toyoda, Y. Metalorganic vapor phase epitaxial growth of a high quality GaN film using an AlN buffer layer. *Applied Physics Letters* **48,** 353–355 (1986).

156. Ishikawa, H *et al.* High-Quality GaN on Si Substrate Using AlGaN/AlN Intermediate Layer. *physica status solidi (a)* **176,** 599–603 (1999).

157. Chen, K. J. *et al.* GaN-on-Si power technology: Devices and applications. *IEEE Transactions on Electron Devices* **64,** 779–795 (2017).

158. Ng, T. K. *et al.* Group-III-nitride and halide-perovskite semiconductor gain media for amplified spontaneous emission and lasing applications. *Journal of Physics D: Applied Physics* **54,** 143001 (2021).

159. Li, L. *et al.* Efficient photon collection from a nitrogen vacancy center in a circular bullseye grating. *Nano letters* **15,** 1493–1497 (2015).

160. Djalalian-Assl, A. *Dipole emission to surface plasmon-coupled enhanced transmission in diamond substrates with nitrogen vacancy center-near the surface* in *Photonics* **4** (2017), 10.

161. Andersen, S. K. *et al.* Hybrid plasmonic bullseye antennas for efficient photon collection. *Acs Photonics* **5,** 692–698 (2018).

162. Wan, N. H. *et al.* Efficient extraction of light from a nitrogen-vacancy center in a diamond parabolic reflector. *Nano letters* **18,** 2787–2793 (2018).

163. Babinec, T. M. *et al.* A diamond nanowire single-photon source. *Nature nanotechnology* **5,** 195–199 (2010).

164. Barclay, P. E., Santori, C., Fu, K.-M., Beausoleil, R. G. & Painter, O. Coherent interference effects in a nano-assembled diamond NV center cavity-QED system. *Optics Express* **17,** 8081 (2009).

165. Johnson, S. *et al.* Tunable cavity coupling of the zero phonon line of a nitrogen-vacancy defect in diamond. *New Journal of Physics* **17,** 122003 (2015).

166. Gould, M., Schmidgall, E. R., Dadgostar, S., Hatami, F. & Fu, K.-M. C. Efficient extraction of zero-phonon-line photons from single nitrogen-vacancy centers in an integrated gap-on-diamond platform. *Physical Review Applied* **6,** 011001 (2016).

167. Sipahigil, A. *et al.* An integrated diamond nanophotonics platform for quantum-optical networks. *Science* **354,** 847–850 (2016).

168. Dolan, P. R. *et al.* Robust, tunable, and high purity triggered single photon source at room temperature using a nitrogen-vacancy defect in diamond in an open microcavity. *Optics Express* **26,** 7056 (2018).

169. Janitz, E., Bhaskar, M. K. & Childress, L. Cavity quantum electrodynamics with color centers in diamond. *Optica* **7,** 1232–1252 (2020).

170. Marseglia, L *et al.* Nanofabricated solid immersion lenses registered to single emitters in diamond. *Applied Physics Letters* **98,** 133107 (2011).

171. Rogers, L. J. *et al.* Multiple intrinsically identical single-photon emitters in the solid state. *Nature Communications* **5,** 1–2. arXiv: 1310.3804 (2014).

172. Jiang, Q. *et al.* Focused-ion-beam overlay-patterning of three-dimensional diamond structures for advanced single-photon properties. *Journal of Applied Physics* **116,** 044308 (2014).

173. Wang, X. *et al.* Electrical control of coherent spin rotation of a single-spin qubit. *npj Quantum Information* **6** (2020).

174. Knauer, S., Hadden, J. P. & Rarity, J. G. In-situ measurements of fabrication induced strain in diamond photonic-structures using intrinsic colour centres. *npj Quantum Information* **6,** 2–7 (2020).

175. McKenzie, W. R., Quadir, M. Z., Gass, M. & Munroe, P. Focused ion beam implantation of diamond. *Diamond and Related Materials* **20,** 1125–1128 (2011).

176. Abobeih, M. *et al.* Fault-tolerant operation of a logical qubit in a diamond quantum processor. *Nature* **606,** 884–889 (2022).

177. Pompili, M. *et al.* Realization of a multinode quantum network of remote solid-state qubits. *Science* **372,** 259–264 (2021).

178. Popovic, Z. D., Sprague, R. A. & Neville Connell, G. A. Technique for monolithic fabrication of microlens arrays. *Applied Optics* **27,** 1281 (1988).

179. Daly, D., Stevens, R. F., Hutley, M. C. & Davies, N. The manufacture of microlenses by melting photoresist. *Measurement Science and Technology* **1,** 759–766 (1990).

180. Kang, S. Replication technology for micro/nano optical components. *Japanese Journal of Applied Physics* **43,** 5706 (2004).

181. Kirchner, R. & Schift, H. Thermal reflow of polymers for innovative and smart 3D structures: A review. *Materials Science in Semiconductor Processing* **92,** 58–72 (2019).

182. Kim, T. *et al. A fabrication of GaN micro-lens* in *1997 Digest of the IEEE/LEOS Summer Topical Meeting: Vertical-Cavity Lasers/Technologies for a Global Information Infrastructure/WDM Components Technology/Advanced Semiconductor Lasers and Application* (1997), 54–55.

183. Gu, E *et al. Bifocal and negative microlens arrays in hard optical materials* in *The 17th Annual Meeting of the IEEELasers and Electro-Optics Society, 2004. LEOS 2004.* **1** (2004), 360–361.

184. Lee, C., Dawson, M. & Gu, E. Diamond double-sided micro-lenses and reflection gratings. *Optical Materials* **32,** 1123–1129 (2010).

185. Liu, H., Herrnsdorf, J., Gu, E. & Dawson, M. D. Control of edge bulge evolution during photoresist reflow and its application to diamond microlens fabrication. *Journal of Vacuum Science & Technology B* **34** (2016).

186. Jin, N. *et al.* Scalable fabrication of ultrahigh-finesse micromirrors with variable geometry. *arXiv e-prints,* arXiv–2203 (2022).

187. C.L. Lee. *Dissertation on Micro-lenses* PhD thesis (2010).

188. Liu, H. *Diamond processing for advanced photonic devices* PhD thesis (University of Strathcylde, 2016).

189. Li, Y., Zhang, Y., Liu, L. & Yang, C. Diamond micro-lenses with variable height using self-assembly silica-microsphere-monolayer as etching mask. *Materials Today Communications* **11,** 119–122 (2017).

190. Li, L. *et al.* Nanofabrication on unconventional substrates using transferred hard masks. *Scientific reports* **5,** 7802 (2015).

191. Li, L., Schröder, T., Chen, E. H., Bakhru, H. & Englund, D. One-dimensional photonic crystal cavities in single-crystal diamond. *Photonics and Nanostructures-Fundamentals and Applications* **15,** 130–136 (2015).

192. Bayn, I *et al.* Fabrication of triangular nanobeam waveguide networks in bulk diamond using single-crystal silicon hard masks. *Applied Physics Letters* **105** (2014).

193. Franz, G. *Low pressure plasmas and microstructuring technology* 517–557 (2009).

194. Ottevaere, H. *et al.* Comparing glass and plastic refractive microlenses fabricated with different technologies. *Journal of Optics A: Pure and Applied Optics* **8,** S407 (2006).

195. Aikens, D. M. *Meaningful surface roughness and quality tolerances* in *International Optical Design Conference* (2010), ITuD3.

196. Linghu, C., Zhang, S., Wang, C. & Song, J. Transfer printing techniques for flexible and stretchable inorganic electronics. *npj Flexible Electronics* **2,** 26 (2018).

197. Kim, J.-H., Aghaeimeibodi, S., Carolan, J., Englund, D. & Waks, E. Hybrid integration methods for on-chip quantum photonics. *Optica* **7,** 291–308 (2020).

198. Kaur, P. *et al.* Hybrid and heterogeneous photonic integration. *APL Photonics* **6** (2021).

199. Kim, J.-H. *et al.* Hybrid integration of solid-state quantum emitters on a silicon photonic chip. *Nano letters* **17,** 7394–7400 (2017).

200. Splitthoff, L. J. *et al.* Gate-tunable kinetic inductance in proximitized nanowires. *Physical Review Applied* **18,** 024074 (2022).

201. Kim, S., Liu, N. & Shestopalov, A. A. Contact Printing of multilayered thin films with shape memory polymers. *ACS nano* **16,** 6134–6144 (2022).

202. Choi, M. *et al.* Stretchable active matrix inorganic light-emitting diode display enabled by overlay-aligned roll-transfer printing. *Advanced Functional Materials* **27,** 1606005 (2017).

203. Wang, Y. *et al.* Programmable micro-transfer-printing for heterogeneous material integration. *AIP Advances* **12** (2022).

204. Ismail, N. & Ferreira, P. M. Active elastomeric composite dense array stamp for micro-transfer printing. *Procedia Manufacturing* **48,** 64–70 (2020).

205. Li, L. *et al.* Coherent spin control of a nanocavity-enhanced qubit in diamond. *Nature communications* **6,** 6173 (2015).

206. Kou, R. *et al.* Inter-layer light transition in hybrid III-V/Si waveguides integrated by μ-transfer printing. *Optics Express* **28,** 19772–19782 (2020).

207. Wang, C. *et al.* Programmable and scalable transfer printing with high reliability and efficiency for flexible inorganic electronics. *Science advances* **6,** eabb2393 (2020).

208. Wu, Y., Ma, J., Su, P., Zhang, L. & Xia, B. Full-color realization of micro-LED displays. *Nanomaterials* **10,** 2482 (2020).

209. Zhou, X. *et al.* Growth, transfer printing and colour conversion techniques towards full-colour micro-LED display. *Progress in Quantum Electronics* **71,** 100263 (2020).

210. Meitl, M. A. *et al.* Transfer printing by kinetic control of adhesion to an elastomeric stamp. *Nature materials* **5,** 33–38 (2006).

211. Feng, X. *et al.* Competing fracture in kinetically controlled transfer printing. *Langmuir* **23,** 12555–12560 (2007).

212. Novoselov, K. S. *et al.* Electric field effect in atomically thin carbon films. *science* **306,** 666–669 (2004).

213. Castellanos-Gomez, A. Why all the fuss about 2D semiconductors? *Nature Photonics* **10,** 202–204 (2016).

214. Woods, L. *et al.* Materials perspective on Casimir and van der Waals interactions. *Reviews of Modern Physics* **88,** 045003 (2016).

215. Nikolić, H. Proof that Casimir force does not originate from vacuum energy. *Physics Letters B* **761,** 197–202 (2016).

216. Izadi, H., Stewart, K. M. & Penlidis, A. Role of contact electrification and electrostatic interactions in gecko adhesion. *Journal of the Royal Society Interface* **11,** 20140371 (2014).

217. Ahmed, N., Dagdeviren, C., Rogers, J. A. & Ferreira, P. M. Active polymeric composite membranes for localized actuation and sensing in microtransfer printing. *Journal of Microelectromechanical Systems* **24,** 1016–1028 (2014).

218. Jevtics, D. *et al.* Spatially dense integration of micron-scale devices from multiple materials on a single chip via transfer-printing. *Optical Materials Express* **11,** 3567–3576 (2021).

219. McPhillimy, J. *et al.* Automated Nanoscale Absolute Accuracy Alignment System for Transfer Printing. *ACS Applied Nano Materials* **3,** 10326–10332 (2020).

220. Trindade, A. *et al.* Heterogeneous integration of gallium nitride light-emitting diodes on diamond and silica by transfer printing. *Optics express* **23,** 9329–9338 (2015).

221. Rae, K. *et al.* InGaN μLEDs integrated onto colloidal quantum dot functionalized ultra-thin glass. *Optics Express* **25,** 19179–19184 (2017).

222. Rae, K. *et al.* Transfer-printed micro-LED and polymer-based transceiver for visible light communications. *Optics Express* **26,** 31474–31483 (2018).

223. Li, L. *et al.* Heterogeneous integration of microscale GaN light-emitting diodes and their electrical, optical, and thermal characteristics on flexible substrates. *Advanced Materials Technologies* **3,** 1700239 (2018).

224. Ghosh, S. *et al.* Design of step-graded AlGaN buffers for GaN-on-Si heterostructures grown by MOCVD. *Semiconductor Science and Technology* **38,** 044001 (2023).

225. Hsueh, C.-H. Modeling of elastic deformation of multilayers due to residual stresses and external bending. *Journal of Applied physics* **91,** 9652–9656 (2002).

226. Spiridon, B. *et al.* Method for inferring the mechanical strain of GaN-on-Si epitaxial layers using optical profilometry and finite element analysis. *Optical Materials Express* **11,** 1643–1655 (2021).

227. Ghosh, S. *et al.* Origin(s) of Anomalous Substrate Conduction in MOVPE-Grown GaN HEMTs on Highly Resistive Silicon. *ACS Applied Electronic Materials* **3,** 813–824 (2021).

228. Fairclough, S. *et al. Direct evidence of an Al alloyed SiNx interlayer within an ammonia predosed AlN/Si interface via STEM-EELS* in *Proceedings of Electron Beam Spectroscopy for Nanooptics 2021 (EBSN2021)* (2021).

229. Yeung, T., Le Sage, D, Pham, L. M., Stanwix, P. & Walsworth, R. L. Anti-reflection coating for nitrogen-vacancy optical measurements in diamond. *Applied Physics Letters* **100** (2012).

230. Baranski, M. *et al.* A simple method for quality evaluation of micro-optical components based on 3D IPSF measurement. *Optics Express* **22,** 13202 (2014).

231. Franzen, A. *http://www.gwoptics.org/ComponentLibrary/* 2022.

232. Laws, G. M., Larkins, E. C., Harrison, I., Molloy, C. & Somerford, D. Improved refractive index formulas for the AlxGa1-xN and InyGa1-yN alloys. *Journal of Applied Physics* **89,** 1108–1115 (2001).

233. Demtröder, W. *Experimentalphysik 2 - Elektrizität und Optik* (2009).

234. Nussbaum, P., Völkel, R., Herzig, H. P., Eisner, M. & Haselbeck, S. Design, fabrication and testing of microlens arrays for sensors and microsystems. *Pure and Applied Optics (Print edition) (United Kingdom)* **6,** 617–636 (1997).

235. Kim, M.-S., Scharf, T. & Herzig, H. P. Small-size microlens characterization by multiwavelength high-resolution interference microscopy. *Optics Express* **18,** 14319 (2010).

236. Lee, G. J., Kim, H. M. & Song, Y. M. Design and Fabrication of Microscale, Thin-Film Silicon Solid Immersion Lenses for Mid-Infrared Application. *Micromachines* **11** (2020).

237. Kurtsiefer, C., Zarda, P., Mayer, S. & Weinfurter, H. The breakdown flash of silicon avalanche photodiodes-back door for eavesdropper attacks? *Journal of Modern Optics* **48,** 2039–2047 (2001).

238. Cheng, X. *et al.* Additive GaN solid immersion lenses for enhanced photon extraction efficiency from diamond color centers. *ACS photonics* (2023).

239. Knight, P. & Walmsley, I. UK national quantum technology programme. *Quantum Science and Technology* **4,** 040502 (2019).

240. Acín, A. *et al.* The quantum technologies roadmap: a European community view. *New Journal of Physics* **20,** 080201 (2018).

241. Pfaff, W. *et al.* Demonstration of entanglement-by-measurement of solid-state qubits. *Nature Physics* **9,** 29–33 (2013).

242. Robledo, L. *et al.* High-fidelity projective read-out of a solid-state spin quantum register. *Nature* **477,** 574–578 (2011).

243. Kimble, H. J. The quantum internet. *Nature* **453,** 1023–1030 (2008).

244. Ghosh, S. *et al.* Origin (s) of anomalous substrate conduction in MOVPE-Grown GaN HEMTs on highly resistive silicon. *ACS Applied Electronic Materials* **3,** 813–824 (2021).

245. Simmonds, R. D., Salter, P. S., Jesacher, A. & Booth, M. J. Three dimensional laser microfabrication in diamond using a dual adaptive optics system. *Optics express* **19,** 24122–24128 (2011).

246. Griffiths, B. *et al.* Microscopic processes during ultrafast laser generation of Frenkel defects in diamond. *Physical Review B* **104,** 174303 (2021).

247. Stephen, C. *et al.* Deep three-dimensional solid-state qubit arrays with long-lived spin coherence. *Physical Review Applied* **12,** 064005 (2019).

248. Baba, M., Sasaki, T., Yoshita, M. & Akiyama, H. Aberrations and allowances for errors in a hemisphere solid immersion lens for submicron-resolution photoluminescence microscopy. *Journal of applied physics* **85,** 6923–6925 (1999).

249. Paskov, P. *et al.* Emission properties of a-plane GaN grown by metal-organic chemical-vapor deposition. *Journal of Applied Physics* **98** (2005).

250. Christen, I. *et al.* An integrated photonic engine for programmable atomic control. *arXiv preprint arXiv:2208.06732* (2022).

251. Brown, R. H. & Twiss, R. Q. LXXIV. A new type of interferometer for use in radio astronomy. *The London, Edinburgh, and Dublin Philosophical Magazine and Journal of Science* **45,** 663–682 (1954).

252. Maze, J. R. *et al.* Nanoscale magnetic sensing with an individual electronic spin in diamond. *Nature* **455,** 644–647 (2008).

253. Berthel, M. *et al.* Photophysics of single nitrogen-vacancy centers in diamond nanocrystals. *Physical Review B - Condensed Matter and Materials Physics* **91,** 1–13. arXiv: 1501.03714 (2015).

254. Gruber, A *et al.* Scanning confocal optical microscopy and magnetic resonance on single defect centers. *Science* **276,** 2012–2014 (1997).

255. Siyushev, P *et al.* Monolithic diamond optics for single photon detection. *Applied physics letters* **97,** 241902 (2010).

256. Zwiller, V. & Björk, G. Improved light extraction from emitters in high refractive index materials using solid immersion lenses. *Journal of Applied Physics* **92,** 660–665 (2002).

257. McPhillimy, J. *et al.* High accuracy transfer printing of single-mode membrane silicon photonic devices. *Optics Express* **26,** 16679–16688 (2018).

258. McPhillimy, J. *et al.* Automated nanoscale absolute accuracy alignment system for transfer printing. *ACS applied nano materials* **3,** 10326–10332 (2020).

259. Margariti, E. *et al. Continuous roller transfer-printing and automated metrology of> 75,000 micro-LED pixels in a single shot* 2023.

260. Yurgens, V. *et al.* Low-charge-noise nitrogen-vacancy centers in diamond created using laser writing with a solid-immersion lens. *ACS Photonics* **8,** 1726–1734 (2021).

261. Balasubramanian, G. *et al.* Nanoscale imaging magnetometry with diamond spins under ambient conditions. *Nature* **455,** 648–651 (2008).

262. Maletinsky, P. *et al.* A robust scanning diamond sensor for nanoscale imaging with single nitrogen-vacancy centres. *Nature nanotechnology* **7,** 320–324 (2012).

263. Rondin, L *et al.* Nanoscale magnetic field mapping with a single spin scanning probe magnetometer. *Applied Physics Letters* **100** (2012).

264. Momenzadeh, S. A. *et al.* Nanoengineered diamond waveguide as a robust bright platform for nanomagnetometry using shallow nitrogen vacancy centers. *Nano Letters* **15,** 165–169 (2015).

265. Radtke, M., Bernardi, E., Slablab, A., Nelz, R. & Neu, E. Nanoscale sensing based on nitrogen vacancy centers in single crystal diamond and nanodiamonds: achievements and challenges. *Nano Futures* **3,** 042004 (2019).

266. Rohner, D *et al.* (111)-oriented, single crystal diamond tips for nanoscale scanning probe imaging of out-of-plane magnetic fields. *Applied Physics Letters* **115** (2019).

267. Barry, J. F. *et al.* Sensitivity optimization for NV-diamond magnetometry. *Reviews of Modern Physics* **92.** arXiv: 1903.08176 (2020).

268. Hedrich, N., Rohner, D., Batzer, M., Maletinsky, P. & Shields, B. J. Parabolic diamond scanning probes for single-spin magnetic field imaging. *Physical Review Applied* **14,** 064007 (2020).

269. Scholten, S. C. *et al.* Widefield quantum microscopy with nitrogen-vacancy centers in diamond: Strengths, limitations, and prospects. *Journal of Applied Physics* **130,** 1–22. arXiv: 2108.06060 (2021).

270. Ibrahim, M. I., Foy, C., Englund, D. R. & Han, R. High-scalability CMOS quantum magnetometer with spin-state excitation and detection of diamond color centers. *IEEE Journal of Solid-State Circuits* **56,** 1001–1014 (2020).

271. Abrahams, G. *et al.* An integrated widefield probe for practical diamond nitrogen-vacancy microscopy. *Applied Physics Letters* **119** (2021).

272. Schloss, J. M., Barry, J. F., Turner, M. J. & Walsworth, R. L. Simultaneous broadband vector magnetometry using solid-state spins. *Physical Review Applied* **10,** 034044 (2018).

273. Edelstein, A. Advances in magnetometry. *Journal of Physics Condensed Matter* **19** (2007).

274. Edelstein, A. *et al.* Advances in magnetometry through miniaturization. *Journal of Vacuum Science and Technology A: Vacuum, Surfaces, and Films* **26,** 757–762 (2008).

275. Hirohata, A., Samiepour, M. & Corbetta, M. in *Electrical Atomic Force Microscopy for Nanoelectronics* 231–265 (Springer, 2019).

276. Mamin, H. J., Rugar, D, Chui, B. W. & Budakian, R. Single spin detection by magnetic resonance force microscopy. *Nature* **430,** 329–332 (2004).

277. Qnami. *Quantilever MX data sheet* tech. rep. November (2021).

278. Qnami. *Quantilever MX+ data sheet* tech. rep. November (2022).

279. Taylor, J. M. *et al.* High-sensitivity diamond magnetometer with nanoscale resolution. *Nature Physics* **4,** 810–816 (2008).

280. Fabre, F *et al.* Characterization of room-temperature in-plane magnetization in thin flakes of Cr Te 2 with a single-spin magnetometer. *Physical Review Materials* **5,** 034008 (2021).

281. Finco, A. *et al.* Imaging topological defects in a noncollinear antiferromagnet. *Physical Review Letters* **128,** 187201 (2022).

282. Misonou, D. *et al.* Construction and operation of a tabletop system for nanoscale magnetometry with single nitrogen-vacancy centers in diamond. *AIP Advances* **10** (2020).

283. Suter, K. *et al. Tuning Fork AFM with Conductive Cantilever* in *AIP Conference Proceedings* **696** (2003), 227–233.

284. Guo, M. *et al.* A flexible nitrogen-vacancy center probe for scanning magnetometry. *Review of Scientific Instruments* **92** (2021).

285. Fuchs, P., Challier, M. & Neu, E. Optimized single-crystal diamond scanning probes for high sensitivity magnetometry. *New Journal of Physics* **20,** 125001 (2018).

286. Brouri, R., Beveratos, A., Poizat, J.-P. & Grangier, P. Photon antibunching in the fluorescence of individual color centers in diamond. *Optics letters* **25,** 1294–1296 (2000).

287. Beveratos, A., Brouri, R., Gacoin, T., Poizat, J.-P. & Grangier, P. Nonclassical radiation from diamond nanocrystals. *Physical Review A* **64,** 061802 (2001).

288. Zhang, J. L. *et al.* Complete coherent control of silicon vacancies in diamond nanopillars containing single defect centers. *Optica* **4,** 1317–1321 (2017).

289. Brouri, R., Beveratos, A., Poizat, J.-P. & Grangier, P. Single-photon generation by pulsed excitation of a single dipole. *Physical Review A* **62,** 063817 (2000).

290. Beveratos, A., Brouri, R., Poizat, J.-P. & Grangier, P. in *Quantum Communication, Computing, and Measurement 3* 261–267 (Springer, 2002).

291. Kitson, S., Jonsson, P, Rarity, J. & Tapster, P. Intensity fluctuation spectroscopy of small numbers of dye molecules in a microcavity. *Physical Review A* **58,** 620 (1998).

292. Basché, T., Moerner, W., Orrit, M & Talon, H. Photon antibunching in the fluorescence of a single dye molecule trapped in a solid. *Physical review letters* **69,** 1516 (1992).

293. Guilhabert, B. *et al.* Advanced Transfer Printing With In-Situ Optical Monitoring for the Integration of Micron-Scale Devices. *IEEE Journal of Selected Topics in Quantum Electronics* **29,** 1–11 (2022).

294. Yan, R., Gargas, D. & Yang, P. Nanowire photonics. *Nature photonics* **3,** 569–576 (2009).

295. Couteau, C., Larrue, A., Wilhelm, C. & Soci, C. Nanowire lasers. *Nanophotonics* **4,** 90–107 (2015).

296. Johnson, J. C. *et al.* Single nanowire lasers. *The Journal of Physical Chemistry B* **105,** 11387–11390 (2001).

297. Johnson, J. C. *et al.* Single gallium nitride nanowire lasers. *Nature materials* **1,** 106–110 (2002).

298. Vanmaekelbergh, D. & Van Vugt, L. K. ZnO nanowire lasers. *Nanoscale* **3,** 2783–2800 (2011).

299. Ma, Y., Guo, X., Wu, X., Dai, L. & Tong, L. Semiconductor nanowire lasers. *Advances in optics and photonics* **5,** 216–273 (2013).

300. Eaton, S. W., Fu, A., Wong, A. B., Ning, C.-Z. & Yang, P. Semiconductor nanowire lasers. *Nature reviews materials* **1,** 1–11 (2016).

301. Gao, Q. *et al.* Selective-area epitaxy of pure wurtzite InP nanowires: high quantum efficiency and room-temperature lasing. *Nano letters* **14,** 5206–5211 (2014).

302. Guilhabert, B. *et al.* Transfer printing of semiconductor nanowires with lasing emission for controllable nanophotonic device fabrication. *ACS nano* **10,** 3951–3958 (2016).

303. Jevtics, D. *et al.* Integration of semiconductor nanowire lasers with polymeric waveguide devices on a mechanically flexible substrate. *Nano Letters* **17,** 5990–5994 (2017).

304. Xu, W.-Z. *et al.* Vertically emitting indium phosphide nanowire lasers. *Nano letters* **18,** 3414–3420 (2018).

305. Jevtics, D. *et al.* Characterization, selection, and microassembly of nanowire laser systems. *Nano Letters* **20,** 1862–1868 (2020).

306. Almeida, V. R., Panepucci, R. R. & Lipson, M. Nanotaper for compact mode conversion. *Optics letters* **28,** 1302–1304 (2003).

307. Mu, X., Wu, S., Cheng, L. & Fu, H. Edge couplers in silicon photonic integrated circuits: A review. *Applied Sciences* **10,** 1538 (2020).

308. Scarcella, C. *et al.* Pluggable single-mode fiber-array-to-PIC coupling using micro-lenses. *IEEE Photonics Technology Letters* **29,** 1943–1946 (2017).

309. Gehring, H *et al.* Low-loss fiber-to-chip couplers with ultrawide optical bandwidth. *APL Photonics* **4** (2019).

310. Lindenmann, N *et al.* Photonic wire bonding: a novel concept for chip-scale interconnects. *Optics express* **20,** 17667–17677 (2012).

311. Lindenmann, N. *et al.* Connecting silicon photonic circuits to multicore fibers by photonic wire bonding. *Journal of lightwave Technology* **33,** 755–760 (2014).

312. Gehring, H., Eich, A., Schuck, C. & Pernice, W. H. Broadband out-of-plane coupling at visible wavelengths. *Optics letters* **44,** 5089–5092 (2019).

313. Yu, S. *et al.* Free-Form Micro-Optics Enabling Ultra-Broadband Low-Loss Off-Chip Coupling. *Laser & Photonics Reviews,* 2200025 (2023).

314. Carlson, D. R. *et al.* Ultrafast electro-optic light with subcycle control. *Science* **361,** 1358–1363 (2018).

315. Octave-Photonics. *Supercontinuum-Generation Devices* tech. rep. (2022).

316. Kostovski, G., Stoddart, P. R. & Mitchell, A. The optical fiber tip: an inherently light-coupled microscopic platform for micro-and nanotechnologies. *Advanced Materials* **26,** 3798–3820 (2014).

317. Xiong, Y. & Xu, F. Multifunctional integration on optical fiber tips: challenges and opportunities. *Advanced Photonics* **2,** 064001–064001 (2020).

318. Gissibl, T., Thiele, S., Herkommer, A. & Giessen, H. Sub-micrometre accurate free-form optics by three-dimensional printing on single-mode fibres. *Nature Communications* **7,** 11763 (2016).

319. Smythe, E. J., Dickey, M. D., Whitesides, G. M. & Capasso, F. A technique to transfer metallic nanoscale patterns to small and non-planar surfaces. *ACS nano* **3,** 59–65 (2009).

320. Schroder, T., Schell, A. W., Kewes, G., Aichele, T. & Benson, O. Fiber-integrated diamond-based single photon source. *Nano letters* **11,** 198–202 (2011).

321. Wang, B. *et al.* Transfer printing and nanomanipulating luminescent photonic crystal membrane nanocavities. *Journal of Applied Physics* **111** (2012).

322. Pingault, B. *et al.* Coherent control of the silicon-vacancy spin in diamond. *Nature communications* **8,** 15579 (2017).

323. Berhane, A. M. *et al.* Bright room-temperature single-photon emission from defects in gallium nitride. *Advanced Materials* **29,** 1605092 (2017).

324. Zhou, Y. *et al.* Room temperature solid-state quantum emitters in the telecom range. *Science advances* **4,** eaar3580 (2018).

325. Nguyen, M. *et al.* Effects of microstructure and growth conditions on quantum emitters in gallium nitride. *APL Materials* **7,** 081106 (2019).

326. Bishop, S. *et al.* Enhanced light collection from a gallium nitride color center using a near index-matched solid immersion lens. *Applied Physics Letters* **120,** 114001 (2022).

327. Lohrmann, A., Johnson, B., McCallum, J. & Castelletto, S. A review on single photon sources in silicon carbide. *Reports on Progress in Physics* **80,** 034502 (2017).

328. Radulaski, M. *et al.* Scalable quantum photonics with single color centers in silicon carbide. *Nano letters* **17,** 1782–1786 (2017).

329. Wang, J. *et al.* Bright room temperature single photon source at telecom range in cubic silicon carbide. *Nature communications* **9,** 4106 (2018).

330. Widmann, M. *et al.* Bright single photon sources in lateral silicon carbide light emitting diodes. *Applied Physics Letters* **112** (2018).

331. Chen, Y.-C. *et al.* Laser writing of individual nitrogen-vacancy defects in diamond with near-unity yield. *Optica* **6,** 662–667 (2019).

332. Lukin, D. M. *et al.* 4H-silicon-carbide-on-insulator for integrated quantum and nonlinear photonics. *Nature Photonics* **14,** 330–334 (2020).

333. Mu, Z. *et al.* Coherent manipulation with resonant excitation and single emitter creation of nitrogen vacancy centers in 4H silicon carbide. *Nano letters* **20,** 6142–6147 (2020).

334. Bourassa, A. *et al.* Entanglement and control of single nuclear spins in isotopically engineered silicon carbide. *Nature Materials* **19,** 1319–1325 (2020).

335. Wang, J. *et al.* ICP etching of SiC. *Solid-State Electronics* **42,** 2283–2288 (1998).

336. Hossain, T. K. *et al.* The fabrication of suspended micromechanical structures from bulk 6H-SiC using an ICP-RIE system. *Journal of Micromechanics and Microengineering* **16,** 751 (2006).

337. Di Cioccio, L, Le Tiec, Y, Letertre, F, Jaussaud, C & Bruel, M. Silicon carbide on insulator formation using the Smart Cut process. *Electronics Letters* **32,** 1144–1145 (1996).

338. Calusine, G., Politi, A. & Awschalom, D. D. Silicon carbide photonic crystal cavities with integrated color centers. *Applied Physics Letters* **105** (2014).

339. Martini, F. & Politi, A. Linear integrated optics in 3C silicon carbide. *Optics express* **25,** 10735–10742 (2017).

340. Ko, S.-D., Hamelin, B., Yang, J. & Ayazi, F. *High-Q monocrystalline silicon carbide disk resonators fabricated using drie of thick SiC-on-insulator substrates* in *2018 IEEE Micro Electro Mechanical Systems (MEMS)* (2018), 996–999.

341. Garrisi, F., Chatzopoulos, I., Cernansky, R. & Politi, A. Silicon carbide photonic platform based on suspended subwavelength waveguides. *JOSA B* **37,** 3453–3460 (2020).

342. Wang, Y., Lin, Q. & Feng, P. X.-L. Single-crystal 3C-SiC-on-insulator platform for integrated quantum photonics. *Optics Express* **29,** 1011–1022 (2021).

343. Sardi, F *et al.* Scalable production of solid-immersion lenses for quantum emitters in silicon carbide. *Applied Physics Letters* **117,** 022105 (2020).

344. Bekker, C. *et al.* Scalable fabrication of hemispherical solid immersion lenses in silicon carbide through grayscale hard-mask lithography, 1–9. arXiv: 2301.07705 (2023).

345. Johnson, M., Zvanut, M. & Richardson, O. HF chemical etching of SiO 2 on 4H and 6H SiC. *Journal of Electronic Materials* **29,** 368–371 (2000).

346. Guo, J. *et al.* Chip-based laser with 1-hertz integrated linewidth. *Science advances* **8,** eabp9006 (2022).

347. Spierings, G. Wet chemical etching of silicate glasses in hydrofluoric acid based solutions. *Journal of Materials science* **28,** 6261–6273 (1993).

348. Tanaka, H., Takeda, M. & Sato, K. Si (100) and (110) etching properties in 5, 15, 30 and 48 wt% KOH aqueous solution containing Triton-X-100. *Microsystem Technologies* **23,** 5343–5350 (2017).

349. Pal, P. *et al.* High speed silicon wet anisotropic etching for applications in bulk micromachining: a review. *Micro and Nano Systems Letters* **9,** 1–59 (2021).

350. Weyher, J. *et al.* Chemical etching of GaN in KOH solution: role of surface polarity and prior photoetching. *The Journal of Physical Chemistry C* **126,** 1115–1124 (2022).

351. Mileham, J. *et al.* Patterning of AlN, InN, and GaN in KOH-based solutions. *Journal of Vacuum Science & Technology A: Vacuum, Surfaces, and Films* **14,** 836–839 (1996).

352. Ni, H., Lee, H.-J. & Ramirez, A. G. A robust two-step etching process for large-scale microfabricated SiO2 and Si3N4 MEMS membranes. *Sensors and Actuators A: Physical* **119,** 553–558 (2005).

353. Rinke, T. & Koch, C. *Photolithography - Basics of microstructuring* (MicroChemicals, 2017).

354. Direct Laser Writing. *KNMF Laboratory for Micro- and Nanostructuring (KIT)* (2023).

355. Schumacher, U. Basics of plasma physics. *Plasma Physics: Confinement, Transport and Collective Effects,* 1–20 (2005).

356. Pearton, S., Shul, R. & Ren, F. A review of dry etching of GaN and related materials. *Materials Research Society Internet Journal of Nitride Semiconductor Research* **5,** e11 (2000).

357. Pearton, S. J., Douglas, E. A., Shul, R. J. & Ren, F. Plasma etching of wide bandgap and ultrawide bandgap semiconductors. *Journal of Vacuum Science & Technology A* **38** (2020).

358. Khanaliloo, B., Mitchell, M., Hryciw, A. C. & Barclay, P. E. High-Q/V monolithic diamond microdisks fabricated with quasi-isotropic etching. *Nano Letters* **15,** 5131–5136 (2015).

359. Khan, F. A. & Adesida, I. High rate etching of SiC using inductively coupled plasma reactive ion etching in SF6-based gas mixtures. *Applied Physics Letters* **75,** 2268–2270 (1999).

360. Ryu, J. H., Byoung Hoon Kim & Sung Jin Yoon. *Characterization of thin carbonized photoresist layer and investigation of dry strip process through real-time monitored variable temperature control* in *28th Annual SEMI Advanced Semiconductor Manufacturing Conference (ASMC)* (IEEE, 2017), 102–106.

361. Martinu, L. & Poitras, D. Plasma deposition of optical films and coatings: A review. *Journal of Vacuum Science & Technology A: Vacuum, Surfaces, and Films* **18,** 2619–2645 (2000).

362. Blateyron, F. *Introduction to stylus profilometers* 2022.

363. Hill, P. *Heterogenous integration of diamond with non-native substrates* PhD thesis (University of Strathclyde, 2019).

364. MikroMash. *HQ:NSC15/Al BS* 2023.

365. Nanosensors. *SSS-NCH* 2023.

366. Purcell, E. M. Spontaneous emission probabilities at radio frequencies. *Physical Review B* **69,** 681 (1946).

367. Faraon, A., Barclay, P. E., Santori, C., Fu, K. M. C. & Beausoleil, R. G. Resonant enhancement of the zero-phonon emission from a colour centre in a diamond cavity. *Nature Photonics* **5,** 301–305. arXiv: 1012.3815 (2011).

368. Liu, J. & Tan, J. *Confocal microscopy* (Morgan & Claypool Publishers, 2016).

369. McConnell, G., Amos, W. & Wilson, T. Confocal microscopy (2011).

370. Hadfield, R. H. Single-photon detectors for optical quantum information applications. *Nature photonics* **3,** 696–705 (2009).

371. Izhnin, I. I. *et al.* Single-photon avalanche diode detectors based on group IV materials. *Applied Nanoscience,* 1–11 (2022).

372. ID Quantique SA. *Photon counting for brainies* 2021.

373. ID Quantique SA. *ID120 Visible Single-Photon Detector Datasheet* 2021.

374. Giese, C., Quellmalz, P. & Knittel, P. Development of All-Diamond Scanning Probes Based on Faraday Cage Angled Etching Techniques. *MRS Advances* **5,** 1899–1907 (2020).

B Acknowledgement

I am extremely thankful for the great support I received throughout my PhD. The University of Strathclyde and the Institute of Photonics in particular will always remain places of tremendous personal growth stimulated by the many challenges that I was exposed to.
First and foremost I want to thank Prof. Michael Strain, he has been a great role model and would always make time for discussions. I admire him for his hard and passionate working ethic that combined with his brilliance and organizational skills makes him such a tremendously effective person. I know few people that take on so much responsibility. It was a great pleasure to work with you and it was lovely to meet your fantastic family!
I was very lucky to be additionally supervised by a visionary technologist, Prof. Martin Dawson. He initiated the GaN micro-lens work with a small comment and I am very happy that I followed up on his targeted and even subtle advice. Simply by observing him I learned a lot about the art of leading people in a polite and soft spoken manner. Thank you especially for highlighting the DocDoc conference, I am sure it will be great fun.
I enjoyed many interactions with my Fraunhofer supervisor Loyd McKnight, including a great trip to Germany visiting the Fraunhofer institutes IAF in Freiburg and HHI in Berlin as well as our shared participation at the Fraunhofer event 'Futuras in Res' together with Simon Andrews. Loyd has a special place in my heart and his bold, practical and creative approach to work and as it seems life have inspired me. Thank you for your example!
From my coworkers I want to specially thank Sean Bommer, Eleni Magariti, Dimitars Jevtics and Jack Smith. You all have accompanied me on the full journey of my PhD and I feel very connected to all of you. Thank you Sean for all the great little chats and for opening my horizon in terms of systems development, thank you Eleni for all our great conversations, thank you Dimitars for taking care of me and your bold example and thank you Jack for your witty humour. I enjoyed working with all of you very much.
I want to thank Matej Hejda for his friendship and example of a highly effective and passionate researcher. Thank you Emma Butt for your clean room expertise and friendliness. I want to thank Lucia Caspani for our lovely chats and moral support. I thank Yunzhou Cheng for his approachable and caring behaviour in the clean room that has helped so many of us! I thank Enyuan Xie for his boldness and expertise.
Special thanks go to Jim Sweeney and Ronny Rogers, our clean room technicians over the years. When I heard that Jim would leave the department I started to cry in the clean room! You both have supported my work tremendously with your fight against entropy. My salute!
Similarly special thanks to Sharon and Lorraine who keep the institute running. You are both such lovely people and you contribute a lot to the IOP family feeling!
I want to thank all the other members of our group, especially Zhibo Li, Elise Burns and Adnan, the members of the Institute of Photonics and coworkers at Fraunhofer UK. This special environment has facilitated my personal growth and has given me a very wide range of opportunities, especially for the great conversations which I had with so many of you.
My final thanks go to my mother, father, sister and wife Henrike. What you have done for me over the years fills me with gratitude and I deeply love you. My father passed away during my PhD which has shaped me in many ways. I love you dad.

C Copyright Statement

This thesis is the result of the author's original research. It has been composed by the author and has not been previously submitted for examination which has led to the award of a degree.

Date: 15/10/2023 Signed: Nils Kolja Freier

D Microfabrication methods

In this section we are going to look at the different clean-room based micro-fabrication methods employed in this thesis. After ISO norm 14644-1:2015 a clean room is a 'room within which the number concentration of airborne particles is controlled and classified, and which is designed, constructed and operated in a manner to control the introduction, generation and retention of particles inside the room.' Microfabrication refers to the layer-by-layer removal or addition of thin films consisting of materials such as semiconductors, metals and organics at targeted locations defined by lithographic patterns forming functional device architectures (electronic, photonic, mechanical etc.) along the chip surface. Due to this layer based processing and the micrometer size and distances of for example wires or waveguides on a microchip, airborne dust particles can severely affect the process yield. They might for example physically shield the deposition of a metal contact layer on several transistors and therefore destroy their functionality. The airflow in the clean room facility used in this work was directed outwards from each room (positive pressure generated by filtered air) to avoid airborne travel of particles from outside of the clean room. The clean room is commissioned with class 10,000 (ISO 7) meaning 10,000 particles/cubic foot of size $> 0.5\,\mu$m are permitted after ISO norm.
The main semiconductor substrates used for this thesis are HPHT single crystalline diamond (SCD) substrates overgrown by CVD prepared by the Fraunhofer Instituite for Solid State Physics in Freiburg (IAF) with a size of roughly 4x4x0.5 mm, commercially available cut and polished CVD SCD membranes from Element6 [16], with 2x2 mm lateral size and $30\,\mu$m thickness and ultra low nitrogen concentration (< 5 ppb), and GaN thin films grown on 1 mm thick 6 inch slightly n-doped Si wafers ($10^{13} - 10^{16}$ 1/cm^3 carrier concentration, likely phosphor) with the epilayer thickness ranging between 2.2 and $4\,\mu$m. Commercially available 4 inch Si wafers in (100) orientation (1-sided polishing, n-doping with phosphor, 1-10 Ohm/cm resistivity) were used as carrier wafers for dry etching, witness samples and resist reflow test pieces. Cover glass slides are either borosilicate or Schott D 263 M glass with thickness ranging between 100-200 μm. In the following we will refer to each substrate and how it is handled. A rectangular cut from a wafer is commonly referred to as a die and the lateral cutting process is called dicing.

D.1 Sample preperation, cleaning and wet chemical etching

We are quickly going to look into different steps to prepare the substrates in the right size for manual handling and at typical surface cleaning procedures to remove foreign particles from the substrate before processing as well as removing previously deposited or spin coated thin films. We will also discuss the wet chemical etching of Si which is heavily used in this work to suspend GaN-on-Si membrane devices. A useful resource for standard process parameters of solvents, resists and wet etchants can be found on the website 'microchemicals.com'.

D.1.1 Cleaving

4 inch Si-(100) wafers are cleaved with metal tweezers from the backside of the wafer generating rectangular dies with sizes ranging between 10x10 - 25x25 mm^2. For processing thick photoresist a

size of at least 15x15 mm^2 is recommended to avoid resist bulging at the edge of the chip to affect the device performance (any kind of substrate).

D.1.2 Wafer saw

The 6 inch 1 mm thick GaN-on-Si wafers used in this work are received in quarters with the [110] direction marked by a notch (this is the direction in which a potassium hydroxide wet etch laterally removes Si with around 1 μm/min). To avoid potential damage to the wafer during a manual cleaving process the clean room technician cut them into regular 15x15 mm^2 dies using the 'DAD3220 Disco Automatic Wafer Saw'.

D.1.3 Cleaning with organic solvents

To remove accumulated particles the sample is cleaned immediately before processing (for example spin coating). For a well precleaned surface that is stored in a clean room cabinet it is usually sufficient to employ a standard cleaning procedure by placing the sample 5 min in acetone, 5 min in methanol and 5 min in isopropanol (IPA) in an ultrasonic bath with subsequent drying under N_2 flow.
Non-critical samples are loaded together on a sample tray and dipped from one solvent into the other, while for high-quality cleaning each sample is placed in its own beaker, diluting the solution 3x with the next solvent between applying the ultrasonic bath. Acetone is the strongest solvent, while methanol and isopropanol are supposedly mostly used to remove potential residues from the previously applied solvent, respectively. If samples are to be spin coated, the sample is then placed 10 min on a hotplate at > 100°C (real surface temperature) to evaporate water residues to enhance the resist adhesion to the surface.
The same standard solvent clean can also be used to remove photoresist after a dry etching or a failed photolithography process resetting the surface.

D.1.4 Acid cleaning and etching

Acid and base wet etching are powerful techniques to dissolve semiconductor materials in a controlled manner. We will discuss a few of such chemical etches in the following.
Self-heating **piranha solution** is used to clean diamond surfaces from any organic residues left after Scaife or chemical mechanical (CMP) polishing procedures: 20 min in 30 ml 95-98 % sulphuric acid H_2SO_4 aqueous solution mixed with 10 ml $>$ 30 % hydrogen peroxide H_2O_2 aqueous solution, yielding $\approx 80-85$°C after mixing in a PTFE beaker. If well cut and polished diamond membranes are cleaned in such a way, they can be transferred to a small solvent cleaned Si die using an IPA drained clean room cloth or a vacuum pipette.
Premixed **buffered oxide etch (BOE)** (HF:NH_4F 1:7 ratio, 12.5 % HF weight) is used to remove silica glass hard masks in a controlled manner. The etch rate depends on the quality of the SiO_x with around 80 nm/min (21°C) expected for high quality films [347]. The SiO_x used in this thesis (deposited by plasma enhanced chemical vapour deposition (PECVD) in house, see below) usually yielded much faster etch rates with sometimes whole areas delaminating which indicates a low film quality. Etching through photoresist (Microposit SPR220-7.0) windows is found to be slowly terminating even though a surfactant is present in the mixture.

The lateral removal of Si in an anisotropic wet **potassium hydroxide (KOH)** etch is of crucial importance for this work. Standard process conditions are: 26.6 g KOH pallets are dissolved in 40 ml water (yielding 40 % in weight) at 85 ± 3°C in a heated water bath. The water is prewarmed when adding pallets and a stir magnet is used at 200-300 rpm to continuously mix the solution. Lateral etching along the [110] crystal direction of Si-(111) substrates is exploited to create suspended GaN/AlGaN/AlN membranes. Usually the lateral etch rate under typical conditions is around 1 μm/min in reasonable agreement with literature [348]. The etch rate here might depend on the height and orientation of the exposed Si (110) plane and might be additionally delayed by a SiO_x layer. Si is also effectively etched along the (100) plane with similar speed leading to pyramidal etch shapes for Si wafer with a (100) surface orientation [348, 349]. GaN/AlGaN/AlN membrane devices are also getting attacked by the KOH solution [350, 351] and are generally protected by a layer of PECVD SiO_x which dissolves with around 60-70 nm/min etch rate, which is 6-7x higher what would be expected from a higher quality plasma deposited SiO_2 film [352]. We also tested in-house deposited SiN_x as hard mask which showed good resistance to the KOH in agreement to literature [352], but seemed to be too porous to act as a protective layer.

D.1.5 Matrix plasma asher

The 'Matrix 105 Plasma Asher Descum' is used for photoresist removal or for surface activation of cover glass substrates to promote the adhesion between the glass and SU8 photoresist. An oxygen plasma discharge is created and reactive radical species diffuse to the target wafer or die removing organic resists with etch rates of around 1 μm/min. The applied process conditions are 3.75 Torr pressure, MFC1= 35 % and 500 W RF power and a substrate temperature of $T_S = 250$°C.

D.1.6 Oxygen barrel asher

A barrel plasma asher (Diener Pico) is used for removal of the optical adhesive Norland 61 by direct exposure to a weak O2 plasma on an unheated sample stage.

D.2 UV photolithography

Binary photolithography refers to the patterning of an organic thin film called photoresist by exposure to UV light and successive removal of the exposed (positive resist) or unexposed (negative resist) film areas by placing the die in a liquid developer solution. The patterned photoresist is then used to mask areas of the sample during successive plasma or wet chemical exposure for material removal (etch mask) or deposition (lift-off, not used in this work). Grayscale lithography refers to the partial removal of the resist film as a function of lateral position leading to 3D polymer shapes that can be transferred into the semiconductor. In the following we will go through the steps employed to pattern substrates with the most important photoresist thin films used in this work. A description of useful techniques for successful microstructuring using photolithography can be found in [353] which is used as a general reference in this subsection.

D.2.1 Spin coating

Spin coating describes the process of spreading a diluted and thus less viscous photoresist on top of a clean die or wafer surface by quickly rotating the substrate so that centrifugal forces flatten the applied resist bubble into a thin film of desired thickness. The resist dries during the spinning process, becoming more viscous over time and finally reaching a steady state. The final film thickness can be tuned by changing the amount of solvent in the resist before application or the time characteristic of the spin.
In this work the spin is started after the resist bubble is applied and the spin coaters are used with an open lid. The resists Microposit SPR220-4.5 and SPR220-7.0 are poured from the bottle into small plastic beakers and then applied on the die filling the full substrate with a thick bubble, while Microposit S1805 is applied from a syringe with a 0.2 μm pore sized filter and SU8-2002 is applied using a syringe with 0.45 μm filter.
Generally a thinner resist film can lead to higher resolution patterns due to minimal spread of diffracted light in the film and quick development time and therefore low dark erosion of unexposed areas. Due to the high aspect ratio of the micro-lens membrane structures created in this work, mainly thick photoresist films with 4-7 μm thickness were used (Microposit SPR220). With such highly viscous resist a bulge tends to form at the edge of the substrate after spinning, preventing ideal contact with lithography masks. Mask-less photolithography is therefore here advantages. This edge bulge also prevents the use of the full surface of the semiconductor chip, making it particularly challenging to fabricate devices on small substrates such as the SC diamonds used in this thesis.
After spinning the photoresist thin film is baked on a hotplate (soft bake) to remove remaining solvent that would deteriorate the adhesion and resist contrast. In thick photoresist films rehydration periods using the ambient humidity are adopted immediately before and/or after UV exposure to stabilize the development time for repeatable results. This is even more important because the mask-less laser writing lithography method widely employed in this work exposes the resist in a sequential manner. With insufficient rehydration of the film this is found to lead to spatially varying development speed on the sample, something especially undesirable for the gray scale lithography techniques we are going to discuss. For some resists like the SU8 epoxy family an additional post exposure bake (PEB) on a hotplate needs to be applied to thermally activate the cross linking of the resist initiated by the UV light exposure. Standard spin recipes, soft baking, PEB and rehydration conditions are given in Tab. D.1. The film thickness depends also on the substrate size which makes it necessary to perform test runs for highly sensitive exposures such as gray scale lithography on the same die size and material. The primer hexamethyldisilazane (HMDS) is applied with a pipette to the solvent cleaned sample surface after the high temperature bake and cool down and generally the same spin recipe as for the resist is then employed to spread the primer. The primer increases the resist adhesion to the semiconductor surface, something critically important for high-aspect ratio features.

Table D.1: Thin film coating conditions for various resists with the set point temperatures given. MD stands for Microdeveloper and PGMEA for propylene glycol methyl ether acetate. For SPR220-4.5 the optimized grayscale recipe is given.

Resist	Thickness [μm]	Primer	Spin recipe	Soft bake	PEB	Rehydration procedure	Development
S1805	$\approx$ 0.5	HMDS	10 s at 500 rpm, 60 s at 4000 rpm, 100 rpm/s ramp	1 min 115°C	-	-	30 s 1:1 H_2O:MD
SPR220-4.5	$\approx$ 4.2	HMDS	60 s at 4000 rpm, 100 rpm/s ramp	2 min 105°C	-	1 h before and 1 h after exposure	1 min 40 s 2:1 H_2O:MD
SPR220-7.0	$\approx$ 7.0	HMDS	60 s at 4000 rpm, 100 rpm/s ramp	2 min 105°C	-	35 min after exposure	1 min 15 s 1:1 H_2O:MD
SU8-2002	$\approx$ 1.8	Matrix asher	10 s at 500 rpm, 30 s at 2500 rpm, 30 s at 4000 rpm, 100 rpm/s ramp	1 min 95°C	2 min 95°C	-	40 s PGMEA, 10 s IPA, 10 s PGMEA, 20 s IPA
SU8-5	$\approx$ 3.4	Matrix asher	60 s at 3000 rpm	5 min 95°C	5 min 95°C	-	60 s PGMEA, 10 s IPA, 30 s PGMEA, 20 s IPA
SU8-100	$\approx$ 50/35	Matrix asher	10 s at 500 rpm, 30 s increasing from 3000 rpm, 60 s at 5000/7000 rpm, 2 rpm/s ramp	5/10 min 65°C, 15/30 min 95°C	4/5 min 95°C	-	5/6 min PGMEA, rinse in IPA

D.2.2 Hotplates

The three hotplates used for resist baking and photoresist reflow are found to exhibit a temperature offset between setpoint and surface temperature. The measured surface temperature can be 10s of degrees lower than the set point temperature and probably depends on the air flow conditions in the resist flow box. The surface temperature might fluctuate on a daily/monthly/yearly basis. Tab. D.2 gives a small overview of possible discrepancies.

This was only discovered after several years of work in the clean room facility and initially no note was taken of which hotplate was exactly used during a spin or resist reflow step. The given temperature values in this thesis are based on the set point in each case. Therefore it is recommended to take the hotplate temperature found in this work as a approximate scale that not directly transferable to another facility and differences found when reproducing results might be due to different hotplates used. Generally for establishing a certain recipe, the same hotplate and settings are employed in several iterations of the UV dose and development time leading to good results. Recalibration of a process is

always possible as long as enough solvent is removed from the thin film to properly function.

Table D.2: Exemplary values of the set point vs. measured surface temperature of the right and left hot plate in the spinner flow box cabinet.

Set point [°C]	Measured surface temperature [°C]
105 (right)	90 ± 4
123 (right)	105 ± 4
150 (left)	108 ± 4

D.2.3 Hard bake and use of vacuum oven

A Memmert vacuum oven is adapted to hard bake the thick SPR220 photoresists before exposure to any plasma in the successive dry etching steps. The hard bake removes more of the remaining solvent from the thin film and stabilizes the resist features. It is found that applying 60°C for 48 h at 10 mBar pressure leads to highly stable resist without significant signs of thermally induced reflow which can be used to pattern materials both in the capacitively and inductively coupled plasma machines discussed below. SU8-2002 is usually hard baked on a hotplate for 10 min at 95°C.

D.2.4 Mask aligner

Some of the initial lithography shown in this work is carried out with the mask aligner 'Karl Suss MA6', which is otherwise not used. This includes for example the first successfully generated diamond micro-lenses from SPR220-7.0. In a mask aligner like this a glass substrate (4 inch squared used here) is patterned with a thin-film chromium mask and brought into μm-close proximity to the surface of the sample. The chromium layer shields parts of the resist while the counterpart is illuminated by a mercury-discharge lamp. Depending on resist thickness and substrate flatness, the minimum feature size can be as low as 1 μm.

D.2.5 Direct write laser lithography

The 'DWL66+' laser lithography system from 'Heidelberg Instruments' is the main tool used for photolithography in this thesis. This includes the definition of polymer lenses and overlay patterns for suspension of GaN thin-film lenses from the growth substrate. The tool operates a 375 nm UV laser which is automatically focused into the coated resist thin film with the help of a red interferometer laser that does not expose the resist. The write head objective focusing both lasers is then scanned laterally above the surface while constantly maintaining the objective-substrate distance with the help of the interferometer laser. Fig. D.1 illustrates how this is implemented: The scanning motion of the laser is realized by synchronizing continuous 1D beam scanning with a parallel orthogonal stage movement. The beam scanning is realized by acousto-optic deflection (AOD) defining a stripe of 30-75μm width. These stripes are then connected by successive stage movements along the laser scanning direction achieving stitching. The lateral stage movements are similarly controlled by red interferometer lasers leading to closed-loop sub-50 nm stage positioning accuracy. The photomask is defined digitally and

applied by modulation of the laser intensity with an acousto-optic modulator (AOM) that is synchronized with the beam position. This allows rapid prototyping by design alterations from run to run. This tool additionally has a 8-bit grayscale capability, meaning that the local dosage can be varied in 256 fine steps to partially expose resist creating 3D micro-structures. This feature is exploited to fabricate micro-lenses with controllable shape and dimensions.

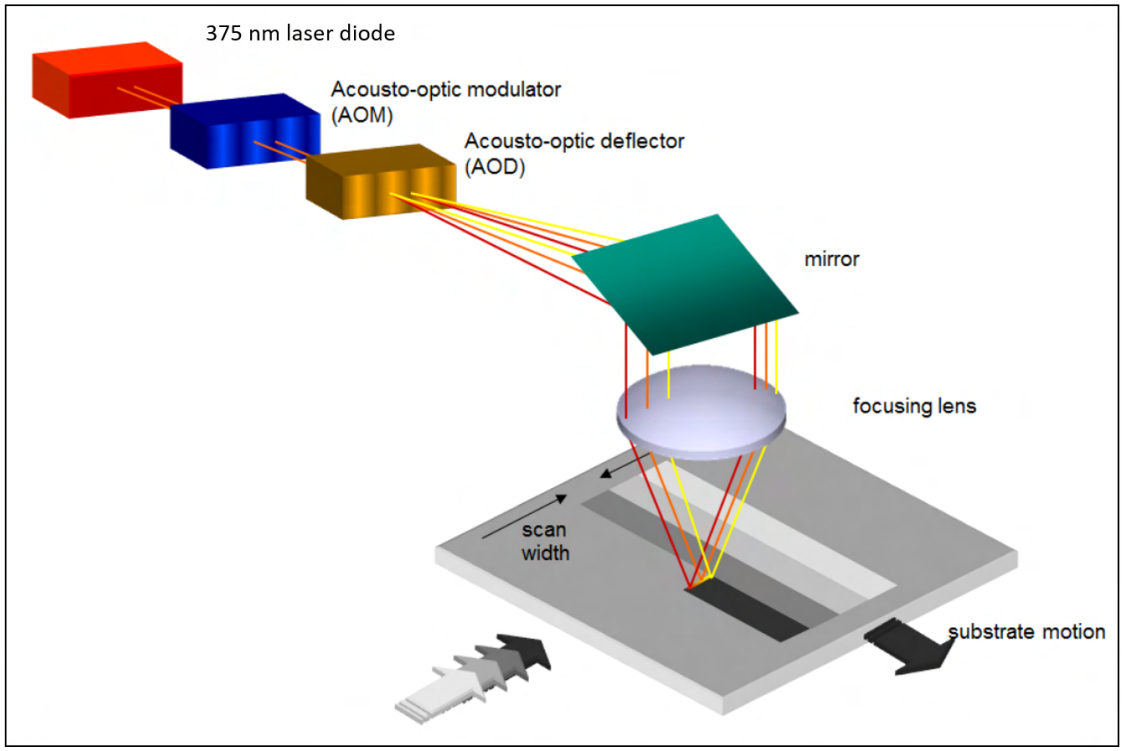

Figure D.1: Illustration of the optical path and synchronized stage movements of the DWL66+, taken from [354].

Table D.3: DWL66+ specifications based on the mounted write head.

Write head	**HiRes**	**5 mm**
Numerical aperture	0.9	0.65
Min. feature size [μm]	0.3	0.8
Min. line separation [μm]	0.5	1.0
Depth of focus [FWHM, μm]	0.9	2.0
Edge roughness [3σ, nm]	50	70
Overlay alignment accuracy [3σ, nm]	500	500
Write speed [mm^2/min]	2	30
Stripe width [μm]	30	75

The user can choose between two different write heads containing different objective lenses with the specifications given in Tab. D.3. The 'HiRes' write head is used for the definition of photoresist lenses while the '5 mm' head is mainly employed to expose successive overlay patterns to define the membrane devices for suspension.

The user has control over two main parameters: The exposure dose and the z-position of the write head with respect to the found auto-focus position (focus offset). Typically spin recipe and development time

are fixed before the exposure and then the dosage and focus offset parameters are carefully optimized in a $n \times m$ matrix exposure of a small test pattern, ideally on the same substrate used for the device structure. Because a single laser line is used for the UV exposure of the resist the development results tend to be very sensitive to the respective film thicknesses of the substrate, epilayer and resist due to thin film interference. Anti-reflection coatings are not used in this work.

D.2.6 Development

In the so-called development step the UV exposed pattern is transferred into the photoresist film by removing exposed or unexposed part of the resist selectively due to light induced changes of the resist solubility. For a positive photoresist the solubility of the resist is locally increased by the light exposure, while for a negative resist the polymer is crosslinked and less soluble in the developer solution [353].
The mainly employed development recipes are already included in Tab. D.1. For repeatable results in grayscale lithography the volume of developer and DI water is monitored and the last 100-200 ml in the developer storage bottle are avoided, because its development rate seems to change over time due to exposure to air. The development rate also critically depends on how the user manually handles his sample in the solution. Shaking the substrate in the development beaker or constantly mixing the solution might increase the development rate significantly, but too strong movement might lift high aspect ratio features off the substrate. In this work mostly slow substrate movements are employed to homogenize the development across the sample without destroying the resist structures. This avoids the built-up of clouds of higher resist concentration in some corners of a pattern.

D.3 Plasma driven material removal and deposition

Plasma based dry etching and deposition techniques are fundamental to microfabrication. A plasma is a partly ionized gas which is governed by complex collective behaviour of its constituent particles which are coupled to external and self-generated electromagnetic fields which makes a plasma generally very complex to describe [193, 355]. We are specifically looking at low-pressure plasmas inside vacuum chambers that are constantly maintained by the application of an external radio frequency field providing the energy that is constantly lost if electrical charges are terminated at the chamber walls or light is emitted under recombination of free electrons with ionized atoms [193].
Simply speaking the externally applied field causes atoms to inelastically scatter under the emission of electrons, which then causes further acceleration of these now charged particles and additional inelastic collisions causing an avalanche effect. Generally the free electrons are much faster due to their lower mass, leading to separate thermal equilibirum conditions for electrons and ions [193].
In this state of matter we can make use of heightened chemical reactivity of the gas components. For example the dissociated gas molecules might react with the sample surface building volatile compounds that can be removed from the chamber under constant gas flow and vacuum pump out.

D.3.1 Reactive ion etching

Reactive ion etching (RIE) is a plasma based process that successively removes material from a surface in layer-by-layer fashion with anisotropy being one of the most important advantages over wet chemical

etching techniques. This means that the material can be removed in a primary direction, usually downwards [193, 356, 357].

gas	E_{diss} [eV]	E_{ion} M^+, M_2^+ [eV]	$n_{\text{ion}}/n_{\text{diss}}$
H_2	4.49	13.59, 15.4	112 ppm, 18 ppm
O_2	2.57	13.62, 12.0	16 ppm, 80 ppm
CH_4	4.5	12.6	15
F_2	1.59	15.7, 17.42	0.7 ppm, 0.1 ppm
Cl_2	2.51	11.02, 12.96	201 ppm, 29 ppm

Figure D.2: Dissociation energy E_{diss}, ionisation energy E_{ion} of radicals (M^+) and molecules (M_2^+) and theoretically expected ion density n_{ion} per density of dissociated gas radicals n_{diss} given for both ionization of free radicals (left value) and ionization of molecules (right value) for $T_e = 3\,\text{eV}$, taken from [193].

The sample is placed in a vacuum chamber ($< 0.5\,\text{mTorr}$) which is then purged with etch gases like CHF_3, Cl_2 or O_2 and inert buffer gases like Ar. In the capacitively coupled RIE tools employed in this work a plasma is then generated by applying a RF power (typically at 13.56 MHz [356]) driving a plate condensator inside the chamber. The sample sits on one of these condensator plates and works either as extension of the electrode or as dielectric. This RF field then maintains a low-pressure plasma fed by the continuous neutral gas stream.

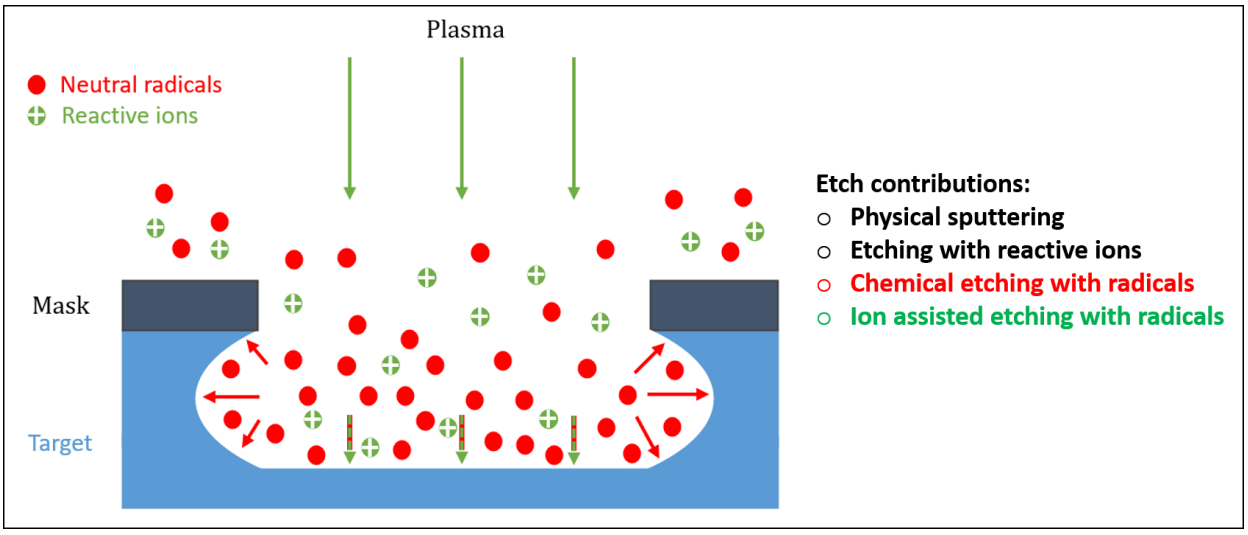

Figure D.3: Illustration of the different contributions to 'reactive ion etching': Sputtering with ions and fast neutrals (mainly anisotropic), chemical etching with reactive ions (anisotropic), thermally-induced chemical etching with neutral radicals (isotropic), ion-assisted chemical etching with neutral radicals (anisotropic). Radicals are indicated in red and ions in green with + signs, based on [193].

The target material is removed from the surface by a combination of four processes as described in the caption of Fig. D.3. The principle goal is the formation of volatile etch products containing the atoms of the targeted sample surface in a cycle of absorption of reactive species, reactions with the surface and desorption of the final product. This allows to remove the material through the gas phase as the chamber is constantly connected to a vacuum pump and fresh process gas is continually streaming in. Depending on the gas mixture and process conditions like chamber pressure, RF power and resulting

DC bias, the balance between different etch contributions can be altered [193].
In a simple model the density of dissociated gas molecules and ionized atoms and molecules in the plasma can be described by the electron temperature T_e. Fig. D.2 compares ion to radical concentrations for different plasma chemistry with $T_e = 3\,\text{eV}$ typical for RIE tools [193]. Because the dissociation energy is much lower than the ionization energy, neutral free radicals exist in much higher concentration than ionized radicals or molecules. The name reactive ion etching is therefore actually misleading: Thermally-induced and/or ion-assisted chemical etching with neutral radicals are expected to be the dominant processes in capacitively coupled RIE tools [193].
Ion sputtering can assist the chemical etching of the surface with the highly reactive radicals for example in the following manner: Lets assume the average ion energy is sufficient to desorb chemical etch products of the semiconductor and the gas radicals from the surface, but is not sufficient to break the bonds of the pure target material without such reactions. Such an etch can be anisotropic if the assisting ions collide with the surface at normal incident mainly, leading to heavily enhanced etch rates in the vertical but not lateral direction. This makes it possible to create nearly vertical sidewalls in an etch pattern. High chamber pressure can lead to more inclined ion trajectories while pure physical sputtering does not allow the fabrication of vertical sidewalls [193].
Assisted desorption is only one possibility how ion sputtering can enhance chemical etching: Microdamaging the surface for increased radical adsorption, removal of reaction-inhibiting molecules from the surface and activation of chemical reactions by transfer of kinetic energy are other possible processes. An isotropic etch occurs if the chemical etch products of neutral radicals with the sample surface are volatile without ion bombardment and no surface passivation mechanism occurs. Often, chemical etching is selective to crystal planes and therefore sometimes referred to as quasi-isotropic etching [358]. The plasma environment also assists chemical reactions through the bombardment with electrons.
The combination of successive isotropic etch steps with side wall passivation and ion bombardment can lead to overall anisotropic etch profiles, like in the famous Bosch process for deep RIE-based Si etching. Here sidewall passivization of Si in SF_6 plasma discharges happens by polymerisation of SF_2 films [193].
It is to note that adding a new gas type to the plasma does not simply expose the surface to a new reactant, but changes the composition of the plasma itself: The different gas molecules and atoms kinetically interact and can chemically react with each other. Also depending on the etch recipe and tool, etch rates and the dominant etch process can vary laterally on a wafer [193].
'Oxford Plasmalab 80 Plus' RIE tools are adapted for this work which are designed for 3-inch wafer-scale processing. Tab. D.4 summarizes the standard etch recipes used for etching in-house fabricated thin films: Plasma enhanced chemical vapour deposition (PECVD, recipes and principle see below) creates conformal SiO_x and SiN_x hard masks. Etch rates are determined with a white light reflectometer (see description below) on Si-(100) substrates. Tab. D.5 includes two recipes used for Si etching with SF_6 plasmas. A minimum relative etch rate error of 10 % is assumed adding to spread from varying measurement results.
Known volatile etch products of Si, $Si0_x$, SiN_x in CHF_3 and SF_6 plasmas are SiF_x, O_2, N_2, CO_x and CF_x [193, 359]. Fluorine based etching of Si compounds has a strong isotropic chemical etching character [193], which is counteracted in recipes #1-3 by high RF power generating a large DC bias towards the substrate leading to an anisotropic etch. CHF_3 plasmas are found to neither effectively attack Si nor GaN, which makes it necessary to use SF_6 based plasmas to etch Si (Tab. D.5). At the same time the negligible etch rate of GaN allows us to remove deposited hard masks from lens devices with dry

etching, because the GaN effectively acts as an etch stop.
Sufficiently dried SPR220-7.0 can be etched without significant resist carbonization - sometimes referred to as resist 'burning' - which usually distorts the shape of the resist pattern due to accumulating thermal load [360]. The carbonization occurs in the top layers of the resist and is linked to hydrogen depletion due to the ion bombardment. The carbonized layer generally has lower chemical reactivity than the resist, resulting in lowered etch rates and sometimes difficulties when removing 'burned' resist [360].

Table D.4: Experimentally determined etch rates of resists, Si-(111) substrates of the GaN-on-Si samples, hard mask materials and GaN thin films in the dedicated RIE tool for etching the in-house deposited SiO_x hard mask, n.d. stands for 'no data'. Etch rates may vary over time in the cleaning cycle of the machine.

Recipe	SPR220-7.0 [nm/min]	Si-(111) [nm/min]	PECVD SiO_x [nm/min]	PECVD SiN_x [nm/min]	GaN [nm/min]
#1 mleSiO2 120 W RF 5 sccm CHF_3 15 sccm Ar 30 mTorr	4 ± 1	negligible	25 ± 5	8 ± 3	negligible
#2 IOP_SiO2 200 W RF 5 sccm CHF_3 15 sccm Ar 30 mTorr	n.d.	negligible	40 ± 4	n.d.	n.d.

Table D.5: Experimentally determined etch rates the Si-(111) substrates of the GaN-on-Si samples, the in-house deposited SiO_x hard mask and GaN thin-film in the dedicated RIE etching machine for metal and Si etching, n.d. stands for 'no data'.

Recipe	SPR220-7.0 [nm/min]	Si-(111) [nm/min]	PECVD SiO_x [nm/min]	GaN [nm/min]
#3 Si_etch2 300 W RF 60 sccm SF_6 10 sccm Ar 10 sccm O_2 50 mTorr	n.d.	630 ± 50	150 ± 20	20 ± 5
#4 SCREAM1 50 W RF 100 sccm SF_6 8 sccm O_2 25 mTorr	30 ± 10	135 ± 20	17 ± 3	n.d.

The SF_6 based recipe #3 is minimally used during the thesis to etch Si due to its low selectivity over the PECVD SiO_x hard mask. Recipe #4 is a highly versatile Si etch process allowing to use thick photoresist without significant carbonation (if the resist is sufficiently dried) and PECVD SiO_x as mask

with reasonable selectivity. It is the main process used in this work to etch Si and is generally isotropic which generates undercut etch profiles, even though the isotropy is found stronger if etching Si with (100) surface orientation.

D.3.2 Inductively coupled plasma reactive ion etching

The inductively coupled plasma reactive ion etching (ICP-RIE, ICP) tool 'STPS Multiplex system' is used to effectively etch the large band gap semiconductors diamond and GaN, compare Fig. D.4 a) for an image of the machine. It is also sometimes used to etch the Si-(111) GaN-on-Si substrates, which is not advised to future users as the p-doping of the Si wafers might lead to chamber contamination.
In an ICP etcher a RF drive is applied to a magnetic coil to generate a strong plasma discharge inside a vacuum chamber with electrons trapped in the centre, while an additional RF drive is applied to the sample wafer which acts as a condensator plate [356, 357]. This allows to control the ion density in the plasma (coil power) and the ion flux and energy hitting the sample surface (platen power) somewhat independently and creates higher etch rates at lower gas pressures than capacitively coupled RIE tools can achieve [356, 357].

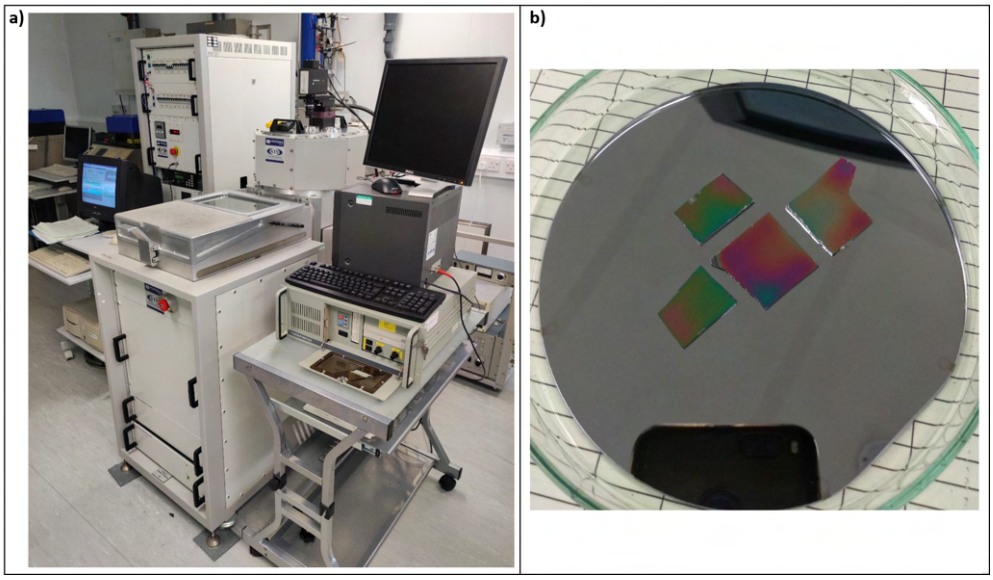

Figure D.4: Photographs of a) the ICP etching machine mainly used in this work (STPS Multiplex, Cl_2, Ar, O_2), b) a Si carrier wafer with 4 GaN-on-Si test pieces after global epilayer thinning, illustrating the varying etch rate / initial epilayer thickness at different positions within in the ICP / growth plasma with differing colours indicating different film thickness.

Because of its much higher degree of ionization ICP-RIE deservers the name 'reactive ion etching' better and is able to break the bonds of high-strength materials such as diamond (3.5 eV), GaN (2.2 eV) and AlN (2.9 eV) [356, 357]. For example III/V semiconductors can generally be effectively etched with a chlorine-based ICP. Cl^+ is here the predominant reactive species, which we will exploit in this work. The lower operating pressure allows to etch smooth anisotropic profiles, because the ions scatter less before they hit the target surface [193].
Crucially important for successful etching with resist masks in ICP machines is to keep the substrate temperature low. Si-(100) carrier wafers are used to mount sample dies as shown in Fig. D.4 b) which are cooled via helium gas from the backside of the wafer when placed in the ICP machine. To ensure

good thermal contact to the cooled carrier wafer a small amount of specialized wax bonding agent that was provided by the vendor is spread on the carrier wafer. This is usually performed on a hotplate with set point temperature between 80-105°C using metal tweezers to generate a thin film a bit smaller than the sample die. Next the sample is placed on the wax and the carrier wafer is quickly removed from the hotplate to avoid photoresist reflow before etching. Alternatively the Memmert vacuum oven can be used for bonding at 60°C and 10 mBar by placing the samples on the cold wax film and then adding the wafer to the oven for 5 min without danger of reflow.

Volatile etch products of diamond, GaN, AlGaN, AlN, Si and SiO_x in chlorine-based plasmas are CCl_x, $GaCl_x$, $AlCl_x$, N_2, $SiCl_x$ and O_2 [357]. Chlorine is a less reactive halogen than fluorine which leads to reduced etch rates and isotropy, but fluorine-based plasmas cannot effectively etch III/V semiconductor compounds mainly because of its low vapour pressure.

In oxygen-based plasmas, diamond can be removed in the form of CO_x [357]. Oxygen etching is tested due to reports of lower etch selectivity over photo resist compared to chlorine-based plasma chemistry [113, 128, 129]. A lower etch selectivity would allow the fabrication of higher diamond micro-lenses from the same photoresist lens.

Tab. D.6 shows the ICP etch results for diamond, GaN, AlGaN, AlN, resist, PECVD SiO_x and Si etching: Diamond etching is performed using recipes #1 (Ar/Cl_2) and #2 (Ar/O_2) yielding similar etch selectivity towards SPR220-7.0 photoresist with the resist exhibiting around 9-11x faster etch rates than diamond. This leads to very shallow etch depth of diamond micro-lenses fabricated by the shape transfer of resist bubbles (reflow method). The Ar/O_2 etching recipe used is based on the PhD thesis from C.L. Lee, who found only 7x lower diamond etch rate when using 15 instead of 10 sccm Ar flow.[3]

GaN, AlGaN, AlN and Si etching is executed with the Ar/Cl_2 based recipes #3-5. Recipe #3 is given for reference purposes and is used for Si trench etching in some cases, but this has supposedly led to contamination of the ICP chamber due to the p-doping content in the GaN-on-Si substrates. Recipe #4 is the most important recipe employed in this work and allows to etch GaN micro-lenses and trenches into the GaN/AlGaN/AlN epilayer on Si substrates. Recipe #5 is used in the initial project stages for test etching in an alternative ICP etcher (STPS LPX) with the pressure difference in the recipe probably stemming from the different chamber design. All three recipes have the same gas ratio composition yielding similar relative etch rates between the different materials.

The GaN micro-lens etch recipe #4 is optimized to minimize resist carbonization by reducing the inductively and capacitively coupled RF power. It is found that a staged execution of the recipe in 2.5 min steps with a 2 min Ar purge at full capacity between steps (or 3x vacuum pump out and purge if the sample is released between etches for investigation) seems to further reduce resist carbonization and micro-masking. This is probably due to reduced temperature of the chamber walls which might contribute to overall sample heating. Is is observed that the average etch rate reduces in the AlGaN/AlN buffer layer when $Al_xGa_{1-x}N$ with $x > 0.33$ is reached, which is in agreement with reports in literature and matches the expectation due to the higher bond strength in AlN [356, 357].

[3] The thesis is unfortunately not published

Table D.6: Experimentally determined etch rates of SC diamond, different parts of the GaN-on-Si epilayer, resist used for lens and trench etching, PECVD silica and the Si growth substrates of the GaN material in the ICP-RIE tool 'STPS Multiplex system'. Values that are taken from other users are marked with their initials in brackets (Enyuan Xie: EX, Paul Hill: PH), n.d. stands for 'no data'. Etch times are given including ca. 15 s DC bias built up, which can make it difficult to reproduce absolute etch rates if other etch interval lengths are used. Recipe number #5 was executed in an alternative ICP etcher (STPS LPX).

Recipe	Diamond [nm/min]	GaN [nm/min]	$Al_xGa_{1-x}N$ $x < 0.33$ [nm/min]	$Al_xGa_{1-x}N$ $x > 0.33$ [nm/min]	Resist [nm/min]	PECVD SiO_x [nm/min]	Si (111) [nm/min]
#1 (Cl_dia) 400 W coil 300 W platen 40 sccm Cl_2 25 sccm Ar 5 mTorr	68 ± 5	n.d.	n.d.	n.d.	610 ± 70 (SPR220-7.0)	155 ± 25 (PH)	n.d.
#2 [129] 400 W coil 40 W platen 40 sccm O_2 10 sccm Ar 5 mTorr	60 ± 10	n.d.	n.d.	n.d.	650 ± 100 (SPR220-7.0)	n.d.	n.d.
#3 (KHSGaN4) 400 W coil 200 W platen 30 sccm Cl_2 10 sccm Ar 20 mTorr	n.d.	500 ± 50 (EX)	n.d.	n.d.	400 ± 40 (S1818, EX)	70 ± 10	420 ± 100
#4 (GaNLens) 200 W coil 70 W platen 30 sccm Cl_2 10 sccm Ar 20 mTorr	n.d.	155 ± 15	155 ± 15	110 ± 15	205 ± 15 (SPR220-4.5)	n.d.	140 ± 15
#5 (*mLED3*) 400 W coil 200 W platen 30 sccm Cl_2 10 sccm Ar 5 mTorr	n.d.	320 ± 30	320 ± 30	290 ± 30	380 ± 30 (SPR220-4.5)	n.d.	330 ± 30

D.3.3 Plasma enhanced chemical vapour deposition

Plasma enhanced chemical vapour deposition (PECVD) is an inversion of the reactive ion etch process in which by careful choice of the precursor materials, selected gas pressure and provision of thermal energy to the growth substrate the accumulation of a desired material on the sample surface is stimulated in a plasma environment [193, 361]. PECVD deposition is generally conformal - meaning it grows laterally on exposed sidewalls - and mostly leads to amorphous thin films [361].
In this work the PECVD tool 'Oxford Plasmalab 80 Plus' is used which is based on an capacitively coupled RF (13.56 MHz) plasma in a vacuum chamber (parallel plate style), completely analogue to the used RIE etching tools. Tab. D.7 summarizes the standard deposition recipes for conforming hard mask materials with unspecified stoichiometry. The surface roughness of such deposited films is found by atomic force microscopy for SiO_x on the order of 7 nm root-mean-squared (r.m.s.) on few μm^2 footprint. This is quite high compared to the polished diamond or GaN epitaxial surfaces with r.m.s. roughness generally on the order of 0.5 nm. Both films are likely to contain considerable amount of hydrogen due to the choice of precursors [361]. The SiN_x films are produced with an ammonia free recipe leading to very low deposition rates. Low frequency RF based systems such these generally yield lower PECVD film quality than tools operated in the GHz regime [361].

Table D.7: Experimentally determined deposition rates of hard mask materials, n.d. stands for 'no data'.

Recipe	PECVD SiO_x [nm/min]	PECVD SiN_x [nm/min]
Oxide200 70 W RF 170 sccm SiH_4 710 sccm N_2O 1 Torr, $T_S = 300\,°C$	40 ± 5	n.d.
Ammonia free nitride 150 W RF 15 sccm SiH_4 900 sccm N_2 1 Torr, $T_S = 300\,°C$	n.d.	7 ± 3

D.4 Quality and dimension control

Process control allows the targeted fabrication of microstructures following the designed layout. In this subsection we name all used methods, describe their working principle and highlight their importance for the work.

D.4.1 Optical microscope

A 'Leica DMR' optical microscope is used to collect images of samples at different stages of the micro-fabrication process with 5-50x magnification using a Thorlabs colour camera. Microscope inspection is

a very powerful tool that was extensively used to keep track of the fabrication process and document the work done.

D.4.2 Stylus profilometer

Stylus profilometer use a sharp typically conical probe tip to assess the topology of a sample. The tip is brought into contact with the sample surface under application of a specified torque and then moved linearly while monitoring the differential changes of the tip holder angle to reconstruct the 1D height profile [362]. The height feedback might be measured by a laser reflection from the deflecting tip holder or other means such as an inductive transducer or a piezoelectric element converting position changes into electrical signals [362]. Two different stylus profilometers are used in this work, but we are mainly relying on the AlphaStep due to its smaller tip size. The tip diameter becomes important if the measured structure is of comparable size or has a very high aspect ratio, because the measured profile is a convolution of the tip and surface topology.
The stylus profiler **'Veeco Dektak3'** uses a diamond tip with a diameter on the order of 12.5 μm limiting the feature size that can be investigated. The vertical repeatability is estimated to lay in the 10-50 nm regime.
The stylus profiler **'KLA Tencor Alpha-Step IQ'** utilizes a diamond tip with a diameter on the order of 5 μm and is specified with up to 1 nm vertical repeatability. Typical measurement conditions are 500 μm scan length and 500 Hz sampling rate at 20 μm/s speed with 20 μm vertical range (calibrated by a commercially available standard for step height). The tool is extensively used for measurements of resist height after development and etch depth progression in the ICP and RIE systems. Initially it is also used to analyse some larger scale (120 μm) grayscale lithography patterns.

D.4.3 Optical profiler

The optical profiler 'Wyko NT1100' uses visible white light interferometry to generate 3D scans of a reflective sample via an objective lens. The reflected beam from the sample is interfered with a reference beam on a CCD via a 50:50 beamsplitter leading to interference fringes if the optical path lengths are matched. The lateral sample size can be up to several mm, while the height resolution can be sub-wavelength due to the use of a broadband probe beam with short coherence length that allows the fringe contrast to fall off very rapidly if the optical path lengths of both interferometer arms are diverging [363].
The tool is mainly employed to investigate the thickness and uniformity of SC diamond membranes with around 10-30 μm thickness after bonding to a Si die and is not of crucial importance for this work because the investigated lenses were generally to small or too steep to be investigated with this tool.

D.4.4 White light reflectometer

The 'Filmetrics F20' white light reflectometer measures the reflection spectrum of a sample with respect to a Si wafer calibration reference on an area of ca. 2-3 mm diameter by using a fibre coupled optical probe head. The user inputs a guess for the layer stack and the data is fitted according to the theoretical expectations to determine the thickness of deposited or etched thin films during the microfabrication process. Thin film thicknesses can range between 15 nm and 50 μm. This highly useful technique is

employed for process control by using small Si dies that are exposed to the same plasma conditions for example the GaN-on-Si dies. In this way deposition and etch rates can be reasonably well tracked, even though the exact rates might depend on the die size and complexity of the already microfabricated pattern.

D.4.5 Atomic force microscope

A vibration shielded 'Park Systems' atomic force microscopy (AFM) is used to assess the 3D surface topology if the high measurement precession is required. This mostly includes the measurement of the r.m.s. roughness of important surfaces with typically 3x3 μm^2 scan sizes and the careful monitoring of the diamond and GaN micro-lens shapes created.
In this AFM tool a Si cantilever with a sharp tip is scanned over a sample surface to probe the force landscape in 2D using a piezo controller for vertical movements. The force landscape usually correlates with the surface topology. The tool is operated under ambient conditions on a vibration isolation plate without shielding against air turbulence. 'Tapping mode' is applied in which the cantilever is constantly driven to oscillate close to its mechanical resonance frequency while the oscillation amplitude is held constant during the scan with feedback from the measured tip deflection fed into the PID controller adjusting the vertical position of the piezo. The cantilever deflection is monitored by pointing a laser beam on the cantilever backside which is reflected onto a 4-field photodiode.

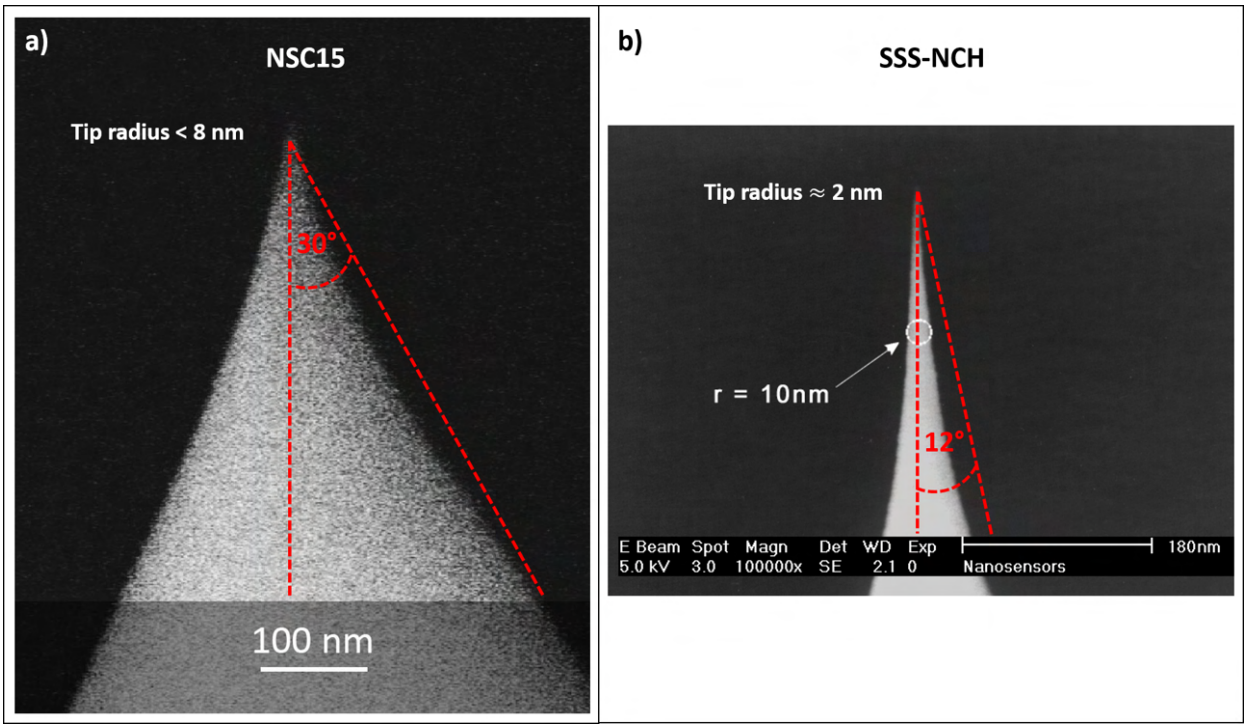

Figure D.5: SEM images of the used AFM tips in this thesis with a) a standard NSC15 cantilever tip, adapted from [364], b) a SuperSharpSilicon SSS-NCH cantilever tip, adapted from [365]. The exact shape is expected to vary from tip to tip and is also expected to change depending on how often the tip is used and under which settings.

Typical settings for a large scale AFM scan include 128x128 or 256x256 px^2, (10x10 - 40x40) μm^2 scan sizes, 11.1 nm setpoint at 20 nm cantilever amplitude monitoring the output from the 'Z detector' rather than 'Topology' in large z range mode with up to ±4 μm range, 2.0-2.5 gain and 0.3-0.5 Hz scan speed.

Surface roughness scans are usually executed with 512x512 px^2 on 3x3 μm^2 scan sizes with lower gain at 1.5 and typically 0.5 Hz (large or small z range is used with minimal difference found).
The use of the 'Z detector' output allows more precise measurements of structures with $> 1\,\mu$m height with the 'Topology' setting severely underestimating the height. Careful calibration of both xy and z axis were carried out to ensure proper operation and are recommended to check for new users.
Two different types of AFM tips (NSC15 and SSS-NCH) are used throughout the thesis and marked in the caption of the respective figure. Fig. D.5 shows SEM images of typical tips from both categories on roughly the same scale for comparison. We can see that both probes are expected to deliver a nearly convolution-free surface shape of any investigated structure with an onset angle lower than 60°. For some of the really high aspect ratio micro-lenses close to hemispherical lenses measured in this thesis we can expect that the AFM tip shape enlarges the diameter by a couple of 100 nm if NSC15 tips are used, but the measurement result is expected to be unaffected by the tip shape in the upper part of the lenses. Due to a learning effect of the author some AFM results in the thesis might exhibit up to 15 % error along all 3 axis based on the data collected during calibration.[4] This includes for example the measurements carried out on monolithic diamond micro-lenses which were luckily below 1 μm in height, leaving the error mostly to the x and y dimensions. Fortunately for the highly optimized grayscale processing and integration of single micro-lenses with diamond and NV centres, these issues were resolved. Some of the measurements on GaN micro-lens arrays were post calibrated using the expected peak pitch.

D.4.6 Scanning electron microscope

The 'Hitachi S-3000N' scanning electron microscope (SEM) is used to obtain quasi-3D images with 10s to 100s of nm resolution of the created microstructures. In a SEM like this the target surface is bombarded with a focused electron beam. During the lateral scanning of this beam the secondary electron emission from the surface is monitored at each position to deliver imaging contrast. This SEM employs a rather low quality thermal tungsten filament as electron source which limits the resolution in comparison to field emission sources. A strength of this particular SEM is the quick pumping time and it is extensively used to image GaN micro-lenses and the microfabrication steps leading to suspended membrane devices, delivering insight into process optimization. Charge up effects on dielectric samples like these can limit the image quality due to coulomb interaction with the beam, but metal coating was found to be unnecessary in this work. A huge strength of SEM imaging is the large depth of focus. Typical experimental conditions are 5-25 keV acceleration voltage at 40° sample tilt.

[4] Experimental errors included to trust the original calibration, usage of the wrong height readout, operation without xy closed loop.

E Micro-lens fabrication: Additional information

In this section we will provide additional collected data relevant for the fabrication of diamond and GaN micro-lenses.

E.1 Temperature dependence of the resist reflow method

The data shown in Fig. E.1 and E.2 illustrates how the reflow temperature can be used to fine tune the radius of curvature of the resist bubble. Fig. E.2 shows specifically pedestals which are preshaped with grayscale lithography in the DWL66+ laser lithography tool.

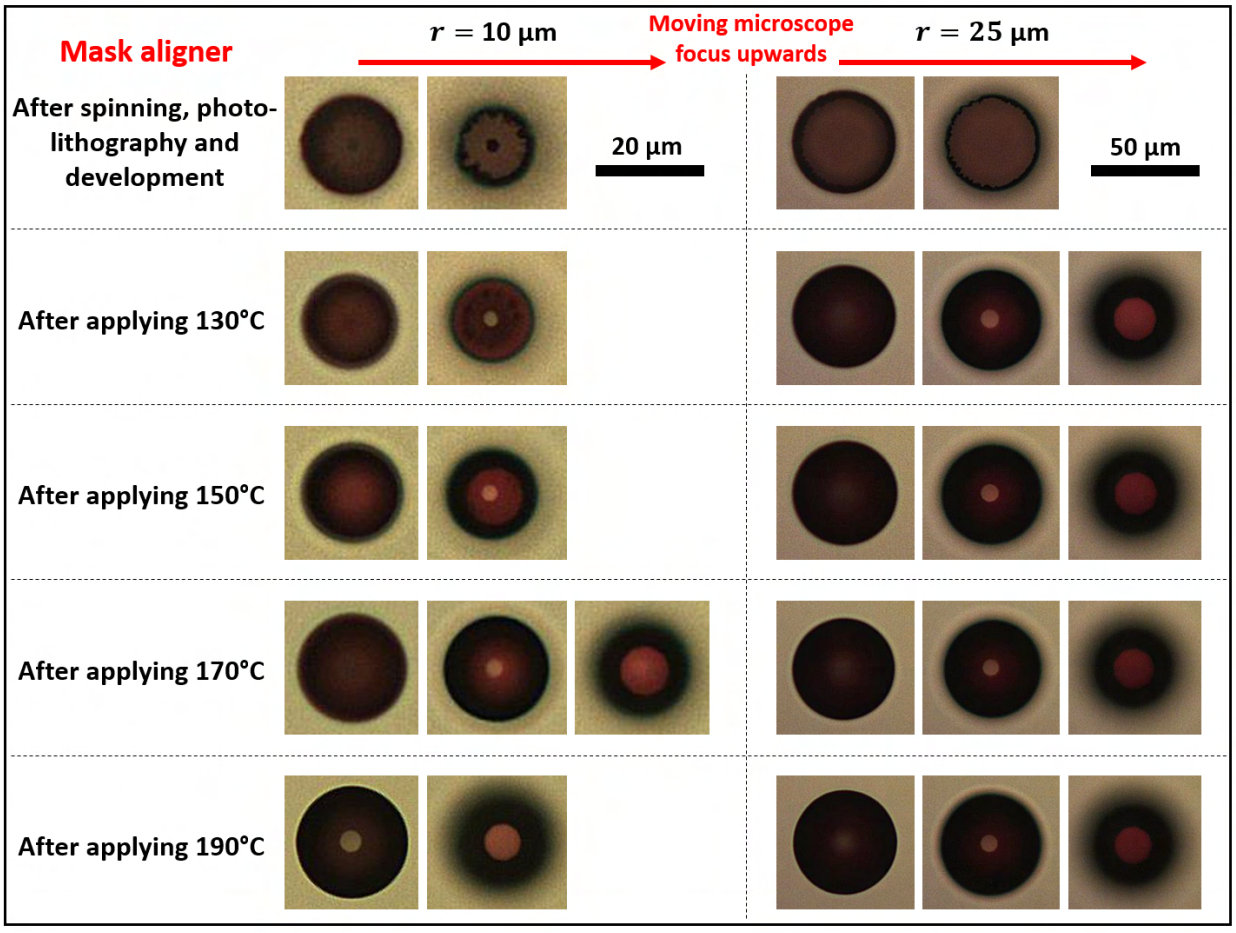

Figure E.1: Microscope images of SPR220-7.0 photoresist pedestals under stepwise thermal reflow fabricated with the mask aligner. Each temperature is applied for 3 min. The nominal radius is given, while the scale bars apply to all images in the respective column. The closely neighboured images in each row correspond to increasing microscope focus height of the same device.

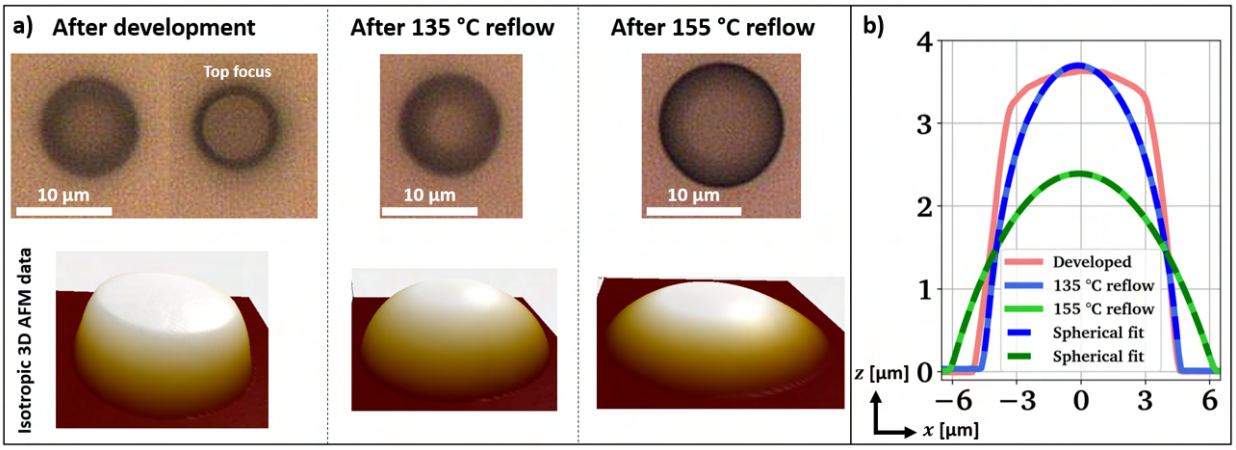

Figure E.2: Shape transformation of SPR220-4.5 photoresist pedestals fabricated with the DWL66+ laser lithography system with grayscale preshaping under increasing reflow temperature with a) microscope images and b) AFM profile data (NSC15).

E.2 Grayscale lithography: How to optimize

This section contains further information on resist grayscale optimization, for which two methods are available (follow the DWL66+ tool documentation for details). Fig. E.3 illustrates what can be achieved if the graytable is directly manipulated without the use of the AIC menu.

Fig. E.4 a) shows tests of the tool stability from run to run, keeping all other conditions stable while b) ilustrates that resist reflow cannot be used to smooth the surface of developed resist without shape distortions. The found surface roughness might be especially high because the more primitive grayscale correction without use of the AIC menu is used here. It is likely that the ICP etching creates a smoothening effect as we generally find much lower r.m.s. surface roughness around 3 nm on finalized GaN lenses even if pure grayscale lithography is employed (only tested with AIC grayscale).

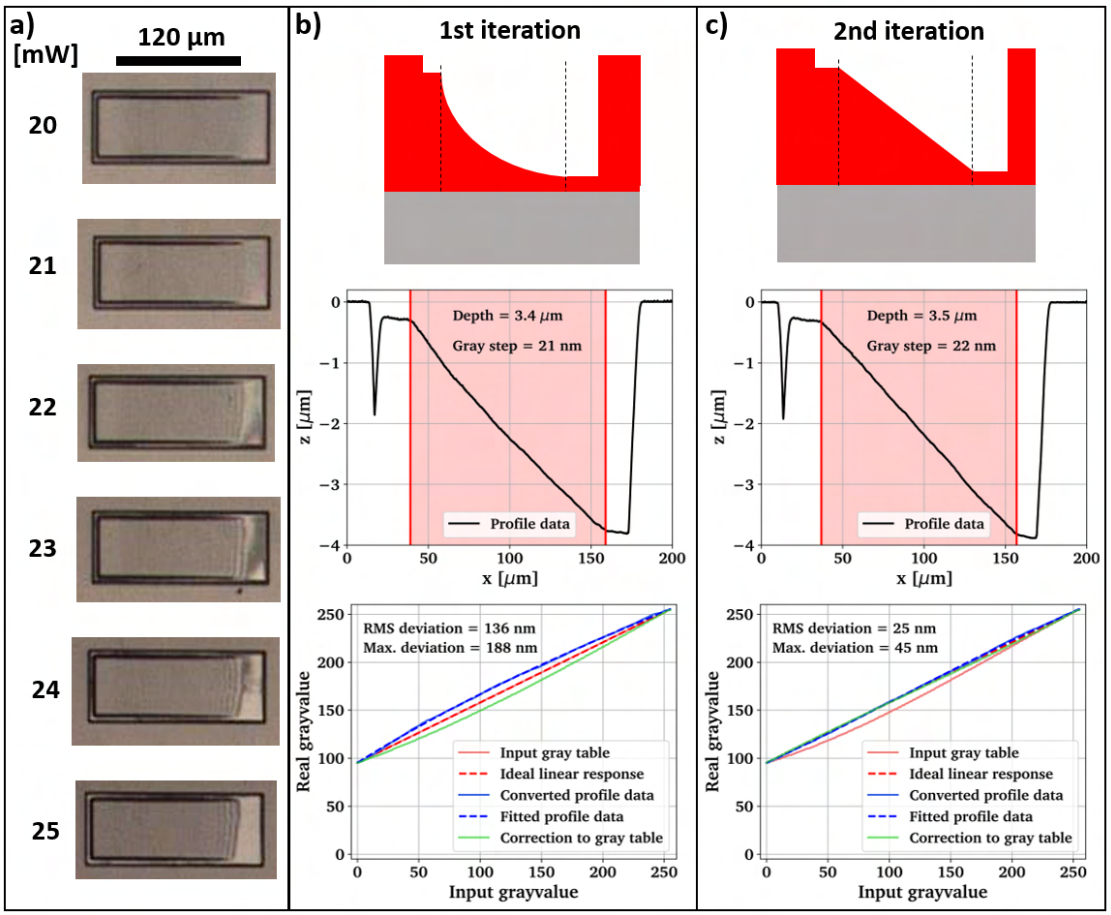

Figure E.3: Grayscale optimization for a linear slope in SPR220-4.5 photoresist, a) microscope images showing the effect of varying overall dosage on the depth of the slope inside the resist film, b) and c) showing the alpha step data in comparison to the designed profile in 1st and 2nd iteration based on proportional correction respectively after optimizing depth and dosage range.

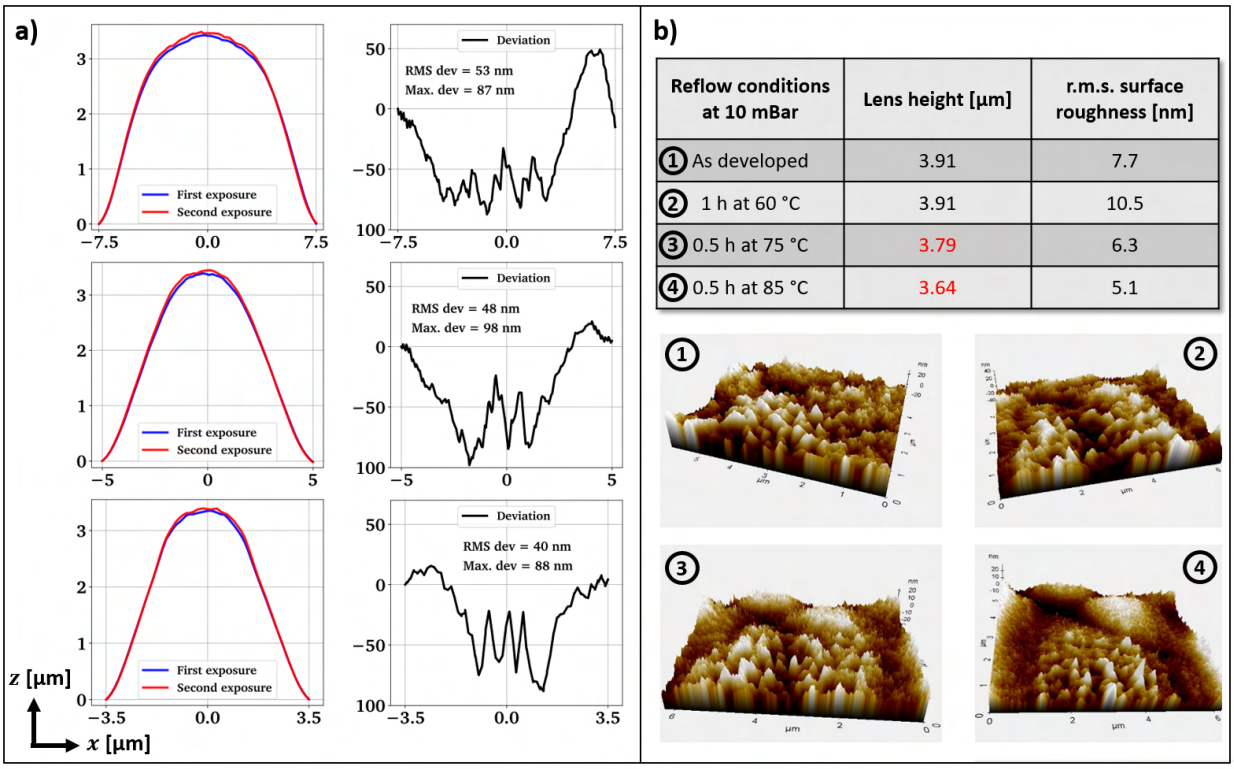

Figure E.4: a) Stability test of DWL66+ grayscale exposure using SPR220-4.5. The same pattern is repeated twice on the same substrate during the same exposure run and then developed in one step, shown are the AFM profile data with deviations between the 1st and 2nd exposure, b) resist grayscale lens smoothening effects caused by applying a hard bake in the Memmet vacuum oven. Lens height and r.m.s. roughness are measured with AFM (NSC15), the 3D AFM data of the roughness scans is shown after each successive hard bake.

E.2.1 Highly optimized spherical GaN lenses using grayscale lithography

This subsection contains detailed plots of how the optimized spherical GaN micro-lenses shown in Chapter 2 are achieved using iterative AIC grayscale correction with self-written python code following a mix of proportional, look-up and average correction methods. The AIC correction adjusts the intensity at each graylevel for the whole exposed design. The data shown in Fig. E.5 and E.8 show the already optimized resist lenses after several iteration runs.

Fig. E.10 contains plots describing the iterative intensity file adjustment in more detail, here with the example of additional adjustments that could be made based on the finally etched GaN lens shape rather the photoresist lens shape.

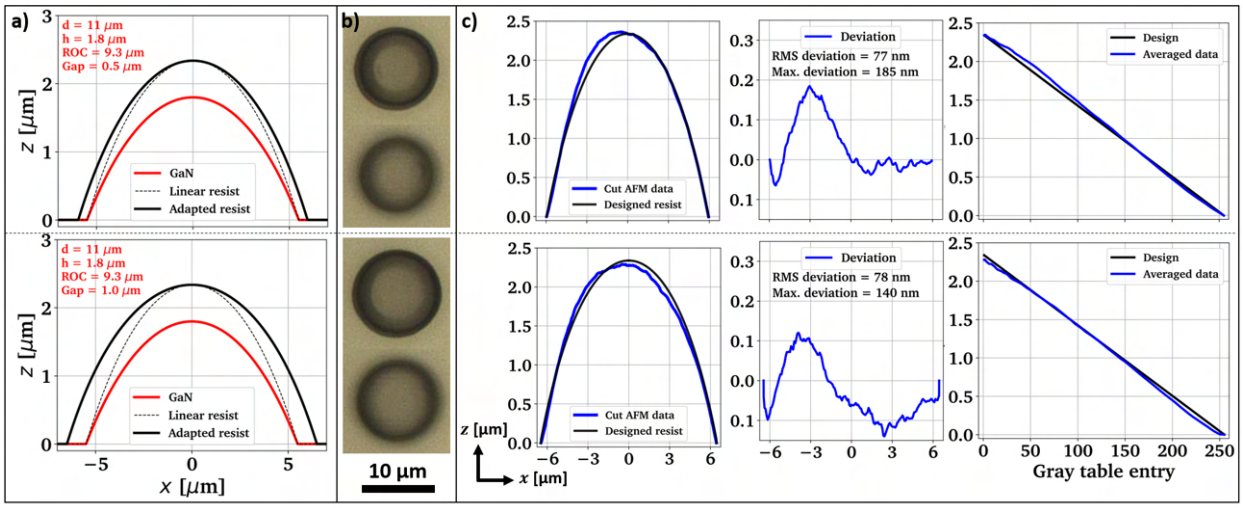

Figure E.5: GaN lenses with 11 μm nominal diameter: A simple optimization procedure is applied to take the lateral lens etching into account. The resist profile (black) is first backcalculated from the desired spherical GaN lens profile (red) based on the ICP etch selectivity. Then, a parabolic correction is added to the resist profile, creating a gap. a) Overview of designed resist profiles, b) microscope images after optimized grayscale lithography, c) AFM profile analysis and comparison of the resist profile to the design (NSC15). The visible asymmetry is likely due to an asymmetric AFM tip.

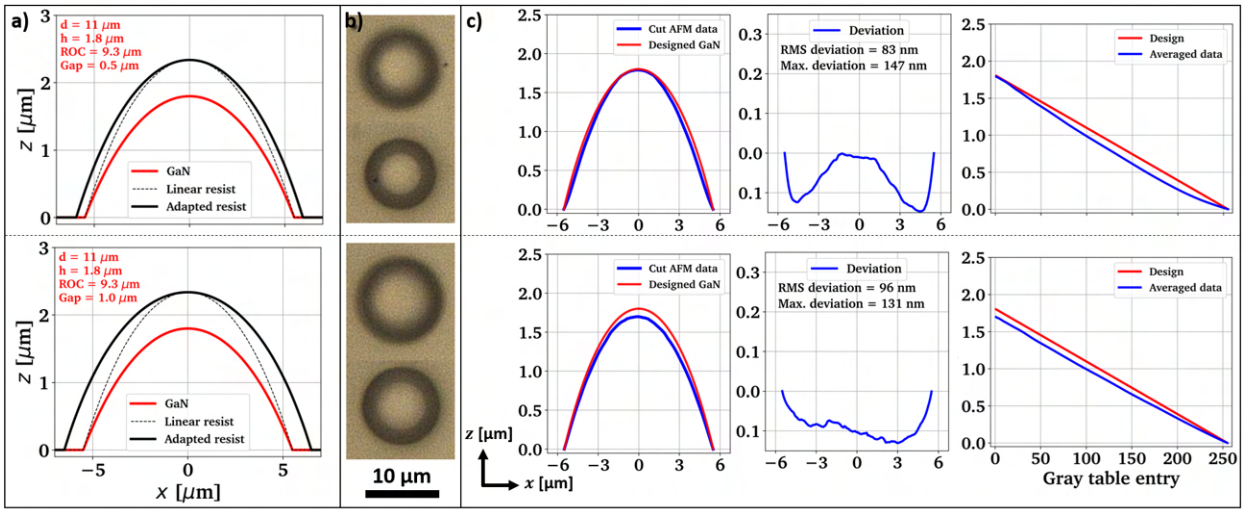

Figure E.6: The same lenses from Fig. E.5 after Ar/Cl_2 based low-bias ICP etching. a) Design of resist and GaN lens profile, b) microscope images of GaN lenses after etching, c) AFM linescan based comparison of the etched GaN-on-Si micro-lens profiles to the input design (SSS-NCH).

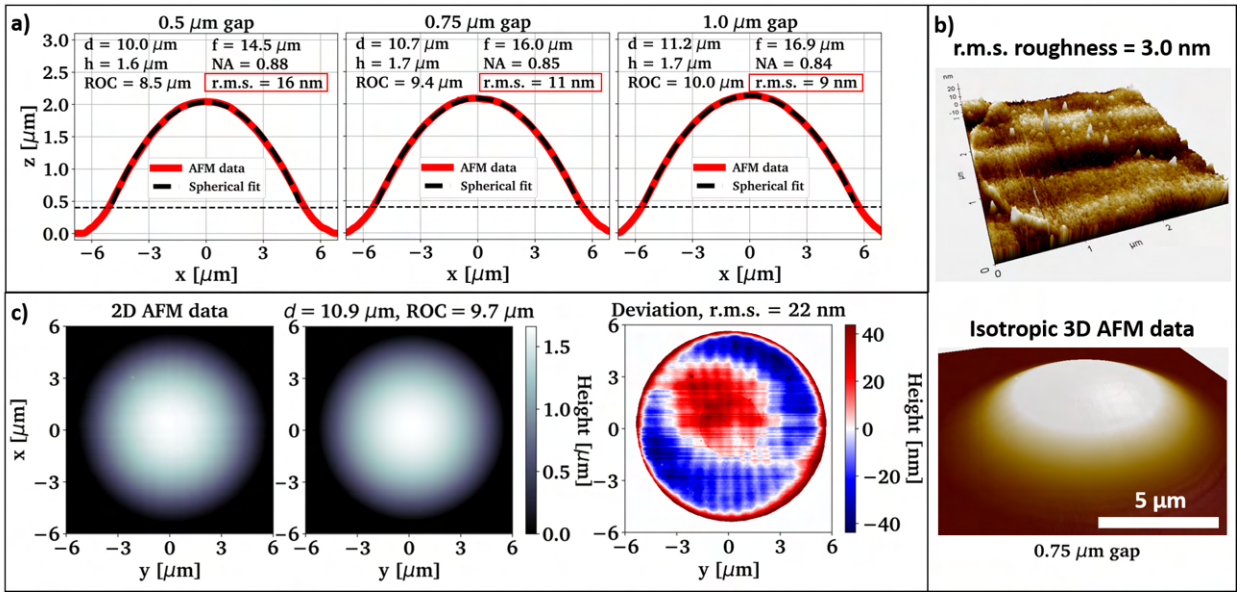

Figure E.7: Detailed AFM analysis of the etched 11 μm diameter GaN-on-Si micro-lenses (SSS-NCH), a) linescan data with spherical fits in dependence of the design gap, b) surface roughness measured on top of a GaN micro-lens with real scale 3D representation, c) 2D spherical fitting of a micro-lens with 0.75 μm gap.

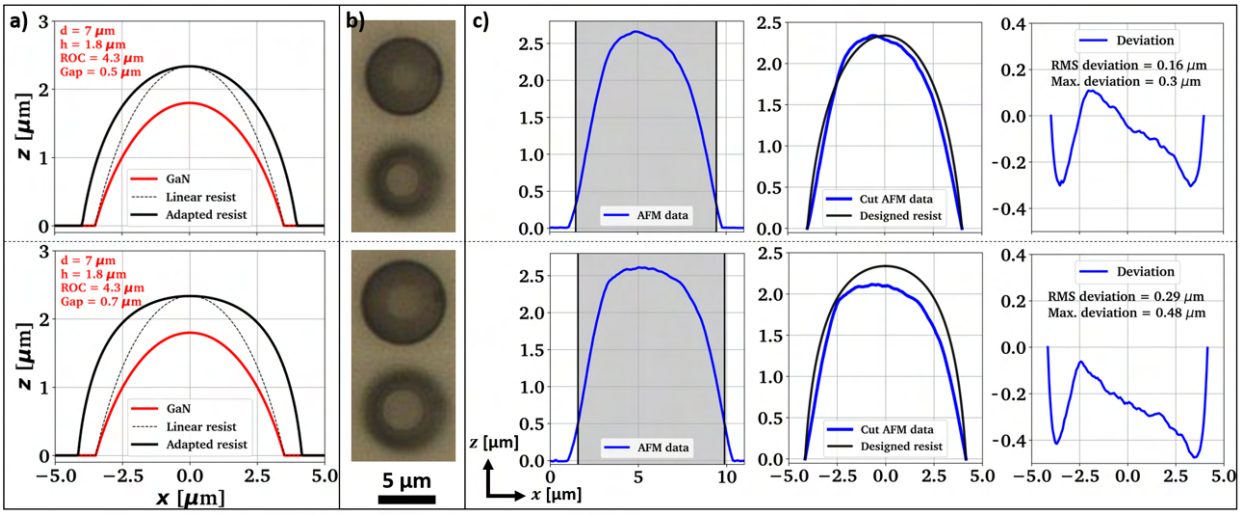

Figure E.8: GaN lenses with 7 μm nominal diameter: A simple optimisation procedure is applied to take the lateral lens etching into account. The resist profile (black) is first backcalculated from the desired spherical GaN lens profile (red) based on the ICP etch selectivity. Then, a parabolic correction is added to the resist profile, creating a gap. a) Overview of designed resist profiles, b) microscope images after optimised grayscale lithography, c) AFM profile analysis and comparison of the resist profile to the design (NSC15). The visible asymmetry is likely due to an assymetric AFM tip.

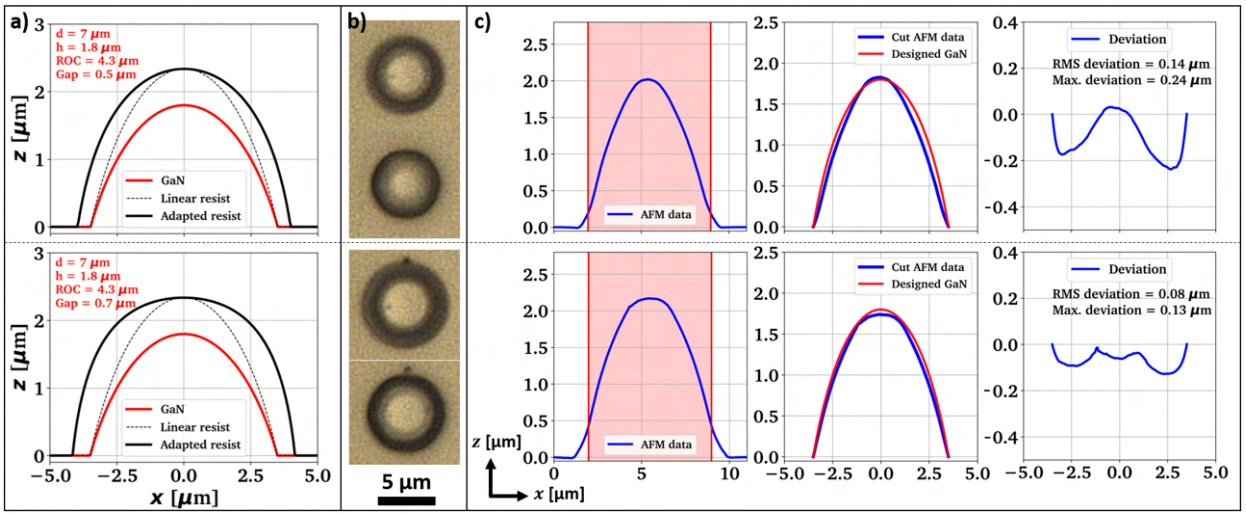

Figure E.9: The same lenses from Fig. E.8 after Ar/Cl_2 based low-bias ICP etching. a) Design of resist and GaN lens profile, b) microscope images of GaN lenses after etching, c) AFM linescan based comparison of the etched GaN-on-Si micro-lens profiles to the input design (SSS-NCH).

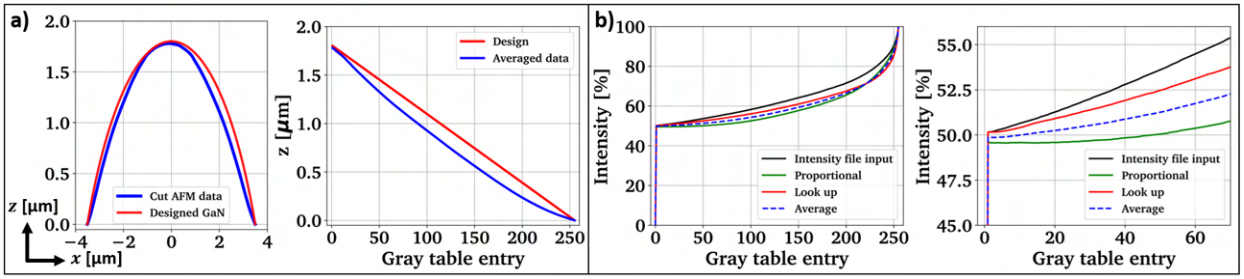

Figure E.10: Feedback for further optimization: The final lens profile could be used to adapt the intensity graytable. a) AFM linescan on a etched GaN lens with 0.6 μm design gap (SSS-NCH), and the resulting z profile backcalculated to the graytable entries, b) generation of new intensity files by 3 different methods based on the collected data.

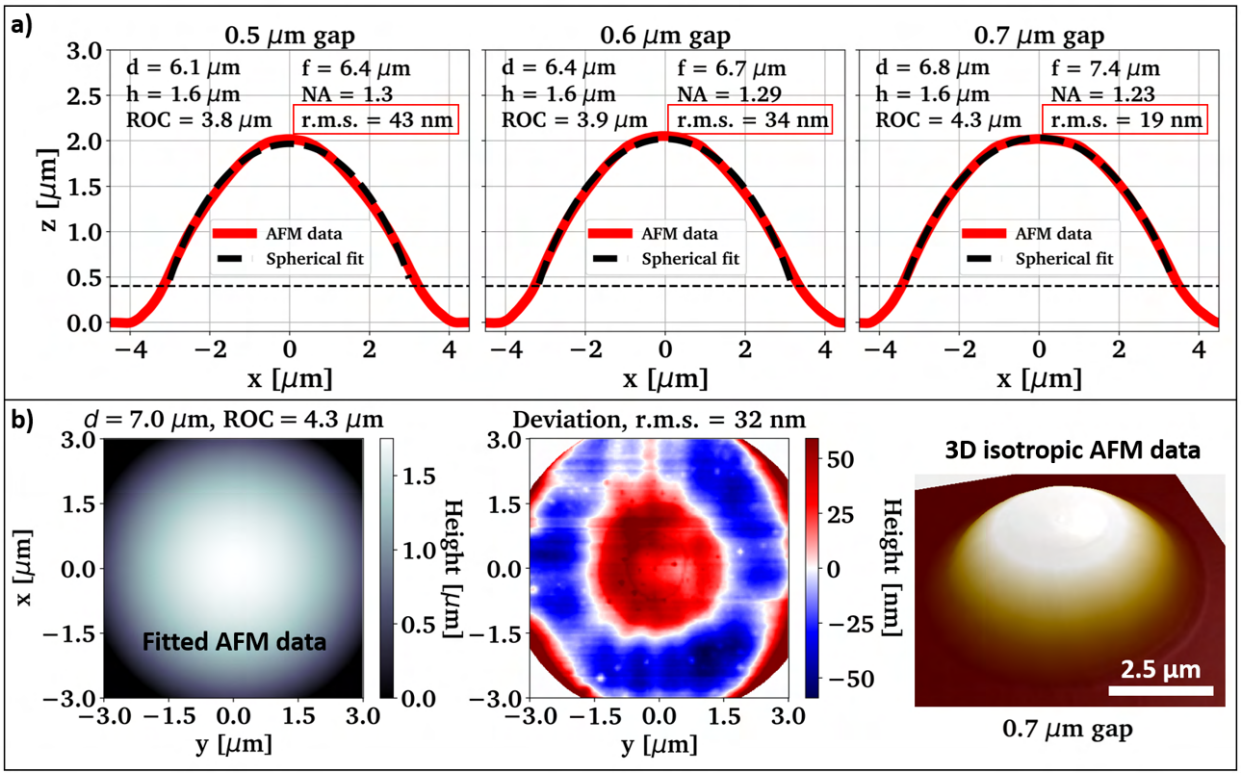

Figure E.11: Detailed AFM analysis of the etched 7 μm diameter GaN-on-Si micro-lenses (SSS-NCH), a) linescan data with spherical fits in dependence of the design gap, b) 2D spherical fitting of a micro-lens with 0.7 μm gap and 3D real scale representation.

E.3 Typical device layout

Fig. E.12 shows a typical layout optimized for grayscale lithography. The large x spacing between the devices allows to separate the devices from the Si deep etch into the substrate. The buffer region reduces edge effects on the array, optimally the most outer devices might not contain a pattern and serve as dummy buffer devices to homogenize the development behaviour across the devices. The outer frame is useful to control the photoresist thickness after development with a profilometer. Additionally we recommend the use of test patterns next to the device to check power and focus settings on a known pattern such as a 10x10 μm^2 chess board.

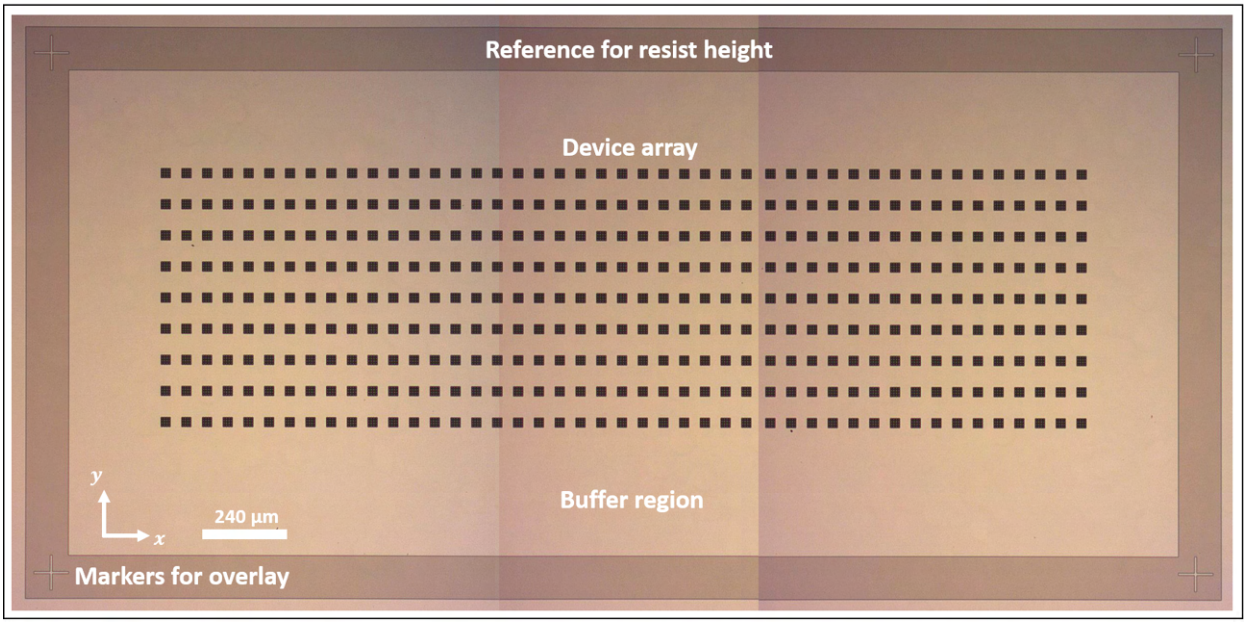

Figure E.12: Typical device layout for the creation of membrane devices, here with dense resist micro-lens arrays (SPR220-4.5) with 30 μm footprint, 60 μm pitch in y and 90 μm pitch in x direction (which is the fast Si etch direction along <110>).

E.4 Monolithic diamond lenses

In the following we provide a detailed schematic illustrating how HPHT diamond substrates can be embedded into optical Norland, compare Fig. E.13. A similar process might be adapted to inlay thin diamond membranes ($< 30\,\mu$m). Alternatively such membranes can be carefully fixated on a 4 inch Si carrier wafer by using nail polish - spinning on a large substrate like this might also reduce the edge bead especially when choosing high spin speeds > 5000 rpm. The microscope images in Fig. E.14 and E.15 show additional monolithic diamond processing corresponding to the lenses shown in Chapter 2. The lenses in Fig. E.15 correspond to the devices used for the focal length measurements in Chapter 3.

E.4.1 Embedding procedure for small diamond substrates before lithography

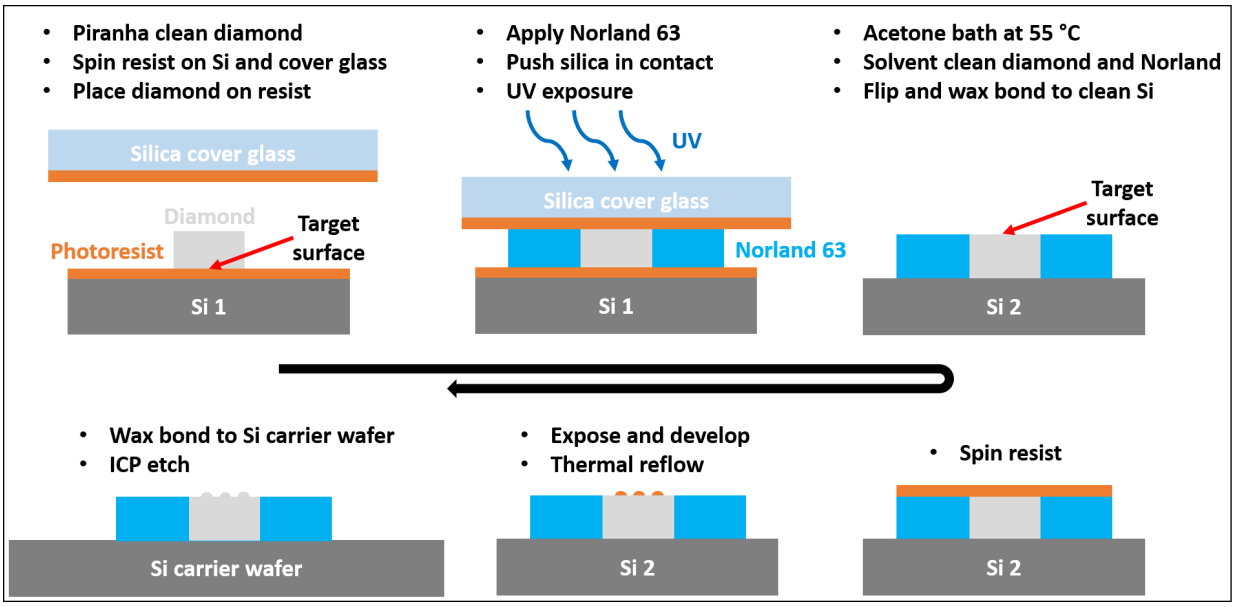

Figure E.13: Schematics illustrating embedding, photolithography and lens etching processes employed with 4x4x0.5 mm single crystalline diamond substrates using the optical adhesive Norland 63.

E.4.2 Etched diamond lenses

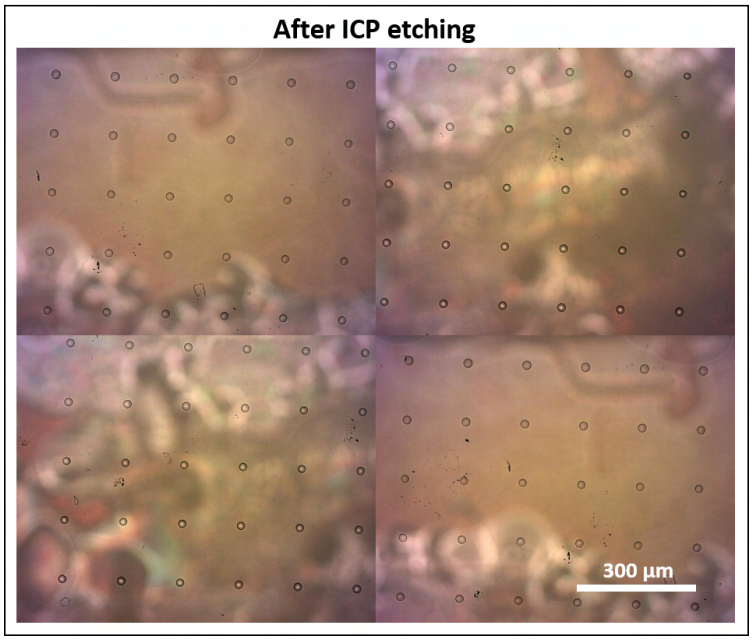

Figure E.14: Incomplete overview of a diamond micro-lens array with 150 μm pitch created from a single layer SPR220-7.0 on a single crystalline diamond substrate using the mask aligner for exposure and the reflow method to shape the lenses (20 μm nominal diameter).

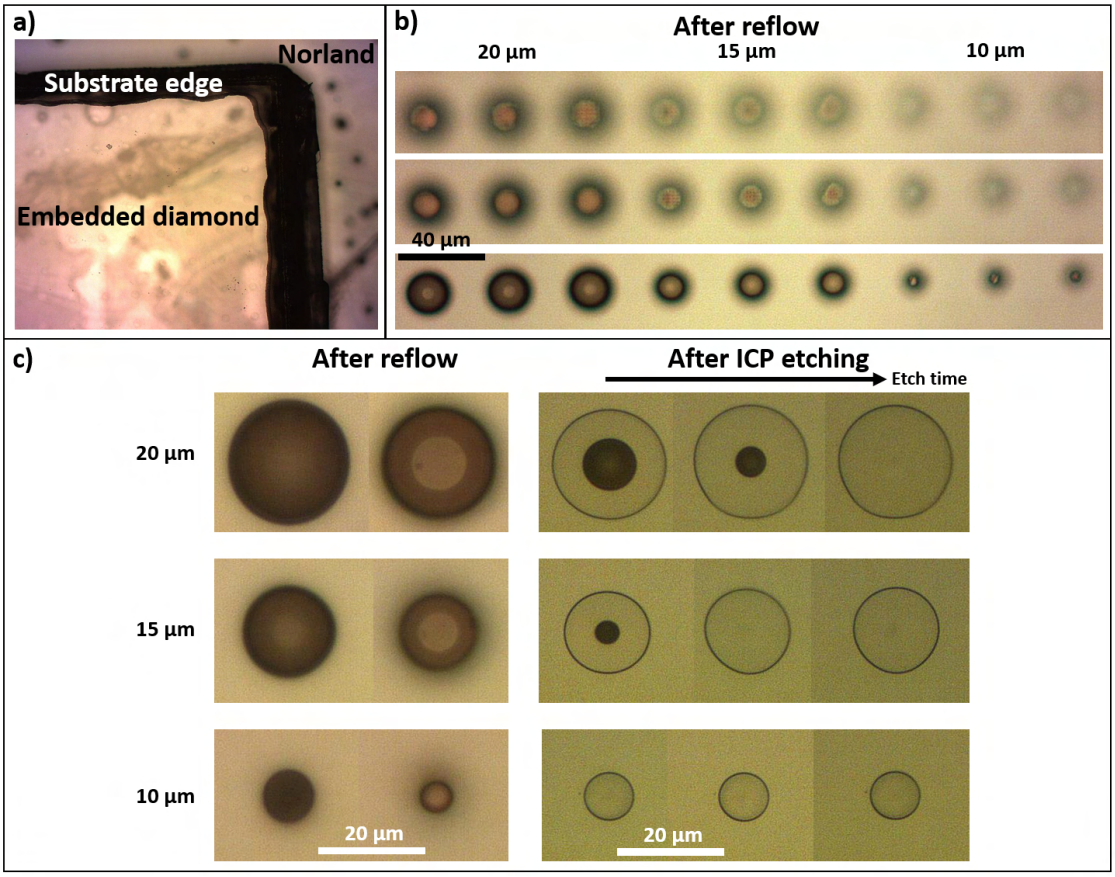

Figure E.15: Double layer processing of SPR220-7.0 using the DWL66+ laser lithography system. a) Microsocpe image of the diamond substrate embedded into Norland 63 before spinning, b) photoresist lenses with varying diameter at three different focus positions imaging the backside of the diamond substrate, c) high magnification microscope images of resist lenses after reflow and Ar/Cl_2 based ICP etching (10, 12.5 and 16 min etching time respectively). The scale bars in c) apply to all images in this box.

E.5 GaN micro-lenses: First test on sapphire

Fig. E.16 documents the first etching test of GaN micro-lenses in Ar/Cl_2 plasma using a GaN-on-sapphire template. The samples are etched using the mLED3 recipe in ICP2.

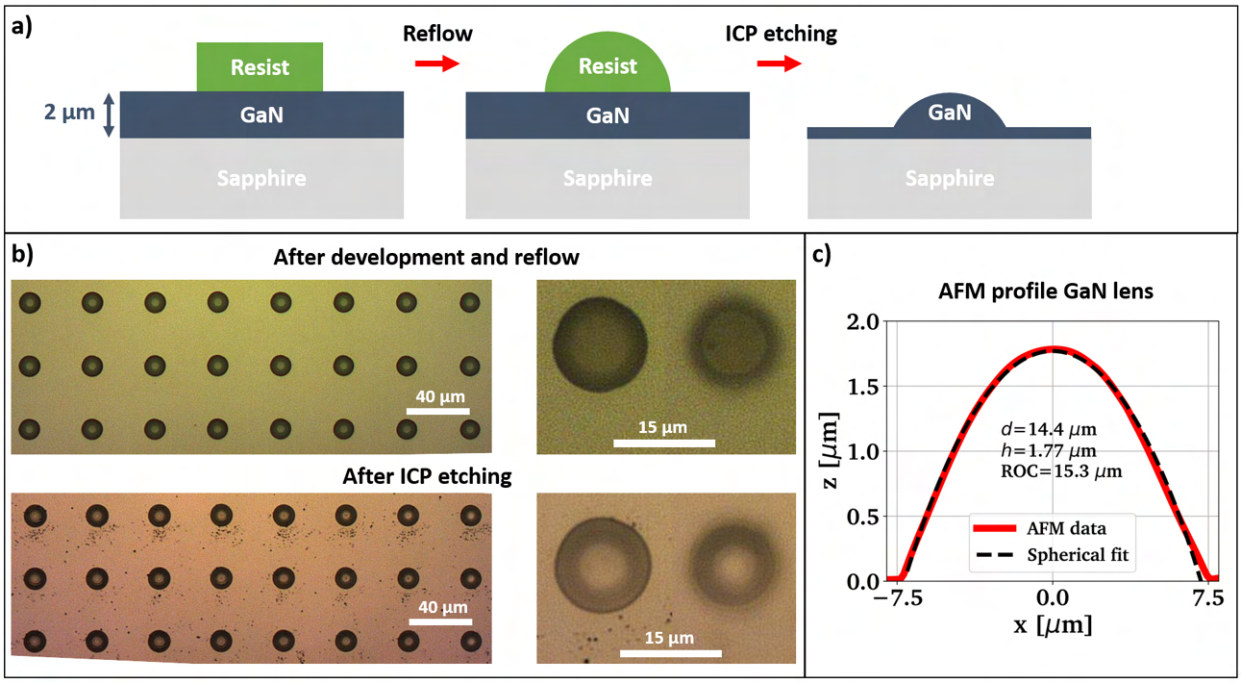

Figure E.16: Result of first GaN test etching using the DWL66+ and SPR220-7.0 employing a variant of the Ar/Cl_2 etch recipe in the alternative ICP etcher. a) Schematic of the process flow and layer stack, b) microscope images after reflow (165 °C) and ICP etching (7.5 min), c) AFM profile of the nominally 10 μm diameter GaN lens after etching (NSC15).

E.6 GaN micro-lens arrays

The following Fig. E.17 and E.18 illustrate how larger scale GaN lens arrays and GaN pillars are designed and etched using grayscale lithography and the optimized Ar/Cl_2 ICP GaN lens etching recipe.

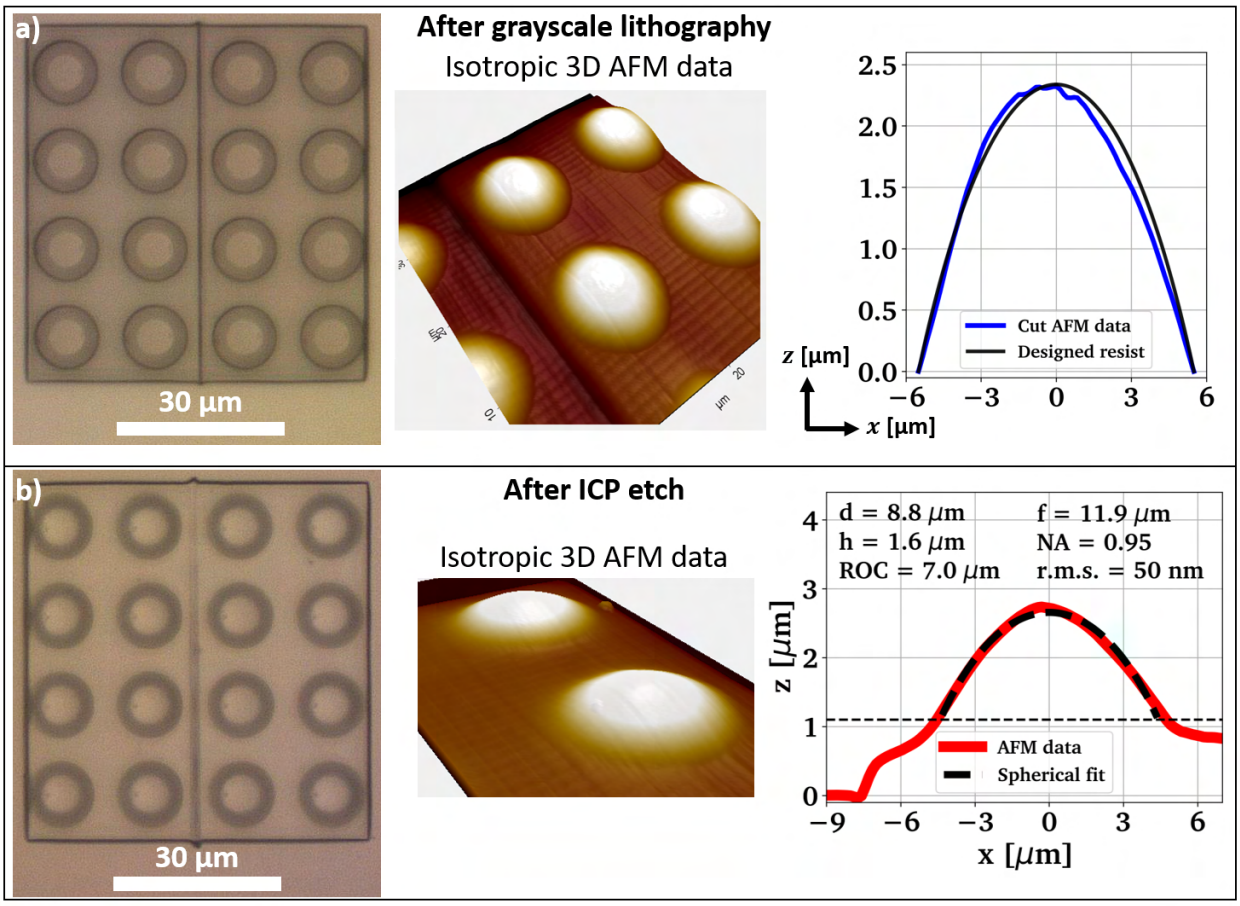

Figure E.17: 4x4 micro-lens array on a 60x60 μm^2 mesa and nominally 11 μm lens diameter with 15 μm pitch. Microscope images of a) photoresist lenses after optimized grayscale lithography and b) after low-bias Ar/Cl_2 etch transfer into the GaN-on-Si layer with corresponding AFM data (NSC15).

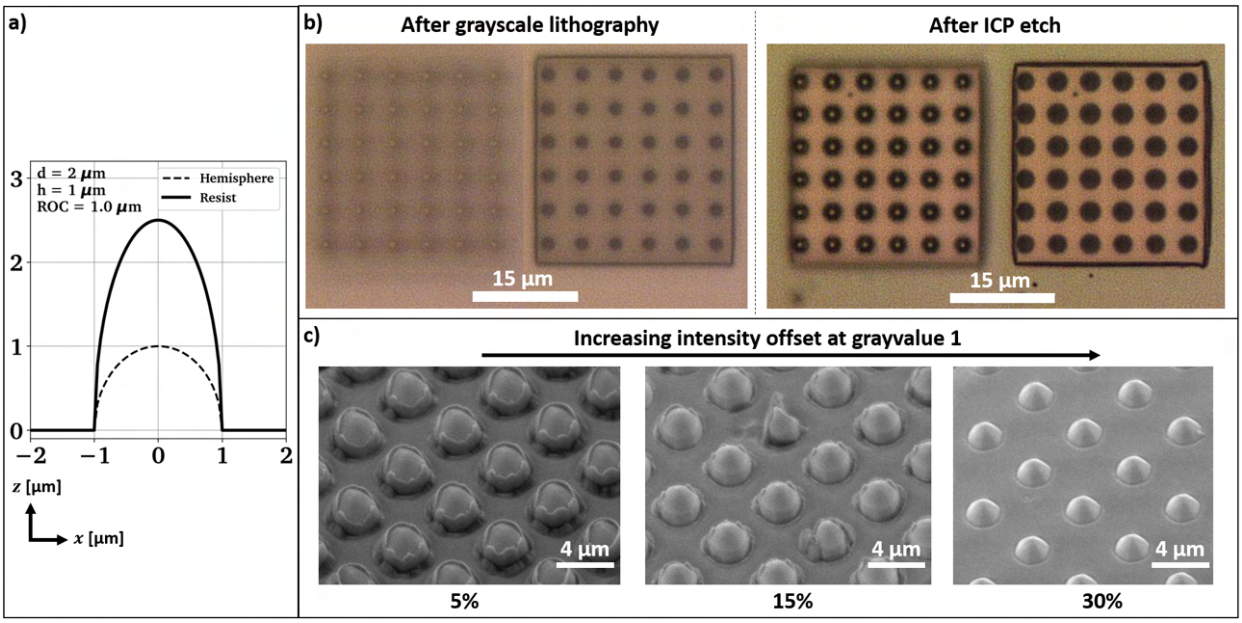

Figure E.18: Failed attempt to fabricate narrow GaN micro-pillars with rounded end-facets. The idea was to exploit the lateral etch components in the ICP process to generate sub-micron pillar diameters. a) Design layout of the resist for grayscale lithography, b) microscope images after grayscale lithography and ICP etching, c) Tilted SEM images (40°) after ICP etching showing the result for different intensity offset values in the grayscale exposure.

F Hybrid integration: Additional information

Here we provide additional information regarding Chapter 3.

F.1 Micro-stamp fabrication

The detailed micro-stamp fabrication is shown in Fig. F.1 and F.2 using a 6:1 weight ratio of polymer to curing agent.

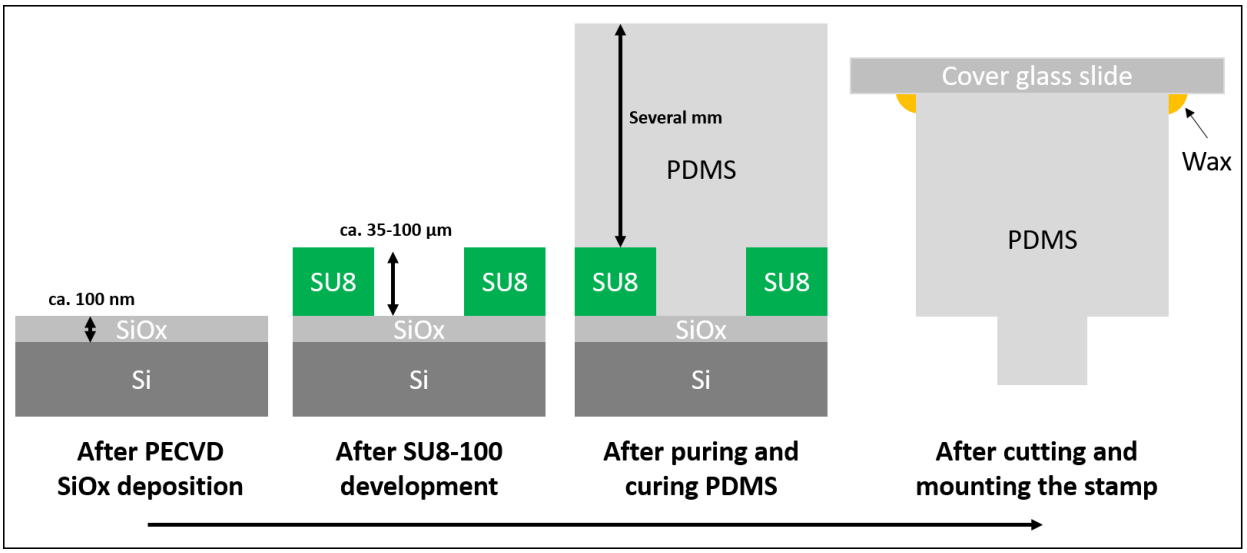

Figure F.1: Schematic of the standard process for PDMS μ-stamp fabrication used in this work.

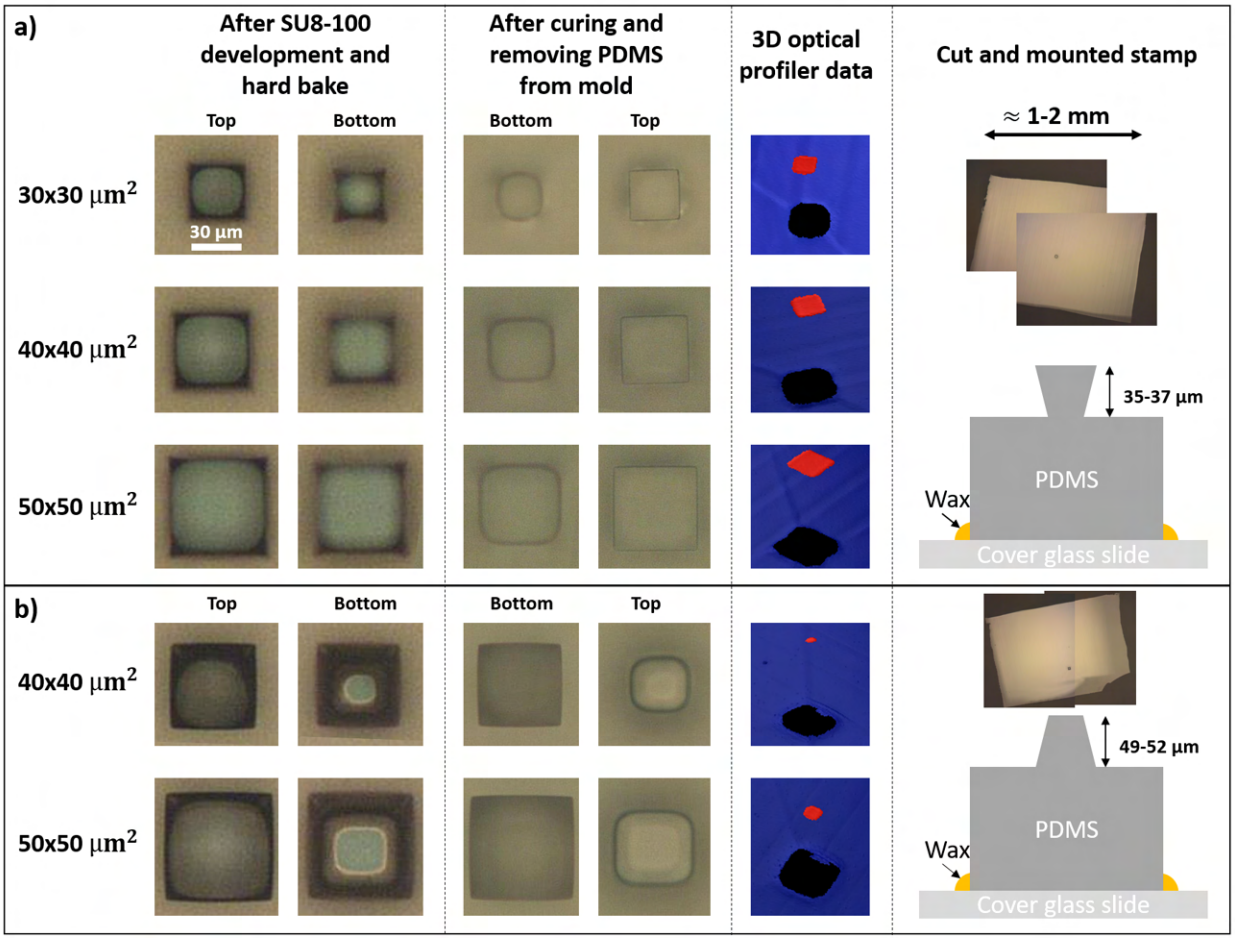

Figure F.2: μ-stamp fabrication using the DWL66+ and fast spun SU8-100. a) ca. 35 μm high PDMS μ-stamp in the shape of inverted truncated pyramids, b) ca. 50 μm high PDMS μ-stamp in the shape of truncated pyramids. The most top stamp design was mostly used for printing GaN micro-lenses in this work. The given scale bar applies to all images.

F.2 Micro-lens array processing and printing

For completeness we include the detailed fabrication documentation for the achieved suspended GaN micro-lens arrays. The intensity offset and laser power is swept on these substrates in triplets of three, leading to slightly different etch depth and therefore membrane bow for the finalized devices. For tests, columns with least interference fringes in the collapsed region are selected.

As a highlight, Fig. F.6 documents how a AFM cantilever is used to break the anchors of 2x2 micro-lens arrays with a thinned anchor geometry.

F.2.1 2x2 micro-lenses on 30x30 μm^2 square membranes

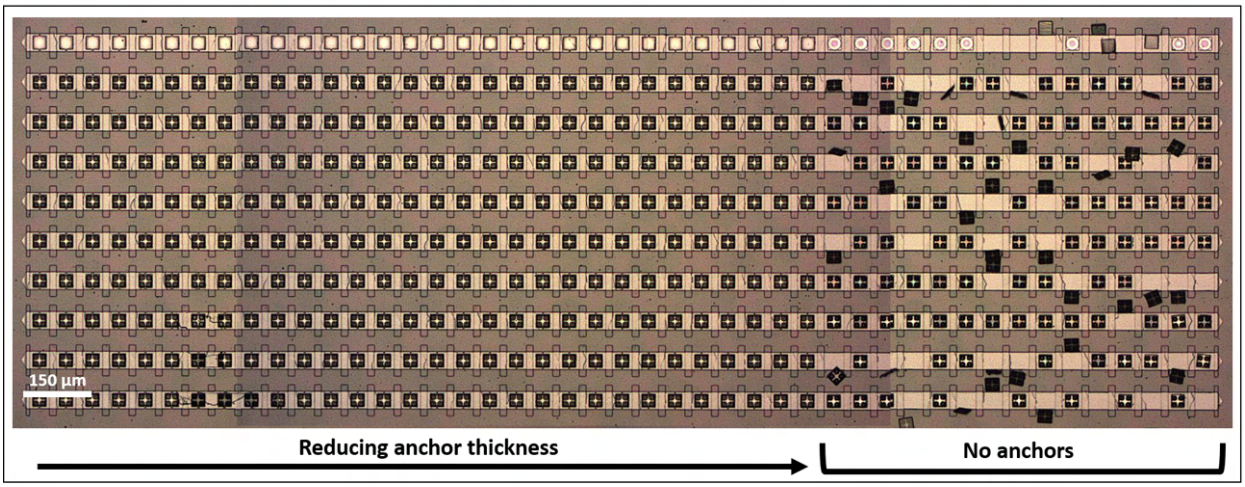

Figure F.3: Example process: 2x2 micro-lens arrays. Typical yield of the optimized micro-fabrication process. On the right hand side of the substrate, no anchors are employed, leading to the loss of devices during hard mask removal (10-11).

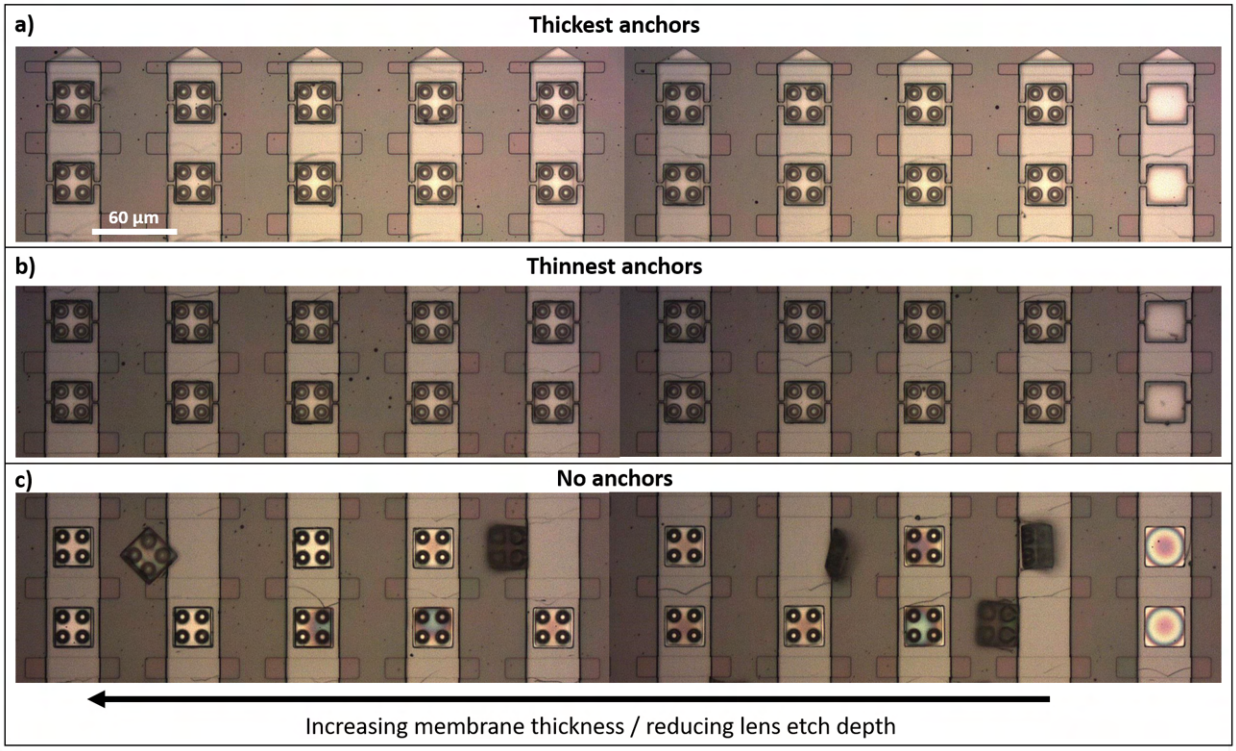

Figure F.4: Example process: 2x2 micro-lens arrays. Microscope images showing regions with a) thickest, b) thinnest and c) no anchors after lateral suspension and SiO_x hard mask removal (11). Due to varied overall exposure dose during lens and mesa lithography, the membrane thickness increases from right to left. The devices in c) are bonded to the etched Si substrate, revealing the absence of interference fringes for thicker membranes. The collapsed membranes without lenses on the right hand side of c) show clear fringes, indicating a device membrane bow. The scale bar in a) corresponds to all images.

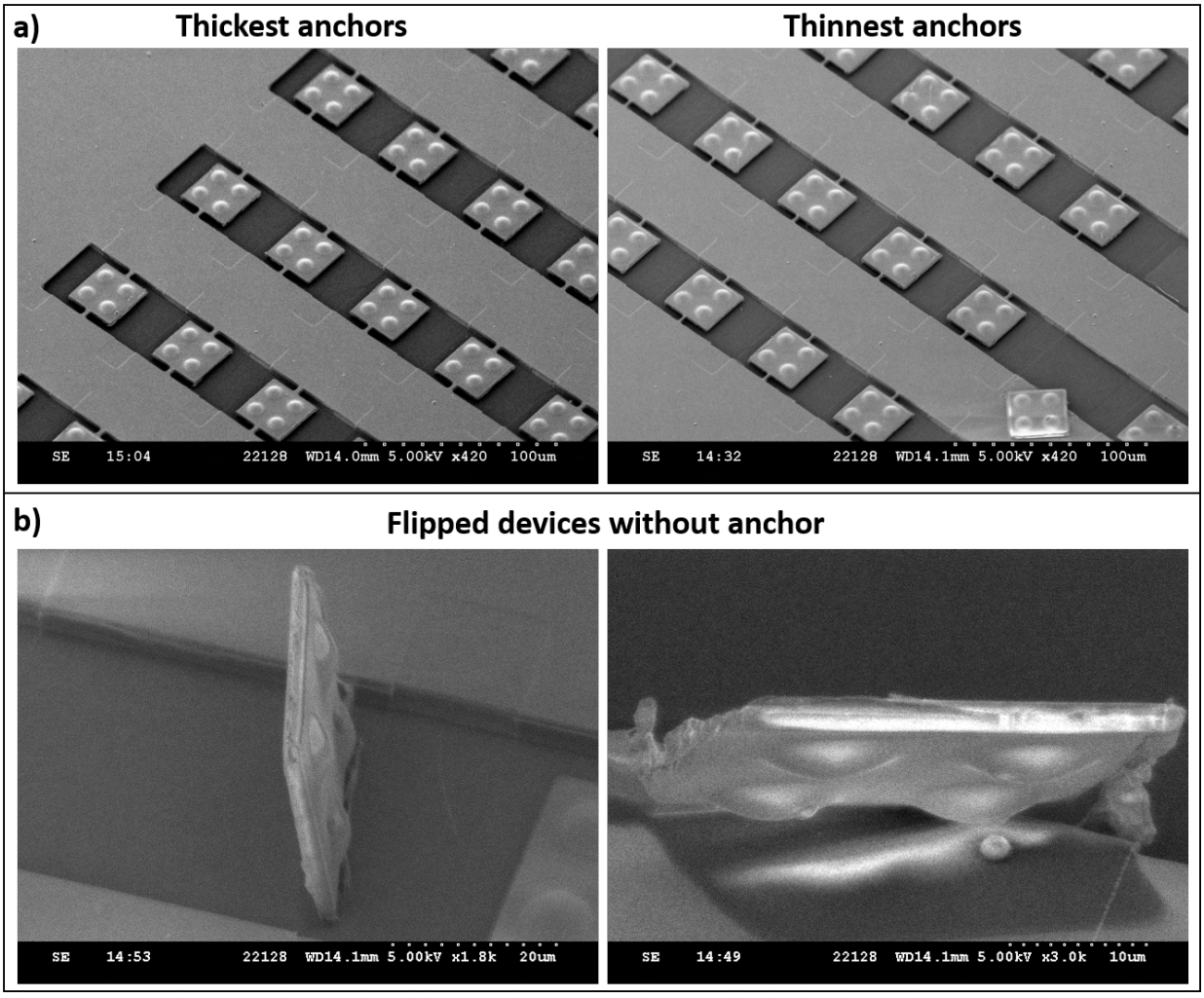

Figure F.5: Example process: 2x2 micro-lens arrays. Tilted SEM images (40°) after process step (11), a) overview of thickest and thinnest devices, b) images of upright standing devices which flipped during hard mask removal (10-11).

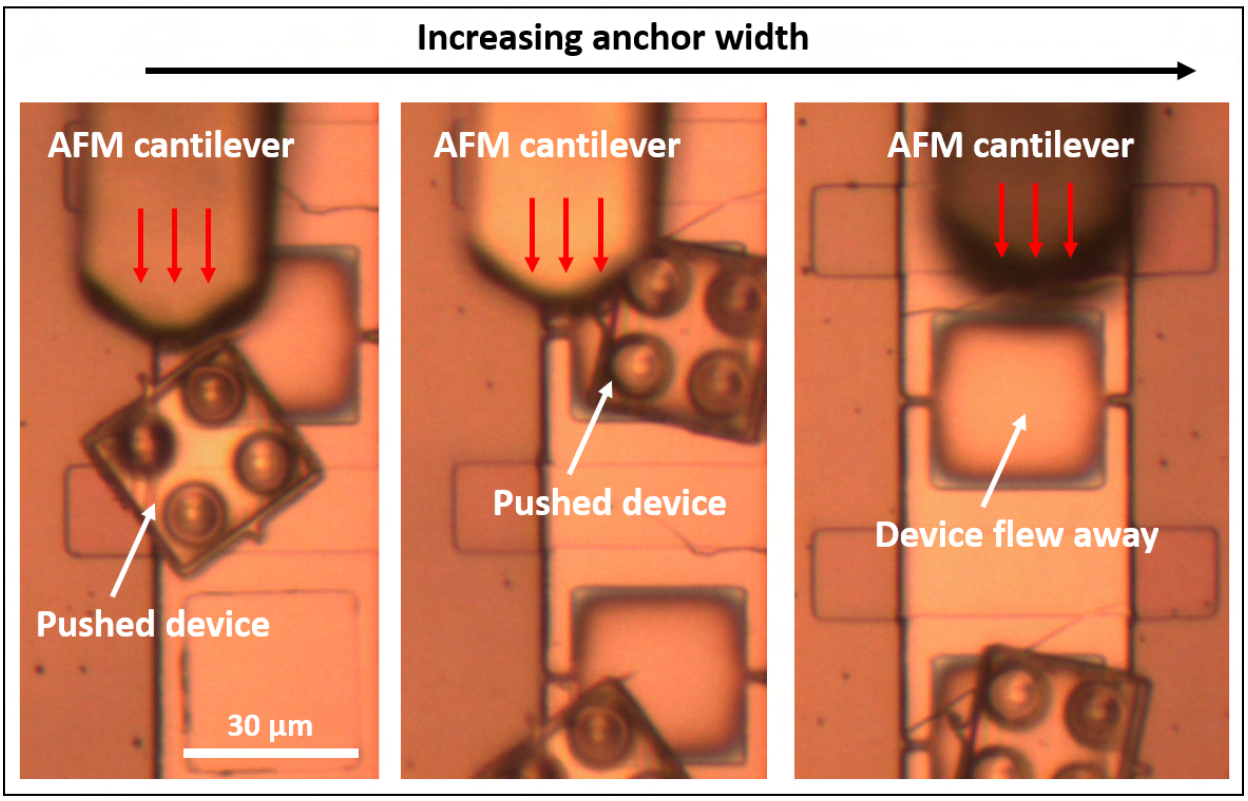

Figure F.6: In-situ images (inside the transfer print tool) of using an AFM cantilever to break the thinnest 3 anchors of 2x2 micro-lens array devices (30x30 μm^2, compare Fig. 3.12-3.19) in the same column successively (left to right). These anchors proved to be to strong for device lift off with a PDMS stamp despite the applied extra thinning of the surrounding epilayer. The cantilever slowly approaches one anchor in 1 μm steps, leading either to anchor breakage and micron-scale device movement or to flipping the GaN lens array away (most right image). The scale bar applies to all images.

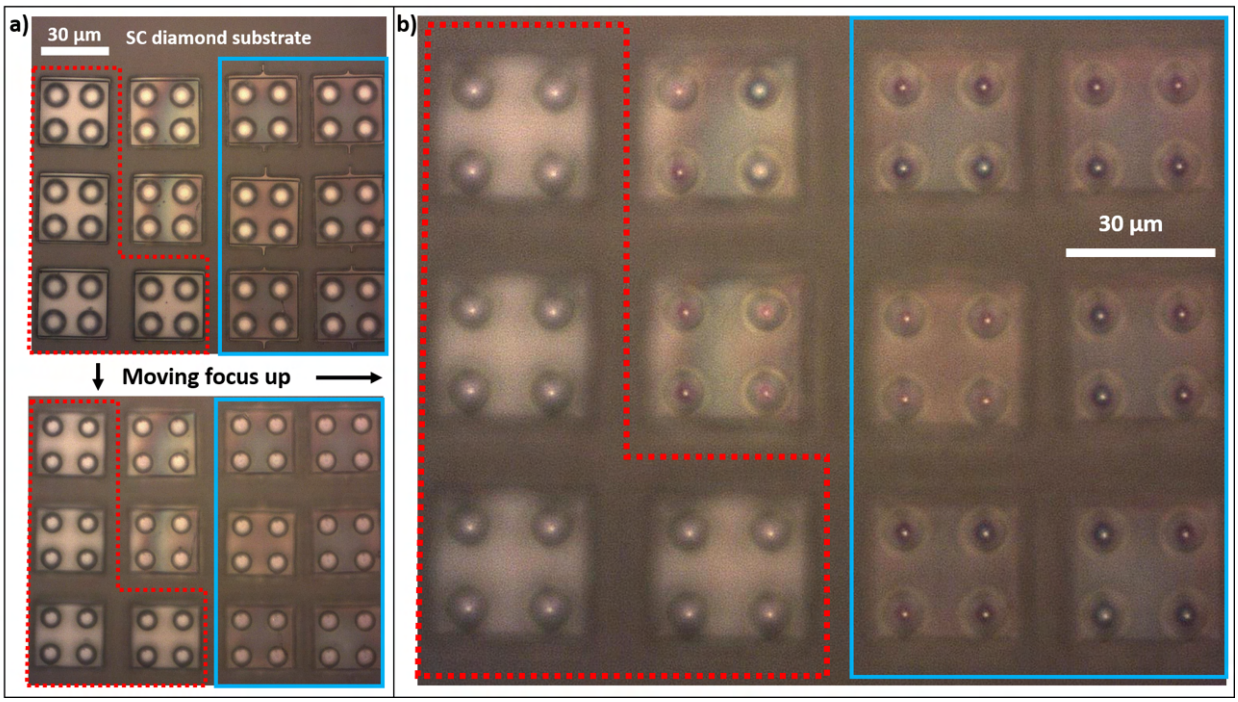

Figure F.7: Transfer printed GaN lens arrays with similar AlGaN/AlN membrane thickness (same total laser power) without (left) and with anchors (right). 4 out of 6 devices without anchor seem to exhibit good contact with the single crystalline diamond substrate below (red), while 2 exhibit colour fringes potentially due to debris (unmarked). All six devices with anchors were broken off with the AFM cantilever prior printing (see previous figure) and exhibit significant colouring after print integration, suggesting that the anchor points prevent a full device contact (blue).

F.2.2 4x4 micro-lenses on 30x30 μm^2 membranes

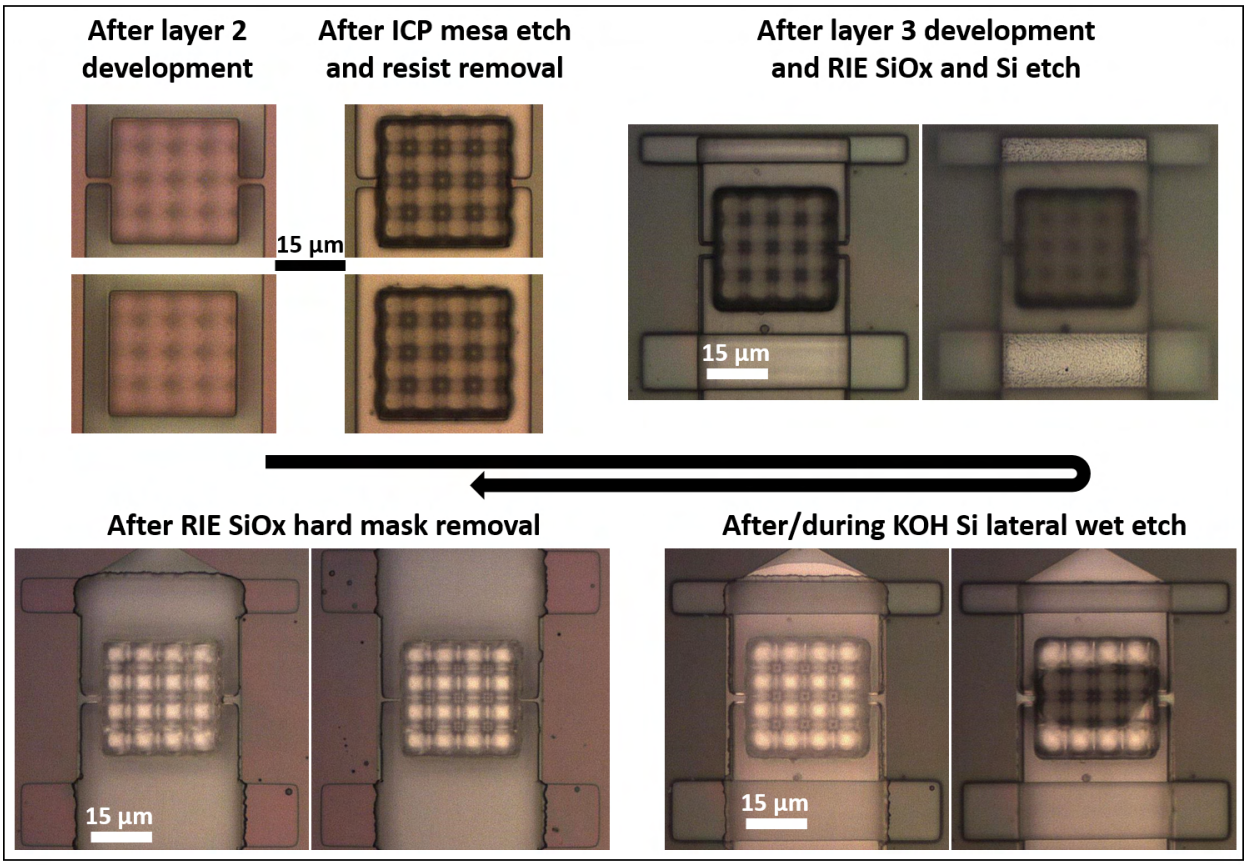

Figure F.8: Membrane processing and suspension of dense 4x4 micro-lens arrays on 30x30 μm^2 footprint (previously discussed in Fig. 2.24). The process flow is similar for all GaN lens arrays and is discussed in detail in Fig. 3.10.

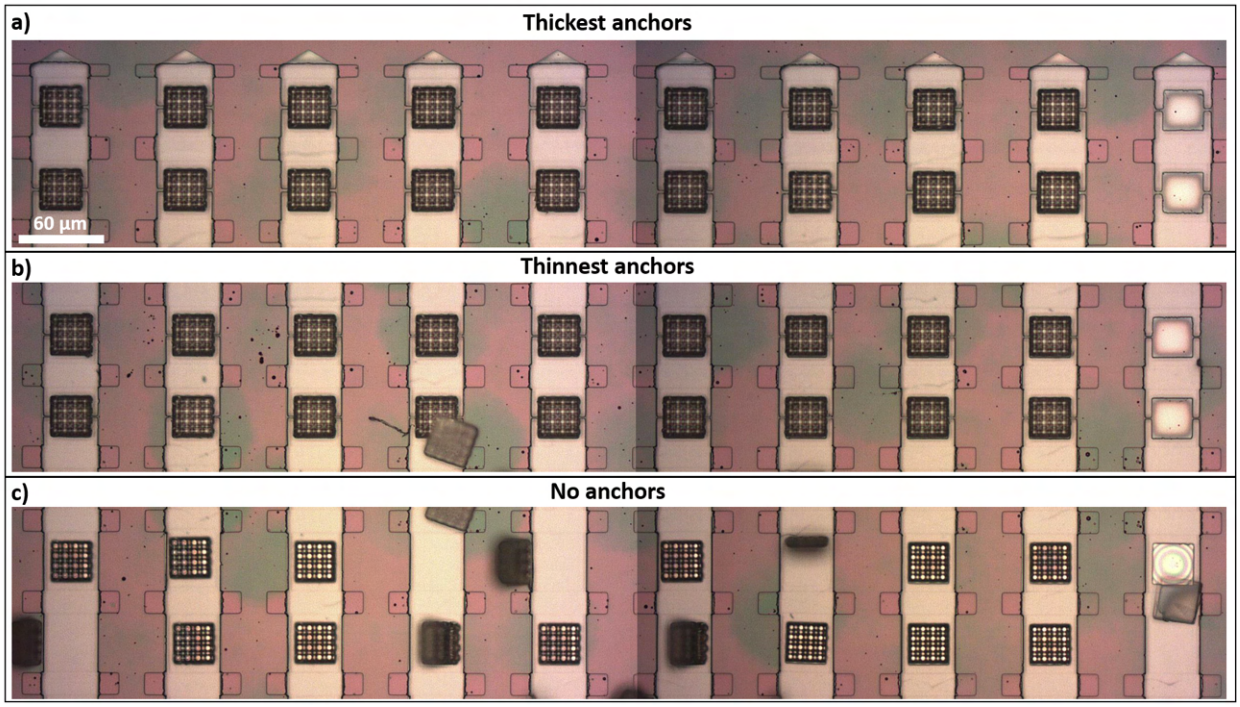

Figure F.9: Yield of dense 4x4 micro-lens arrays on 30x30 μm^2 footprint after finalized micro-fabrication in different areas of the donor chip. The scale bar applies to the images in a), b) and c).

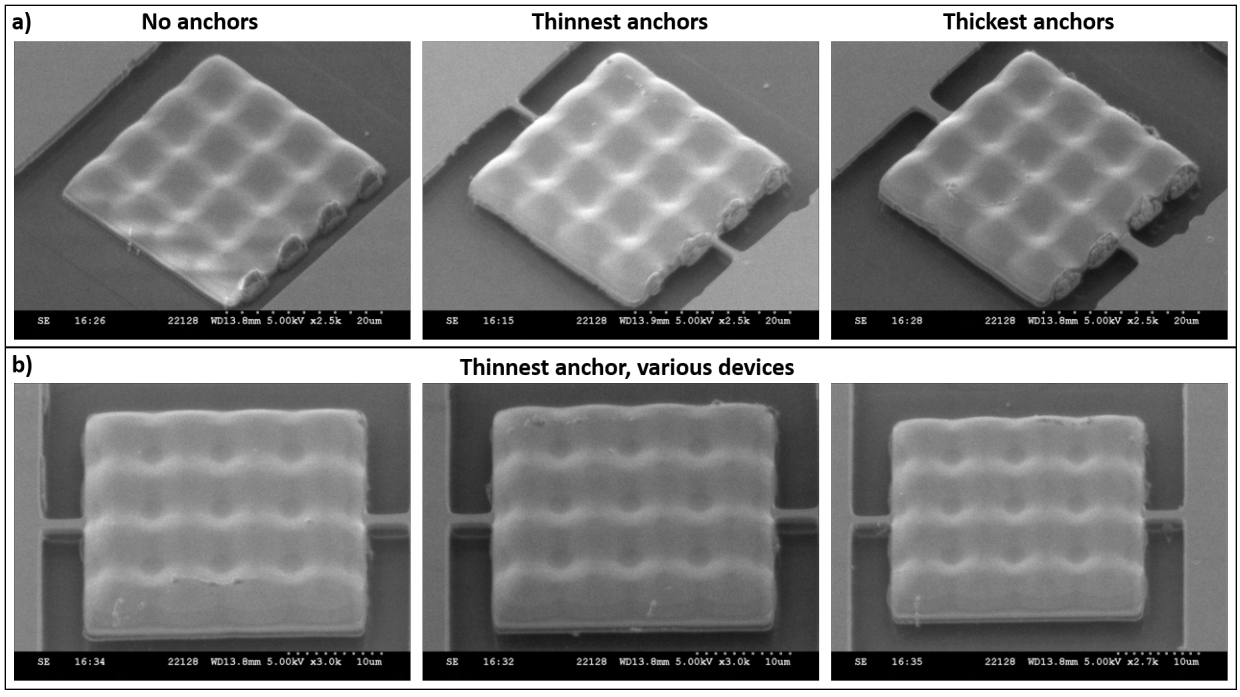

Figure F.10: Tilted SEM images (40°) of dense 4x4 micro-lens arrays on 30x30 μm^2 footprint after finalized micro-fabrication from two different perspectives in a), b). The thinnest anchors prove to break under pressure from a PDMS stamp in the transfer print tool.

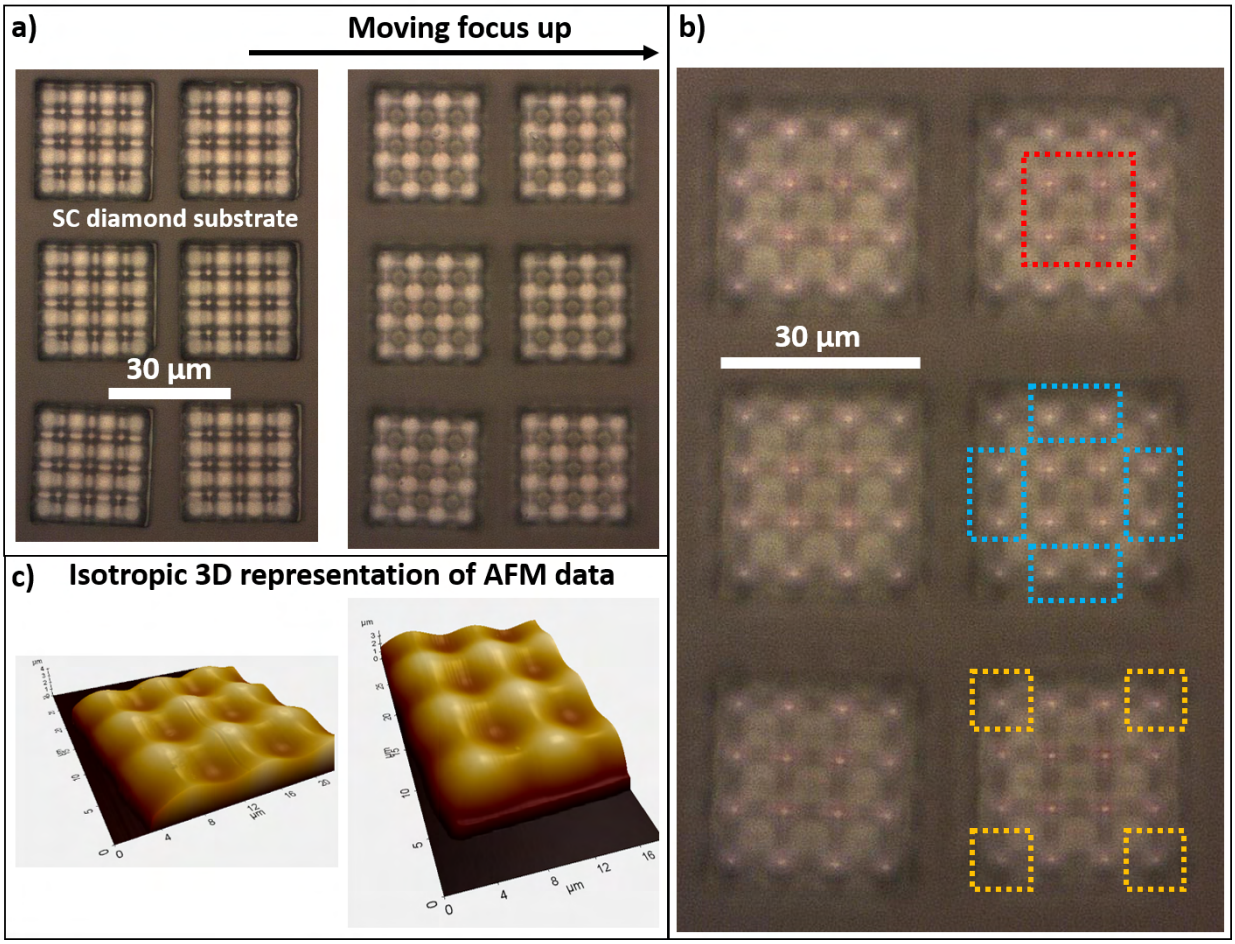

Figure F.11: Transfer printing of dense 4x4 micro-lens arrays on 30x30 μm^2 footprint without anchors onto single crystalline diamond substrates. When moving the focus upwards from a) to b), slight coloration of the GaN lens foci appears. These devices were preselected on their Si growth substrate (collapsed) for minimal coloration indicating device flatness and are probably the flattest devices available. The marked lenses refer to similar exposure conditions, as edge effects are observed to have influenced the lens height in dependence on position within the array, c) real scale 3D AFM representation of similar transfer printed devices on a different diamond substrate (SSS-NCH).

F.2.3 4x4 micro-lenses on 60x60 μm^2 membranes

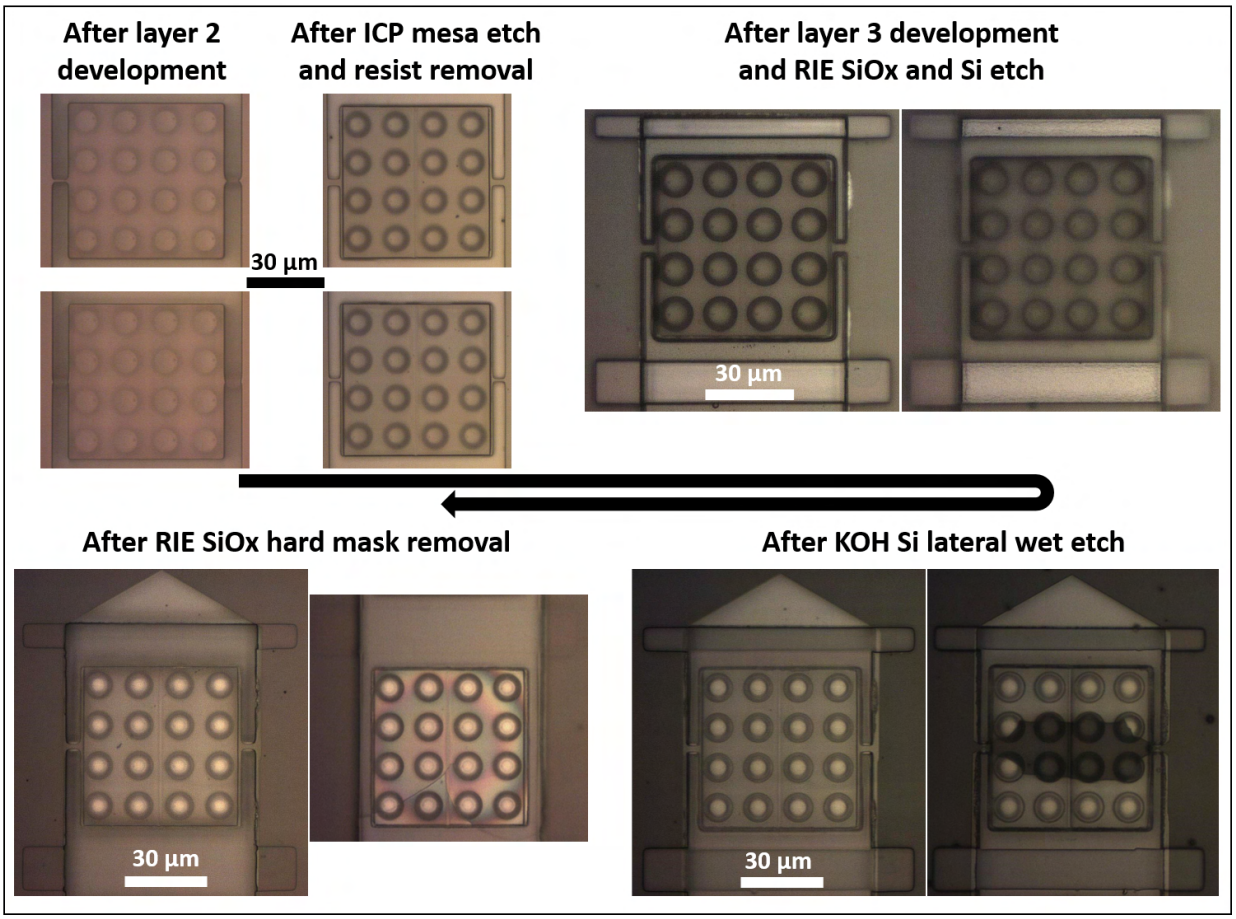

Figure F.12: Membrane processing and suspension of 4x4 micro-lens arrays on 60x60 μm^2 footprint (previously discussed in Fig. E.17). The process flow is similar for all GaN lens arrays and is discussed in detail in Fig. 3.10.

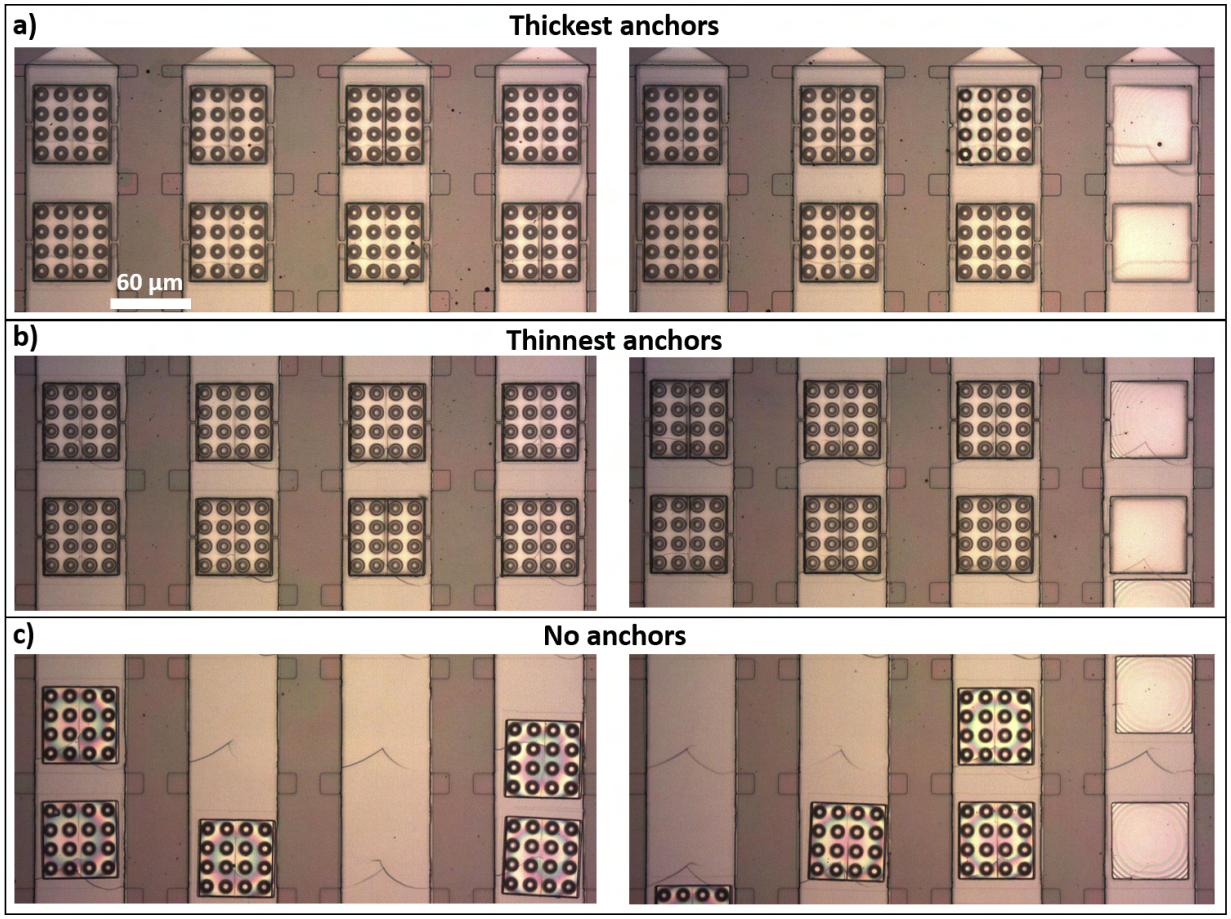

Figure F.13: Yield of 4x4 micro-lens arrays on 60x60 μm^2 footprint after finalized micro-fabrication in different areas of the donor chip. The scale bar applies to the images in a), b) and c).

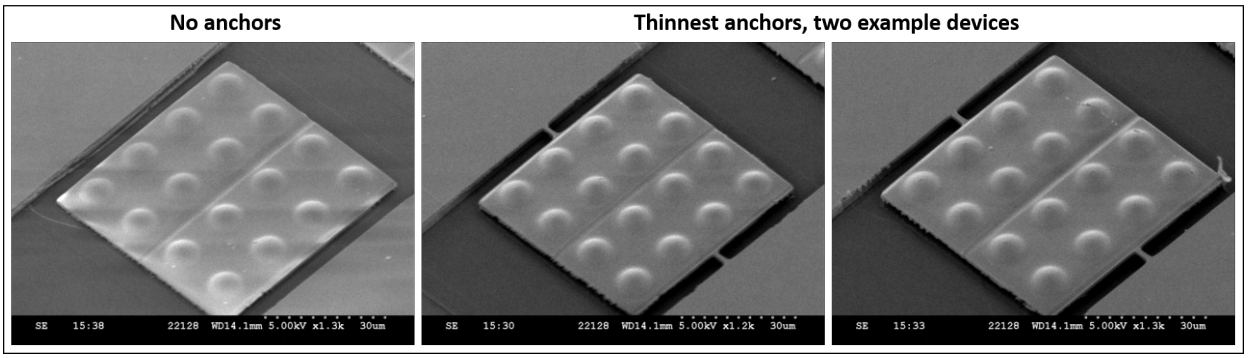

Figure F.14: Tilted SEM images (40°) of 4x4 micro-lens arrays on 60x60 μm^2 footprint after finalized micro-fabrication.

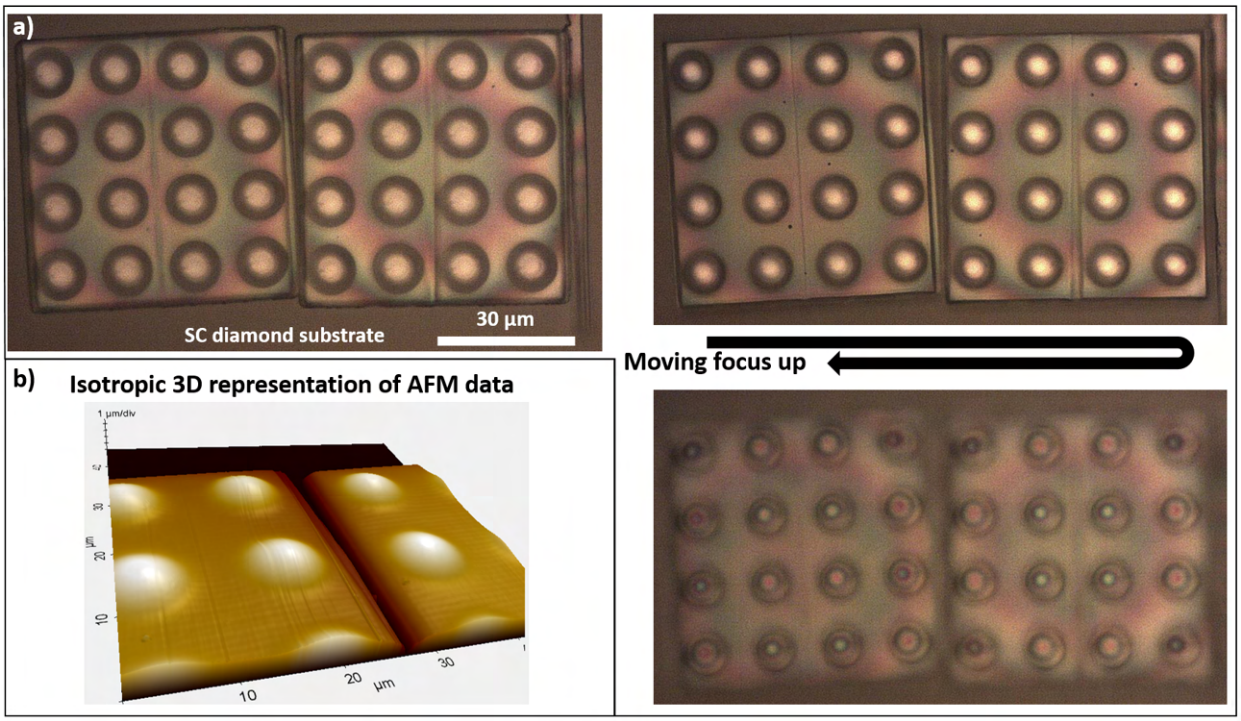

Figure F.15: Transfer printing of 4x4 micro-lens arrays on 30x30 μm^2 footprint without anchors onto single crystalline diamond substrates. Clear color fringing appear throughout the membranes, b) real scale 3D AFM representation of these transfer printed devices (SSS-NCH).

F.2.4 6x6 micro-pillar arrays on 30x30 μm^2 membranes

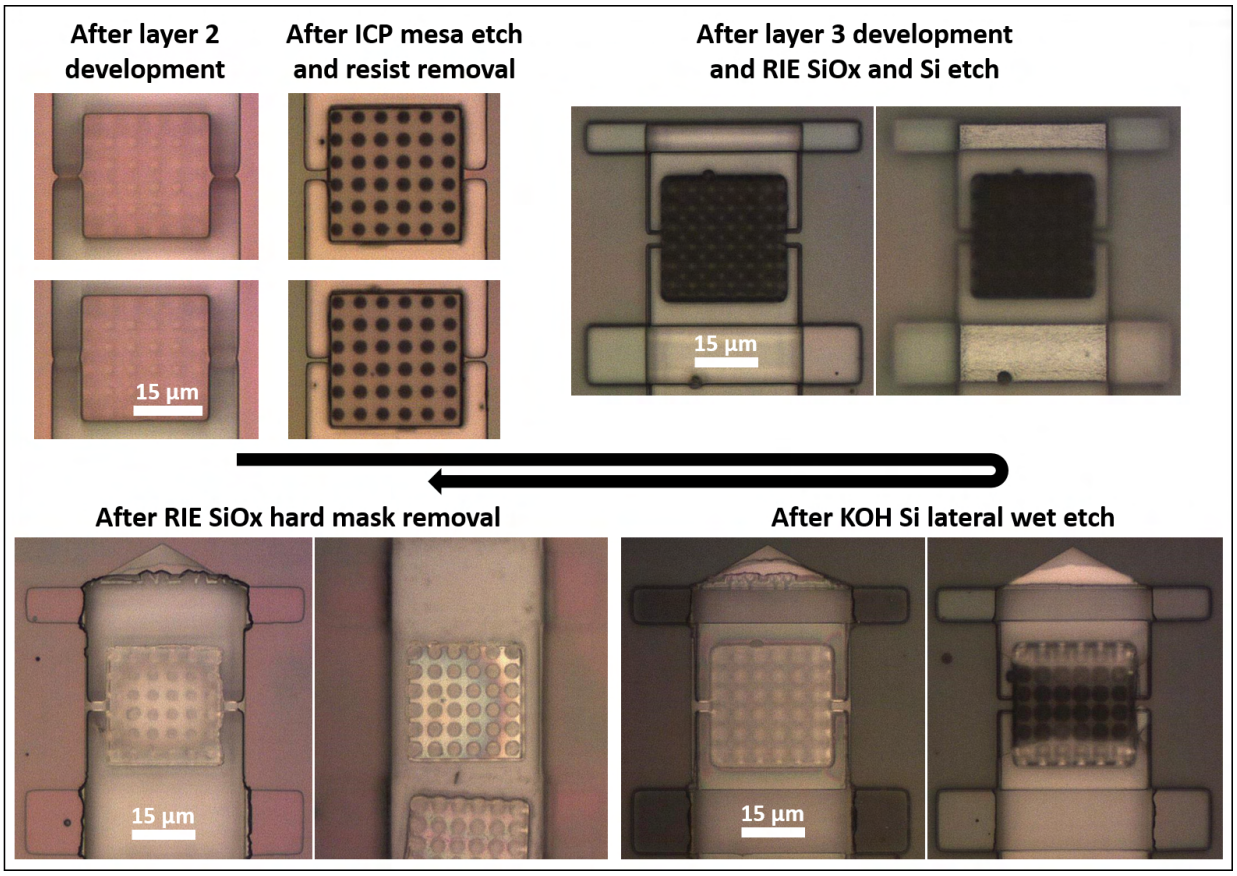

Figure F.16: Membrane processing and suspension of 6x6 micro-pillar arrays on 30x30 μm^2 footprint (previously discussed in Fig. E.18). The process flow is similar for all GaN arrays and is discussed in detail in Fig. 3.10.

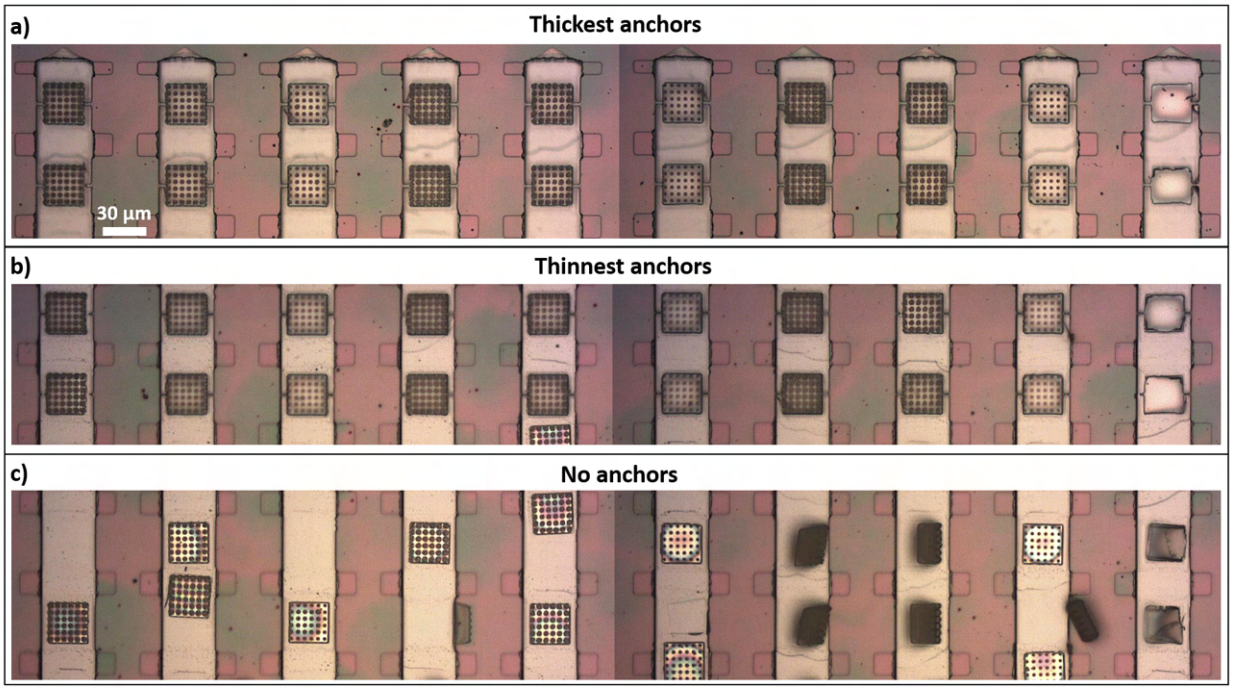

Figure F.17: Yield of 6x6 micro-pillar arrays on 30x30 μm^2 footprint after finalized micro-fabrication in different areas of the donor chip. The scale bar applies to the images in a), b) and c).

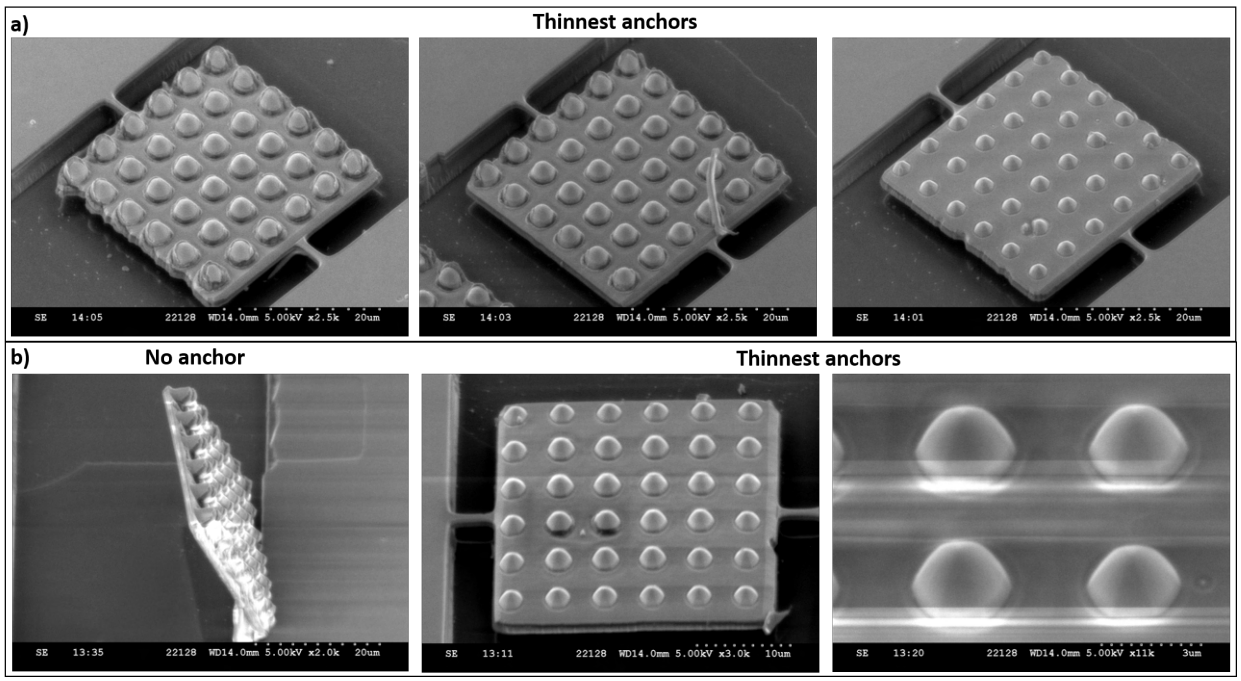

Figure F.18: Tilted SEM images (40°) of 6x6 micro-pillar arrays on 30x30 μm^2 footprint after finalized micro-fabrication. a) shows devices with increasing intensity offset yielding smaller devices at similar membrane thickness, b) shows some additional examples, including an image of an upright standing membrane exhibiting a clear bow (this wafer had -46 μm wafer bow).

F.3 Milestone: Low surface roughness bottom surface

In this subsection we show the data of the first attempt to suspend GaN/AlGaN/AlN membranes containing micro-lenses. The epilayer is etched in ICP2 using the mLED3 recipe. As no silica protection

layer is employed both membranes and lenses are getting heavily etched by the KOH solution used to suspend the devices. Fig. F.21 specifically shows how a flat membrane is picked up with a PDMS stamp (fabircated by Dimitars Jevtics) and the AlN backside is analysed with the AFM confirming an atomically smooth bottom surface.

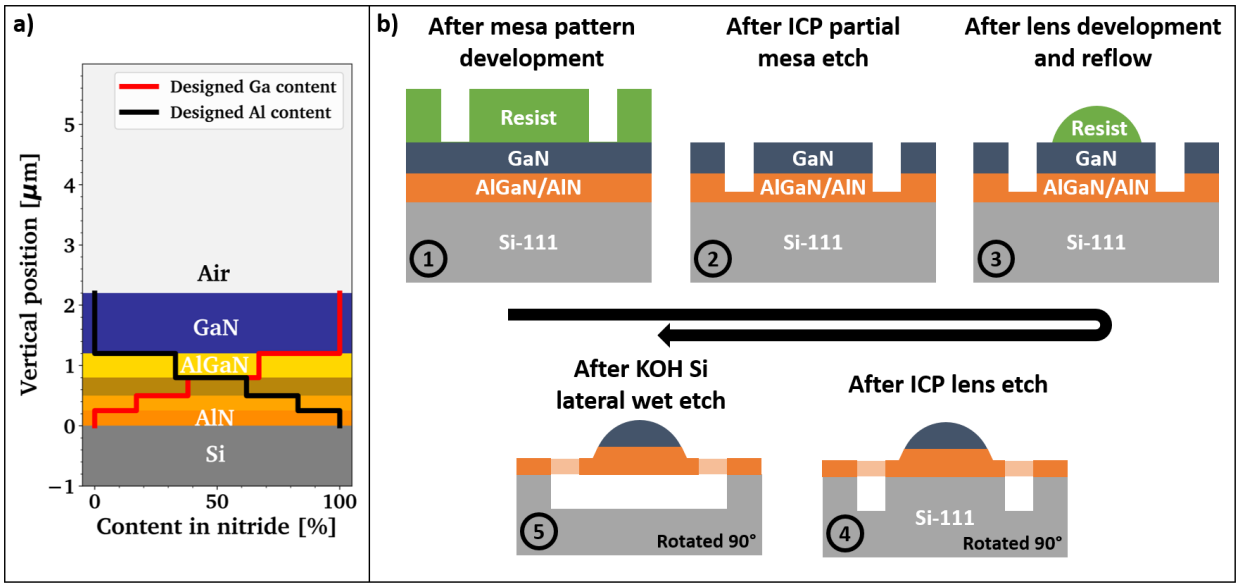

Figure F.19: Initial test of hybrid lens-membrane fabrication using a stepped AlGaN buffer layer and 1 μm thick GaN-on-Si. a) Schematic showing the designed Ga and Al content in the epilayer used, b) process flow employed to test the suspended lens fabrication.

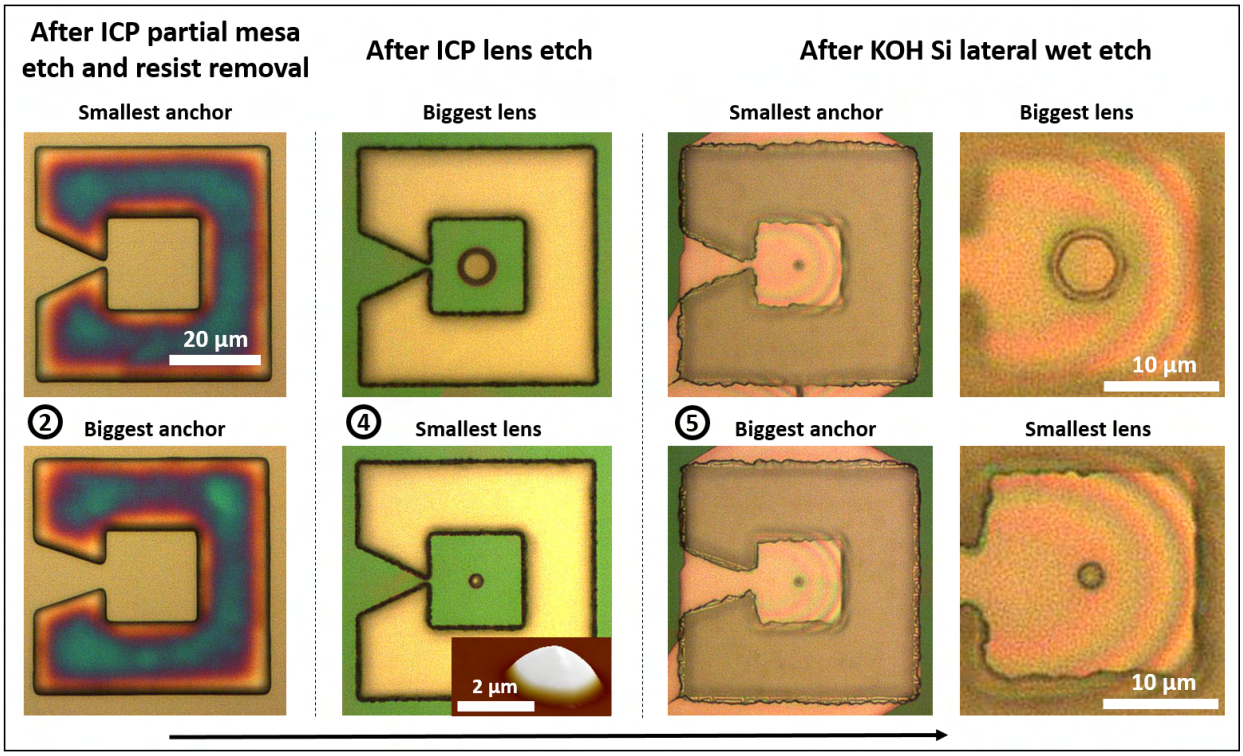

Figure F.20: Initial test of hybrid lens-membrane fabrication using a stepped AlGaN buffer layer and 1 μm thick GaN-on-Si. Microscope images at process steps (2), (4) and (5) with respect to Fig. F.19 b). Final anchor width and lens diameter are varied, SPR220-4.5 is used both for platelet and lens definition (DWL66+ and simple reflow method). The scale bar in the top right applies to the 6 most left images.

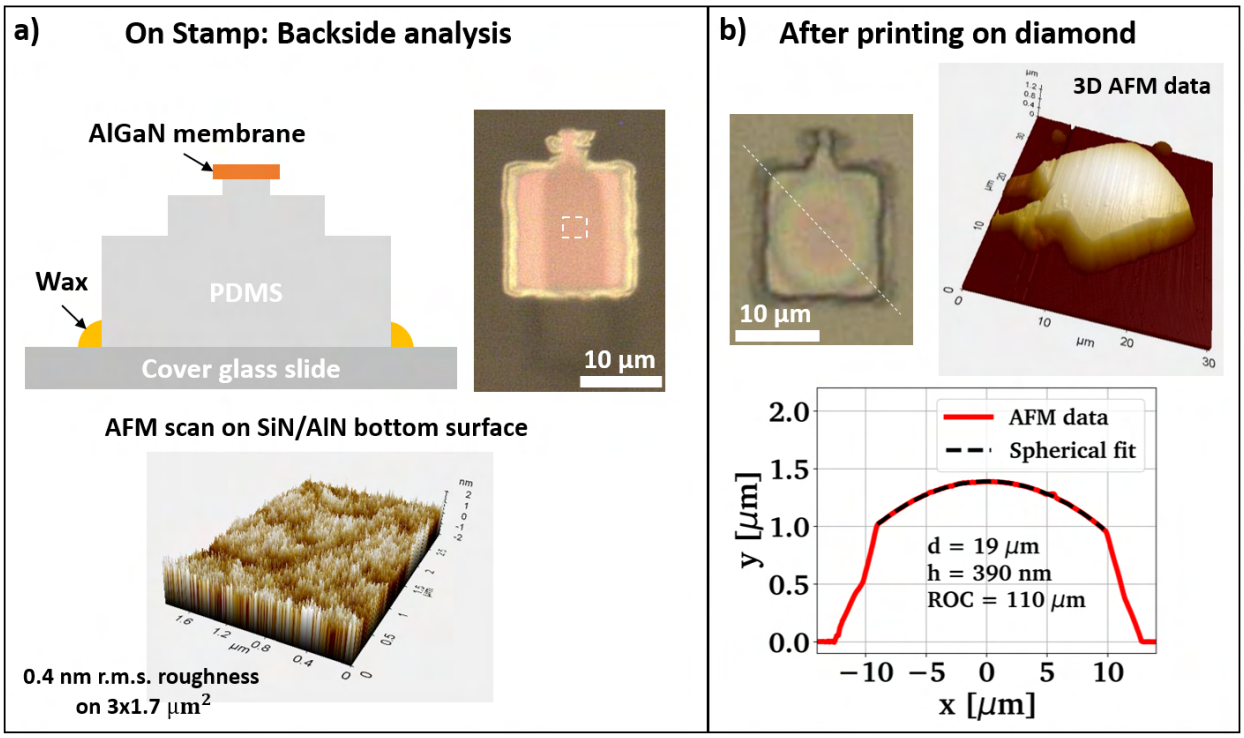

Figure F.21: Initial test of hybrid lens-membrane fabrication using a stepped AlGaN buffer layer and 1 μm thick GaN-on-Si. a) In-situ AFM backside analysis of a AlGaN membrane after pick-up with the transfer print tool by placing the stamp on the AFM sample stage, b) AFM analysis of the printed membrane released on diamond by wet IPA assistance. NSC15 is used in both cases.

F.4 Systematic study of membrane protection

Following the argumentation in the main text we systematically test the conditions that might allow micro-lens membrane protection by employing 2 instead of 3 lithography steps without much success. We show more detailed results, including for thicker epilayer membranes (Fig. F.24), a thin epilayer combined with a Si deep etch using thick photoresist as mask (Fig. F.25 and F.26), as well as angle dependend recess etch testing using both silica and SiN hard masks in various thickness (Fig. F.27 to F.34).

In summary we find that for a significantly thinned epilayer the device protection does not work without the introduction of a third lithography step, even though good suspension yield might be achieved.

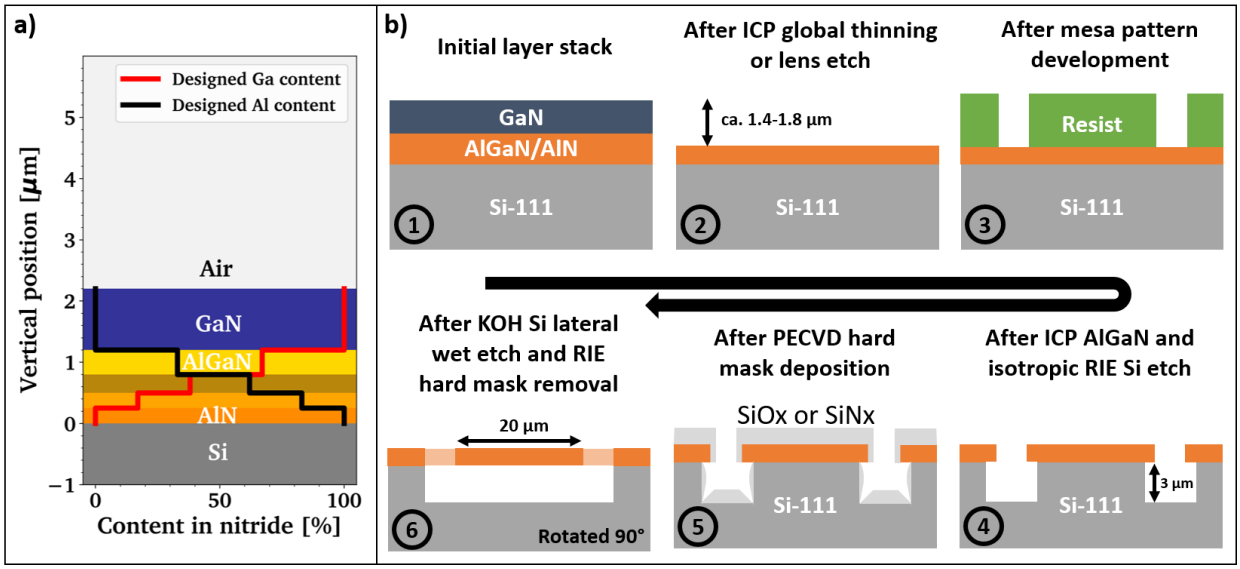

Figure F.22: Systematic study of membrane protection during KOH lateral Si etch. a) Schematic of the employed epilayer of GaN-on-Si, b) process flow for testing an isotropic Si RIE etch to create a recess below the membrane (4) for KOH wet etch access after membrane protection with a PECVD hard mask (5). For some devices shown in the following figures the global ICP thinning step was either not performed or performed with SPR220-4.5 reflown resist lenses and step (4) is varied between isotropic and anisotropic Si etching.

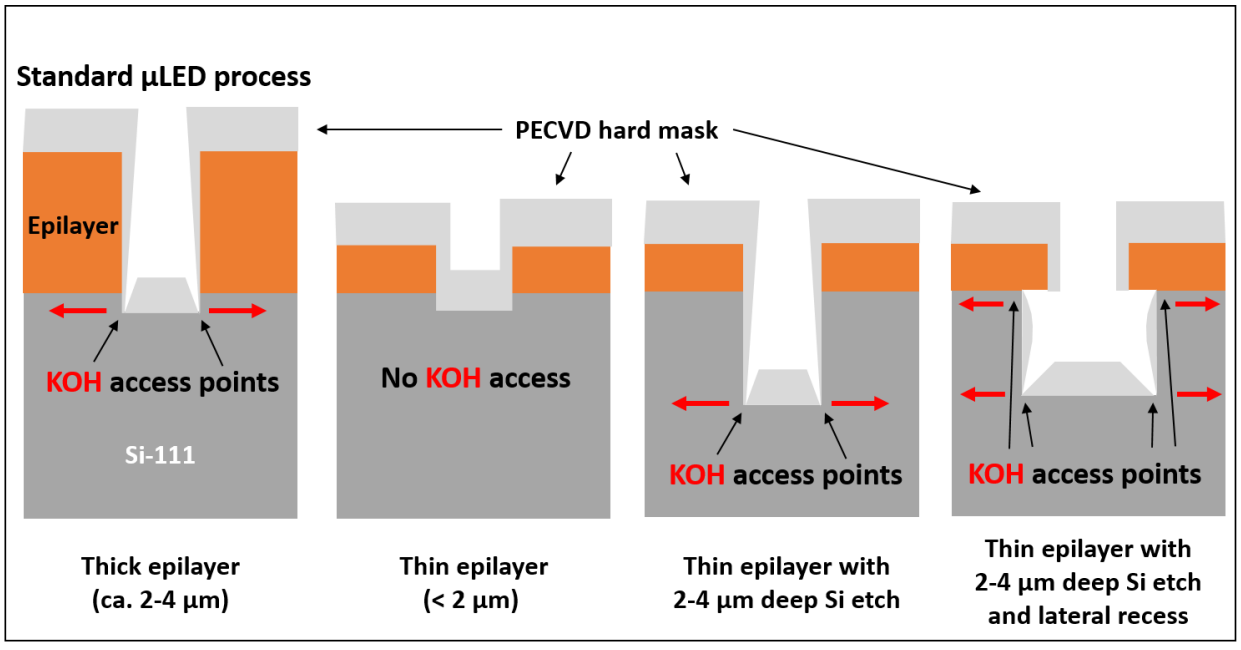

Figure F.23: Discussion of process step (5) in Fig. F.22 b). Schematics explaining variations of epilayer thickness and Si etch depth with constant hard mask thickness, the later depending on the size of the membrane that is to be suspended. The most right schematic indicates the use of an isotropic Si RIE step.

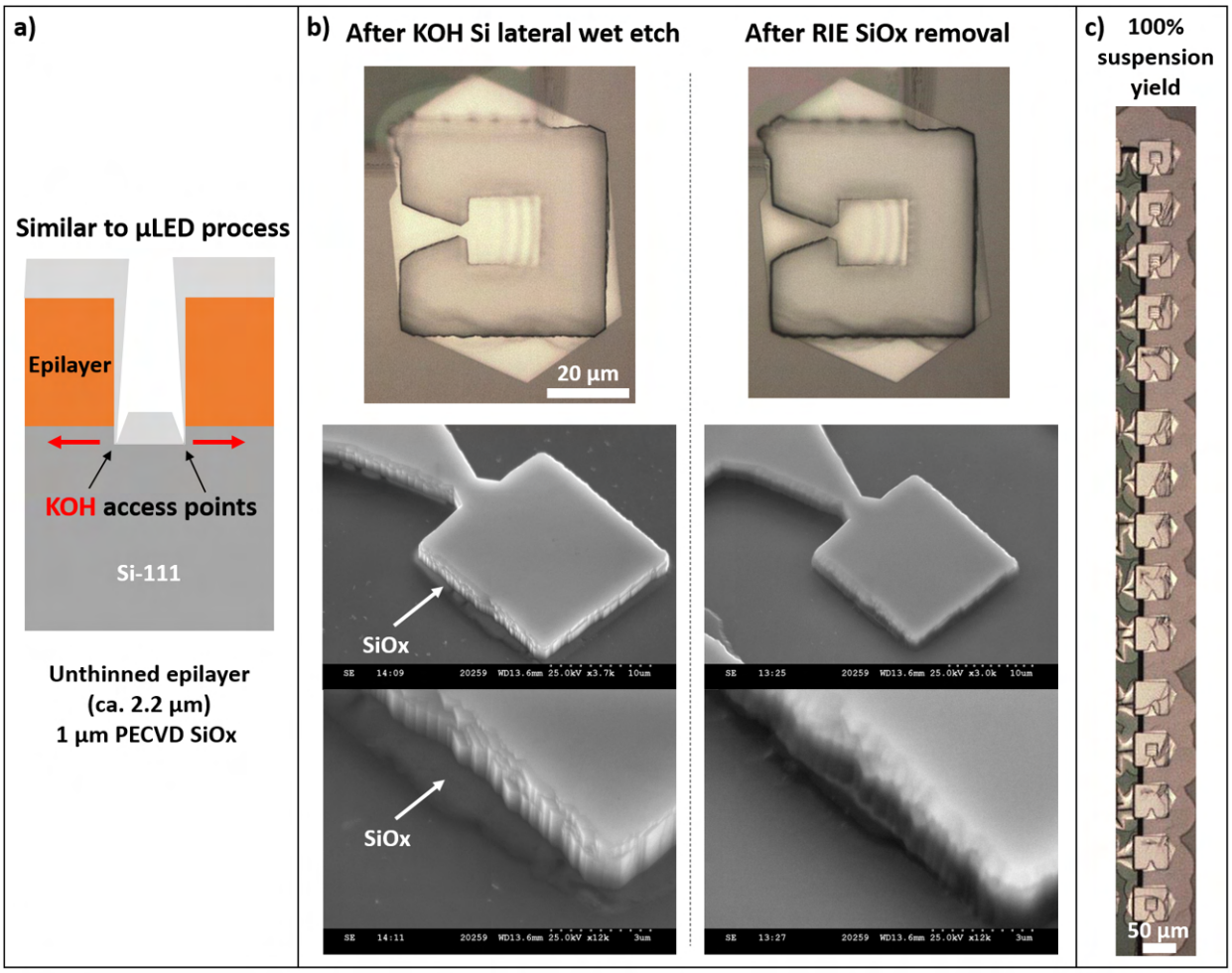

Figure F.24: Case 1: Thick epilayer and shallow anisotropic Si etch. a) Schematic of the epilayer corresponding to the shown microscope images of processed membranes after suspension in b) and c). In c) the SiO_x hard mask is still present. The scale bar in b) corresponds to both images, while the SEM images are taken with 40° sample tilt. SPR220-4.5 was applied to define the membranes.

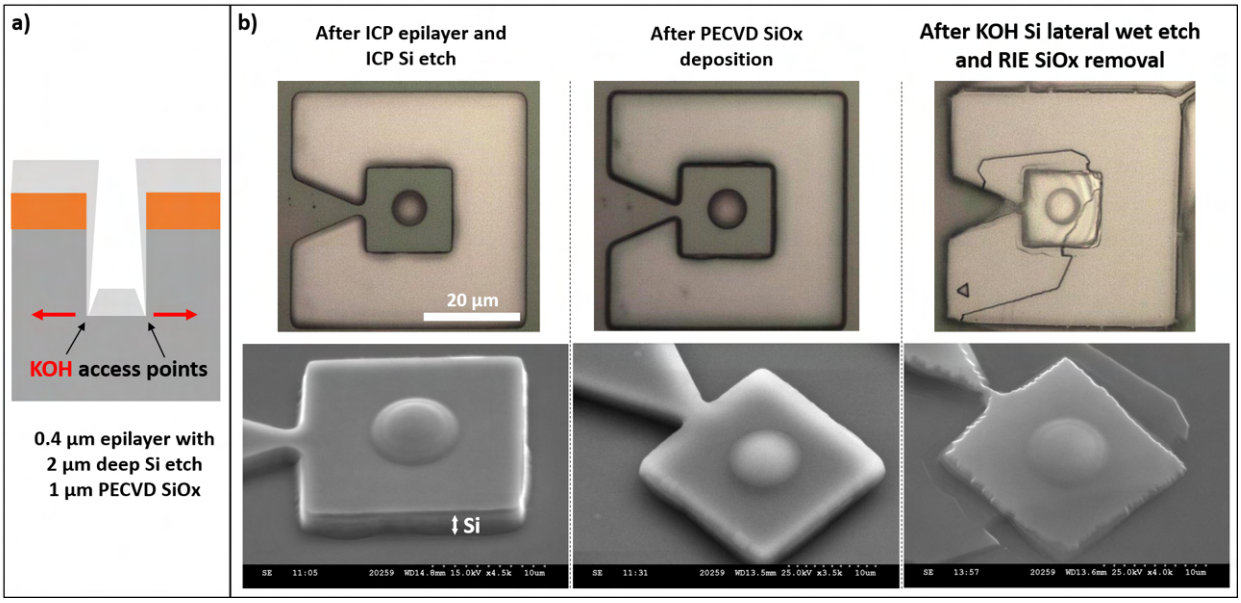

Figure F.25: Case 3: Thin epilayer and deep anisotropic Si etch. a) Schematic of the epilayer corresponding to the shown microscope and tilted SEM images (40°) of processed membranes in b). SPR220-4.5 was applied to both define the membranes and lenses. The scale bar applies to all three microscope images.

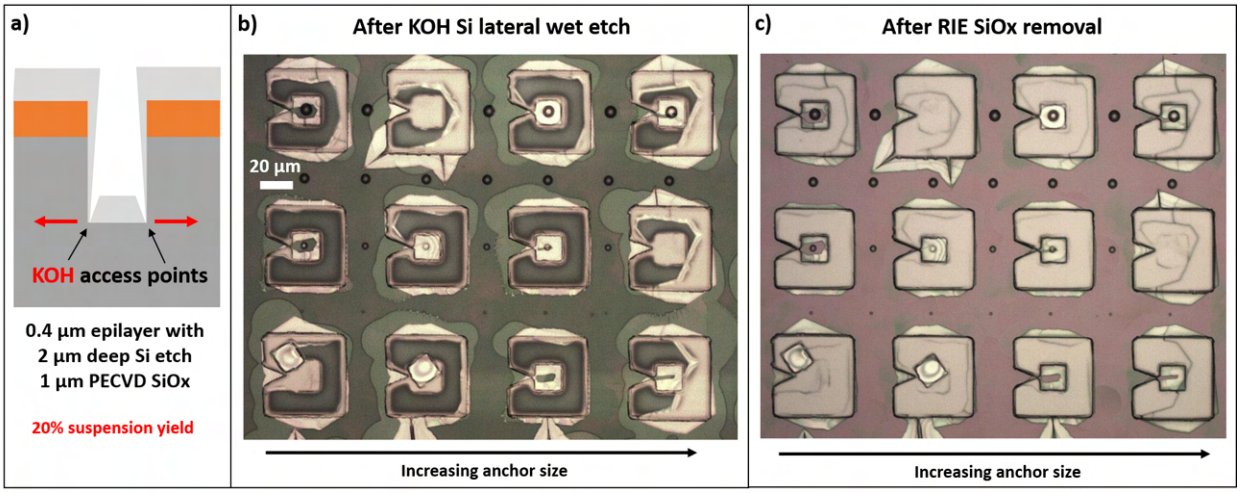

Figure F.26: Case 3: Thin epilayer and anisotropic deep Si etch. Yield discussion for the same chip discussed in Fig. F.25. a) Schematic of the epilayer, b)/c) show the same sample region illustrating typical results in an overview. The green areas inside the trenches in b) seem to correspond to a thin layer of suspended SiO_x. The scale bar in b) applies similarly to the image in c).

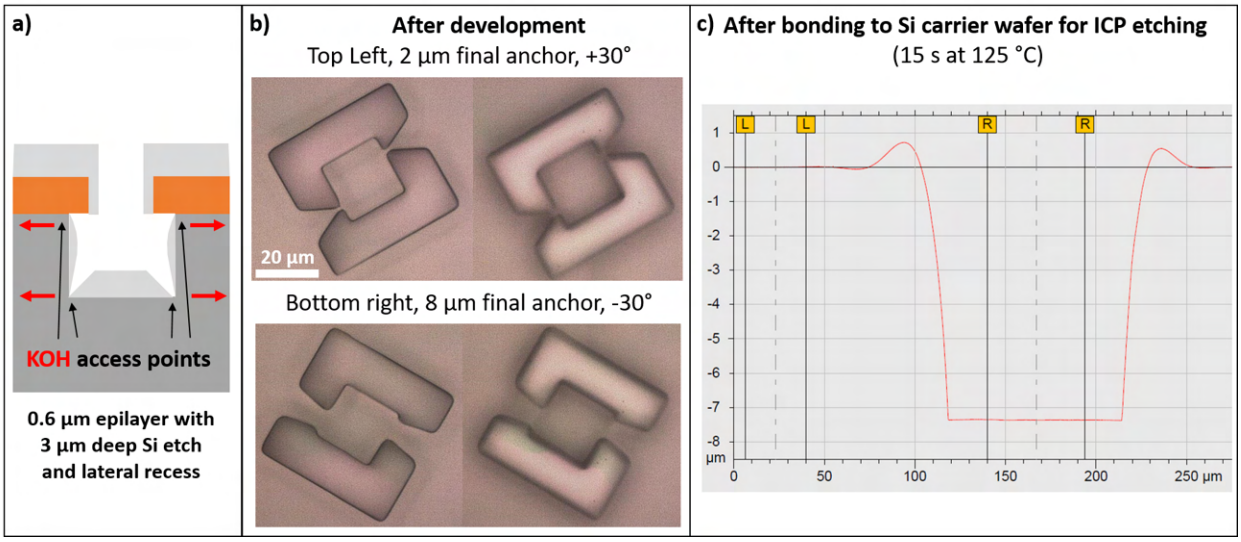

Figure F.27: Case 4: Thin epilayer and isotropic deep Si etch, directly corresponding to the process flow shown in Fig. F.22 b). a) Schematic of the epilayer, b) microscope images taken after initial development of SPR220-7.0 forming membranes. The final anchor width is varied giving rise to different taper angles, which is found to effect the KOH underetch. The influence of a rotational misalignment vs. the (110) direction of the Si(111) substrate is simultaneously tested in this fabrication run performed on 4 samples in parallel with varying PECVD hard mask thickness and composition. c) AlphaStep line profile in a reference trench, showing reflow of the thick photoresist caused by slightly elevated temperature during bonding the chips to the Si carrier wafer before ICP etching.

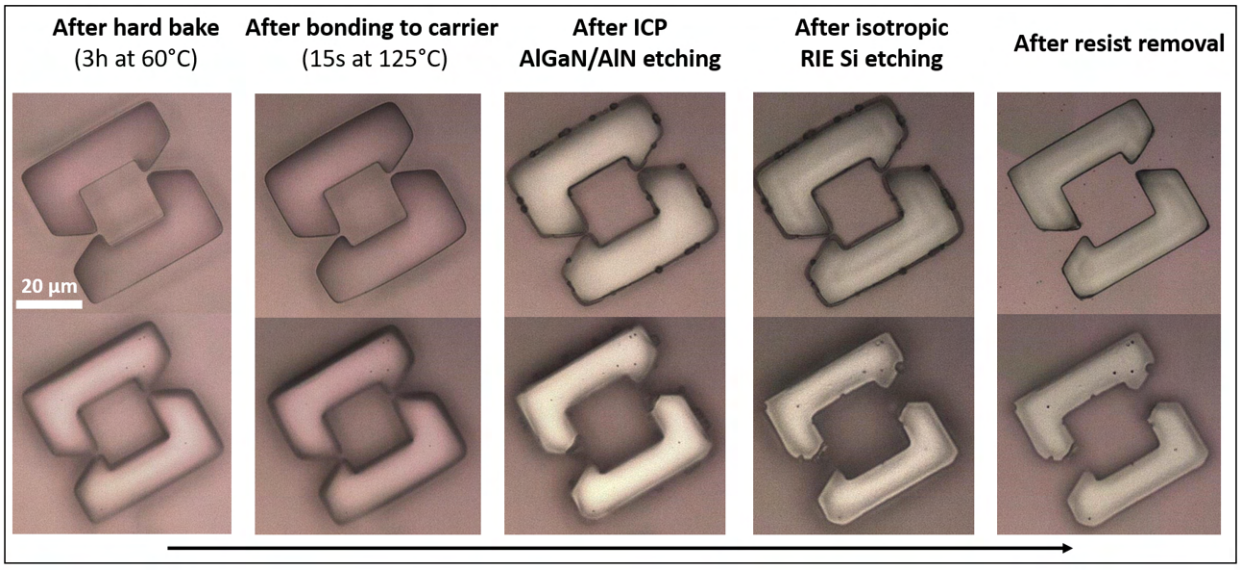

Figure F.28: Case 4: Thin epilayer and isotropic deep Si etch. Detailed microscope images indicating the effects of ICP-RIE and RIE process on the resist pattern at +30° rotation vs. the correct crystal orientation. The resist pattern was not sufficiently hard baked, resulting in loss of shape during etch transfer. The scale bar applies to all images.

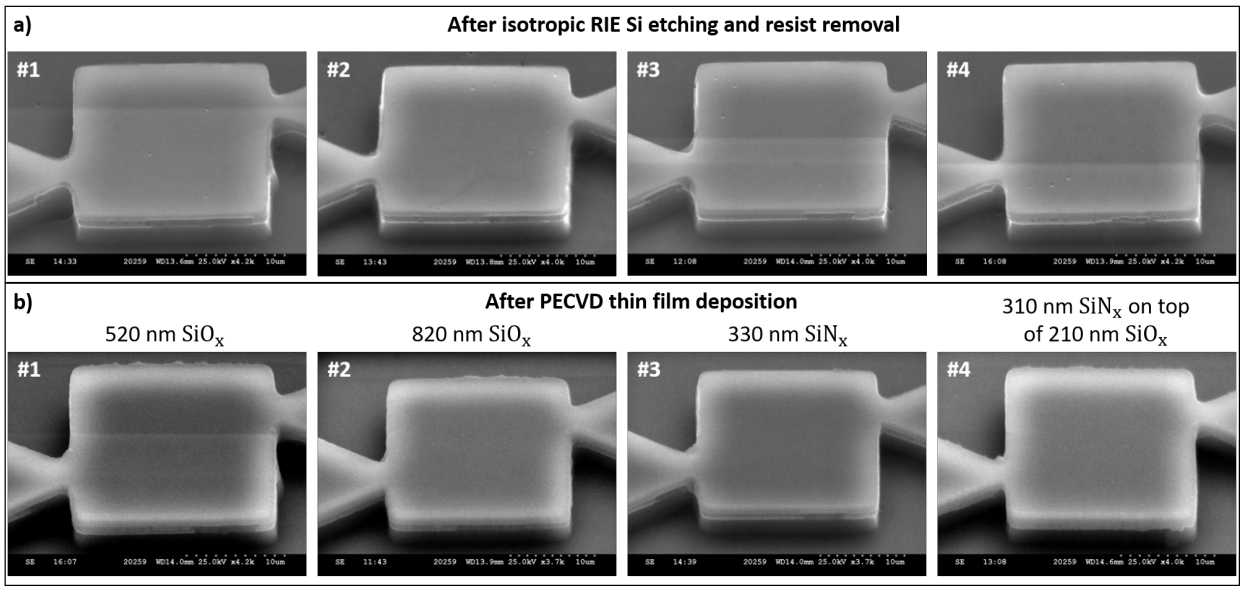

Figure F.29: Case 4: Thin epilayer and isotropic deep Si etch. Tilted SEM images (40°) of 4 samples processed in parallel a) after Si deep etch and b) after applying variations of hard mask thickness and composition for systematic testing. These devices correspond to roughly the correct crystal orientation.

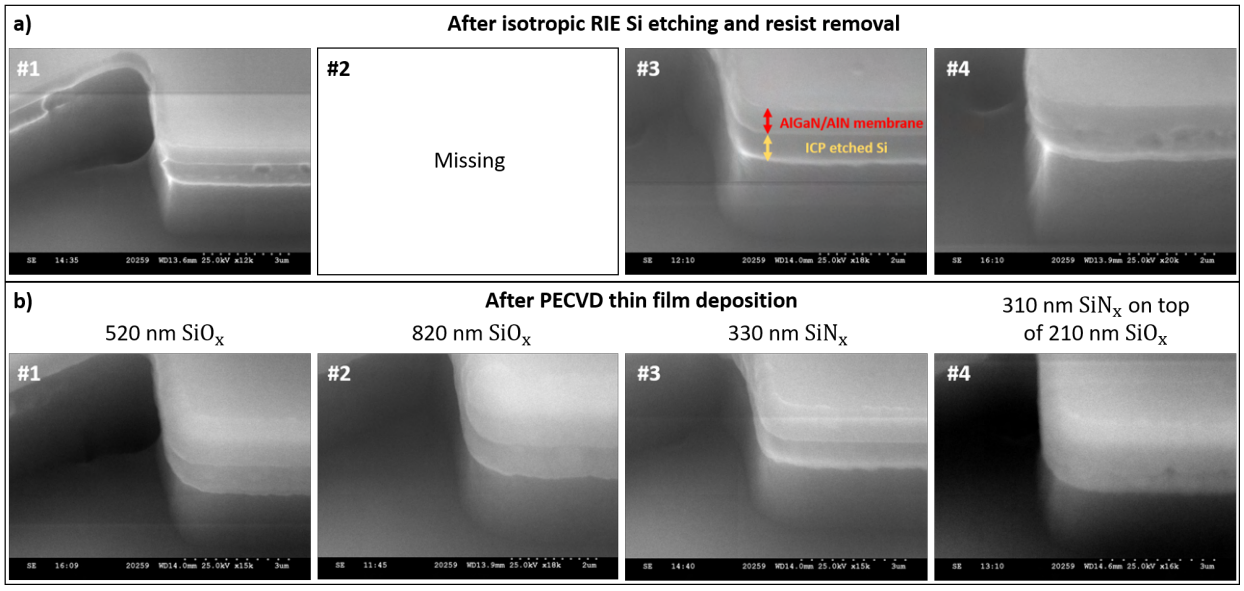

Figure F.30: Case 4: Thin epilayer and isotropic deep Si etch. Zoom into the same devices displayed in Fig. F.29. Tilted SEM images (40°) of 4 samples processed in parallel a) after Si deep etch and b) after applying variations of hard mask thickness and composition for systematic testing. The visible step in the membrane seems to stem from a slight ICP over etch into the Si substrate, that might have been protected by reflown resist during the Si deep etch creating the recess. These devices correspond to the correct crystal orientation.

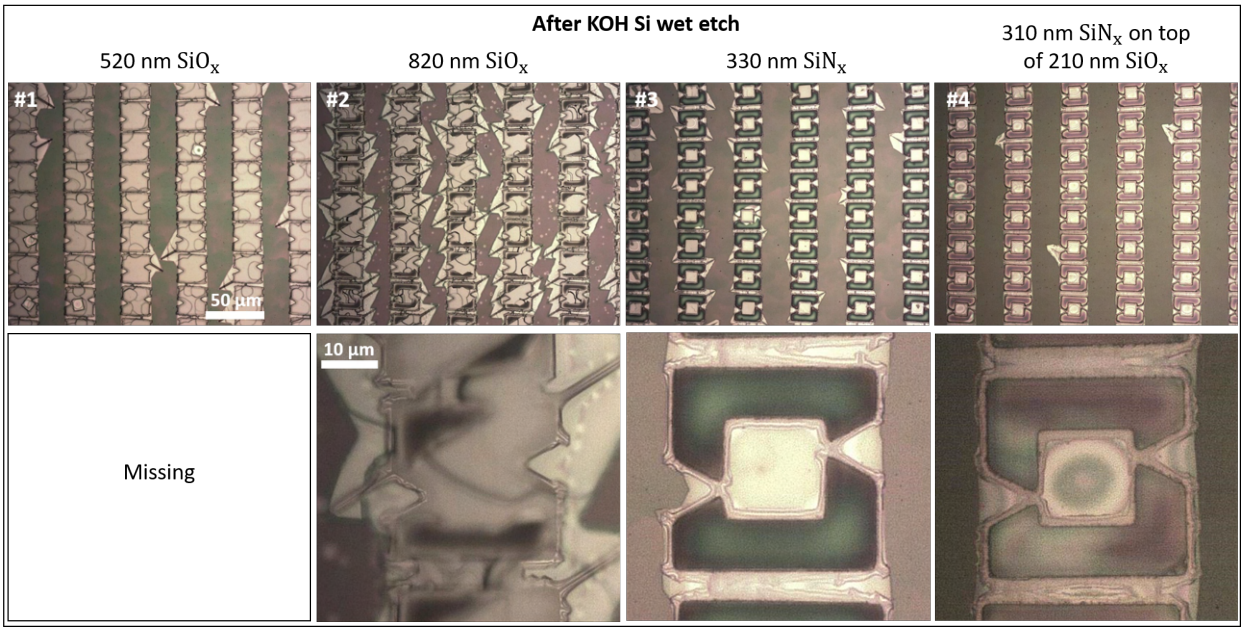

Figure F.31: Case 4: Thin epilayer and isotropic deep Si etch. **Thinnest anchors.** Small and large magnification microscope images of the 4 different samples after KOH wet etch but with the hard mask present. The shown devices correspond to the roughly the correct crystal orientation (device to device rotational variation in each column is 1°).

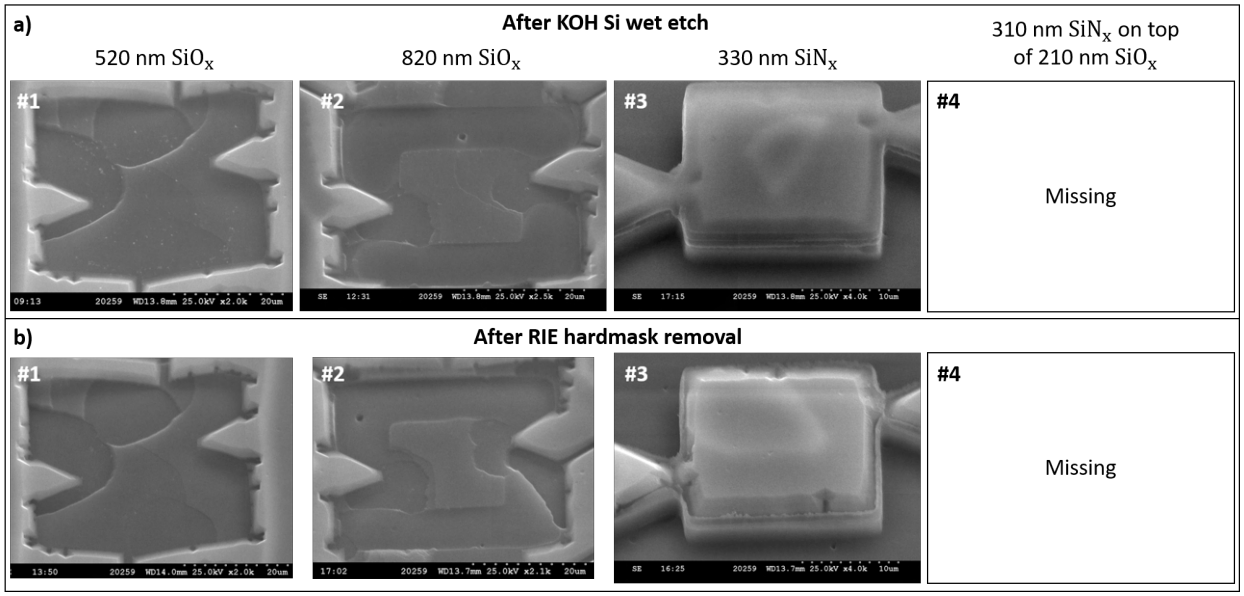

Figure F.32: Case 4: Thin epilayer and isotropic deep Si etch. **Thinnest anchors.** Tilted SEM images (40°) of the 4 different samples after a) KOH wet etch and b) RIE based hard mask removal. The shown devices correspond to the roughly the correct crystal orientation.

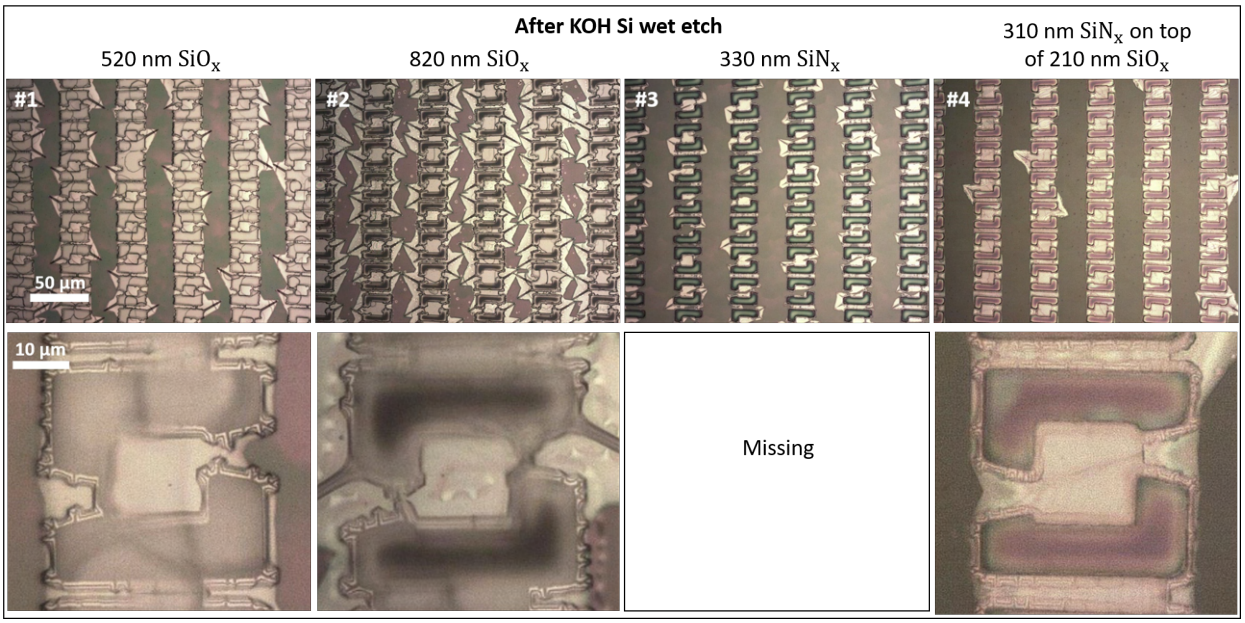

Figure F.33: Case 4: Thin epilayer and isotropic deep Si etch. **Thickest anchors.** Small and large magnification microscope images of the 4 different samples after KOH wet etch but with the hard mask present. The shown devices correspond to the roughly the correct crystal orientation (device to device rotational variation in each column is 1°).

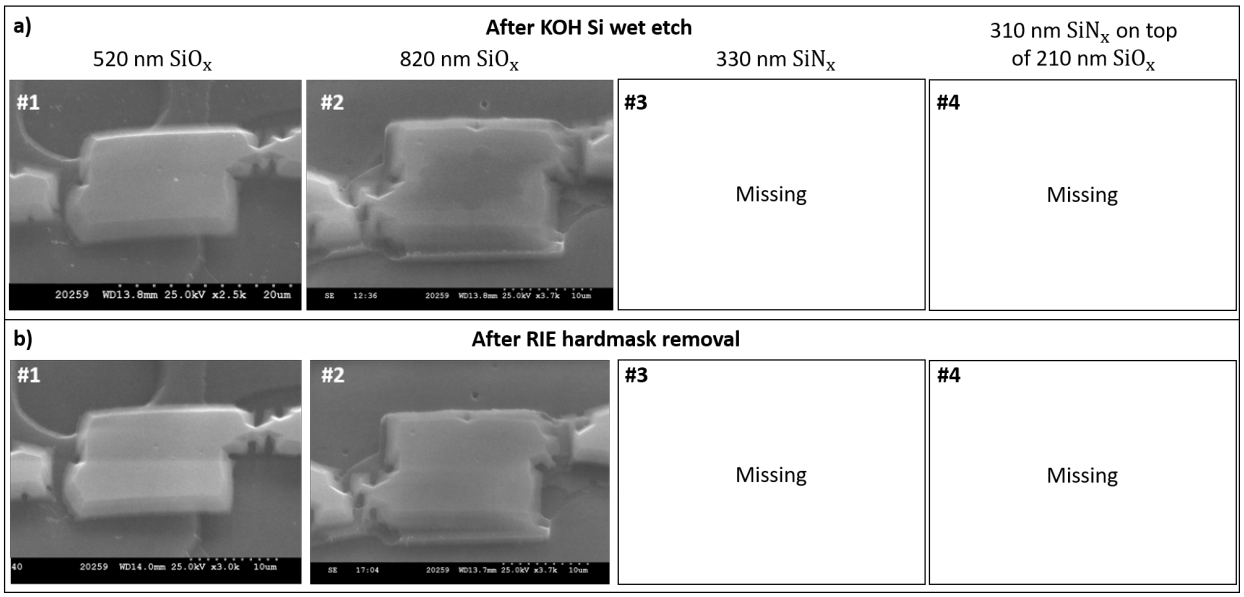

Figure F.34: Case 4: Thin epilayer and isotropic deep Si etch. **Thickest anchors.** Tilted SEM images (40°) of the 4 different samples after a) KOH wet etch and b) RIE based hard mask removal. The shown devices correspond to the roughly the correct crystal orientation.

F.5 Test of recess Si etch and SiN hard mask for lens protection with optimised epilayer

Here we provide additional data on the recess etch which we combined with a SiN hard mask to protect lens devices as already discussed in the main text in Chapter 3. Except for the lens protection the suspension yield is very high and print tests show reasonable device flatness.

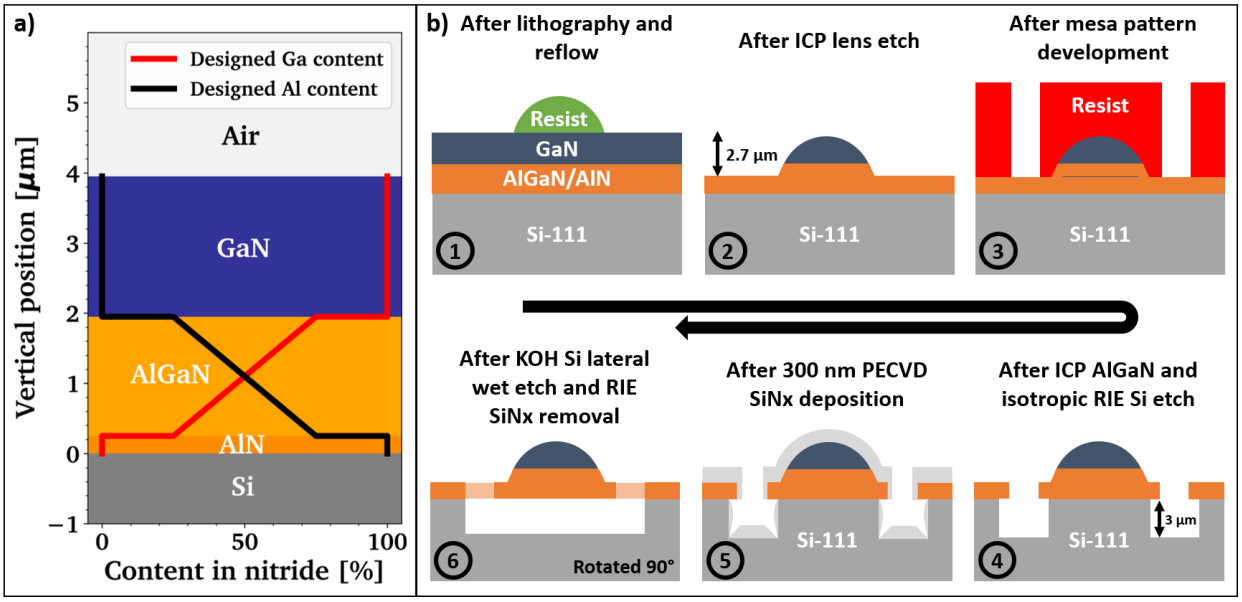

Figure F.35: Test of Si recess etch with SiN hard mask and optimised epilayer stack (-2 μm wafer bow) depicted schematically in a), b) process flow applied to this sample. Lenses are fabricated from SPR220-4.5 (green) and platelets are formed with SPR220-7.0 (red).

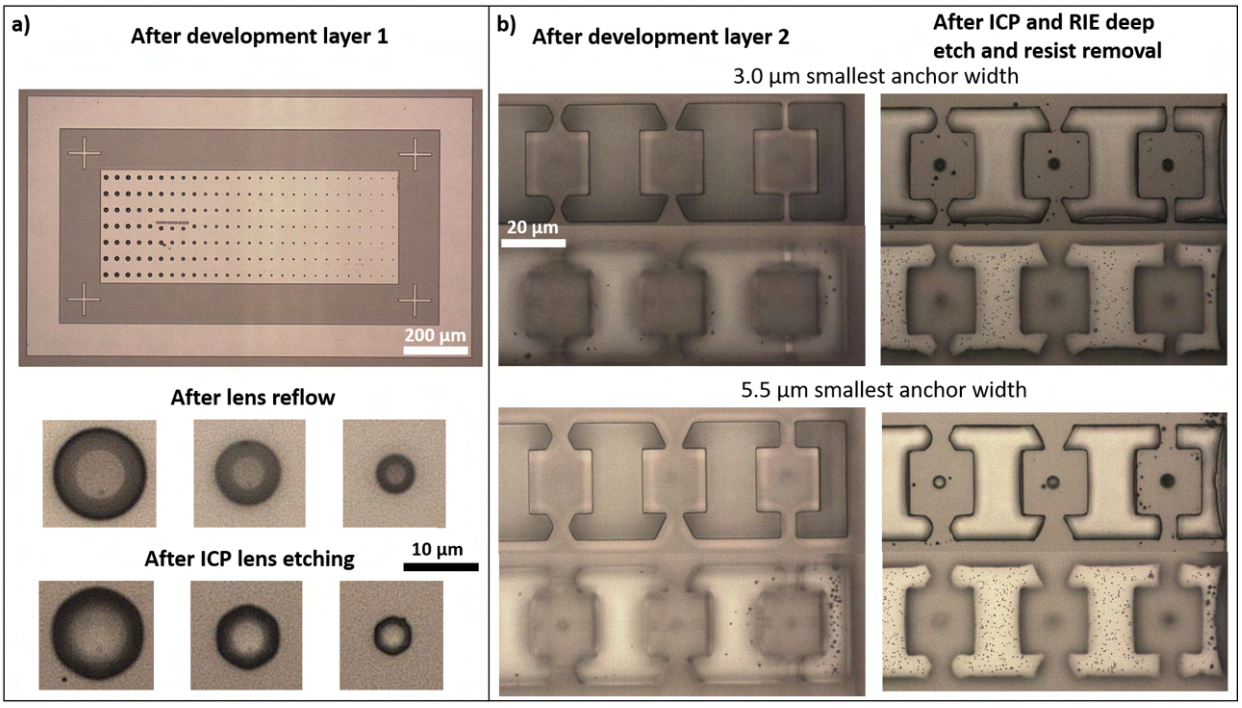

Figure F.36: Test of Si recess etch with SiN hard mask and optimised epilayer stack (-2 μm wafer bow). a) Layout after lens development and large magnification microscope images of lenses with varying sizes (14, 8, 4 μm nominal diameter) after reflow and ICP etch transfer into the GaN layer stack, b) microscope images of the three tested symmetric anchor geometries (bow tie, taper and straight) after resist mesa overlay (3) and ICP AlGaN and RIE isotropic Si etch (4). The smallest anchor width is given in each case, the angle is set to 26.6° avoiding interference with other preferred etch planes in Si (e.g. at 30°). The scale bars apply to the respective images in the surroundings.

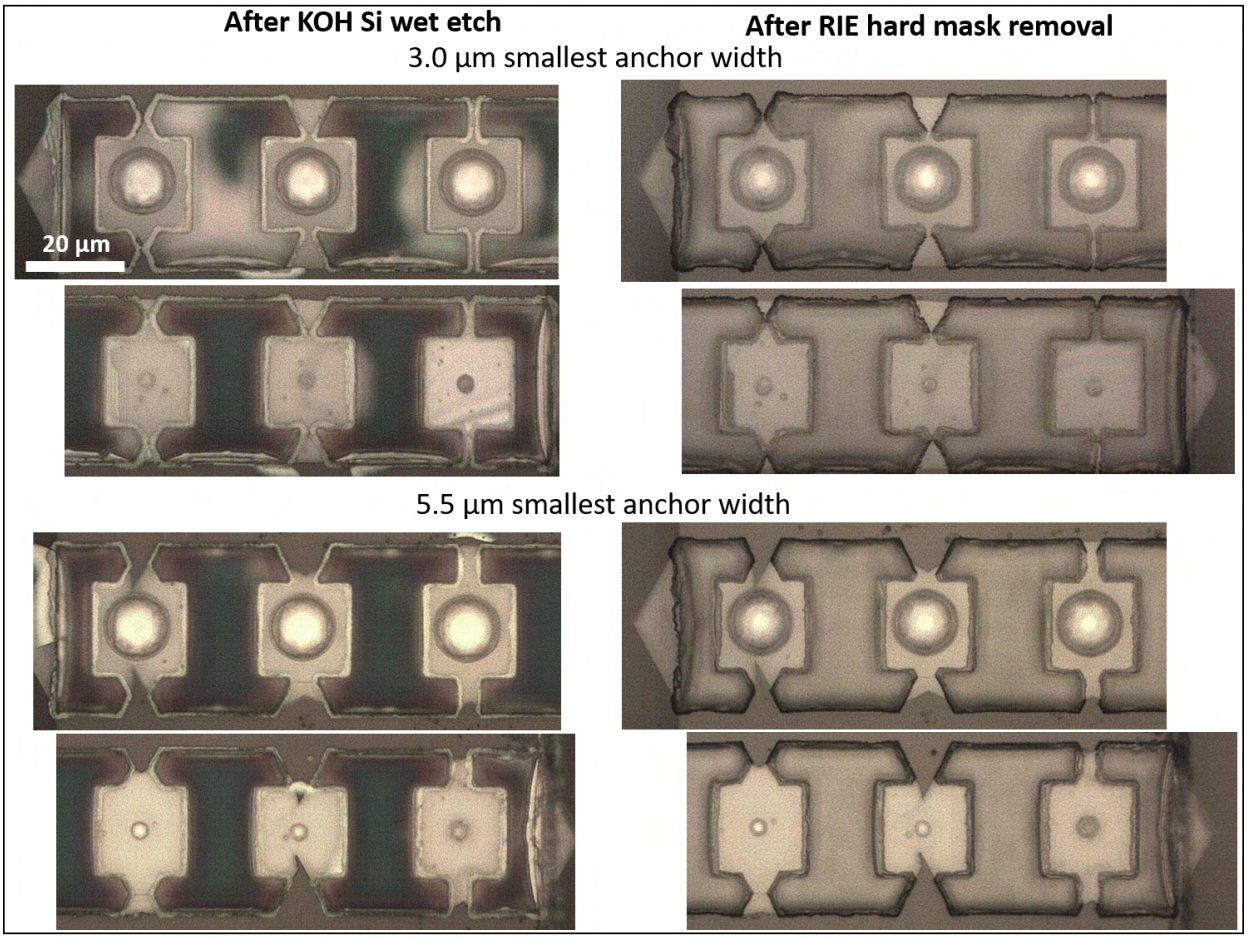

Figure F.37: Test of Si recess etch with SiN hard mask and optimised epilayer stack (-2 μm wafer bow). Microscope images of thickest and thinnest anchors with largest and smallest micro-lenses respectively (3 to 16 μm nominal diameter) after KOH suspension etch and after RIE SiN_x removal (same devices are shown left and right), finalizing the device fabrication. The scale bar applies to all images.

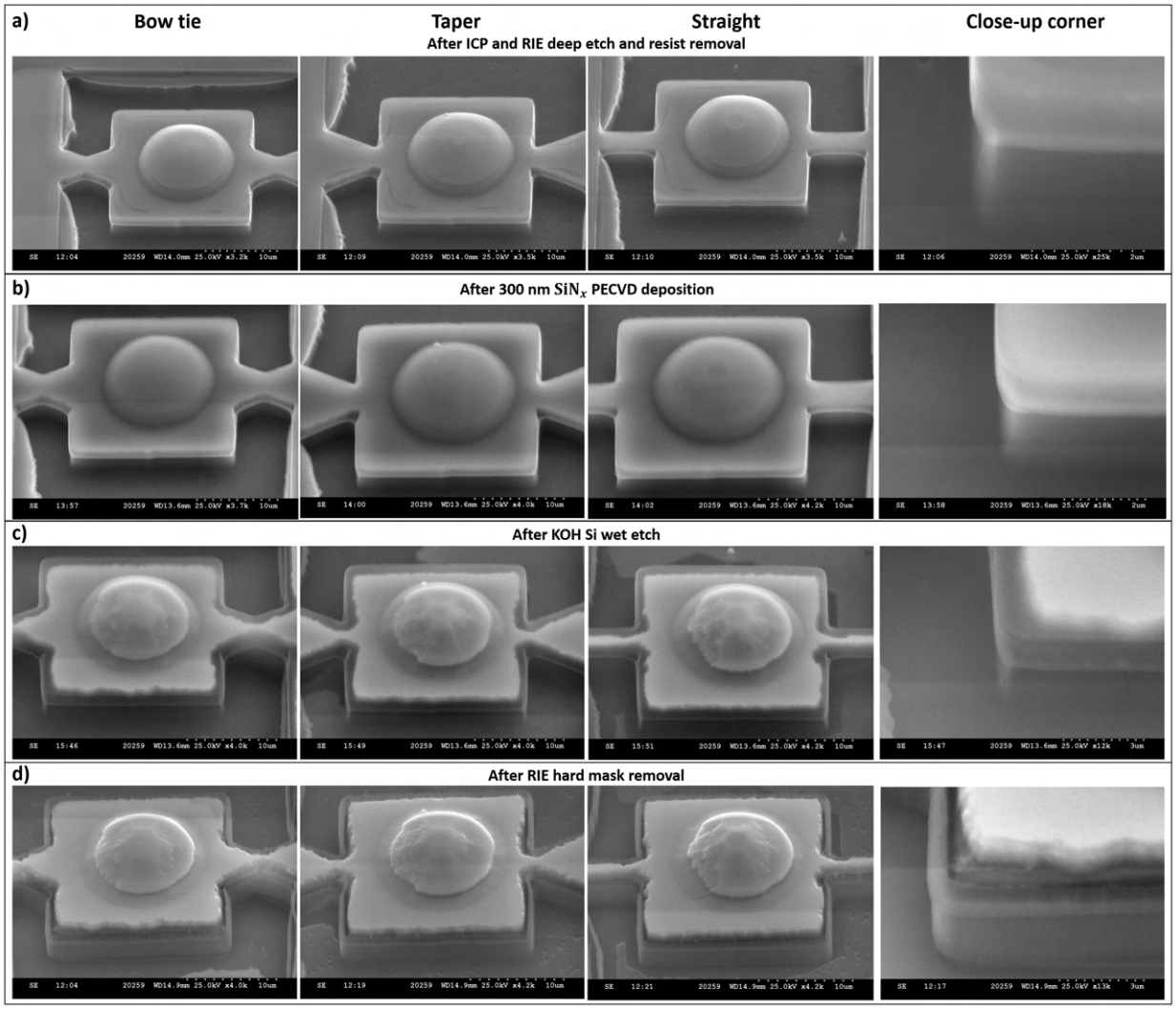

Figure F.38: Test of Si recess etch with SiN hard mask and optimised epilayer stack (-2 μm wafer bow). Tilted SEM images (40°) of the three different anchor geometries for the smallest anchor width (3 μm) and lenses with 16 μm nominal diameter, after a) Si deep etch (4), b) SiN_x deposition (5), c) KOH lateral Si etch for device suspension and d) removal of the remaining SiN_x hard mask with RIE (6). The same device is imaged in each column after the respective process step.

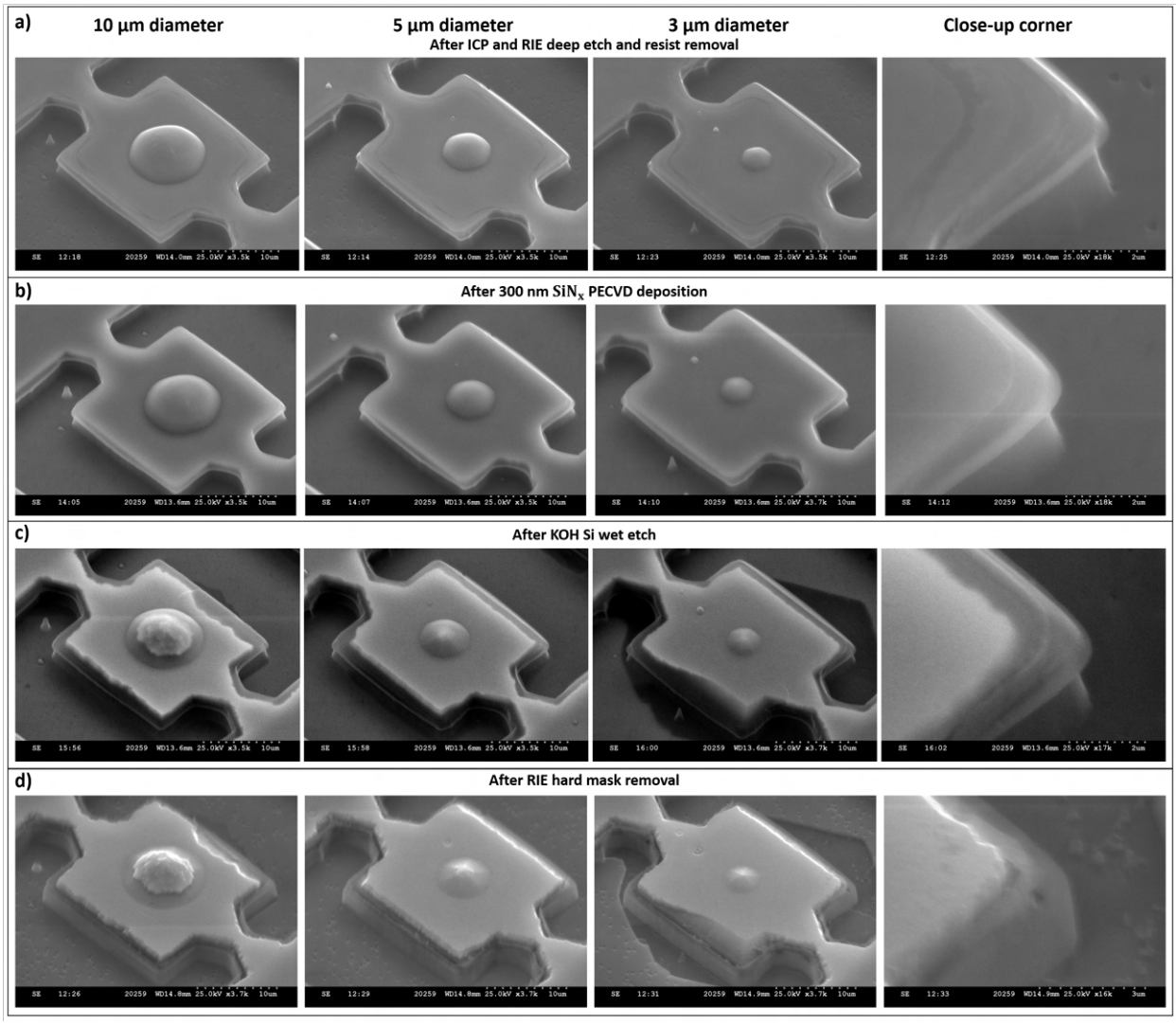

Figure F.39: Test of Si recess etch with SiN hard mask and optimised epilayer stack (-2 μm wafer bow). Tilted SEM images (40°) of 3 bow tie devices with smallest anchor width (3 μm) and lenses with 10, 5 and 3 μm nominal diameter, after a) Si deep etch (4), b) SiN_x deposition (5), c) KOH lateral Si etch for device suspension and d) removal of the remaining SiN_x hard mask with RIE (6). The same device is imaged in each column after the respective process step.

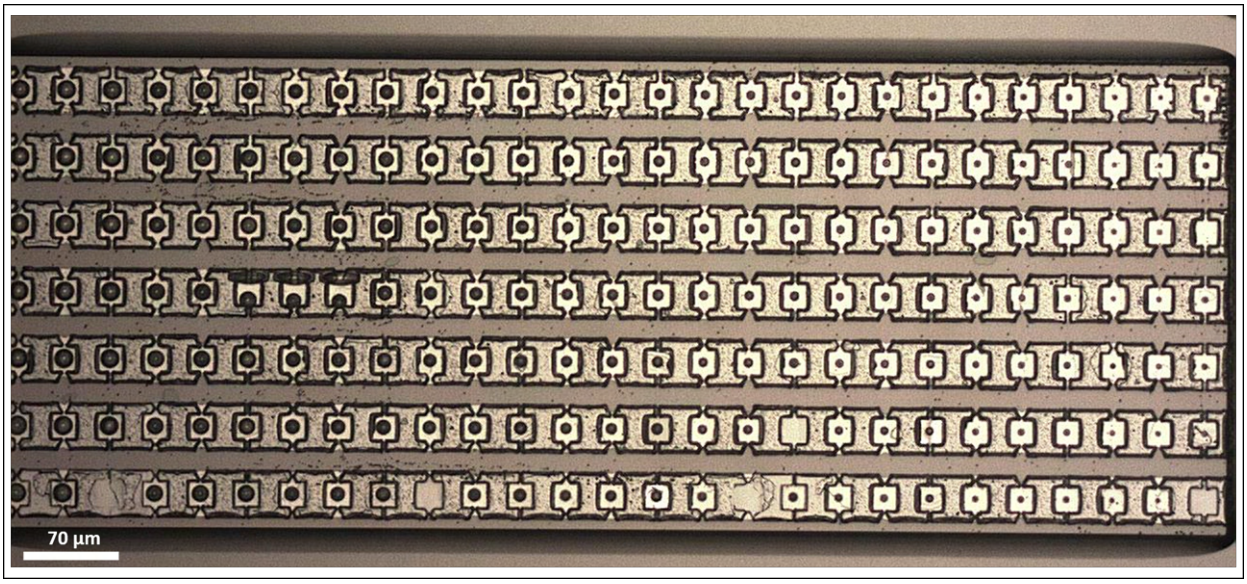

Figure F.40: Test of Si recess etch with SiN hard mask and optimised epilayer stack (-2 μm wafer bow). Device yield after hard mask removal. Three of the missing devices are removed by transfer printing and are shown in the following figure.

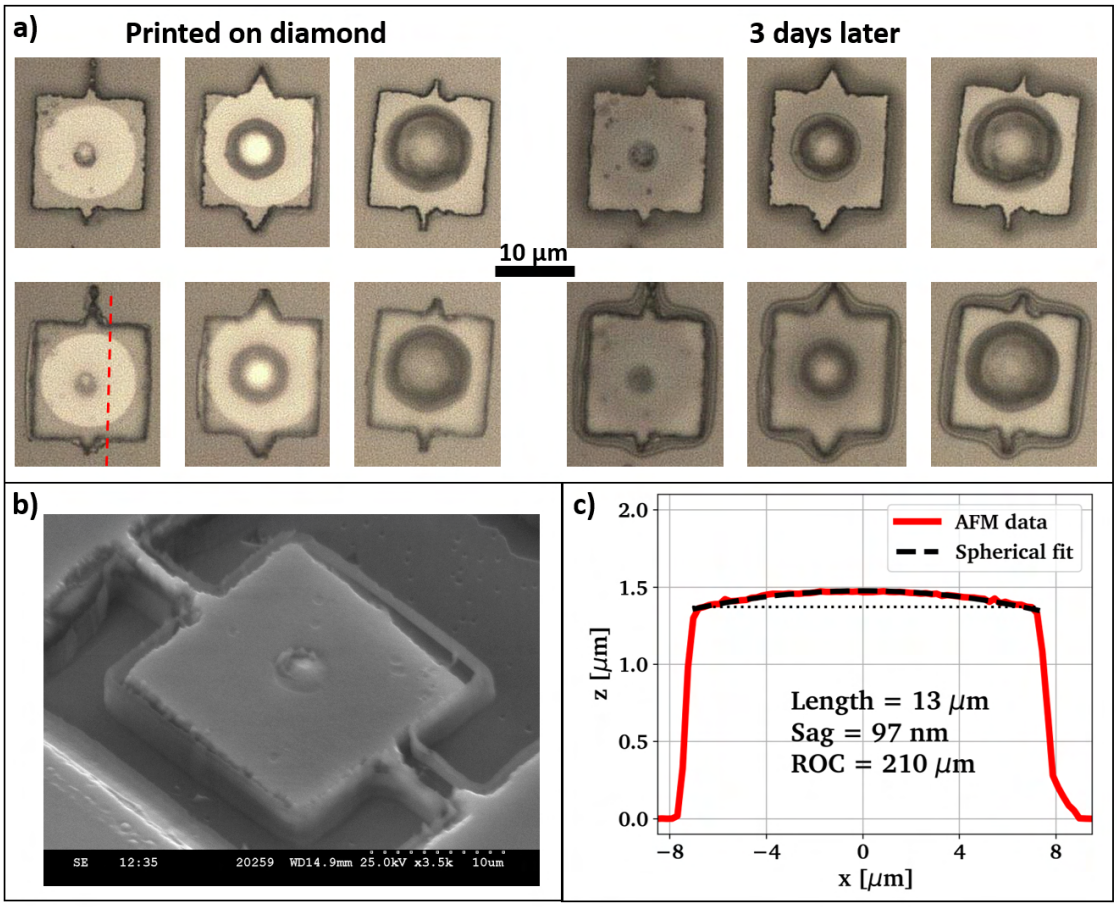

Figure F.41: Test of Si recess etch with SiN hard mask and optimised epilayer stack (-2 μm wafer bow). a) Three devices with varying lens diameter (3, 10, 16 μm) are transfer printed onto a polished single crystalline diamond substrate. The contact changed significantly after three days with liquid seemingly accumulating around the devices. b) Tilted SEM image (40°) of the bottom left membrane device before transfer printing, c) AFM line scan across the red line indicated in the microscope image in a) of the same device (NSC15) after printing on diamond.

F.6 Milestone: Lens protection during suspension etch

As discussed in the main text we show here the first suspension results that combine high yield with successful micro-lens protection in more detail. The lens protection is achieved by opening trenches between the lens devices leaving a micrometer thick protective layer of SiO_x around the devices.

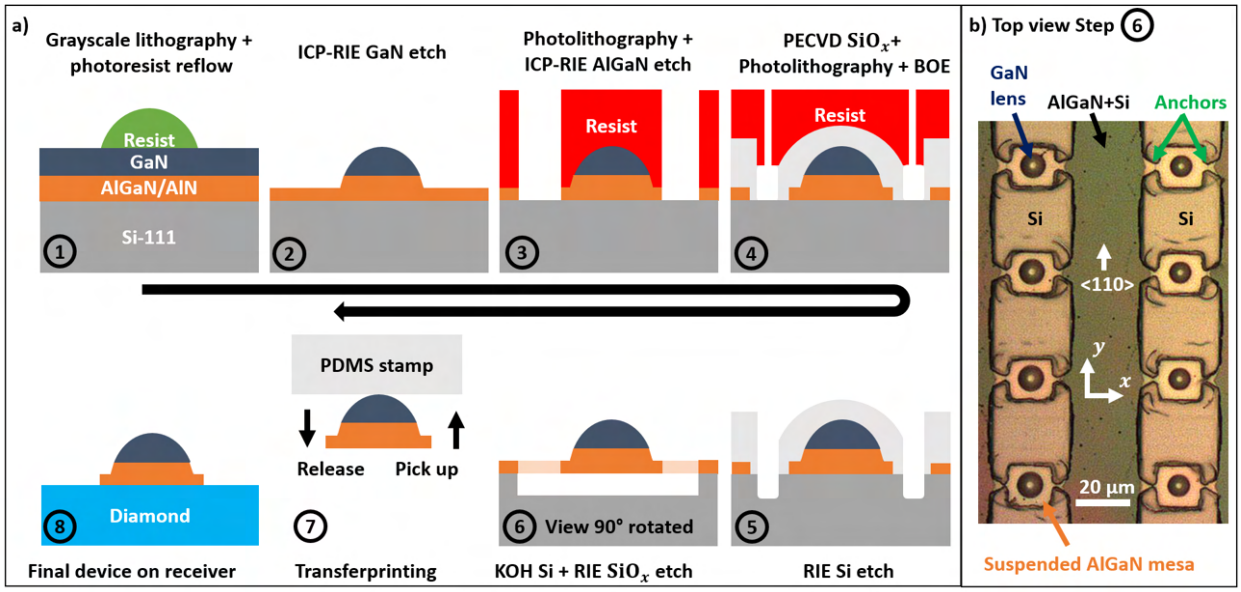

Figure F.42: 1st fabrication with conserved GaN lenses after suspension and hard mask removal. a) Schematics of the process flow. The key change appears in step (4) with adding an extra layer of SiO_x protection to the sidewalls of the membrane devices. For lens fabrication SPR220-4.5 is used, while both layer two and layer three (3,4) are formed with SPR220-7.0, b) microscope image showing the successfully suspended GaN micro-lenses on square platelets, using tapered anchors.

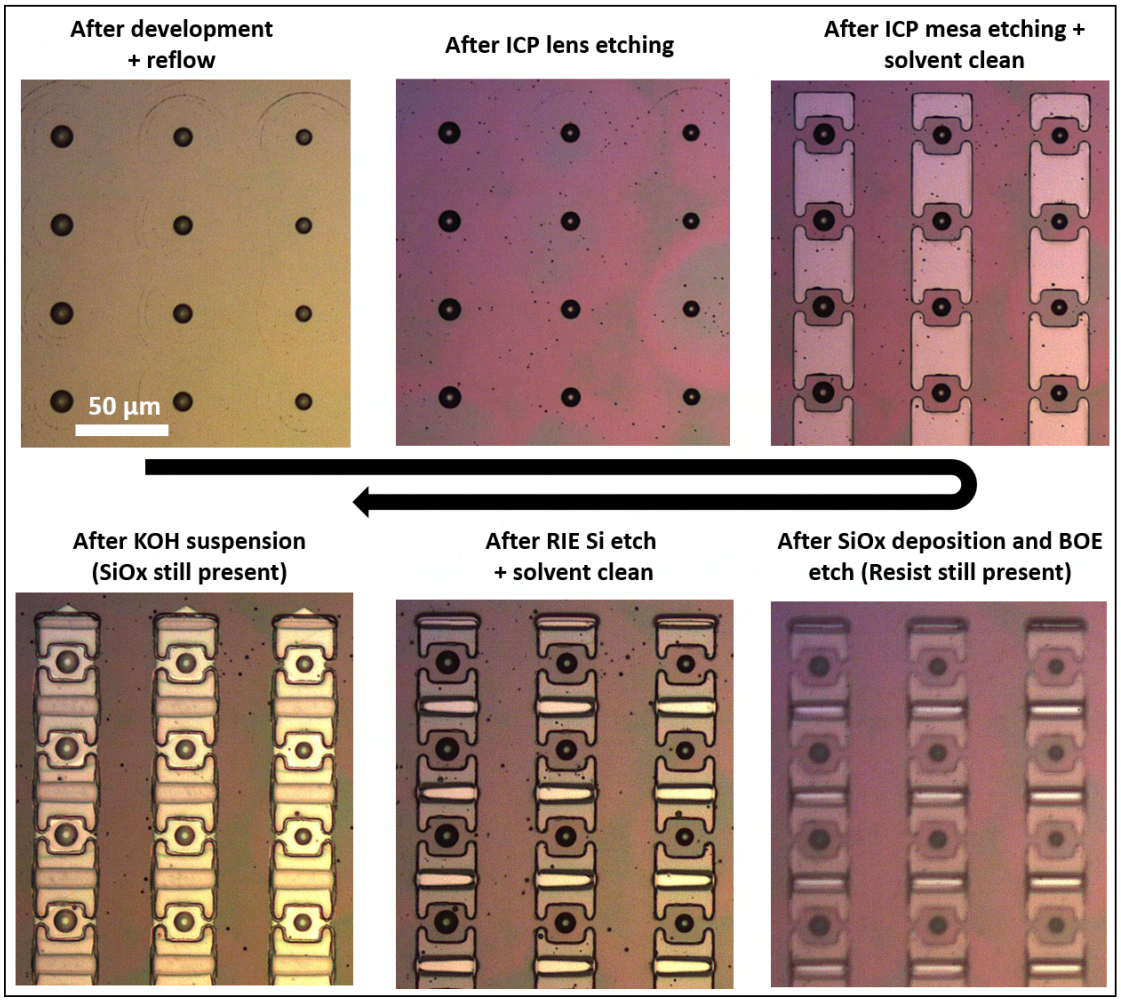

Figure F.43: 1st fabrication with conserved GaN lenses after suspension and hard mask removal. Microscope images of the same sample area after successive processing steps. Lenses are fabricated with grayscale preshaping and photoresist reflow. The silica hard mask is removed selectively by applying a BOE wet etch through resist windows in the bottom right image. The scale bar applies to all images.

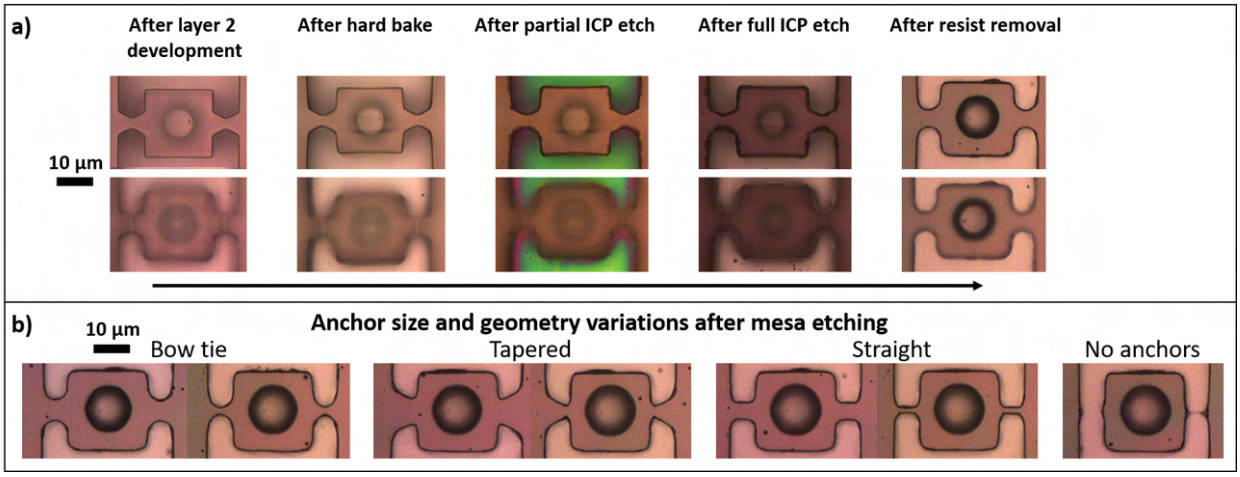

Figure F.44: 1st fabrication with conserved GaN lenses after suspension and hard mask removal. a) Microscope images showing the mesa etching in layer 2 (3). The lens fabrication on this sample is already shown in detail in Fig. 2.17-2.20. The middle image is taken before the Si substrate is exposed, illustrating how the color of the thin film indicates remaining AlGaN/AlN material. The Si substrate is then finally reached. b) Anchor styles and sizes employed on this substrate after etching and resist removal. Nominally, the smallest anchor width is sweeped between 1-4 μm. The scale bars apply to all images in each box.

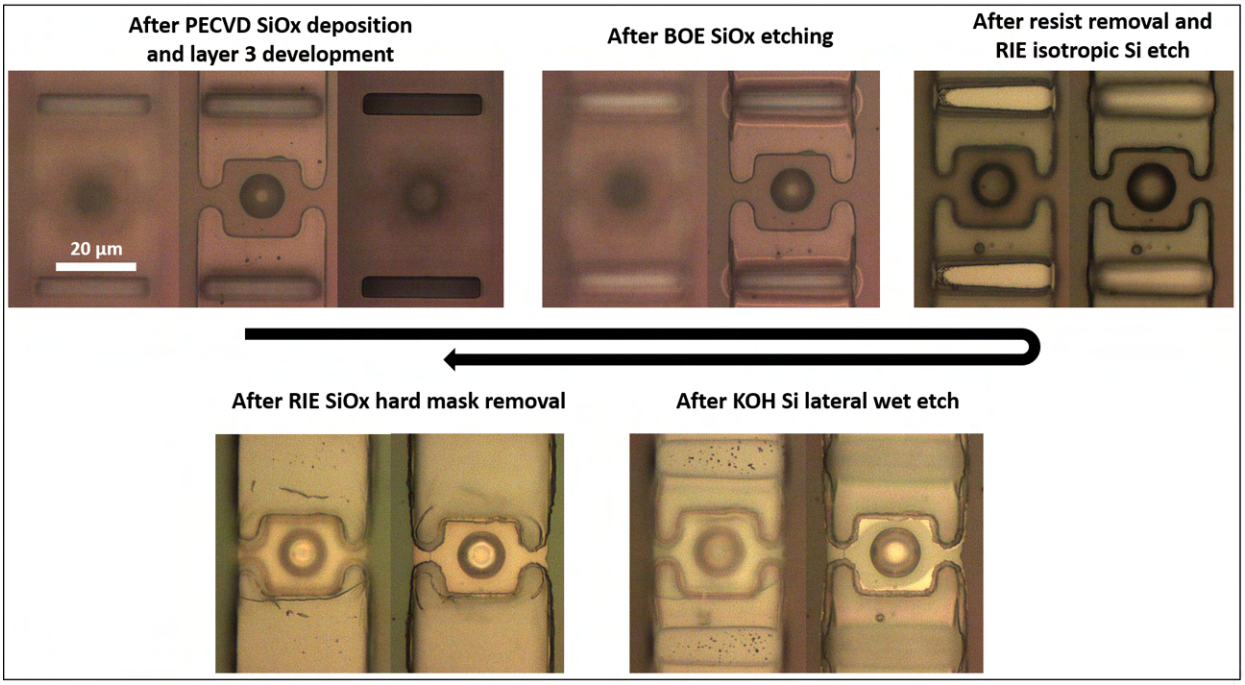

Figure F.45: 1st fabrication with conserved GaN lenses after suspension and hard mask removal. Micrsoscope images following the same device from process step (4) to (6). Windows are opened in SPR220-7.0 after depositing the SiO_x hard mask (below the resist). Wet etching of SiO_x is applied between lens device membranes, leaving a several μm-thick protective layer on the side walls. The trench in the SiO_x is then transferred into the Si substrate below, generating a (110) access plane for the KOH etch to suspend the membranes effectively. The SiO_x hard mask is removed with RIE. The scale bar applies to all images.

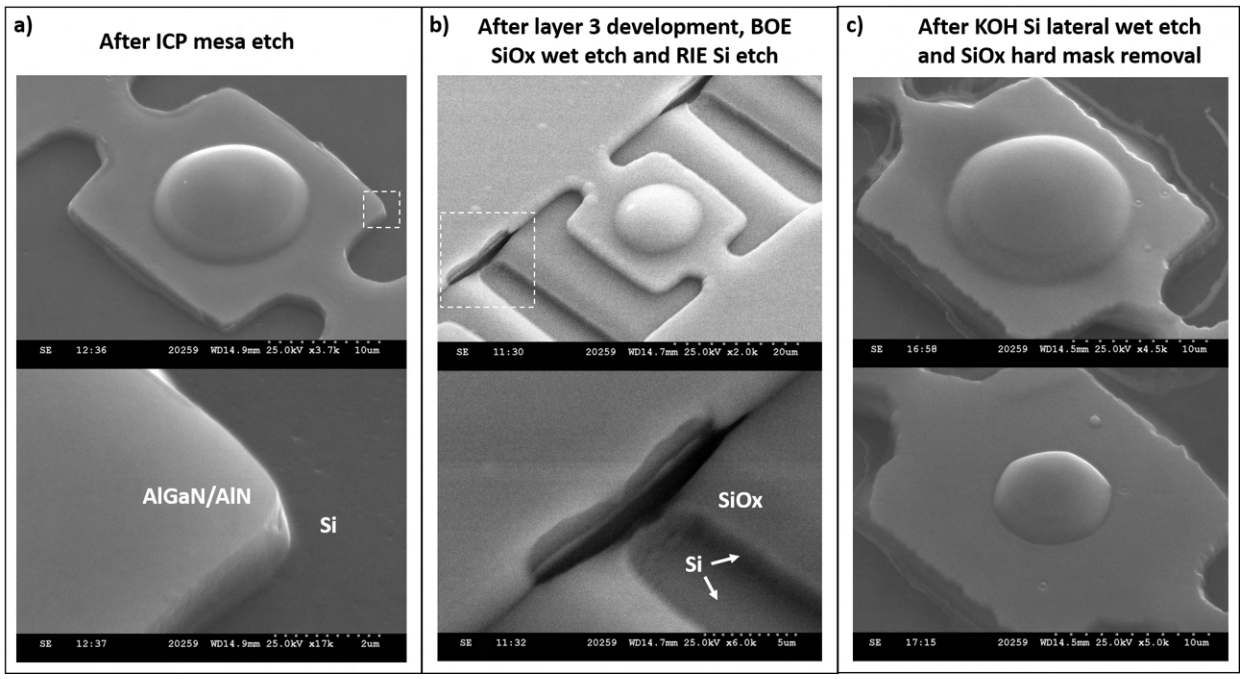

Figure F.46: 1st fabrication with conserved GaN lenses after suspension and hard mask removal. Tilted SEM images (40°) of different devices after successive processing steps, with magnified views in a) and b) showing the sidewall of the AlGaN mesa and the wet and dry etching profile in SiO_x and Si respectively. c) shows two suspended membrane devices after hard mask removal with conserved GaN microlenses of 16 and 8 μm nominal diameter.

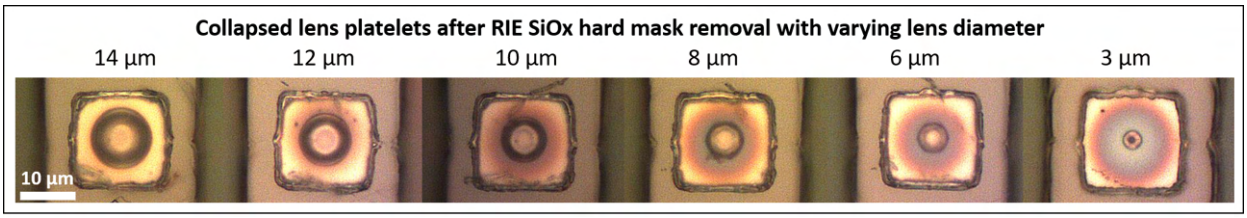

Figure F.47: 1st fabrication with conserved GaN lenses after suspension and hard mask removal. Series of suspended lens membranes without anchors, which collapsed to the Si substrate after SiO_x hard mask removal. Interference fringes increase with diminishing lens diameter indicating an influence of the GaN micro-lens on the strain in the overall membrane. The scale bar applies to all images.

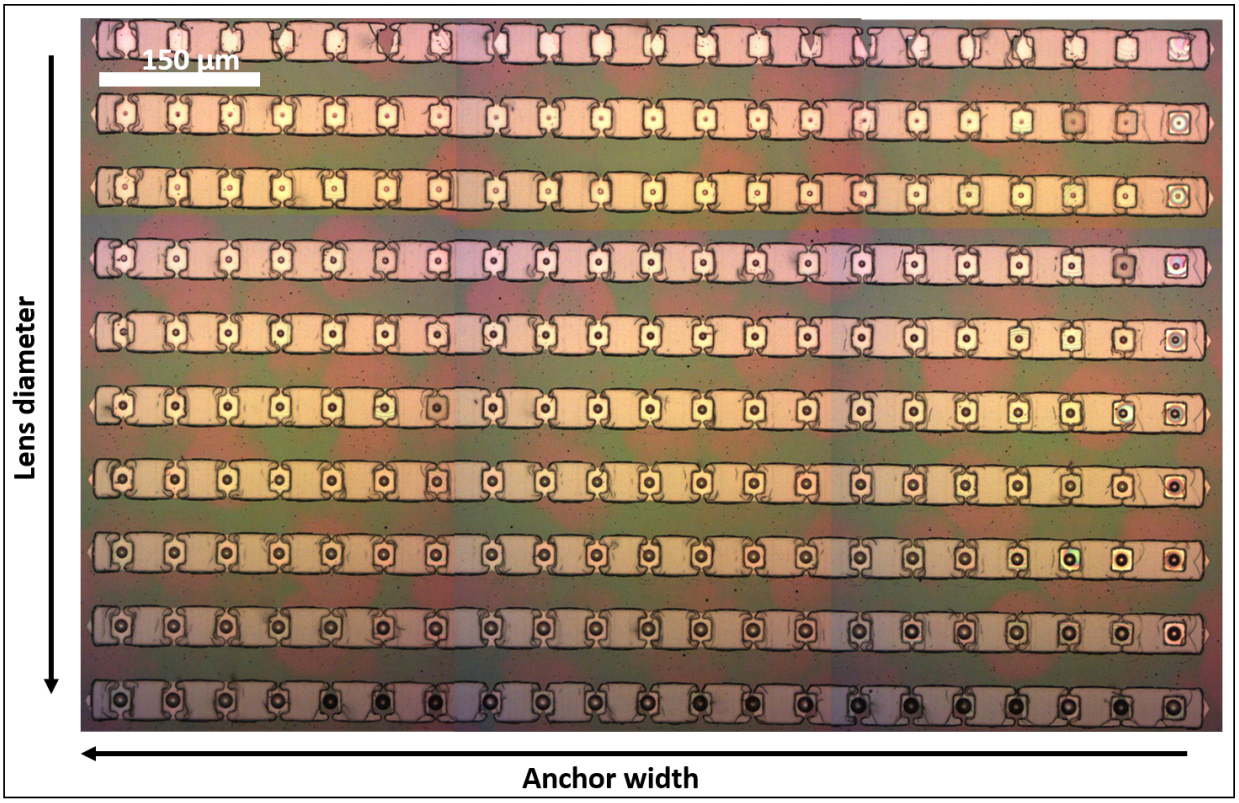

Figure F.48: 1st fabrication with conserved GaN lenses after suspension and hard mask removal. Device yield on the full die. Some devices in the top and bottom row are not successfully suspended, otherwise the suspension yield is 99 %.

F.7 Surface quality of GaN lenses and single crystalline diamond surfaces

Fig. F.49 contains the surface roughness analysis of the surface of a single crystalline diamond membrane from Element 6 as well as the roughness measurement on top of a GaN micro-lenses printed on diamond fabricated by grayscale preshaping, resist reflow and low bias Ar/Cl_2 ICP etch transfer.

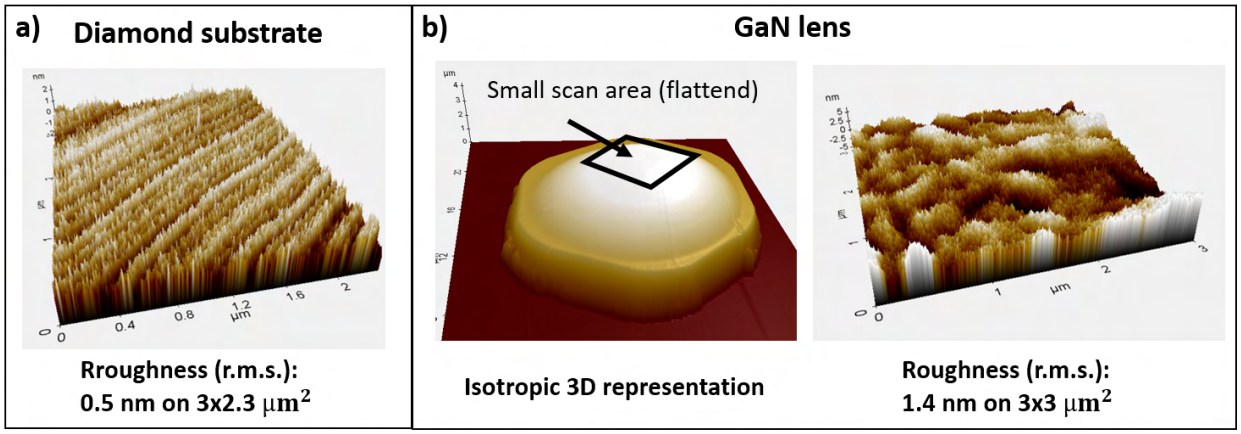

Figure F.49: Devices with optimized etch depth and device membrane size, surface roughness analysis of the relevant surfaces. a) 3D representation of an AFM roughness scan on the diamond substrate close to the printed lens devices (NSC15), b) real scale 3D representation of the GaN lens device (1) from Fig 3.29 and 3D representation of a flattened AFM roughness scan taken on top of the GaN micro-lens after transfer printing.

G Simulation methods

We will quickly discuss the simulation methods used in this thesis in more detail after a short introduction into modelling of light based on common optics text books such as [2, 3, 5, 6]. For optical applications where diffraction is negligible, light can be approximated as rays that are reflected, transmitted and refracted, following Snell's law and the Fresnel equations. This is useful to calculate the beam propagation in macroscopic lens systems in free ray optics, but is also still reasonably valid for micro-lenses with $>20\,\mu$m diameter, as long as VIS light is used.
If the feature size of a structure in interaction with light comes closer to the wavelength λ_n in the medium, the wave properties of light become more dominant and effects like diffraction and interference have to be taken into account. Practically, the light propagation from a dipole source in arbitrary geometries or guided field profiles in waveguides can then be calculated with numerical methods.
For example the modes and effective index of slab waveguides with one dimensional confinement can be calculated analytically from Maxwell's equations. The mode profiles and propagation constants in channel waveguides can be derived from the analytical solutions for special cases like low confinement. But for well confining waveguides, the field has substantial components polarized in the direction of propagation and most approximations from analytical solutions fail.
Therefore, numerical solutions for the Maxwell equations in media are needed under such conditions. Similarly we have seen in Chapter 3 that micro-lenses with a diameter on the order of $10\,\mu$m already provoke significant diffraction effects that break down the ray optics picture. We will now introduce the modelling approach used in this thesis, 3D FDTD for micro-lenses in interaction with dipole sources and waveguided modes calculated by FDE analysis within the FDTD software suite.

G.1 Finite difference time domain solver

The 'Ansys Lumerical' finite difference time domain (FDTD) solver allows to monitor the development of light fields in arbitrary, omnidirectional 3D geometries by solving the classical Maxwell equations fully vectorial in dielectric and metal media using overlayed separate grids for the electric and magnetic field while operating in the time domain with a finite number of steps. The Maxwell wave equation is solved with finite differences using discrete space and time coordinates instead of smooth derivatives, giving the method its name. This applies similarly to the finite difference element (FDE) method. The differently polarized components of the fields at one 'mesh point' are attributed to different spatial positions in the Yee unit cell, giving computational advantage.
In contrast to the FDE solver, which works in the frequency domain, in FDTD sources emit a light pulse that is tracked inside the simulation region probing the broadband system response. Via Fourier transformation, the continuous wave solution for the frequency range of the excitation pulse can be monitored with predefined detector surfaces. Spatial field profiles, transmission through a detector surface or Poynting vector analysis are standard results. It is to note, that the interpolation from time domain to continuous wave results relies on a linear response of the material in interaction with the light field.
To perform a FDTD simulation, the following components have to be set up and defined.

- Modelled geometry with defined material properties

- Simulation region with suitable boundary conditions
- Source or sources to emit a light pulse with a defined spatial and temporal profile into the simulation region
- Detector surfaces to monitor the development of the light field in an area of interest

Set up and result extraction can be fully scripted in the 'Ansys Lumerical' scripting language to perform automatized and parallel simulations. The material properties and geometry can be set up similarly to the FDE solver from Lumerical. Generally we use the refractive index catalogue provided by refractiveindex.info, which collates the dispersion formulas derived in the scientific literature. The mesh can be defined in a continuous manner or with an automated meshing protocol, that takes larger mesh spacing for low index materials into account to save computational power. To describe crucial parts of the structure with high spatial accuracy, an overlay mesh can be defined which is employed to approximate the lens geometry and diamond micro-pillars in more detail. Typically a 50 nm mesh size is used with 35 nm mesh size in the region of the GaN micro-lens.
Because the light fields in FDTD simulations are not necessarily guided, absorbing boundary conditions with perfectly matched layers (PML) are employed. Symmetries of the geometry and source can be exploited to define symmetric and anti-symmetric boundary conditions to reduce the size of the simulation region by a factor of 2, 4 or 8. This can be specifically useful to reduce the memory requirements and simulation time, as shown in Tab. G.1.
Possible sources are a plane wave, Gaussian beams, dipole emitters, FDE calculated modes or self defined input fields from other simulations. With a dipole emitter, the back-action of the emitted light field on emitting dipole is taken into account and allows the calculation of the Purcell factor in the weak coupling regime, as discussed later in this section.
FDTD simulations are, when properly set up, the most accurate and universal way to simulate light propagation in a classical, macroscopic manner, because the meshing and material parameters are the only approximations made within the approach. But compared to FDE the computational power used is much higher, especially because of the 3D character of the simulation.

Table G.1: How memory and time requirements scale in FDTD simulations with vacuum wavelength λ and grid step size Δx. Increasing the size of the simulation region has a similar effect as reducing the step size.

	3D	2D
Memory requirement	$\propto \left(\frac{\lambda}{\Delta x}\right)^3$	$\propto \left(\frac{\lambda}{\Delta x}\right)^2$
Simulation time	$\propto \left(\frac{\lambda}{\Delta x}\right)^4$	$\propto \left(\frac{\lambda}{\Delta x}\right)^3$

G.2 Embedded in FDTD: Finite difference eigenmode solver

The 'Ansys Lumerical' finite difference eigenmode (FDE) solver evaluates the macroscopic Maxwell equations in media for a 2D slice through a waveguiding structure and can be used to find the field profile of a guided mode, as well as its polarization, effective refractive index, dispersion, propagation and bend loss. The full vectorial Maxwell equations are solved on two overlapping rectangular grids

for the electric and magnetic fields $\vec{E}$ and $\vec{B}$ with the following ansatz at a single vacuum wavelength $\lambda = \frac{c}{2\pi\omega}$:

$$\vec{E}(x,y,z,t) = \vec{E}(x,y) \cdot e^{i(-\omega t+\beta z)} \qquad \vec{B}(x,y,z,t) = \vec{B}(x,y) \cdot e^{i(-\omega t+\beta z)} \tag{G.1}$$

where ω is the angular frequency of the light field, x, y and z spatial coordinates and t the time. The ansatz includes static mode profiles that propagate along the z direction. The effective refractive index n_{eff} of these modes can be calculated from the effective wavenumber β:

$$n_{eff} = \frac{c\beta}{\omega} \tag{G.2}$$

The method takes the full geometry and boundary conditions between media into account and is limited mainly by the mesh accuracy. The solutions are always orthogonal to each other, because they are the result of a matrix Eigenwert problem. The simulations are 2D, therefore the calculation time is comparably short and the needed computational power low compared to for example FDTD simulations, see also Tab. G.1.

The solver is used to find confined waveguide modes and the boundary conditions are usually set to metal, which means 100 % reflective surfaces. Therefore, the simulation region has to be large enough, so that the evanescent tail of the found modes has dropped over several orders of magnitude at the border.

G.3 Purcell effect

We will quickly discuss the connection between the classical and quantum mechanical picture of Purcell enhancement based on reference [2]. The Purcell effect describes the enhancement of the spontaneous emission rate γ (the inverse of the radiative life time τ) of a quantum emitter caused by an inhomogeneous environment. It was first proposed by Purcell in 1946 [366]. In quantum electro dynamics, γ is connected to the partial local density of states (LDOS) ρ_p of the light field. For weak coupling between the quantum emitter and light field, the spontaneous emission rate of a two level quantum system is directly proportional to the LDOS.

γ can only be derived correctly using quantum electrodynamics. However the enhancement of the spontaneous emission rate due to an inhomogeneous environment $F_P = \frac{\gamma}{\gamma_0}$ (Purcell factor) equals the enhancement that a classical dipole experiences due to back action of its own backscattered field, with γ_0 being the equivalent emission rate in a free space environment [2]. Therefore the classical simulations used in this thesis to solve Maxwell's equations on a grid can calculate F_P.

For example the Purcell factor F_P of a dipole emitter inside a cavity, whose dipole moment is aligned to the maximum electric field of the cavity mode and no spectral detuning, can be approximated by evaluating Eq. (G.3) [367]:

$$F_P(\lambda) = \frac{3}{4\pi^2}\left(\frac{\lambda}{n}\right)^3 \frac{Q}{V} = \frac{\gamma}{\gamma_0} \tag{G.3}$$

with the wavelength $\frac{\lambda}{n}$ inside a cavity with quality factor Q and mode volume V. Q is defined as the ratio between the stored energy and the total power loss rate times the resonance frequency of the resonator. It indicates for how many cycles the resonator will hold power, after pumping stops.

The increase of the LDOS leading to the emission enhancement may be understood to stem from the

large number of available optical states in the cavity. Therefore the emission at the cavities resonant wavelengths is highly increased and the spatial emission pattern is distorted because the additionally emitted photons are emitted into the cavity mode. Furthermore the emission of photons with off-resonant wavelength into the cavity mode is suppressed. This simply means that Purcell enhancement is directionally sensitive.

In this work we have considered the NV^- centre in μm-proximity to a planar diamond air interface with roughly unmodified Purcell enhancement compared to bulk diamond, but also in nm-proximity to the tip of a diamond micro-pillar in which case the Purcell enhancement alters the emission spectrum and direction. A dipole emitter in a bulk dielectric is expected to show a Purcell factor $F_p > 1$ (leading to a reduction of the radiative life time) [2], explaining the observed increase of fluorescence lifetime of NV^- centres in nanodiamonds where the dielectric environment on the length scale of the emission wavelength is dominated by air instead of diamond [7].

H Hardware and software development for a confocal photoluminescence microscope with single photon sensitivity

In this section we are going to document the development of a confocal microscope optimized for light detection from single nitrogen vacancy centres in diamond. The tool will be capable of generating photoluminesence maps in 3D and the collection of $g^2(\tau)$ autocorrelation measurements to verify the nature of single emitters and has been used in Chapter 4.
Initially we will discuss the basic principle and equations that govern confocal microscopy, pin point the design criteria that were driving this work and give a full description of the home-built confocal setup in terms of hard- and software. After analysing the system performance we are showing measurements from three collaborative projects that are supported by the development of this tool but are outside the general scope of this thesis.

H.1 Review: Principles of confocal photoluminescence microscopy

Simply speaking confocal photoluminescence microscopy is a free-space optics technique that makes use of a μm-sized aperture to restrict the light collection to roughly the same focal volume in which the specimen is excited by the pump source, typically a laser [368]. As a consequence a 3D sectioning ability emerges which is extensively used in the context of micro-biology and semiconductor physics to isolate the system of interest spatially from the background. As illustrated in Fig. H.1 a confocal microscope essentially images the focal plane of the microscope objective lens system onto a pinhole and therefore requires to scan either the beam path or the sample to generate an image. This stands in contrast to wide field microscopy techniques which gather an image in a single shot when using an array-based light detector such as a CCD or CMOS camera.
Even an ideal imaging system cannot image a point source into one spot because its limited aperture size causes diffraction. The diffraction limited projection of a point source in an imaging system such as a lens is called the point spread function (PSF) or intensity point spread function (IPSF)) if expressed in terms of intensity [368]. We are interested in calculating the resolution of a confocal microscope system using the PSF concept, assuming that a collimated laser beam can be seen as a point source placed at infinity. If we consider a point source emitting monochromatic linearly polarized classical light we can calculate the IPSF by scalar diffraction theory [368].
As indicated in Fig. H.1 the objective lens system is shared between the excitation and detection beam path in our specific setup and we are considering non-resonant excitation of photoluminescent emitters. Therefore we can look at the point spread function from different perspectives: The ideal IPSF of the excitation laser at λ_{pump} in the objective plane can be calculated by [369]

$$\mathrm{FWHM}_{\mathrm{lateral}} = 0.51\frac{\lambda}{\mathrm{NA}} \tag{H.1}$$

and

$$\mathrm{FWHM}_{\mathrm{axial}} = 0.88\frac{\lambda}{1-\sqrt{1-\mathrm{NA}}}. \tag{H.2}$$

with the maximum of the IPSF laying on the optical axis in the image plane, which in this case is the sample plane. The numerical aperature (NA) corresponds here to the objective NA. If we would image the laser spot onto a CCD camera at the position of the pinhole/detector arrangement we will need to take the image magnification $M = f_{\mathrm{TL}}/f_{\mathrm{objective}}$ into account, resulting in

$$\mathrm{FWHM}_{\mathrm{lateral,real}} = \mathrm{FWHM}_{\mathrm{lateral,CCD}}/M \tag{H.3}$$

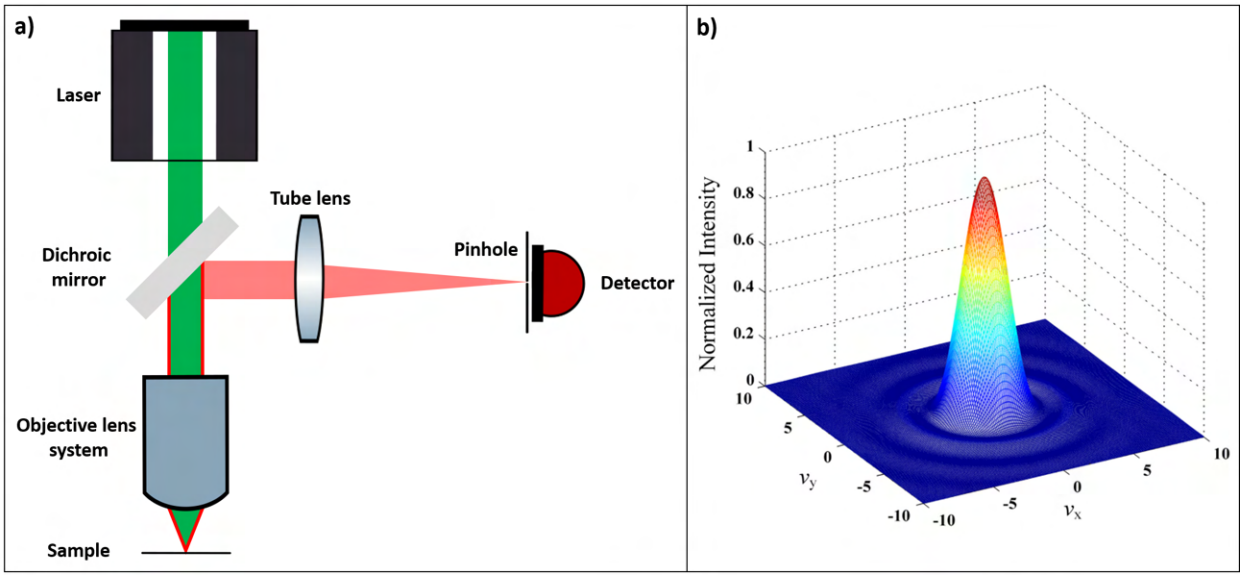

Figure H.1: a) Schematic illustrating the simplified beam path of the reflection mode confocal microscope system used in this work. Parallel light bundles indicate a collimated beam with the colours indicating pump (green) and photoluminescence (red) light, b) intensity point spread function in the image plane of an ideal point source (Airy rings) as function of generalized transverse optical coordinates, adapted from [368].

If we are using the system as a reflective laser scanning microscope with laser light leaking through the dichroic mirror the system resolution would be theoretically expected to increase if an infinitesimally small pinhole is used because the image of the excitation point source in the sample plane can be thought of being convoluted (implying multiplication in the Fourier plane) with the PSF of the pinhole imaged onto the sample plane [368, 369]. This effectively reduces the size of the system IPSF at the cost of count rate. We are going to choose the size of the pinhole as such that the main lobe of the PSF of the tube lens will always fully pass through the pinhole diameter, effectively using the pinhole to reject light from other planes of interest by multiplication of the two PSFs, but not to increase the resolution below the equations given above. For realistic pinhole sizes as such the expected axial size of the confocal IPSF in the sample plane can be modified according to [369]

$$\mathrm{FWHM}_{\mathrm{axial,CM}} = 0.67\frac{\lambda}{1-\sqrt{1-\mathrm{NA}}}\cdot\sqrt{1+\frac{\mathrm{NA}_{\mathrm{TL}}D_{\mathrm{pinhole}}}{1.22\lambda}} \tag{H.4}$$

with the numerical aperture of the tube lens $\mathrm{NA}_{\mathrm{TL}}$ the diameter of the pinhole D_{pinhole}. If the emission from a point emitter is considered, we can insert its emission wavelength $\lambda_{\mathrm{emitter}}$ instead of λ_{pump} into

the equation as a lower bound.

H.2 Review: Si-based single photon avalanche diodes

Single photon avalanche diodes are purposefully built photodiodes that are operated beyond the breakdown voltage of their pn-junction in a Geigermode, which allows them to detect single photons with high efficiency [370, 371]. They mimic the working principle of a classical photomultiplier tube on a CMOS compatible solid state platform by adding a resistive p-doped layer into the typical design of a p^+-i-n^+ photodiode leading to a p^+-i-p-n^+ layout, compare Fig. H.2 a) for an example of the layer stack [370, 371].

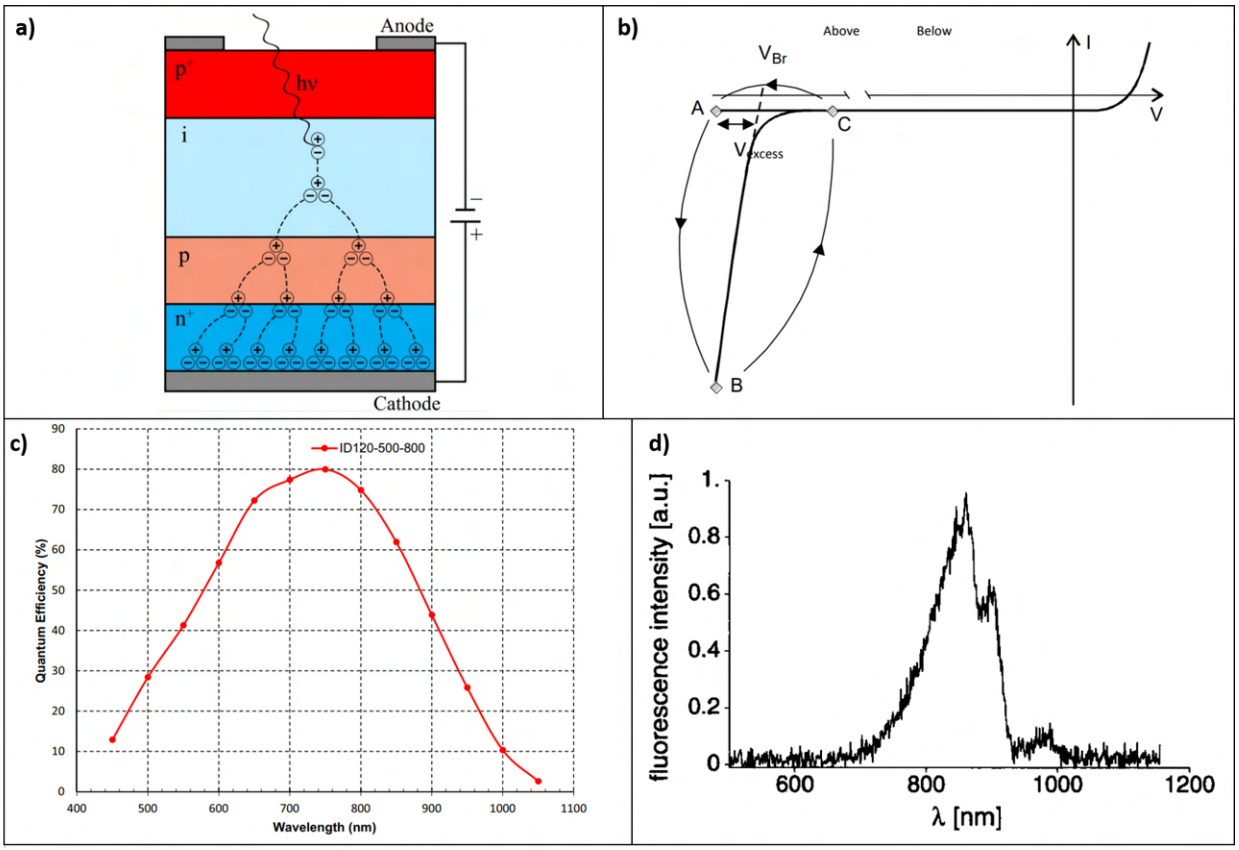

Figure H.2: a) Cross section of a typical SPAD with schematics illustrating the working principle, adapted from [371], b) typical shape of the I-V curve of a SPAD detector with marked operation points, adapted from [372], c) quantum efficiency in dependence of wavelength for ID120-500-800 Si single photon detectors from ID Quantique, adapted from [373], d) normalized break-down flash spectrum of a Si SPAD, adapted from [237]

If an electron-hole pair is created by an incident photon in the intrinsic region the electron is drawn to the cathode contact by the high reverse bias leading to an avalanche of further electron-hole pairs initiated by the high resistivity in the p-layer. Fig. H.2 b) contains a schematic of the operation in the I-V curve: The excess bias above the break down voltage V_{excess} leaves the device in a metastable state (A). Any disturbance with enough energy, such as a single incident photon can now cause a return to the I-V curve (B) and a quenching circuit quickly stabilizes the SPAD by reducing the applied voltage before physical damage can occur (C), while the control electronics generate an electrical pulse indicating the triggering event. Then the cycle is restarted.

Fig. H.2 c) contains the quantum efficiency response curve from the ID Quantique detectors employed, showing nearly 80% peak efficiency with an appropriately operated device and under sufficiently low photon influx. The figure in d) shows the spectrum measured for photons emitted from Si SPADs due to the phenomenon of the break-down flash generated by hot-carriers that recombine under light emission [237]. This effect can generate optical cross talk between SPAD detectors in a HBT arrangement, something also observed in the home-built setup. We counteract the effect by adding a 750 nm short pass premium filter which dramatically reduces but does not fully eliminate the effect.

H.3 Outline of the work

The setup is designed to achieve the following capabilities:

- Collect photoluminescence from a diffraction limited three dimensional volume for tomography of complex samples with the option to switch to a larger detection area
- Single photon sensitivity in the $\lambda = 600 - 900$ nm wavelength window
- Gathering $g^2(\tau)$ second order autocorrelation statistics of the detected photon stream from targeted positions
- Relative position detection of emitter distributions with respect to alignment markers
- Compatibility with future addition of edge detection from photonic integrated circuits

H.4 Hardware description

A schematic of the home-built confocal microscope setup is shown in Fig. H.3. In the following we will go through photographs of the different parts of the setup and explain the components and their purpose in detail.

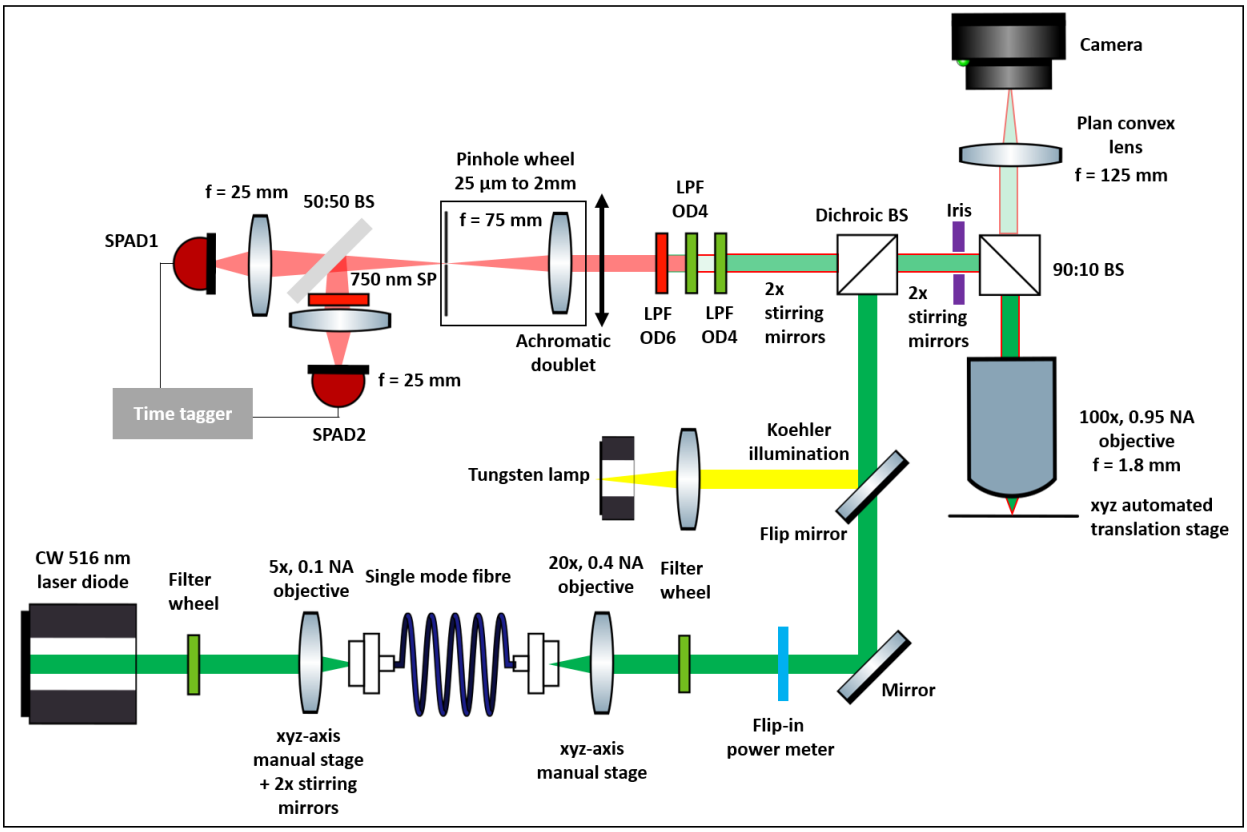

Figure H.3: Schematic showing the components of the home-built confocal microscope system with single photon sensitivity with closed-loop automated stage movements for scanning the laser spot over the sample. The setup is optimised for the 100x objective lens, but 50x and 10x objectives can also be easily mounted. Abbreviations are long pass filter (LPF), short pass (SP) filter, beam splitter (BS), numerical aperature (NA), continuous wave (CW), single photon avalanche photodiode (SPAD).

The laser coupling section is shown in Fig. H.4 a) with the laser beam path indicated in green. A single mode green laser diode (Sharp GH0521DE2G, 130 mW) with measured $\lambda = 517 \pm 2$ nm wavelength is mounted in an actively cooled housing (Thorlabs LDM56) and operated with a constant current power supply (Thorlabs LDC200C) while the temperature is monitored and corrected by a thermoelectric temperature controller (Thorlabs TED200C). Typical settings are 270 mA constant current and 25°C (10,000 Ω). The laser beam is collimated using an anti-reflection coated asphere and reflected twice via silver mirrors while passing through a filter wheel with optical density filters before the beam is focused on the facet of an angled single mode fibre (Thorlabs P3-460B-FC-2) with a 5x objective lens system (infinity corrected, NA= 0.1) for spatial cleaning of the asymmetric laser diode mode profile. The fibre facet is mounted on a xyz manual translation stage (Elliot Gold, 20 nm resolution) for precise coupling. It is found that up to 60 mW output power coupling can be achieved behind the fibre when imaging the laser mode 1:1 on the inpout fibre facet using a suitable asphere, but then the laser power tends to vary heavily over time due to thermal effects. With the low-NA objective the lens facet is overfilled and then additionally defocused to further enlarge the beam leading to 5-6 mW stable output power.

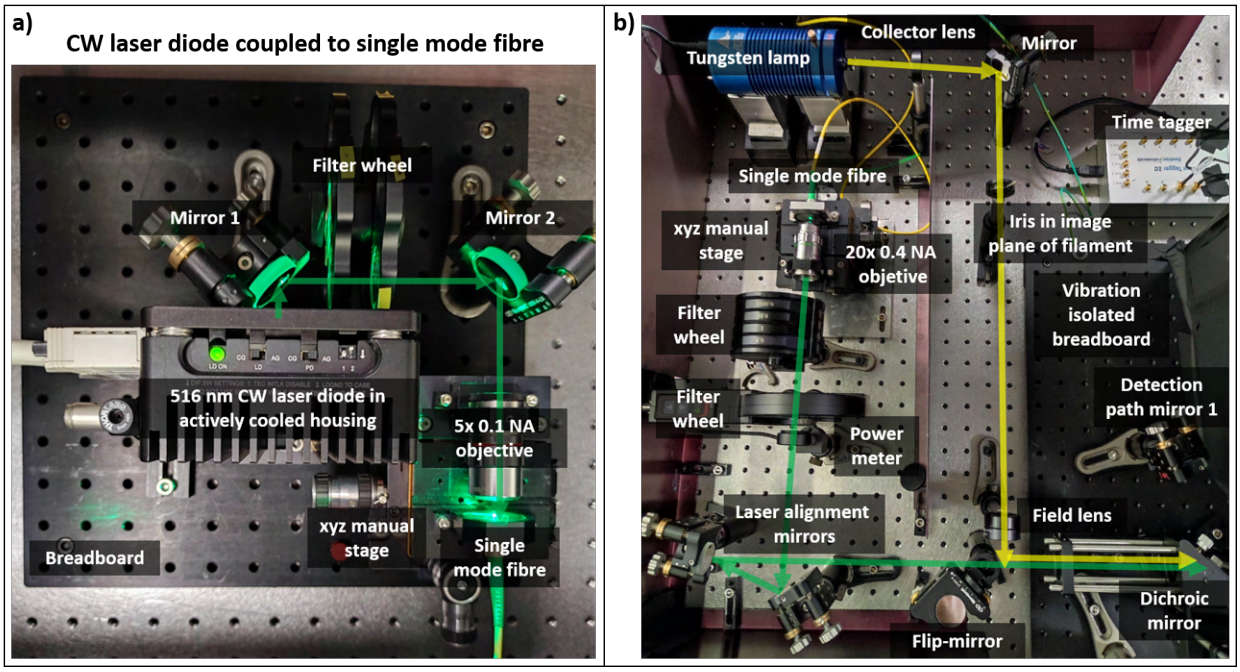

Figure H.4: Photos of the setup as built in the laboratory. a) Breadboard based coupling of a 517 nm continuous wave laser diode into a single mode fibre for beam cleaning, b) laser (green) and tungsten lamp (yellow) input paths into the optical column, which starts at the dichroic mirror in the bottom right of the photo.

The next section of the optical setup is shown in Fig. H.4 b). The cleaned laser mode exits the single mode fibre and is collimated using an infinity corrected 20x objective (Olympus ULDW MSPlan, NA= 0.4) which is mounted on a xyz manual stage (Elliot Gold, 20 nm resolution). This leads to a Gaussian beam profile with a diameter of approximately 2-3 mm (determined by eye, depends on power), which is a bit smaller than the entrance pupil diameter of the infinity corrected 100x objective which is mainly used for measurements (Olympus MSPlan, NA= 0.95). This results in both a small spot size and low waste of optical power. A manual and an automated filter wheel (Thorlabs FW102C) loaded with a wide range of neutral density filters give control of the laser power which is measured by a photo diode power sensor (Thorlabs S120VC,< 50 mW 200-1100 nm) on a flip mount. The laser is than aligned to the cage system containing the optical microscope column via two silver mirrors. The first optical element is the dichroic mirror (Thorlabs DMPL567) in the bottom right of Fig. H.4 b).

Another part of this section of the setup is the white light illumination source employed to navigate the sample. The filament of a tungsten lamp (Ocean optics HL-2000-FHSA) is imaged onto a nearly closed iris ($\approx \varnothing 1$ mm) using a collector lens ($f \approx$10s of mm, plano-convex). A field lens ($f = 200$ mm, plano-convex) reimages the filament onto the back focal plane of the 100x objective (not visible in the image) to achieve reasonably homogenous illumination conditions in a Köhler like arrangement. The white light path in is coupled into the microscope cage system via a flip mirror.

An image of the cage mounted optical column and sample stage is shown in Fig. H.5 a). The column contains the dichroic mirror employed to prefilter the laser reflected light and transmit excited photoluminescence above $\lambda = 567$ nm to the detector section. Two periscope mirrors increase the height of the beam path which is then split vertically by a 90R/10T beam splitter cube (Thorlabs BS028, A coated) focusing most of the laser light through the 100x objective on the sample surface. The beam splitter cube allows to image the sample surface on a CCD camera (Thorlabs DCC1645C) with a tube

lens (Thorlabs LA1986-A, $f = 125\,\text{mm}$). The sample is mounted on an automated closed-loop xyz slip-stick piezo stage with several 31x31x12 mm large travel (Smaract SOM-505020, uni-directional repeatability of 50-100 nm with MSC2 controller). The sample stage is elevated to facilitate bottom illumination and edge coupling in future experiments.

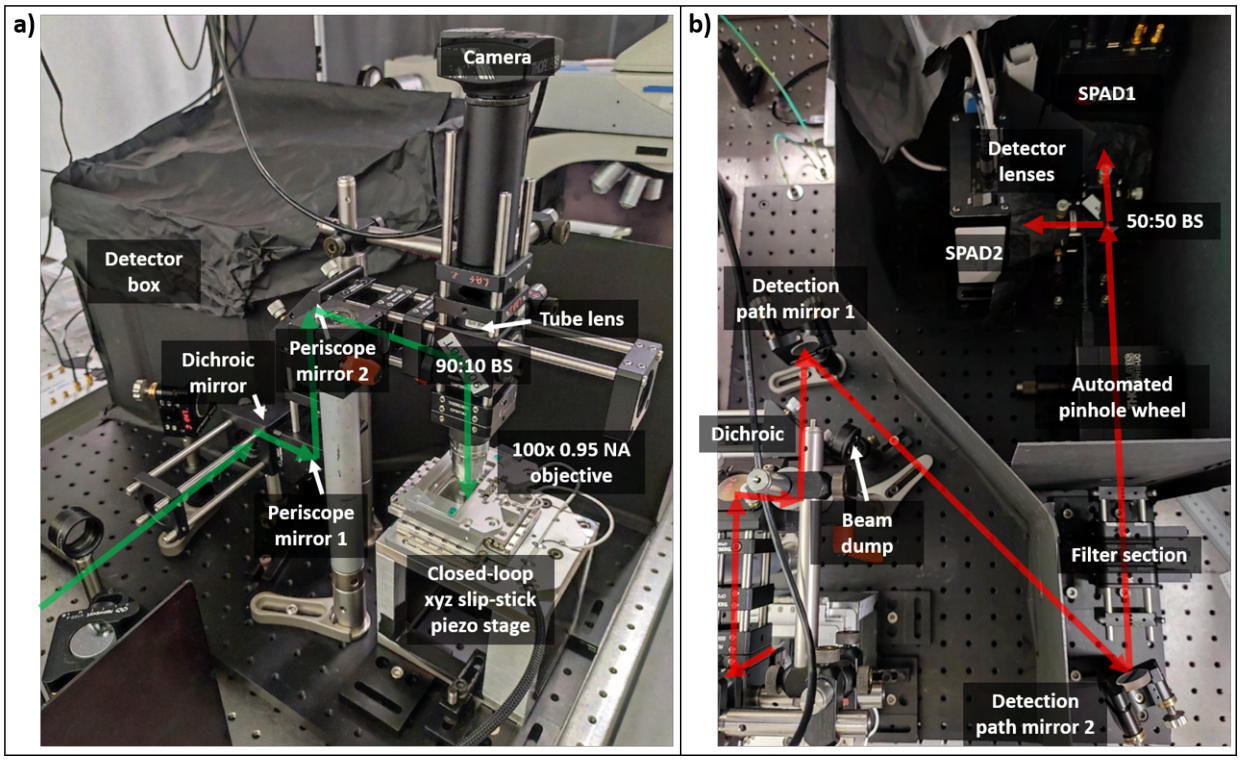

Figure H.5: Photos of the setup as built in the laboratory. a) Optical column accessed via two periscope mirrors and the closed-loop piezo based stage with several cm range in x, y and z on a stage holder, potentially allowing bottom illumination. The laser path towards the sample is indicated in green, b) Detection path of the microscope with the photoluminescence response of the sample indicated in red. The detector box is opened for the photo.

The beam path of the photoluminescence response from the sample (red) is shown in Fig. H.5 b). The emitted fluorescent light from the excited sample volume is recollimated through the 100x objective in reflection mode, passes the periscope and dichroic in the opposite direction and is aligned to the detection path with two silver mirrors. A cage based filter section (Thorlabs CFS1/M) allows to add three filters into the beam path: 2x soft coated 550 nm long pass (Measured around OD4, Thorlabs FEL0550), 1x hard coated 650 nm long pass (Thorlabs FELH0650). By default all three are used in photoluminescence experiments, which effectively means that the phonon sideband of the NV^- centre is detected without the ZPL. The filter section is aligned to the second cage system containing an HBT arrangement of two silicon single photon avalanche photodiodes (SPAD, IDQuantique ID120-500-800) with an automated pinhole wheel (Thorlabs MPH16-B, 25 μm-2 mm pinhole diameter) inserted in between. This contains a B-coated achromatic doublet with $f = 75\,\text{mm}$ to focus the collimated beam onto the pinhole. Without recollimation the beam now passes a 50:50 plate beam splitter (Thorlabs BSW29R, B-coated) and is focused on the ca. 500 μm large detector area of the respective SPAD using B-coated plano-convex lenses (Thorlabs LA1951-B) mounted with xy manual translation stages.
Si SPADs emit light between $\lambda = 700 - 1000\,\text{nm}$ wavelength due to the "break down flash" [237] which causes false counts on the respective other detector in this arrangement. The origin of the reflection

that couples both SPADs together is not exactly known, presumingly light is reflected either by the pinhole wheel or the optical components before the pinhole (pinhole lens, filters). A 750 nm short pass filter (Thorlabs FESH0750) is permanently added in front of SPAD2 to reduce the effect without cutting into the NV^- centre emission spectrum. For optimal HBT measurements the SPAD detectors are deliberately misaligned in an asymmetric way along the optical axis, meaning that one lens is slightly too far and the other slightly too close to their respective SPADs which overfills the detectors but maintains reasonable quantum efficiency.
The detection events triggered on both SPADs are collected via a time tagger (Swabian Instruments Time Tagger 20) which is interfaced with the PC via USB, compare Fig. H.4 b) in the top right for an image. Detection events and sample position are synchronized using a self-developed Python-based GUI which is discussed in detail in the next section.
As we can see in both Fig. H.4 and Fig. H.5, the cage based optical column and detection section are mounted on a vibration isolation plate with eight sorbothane isolators (Thorlabs AV4/M), because the optical table employed only passive vibration isolation leading to significant oscillations between sample and microscope objective clearly visible on the imaging camera. This additional passive isolation is found to work very well contributing to the stability of the setup.

We note that fibre coupling with the automated pinhole is trickier than expected. The Thorlabs automated pinhole has a SMA connector, allowing to couple the spatially filtered light to an optical fibre, e.g. leading to a spectrometer. The datasheet recommends to use 400-1000 μm fibre core with 0.22 NA – if a smaller fibre core is used, it is found that significant amount of light is lost if a small pinhole size like 25 μm is used with a 100 or 50 µm fibre core, potentially due to a lateral misalignment of the connector centre to the small pinholes on the wheel It is found that the pinhole wheel seems to be laterally offset from the centre of the cage system which can be attached to the front of the pinhole and is now blocked by the detector box, compare Fig. H.6 for an illustration. The user is free to use the 2 mm pinhole and for example a 50 µm fibre core, then using the fibre as a pinhole before coupling to a detector or spectrometer.

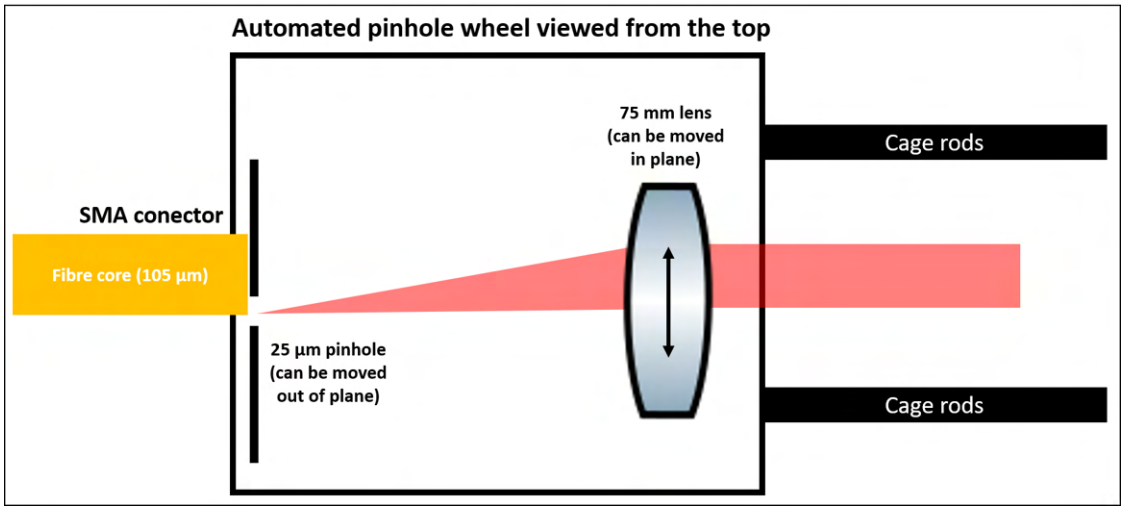

Figure H.6: Warning for the user: Schematic depicting an interpretation of the findings when trying to couple to fibres with 105 and 50 μm fibre core diameter using the automated pinhole wheel at the lowest pinhole diameter (25 μm). Due to large manufacturing tolerances, Thorlabs recommends the use of 400-1000 μm fibre core diameter for collection if fibre coupling is chosen for example to add a spectrometer to the setup.

H.5 Software description

This guide quickly describes the main functionality of the Python-based GUI that can be used to run the home built confocal microscope system in 507f. A couple of variables are set by default (e.g. the region of interest of the camera, default stage velocity and acceleration) and can be changed at the very top of the "Application.py" file that brings together the different components of the script.
The GUI allows to interface the SmarAct slip-stick piezo stage, the Swabian Instruments TimeTagger which is used to accumulate the events from the single photon avalanche photodetectors from ID Quantique, and the Thorlabs camera used to image the sample surface. The Python project is organised in a hierarchical manner, making use of Python's object based programming and therefore native ease to implement modules. The GUI is separated into 7 main panels, which will be described in detail in the following.

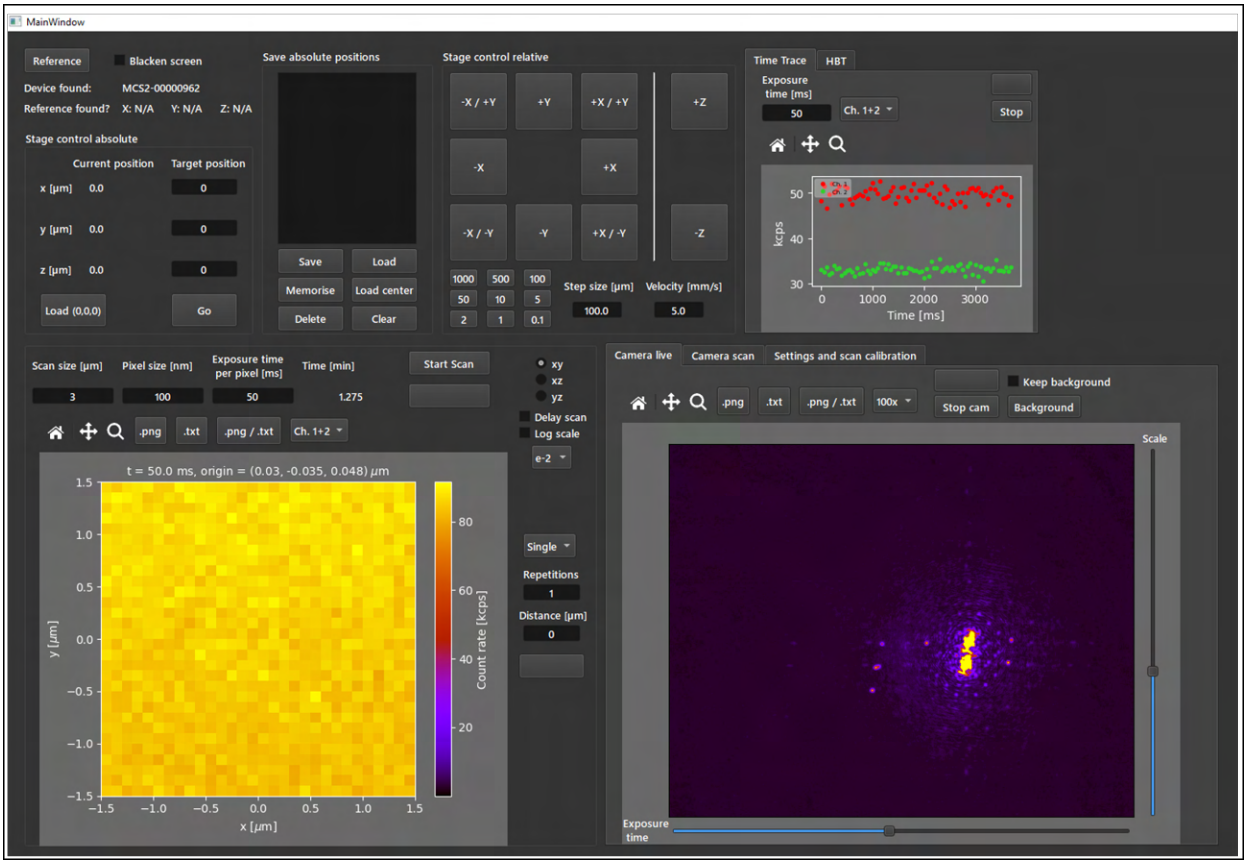

Figure H.7: Python based graphical user interface of the home-built confocal setup. The user can access the stage, record time traces and photon statistics, perform confocal imaging scans in 3D and interact with the camera live view. Both scan and camera panels have a 'click to extract position' feature, that allows the user to quickly navigate on the sample.

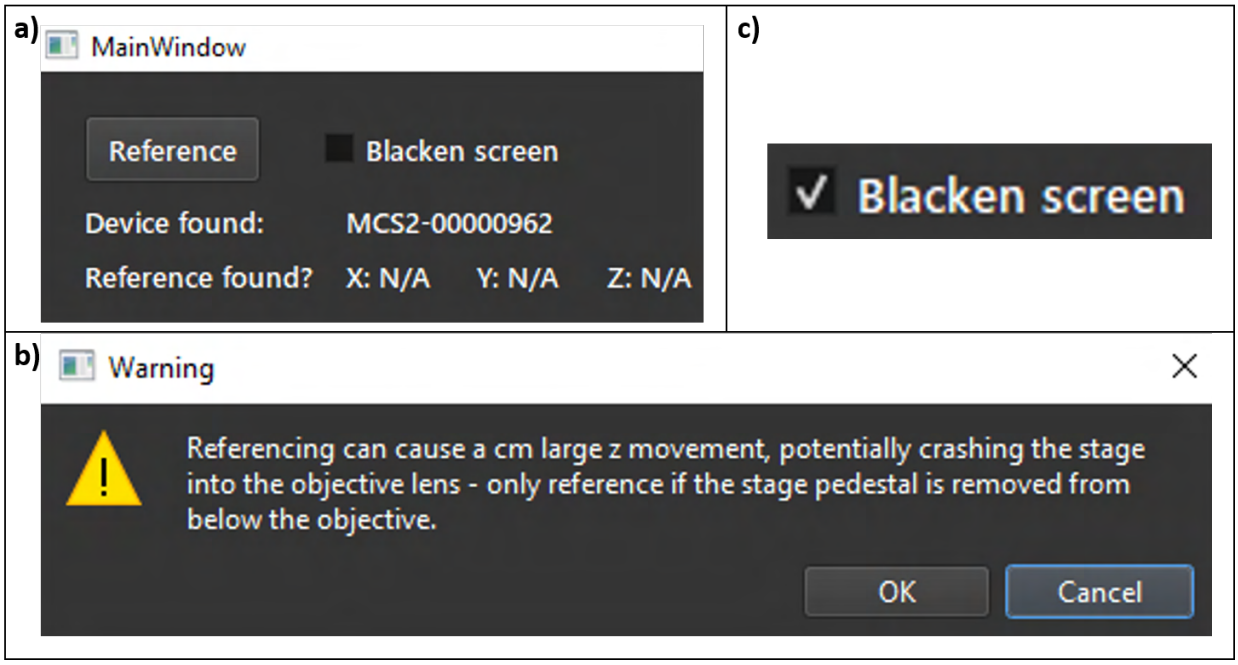

Figure H.8: Python based graphical user interface of the home-built confocal setup with a) the top left of the main panel containing the reference control button and the detected device. b) The warning window that opens if the 'Reference' button is pressed to avoid crashes of the stage with the objective, c) in this part of the menu the user can choose to overlay the screen with black color in full screen if a confocal scan or photon statistic collection is started to reduce background light. The screen turns back to normal when the measurement is finished.

In the top left part of the main window, the GUI allows for stage referencing, which refers to the homing procedure of the stage and is executed after clicking the "Reference" button. It is not required to reference the stage for operation, but it might allow the user to return to a previously defined coordinate system, as the stage position is lost when the MSC2 stage controller is turned off. The referencing can cause significant z-movements, so the software includes a warning before execution to prevent crashing the stage into the objective. After successful referencing, "Reference found?" will be answered by "Yes" next to the respective stage axis. If a problem occurs or the used needs to calibrate the stage, please use the "Precision Tool Commander" from SmarAct to access the stage properties and calibration procedures, following the respective datasheets.
By ticking "Blacken screen" the main monitor is automatically overlaid with a black rectangle if a scan or HBT measurement is started. This feature proved generally unnecessary, because the detector boxing is good enough to block the monitor light.

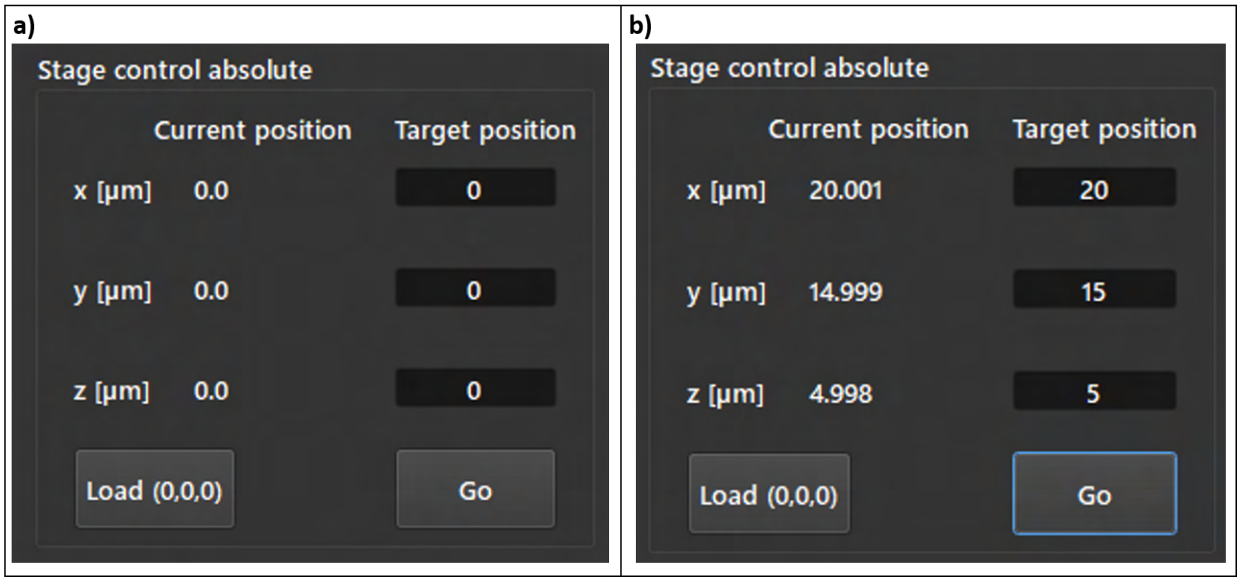

Figure H.9: Python based graphical user interface of the home-built confocal setup, showing the control panel for the absolute position of the closed-loop automated stage. a) shows the condition of the panel at initialization and b) after executing the movement to the target position using the 'Go' button.

The "Stage control absolute" control panel allows the user to drive the stage to arbitrary stage positions within the movement limits. The origin refers either to the home position if the stage is referenced, or to the position during start-up if the MSC2 controller has been turned off and is restarted without referencing. The stage has a closed loop-position control via an encoder system, which can repeat and keep positions with $100-200\,\text{nm}$ accuracy (by datasheet and experience). In order to move to a new position, the user can manually enter the target position in μm and the stage will execute the movement after the "Go" button is clicked. Load (0,0,0) simply allows to overwrite the target position with (0,0,0). The coordinate system and camera display are setup to match the user's intuition when standing in front of the optical table: The x-axis is orientated along the edge of the optical table, the y-axis is in-plane perpendicular to the x-axis, while the z-axis is orientated along the optical axis, indicating the height or distance of objetive and sample. To ease navigation, a positive x-motion refers to the stage moving to the left, resulting in the camera image/laser focus moving to the right in the reference frame of the sample. Similarly, a positive y-motion moves the stage towards the user, resulting in the camera image/laser focus moving in plane "upwards" when imagining the sample reference frame being fixed and viewed along the optical axis. A positive z-movement indicates that the stage is moved downwards, yielding the focussed laser spot to move upwards out of plane in the sample reference frame. This choice has the particular advantage that the real orientation of features on the sample match the display in the GUI.

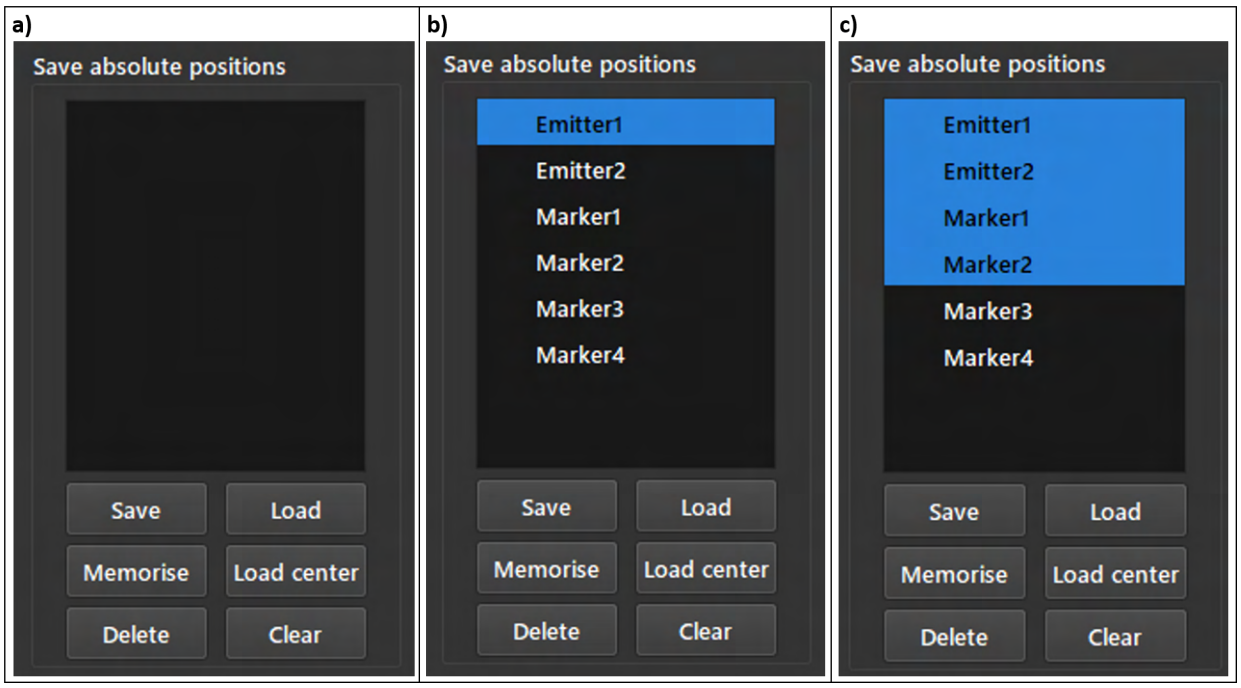

Figure H.10: Python based graphical user interface of the home-built confocal setup, showing the panel used to save stage positions a) after program start up, b) after several positions have been saved and named and c) with multiple positions marked, allowing the user to find the geometric center of these positions by pressing 'Load center'.

"Save absolute position" allows the user to save the current stage position with the "Save" button, and name it appropriately by double clicking onto the created entry in the list. They can "Load" any saved position into the target position of the "Stage control absolute" panel, but for the stage to move, "Go" must still be clicked. "Memorise" creates a hard memory entry of the selected position, so it will be recovered even if the software is closed or crashes. "Load centre" allows to quickly load the geometric average of several selected positions into the target position. "Delete" allows single entries to be deleted, while "Clear" deletes all entries and erases the memory.

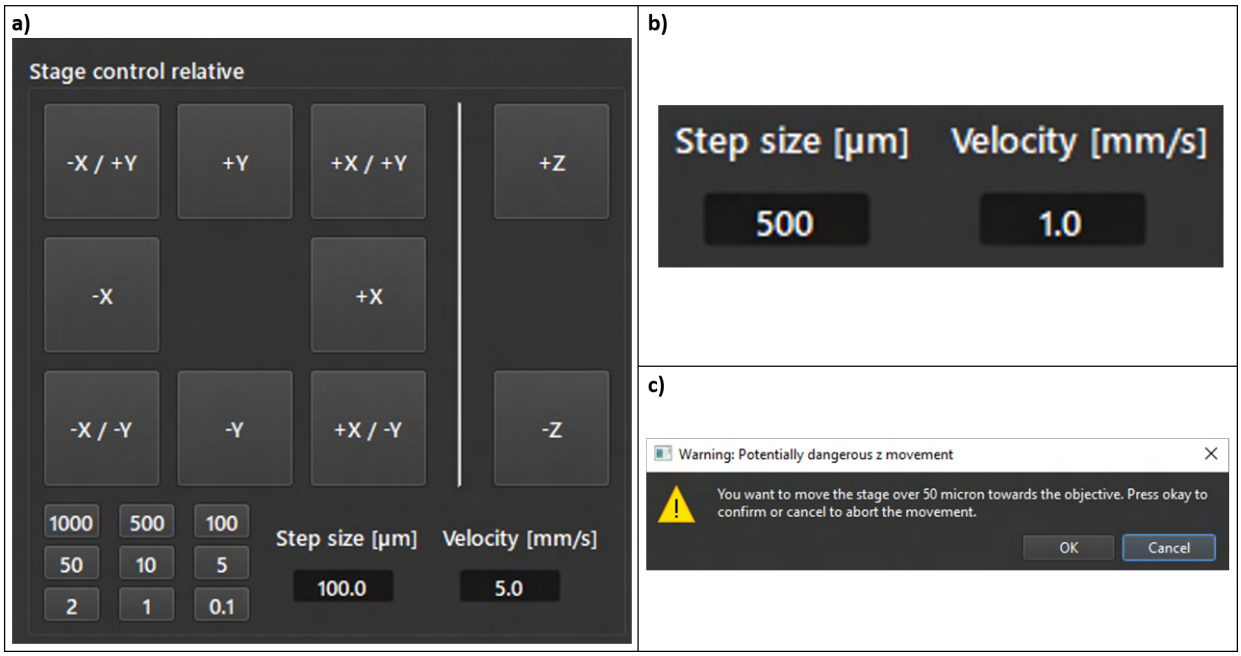

Figure H.11: Python based graphical user interface of the home-built confocal setup, showing in a) a detailed view of the push buttons causing relative stage movements, b) step size and velocity selection boxes and c) the message box that appears if the user attempts to lift the stage further than 50 μm, which could potentially crash the sample and stage into the objective lens.

The "Stage control relative" panel enables the user to explore their sample with intuitive push buttons along all three axis. The buttons in the bottom left corner (1000, 500, ..., 0.1) are designed to quickly change the step size in the range of typical requirements. The user can also manually adjust the velocity of the stage motion. If an upwards movement (-Z button) greater than 50 μm is requested, the user needs to accept a warning before the movement is executed. Again, this feature is supposed to prevent accidental crashes of the sample into the objective lens system.

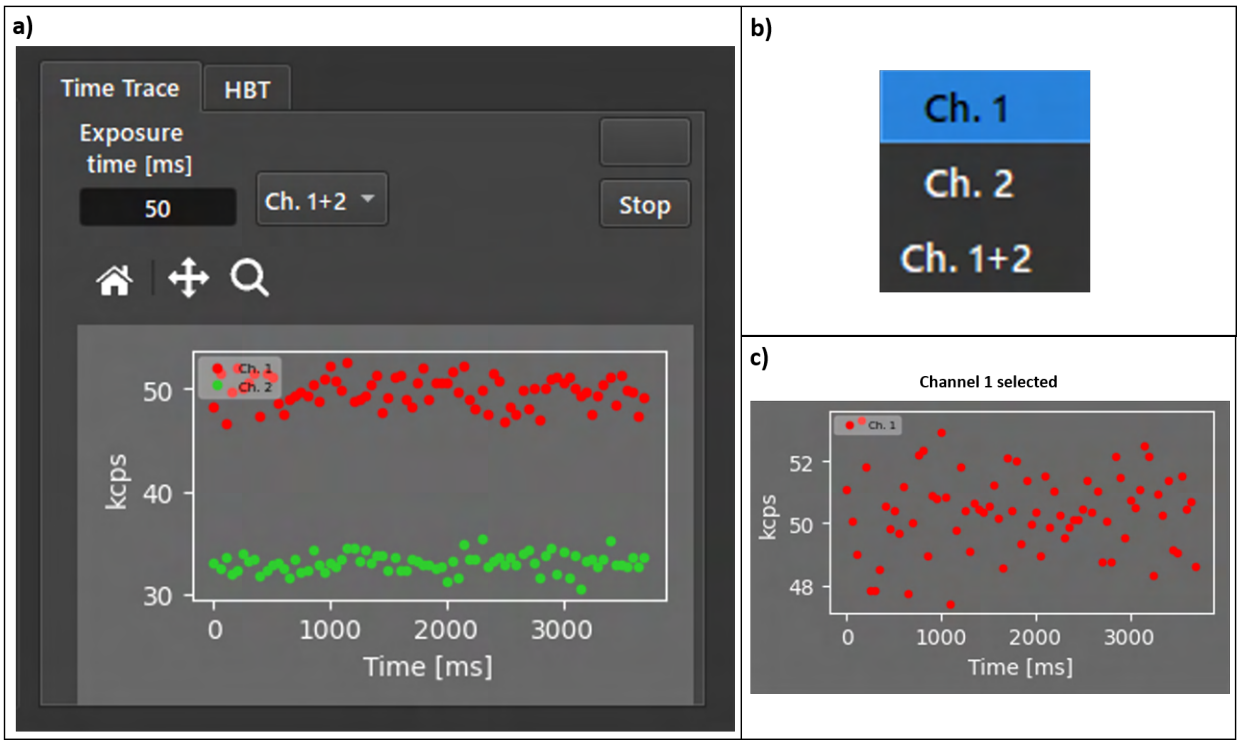

Figure H.12: Python based graphical user interface of the home-built confocal setup, in a) with a detailed view of the time trace panel. b) shows the drop down menu that appears if the channel selection is changed, c) output of the time trace graph with only channel 1 selected.

The "Scan" panel delivers the main functionality of the software: The readings from the SPAD detectors are accumulated for a set "Exposure time" at a certain stage position and the sample is raster scanned in order to create a scanned image of the sample (either delivering contrast by spatially varying reflectivity or photoluminescence emission). The user can choose the "Scan size", which refers to the edge length of the square scan, and the "Pixel size", which refers to the pitch between neighbouring measurement points in the raster scan. The software estimates the measurement time due to the selected amount of pixels times the exposure time in addition to typical delays due to communication and stage movement. The user can select to use the counts from one or both of the two ID120 SPAD detectors by changing the Channel in the drop down menu, as indicated above (Ch. 1, Ch. 2, Ch. 1+2). A scan is always executed symmetrically around the current stage position (marked (0,0) in the displayed scan map), meaning the stage will move so that the laser hits the top left of the image and start a raster scan from left to right and from top to bottom. Finally, the stage will return to the initial position at (0,0), and this origin is displayed above the displayed scan image in terms of global stage position. This allows the user to keep track of the relative positions of consecutive scans. The unit of the scale is 1000 detector counts per second, short kcps.

Furthermore, the user can choose in which plane the scan is to be executed, "xy", "xz" or "yz". A rotation ability of this sectioning ability is not implemented. If the user wants to execute a time consuming measurement under dark room conditions, he can tick "Delay scan" to gain 20 s in order to orderly leave the room before the measurement is executed. The "Log scale" box allows to switch between linear and logarithmic scale, while the lower bound of the displayed count rate values can be chosen with the drop-down menu below. The created map auto-updates every few rows in order to display the progress without slowing down the scan while the upper bound of the displayed count rate auto-updates to the

adhere highest measured value.

After or during a scan, the user can zoom into the scan using the looking glass on the top left of the scan map display. They can zoom to original view by pressing the home button (the little house) or zoom out by activating the zoom feature with the right mouse button. The arrow panel between these two buttons allow to move the scan content left to right and top to bottom.

A scan can be saved both as .png and .txt file, or both at the same time. The respective buttons open a windows explorer dialogue window to determine the file location, as depicted below in the case of the HBT measurement panel. The .png file always contains the current view of the data, while the .txt file always contains all data of the full array currently loaded.

If the user wants to accumulate a full 3D dataset, he can use the multi scan feature by selecting “Multi” instead of “Single” in the drop-down menu on the right hand side of the displayed scan image. This allows them to choose the amount of 2D scans they want to execute and the respective distance between these scans along the non-selected spatial axis (e.g. the z-axis if the “xy”-plane is selected). The multi scan will be performed symmetrically around the current stage position, meaning that if the “xy”-plane is selected, the stage will conduct a relative movement upwards first (“-Z”), then pass scan by scan through the initial position till reaching an equally distant position below the initial stage position (“+Z”).

Scans can be stopped any time during the measurement by pressing the “Stop Scan” button that appears below the “Start Scan” button once the measurement is executed. Similarly, a multi scan can be stopped with the “Stop multi” button that appears below the “Distance” editing field. After the multi scan is finished or aborted, the stage returns to the stage position that was held before the multi scan was executed.

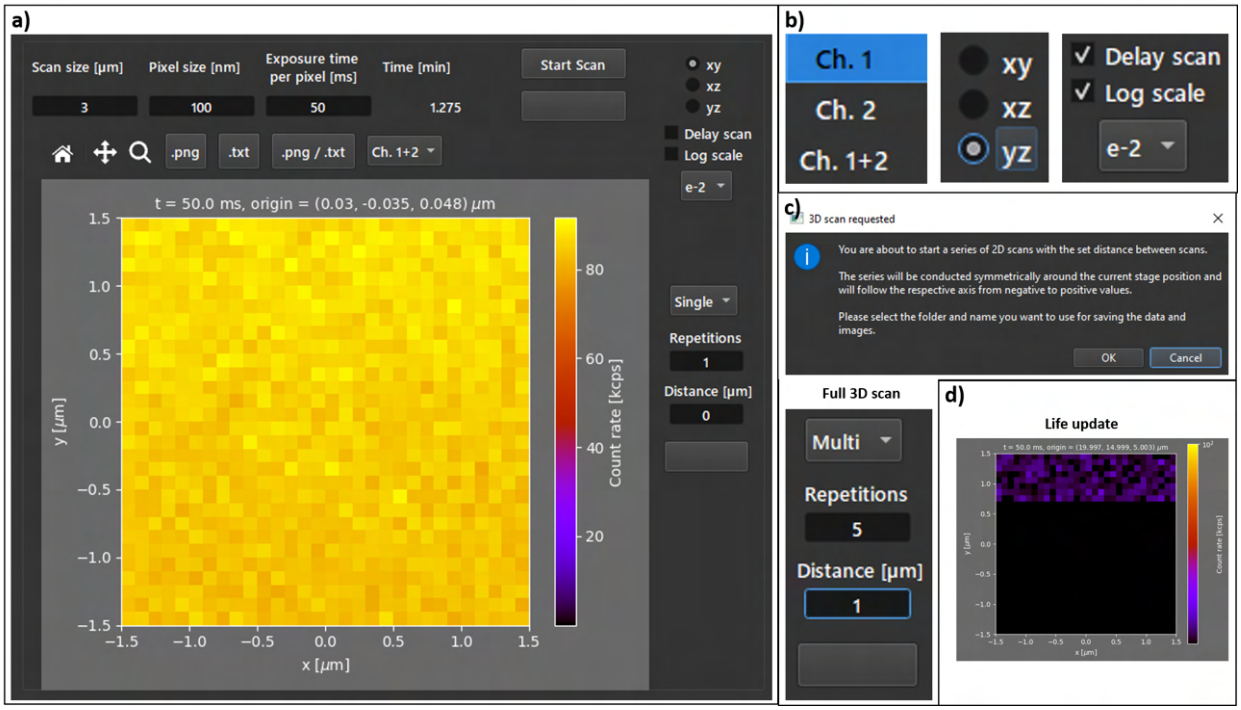

Figure H.13: Python based graphical user interface of the home-built confocal setup, in a) with the scan panel in more detail, b) close ups of the drop down menu for channel selection, plane selection and check boxes for delaying the measurement for 20 s or plotting the results in log scale, c) the message box that pops up if the user wants to perform a full 3D multi scan, in this example with 5 successive scans separated by 1 μm, d) illustration of the life update feature that is performed 4-5 times during the scan showing the so far accumulated measurement.

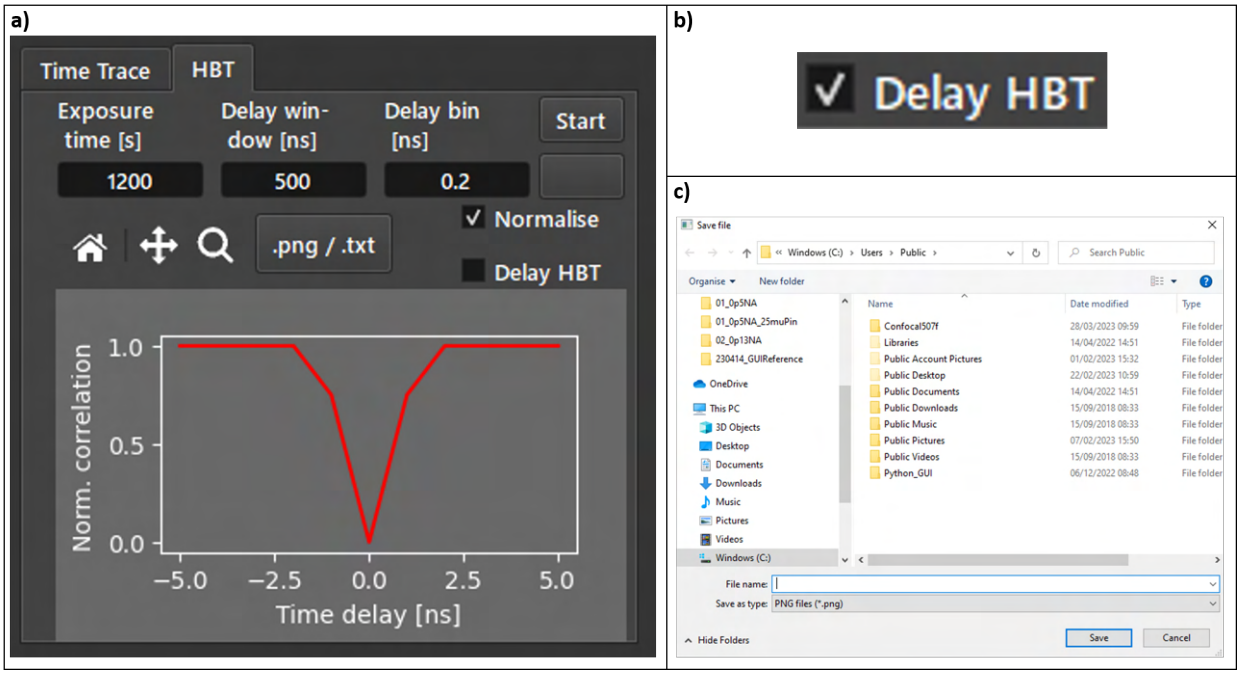

Figure H.14: Python based graphical user interface of the home-built confocal setup, showing the HBT panel for collection of the second order autocorrelation $g^2(\tau)$ in a fully automated way in a), b) showing the button stat allows to delay the start of the measurement by 20 s and c) the explorer window that opens if '.png/.txt' is pressed to save the data (the same window appears if the data is saved in the scan and the camera panel).

The "Time Trace" and "HBT" menu allow direct access to the TimeTagger functionalities within the Python GUI.

In the "Time Trace" tab, a timeline of the measured count rate is accumulated. The user can chose the exposure time and the displayed channels, very similar compared to the "Scan" panel. If the time trace was running the user needs to "Stop" and "Start" the time trace in order to update the exposure time.

The "HBT" panel allows to take a second order autocorrelation function of the incident light using both SPAD detectors simultaneously. It uses the intrinsic "Correlation" function of the TimeTagger, which can be used with and without normalisation. If not normalised, it forms a histogram containing the number of incidents with detector 1 clicking before or after detector 2 as function of the time delay between the events calculated between all recorded count events within the specified "Delay window". The normalisation takes the total amount of recorded events on both channels, the "Exposure time" (meaning the total measurement time to accumulate the histogram) and the "Delay bin" size (the discretisation of the time delay axis) into account, arriving at the second order autocorrelation function. This function is supposed to show vanishing values for zero time delay when considering single photon sources. It is recommended to tick the "Normalise" box, because the user will not be able to accurately normalise the data otherwise.

Similar to the "Scan" panel, the HBT data can be saved and the HBT scan be delayed by 20 s in order to allow the experimenter to leave the room in case a long "Exposure time" is chosen.

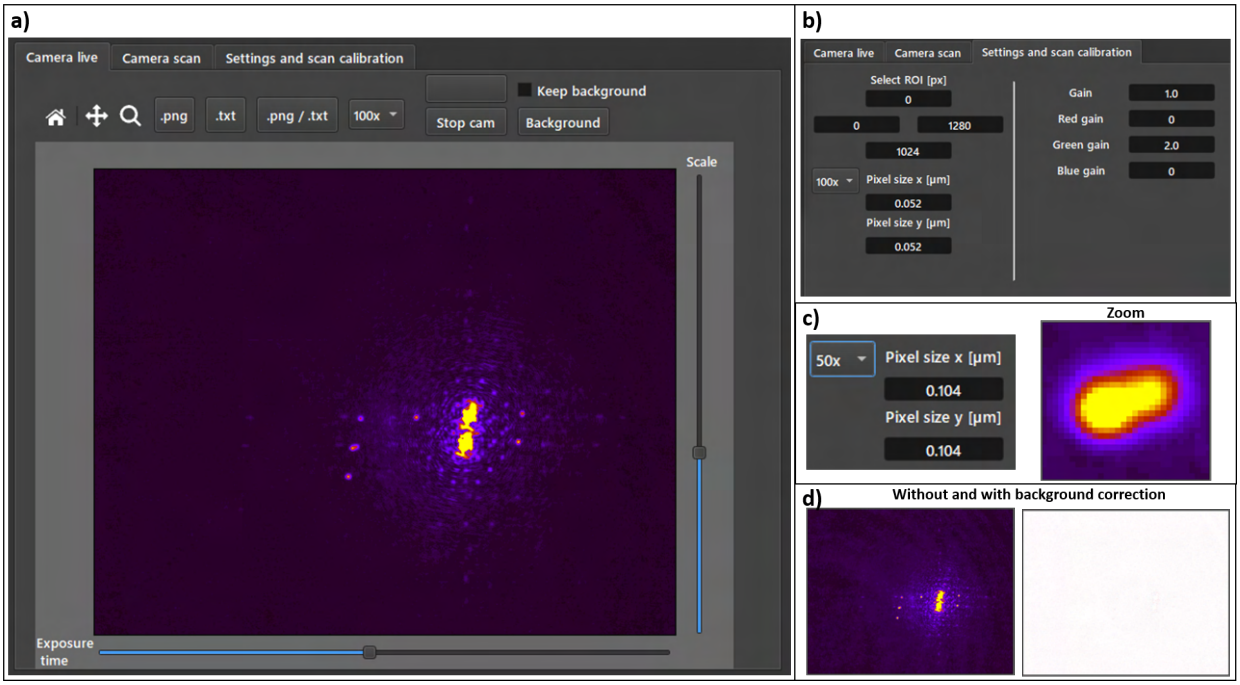

Figure H.15: Python based graphical user interface of the home-built confocal setup, with the camera live panel in a), b) shows the camera settings and pixel size calibration, with a change of magnification indicated in c) together with the zoom feature, that allows the user to magnify a part of the camera image, d) shows the effect of an applied background correction (which changes the color map and allows for positive and negative deviations from the background).

The camera panel in the bottom right of the GUI allows to interface the DCC1645-C Thorlabs camera currently used in the setup. The camera can be started using the “Start Cam” button in the “Camera live” tab and the CCD data is then displayed below. The upper bound of the plot scale can be varied between 0 and 255 with the “Scale” slider on the right hand side, while the exposure time of the camera can be varied below within reasonable limits. The colour camera is operated in grayscale mode. Similar to the functionality of the “Scan” and “HBT” panels, the user can zoom into the displayed image and save them as .png/.txt file, where the .png contains the currently selected view on the data and the .txt file the full data array. A drop-down menu allows to select different types of objectives, 100x, 60x and 50x, which all have been used and tested with the setup. This is mainly important if the user wants to use the “click and move” feature, which allows to load the position of an object in the camera image into the stage target position of the “Stage control absolute” panel. This requires that the projected pixel size of the CCD in the sample plane is calibrated with the magnification of the optical system. The DCC1645-C camera has a square pixel size of 3.6 µm, which is demagnified by 70x in the sample plane if the microscope is set up with the 100x objective and a 125 mm imaging lens. For each objective, the pixel size is already preconfigured, but can be changed by the user for fine adjustments in the “Settings and scan calibration tab”. Here the user can also select the region of interest of the CCD sensor, which requires to restart the camera in the “Camera live” tab to have any effect. Similar, gain settings of the sensor can be modified, and are set to high green gain by default to avoid chromatic aberration between the laser and green filtered illumination light (the white light source is reflected by the dichroic).
A background correction allows to remove permanent features or reduce the effects of inhomogeneous illumination. After pressing the “Background” button in the “Camera live tab”, the current view is taken as background, the colour map is changed to white (0), red (+) and blue (-) for positive and negative

deviations from the background. If the background is to be kept after restarting the camera (a restart automatically happens when an HBT measurement or confocal scan is executed), the user has to tick "Keep background".
The "Camera scan" tab contains controls to quickly map the sample surface with white light illumination by stitching together camera images. The software calculates the field of view based on the selected region of interest and calibrated pixel size of the camera, which are displayed as "Steps x" and "Steps y". The user can choose the number of images that are stitched in x and y with "nx" and "ny", and the software displays the total size of the covered area as "Size x" and "Size y". Based on the image acquisition time and stage movement delays an approximate scan time is displayed as "Time". If the user wants to apply the background taken with the "Camera live" tab, he has to select "Apply background". The "click and move" feature also works in the displayed camera scan, allowing the user to quickly navigate the full sample (he still needs to press "Go" after the target position is changed in the "Stage control absolute" panel). Two examples of stitched images without and with background correction are shown on the right hand side of the following image.

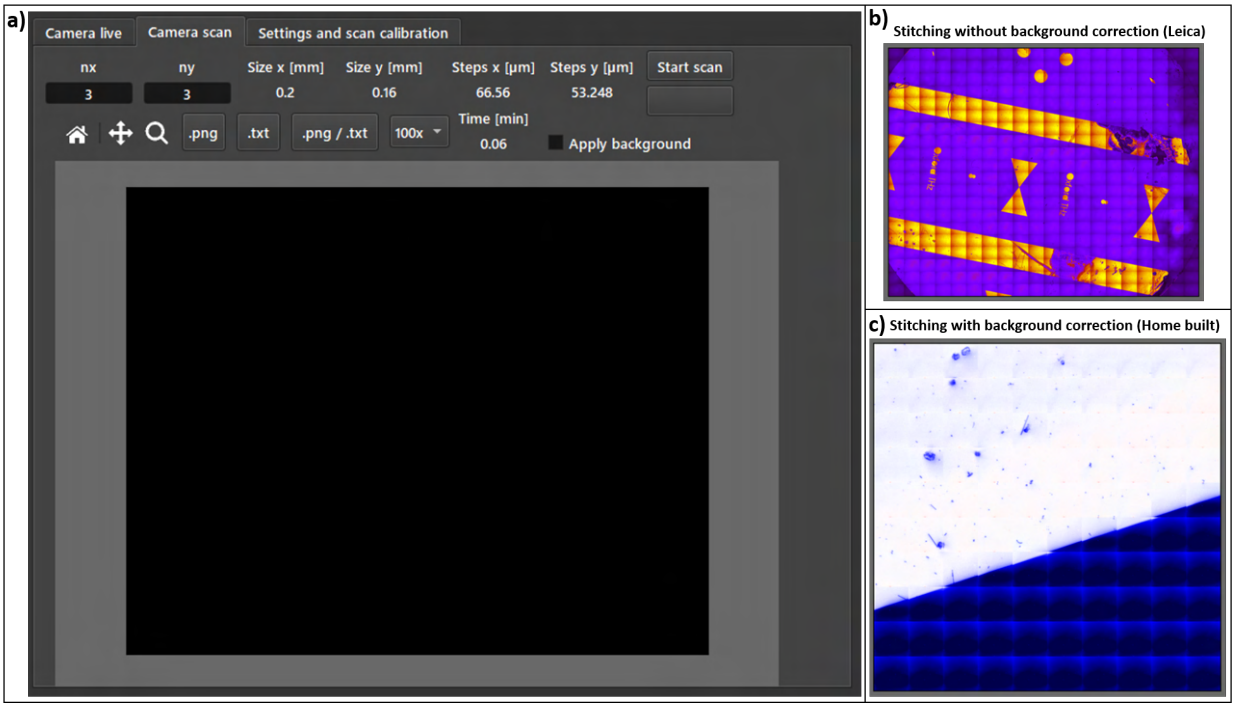

Figure H.16: Python based graphical user interface of the home-built confocal setup, a) showing the panel for stitching camera images together, forming a macro view of the sample. b) and c) show examples of stitched images at low and large magnification, both taken on a round quartz substrate with gold pattern. The edge of the round substrate with 15 mm diameter is clearly visible in b). This feature can be used to quickly scan the sample in search for localized devices, the 'click and extract position' feature is implemented here as well, allowing for quick navigation in the enlarged field of view.

H.6 SPAD calibration and alignment

The **SPAD detectors** can be individually interface with the "ID120" labview software provided by the manufacturers. Only one SPAD can be addressed by the software at the same time, so the USB of the other SPAD needs to be disconnected / unplugged. The user can adjust the bias across the active area in V, the target cooling temperature of the Peltier element in °C, and the threshold voltage that

distinguishes counts from noise in V.
Typical settings are:

- SPAD1: 210 V bias, -45 °C, 0.1 V threshold (ca. 100 cps dark counts) - 1518924M110
- SPAD2: 200 V bias, -45 °C, 0.1 V threshold (ca. 500 cps dark counts) - 1651018M110

The low cooling temperature is close to the limit of -50°C to reduce dark counts, while the bias lays around 30-40 V above the breakdown voltage of the respective detector, resulting in a compromise of reasonable quantum efficiency and use of the full dynamic range of up to 1000 kcps, while keeping away from an over biased regime in which the after pulsing probability might rise. The dead time is specified to 1μs, but measured to be $\approx$ 400 ns (datasheet provided by manufacturer) – still any measured count rate above 1000 kcps might be due to after pulsing effects.
It is important to keep in mind that these detectors are highly non-linear due to saturation behaviour at increased photon flux. If a power series is to be taken, the user first needs to carefully assess how the detector reacts to linear increases in laser power to calibrate the measured count rates with respect to each other. Example measurements of the SPAD saturation behaviour at different detector bias is given in Fig. H.17. We show a potential method to calibrate the detector response in Fig. H.18 which is applied to the most data shown in this thesis. It is valid till a measured count rate of around 300 kcps, leading to up to a predicted count rate of 1000 kcps.

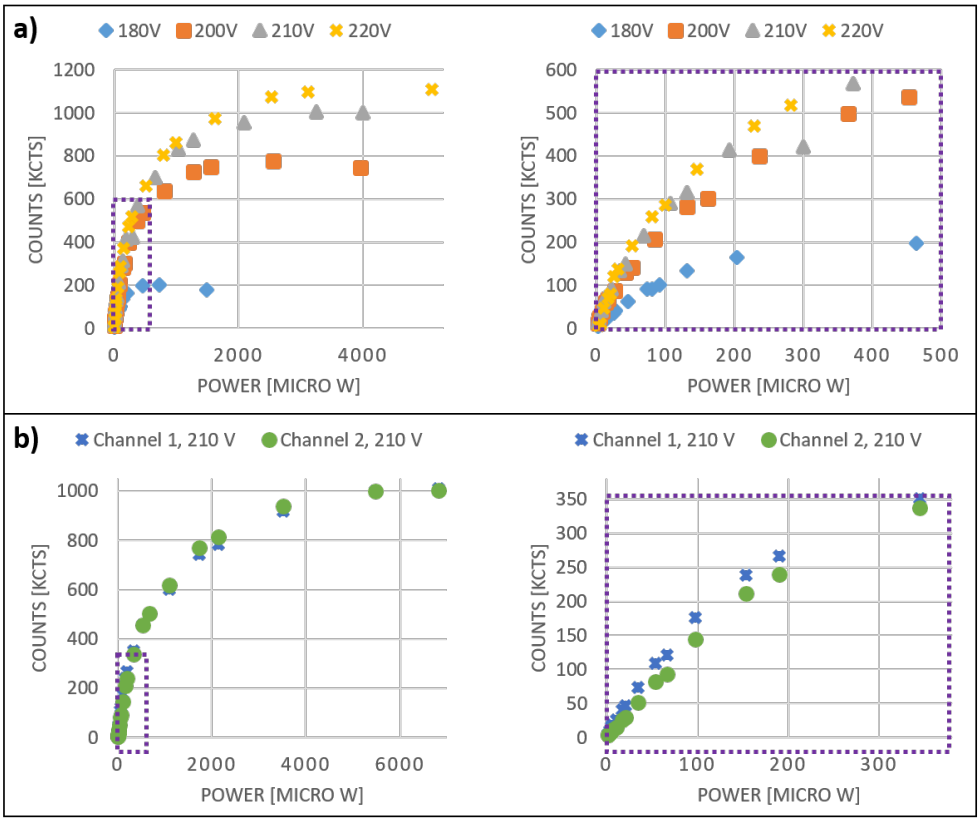

Figure H.17: SPAD detector performance under varying laser power and a simple reflection from gold, collected here with a 105 μm fibre core and the 25 μm pinhole (explaining the low sensitivity). a) response curves of channel 1 (the SPAD in a straight line behind the pinhole in the free space configuration) at constant $T = -45\,°C$ and varying bias voltage probed by linearly rising laser power, b) response curves of channel 1 ($T = -45\,°C$) and channel 2 $T = -40\,°C$ (warning: the SPAD originally used as channel 2 has been exchanged because of high dark count rates on the order of 5000 Hz), showing reasonably balanced detector response when using a 50:50 fibre beam splitter. If not otherwise stated all other shown data in this thesis corresponds to free space SPAD coupling as shown in Fig H.3.

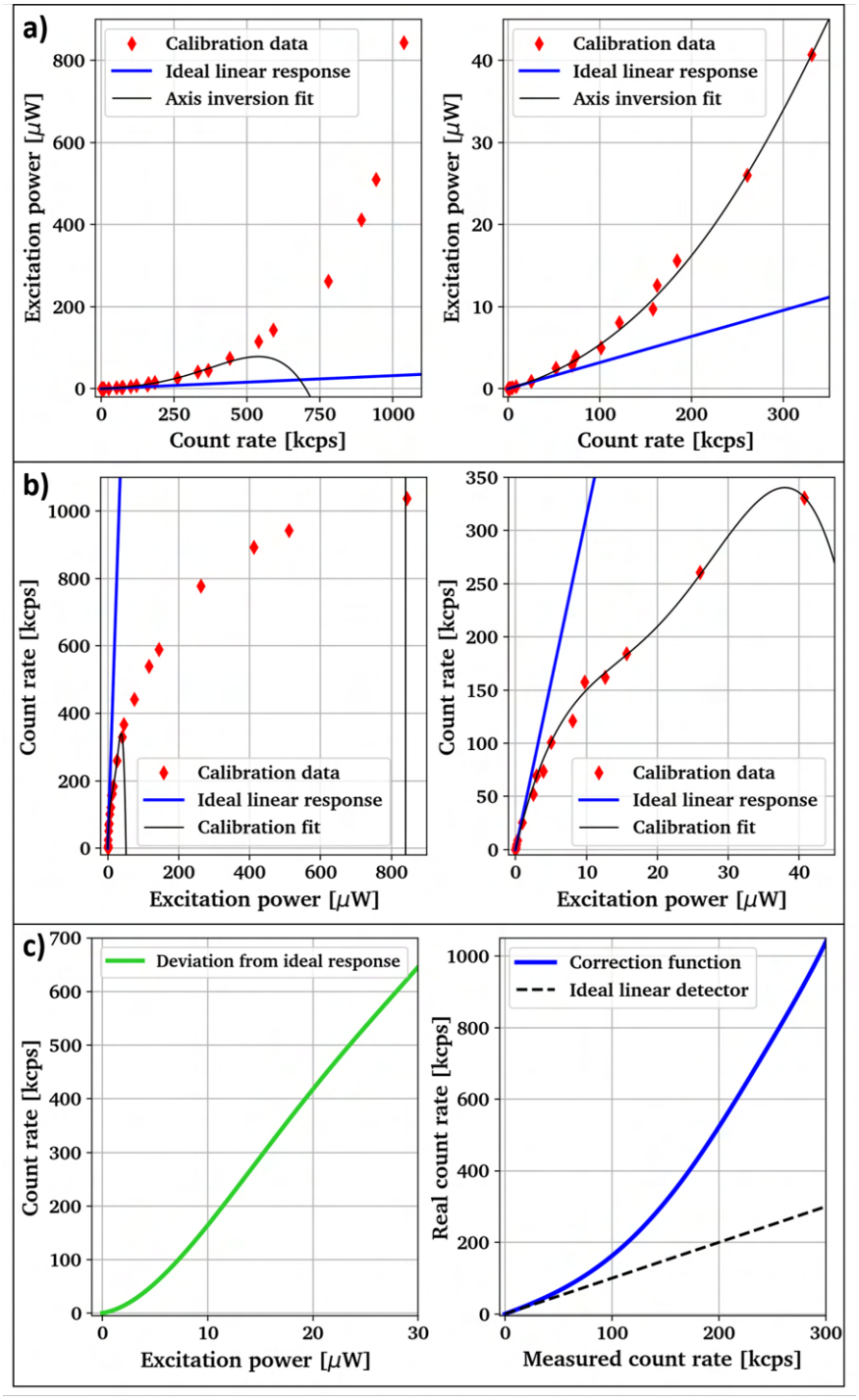

Figure H.18: Method applied to linearise the detector response for channel 1 with cooling temperature $T = -45\,°C$ and 210 V detector bias. The right hand side images in a) and b) show a zoom into the data on the left hand side respectively. In a) a 5th order polynom is fitted to the inverted detector response to receive a model for the excitation power as function of count rate, while the axis are turned around in b), repeating the fitting procedure. In both cases the ideal linear detector response is modelled by a linear fit of the first 5 data points, resulting in c) a plot of successively rising deviation from the ideal linear detector response with rising excitation power. The fits applied in a) and b) are roughly valid up to 300 kcps measured count rate. Therefore we can back-calculate the 'real photon influx' based on the measured count rate by combining 11 fit parameters for the inversion function. The result is depicted in c) on the right hand side with the black dotted line indicating the ideal linear response.

Alignment

We now quickly discuss the alignment of the microscope system. The part of the setup before the detection path is considered to be aligned if

- the input laser beam is collimated and well aligned to the cage system
- The camera position is adjusted so that the laser focus in the camera matches a sharp image of the sample surface features under white light illumination (filtered green by the dichroic and green gain settings of the camera)

This simply means that the laser is actually focused in the plane of the substrate surface. And that the resulting reflected laser light from the sample is similarly collimated if the laser is focused on the substrate. The latter should automatically be the case if the two conditions given above are met.

Laser collimation, alignment and camera adjustment

The laser can be simply collimated by observing the output of the 20x objective over a large distance on a measurement card and adjusting the z-position of the objective if necessary. Then the user can align to the cage system using alignment targets. Afterwards the cage mirrors can be used to guide the beam in the centre of the cage. The laser beam seems to suffer from astigmatism, either due to 20x collimation objective, the dichroic mirror or the imaging lens – but it does not seem to disturb the systems performance. Initially, laser focus and a sharp image of the sample surface might not overlap, which indicates that the camera position along the optical path needs to be adjusted or the 20x coupling objective needs adjustment. This will not usually be the case if the system is aligned already, but might become necessary if a new imaging lens is mounted or the camera is exchanged.

The user can then iteratively change the camera position and refocus the laser, till both focus and image plane overlap within the tolerance given by the depth of focus. The user can then again adjust the laser position in the camera with the upper periscope mirror to minimize beam walk when moving the stage along the z-axis. If under these conditions, the reflected laser beam leaking through the dichroic mirror (the user will need to increase laser power to several 100 μW to see this) is focusing or defocusing even though the laser is focused on the image of the sample on the CCD, a slight z-adjustment of the 20x collimation objective becomes necessary.

A 20x objective z-movement might cause the laser to slightly change direction, which makes realignment to the cage system with the two stirring mirrors of the laser in front of the flip-mirror necessary. The user then needs to adjust the camera position again to overlap the sharp sample image under broadband illumination with the laser focus and recheck the collimation of the reflected leaser light in the detection path using a sample with small distinct features that are visible in the widefield microscope image.

Alignment of the detection path

Aligning Pinhole and SPAD detectors: The detection path is built in such a way that the cage-based filter section is on the same hole pattern and height as the cage system containing the SPADs and the beam splitter plate. To check or improve this alignment the user can remove the pinhole from the optical path and connect both cage systems with long cage rods. The height of the pinhole housing needs careful manual alignment, while a 1D translation stage allows to move the pinhole laterally in the beam path. The optimal lateral position of the pinhole lens seems to be if the pinhole lens is pushed further left than the centre position in its housing (controlled with the Allen key). The user can check the pinhole

housing alignment by aligning the reflected beam of the focused laser on a flat substrate to the filter section, optimizing the transmission through a pinhole $< 50\,\mu$m diameter and then checking whether the beam hits the cage system of the SPAD detectors in the centre.

The user might need to iteratively adjust the pinhole housing position (height and lateral position) and then optimize the pinhole lens and pinhole wheel position to find the ideal alignment. To optimize focusing the beam on the active area of the SPADs (ca. 500 μm diameter), the user can manipulate the xy position of the cage-mounted 25 mm lenses, which adds significant tolerance to misalignment of the pinhole housing.

This optimization should be conducted if the rest of the setup is aligned to satisfaction, using the reflected collimated laser beam focused on a flat substrate. Example data after full system alignment from a sample that has some distinct structures around a flat area is shown in Fig. H.19. The features help to map the laser focus to the sample plane by comparing it to the broadband illumination from the filtered tungsten lamp.

For optimal HBT measurements, the SPAD detectors can be deliberately misaligned in an asymmetric way along the optical axis, for example: Push lens 1 only slightly too far away from SPAD1 and push lens 2 too close to SPAD2. This overfills both detectors, but maintains reasonable quantum efficiency on SPAD1, while SPAD2 loses more potential counts.

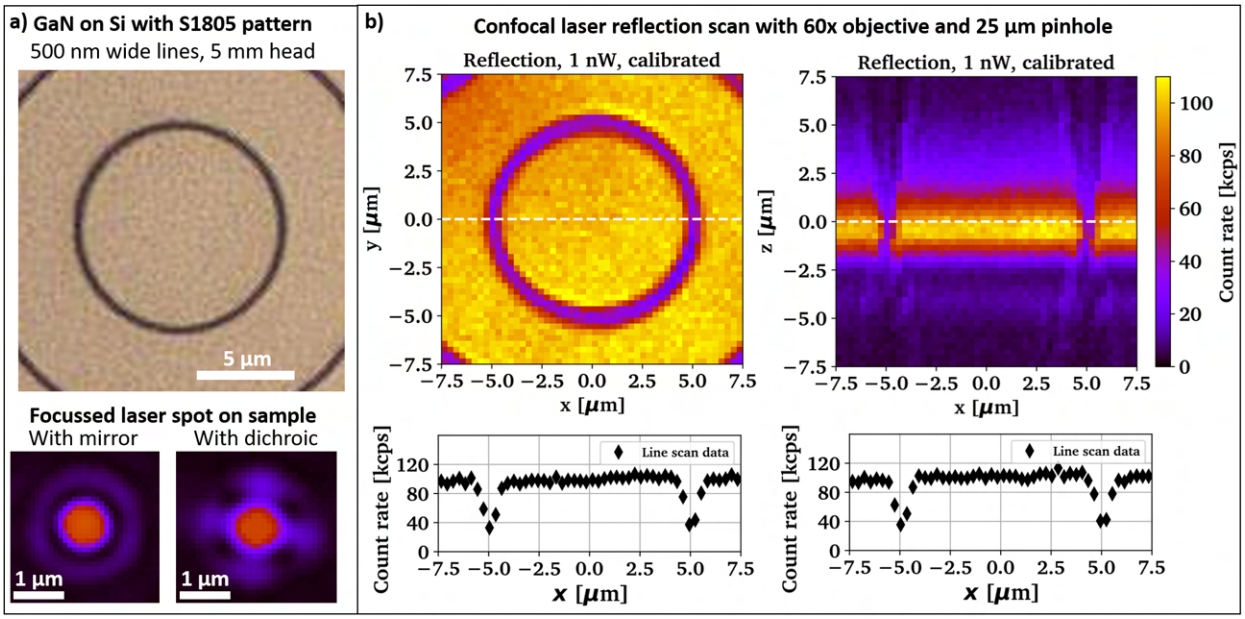

Figure H.19: Alignment of camera and focus plane after laser beam collimation by adjusting the camera position along the optical column. a) A GaN-on-Si substrate (4 μm epilayer) is patterned with a sharp S1805 resist pattern with 500 nm linewidth and used as a target for focusing. We experienced some issues with strain in the dichroic beamsplitter plate, which was replaced by a thicker version later on. Still, the dichroic seems to introduce astigmatism into the focus, here significantly distorting the shape of the focused laser beam (bottom images), b) result of aligning the laser focus (beam collimated before objective) to a sharp image of the sample plane, here using a 60x objective with NA=0.85, which was later replaced by the 100x standard objective. Shown are calibrated xy (left) and xz (right) scans with the white dotted lines indicating the shared plane between both scans, confirming the operation of the microscope as a confocal laser scanning system (no additional filters applied, the laser leaks through the dichroic mirror). The shown line scans equally follow the white dotted lines. The count rate calibration described above was applied to the maps, enhancing the contrast.

H.7 Analysis of system performance

We characterize the measured laser spot in Fig. H.20 and find that we significantly underfil all used objective lenses with the chosen beam diameter. The diffraction limited spot size expected at $\lambda = 517\,\text{nm}$ is FWHM = 280, 530 and 880 nm for an NA of 0.95, 0.5 and 0.3 respectively, employing equation H.1. The z-sectioning ability of the setup is demonstrated by measured laser reflection scans in Fig. H.21. In terms of axial resolution we expect from Eq. (H.4) FWHM = $0.8, 1.1, 1.3, 1.6, 2.5$ and $4.9\,\mu$m at $\lambda = 517\,\text{nm}$ wavelength with the measured data outperforming the predictions.
In Fig. H.22 we show an example PL measurement on a bright self-assembled CdSe sphere consisting of nano platelets, confirming proper operation of the tool.

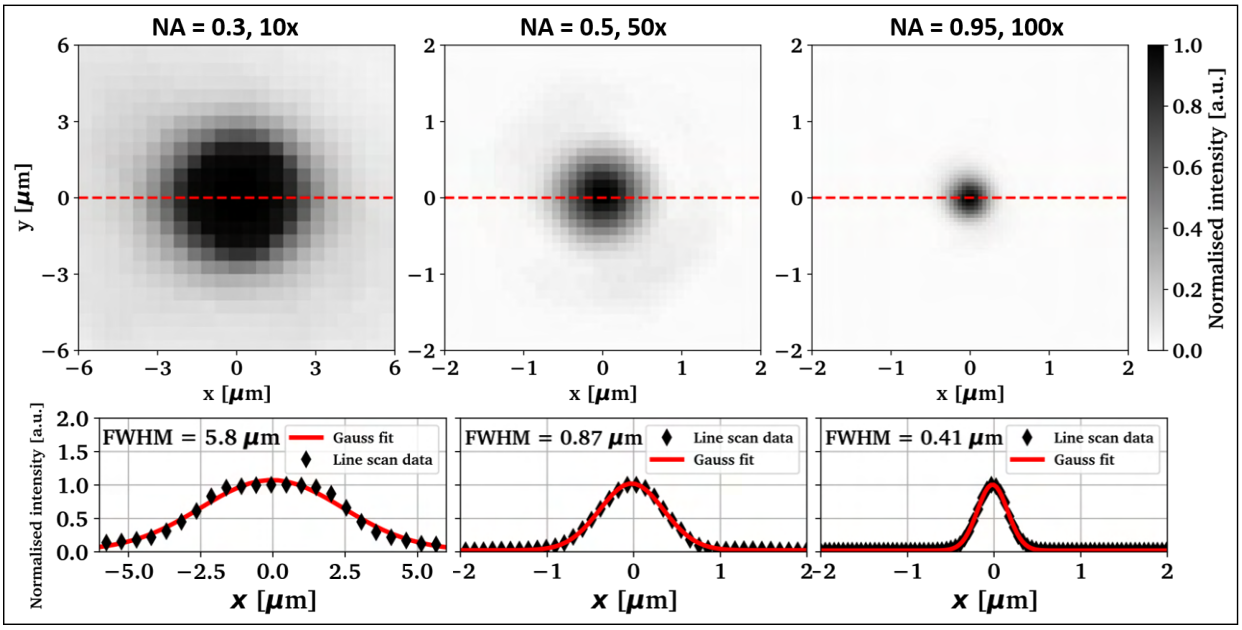

Figure H.20: Measured laser spot size in the sample plane projected onto the CCD camera in dependence on the objective lens used. Measurements were performed on the same day with the beam diameter optimized for the 100x objective. The 10x objective is heavily underfilled, leading to an unusually large spot size compared what could be expected at this NA. Line scans are taken along the red dotted lines in the xy maps above. The pixel size is calculated from the nominal magnification using $f = 125\,\text{mm}$ for the tube lens and the given CCD pixel size from the camera data sheet.

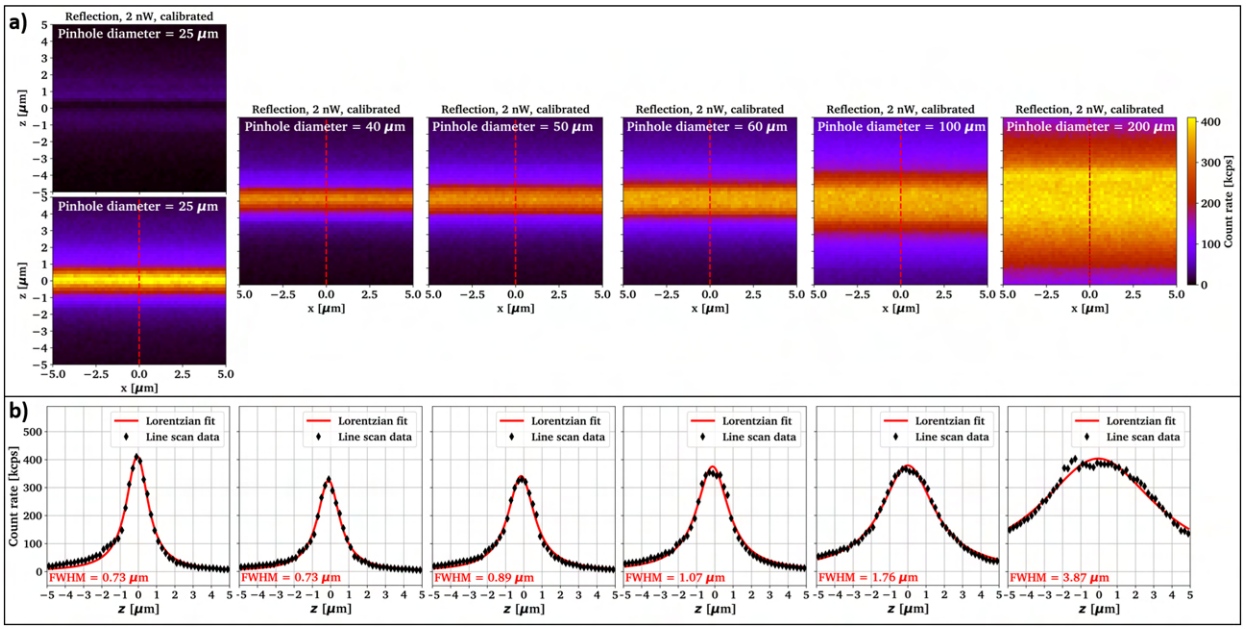

Figure H.21: Measurement of the z-sectioning ability of the confocal microscope using the 100x objective with NA=0.95 and varying pinhole sizes from the automated pinhole wheel with all other settings are held constant (including laser power). a) xz laser reflection scans from a gold film on quartz, not normalized, but linearised with the measured detector response function. Variations in maximum power are most likely to due incomplete realignment of the detection path when changing the pinhole size, seeming optimally adjusted for the standard 25 μm pinhole. The top left image corresponds to a map obtained with a different filter wheel section in the beam path, destroying the alignment. b) Corresponding line scan data from the red dotted lines in a), fitted with a Lorentzian lineshape function.

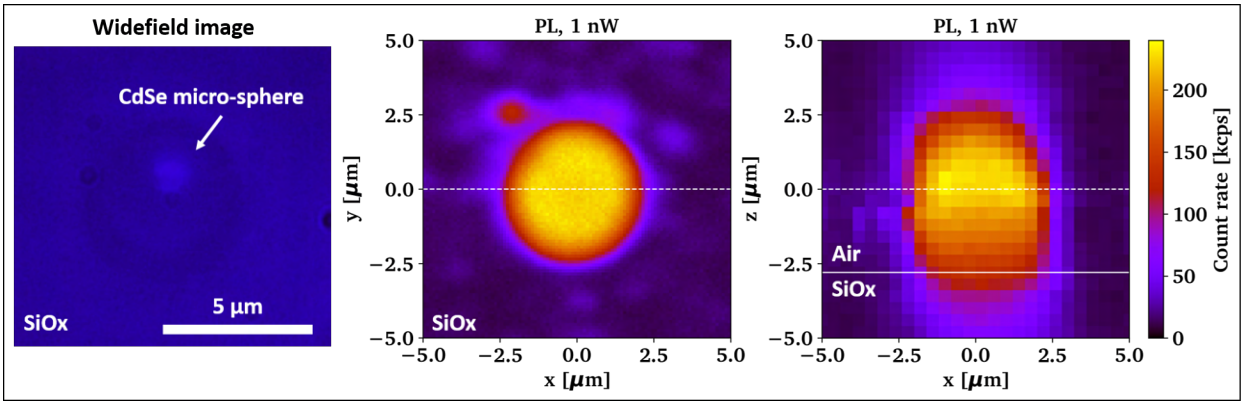

Figure H.22: Example for a photoluminescence measurement with the 100x objective and 100 μm pinhole and both SPAD detectors used simultaneously. The two PL maps are taken with all three long pass filters inserted into the beam path. The sample consisted of CdSe microspheres assembled from nanoplatelets and dropcasted on a microscope slide. These show bright red photoluminescence emission under very dim green laser excitation. The white dotted lines indicate the shared plane between both scans, showing the 3D resolution of the confocal PL setup. 2x 550LP, 1x 650 LP filters are used for the PL maps. No count rate calibration is applied.

H.8 Example projects using the developed confocal microscope setup

In order to motivate the development of the tool further we present preliminary results from three different potential nanophotonics projects.

H.8.1 Preselection of nanowire lasers on growth substrate for integration via transferprinting

Initiated by Dimitars Jevtics, we present measurement results on InP nanowires on their growth substrate. The wires are similar to the ones used in Chapter 5 and show length and quality deviations. The geometry is illustrated in Fig. H.23.

We compare reflection and photoluminescence images taken on the top facets of the upright standing nanowires and find significant differences between the two, as illustrated by the plots in Fig. H.24 to H.26. We can resolve single nanowires, most probably due to efficient waveguiding into the wire mixing reflections from the top facet and bottom impedance mismatch.

More detailed analysis and modelling of such data might provide insight on how to preselect the best nanowires for transfer print integration. The reflection scans are expected to deliver information about the top facet quality as well as the nanowire height. Due to the density of the wires on the growth substrate we can expect that short wires are shielded by the surrounding wires which would need to be taken into account. Wider spaced wires might be used instead. The photoluminescence emission might additionally contain information about the crystalline and surface quality of the wires.

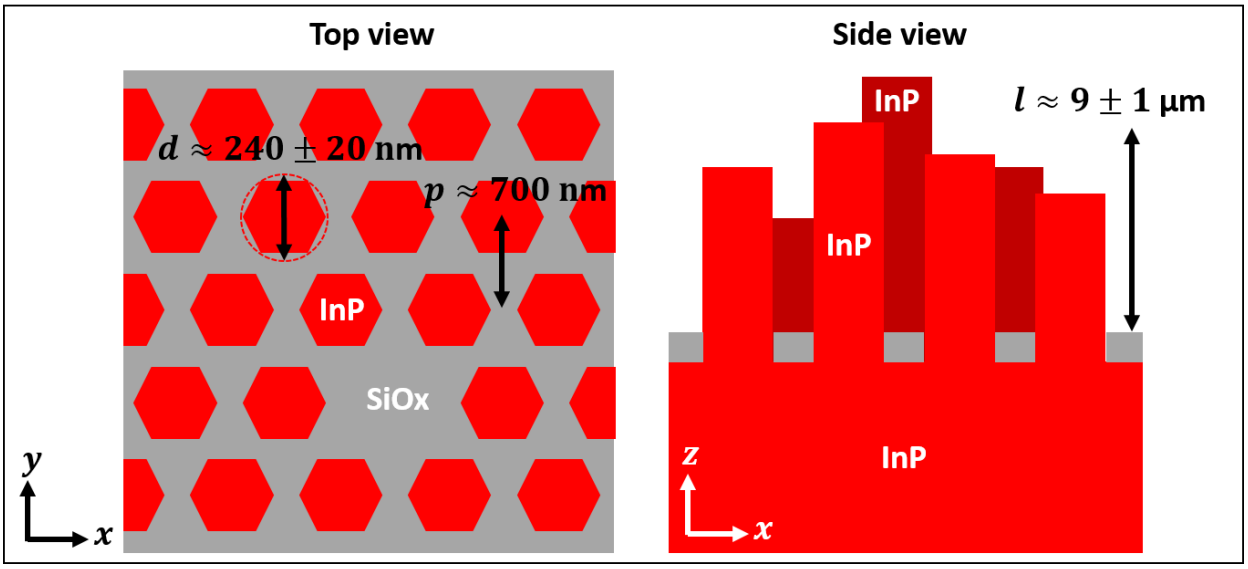

Figure H.23: Schematics showing a) a top view and b) a side view of InP nanowires grown from a patterned InP substrate (SiO_x mask) with nanowire growth sites arranged hexagonally. Not every site necessarily contains a successfully grown nanowire with height variations only being one of many potential differences between individual devices.

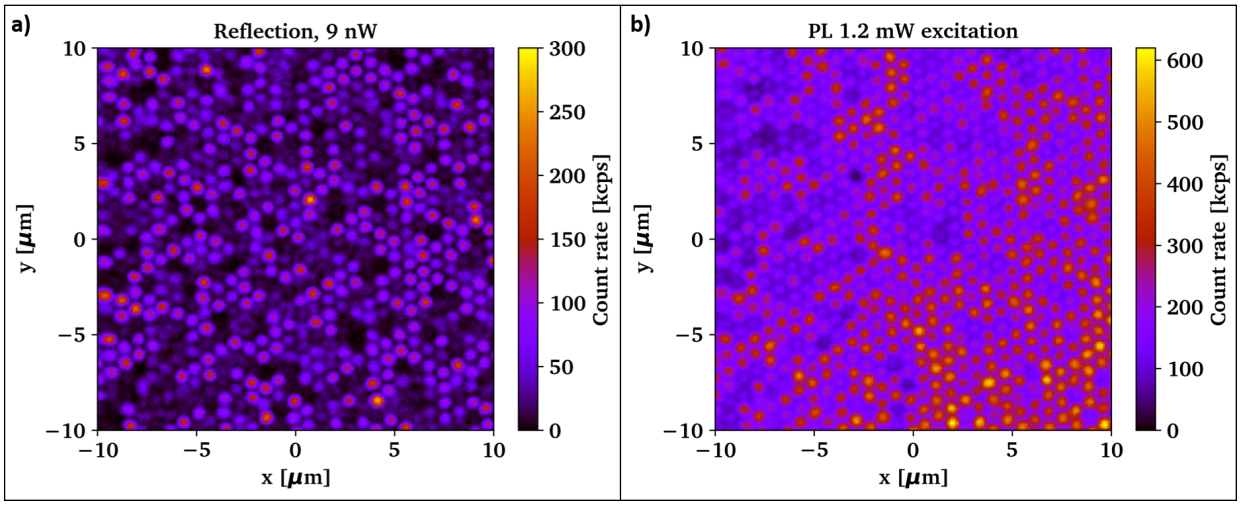

Figure H.24: a) Reflection and b) photoluminescence map taken near the top facets of InP nanowires on their growth substrate at the same xyz position. While the refleciton image seems reasonably homogeneous, a clear trend towards potentially more emissive devices can be seen in b). The 100x objective is used with 40 μm pinhole. 2x 550LP, 1x 650 LP filters are used for the PL maps.

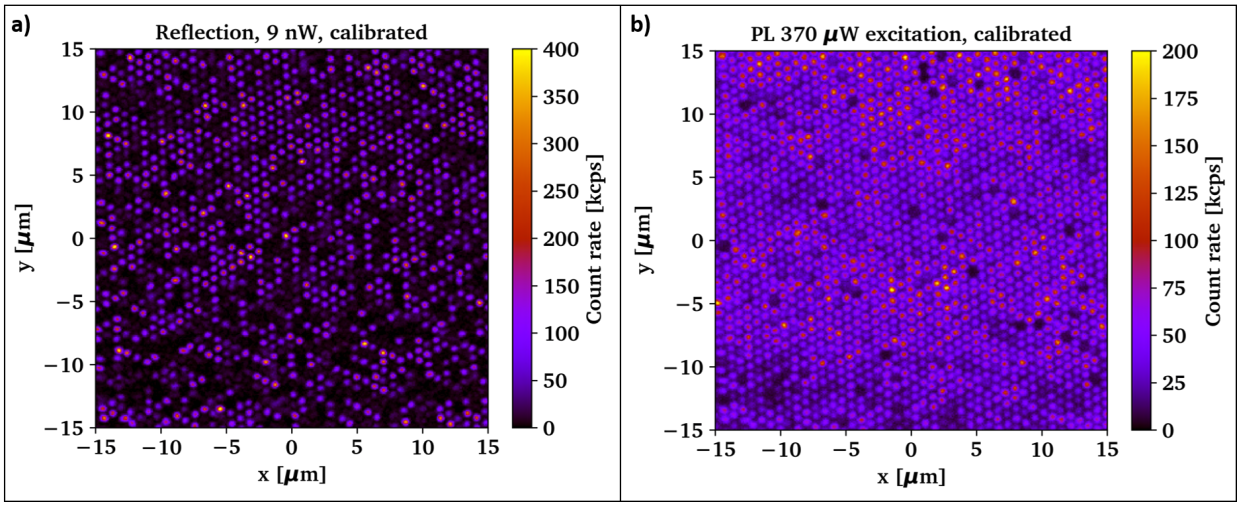

Figure H.25: a) Reflection and b) photoluminescence map taken near the top facets of InP nanowires on their growth substrate at the same xyz position. Again both images dont seem to correlate well, with the PL map revealing bands of brighter and darker devices. The 100x objective is used with 25 μm pinhole for best possible resolution and the data is linearised with the measured detector response function. 2x 550LP, 1x 650 LP filters are used for the PL maps.

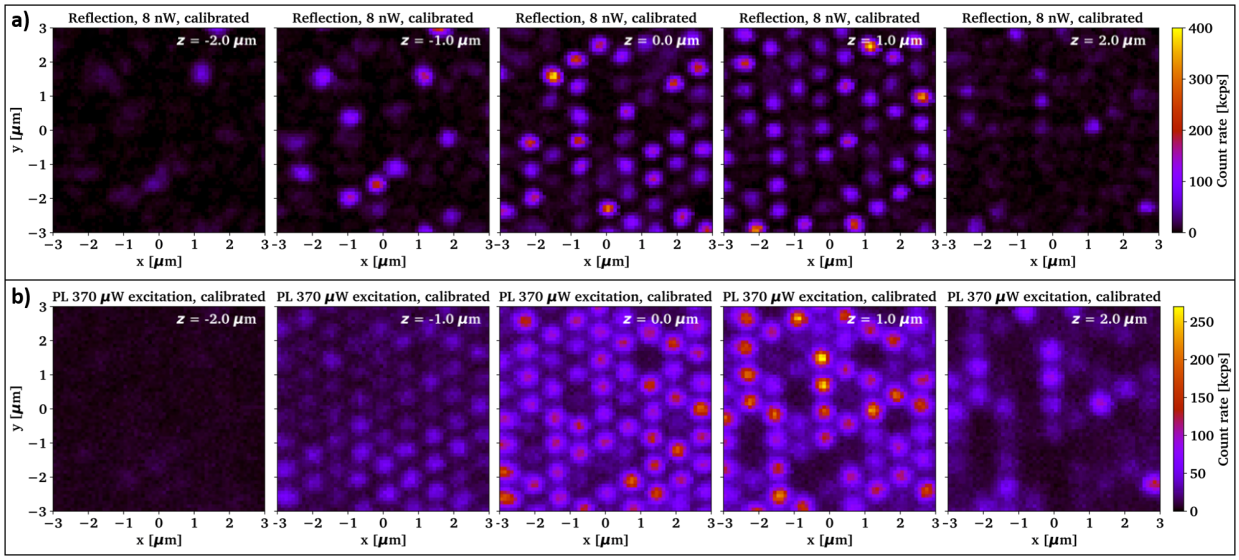

Figure H.26: Depth scans in both a) reflection and b) photoluminescence mode, targeting the InP nanowire top facets on their growth substrate taken at the same xy position. The 100x objective is used with 25 μm pinhole for best possible resolution and the data is linearised with the measured detector response function. 2x 550LP, 1x 650 LP filters are used for the PL maps.

H.8.2 Hybrid integration of suspended diamond structures with integrated photonic circuits

In collaboration between the Fraunhofer IAF in Freiburg (Christian Giese and Quankui Yang are the lead scientists [138, 374]) and Fraunhofer CAP in Glasgow we investigate the potential to integrate high-quality NV centre hosted in suspended single crystalline diamond with dielectric waveguides for light delivery. Here we use SU8 polymer waveguides for initial testing.

Fig. H.27 shows the Faraday cage etching capabilities provided by Christian Giese at IAF, which allows to suspend SC diamond waveguides with triangular cross section. Using angled nitrogen implantation NV clusters are implemented into the waveguide tip and we are able to map these emitters with our home-built confocal microscope as shown in Fig. H.28. More advanced photonic waveguide structures like a tapered waveguide with integrated Bragg mirror and suspended ring resonators are shown in c) for future device tests.

Fig. H.29 and H.30 contain initial simulation and printing results which demonstrate that we are able to manipulate these systems effectively by transfer printing. Polymer waveguides like SU8 exhibit way to much auto-fluorescent emission to carry single photon emitters and future project work might be directed at integration with low-loss SiN waveguides or similar semiconductor platforms. The confocal microscope setup can inform the transfer print integration by mapping the most suitable devices beforehand.

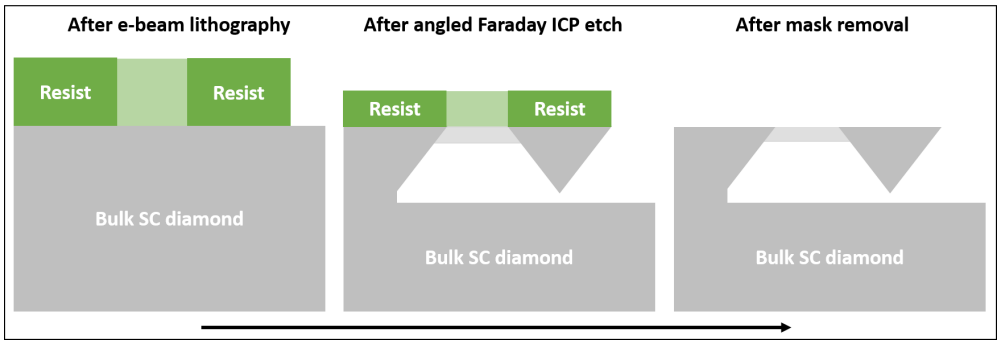

Figure H.27: Schematic of the angled diamond processing done at Fraunhofer IAF by Christian Giese using ICP-RIE plasma etching with angled Faraday cages to guide the ions of the plasma to undercut devices from bulk. The transparent regions show narrow parts of the pattern (when viewed from the top) that are easily suspended and work as tethers or anchors to prevent collapsing of the diamond device structures.

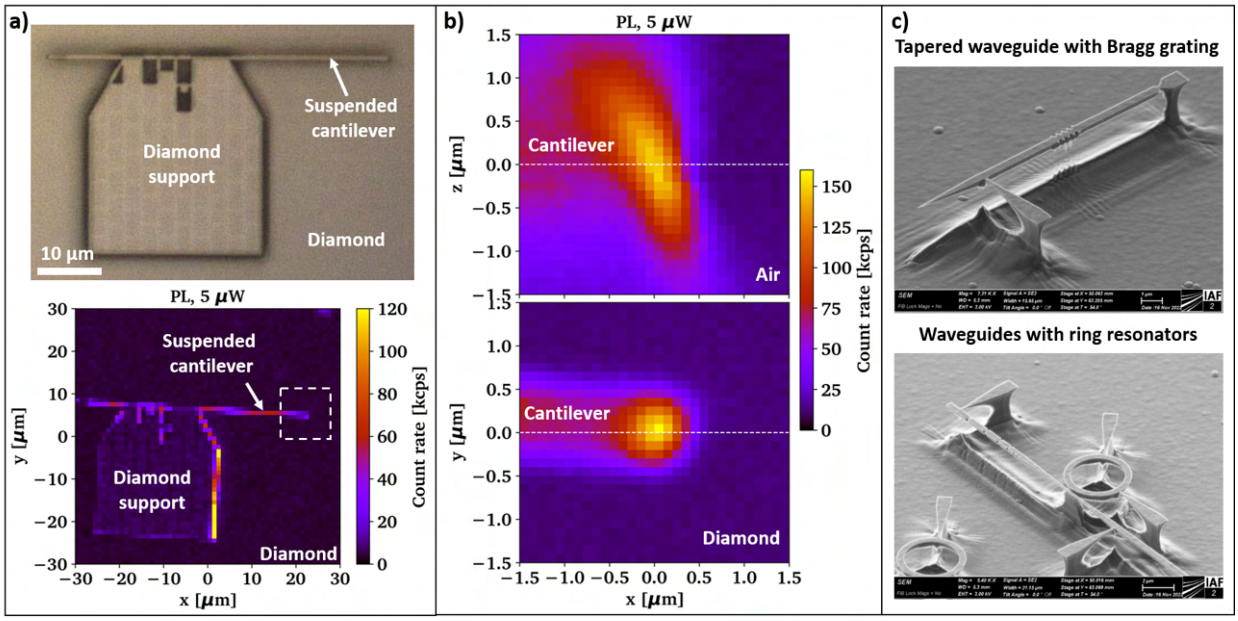

Figure H.28: Overview of some diamond devices containing nitrogen vacancy centres produced by IAF for transfer printing tests and photonic integration at FCAP. a) Microscope image and confocal PL map (100x, 100 μm pinhole, 2x 550LP, 1x 650 LP) of two similar suspended diamond cantilevers, which were irradiated with nitrogen under an angle for targeted nitrogen vacancy generation at the right tip of the cantilever device, b) zoom into the large scale PL map at the bottom of a), showing localised red emission from the cantilever tip in 3D, most likely corresponding to clusters of NV centres. c) SEM images of more advanced photonic devices etched at IAF.

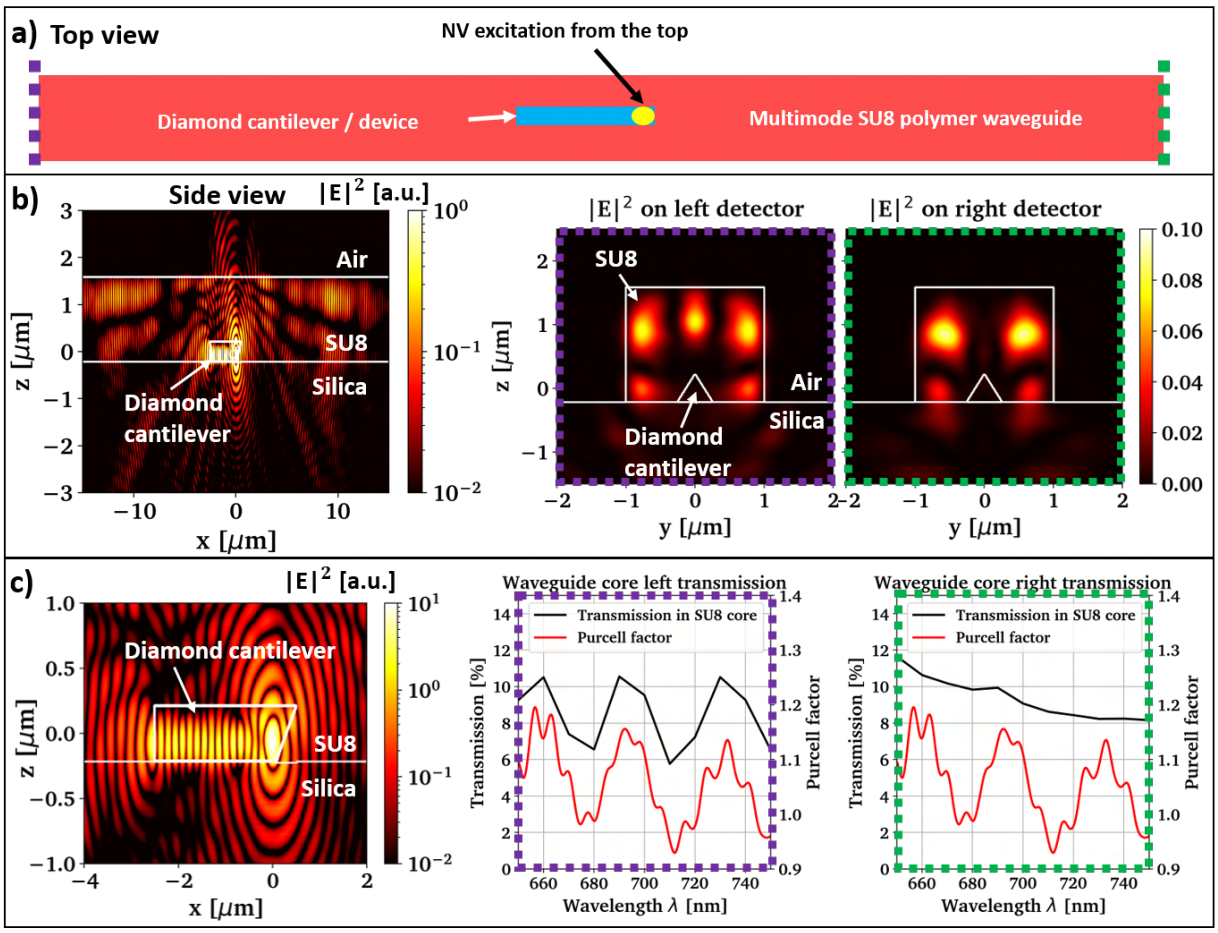

Figure H.29: Simulations of an initial test geometry. Bright diamond devices could be coupled to SU8 polymer waveguides to investigate the potential sensitivity of the confocal microscope setup when adding an edge detection module to gather light from waveguide facets with single photon sensitivity. a) Simple device layeout with the diamond cantilever printed on a glass substrate and overlayed with an SU8 waveguide. Top excitation and sideways collection of the PL response is one of the aims of the project. b) FDTD simulations with cross sections through the simulation region at $\lambda = 650\,\text{nm}$ wavelength assuming 500 nm edge length for a 3 μm long diamond cantilever with isoscele trianglur cross section incorporated into a 1.8x2.0 μm^2 high and wide SU8 waveguide on a standard SiO_2 substrate. A single dipole emitter is placed close to the tip of the diamond cantilever to mimick NV center emission. The left plot shows the full simulation region in side view, while the two right plots correspond to the two end facets of the waveguide, indicating lossy multimode coupling. c) (left) Zoom into the cross section shown on the left in b), (right) transmission and Purcell factor extracted from the waveguide end facet monitors and the dipole respectively, showing a total coupling efficiency around 16 % (adding both sides).

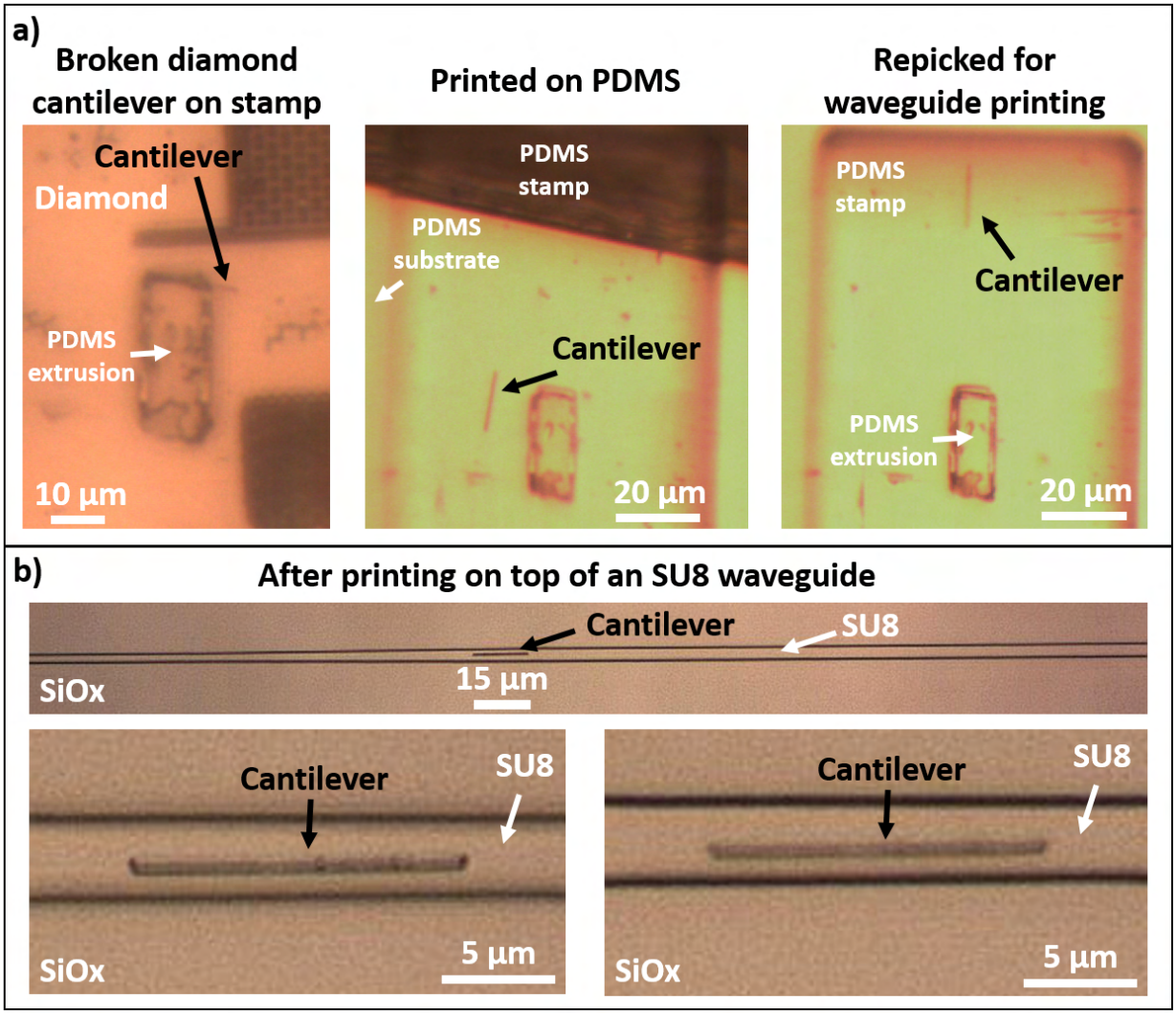

Figure H.30: Test print of a diamond cantilever device from the same sample as the device shown Fig. H.28 a). a) A PDMS stamp with a 10x40 μm additional extrusion is brought into contact with a suspended cantilever and breaks it by applying a shearing force (lateral stage movement). The diamond cantilever is then printed on an intermediate PDMS substrate for realignment and finally repicked with the desired orientation, b) then the cantilever is released on top of a SU8 waveguide on a borosilicate glass cover slip. Courtisy to Dimitars Jevtics who performed this printing.

H.8.3 Identification of single photon emitters in nanodiamonds for integration via transfer printing

As part of the Fraunhofer QDOS project we also look into the identification of nanodiamonds that contain single NV centres for transfer print based integration with photonic circuitry. Fig. H.31 contains some initial results with dense and sparse nanodiamond spreading on Si substrates.

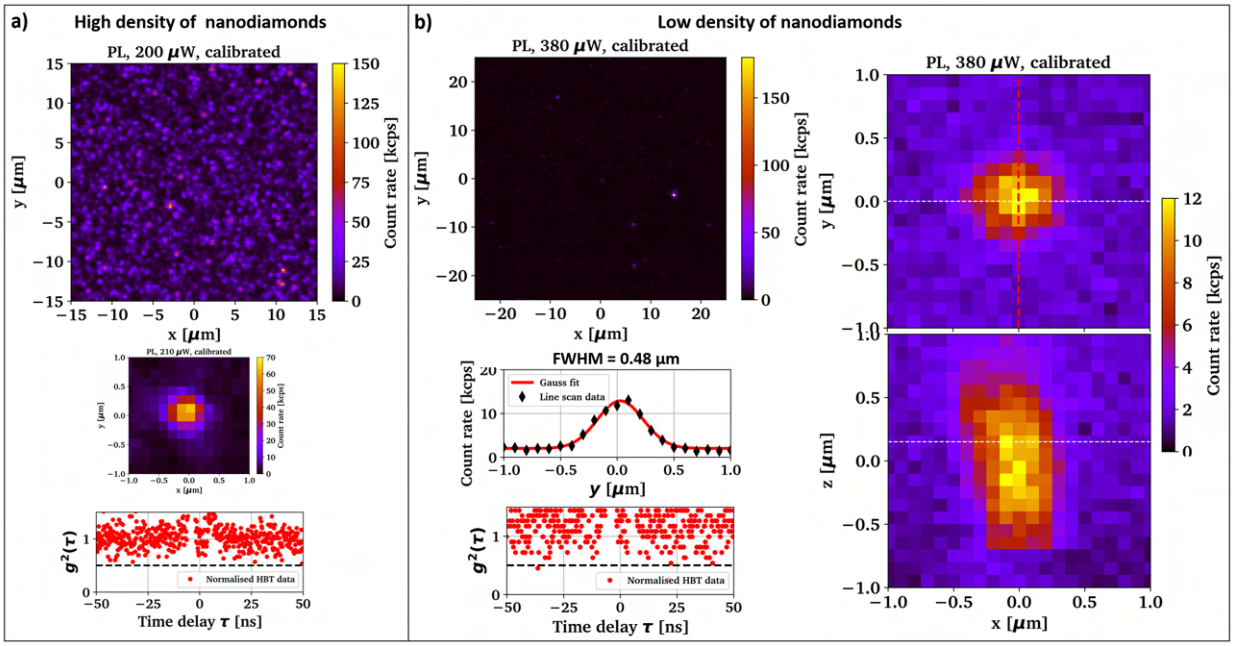

Figure H.31: Large scale preselection of commercially available nanodiamonds with single NV centres for transfer print based integration. a) High density of nanodiamonds in a PVA thin film on Si substrate, including large and small scale PL maps and the corresponding autocorrelation statistic for the emitter cluster shown above, b) Small density of nanodiamonds spun from aqueos solution on a Si substrate, with a large PL overview scan in the top left, two small scale PL maps of a single emitter candidate on the right hand side (white dotted lines indicate the shared plane between the scans), line scan following the red dotted line in the top right scan and the corresponding autocorrelation measurement on this emitter cluster showing no anti-bunching. PL maps and HBT measurements are taken with 100x, 25 μm pinhole (only the top left scan in a) used a 40 μm pinhole), 2x 550 nm LP, 1x 650 nm LP.

I Shallow NV emitter: Addtional information on failed samples

In the following we present some additionally measured photoluminescence and AFM data taken on the three samples we received from IAF, targeting the growth of NV clusters at controlled shallow distance below the diamond surface. Fig. I.2 to I.4 contain data not shown before, illustrating how high surface roughness might still allow transfer printing based integration but seems to frustrate enhancement of light emission. The high roughness and nano-lens like features on sample #1 might actually contribute to the high count rate measured on this sample. Fig. I.1 and I.5 are already shown in the main text and added here for reference.

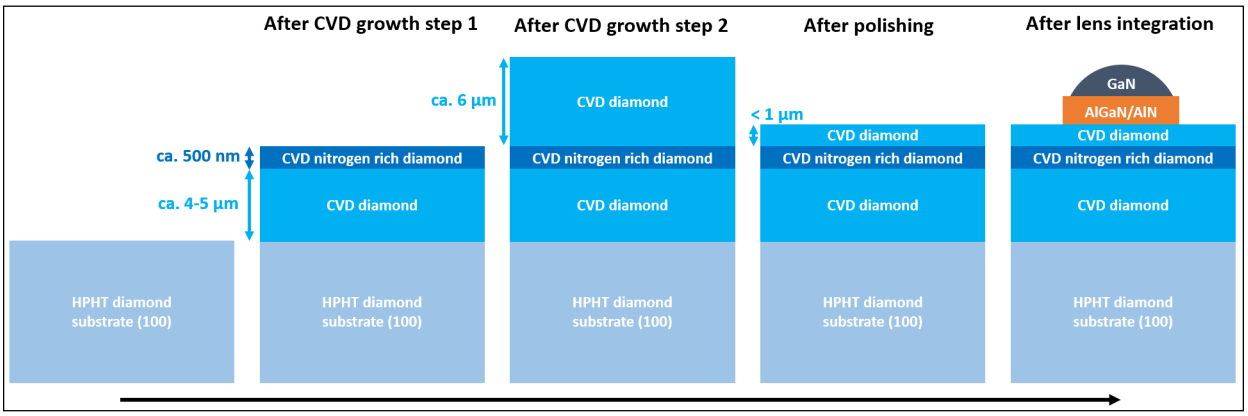

Figure I.1: Chemical vapour deposition based growth process (Fraunhofer IAF) including a 500 nm thin delta doped layer with NV^- centers (ca. 30 ppb) forming from nitrogen impurities (ca. 10 ppm). Overgrowth of the nitrogen rich layer with successive Scaife polishing was used to achieve vertical position control and a smooth surface finish.

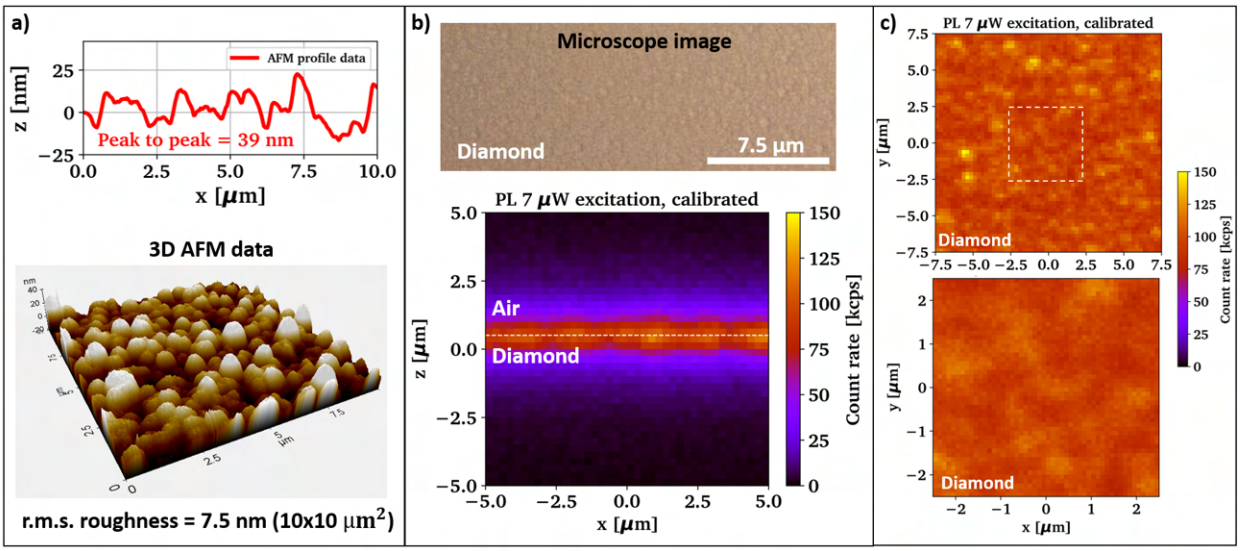

Figure I.2: Sample #1: Failed Scaife polishing but bright emission from the surface layer (after piranha acid clean). a) AFM line scan and 3D presentation of the surface roughness (SSS-NCH) taken close to the sample center, b) microscope image of the surface and PL xz scan, c) xy PL maps in the bright surface layer on two different scales. PL maps are linearised and taken with 100x objective, 40 μm pinhole, 2x 550 nm LP, 1x 650 nm LP.

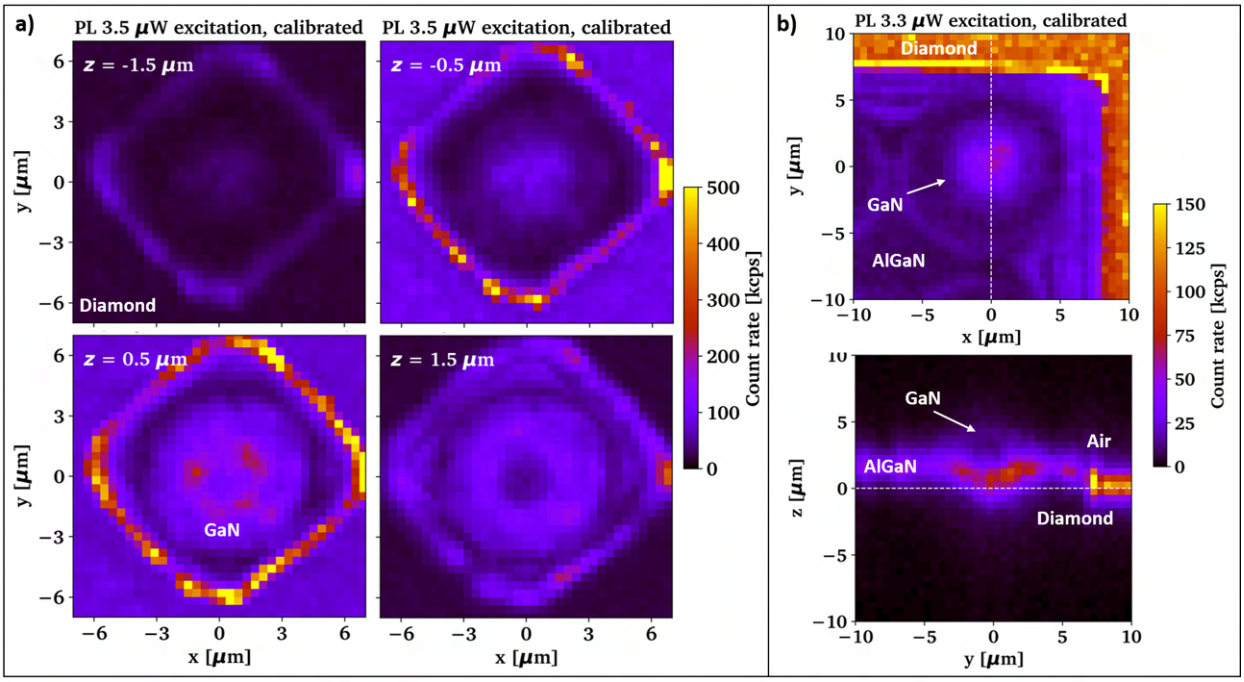

Figure I.3: Sample #1: Photoluminescence maps after transfer printing a) the single GaN micro-lens shown in Fig. 4.5 a) with 4 xy scans at different depth but same xy position, b) a GaN micro-lens array similar to what is shown in Fig. 4.5 b). The white dotted lines indicate the shared planes between the scans. PL maps are linearised and taken with 100x objective, 40 μm pinhole, 2x 550 nm LP, 1x 650 nm LP.

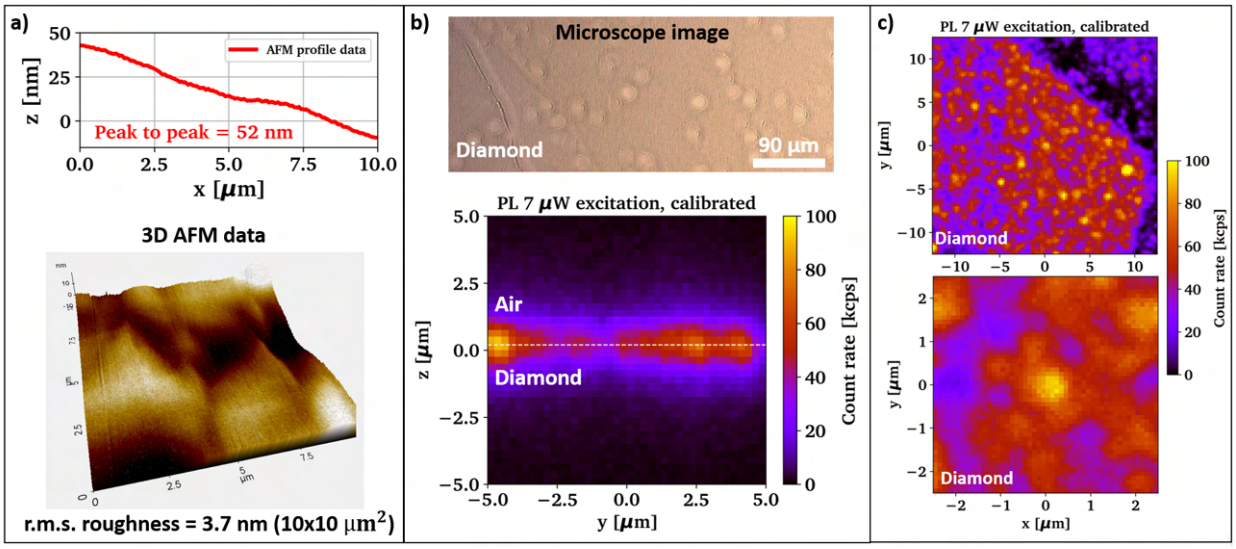

Figure I.4: Sample #2: Neither overgrowth nor polishing applied to this sample, so the bare nitrogen rich layer lays at the top of the substrate (after piranha acid clean). a) AFM line scan and 3D presentation of the surface roughness (SSS-NCH) taken close to the sample centre, b) microscope image of the surface and PL xz scan, c) xy PL maps in the bright surface layer on two different scales. PL maps are linearised and taken with 100x objective, 40 μm pinhole, 2x 550 nm LP, 1x 650 nm LP.

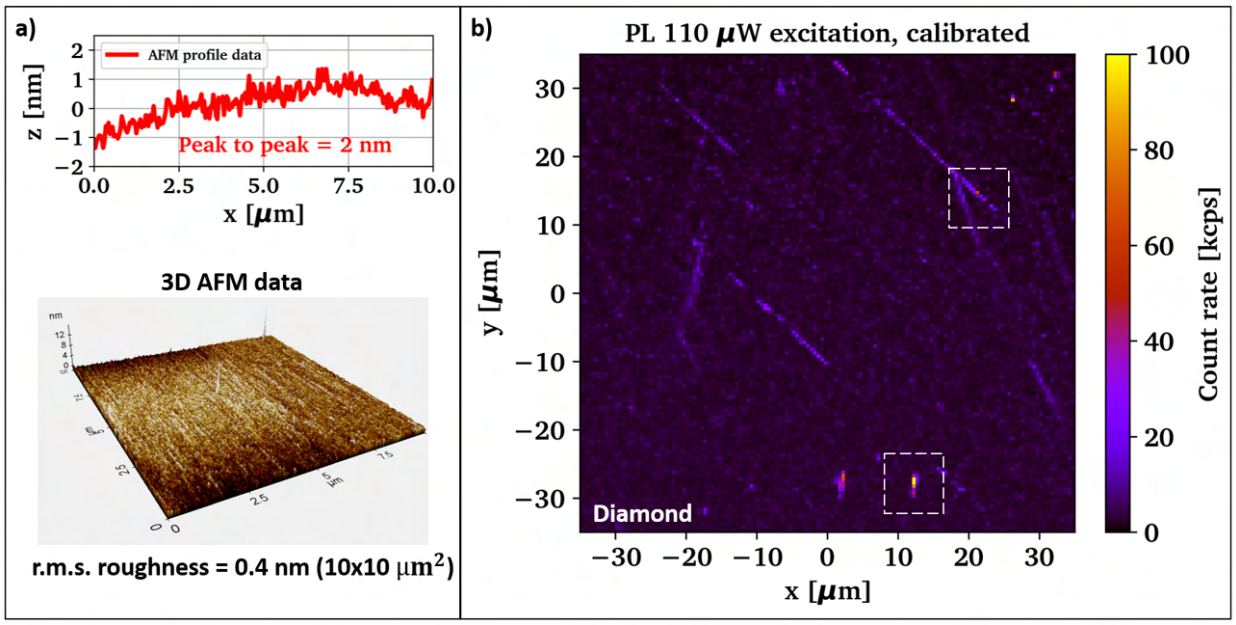

Figure I.5: Sample #3: Successfully polished surface, but the nitrogen rich layer seems to have been removed to a large extent (after piranha acid clean). a) AFM line scan and 3D presentation of the surface roughness (SSS-NCH) taken close to the sample centre, b) xy PL map in the surface layer with two interesting emitter formations marked (100x objective, 40 μm pinhole, 2x 550 nm LP, 1x 650 nm LP). The scan origin matches the origin of the whole sample, using the corners of the diamond as alignment markers. The following transfer print process was based on the here retrieved emitter positions (1st round of printing).